

❖ *By Scientific Research the Country will Develop and Flourish* ❖

Republic of Iraq
Ministry of Higher Education and Scientific Research
University of Technology
Control and Systems Engineering Department



Full Papers Conference Proceeding

January 30-31, 2011

**The Engineering Conference of
Control, Computers and Mechatronics
(ECCCM 2011)**

January 30-31, 2011

**Full Papers Conference
Proceeding**

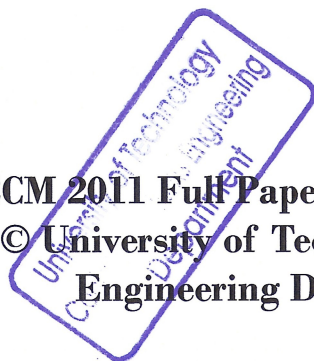
Organized by:

**Control and Systems Engineering Department
University of Technology
Baghdad-Iraq**

**Address: Al-Sina'a St. 52, P. O. Box 18310
Website: <http://www.uotechnology.edu.iq>
E-mail: conf_cse_uot@yahoo.com**

WELCOME

ECCCM 2011 Full Papers Conference Proceeding
Copyright © University of Technology - Control and Systems
Engineering Department, 2011



Contents

Contents	I
-----------------------	---

About the Conference:

Conference Topics	V
Conference Supervising Committee	V
Scientific Committee	V
Organizing Committee	V
Secretary of the Organizing Committee	VI
Control and Systems Engineering Department in brief	VI

Topic 1 - Automatic Control and Its Applications:

Positively Invariant Sets in Sliding Mode Control Theory with Application to Servo Actuator System with Friction	2
Generalized PID Controller Based on Particle Swarm Optimization	14
Tuning of PID Controller Based on Foraging Strategy for Pneumatic Position Control System	22
Tuning Model Reference Adaptive Controller for AVR of Synchronous Generator	34
Transient Voltage Stability Enhancement Using Fuzzy Logic Controller Techniques	42
Sensorless Fuzzy Logic-Based Speed Control of Permanent Magnet Stepper Motor	51
Integrated PID Like Adaptive Fuzzy Neural Network for Nonlinear System Control	60
Design of ON-Line Tuned Idle Speed Controller for an Automotive Engine	65
Optimal Controller Design for Dynamic Systems with Perturbed Time-Varying Delay ...	75
Limitation & optimization of governor speed regulation factor of power system Station	82

Topic 2 - Robots and their Applications:

Human Arm Simulation Based on Matlab with Virtual Environment	90
Measurement of Human Leg Joint Angle through Motion Based on Electromyography (EMG) Signal	100
The Use of Virtual Reality to Demonstrate Trajectory planning and Control of a 3-DOF Underactuated Robot in a Horizontal Plane in Real-Time	110
Design and Simulation of Fuzzy Like PD Controller for Autonomous Mobile Robot	121

Topic 3 - Modeling and Measurements:

Texture Identification by Using Neuro-Wavelet Technique.....	129
Performance Comparison of Two Neural Network Identifiers for Space Vector Modulation	134
Multiwavelet Transform and Multi-Dimension-Two Activation Function Wavelet Network Using for Person Identification.....	145
Modeling and Design of a Suboptimal Controller for a Hydraulic System.....	160
Simulation of Boiler Drum Wall Temperature Differential and its Estimation	171
Developing a 3-D Mathematical Model for Network Topology Based on Graph Theory.....	182
A Simulation Model for Irrigation Scheduling to Maize Crop in Mosul Area	188

Topic 4 - Computer Networks:

Indoor Propagation Modeling for Wireless Local Area Network (WLAN).....	198
Fuzzy-Genetic Controller for Congestion Avoidance in Computer Networks.....	206
Design of a Telemedicine Network for Iraq	213
Web Based Multithreading System.....	224
Remote User Authentication Scheme Using Hiding Information in Image Based on LSB Steganography	230
Computing Nodes and Links Appearances on Geodesics in Network Topologies Using Graph Theory.....	235
RSA Security Enhancement	241

Topic 5 - Computer Software in Engineering Applications:

Proposed Design and Implementation of a Schematic FPGA-Based Binary Arithmetic Multiplier	247
Proposal of Creating Entity-Relationship Table from English Sentences Groups	254
Conversion of English Characters into Braille Using Neural network	263
Hardware Implementation of ANN Trained by GA and PSO Based on FPGA.....	270
Modified Method of Information Hiding Based on Hybrid Encryption and Steganography.....	279
Key Extended-Base DES Algorithm.....	291
Rule Induction Technique for Fingerprint Identification.....	298

Topic 6 - Communications, Sensors and Signal Processing in Modern Control Systems:

Multispectral Fusion for Synthetic Aperture Radar (SAR) Image Based Framelet Transform	305
Low Density Parity Check (LDPC) Codes for Proposed Slantlet Transform OFDM System in a Rayleigh Fading Channels With Perfect and Pilot Channel Estimation for M_ARY PSK Modulation	317
Modeling and Simulation of Intelligent Traffic Light.....	330
Self Heating Calculation and Resistance Measurement Circuit Design of Mezzo-Structure Resistance Temperature Detector (μ SRTD) Sensor	338
Author Index	346

ECCCM 2011

About the Conference

Conference Topics:

1. Automatic Control and its applications.
2. Robots and their applications.
3. Modeling and measurements.
4. Computer Networks.
5. Computer Software in engineering applications.
6. Communications, signal processing and sensors in modern control systems.

Conference Supervising Committee:

Prof. Dr. Kahtan K. M. Al-Khazraji (Chair)
President of University of Technology-Iraq
Prof. Dr. Waladin Khairi Sa'id
Head of Control and Systems Eng. Dept., University of Technology-Iraq
Prof. Dr. Saleh M. Al-Qaraawi
Deputy Head of Department for Scientific Affairs and Postgraduate Studies-Iraq
Dr. Farazdak Rafeek Yasein
Head of Control Engineering Branch-Iraq

Scientific Committee:

Prof. Dr. Waleed Ameen Mahmoud Al-Jawher (Chair)
University of Baghdad-Iraq
Prof. Dr. Rami Abd Al-Kader Maher
Al-Isra Private University-Jordan
Prof. Maher Khader Al-Azzawi
Al-Mustansiriya University-Iraq
Prof. Dr. Adel Hameed Al-Shamari
University of Technology-Iraq
Prof. Dr. Saleh M. Al-Qaraawi
University of Technology-Iraq
Prof. Dr. Mohammed Zaki Al-Faiz
Al-Nahrain University-Iraq
Assist. Prof. Dr. Mohamed Yousif Hassan
University of Technology-Iraq
Dr. Shibly Ahmed Al-Samarraie
University of Technology-Iraq
Dr. Firas Abdulrazzaq
University of Technology-Iraq

Organizing Committee:

Prof. Dr. Waladin Khairi Sa'id (Chair)
Dr. Siba M. Sharef
Assist. Prof. Dr. Arif Abdualrahman
Assist. Prof. Dr. Azad Raheem Kareem
Dr. Farazdak Rafeek Yasein
Dr. Mohamed Jasem Mohamed
Mr. Abdul Mohsin M. Al-Timimi
Mrs. Arij Alaa Hassan
Miss Noor Ayad Yousif

Secretary of the Organizing Committee:

Mr. Waleed Fawwaz Shareef
Mahmood Jehad Ali

Mr. Ali Majeed Mahmood
Amjad Falih Hassan

Control and Systems Engineering Department in brief

Foundation:

The department of Control Systems Engineering was established in 1975, the year of the establishment of the University of Technology. It was then the first one of its kind in Iraq as well as in the Middle East region. The goal of the department is to introduce advanced control technology to advance the industry in Iraq. The department is concerned with the study of various engineering systems that involve electrical, mechanical, hydraulic, and pneumatic components. Typical application fields are steel mills, automobile industries, refineries, computer control, robotics, automation...etc.

Aims:

The department aims are to:-

- (1) Prepare engineering graduates fully equipped with the fundamentals of modern technology in Control and Systems Engineering to meet the requirements of the Iraqi industry.
- (2) Deal with scientific research projects in Control and Systems Engineering.
- (3) Give full technical consultancy to the industrial sector.
- (4) Provide continuing education programs in the field of Control and Systems Engineering.

Main branches:

Currently the department has three branches:

- a. Control Engineering Branch.
- b. Computer Engineering Branch.
- c. Mechatronics Engineering Branch.

Students are streamed to one of the above specializations starting from the Third Year.

Undergraduate studies:

Due to the large request for admission to the department, and limited resources, the department has adopted a policy to accept only the highly qualified students. The number of students admitted and graduated over the years (1977-2010) is: **3020**; (control and systems Engineering 1589, control Engineering 600, Computer Engineering 652 and Mechatronics Engineering 179). Evening classes began in the academic year (1997-1998). The number of students graduated over the years (1997-2010) is **521**; (Control Engineering 254, Computer Engineering 240 and Mechatronics Engineering 27).

Postgraduate studies:

Postgraduate studies began in 1976 to provide highly qualified specialists. The department offers the following postgraduate studies:

1. M.Sc. in Control Engineering.
2. M.Sc. in Computer Engineering.
3. M.Sc. in Mechatronics Engineering.
4. Ph.D. in Control Engineering.
5. Ph.D. in Computer Engineering.
6. Ph.D. in Mechatronics Engineering.

The number of students admitted and graduated over the years (1976-2010) is: Higher Diploma **65** (Applied computers 65); Master **249** (Measurements and Control Engineering 81, Electronic Computers Engineering 58, Control Engineering 25, Computer Engineering 38 and Mechatronics Engineering 47); Doctorate **23** (Control and Computers Engineering 4, Control Engineering 5, Computer Engineering 11 and Mechatronics Engineering 3). The admission to postgraduate studies requires that the applicants must have a B.Sc. degree either in Control Systems Engineering, Computer Engineering or Mechatronics Engineering. The applicant's average grade should not be less than 65% or at least he should be within the top quarter of graduates in his department.

Research interests:

The scientific research in the department is concerned with all branches of Control Engineering, robotics, mechatronics and process control using advanced computer systems and techniques. There is a particular interest in research areas concerned with Computer Engineering, neural networks, artificial intelligence, expert systems and fuzzy logic applications.

The following are typical research activities:

- Stability and control characteristics of microprocessor controlled brushless machine for servo drive.
- Synchro digitizer.
- A PC-based CNC machine controller.
- Kalman estimator design for the boiler drums temperature differentials during start up.
- Static state estimation and neural network application to the continuous monitoring of charge temperature in induction furnaces.
- Estimation of immeasurable molten metal temperature in induction furnaces by Kalman filtering estimation technique.
- Enhancement of boiler drum water level sensor for Al-Mussaib thermal power station.
- Neural network application to drum water level sensing of steam boilers.
- PID controller with on-line Neuro-Tuner for a pressure process.
- PID controller with on-line Fuzzy-Tuner for a pressure process.
- Gear flexibility effect on the dynamic response of spur gears system.
- Gear flexibility effect on the dynamic load factor.

- On-line collision-free motions for kinematically redundant manipulators in constrained configuration space.
- Development of high performance parallel computers system based on LAN.
- Design and implementation of reliable wireless network.
- Simulation of autopilot design using variable structure systems.
- Real time kernel for process control.
- Implementation of a telemetry protocol for packed switch satellite service.
- Increase the GPS performance accuracy and its military applications.

Laboratories:

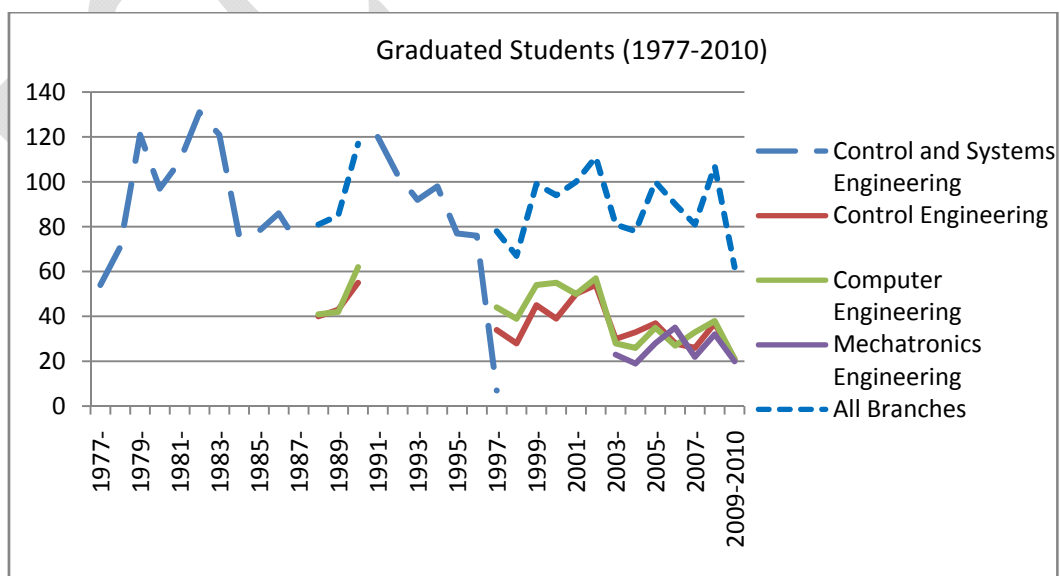
There are many specialized laboratories in the department to support the teaching and training of the students. The labs prepare students to deal effectively and efficiently with practical engineering aspects. Each laboratory can accommodate up to 20 students at one time. These laboratories include: Digital Techniques, Personal Computer, Control, Computer Control, Process Control, Components, Electronics, Electrical, Mechatronics, Research, Communication, Computer Networks and Microprocessor Labs.

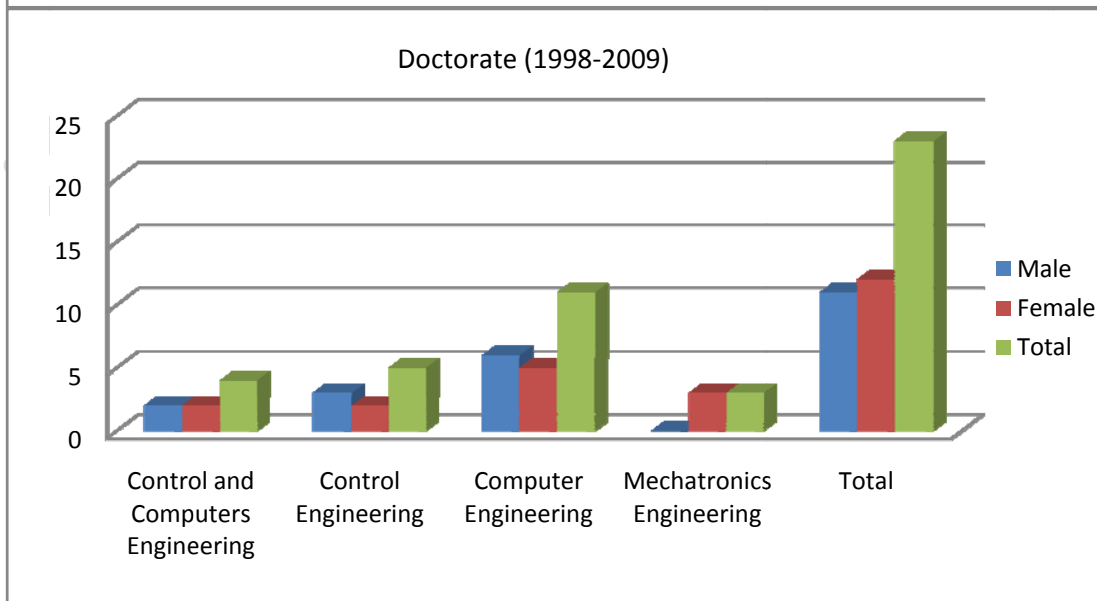
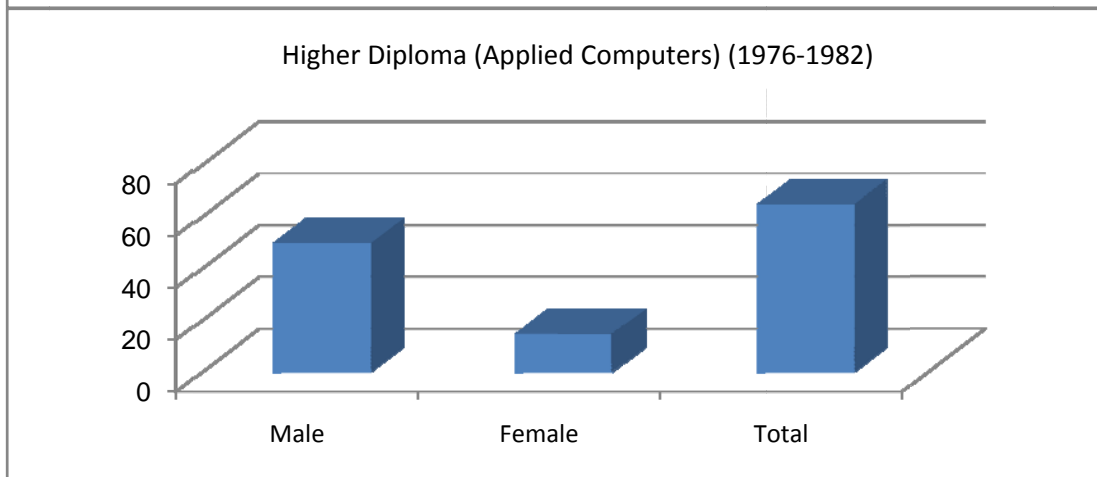
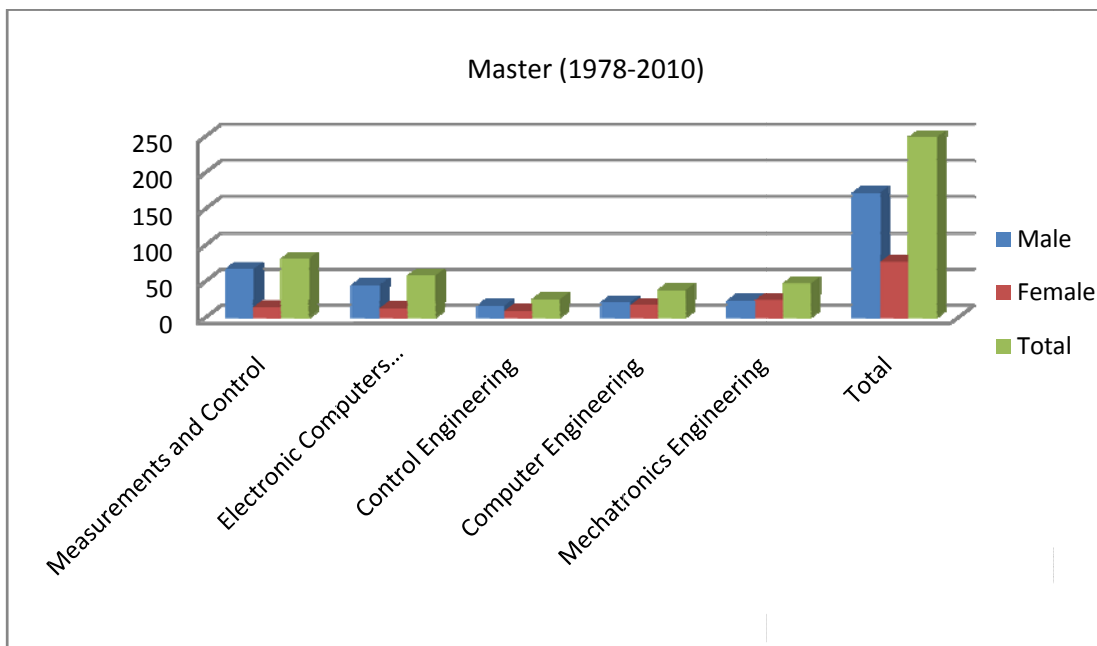
Relationship with industry:

The department has a good relationship with industrial establishments to carry out scientific research projects, consultations, teaching and joint-supervision of postgraduate students, especially in oil refineries, Electricity Board and heavy industries.

Scientific conferences:

The department encourages its staff to participate in scientific seminars and conferences held inside the country and abroad. The department has organized seminars and conferences, the last of which was held in the academic year (2000-2001).





[THIS PAGE IS INTENTIONALLY LEFT BLANK]

ECCCM 2011

Topic 1

Automatic Control and its Applications

Paper Reference: ECCCM 10/16

POSITIVELY INVARIANT SETS IN SLIDING MODE CONTROL THEORY WITH APPLICATION TO SERVO ACTUATOR SYSTEM WITH FRICTION

Dr. Shibly Ahmed Al-Samarraie

Control and Systems Engineering Department
University of Technology
dr.shiblyahmed@yahoo.com

Abstract

In this paper two invariant sets are derived for a second order nonlinear affine system uses a sliding mode controller. If the state started in these sets it will not leave it for all future time. The invariant set is found to be function to the initial condition only, from which the state bound is estimated and used when determining the gain of the sliding mode controller. This step overcomes an arithmetic difficulty that consists of calculating suitable controller gain value that insures the attractiveness of the switching manifold. Also, by using a differentiable form for the approximate signum function in sliding mode controller formula, the state will converge to a positively invariant set rather than the origin. The size of this set is found to be function to the parameters that can be chosen by the designer, thus, it enables us to control the size of the steady state error. The sliding mode controller is designed to the servo actuator system with friction where the derived invariant sets are used in the calculation of the sliding mode controller gain. The friction model is represented by the major friction components; Coulomb friction, the Stiction friction, and the viscous friction. The simulation results demonstrate the rightness of the derived sets and the ability of the differentiable sliding mode controller to attenuate the friction effect and regulate the state to the positively invariant set with a prescribed steady state error.

Keywords: *Positively Invariant Set, Sliding Mode Control, Servo Actuator System, Friction Model.*

1-Introduction

In this paper we are interested mainly to answer the following: *Consider the second order affine system with sliding mode controller*

$\dot{x} = f(x) + g(x) * (-k * \text{sgn}(s)), s = s(x)$
Then, for a certain controller gain value k , what is the area around the origin such that if the state initiated inside this region, it will not leave it and the origin is an attractive point. This area is known as the area of attraction.

The area of attraction forms the so called the positively invariant set. The set notion appears in control theory when we considered three aspects, which are crucial in control systems design, these are: constraints, uncertainties, and design specifications [1]. For the sliding mode controller

$$u = -k * \text{sgn}(s), k > 0$$

the main design step is the calculation of an appropriate value for the controller gain k . This point is important since a large gain value may lead to the chattering problem. So a better estimate to gain value, may help in reducing the amplitude of the chattering behavior (the chattering behavior is frequently appears in sliding mode control system for many reasons such as the non ideality of the switching process [2]). In fact, this work is an issue in this direction. Furthermore, many methods are used to eliminate the chattering in sliding mode control system (see [2]&[3]), but the simplest

method is introduced by Sloten J. J. [4], where the segnum function is replaced by a saturation function. This approximate sliding mode controller introduces a positively invariant set around the origin and its size determined by the design parameters [5]. Khalil H.K. [5], derives the invariant set formed by the sliding mode controller that uses the saturation function as suggested by Sloten. The saturation function is a continuous but not differentiable function; and for this reason we are interested in replacing the segnum function by a continuous and differentiable function, and then derive the positively invariant set formed by the approximate sliding mode controller.

In recent application of control theory, many dynamical systems modeled as interconnected systems where the state of the upper system is unaffected by the actual controller [6]. For this system type a virtual controller is used to control the upper system if the system be in a certain form to enable the application of the so called the Backstepping approach. So, the presence of the disturbances in the upper system will lead to the non-matching property for the control system. The situation becomes more complicated if the disturbances are nonsmooth. This situation makes us use the arc tan function (the continuous and differentiable function), which may be used as a virtual controller for the interconnected system, and derive for it the positively invariant set. The servo actuator system is one of the interconnected system models, where the torque that actuates the mechanical system is not the actual input (for a D.C. motor the voltage is the actual servo actuator system input). Therefore, we select this system to design the sliding mode controller with the aid of the derived positively invariant sets.

2-Invariant Set

The terminologies of the invariant and positively invariant set are defined in this

section, where we refer mainly to the excellent reference [5]. So, consider the second order autonomous system

$$\dot{x} = f(x) \quad (1)$$

Where $x \in \mathcal{R}^2$ and $f(x)$ is a locally Lipschitz map from a domain $D \subset \mathcal{R}^2$ into \mathcal{R}^2 . Let $x(t)$ be a solution to the second order autonomous system in equation (1) and also let $x = 0$ be an equilibrium point; that is $f(0) = 0$. Now, the set M , with respect to the system in equation (1), is said to be invariant set if

$$x(0) \in M \Rightarrow x(t) \in M, \quad \forall t \in \mathcal{R}$$

It means that: if $x(t)$ belongs to M at some time instant, then it belongs to M for all future and past time, i.e., it will never come from a region outside it or leave it for all future time. A set M is said to be a positively invariant set if

$$x(0) \in M \Rightarrow x(t) \in M, \quad \forall t \geq 0$$

In this case the state may be come from outside the positively invariant set but will never leave for all future time. We also say that $x(t)$ approaches a set M as t approaches infinity, if for each $\varepsilon > 0$ there is $T > 0$ such that

$$\text{dist}(x(t), M) < \varepsilon, \quad \forall t > T$$

where $\text{dist}(x(t), M)$ denotes the distance from a point $x(t)$ to a set M . The positive limit point is defined as the limit for the solution $x(t)$ when the time approaches infinity. The set of all positive limit points of $x(t)$ is called the positive limit set of $x(t)$. Accordingly, the asymptotically stable equilibrium is the positive limit set of every solution starting sufficiently near the equilibrium point, while the stable limit cycle is the positive limit set of every solution starting sufficiently near the limit cycle. The solution approaches the limit cycle as $t \rightarrow \infty$. The equilibrium point and the limit cycle are invariant sets, since any solution starting in either set remains in the set for all $t \in \mathcal{R}$. Moreover, let the set of positively limit set for a point p denoted by the ω limit set of p ,

namely $\omega(p)$, then some properties of it are stated in the following fact [7]:

Let M be a compact, positively invariant set and $p \in M$, then $\omega(p)$ satisfies the following properties:

1. $\omega(p) \neq \emptyset$, that is, the ω limit set of a point is not empty.
2. $\omega(p)$ is closed.
3. $\omega(p)$ is a positively invariant set.
4. $\omega(p)$ is connected.

This fact, in later sections, will be helpful in determining the behavior of the state trajectory when it is initiated in a positively invariant set.

3-The First Positively Invariant Set

In the following analysis, the first invariant set for a second order system that use a sliding mode controller is estimated. Consider the following second order affine system

$$\begin{aligned} \dot{x}_1 &= x_2 \\ \dot{x}_2 &= f(x) + g(x)u, \quad g(x) > 0 \end{aligned} \quad (2)$$

Let the controller in equation (2) is the sliding mode controller

$$u = -k \operatorname{sgn}(s), \quad s = x_2 + \lambda x_1, \quad \lambda > 0 \quad (3)$$

Where s is the switching function which it is selected such that the system at the switching manifold ($s = 0$) is asymptotically stable. The main idea behind the selection of the sliding mode controller gain k is that the switching manifold will be attractive. To do that we use the following nonsmooth Lyapunov function

$$V = |s| \quad (4)$$

The switching manifold is guaranteed to be attractiveness if the derivative of the Lyapunov function is negative. Consequently,

$$\begin{aligned} \dot{V} &= \dot{s} * \operatorname{sgn}(s) \\ &= [f(x) - g(x)k * \operatorname{sgn}(s) + \lambda x_2] \operatorname{sgn}(s) \\ &= -[g(x)k - (f(x) + \lambda x_2) * \operatorname{sgn}(s)] \end{aligned} \quad (5)$$

Now if k is chosen such that $\dot{V} < 0$, then the switching manifold is attractive. Thus,

$$k > \max \left| \frac{f(x) + \lambda x_2}{g(x)} \right| = h \quad (6)$$

If k satisfy the inequality (6), then $\dot{V} = 0$ is asymptotically stable. In fact satisfying inequality (6) is the main calculation problem during design process. Formally, we may use a large gain value to ensure satisfying (6), and consequently the area of attraction becomes large. But the gain cannot be chosen freely without limit due to the control saturation. Accordingly, the gain value determined directly the area of attraction size. In this work, we aim to find the invariant set for a second order system that use the sliding mode controller as given in (3), such that when the state initiated in it will never leave for all future time. Hence, the gain is calculated depending on the invariant set size and the region of attraction will include at least the invariant set. In literature, the existence of the invariant set is assumed (by assign the maximum state value) and accordingly the sliding mode controller gain is calculated. In this case the sliding controller will be able to force the state toward the switching manifold at least when it initiated in this invariant set. However, the gain value may be large and again the saturation problem arises. Other designer, uses a certain gain value in the design of sliding controller and, may be, by doing extensive simulations they prove that the area of attraction will include the nominal initial conditions for a certain application [8].

To find the invariant set, we need to derive its bounds. The first bound on the invariant set is derived by using the Lyapunov function given in equation (4). Suppose that we use a certain value for the gain k , and then there is a certain basin of attraction such that the time rate of change of the Lyapunov function is less than zero, namely

$$\dot{V} < 0 \Rightarrow V(t) - V(t_0) < 0$$

or

$$|s(t)| - |s(t_0)| < 0$$

Therefore the switching function level is bounded by:

$$\therefore |s(t)| < |s(t_0)|, \forall t > t_0 \quad (7)$$

Of course the inequality (7) hold due to the action of the sliding mode controller with gain k . However, the inequality (7) shows that the state will lie in a region bounded by

$$-s(t_0) < s(t) < s(t_0), \forall t > t_0$$

but without assign the equilibrium point with respect to the switching function. So we need to show that, as it is known, that the switching manifold is an asymptotically equilibrium manifold due to the sliding mode controller. To prove the stability of $s = 0$, the time derivative of the switching function is found first when k satisfy inequality (6), as follows:

$$\begin{aligned} \dot{s} &= \dot{x}_2 + \lambda \dot{x}_1 = f(x) - g(x)k \operatorname{sgn}(s) + \lambda x_2 \\ \Rightarrow \dot{s} &= -\beta(x) \operatorname{sgn}(s), \quad 0 \leq \beta(x) \end{aligned}$$

Now, we return to the Lyapunov function, equation (4), to find its derivative as:

$$\begin{aligned} \dot{V}(s) &= \dot{s} * \operatorname{sgn}(s) \\ \Rightarrow \dot{V}(s) &= -\beta(x) < 0 \end{aligned}$$

Since $V(0) = 0$ and $\dot{V}(s) < 0$ in the set $\{x \in \mathcal{R}^2: s \neq 0\}$, then $s = 0$ is asymptotically stable (theorem 4-1 in reference [5]). Moreover, we must note that the solution of the dynamical system in (7) at the switching manifold does not exist [9]. This is due to the discontinuity in sliding mode controller formula. Ideally the state will slide along the switching manifold to the origin, i.e., the state trajectory will identify the switching manifold until it reaches the origin. Therefore, the bound given in the inequality (7) becomes:

$$\begin{aligned} 0 &\leq |s(t)| < |s(t_0)| \\ \Rightarrow 0 &\leq s(t) * \operatorname{sgn}(s) < s(t_0) * \operatorname{sgn}(s_0) \end{aligned}$$

But in sliding mode control $\operatorname{sgn}(s) = \operatorname{sgn}(s_0), \forall t > t_0$, thus,

$$0 \leq s(t) * \operatorname{sgn}(s) < s(t_0) * \operatorname{sgn}(s) \quad (8)$$

Accordingly we have

$$\begin{aligned} 0 &\leq s(t) < s(t_0) \text{ for } s > 0 \\ 0 &\geq s(t) > s(t_0) \text{ for } s < 0 \end{aligned} \quad (9)$$

In words, inequality (9) shows that if the state initiated in the positive side of the switching manifold, then the state will stay in an open region bounded by $s = s(t_0)$ and $s = 0 \forall t > t_0$. The same thing is happened if the state initiated with negative switching function level. Inequality (9) is the first bound; the second is derived here for x_1 as follows:

$$\begin{aligned} \dot{x}_1 + \lambda x_1 &= s(t) \\ \Rightarrow d\{e^{\lambda t} x_1(t)\} &= e^{\lambda t} s(t) dt \end{aligned}$$

or

$$e^{\lambda t} x_1(t) - x_1(t_0) = \int_{t_0}^t s(\tau) e^{\lambda \tau} d\tau$$

By taking the absolute for both sides and considering the inequality (7), we obtain

$$\begin{aligned} |e^{\lambda t} x_1(t)| - |e^{\lambda t_0} x_1(t_0)| &\leq |e^{\lambda t} x_1(t) - e^{\lambda t_0} x_1(t_0)| \\ &= \left| \int_{t_0}^t s(\tau) e^{\lambda \tau} d\tau \right| \leq \int_{t_0}^t |s(\tau)| e^{\lambda \tau} d\tau \\ &\leq |s(t_0)| \int_{t_0}^t e^{\lambda \tau} d\tau = \frac{|s(t_0)|}{\lambda} (e^{\lambda t} - e^{\lambda t_0}) \\ &\Rightarrow |e^{\lambda t} x_1(t)| \leq |e^{\lambda t_0} x_1(t_0)| + \frac{|s(t_0)|}{\lambda} (e^{\lambda t} - e^{\lambda t_0}) \\ \Rightarrow |x_1(t)| &\leq |x_1(t_0)| e^{-\lambda(t-t_0)} + \frac{|s(t_0)|}{\lambda} (1 - e^{-\lambda(t-t_0)}) \\ \therefore |x_1(t)| &\leq \max \left\{ |x_1(t_0)|, \frac{|s(t_0)|}{\lambda} \right\} \quad (10) \end{aligned}$$

The result in the inequality (10) is a consequence of the convexity of the set

$$\Psi = \left\{ x_1(t): x_1(t) = \mu|x_1(t_o)| + (1 - \mu) \frac{|s(t_o)|}{\lambda}, 0 \leq \mu \leq 1 \right\}$$

In this case the maximum element of the set is at $\mu = 0$ or at $\mu = 1$. Therefore the invariant set is bounded by the inequalities (9) and (10) in terms of the initial condition only and hence, the invariant set is given by:

$$\Theta = \left\{ x \in \mathcal{R}^2: 0 \leq s(t)sgn(s) < s(t_o)sgn(s), |x_1(t)| \leq \max \left(|x_1(t_o)|, \frac{|s(t_o)|}{\lambda} \right) \right\} \quad (11)$$

The figure below plot the invariant set in the phase plane and one can find geometrically that the bound for $x_2(t)$ inside Ψ is

$$|x_2(t)| \leq \max\{|x_2(t_o)|, |s(t_o)|\} \quad (12)$$

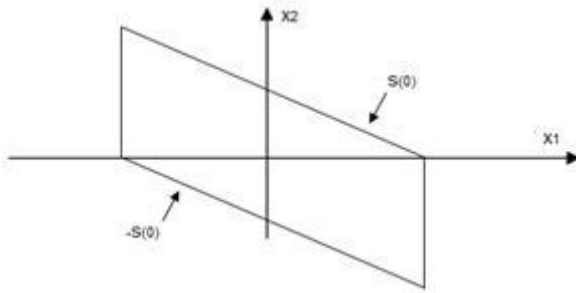


Figure (1): Positively Invariant Set.

4-The Second Positively Invariant Set

In classical sliding mode control theory, there exist a trivial invariant set. This set is the origin of the state space where the controller regulates the state to it and kept make the state there for all future time. The sliding mode control that does the above task is a discontinuous control and it may lead to the chattering problem. Many solutions to the chattering problem are exist in the literatures (see references [2], [3] and [10]). A simplest method to remove chattering is by replacing the segnum function, which it used in sliding mode controller, by an approximate form. This idea is first introduced by J.J. Sloten in [4] by using the saturation function instead of

the signum function. Later, many other approximate segnum functions are used to remove chattering as found in reference [11]. However, when replacing the signum function the state will not be regulated to the origin, instead it will regulated to a certain set around the origin known as the positively invariant set. The size of this set is determined by the design parameters and the approximation form. In the present work the signum function is replaced by the arc tan function, namely

$$sgn_{approx}(s) = \frac{2}{\pi} \tan^{-1}(\gamma s) \quad (13)$$

Where $\tan^{-1}(\gamma s)$ is a continuously differentiable, odd, monotonically increasing function with the properties:

$$\begin{aligned} \tan^{-1}(0) &= 0, \lim_{|s| \rightarrow \infty} \tan^{-1}(\gamma s) = \\ \lim_{\gamma \rightarrow \infty} \tan^{-1}(\gamma s) &= \frac{\pi}{2} sgn(s) \text{ and } sgn(s) * \\ \tan^{-1}(\gamma s) &= \tan^{-1}(\gamma |s|) \geq 0 \end{aligned}$$

Accordingly, the sliding mode controller, given in equation (3), becomes

$$u_{approx} = -\frac{2k}{\pi} \tan^{-1}(\gamma s) \quad (14)$$

Now, let us state the following, and then prove it:

When the sliding mode controller use the approximate signum function as given in equation (13), and the controller gain satisfy the inequality (6), then the state will be regulated to a positively invariant set defined by

$$\Delta_\delta = \left\{ x \in \mathcal{R}^2: |x_1| < \frac{\delta}{\lambda}, |s| \leq \delta \right\} \quad (15)$$

To prove that Δ_δ is a positively invariant set for a second order affine system (equation (3)), we return to use the Lyapunov function in equation (4) which has the time rate of change

$$\begin{aligned} \dot{V} &= \left\{ f(x) - g(x) \frac{2k}{\pi} \tan^{-1}(\gamma s) + \lambda x_2 \right\} sgn(s) \\ &= - \left\{ g(x) \frac{2k}{\pi} \tan^{-1}(\gamma |s|) \right. \\ &\quad \left. - (f(x) + \lambda x_2) * sgn(s) \right\} \end{aligned}$$

For the switching manifold to be attractive \dot{V} must be less than zero,

$$\begin{aligned} & \text{namely} - \left\{ g(x) \frac{2k}{\pi} \tan^{-1}(\gamma|s|) - \right. \\ & \left. (f(x) + \lambda x_2) * \text{sgn}(s) \right\} < 0 \\ & \Rightarrow \frac{2k}{\pi} \tan^{-1}(\gamma|s|) > \max \left| \frac{f(x) + \lambda x_2}{g(x)} \right| = h \\ & \text{or} \\ & k > \frac{\pi h}{2 \tan^{-1}(\gamma|s|)} \end{aligned} \quad (16)$$

Now, let $|s| = \delta$ be the chosen boundary layer, then inequality (16) reveals, for a certain γ , that: *for any δ there is k , such that the state will be regulated to an open region given by*

$$\Gamma = \{x \in \mathcal{R}^2: |s| < \delta\} \quad (17)$$

Accordingly, the gain k will be

$$k = \frac{\alpha \pi h}{2 \tan^{-1}(\gamma \delta)}, \alpha > 1 \quad (18)$$

In addition, to determine γ , equation (18) may be written as:

$$k = \alpha h \beta, \beta > 1 \quad (19)$$

provided that;

$$\gamma \delta = \tan \frac{\pi}{2\beta} \quad (20)$$

The next step in the determination of the invariant set Δ_δ is to found the boundary with respect to x_1 inside Γ . This is done by using the following Lyapunov function

$$V = \frac{1}{2} x_1^2 \quad (21)$$

with the x_1 dynamics, from equations (2) and (3):

$$\dot{x}_1 = -\lambda x_1 + s(t) \quad (22)$$

Therefore the time rate of change for the Lyapunov function is

$$\begin{aligned} \dot{V} &= x_1 \dot{x}_1 = x_1 (-\lambda x_1 + s(t)) \\ &= -\lambda |x_1|^2 + |x_1| |s(t)| \leq -\lambda |x_1|^2 + |x_1| \delta \\ &= -|x_1| (\lambda |x_1| - \delta) \end{aligned}$$

Thus, $\dot{V} \leq 0$ for the following unbounded interval:

$$|x_1| > \frac{\delta}{\lambda} \quad (23)$$

Inequality (23) proves that the state x_1 will reach and stay within the interval $-\frac{\delta}{\lambda} \leq x_1 \leq \frac{\delta}{\lambda}$. This ends the prove that the set $\{x \in \mathcal{R}^2: |x_1| < \frac{\delta}{\lambda}, |s| \leq \delta\}$ is positively invariant for the system in equation (2) that uses a sliding mode controller with the approximate signum function as given in equation (14).

Note that the state inside Δ_δ may or may not reaches an equilibrium point; the situation depends on system dynamics, i.e., the state, instead of that, will reach a limit cycle inside Δ_δ . Consequently, and for the design purpose, δ may be determined according to a desired permissible steady state deviation of the state x_1 and for a selected λ , as a design parameter, as follows:

$$\delta = \lambda * x_{1per}. \quad (24)$$

Thus, the set Δ_δ is now written as:

$$\Delta_\delta = \{x \in \mathcal{R}^2: |x_1| < x_{1per}, |s| \leq \delta\} \quad (25)$$

It is also noted that for arbitrary small x_{1per} , the positively invariant set Δ_δ becomes arbitrary small and it may lead, again, to the state chattering. This case may explain the chattering phenomena as the state oscillation with a very narrow width, i.e., the interval $|x_1| < x_{1per}$, is very small.

5-Sliding Mode Controller Design for Servo Actuator with Friction

Consider the following model for the servo actuator with friction:

$$J\ddot{x} = u - F - T_L \quad (26)$$

Where x is the actuator position, J is the moment of inertia, u is the control signal, F is the friction torque, including the static and dynamic components, and T_L is the load torque. The friction model taken here is a combination of Coulomb friction F_c ,

Stiction friction F_s , and the viscous friction (for more details one can refer to the survey papers [12] & [13]), namely

$$F = F_s e^{-\left(\frac{\dot{x}}{\dot{x}_s}\right)^2} * \text{sgn}(\dot{x}) + F_c \left(1 - e^{-\left(\frac{\dot{x}}{\dot{x}_s}\right)^2}\right) * \text{sgn}(\dot{x}) + \sigma \dot{x}$$

or

$$F = \left\{ F_s e^{-\left(\frac{\dot{x}}{\dot{x}_s}\right)^2} + F_c \left(1 - e^{-\left(\frac{\dot{x}}{\dot{x}_s}\right)^2}\right) + \sigma |\dot{x}| \right\} * \text{sgn}(\dot{x}) \quad (27)$$

Where \dot{x}_s is called the Stribeck velocity and σ is the viscous friction coefficient. In addition, the servo actuator model in equation (26) is considered uncertain with a bounded load torque. The uncertainty in the model parameters reaches to 20% of their nominal values. Now, define $e_1 = x - x_d$ and $e_2 = \dot{x} - \dot{x}_d$, then the system model in equation (26) in state space form (in (e_1, e_2) plane) is written as:

$$\begin{aligned} \dot{e}_1 &= e_2 \\ \dot{e}_2 &= \left(\frac{1}{J}\right) (u - F - T_L) - \ddot{x}_d \end{aligned} \quad (28)$$

In this work the desired position and velocity are taken as in reference [14]:

$$\begin{aligned} x_d &= \frac{1}{16\pi} \sin(8\pi t) - \frac{1}{24\pi} \sin(12\pi t) \Rightarrow |x_d| \leq \frac{5}{48\pi} \\ \dot{x}_d &= \sin(10\pi t) * \sin(2\pi t) \Rightarrow |\dot{x}_d| \leq 1 \end{aligned} \quad (29)$$

Also, the switching function and its derivative are

$$\begin{aligned} s &= e_2 + \lambda e_1 \\ \dot{s} &= \left(\frac{1}{J}\right) (u - F - T_L) - \ddot{x}_d + \lambda e_2 \end{aligned} \quad (30)$$

Where $\ddot{x}_d = 10\pi * \cos(10\pi t) \sin(2\pi t) - 2\pi * \sin(10\pi t) \cos(2\pi t)$ and $|\ddot{x}_d| \leq 12\pi$.

The sliding mode controller is designed for two initial conditions (the position and the velocity at time $t = 0$). The first initial condition lies in the 2nd positively invariant set (see (15)), while in the second case the 1st positively invariant set is according to the initial condition taken which lies outside the 2nd positively invariant set. The controller parameters are calculated for each case in appendices (A) and (B) for the following

nominal parameters and external load values [14]

Table (1): Nominal Servo Actuator Parameters and the External Load values

Par.	Definition	Value	Units
J_o	Moment of inertia.	0.2	kgm^2
F_{so}	Stiction friction.	2.19	Nm
F_{co}	Coulomb friction.	16.69	Nm
\dot{x}_{so}	Stribeck velocity.	0.01	$\frac{rad}{sec}$
σ_o	viscous friction coefficient	0.65	$\frac{Nm \cdot sec}{rad}$
T_{Lo}	External Torque	2	Nm

The simulation results and discussions are presented in the following section.

6-Simulations Result and Discussions

For the first case the state is started from the rest, which means $e(0) = (0,0)$ (this is because $x_d(0) = \dot{x}_d(0) = 0$). In this case the state is initiated inside the 2nd positively invariant set Δ_δ , and accordingly the state will not leave it for $t \geq 0$. The state after that reaches an invariant set (it still inside Δ_δ), namely the ω limit set of the point $e(0)$. For the servo actuator with non-smooth disturbance (the friction), this set is a limit cycle lies inside the positively invariant set Δ_δ (the fact in section 2). Indeed, the state will reach the ω limit set if it is started at any point in Δ_δ . This situation will be demonstrated by the simulation results below.

The approximate sliding mode controller in this case is (the details of the calculations is found in Appendix (A))

$$\left. \begin{aligned} u_{approx} &= -(84/\pi) * \tan^{-1}(141 * s) \\ s &= (\dot{x} - \dot{x}_d) + 25 * (x - x_d) \end{aligned} \right\} (31)$$

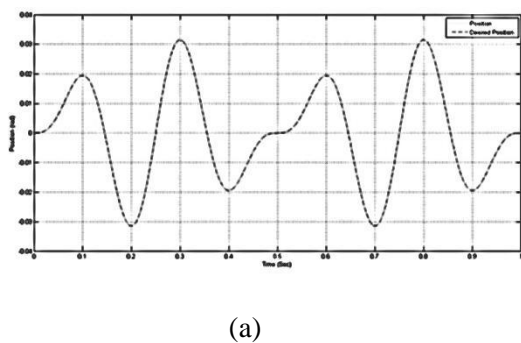
This controller will be able to maintain the state in the following invariant set:

$$\Delta_\delta = \left\{ x \in \mathcal{R}^2: |x - x_d| < \frac{\pi}{3600}, |s| \leq \frac{\pi}{144} \right\} (32)$$

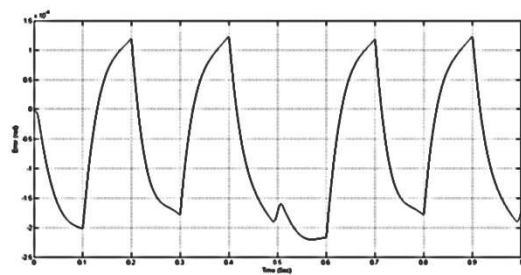
The response of the servo actuator system when started at the origin is shown in figure (2). In this figure the position response is plotted with time and it appears very close to the desired position. This result is

demonstrated when plotting the error and the maximum error shown in the plot, where it does not exceed 1.5×10^{-4} radian. For the velocity, figure (3) plot the time response and again the maximum error, which it does not exceed 6.5×10^{-3} radian per second, reveal the closeness between the velocity response and the desired velocity. The error phase plot is found in figure (4) where the state reaches the ω limit set of the origin point. The ω limit set forms here a non-smooth time varying limit cycle and accordingly, the error state will oscillate for all future time within certain amplitude. The oscillation amplitude has an upper bound decided early by the choice of the permissible error.

The positively invariant set formed by the sliding mode controller, as it is given by (32), enables the same controller to regulate the state when it is started within this set. This situation is verified in figure (5) for two starting points where the state reaches the ω limit set corresponding to each point.

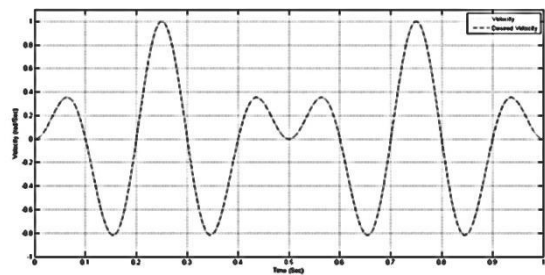


(a)

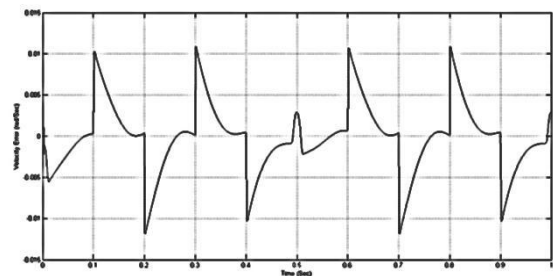


(b)

Figure (2) a) Position and the desired position vs. time (equation (29)). b) The position error for 5second.



(a)



(b)

Figure (3) a) Velocity and the desired velocity vs. time (equation (29)). b) The velocity error for 5second.

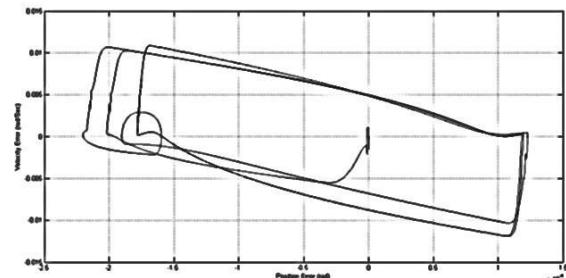
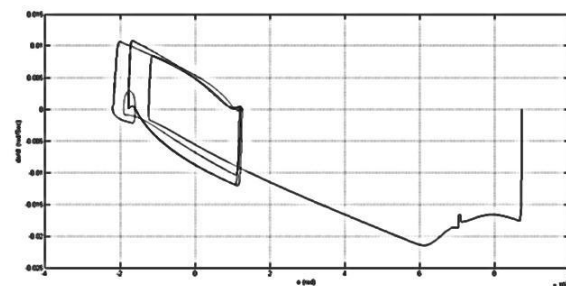
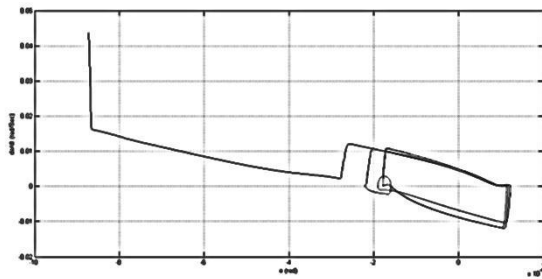


Figure (4) The phase plane plot when the error started at the origin.



(a)



(b)

Figure (5) The phase plane plot a) when the error started at $(e, \frac{de}{dt}) = (\frac{\pi}{3600}, 0)$ b) when the error started at $(e, \frac{de}{dt}) = (-\frac{\pi}{3600}, 2\frac{\pi}{144})$.

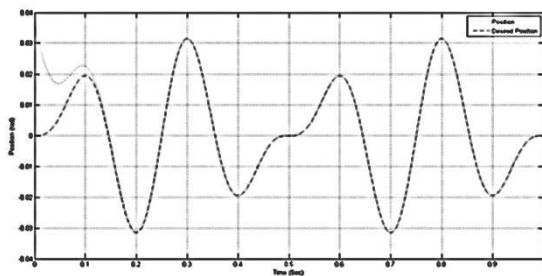
For the second case the sliding mode controller, as calculated in appendix (B), is

$$\left. \begin{aligned} u &= -45 * \text{sgn}(s) \\ s &= (\dot{x} - \dot{x}_d) + 25 * (x - x_d) \end{aligned} \right\} \quad (33)$$

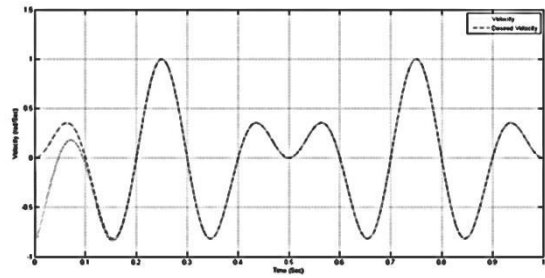
The controller will be able to regulate the error to the origin if it initiated in the following positively invariant set:

$$\Omega = \{x \in \mathcal{R}^2: |s(t)| < 0.875, |x - x_d| \leq 0.035\} \quad (34)$$

The simulation results for the position and the velocity when the state starting at $(x, \dot{x}) = (0.035, 0)$ is shown in figure (6). In this figure the position and the velocity track the desired response after a period of time not exceeding 0.12 second.



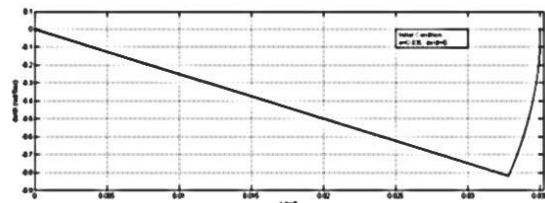
(a)



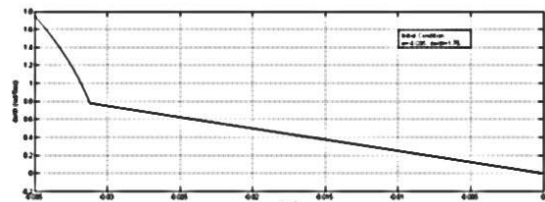
(b)

Figure (6) Servo actuator response for the initial condition $(e, \frac{de}{dt}) = (0.035, 0)$ a) The position vs. time b) velocity vs. time.

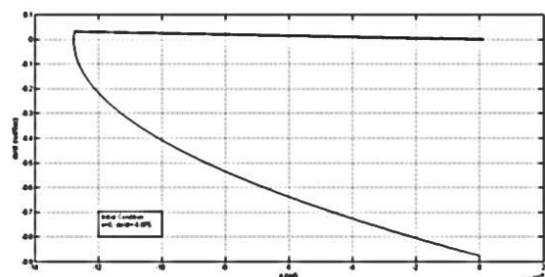
As for the sliding mode controller in (31), the sliding mode controller in (33) will create a positively invariant region (34) such that if the state initiated inside this set, it will be regulated to the origin. This situation is confirmed in figure (7) for three different starting points including the case of figure (6).



(a)



(b)



(c)

Figure (7) Error phase plot for different initial conditions a) $(e, \frac{de}{dt}) = (0.035, 0)$ b) $(e, \frac{de}{dt}) = (-0.035, 1.75)$ c) $(e, \frac{de}{dt}) = (0, -0.875)$.

If it is required to remove the chattering that exists in the system response for the second case, we again replace the segnum function by the arc tan function. In this case we replace the gain $k = 45$ by the following quantity:

$$k = 45 * 1.25 = 57, \quad \beta = 1.25$$

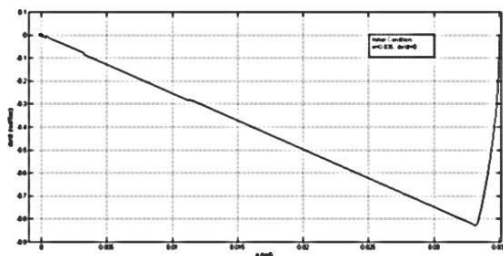
Then, we obtain

$$u = -\left(\frac{114}{\pi}\right) \tan^{-1}(141 * s) \quad (35)$$

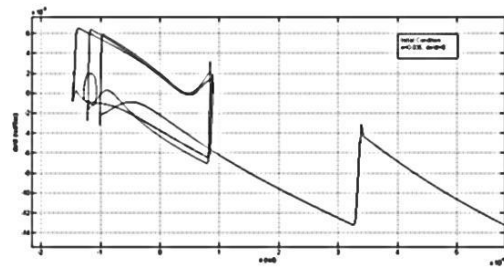
The sliding mode controller in (35) creates a positively invariant set equal to the set given in (34), but in this case the controller will not regulate the error to the origin. Indeed, the controller will regulate the error to enter the 2nd positively invariant set that was given in (32). Mathematically, the 1st and the 2nd sets in (34) and (32) are two positively invariant sets created by the sliding mode controller in equation (35) but with a different set level (see reference [1] for the definition of set level), namely

$$\Delta_\delta \subset \Omega$$

As in figure (7), the phase plane plot for the initial condition $\left(e, \frac{de}{dt}\right) = (0.035, 0)$ is plotted in figure (8) but without chattering around the switching manifold due to replacing the segnum function in equation (33) by the approximate form in (35). Accordingly, the state will enter a smaller positively invariant set and then reach the ω limit set as in case one.



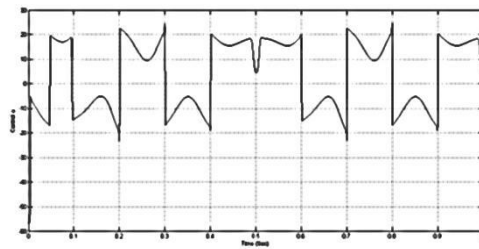
(a)



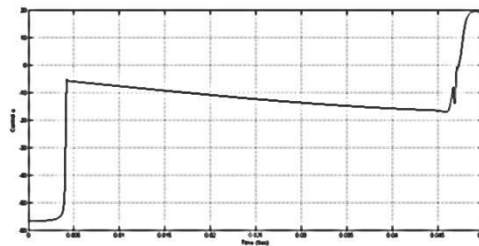
(b)

Figure (8) the phase plane plot when using the controller in (35) a) full phase plot b) small plot around the origin showing the oscillation behavior.

Finally, the chattering behavior is removed due to a continuous control action, where the continuity is revealed in figure (9) with a magnitude lies between $\pm 25 \text{ N.m}$ after a period of time not exceed 0.05 second.



(a)



(b)

Figure (9) The control action vs. time a) plot for 1 second b) plot for 0.05 second.

7-Conclusions

The positively invariant set for a second order affine system that uses a sliding mode controller has been derived. The size of the invariant sets are found functions to the initial condition and consequently to the controller gain and design parameters. The derived sets have been used to calculate the sliding mode controller gain for the servo

actuator. The simulation results prove the invariant property of the derived set and the effectiveness of using them in the calculation of the sliding mode controller. The ability of the approximate sliding mode controller, a continuously and differentiable controller, has been verified when it used to attenuate the effect of a nonsmooth disturbances (the friction) that act on the servo actuator system. The controller maintains the maximum error (the difference between the actual and the desired state) very close to zero and according to the permissible error value specified previously.

References

- [1] F. Blanchini and S. Miani. "Set-Theoretic Methods in Control". Birkhauser, Boston, 2008.
- [2] V. I. Utkin, J. Guldner, and J. Shi. "Sliding Mode Control in Electromechanical Systems". CRC Press. Boca Raton, 1999.
- [3] A. Levant. "Sliding order and sliding accuracy in sliding mode control". *International Journal of Control*, Vol. 58, No. 6, pp. 1247-1263, 1993.
- [4] J.-J. E. Slotine, "Tracking control of nonlinear systems using sliding surfaces", Ph.D. Thesis, Massachusetts Institute of Technology, Dept. of Aeronautics and Astronautics, 1983.
- [5] H. K. Khalil. "Nonlinear Systems". 3rd Edition, Prentise Hall, USA, 2002.
- [6] M. Krstic, I. Kanellakopoulos, and P. Kokotovic. "Nonlinear and Adaptive Control Design". Johnwiley&Sons, 1995.
- [7] S. Sastry. "Nonlinear Systems: Analysis, Stability, and Control". Springer-Verlag New York, 1999.
- [8] Y. Pan, U. Ozguner, and O. H. Dağci. "Variable-Structure Control of Electronic Throttle Valve". *Transaction on Industrial Electronis*, Vol. 55, No. 11, November, pp. 3899-3907, 2008.
- [9] V. I. Utkin. "Sliding Modes in Control and Optimizations". Springer-Verlag, Berlin, 1992.
- [10] L. Hoon. "Chattering suppression in sliding mode control system." Ph.D. Thesis, Mechanical Engineering, Ohio State University, 2007.
- [11] C. Edwards and S. K. Spurgeon. "Sliding Mode Control: Theory and Applications". Tayler & Francis Ltd, 1998.
- [12] B. Armstrong-Hélouvry, P. Dupont, and C. C. de Wit, "A survey of models, analysis tools and compensation methods for the control of machines with friction," *Automatica*, vol. 30, no. 7, pp. 1083–1138, 1994.
- [13] H. Olsson, K. J. Åström, C. Canudas-de-Wit, M. Gäfvert and P. Lischinsky, "Friction models and friction compensation," *Eur. J. Control* 4(3), 176-195, 1998.
- [14] W. F. Xie. "Sliding-Mode-Observer-Based Adaptive Control for Servo Actuator With Friction". *Transaction on Industrial Electronis*, Vol. 54, No. 3, June, pp. 1517-1527, 2008.

Appendix (A)

To design the approximate sliding mode controller we need, first, to calculate h as it is given in (6):

$$h = \max \left| \frac{f(e) + \lambda e_2}{g(e)} \right|$$

$$= \left\{ \frac{\max \left| \left(\frac{-F - T_L}{J} \right) - \ddot{x}_d + \lambda e_2 \right|}{\min \left(\frac{1}{J} \right)} \right\}$$

$$= \max |F| + \max |T_L| + (\max J) * \max |\ddot{x}_d| + \lambda (\max J) * \max |e_2| \quad (A-1)$$

From the set Δ_δ , the following bounds are estimated:

$$\max |e_2| = 2\delta \text{ and}$$

$$\max |\dot{x}| = \max |e_2| + \max |\dot{x}_d| = 2\delta + 1$$

The term $\max |\dot{x}|$ enables the calculation of $\max |F|$ as follows:

$$\max |F| = 1.2 \left\{ F_{so} e^{-\left(\frac{2\delta+1}{x_s} \right)^2} \right\}$$

$$\left. \begin{aligned} &+F_{co} \left(1 - e^{-\left(\frac{2\delta+1}{\dot{x}_s}\right)^2} \right) + \sigma_o(2\delta + 1) \Big\} \\ &\leq 1.2(F_{co} + \sigma_o(2\delta + 1)) \end{aligned}$$

Where F_{so} , F_{co} , and σ_o are the nominal friction parameter values also, we multiply by 1.2 to take into account the uncertainty in system parameters as assumed previously. In addition, we have

$\max|J| = 1.2 * J_o$ and $\min|J| = 0.8 * J_o$ again J_o is the nominal moment of inertia value and finally the load torque is bounded by

$$|T_L| \leq T_{L_{max}} = 1.2T_{L0}$$

Therefore, h becomes a function to the slope of the switching manifold λ and the boundary layer δ .

In sliding mode controller design, we mainly concern in calculating suitable value for the gain k after a proper selection to the switching function $s(x)$ (by proper we mean that the origin is an asymptotically stable after the state reaches the switching manifold $s(x) = 0$). Now, if we set the permissible error and λ as in the following

$$e_{per.} = 0.05 \text{ deg.} = \frac{\pi}{3600} \text{ rad}, \quad \lambda = 25$$

then from (24), we have

$$\delta = \lambda * e_{per.} = \frac{\pi}{144} \Rightarrow |e_1| \leq e_{per.}$$

Accordingly, to find the gain k , we first compute h as follows:

$$\begin{aligned} \max|F| &\leq 1.2(F_{co} + \sigma_o(2\delta + 1)) = 20.84 \\ \Rightarrow h &= 20.84 + 2.4 + 0.24 * 12\pi + 0.24 \\ &\quad * 25 * 2 \frac{\pi}{144} = 32.55 \end{aligned}$$

and then for $\beta = 1.25$, we get

$$k = \alpha * 1.25 * 32.55 = 42, \quad \alpha > 1$$

Also, from equation (20), γ equal to

$$\gamma = \frac{144}{\pi} \tan \frac{\pi}{2.5} = 141$$

Finally, the sliding mode controller to the servo actuator is

$$u_{approx.} = -\frac{84}{\pi} \tan^{-1}(141 * s)$$

$$s = (\dot{x} - \dot{x}_d) + 25 * (x - x_d) \quad (\text{A-2})$$

The sliding mode controller will be able to prevent the state leaving the positively invariant set Δ_δ . That means the error $(x - x_d)$ is less than the permissible limit that specified earlier.

Appendix (B)

In this case we consider the same desired position and velocity as in equation (29) with the following initial condition

$$x = 0.035 \text{ rad}, \quad \dot{x} = 0 \text{ rad/sec.}$$

$$\Rightarrow e(0) = (e_1, e_2) = (0.035, 0)$$

Also, consider the same switching function as in case one ($s = e_2 + 25e_1$). Then, accordingly, the invariant set is given by

$$\Theta = \{x \in \mathcal{R}^2: 0 \leq s(t) < 0.875, |e_1(t)| \leq 0.035\} \quad (\text{B-1})$$

In addition we have

$$\begin{aligned} |e_2(t)| \leq 1.75 &\Rightarrow \max|\dot{x}| = \max|e_2| \\ &+ \max|\dot{x}_d| = 2.75 \text{ rad/sec.} \end{aligned}$$

And then we can calculate $\max|F|$ as in the following:

$$\max|F| \leq 1.2(F_{co} + 2.75 * \sigma_o) = 22.2$$

Thus, as in the first case, h is equal to

$$h = 22.2 + 2.4 + 0.24 * 12\pi$$

$$+ 0.24 * 25 * 1.75 = 44.15$$

The sliding mode controller gain from equation (6) is taken equal to

$$k = 45 > h$$

Finally, the sliding mode controller for the second case is given by

$$u = -45 * \text{sgn}(s)$$

$$s = (\dot{x} - \dot{x}_d) + 25 * (x - x_d) \quad (\text{B-2})$$

If the state initiated inside the positively invariant set as given in (B-1), the sliding mode controller will regulate the error state to the origin irrespective to the uncertainty and the non-smooth components in the servo actuator model.

GENERALIZED PID CONTROLLER BASED ON PARTICLE SWARM OPTIMIZATION

Ali Hussien Mary

Mechatronics Engineering Dept.
Al-Khwarizmy College of Engineering
University of Baghdad
alihussien76@yahoo.com

Abstract

The paper presents the novel application of Particle Swarm optimization (PSO) for the optimal tuning of the new PID controller which is called generalized PID (GPID). In 2009, Zhao Xiaodong, Li Yongqiang, Xue Anke proposed generalized PID (GPID) to improve the time response and control quality of the traditional PID control algorithm. This paper applies the Particle Swarm Optimization (PSO) algorithm for GPID controllers. The main goal is to eliminate the steady state error of the system and minimize the error performance index. The method searches the GPID parameter that realizes the expected step response of the plant. The expected response is defined by the overshoot ratio, the rising time, and the settling time. The numerical result and the experiment result show the effectiveness of the proposed tuning method when the results are compared with the Traditional PID Controller.

Keywords: GPID, PID, Particle Swarm Optimization, Tuning Algorithm.

1- Introduction

Conventional proportional–integral–derivative (PID) controllers have been well developed and applied for about half a century, and are extensively used for industrial automation and process control today. The main reason is due to their simplicity of operation, ease of design, inexpensive maintenance, low cost, and effectiveness for most linear systems. Recently, motivated by the rapidly developed advanced microelectronics and digital processors [1,2]. The study of new generation of PID controllers has drawn significant attention in recent years. Specifically, Zhao Xiaodong, Li Yangquan

,Xue Anke propose A generalized PID algorithm (GPID) is proposed to improve the time response and control quality of the traditional PID control algorithm.

The traditional PID controller is a special case of the generalized PID; this can be shown by comparing the coefficients of GPID and PID. GPID can be obtained by adding higher-order derivative terms in on the form of the traditional PID [3], the tuning method based on PSO (Particle Swarm Optimization) has already been proposed to obtain the optimal PID parameter. This method has not considered the step response of constraints (the overshoot ratio, the rising time, the settling time and so on). This paper presents a new method that obtains the PID parameter realizing the expected step response with the constraints. A proposed method using Particle Swarm Optimization (PSO) is implemented into the GPID tuning tool on a personal computer. The developed tool provides the GPID parameter that realizes the expected step response of the plant. The numerical result and the experimental result show the effectiveness of the proposed a new GPID parameter tuning method.

2- Background

2.1- PID Controller

The PID controller is a linear controller. Fig.1 illustrates the core architecture of a PID controller. The PID controller calculation (algorithm) involves three separate parameters; the Proportional, the Integral and Derivative values. The Proportional value determines the reaction to the current error, the Integral value determines the reaction based on the sum of recent errors, and the Derivative value

determines the reaction based on the rate at which the error has been changing. The weighted sum of these three actions is used to adjust the process via a control element such as the position of a control valve or the power supply of a heating element. The normal PID controller is in the following form [3]

$$u(t) = k_p e(t) + k_i \int e(t) dt + k_d de(t) / dt \quad \dots(1)$$

Where $e(t) = r(t) - y(t)$ is the error between reference input and output. By "tuning" the three constants in the PID controller algorithm, the controller can provide control action designed for specific process requirements

2.2- Generalized PID Controller

Based on the study of traditional PID controller, in 2009 Zhao Xiaodong, Li Yongqiang, Xue Anke proposed generalized PID(GPID) by increasing higher order derivatives terms, In (1), a second order derivative term of $e(t)$ is added, we can get:

$$u(t) = k_p e(t) + k_i \int e(t) dt + k_d de(t) / dt + k_a d^2 e(t) / dt^2 \quad \dots (2)$$

As the physical meaning of the derivative, the first derivative represents the change speed of the error, the second derivative represents the acceleration of the error. In (2), the second derivative added restrains the acceleration of the error getting bigger and makes the system's response more quickly and reduce the overshoot, increase the stability of the system. Thus the controller gains better control effect. However, increasing higher-order derivative also makes some problems, such as increasing the time and the difficulty of setting the parameter and amplifying the noise interference.

3- Particle Swarm Optimization (PSO)

Optimization algorithms are another area that has been receiving increased attention in the past few years by the research community as well as the industry. An optimization algorithm

is a numerical method or algorithm for finding the maxima or the minima of a function operating with certain constraints [5].

Particle swarm optimization (PSO) is a relatively recently devised population-based stochastic global optimization algorithm. PSO has many similarities with evolutionary algorithms, and has also proven to have robust performance over a variety of difficult optimization problems. However, the original formulation of PSO requires the search space to be continuous and the individuals to be represented as vectors of real numbers [6]

Particle swarm optimization originally relates to artificial life (A life) in general and specifically it connects with bird flocking and fish schooling. The Intelligence in PSO as any other swarm technique is a collective intelligence resulting in the collective behaviors of(unsophisticated) individuals interacting locally and with their environment causing coherent functional global patterns to emerge. Particle Swarm Optimization (PSO) which is inspired by the social behavior of bird flocking or fish schooling and Ant Colony Optimization (ACO) which is inspired by behavior of ants are the primary computational parts of swarm intelligence. In 1995, Kennedy and Eberhart first introduced the particle swarm optimization (PSO) method as a stochastic, population-based evolutionary algorithm for problem solving. The key idea of PSO method is to simulate the shared behavior happening among the birds flocks or fish school[7]. Particle Swarm Optimization has more advantages over Genetic Algorithm as follows:

(a). PSO is easier to implement and there are fewer parameters to adjust.

(b). In PSO, every particle remembers its own previous best value as well as the neighborhood best ; therefore, it has a more effective memory capability than GA. (c). PSO is more efficient in maintaining the diversity of the swarm, since all the particles use the information related to the most successful

particle in order to improve themselves, whereas in Genetic algorithm, the worse solutions are discarded and only the new ones are saved; (i.e) in GA the population evolves around a subset of the best individuals[8].

In the PSO algorithm, instead of using evolutionary operators such as mutation and crossover, to manipulate algorithms, for a d-variable optimization problem, a flock of particles are put into the d-dimensional search space with randomly chosen velocities and positions knowing their best values so far (Pbest) and the position in the d-dimensional space. The velocity of each particle, adjusted according to its own flying experience and the other particle's flying experience. For example, the *i* th particle is represented as

$$x_i = (x_{i,1}, x_{i,2}, x_{i,3}, \dots, x_{i,d}) \dots (3)$$

in the d-dimensional space. The best previous position of the *i* th particle is recorded and represented as:

$$Pbest_i = (Pbest_{i,1}, Pbest_{i,2}, \dots, Pbest_{i,d}) \dots (4)$$

The index of best particle among all of the particles in the group is *d gbest_d*. The velocity for particle *i* is represented as $v_i = (v_{i,1}, v_{i,2}, v_{i,3}, \dots, v_{i,d}) \dots (5)$

The modified velocity and position of each particle can be calculated using the current velocity and the distance from Pbest_{*i,d*} to gbest_{*d*} as shown in the following formulas :

$$v_{i,m}^{(t+1)} = w.v_{i,m}^{(t)} + c_1 * rand() * (pbest_{i,m} - x_{i,m}^{(t)}) + c_2 * Rand * (gbest_m - x_{i,m}^{(t)}) \dots (6)$$

$$x_{i,m}^{(t+1)} = x_{i,m}^{(t)} + v_{i,m}^{(t+1)} \dots (7)$$

I=1,2,...n

M=1,2,...m

Where:

n Number of particles in the group

d dimension

t Pointer of iterations(generations)

$v_{i,m}^{(t)}$ Velocity of particle I at iteration t

W Inertia weight factor, c_1, c_2 Acceleration constant

Rand() Random number between 0 and 1

$x_{i,m}^{(t)}$ Current position of particle i at iterations

Pbest_{*i*} Best previous position of the *i*th particle
gbest Best particle among all the particles in the population. Figure 1 show the PSO Steps.

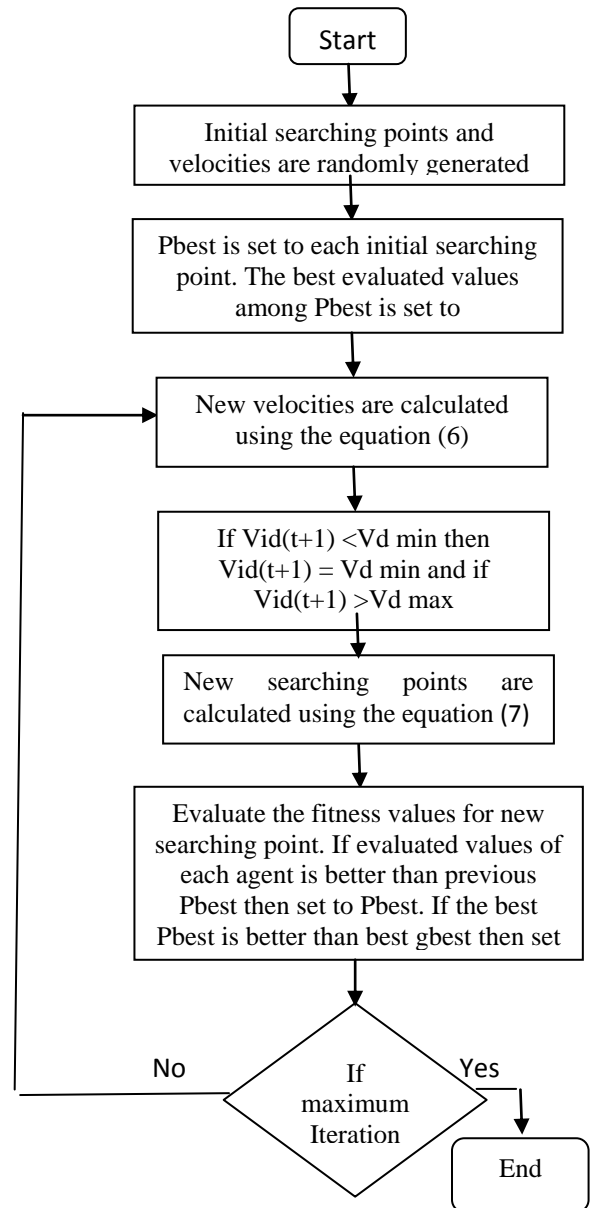


Fig. 1 PSO Algorithm

5-PSO based optimal GPID controller design

This paper describes the application of PSO to the fine-tuning of the parameters for GPID controllers. Such a simple but general approach, having ability for global optimization and with good robustness, is expected to

overcome some weakness of conventional approaches and to be more acceptable for industrial practices. An improved multi-objective optimization method for parameter tuning of GPID controller based on PSO algorithm is proposed, which consists of the following two steps:

Step 1: Scheduling PSO for PID Controller parameters. In this paper, An GPID controller used PSO Algorithms to find the optimal parameters of DC Motor speed control system. The structure of the GPID controller with PSO algorithms is shown in Fig. 4. In the proposed PSO method each particle contains four members k_i, k_p, k_d and k_a . It means that the search space has four dimension and particles must 'fly' in a four dimensional space.

Step 2: Design of Fitness Function

The most crucial step in applying optimization problems is to choose the objective functions that are used to evaluate fitness of each chromosome To evaluate the controller performance, there are always several criterions of control quality are Integral of Time multiplied by Absolute Error (ITAE), Integral of Absolute Magnitude of the Error (IAE), and Integral of the Squared Error (ISE), [9].

$$\left. \begin{aligned} ITAE &= \int_0^{\tau} t |e(t)| dt \\ ISE &= \int_0^{\tau} (e(t))^2 dt, IAE = \int_0^{\tau} |e(t)| dt \end{aligned} \right\} \dots(8)$$

5.1- Multi-Objective PSO

In this paper to evaluate the controller performance and get the satisfied transient dynamic, the fitness function includes the four main transient performance indices, overshoot, rise time, settling time and cumulative error. This lead to using Multi-objective optimization in order gets the desired response

The First Objective: $w_1 J_1$

The Second Objective: $w_2 t_r$

The third Objective: $w_3 \sigma$

The Fourth Objective: $w_4 t_s$

Therefore the fitness function used is designed as [10]

$$J = \frac{1}{w_1 J_1 + w_2 t_r + w_3 \sigma + w_4 t_s} \dots\dots (9)$$

Where J_1 is one of the control quality (defined in eqn(8)), t_r is the rise time, σ is the maximal overshoot, t_s is the settling time with 5% error band, are weighting coefficients. One could adjust all the weighting coefficients in the fitness function based on the specific requests such as rapidity, accuracy and stability of the system. For example if a system with little overshoot value is required, w_4 would be increased appropriately; if a system with fast dynamic responses is required, then w_3 would be increased appropriately. This research has picked the weighting coefficients w_1, w_2, w_3 , and w_4 to cover all the performance indices completely.

6-Simulation Results

For the purpose of showing the effectiveness of the proposed method and the developed tool, numerical examples and experimental examples are studied and simulated using the MATLAB. The DC motor under study has the following parameters: The transfer function of DC motor is

$$\frac{\theta(s)}{v(s)} = \frac{k_b}{JL_a s^3 + (R_a J + BL_a) s^2 + (k_b k_T + R_a B) s} \dots\dots (10)$$

Where, $R=R_a$ =Armature resistance in ohm, $L=L_a$ =Armature inductance in henry, $v=V_a$ =Armature voltage in volts, $e_b=e(t)$ =Back emf voltage in volts, K_b =back emf constant in volt/(rad/sec), $K=K_T$ =torque constant in N-m/Ampere, T_m =torque developed by the motor in N-m, $\theta(t)$ =angular displacement of shaft in radians, J =moment of inertia of motor and load in Kg-m²/rad, B =frictional constant of motor and load in N-m/(rad/sec) .
 $L_a=0.3e^{-3}h, J=6.52e^{-6}Kg\text{-m}^2/\text{rad}.$
 $R_a=1.71\text{ohm}, K_t=0.0445, K_b=.0444\text{volt}/(\text{rad}/\text{sec}),$
 $B=0.5*10^{-3} \text{ N-m}/(\text{rad}/\text{sec}).$

While The PSO parameters are listed in Table 1. Which used to verify the performance of the PID-PSO controller parameters.

Table 1. PSO Parameters

PSO Parameters	Value
Population size	100
w_{min}	0.1
w_{max}	0.6
$C1 = C2$	1.5
Iteration	100

The control parameters were tuned and the simulation results are shown on the following pages. Table 2 shows the results of PSO algorithm running. The table shows the main objective function and transient specifications for tuned GPID and tuned PID.

The PSO Gain tuning algorithm was used to minimize the absolute of controller total error as shown in figure. 2.

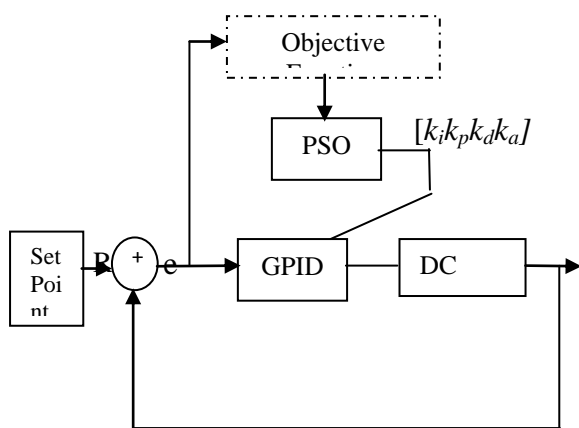


Fig.2 Close loop block diagram of a SISO system with GPID controller.

Table 3 shows the values of the GPID, PID Controllers parameter at different objective function.

Figures 3, 4, and 5 shows the response to the step input signal with desired input (desired Position) 90 based on different tuning techniques. It has been found that the performance of proposed is better than other

technique in term of time response such settling time, rise time and over shoot. Notice, from the step response, that the performance of the proposed technique is better than the other techniques in approach to steady state. Finally from the figures 3, 4 and 5, the response of the GPID is better than PID in all objective function. Figure 6 shows the comparison between PSO and Genetic Algorithm (GA), it may be said that the PSO algorithm gets better performance than GA; table 4 shows the results of this comparison

7- Conclusions

PSO algorithm to tuning the new PID controller which is called GPID is present in this paper. The main goal was to eliminate the steady state error of the system and minimize the performance index.

The position of a DC Motor drive is controlled by GPID-PSO controller. Obtained through simulation of DC motor; the results show that the proposed controller can perform an efficient search for the optimal PID controller. This algorithm successfully tuned the parameters for the four GPID controller parameters.

By comparison with PID controller, it shows that the presented method can improve the dynamic performance of the system in a better way. The GPID-PSO controller is the best which presented satisfactory performances and possesses good robustness (very low overshoot, minimal rise time, Steady state error = 0). The optimizing performance of the PSO algorithm in this application is compared with those of the GA. The transient response analysis is used for these comparisons. At the end of the analysis, the maximum overshoots and the settling times of the control system which is optimized with PSO algorithm are smaller than results of GA algorithm. The results obtained in this paper may be improved the control systems that depend on PID by using GPID.

Table 2 GPID, PID Parameters after Tuning by PSO

Objective Function	Tuned GPID parameters				Tuned PID Parameters		
	K_p	K_i	k_d	k_a	K_p	K_i	k_d
ISE	0.4203	0.0003	16.2854	0.0001	0.0667	0.00002	14.1347
ITAE	0.0565	0.001	5.9621	8.6308	0.0402	0.0002	4.5668
IAE	0.0565	0.0002	5.9621	8.6308	0.0589	0.0001	7.6026

Table 3 GPID, PID Response Specifications after Tuning by PSO

Objective Function	GPID Response			PID Response		
	RiseTime	SettlingTime	Overshoot	RiseTime	SettlingTime	Overshoot
ISE	0.0256	0.0557	7.1100e-006	0.1497	0.2212	0.8566
ITAE	0.1741	0.2821	0.0218	0.2299	0.3660	0.2328
IAE	0.1602	0.2337	1.6574	0.1568	0.2276	1.6425

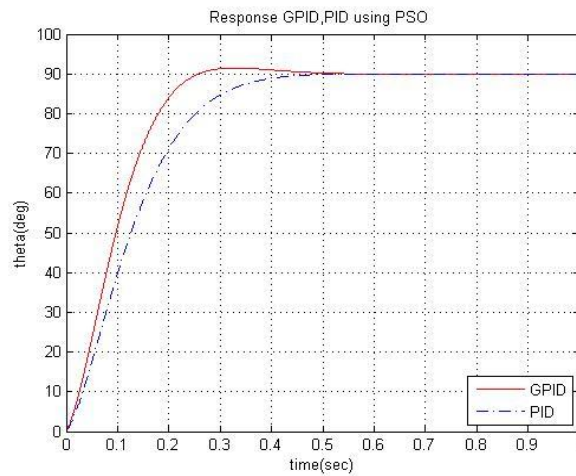


Fig. 3 Response based on ISE

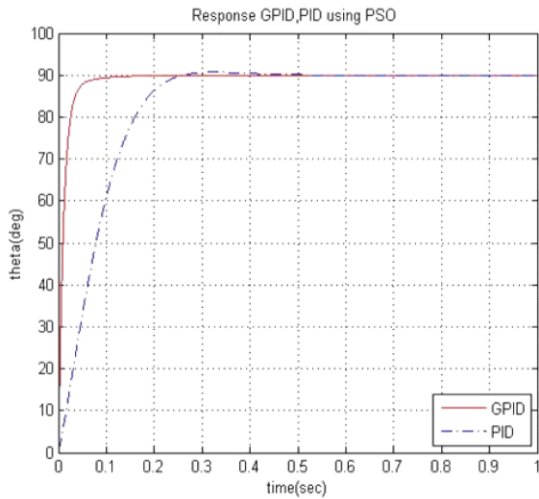


Fig. 4 Response based on ITAE

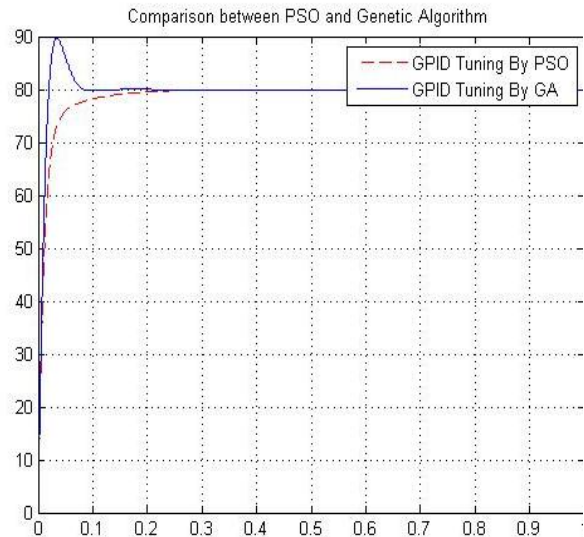


Fig. 6 Comparison between PSO and GA

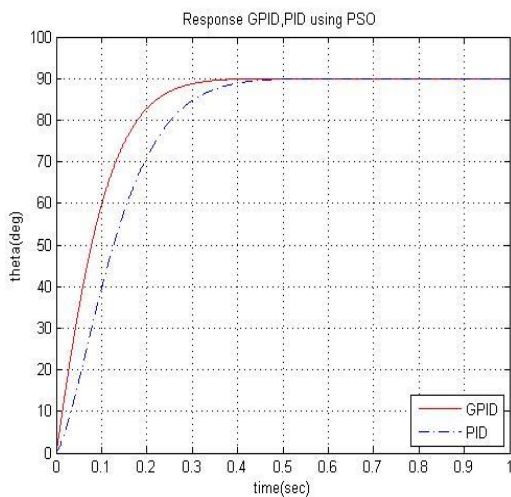


Fig. 5 Response based on IAE

Table4. Comparison between PSO and GA

Tuning Method	Overshoot	Settling Time	Rise Time
PSO	0.0032	0.0681	0.0143
GA	12.040503	0.1091	0.0298

References

- [1] Xu, J., Zeng, X., Mirafzal, B. and Demerdash N.,2006" Application of Optimal Fuzzy PID Controller Design: PI Control for Nonlinear Induction Motor" Proceedings of the 6th World Congress on Intelligent Control and Automation, June 21 - 23, Dalian, China. IEEE Conference.
- [2] Tang K. S., Man K. F., G. and Kwong S., 2001" An Optimal Fuzzy PID Controller " IEEE Transactions On Industrial Electronics, VOL. 48, NO. 4, AUGUST.
- [3] Xiaodong Z., Yongqiang L. and AnkeX.,2009, "The Study of the Generalized PID Algorithm" International Forum on Computer Science-Technology and Applications, IEEE Conference.
- [4] Oi A., Nakazawa1, and Matsui1 T., 2008," Development of PSO-based PID Tuning Method ", International Conference on Control, Automation and Systems Oct. 14-17, in COEX, Seoul, Korea
- [5] Giriraj Kumar S. M. and Anoop J. 2010,"PSO based tuning of a PID controller for a High performance drilling machine" International Journal of Computer Applications (0975 - 8887) Volume 1 – No. 19

- [6] Moraglio A., Chio, C., Togelius J., and Poli R., 2008,"Geometric Particle Swarm Optimization" Journal of Artificial Evolution and Applications Volume , Article ID 143624, 14 pages
- [7] Binwahlan M. S., Johor S.,2009 "Fuzzy Swarm Based Text Summarization" Journal of Computer Science 5 (5):338-346.
- [8] Nasri M. I, pour H. N, and MaghfooriM.,2007"A PSO-Based Optimum Design of PID Controller for a Linear Brushless DC Motor" Proceedings Of World Academy Of Science, Engineering And Technology VOL. 20 APRIL.
- [9] Kim J., Park J., Choe W. and Heo H., 2008,"Auto Tuning PID Controller based on Improved Genetic Algorithm for Reverse Osmosis Plant", World Academy of Science, Engineering and Technology Vol.47 pp: 384- 389.
- [10]CHEN, H. C.,2008"Optimal Fuzzy PID Controller design Of An Active Magnetic Bearing System based On Adaptive Genetic Algorithms" Proceedings of the Seventh International Conference on Machine Learning and Cybernetics, Kunming, 12-15 July .

TUNING OF PID CONTROLLER BASED ON FORAGING STRATEGY FOR PNEUMATIC POSITION CONTROL SYSTEM

Dr. Amjad J. Humaidi

Control and Systems Eng. Dept, University of Technology

aaacontrol2010@yahoo.com

Abstract

Pneumatic servo system has been applied in many industry fields. The system has many advantages, such as high speed, high flexibility and low price. However, application of the system is restricted because the physical parameters have strong nonlinearity, inaccuracy and uncertainty, so that it is very difficult to find an optimal controller by means of traditional control theory. Proportional integral derivative (PID) control is one of the earlier control strategies; it has a simple control structure and can be easily tuned. Optimization of PID controller parameters is one of the recent control solutions; especially when the system is of high complexity. In this paper foraging strategy has been adopted to optimize the gains of PID controller for positioning control of pneumatic system. The foraging theory is based on the assumption that animals search for nutrients in a way that maximizes their energy intake per unit time spent for foraging. The bacterial foraging algorithm is a non-gradient and stochastic optimization technique; as no need to measurement and analytical description. In the work, the optimization model of *E. coli* bacterial foraging has been used and the performance index (cost) is based on Integral Square Error (ISE) for obtaining sub-optimal values of controller parameters. Behavior of bacteria (solutions) over their lifetime has been simulated and the effect of foraging parameters on cost function has been studied.

Keywords: *E. coli* bacterial foraging, pneumatic actuator, PID controller, position control.

1. Introduction

Pneumatically actuated drives are used in widespread applications of modern automation systems mainly for pick-and-place positioning problems. They can be a cheaper alternative to electric and hydraulic systems, especially for light load applications. However, the possibility of application of pneumatic drives is limited in practice by the problems regarding to control these plants. The nonlinear effects of pneumatic systems caused by the phenomena associated with air compressibility, significant friction effects, wide range of air supply pressure, load variations, etc., make them difficult to control pneumatic axis [1,2,3].

Proportional integral derivative (PID) control is one of the earlier control strategies. Its early implementation was in pneumatic devices, followed by vacuum and solid state analog electronics, before arriving at today's digital implementation of microprocessors. It has a simple control structure which was understood by plant operators and which they found relatively easy to tune [4,5,6].

Industrial processes such as pneumatic systems are subjected to variation in parameters and parameter perturbations so that the control system performs poor in characteristics and even it becomes unstable, if improper values of the controller tuning constants are used. Therefore, it becomes necessary to tune the controller parameters to synchronize the controller with the controlled variable, thus allowing the process to be kept at its desired operating condition and to achieve good control performance with the proper choice of tuning constants. Practically all PID controllers made today are based on

microprocessors. This has given opportunities to provide additional features like automatic tuning, gain scheduling, and continuous adaptation (continuously updating the parameters of a controller) [5,6].

The foraging theory is based on the assumption that animals trying to find and consumes nutrients in a manner that maximize energy obtained from nutrient sources per unit time spent for foraging, while at the same time minimizing exposure to risks from predators. If the organism has a decision-making mechanism (e.g., a brain), then one can view this mechanism as the controller and the remainder of organism and environment as the "plant" (process to be controlled) [7,8,9,10].

In foraging, animals conduct an optimization process without use of an analytical expression for the gradient and hence, they perform nongradient optimization for "search". This is because that it is impossible for most animals (e.g., bacteria) to know the mathematical expression for how the nutrient concentration will change as the bacterium makes small changes in position. This is both because it does not have the memory to store it, and also due to the high level of uncertainty about the environment it lives in (e.g., time-varying and stochastically effects).

In the present work, the optimization model of *E. coli* bacterial foraging has been analyzed. Then, this model has been employed for tuning the parameters of PID controller for positioning control of pneumatic system to account for the system variation of parameters.

2. Description of *E. coli* bacterium and its motility behavior

The *E. coli* bacterium is shown in Fig.(1). The *E. coli* bacterium has a control system that enables it to search for a food and try to avoid noxious substances [7, 8].

An *E. coli* bacterium can move in two different ways: it can "run" (swim for a period of time) or it can "tumble", and it

alternates between these two modes of operation its entire lifetime.

Locomotion is achieved via a set of relatively rigid flagella that enable it to swim. If the flagella rotate clockwise, each flagellum pulls on the cell and the net effect is that each flagellum operates relatively independent of the others and so the bacterium "tumble" about (i.e., the bacterium does not have a set direction of movement and there is little displacement) (See Figure (1-a)).

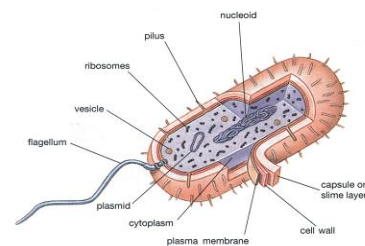


Figure (1) *E. coli* bacterium [8]

If the flagella moves counterclockwise, their effects accumulate by forming a "bundle" and hence, they essentially make a "composite propeller" and push the bacterium so that it runs (swims) in one direction (See Figure (1-a)).

If an *E. coli* is in some substance that is neutral, in the sense that it does not have a food or noxious substances, then the flagella will simultaneously alternate between moving clockwise and counterclockwise so that the bacterium will alternatively tumble and run as shown in Fig.(2.b).

Next, suppose that the bacterium happens to encounter a nutrient gradient as shown in Fig.(2.c). The change in the concentration of the nutrient triggers a reaction bacterium will spend more time swimming and less time tumbling. As long as it travels on a positive concentration gradient, it will tend to lengthen the time it spends swimming (i.e., it runs farther).

On the other hand, typically if the bacterium happens to swim down concentration gradient, it will return to its baseline behavior so that essentially it tries to search for a way to climb back up the gradient.

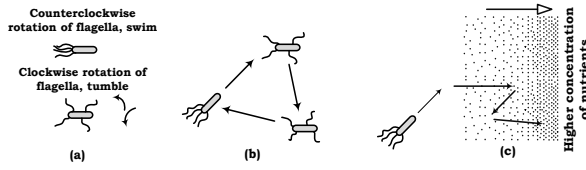


Figure (2) Motility behavior of *E. coli* bacterium
(a) Bundling phenomenon of flagella (b) swimming and tumbling behavior of *E. coli* bacterium in a neutral medium (c) there is a nutrient concentration gradient.

Finally, if the concentration of the nutrient is constant for the region it is in, after it has been on a positive gradient for some time. In this case, the bacterium will return to the same proportion of swimming and tumbling as when it was in the neutral substance so that it returns to its standard behavior.

3. Modeling of *E. coli* bacterial foraging process

To define the model of *E. coli* bacterial foraging, one need to define a population (set) of bacteria, and then model how they execute chemotaxis, swarming, reproduction, and elimination/dispersal [7]. A path through the components of the foraging process is shown as a flowchart in Fig. (3.a).

3.1 Population and Chemotaxis:

Let j, k and ℓ be the indices for the chemotactic, reproduction step and elimination /dispersal event, respectively. Then,

$$P(j, k, \ell) = \{\theta^i(j, k, \ell) | i = 1, 2, \dots, S\} \quad (1)$$

Represents the positions of each member in the population of the S bacteria at the j^{th} chemotactic step, k^{th} reproduction step, and ℓ^{th} elimination-dispersal event. Here, let $J(i, j, k, \ell)$ denotes the cost at the location of the i^{th} bacterium $\theta^i(j, k, \ell) \in \mathbb{R}^p$.

Let N_c be the length of the lifetime of the bacteria as measured by the number of chemotactic steps they take during their life. Let $C(i) > 0, i = 1, 2, \dots, S$ denote the lengths of steps during runs. To represent a tumble, a

unit length random direction, say $\phi(j)$, is generated; this will be used to define the direction of movement after a tumble.

$$\theta^i(j+1, k, \ell) = \theta^i(j, k, \ell) + C(i) \phi(j) \quad (2)$$

so that $C(i)$ is the size of the step taken in the random direction specified by the tumble. If at $\theta^i(j+1, k, \ell)$ the cost $J(i, j+1, k, \ell)$ is better (lower) than at $\theta^i(j, k, \ell)$, then another step of size $C(i)$ in this same direction will be taken, and again, if that step resulted in a position with a better cost value than at the previous step, another step is taken. This swim is continued as long as it continues to reduce the cost, but only up to a maximum number of steps, N_s . This represents that the cell will tend to keep moving if it is headed in the direction of increasingly favorable environments. The flow chart in Fig.(3.b) represents the steps of chemotactic event.

3.2 Swarming Mechanism

The cell secretes attractants to signal other cells that they should swarm together. To model this, let $d_{attract}$ be the depth of the attractant released by the cell (a quantification of how much attractant is released), $w_{attract}$ be a measure of the width of the attractant signal (a quantification of the diffusion rate of the chemical). If the attraction relationship between cell and other is represented by a Gaussian form, then the addition of such relation to the nutrient concentration (cost function) can be given by:

$$J_{cc_attract}(\theta, \theta^i(j, k, \ell)) = \sum_{i=1}^S \left[-d_{attract} \exp\left(-w_{attract}(\theta_m - \theta_m^i)^2\right) \right] \quad (3)$$

Where $m = 1, 2, \dots, p$ and $\theta = [\theta_1, \dots, \theta_2]^T$ is a point on the search domain and θ_m^i is the m^{th} component of the i^{th} bacterium position

The cell also repels a nearby cell in the sense that it consumes nearby nutrients and it is not physically possible to have two cells at

the same location. To model this, let $h_{repellent}$ be the height of the repellent effect (magnitude of its effect) and $w_{repellent}$ be a measure of the width of the repellent. Similarly, if the repelling relationship among bacteria is of Gaussian form, then the contribution of such effect to the cost function is given by

$$J_{cc_repel}(\theta, \theta^i(j, k, \ell)) = \sum_i^S \left[h_{repellent} \exp\left(-w_{repellent}(\theta_m - \theta_m^i)^2\right) \right] \quad (4)$$

The cell-to-cell attraction and repelling effects can be combined in one formula

$$J_{cc}(\theta, P(j, k, \ell)) = \sum_i^S J_{cc}^i(\theta, \theta^i(j, k, \ell)) = \sum_{i=1}^S \left[-d_{attract} \exp\left(-w_{attract} \sum_{m=1}^p (\theta_m - \theta_m^i)^2\right) \right] + \sum_{i=1}^S \left[h_{repellent} \exp\left(-w_{repellent} \sum_{m=1}^p (\theta_m - \theta_m^i)^2\right) \right] \quad (5)$$

The swarming effect is added to the cost function. Therefore, the i^{th} bacterium will hill-climb on

$$J(i, j, k, \ell) + J_{cc}(\theta, P) \quad (6)$$

so that the cells will try to find nutrients, avoid noxious substances, and try to move towards other cells, but not too close to them.

3.3 Reproduction

After N_c chemotactic steps a reproduction step is taken. Let N_{re} be the number of reproduction steps to be taken. Let $S_r = S/2$ be the number of population members who had sufficient nutrients so that they will reproduce (split in two) with no mutation.

For reproduction, the population is sorted in order of ascending accumulated cost (higher accumulated cost represents that it did not get as many nutrients during its lifetime of foraging and hence, is not as "healthy" and thus unlikely to reproduce); then S_r least

healthy bacteria die and the other S_r healthiest bacteria each split into two bacteria, which placed at the same location. This method rewards bacteria that have encountered a lot of nutrients, and allows us to keep a constant population size, which is convenient in coding the algorithm. The flowchart of Fig.(3.c) shows the steps of reproduction event .

3.4 Elimination –dispersal event

If N_{ed} is the number of elimination-dispersal events, each bacterium in the population is subjected to elimination-dispersal event with probability p_{ed} .

4. Dynamic Model of Pneumatic Actuator

Figure (4) shows the position controlled pneumatic system used in the simulations. From Fig.(4), the nonlinear mathematic model of a pneumatic system can be derived as [1,3,11].

$$M \ddot{x} + C \dot{x} + kx = A(P_p - P_n) \quad (7)$$

$$\dot{m}_p = \frac{V_p}{\gamma RT_s} \frac{dP_p}{dt} + \frac{P_p}{RT_s} \frac{dV_p}{dt} \quad (8)$$

$$\dot{m}_n = \frac{V_n}{\gamma RT_s} \frac{dP_n}{dt} + \frac{P_n}{RT_s} \frac{dV_n}{dt} \quad (9)$$

where M is the piston and the load mass, C is the air damping constant, k is the spring constant, A is the bore area, P_p is the pressure in chamber p, P_n is the pressure in chamber n, V_p is the air volume in chamber p, V_n is the air volume in chamber n, c is the ratio of specific heat, R is the universal gas constant, T is the operating temperature, \dot{m}_p is the mass flow rate into chamber p, and \dot{m}_n is the mass flow rate into chamber n.

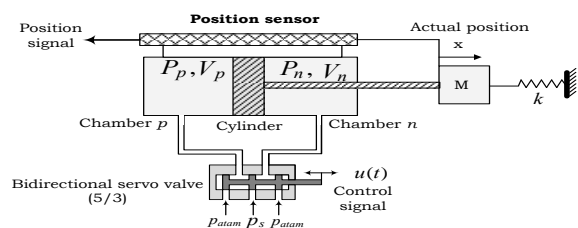
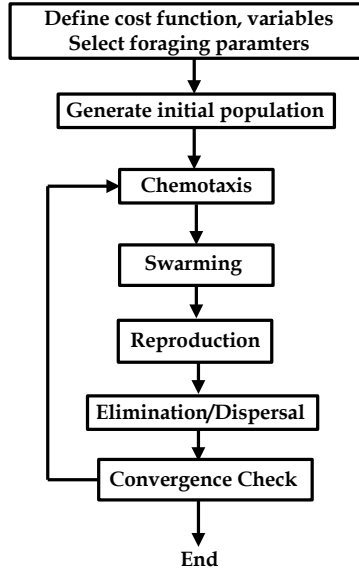
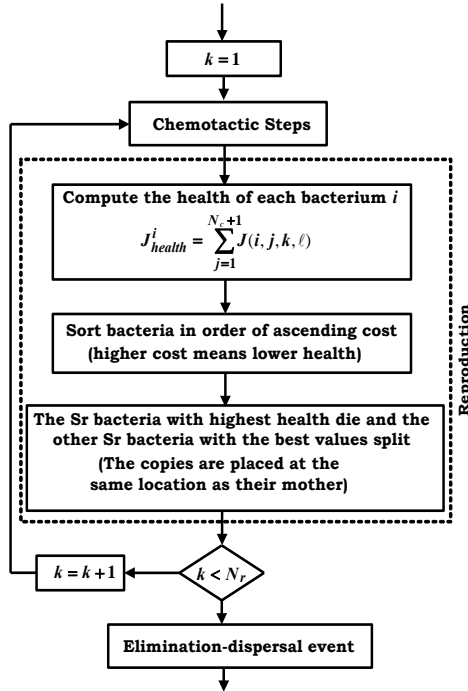


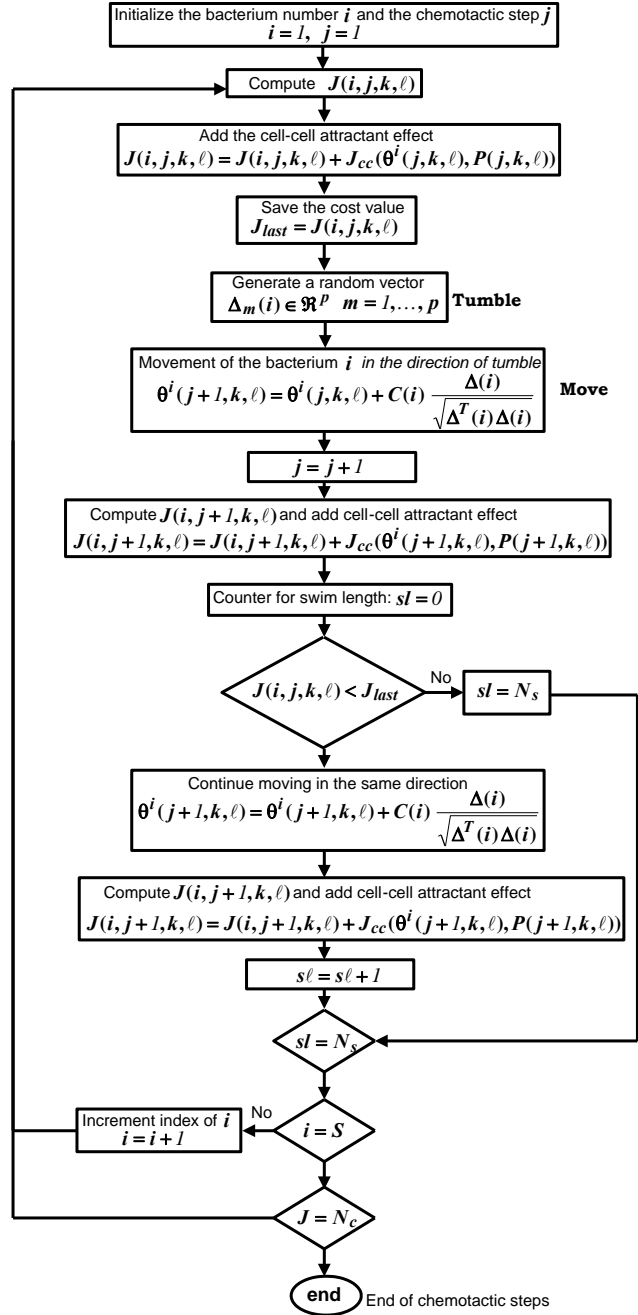
Figure (4) Position controlled pneumatic system



(a) Flow chart of foraging process



(c) Flow chart of reproduction steps



(b) Flow chart of chemotactic steps

Figure (3) (a) Flowchart of foraging process (b) Flowchart of chemotactic steps
(c) Flowchart of reproduction steps

To linearize the system, a small deviation from an initial equilibrium point is considered. Assume that at the equilibrium point, the values of the state variables are $x=0$, $P_p = P_{p0}$, $P_n = P_{n0}$, $V_p = V_{p0}$, $V_n = V_{n0}$. Thus, Eq. (7)–(9) can be rewritten as [1]

$$\Delta \dot{m}_p = \frac{\Delta V_{p0}}{\gamma R T_s} \Delta \dot{P}_p + \frac{P_{p0}}{R T_s} \Delta \dot{V}_p \quad (10)$$

$$\Delta \dot{m}_n = \frac{\Delta V_{n0}}{\gamma R T_s} \Delta \dot{P}_n + \frac{P_{n0}}{R T_s} \Delta \dot{V}_n \quad (11)$$

$$M \Delta \ddot{x} + C \Delta \dot{x} + k \Delta x = A (\Delta P_p - \Delta P_n) \quad (12)$$

Where Δ denotes the small deviation value. If the proportional flow control valve is used, the input valve voltage is proportional to the airflow rate. Assume that mass flow rate is identical in both chambers and displacement of the spool valve is proportional to the valve voltage. Then relation between the input voltage deviation and the flow rate deviation can be written as [1]

$$\Delta \dot{m}_p = K \Delta u, \quad \Delta \dot{m}_n = -K \Delta u \quad (13)$$

By simple volume equation,

$$\Delta \dot{V}_p = A \Delta \dot{x}, \quad \Delta \dot{V}_n = -A \Delta \dot{x} \quad (14)$$

Substitute Eqs.(13) and (14) into Eqs.(10) and (11) and rearrange the equations, the following equations are obtained

$$\Delta \dot{P}_p = -\frac{\gamma A P_{po}}{V_{po}} \Delta \dot{x} + K \frac{\gamma R T}{V_{po}} \Delta u \quad (15)$$

$$\Delta \dot{P}_n = \frac{\gamma A P_{no}}{V_{no}} \Delta \dot{x} - K \frac{\gamma R T}{V_{no}} \Delta u \quad (16)$$

Rearrange Eq. (12), the motion equation then becomes

$$\Delta \ddot{x} = \frac{A}{M} (\Delta P_p - \Delta P_n) - \frac{C}{M} \Delta \dot{x} - \frac{k}{M} \Delta x \quad (17)$$

Assume the state variables vector of the form $x_s = [\Delta P_p \ \Delta P_n \ \Delta x \ \Delta \dot{x}]$, then Eqs.(15)–(17) are then represented in a state-space form,

$$\left. \begin{aligned} \dot{x}_s &= A_s x_s + B_s u \\ y &= C_s x_s \end{aligned} \right\} \quad (18)$$

where

$$A_s = \begin{bmatrix} 0 & 0 & 0 & (-\gamma A P_{po}/V_{po}) \\ 0 & 0 & 0 & (\gamma A P_{no}/V_{no}) \\ 0 & 0 & 0 & 1 \\ (A/M) & (-A/M) & (-k/M) & -C/M \end{bmatrix}$$

$$B_s = \begin{bmatrix} (\gamma K R T/V_{po}) \\ -(\gamma K R T/V_{no}) \\ 0 \\ 0 \end{bmatrix}, \quad C_s = [0 \ 0 \ 1 \ 0].$$

5. E.coli Bacterial Swarm Foraging for Tuning PID controller

The structure of foraging-based PID controller is shown in Fig.(5). Each bacterium represents a solution of the problem and hence it consists of three terms: the first one is the k_p value, the second one

is the k_d value and the third one is k_I . Then the Bacterium vector is given by: Bacterium= $[k_p \ k_d \ k_I]$.

It must be noted here that the range of each gain must be specified, i.e., $k_{p \min} \leq k_p \leq k_{p \max}$, $k_{d \min} \leq k_d \leq k_{d \max}$, $k_{I \min} \leq k_I \leq k_{I \max}$

The most crucial step in applying foraging is to choose the objective functions that are used to evaluate the cost of each bacterium. Some works use *performance indices* as the objective functions. Other works uses mean of the Squared Error (MSE), Integral of Time multiplied by Absolute Error (ITAE), Integral of Absolute Magnitude of the Error (IAE), and Integral of the Squared Error (ISE). In this work, ISE is used to minimize the error signal [12].

Foraging strategy starts with an initial population containing a number of bacteria where each one represents a solution of the problem which performance is evaluated by a cost function. The cost is evaluated after setting the values of controller elements from foraging process, then determining the instantaneous error of the closed-loop behavior. The cost value for a specified solution is the obtained by summing all the squared values of error over the settling time of system behaviour

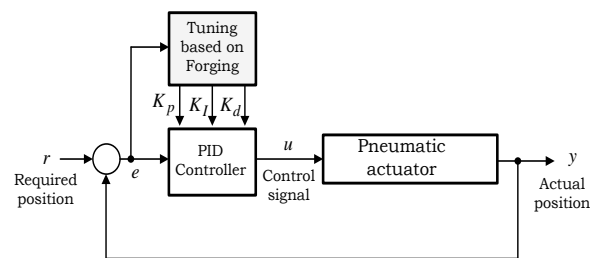


Figure (5) Block diagram of foraging-based Tuning of PID controller

During the search process, the foraging looks for the optimal setting of the PID position controller gains which minimizes the cost function. This function is considered as the evolution criteria for the foraging process.

6. Results

The parameters of foraging process used in the simulated results are listed in Table (2) (see the Appendix). The simulated results have been executed in Matlab package (R2008b) and the numerical solver of pneumatic system of equations is based on fourth-order Runge_Kutta with step size of $1e-4$ sec.

It is worth to note that each bacterium (at every chemotactic step) carries the solution of the three controller terms (K_p , K_d and K_I). Figure (6) shows the behaviors of bacteria solution (values of controller terms) with respect to chemotactic steps. One can see that these solutions are dispersed in the search domain at the first generation and then they converge to a specified region of values at the end of foraging events. Unfortunately, the solutions of all bacteria finally settle at two minimum regions. Actually, this could be attributed to low value of chemotactic steps ($N_c=20$); as the problem does not have sufficient chemotactic steps to find a global minimum. If the chemotactic steps have been increased to ($N_c=50$), all solutions could be reached to a region of global minimum. This is evident in Fig.(7).

Figures (6) and (7) also show the behavior of average cost with respect to chemotactic step. At each chemotactic step, the cost of each bacterium is calculated based on ISE criterion and then the average of all bacteria costs is taken. At every generation and the end of all chemotactic steps, S-solutions of controller terms are available to the controller. Therefore, one can obtain S-plots of closed-loop responses at each generation. At the end of all events, the S-final solutions would give the best values of controller parameters. Applying these final settings to controller parameters, refined S-plots of the closed-response could be obtained. One can see how well the closed-loop response could be improved over the generations of bacteria lives using this foraging process.

Figure (8) shows the behaviors of average cost variation as changing the probability value of elimination/dispersal event occurrence ($P_{ed}=0.1, 0.3, 0.4, 0.5$ and 0.6). The best average cost happens with $P_{ed}=0.1$ and the worse one is found with $P_{ed}=0.6$. One can argue that increasing the probability of elimination/dispersal occurrence would increase the probability of missing the best solutions with low costs and then those with high cost might dominate.

In Fig.(9), the reproduction number has been changed in steps $N_{re}=2,3$ and 6 . Of course, the result in figure is expected as the increasing of reproduction number occurrences would permit the population to attain newer best solutions (solutions with lower cost) and reject the worse ones. In other words, as the number of reproduction occurrences has been increased the promotion of best bacteria can be obtained.

Fixing the probability of elimination-/dispersal at low value ($P_{ed}=0.25$) and increase the number of such event repetitions would permit a few solutions to leave the region of swarming and try to search a newer region at which the cost might be lower (regions with high concentration of nutrients). If happens that such few solution find a lower cost region, then the whole bacteria (solutions) would jump at this new tract.

It is seen from Fig.(10) that increasing the number of elimination/dispersal occurrence would improve the solutions toward a lower cost levels.

Figure (11) shows that lengthening the time interval of bacteria searching (when they are on the gradient) at every chemotactic step has an adverse effect on the average cost. Three values of swim length have been chosen ($N_s=8, 6$ and 5). It is clear from the figure that $N_s=5$ won the best setting that gives the minimum cost average. One can argue that the relation between the cost function and the swim length is dependent on

the considered application. In the present situation, it is expected that the valley of global minimum is of steep edges such that long swim would tend to lead the solution out of the valley minimum; i.e., swimming through its minimum without stopping.

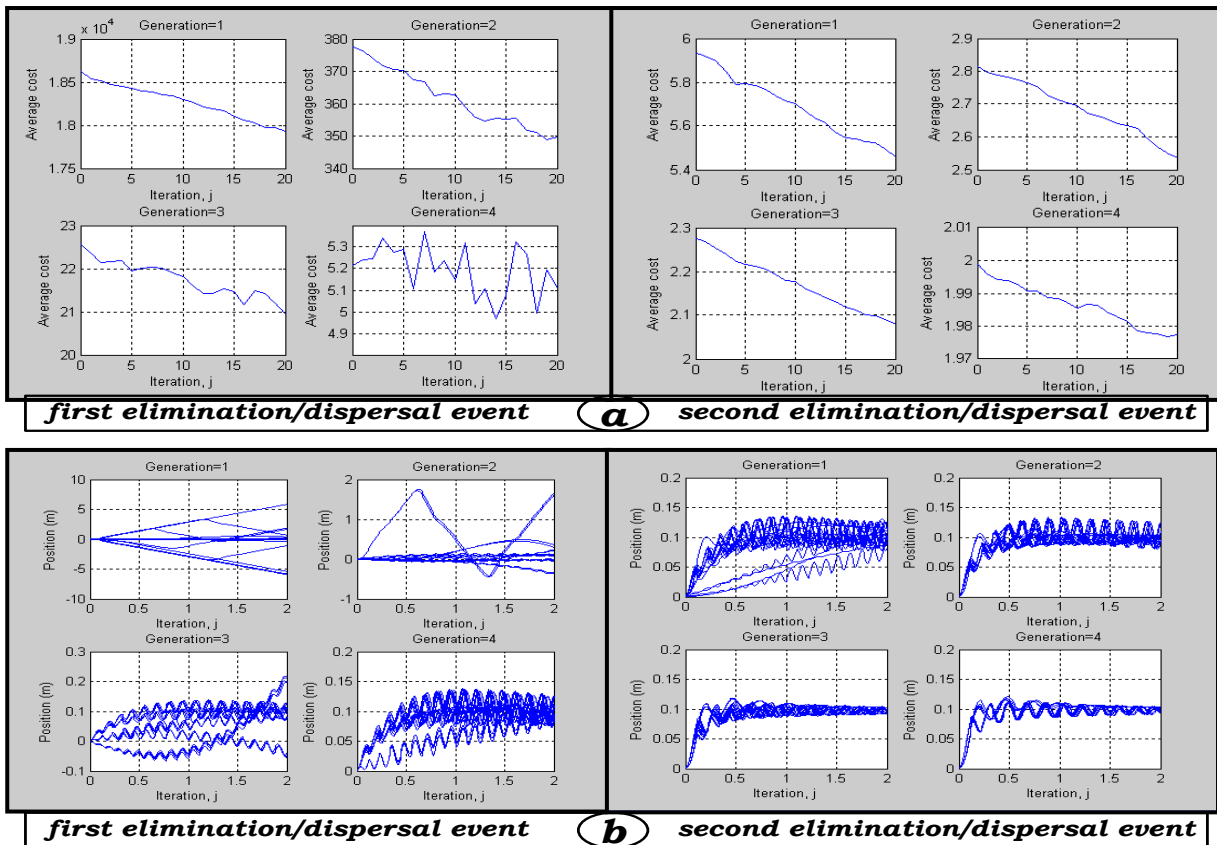
In Fig. (12), the chemotactic steps (per bacteria life time) has been changed at $N_c = 25, 50$ and 75 . For the considered pneumatic problem, it is found that setting $N_c = 50$ show the lowest average cost behavior. Therefore, $N_c = 50$ has been set for all simulations.

7. Conclusion

Based on the above simulated results, the following points could be highlighted:

1. The E. coli optimization model could successively find the sub-optimal values of PID controller which gives the best responses for the pneumatic position control.

2. Increasing the number of chemotactic steps would increase the time required for searching the global minimum. This of course would grant the optimization method a higher chance to lump their solutions at a global minimum.
3. The selection of the probability value of elimination/dispersal event occurrence is problem dependent. In the present pneumatic system, the reaching to the global solution requires a low probability value of this event. Higher value could throw the best solutions away from global minimum and leads to instability problems. However, different system may require different setting of this value.
4. Increasing the reproduction number would enhance the cost measure; as the foraging process could catch new best solutions and repel the worst ones.
5. Increasing the number of elimination/dispersal occurrence would improve the solutions toward a lower cost levels.



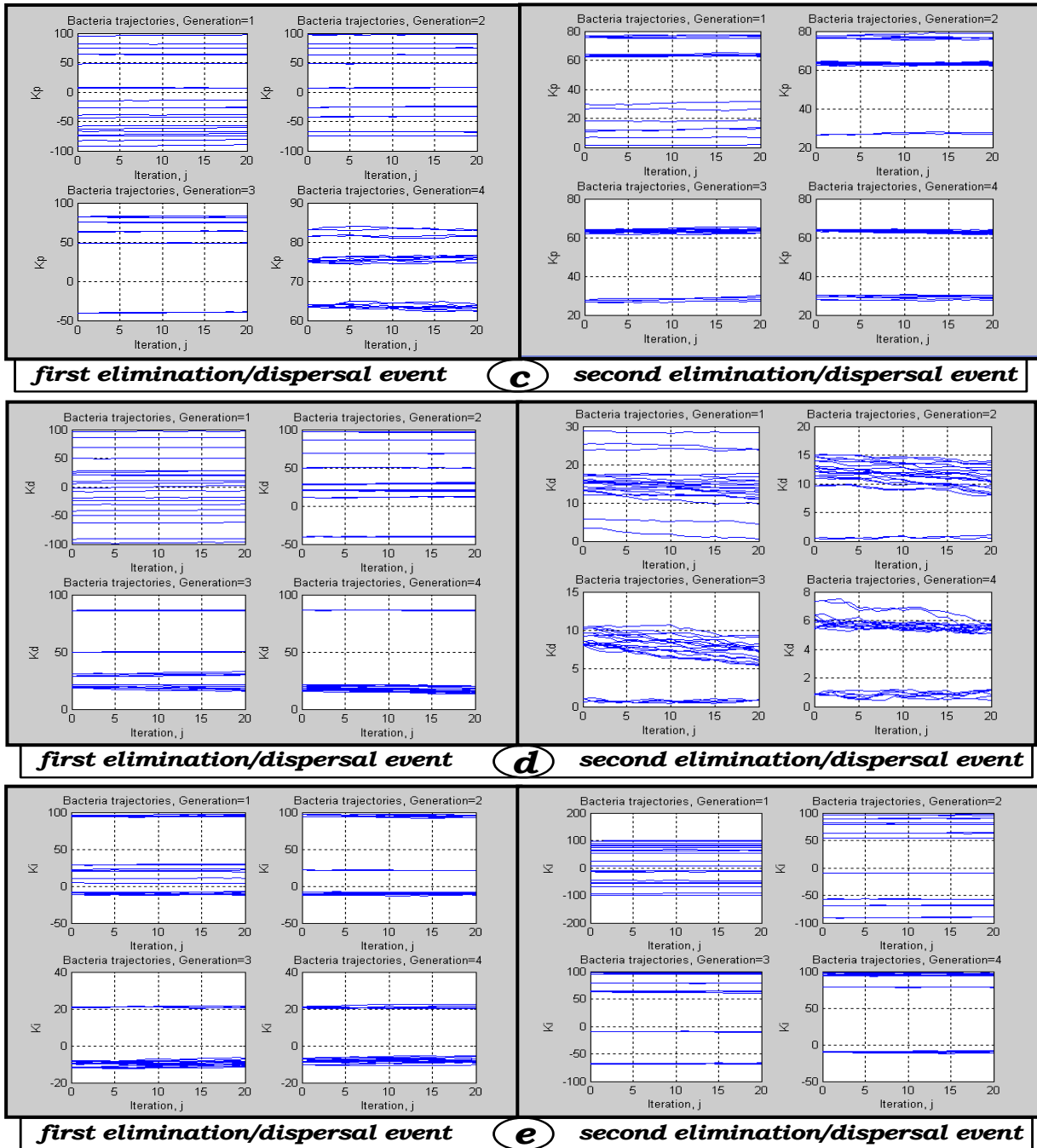
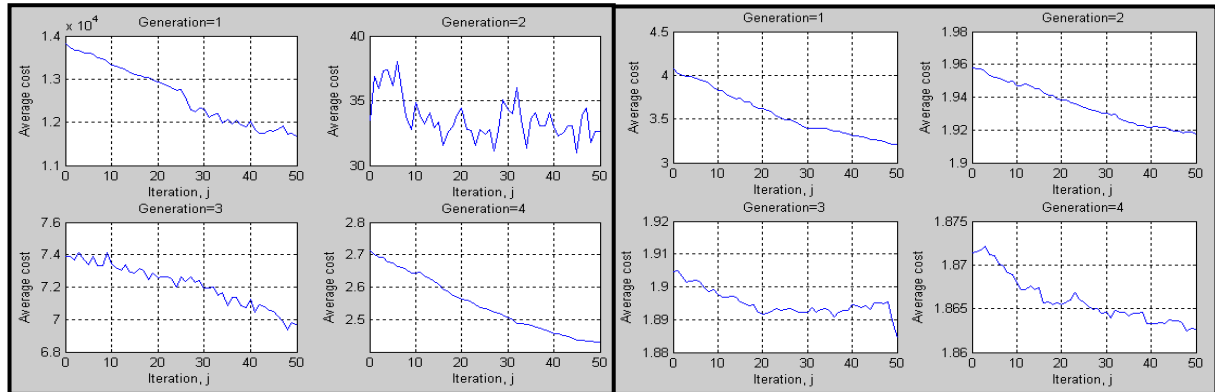
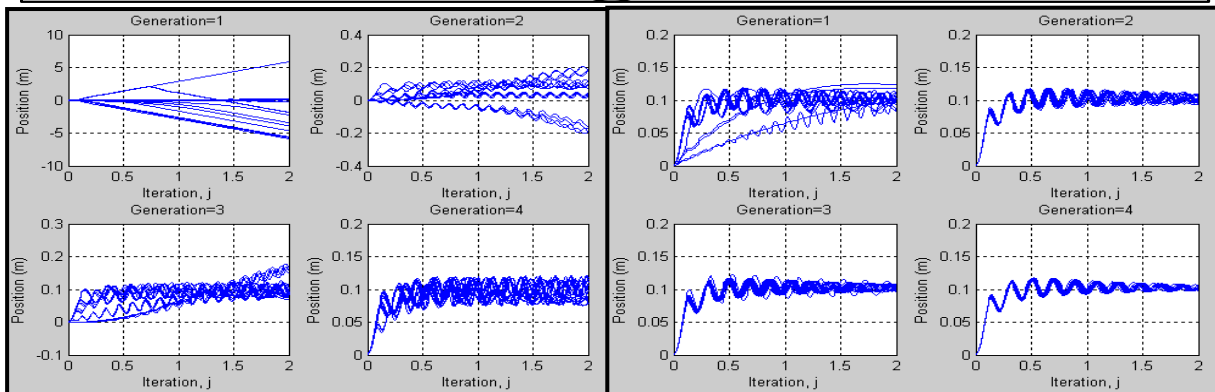


Figure (6) (a) behavior of cost function, (b) position time responses, (c, d, e) behaviors of the PID controller elements over life time of bacteria behavior

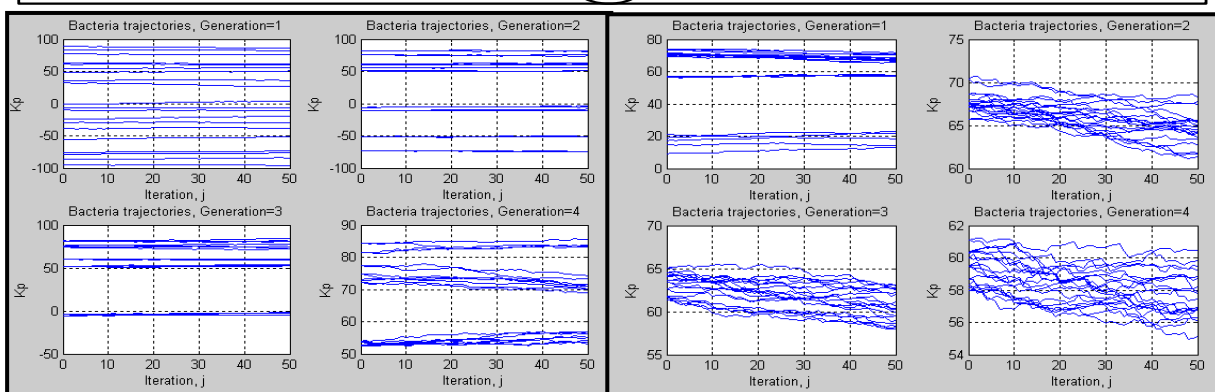
6. Increasing the length of chemotactic steps may have an adverse effect on finding the global solution. The lengthy time may lead the solution to a region beyond the best one and then the global minimum would be lost. Therefore, the setting of this value is problem dependent and it depends on the system complexity and behavior near a global minimum.



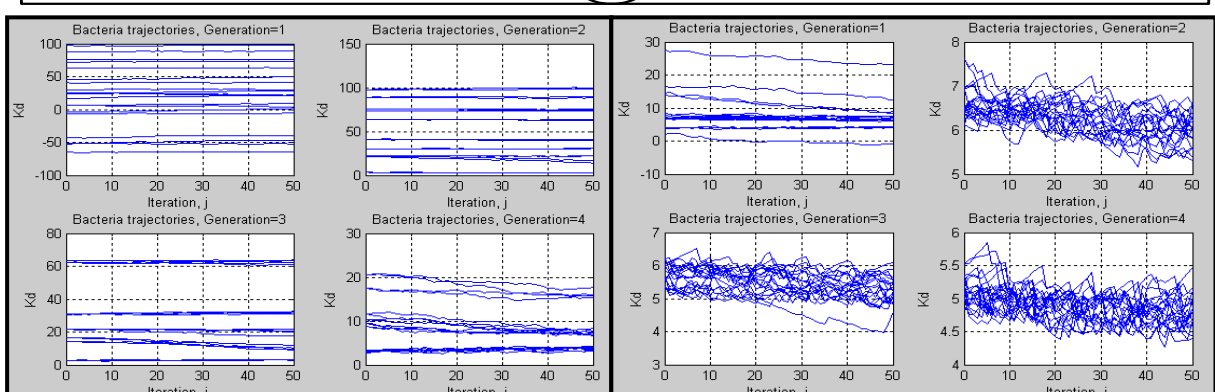
first elimination/dispersal event (a) **second elimination/dispersal event**



first elimination/dispersal event (b) **second elimination/dispersal event**



first elimination/dispersal event (c) **second elimination/dispersal event**



first elimination/dispersal event (d) **second elimination/dispersal event**

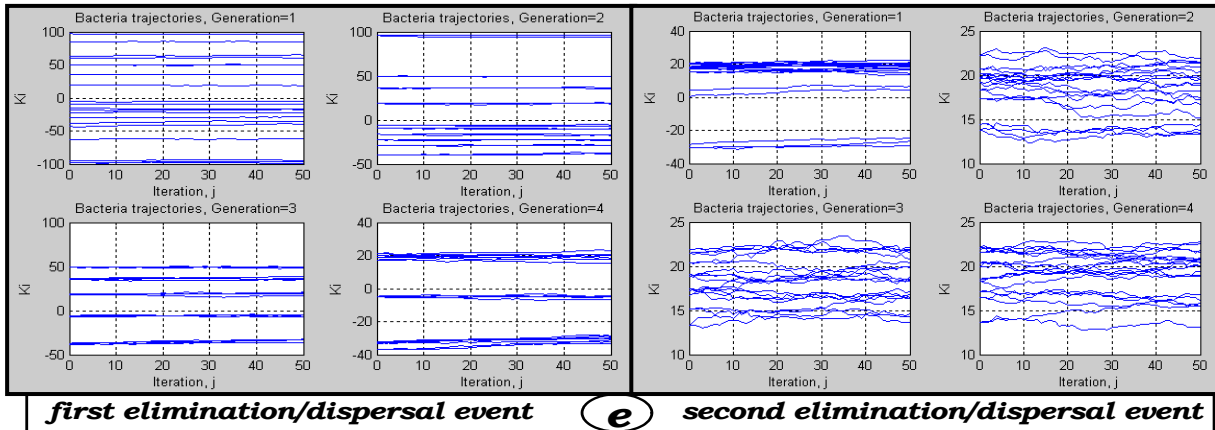


Figure (7) (a) behavior of cost function, (b) position time responses, (c, d, e) behaviors of the PID controller elements over life time of bacteria behavior

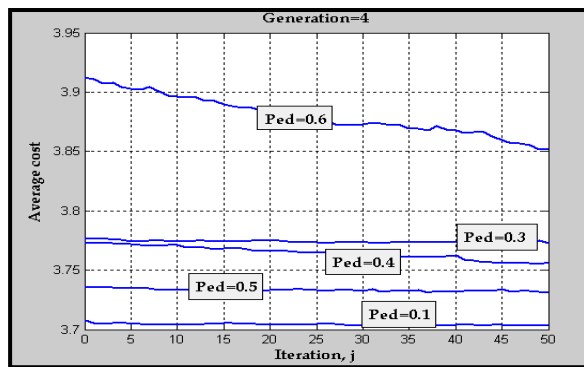


Figure (8) Variation of probability of elimination and dispersal occurrence

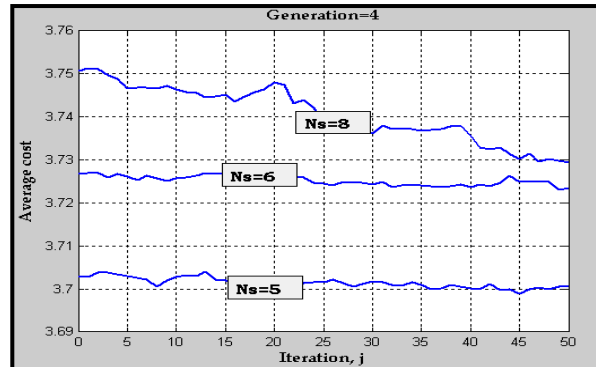


Figure (11) Change the swim length

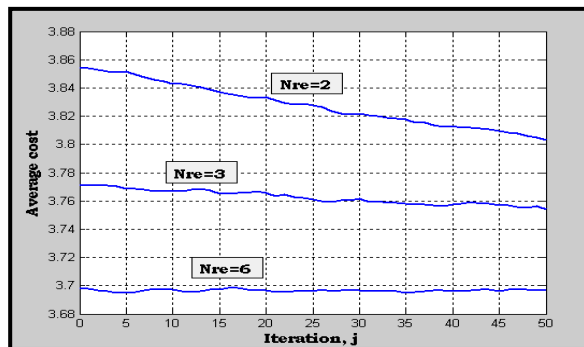


Figure (9) Change the number of reproduction steps

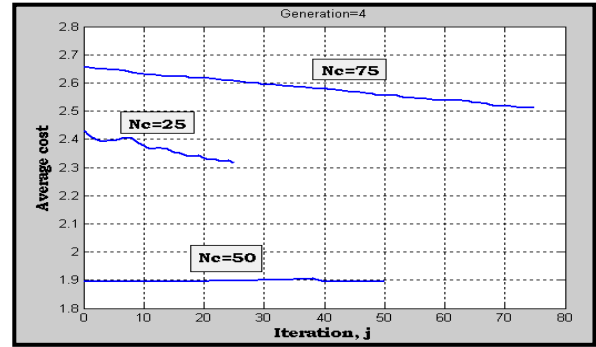


Figure (12) Change the number of chemotactic steps (per bacteria lifetime)

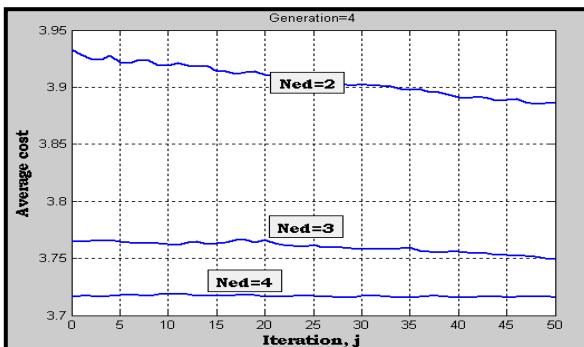


Figure (10) Change the number occurrence of elimination/dispersal events

References:

[1] S. Kaitwanidvilai, M. Parnichkun, "Force control in a pneumatic system using hybrid adaptive neuro-fuzzy model reference control," ELSEVIER, Mechatronics, vol. 15, pp 24-41, 2004.
 [2] B. W. Surgenor, N. D. Vaughan, "Continuous sliding mode control of a pneumatic actuator," Transaction of the ASME, Vol. 119, pp24-41, 2004.

- [3] Hipòlit M., "Control of a Pneumatic Servo-system Using Fuzzy Logic," Proc. of 1st FPNI-PhD Symp. Hamburg, pp. 189-201, 2000.
- [4] Karl J. Astrom and Tore Hagglund, "PID Controllers: Theory, Design and Tuning," Instrument Society of America, 1995.
- [5] DingyuXue, R. Losick and D. Kaiser, "Linear Feedback Control", Society for Industrial and Applied Mathematics, 2007.
- [6] Kyoungkwan AHN, Janghwan HYUN, "Optimization of double loop control parameters for a variable displacement hydraulic motor by genetic algorithms," JMSE, Series C, Vol. 48, No.1, 2005.
- [7] Kavin M. Passino, "Biomimicry for Optimization, Control, and Automation," Springer-Verlag, London, 2005.
- [8] T. Audesirk and G. Audesirk, "Biology: Life on Earth," Prentice Hall, NJ, 5 edition, 1999.
- [9] [9] B. Alberts, D. Bray, J. Lewis, M. Raff, K. Roberts, and J.D.Watson, "Molecular Biology of the Cell," Garland Publishing, NY, 2nd edition, 1989.
- [10] M.T. Madigan, J.M. Martinko, and J. Parker, "Biology of Micro-organisms," Prentice Hall, NJ, 8 edition, 1997.
- [11] Andersen, B., "The Analysis and Design of Pneumatic Systems," New York, John Wiley & Sons, Inc., 1967.
- [12] K. Ogata, "Modern Control Engineering," Prentice-Hall, Inc., 1997.

Appendix

Table (1) lists the system parameters and coefficients, while Table (2) gives the values of various conditions used in the simulated results.

Table (1): Parameters definition and values [1]

Parameter Definition	Value
Temperature (T)	300 K
Ratio of specific heat (γ)	1.4
Air damping coefficient (C)	5 N/m^2
Universal gas constant (R)	287
Proportional valve constant (K)	0.00233 kg/s
Spring constant (k)	20 N/m
Normal pressure in chamber p (P_{po})	$3 \times 10^5 \text{ Pa}$
Normal pressure in chamber n (P_{no})	$3 \times 10^5 \text{ Pa}$
Normal pressure in chamber p (V_{po})	$20 \times 10^{-3} \text{ m}^3$
Normal pressure in chamber n (V_{no})	$20 \times 10^{-3} \text{ m}^3$
Bore area (A)	$2 \times 10^{-3} \text{ m}^2$
Piston mass M	0.4 kg
Supply pressure P_s	400 kPa
Atmosphere pressure (P_{atm})	100 kPa

Table (2): Foraging parameters used in simulations

Parameter Definition	Fig.6	Fig. 7	Fig. 8	Fig.9	Fig.10	Fig.11	Fig. 12
Number of bacteria in the population (S)	20	20	20	40	40	40	40
The length of swim (Ns)	4	4	4	4	4	Var.	4
Number of reproduction steps (Nre)	4	4	4	4	Var.	4	4
Number of chemotactic step (Nc)	20	50	Var.	50	50	50	50
Number of elimination/dispersal events (Ned)	2	2	2	Var.	2	2	2
Number of bacteria splits per generation (Sr)	10	10	10	20	20	20	20
Probability of dispersal occurrence (Ped)	0.25	0.25	0.25	0.25	0.25	0.25	Var.
Height of repellent effect ($h_{rep.}$)	0.1	0.1	0.1	0.1	0.1	0.1	0.1
Width of repellent effect ($w_{rep.}$)	10	10	10	10	10	10	10
Width of attractant effect ($w_{attr.}$)	0.2	0.2	0.2	0.2	0.2	0.2	0.2
Width of attractant effect ($d_{attr.}$)	0.1	0.1	0.1	0.1	0.1	0.1	0.1

TUNING MODEL REFERENCE ADAPTIVE CONTROLLER FOR AVR OF SYNCHRONOUS GENERATOR

Dr. Abdulrahim Thiab Humod

Electrical and Electronic Engineering Department, University of Technology.

abdulrahimhumod@yahoo.com

Abstract

A Tuning Model Reference Adaptive Controller (TMRAC) for a synchronous generator is presented in this paper. The controller performs the function of terminal voltage of the machine. The proposed controller is used to overcome the problems of nonlinearities and parametric uncertainties for Synchronous Generator (SG). The results verify improved performance of TMRAC comparing to conventional Automatic Voltage Regulator (AVR) under various operating conditions.

Keyword: *Mode Reference Adaptive Controller, synchronous generator, Automatic Voltage Regulator (AVR)*

1. Introduction

Synchronous generators are responsible for the bulk of the electrical power generated in the world today. The voltage stability and power quality of the electrical system depend on proper operation of AVR. Synchronous generator excitation control is one of the most important measures to enhance power system stability and to guarantee the quality of electrical power it provides. The main control function of the excitation system is to regulate the generator terminal voltage which is accomplished by adjusting the field voltage with respect to the variation of the terminal voltage [1]. Synchronous Generator in a power system is a non-linear and fast acting which are continuously subjected to load variations [2,3]. Nowadays, Design technology of AVR is being broadly improved. Nonlinearities and parametric uncertainties are unavoidable problem faced in controlling the output voltage of SG when

working alone or with others. Fig (1) shows a block diagram of SG and AVR system [4].

Conventional linear controllers for the synchronous generator consist of the AVR to maintain constant terminal voltage and the turbine governor to maintain constant speed and power at some set point. They are designed to control, in some optimal fashion, the generator around one particular operating point; and at any other point the generator's damping performance is degraded [5].

A number of new control theories and methods have been introduced to design high performance excitation controllers to deal with the problem of transient stability for nonlinear synchronous generator models. Among them the Lyapunov method, singular perturbation methods, feedback linearization and sliding mode control, linear optimal control, the adaptive control method associated with neuro technique, the fuzzy logic control theory [2,6].

The proposed controller in this paper is TMRAC [7]. It is used to design an AVR for a non-linear and fast acting synchronous generators which is subjected to continuously load variations. the controller parameter tuned according to their effect on the rise time, peak over shoot and steady state response where each parameter is examined separately and Parameter are adjusted to overcome their drift. The voltage stability is obtained even though the plant mathematical model is unknown.

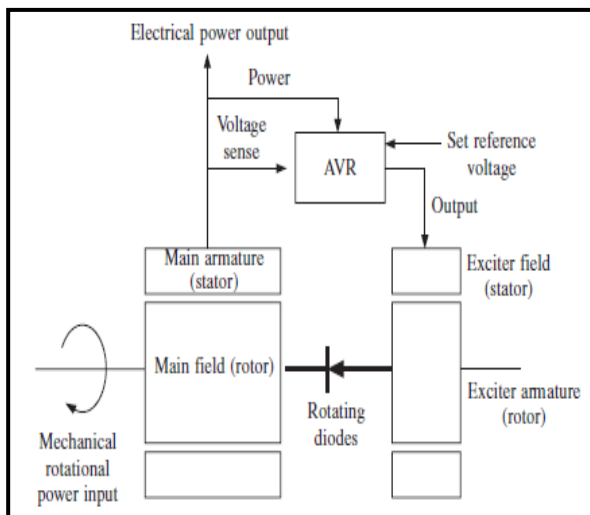


Fig (1) Block diagram of a synchronous generator and AVR

2. Model Reference Adaptive Controller (MRAC)

The MRAS is one of the main approaches to adaptive control. The desired performance can be expressed in term of a reference model. The system consists of two loops. An inner loop, which is an ordinary feedback loop, composed of the plant and the regulator. The parameters of the regulator are adjusted by the outer loop in such away that the error between the plant output and the model output becomes small. The outer loop is thus also a regulator loop. The problem is to determine the adjustment mechanism which brings the error to zero for all command signals. The block diagram of the MRAC is shown in Figure (2).

A single-input single-output system, which may be either a continuous time or a discrete time model, is given by[8]

$$y(t) = \frac{B_p}{A_p} u(t) \quad (1)$$

where $\deg(A_p) \geq \deg(B_p)$

Where u is the control signal and y is the output signal. The symbols A_p and B_p denote polynomials in differential operator. The polynomial A_p assumed to be monic

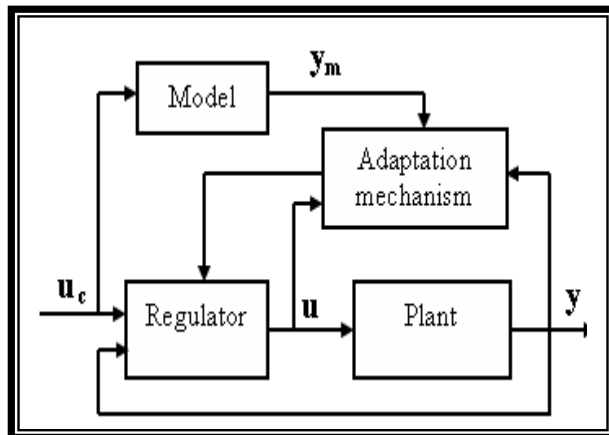


Figure (2) Block Diagram of MRAC [8]

(the first coefficient is unity). The regulator can be found according to the relation between command signal u_c and the desired output signal y_m as

$$y_m(t) = \frac{B_m}{A_m} u_c(t) \quad (2)$$

A general linear control law is

$$R u = T u_c - G y \quad (3)$$

Where R , T and G are polynomials. Figure (3) shows the regulator block diagram.

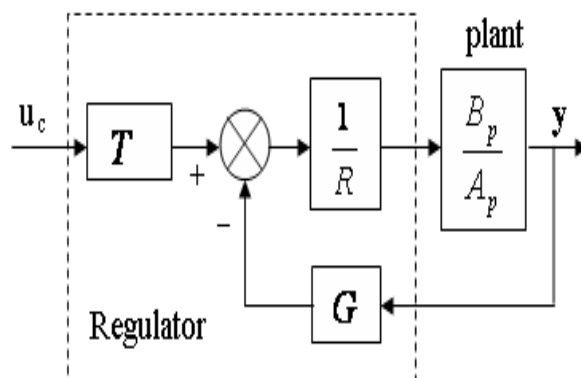


Figure (3): Regulator Block Diagram

$$A_p R + B_p G = B^+ A_0 A_m \quad (4)$$

where A_m is the desired model poles, A_0 is the observer poles (they must have faster

The electrical model of the machine is

$$V_d = R_s i_d + \frac{d}{dt} \varphi_d - \omega_R \varphi_q \quad (13)$$

Where $\varphi_d = L_d i_d + L_{md} (i'_{fd} + i'_{kd})$ and

$$\varphi_q = L_q i_q + L_{mq} i'_{kq}$$

$$V_q = R_s i_q + \frac{d}{dt} \varphi_q + \omega_R \varphi_d \quad (14)$$

$$V'_{fd} = R'_{fd} i'_{fd} + \frac{d}{dt} \varphi'_{fd} \quad (15)$$

Where $\varphi'_{fd} = L'_{fd} i'_{fd} + L_{md} (i_d + i'_{kd})$

$$V'_{kd} = R'_{kd} i'_{kd} + \frac{d}{dt} \varphi'_{kd} \quad (16)$$

Where $\varphi'_{kd} = L'_{kd} i'_{kd} + L_{md} (i_d + i'_{fd})$

$$V'_{kq1} = R'_{kq1} i'_{kq1} + \frac{d}{dt} \varphi'_{kq1} \quad (17)$$

Where $\varphi'_{kq1} = L'_{kq1} i'_{kq1} + L_{mq} i_q$

$$V'_{kq2} = R'_{kq2} i'_{kq2} + \frac{d}{dt} \varphi'_{kq2} \quad (18)$$

Where $\varphi'_{kq2} = L'_{kq2} i'_{kq2} + L_{mq} i_q$

The saturation non linearity can be added to the synchronous generator model by activate the saturation of field current in MATLAB / Simulink program.

4. Determination of Controller Parameters

For the plant has exact mathematical model the controller parameters can be obtained directly by applying equations 4 and 5. But the controller parameters for Synchronous Generator which has nonlinearities and parametric uncertainties can not found directly from equations 4 and 5. The parameters of regulator can be determined as follows

- (1) Set all parameters of the regulator and adaptation gain (γ) to zero.

- (2) Applying test signal to the system (plant and the controller) and observe the response.
- (3) Set an arbitrary value for last coefficient for polynomial T(s) of the regulator parameters then record its effect on the response, change its value until good results obtained.
- (4) Repeat step 3 for other coefficients of polynomial T(s) consequently until the first coefficient.
- (5) Repeat step 3 and 4 for polynomial R(s) and G(s) consequently.

5. Simulation and Results

The AVR for SG with saturation effect of exciter is designed and implemented using the conventional PID and TMRAC which are shown in figures (5 and 6) respectively, and the parameter for SG used in the simulation are shown in table (1).

The study of the regulator parameters

$$T(s) = t_0 s^2 + t_1 s + t_2 ,$$

$$R(s) = s + r_1 \quad \text{and}$$

$$G(s) = g_0 s^2 + g_1 s + g_2$$

effect on the transient and steady state response of SG with zero adaptation gain can be done by applying Simulink program shown in figure(6).

- t₂**: Increase the value of this parameter will tend to decrease the rise time and increase the steady state level as shown in figure (7). Figure (7) shows the responses of different values of parameter t₂ with the present of exciter saturation (upper limit=2 & lower limit=0) and all the other parameters of regulator are set to zero value.
- g₂**: Increase the value of this parameter will tend to decrease the steady state level as shown in figure (8). Figure (8) shows the responses of different values of parameter g₂ with the present of exciter saturation

(upper limit=2 & lower limit=0), parameter $t_2=1000$ and all other the parameters of regulator are set to zero value.

- g_1 : Increase the value of this parameter will tend to decrease the overshoot as shown in figure (9). Figure (9) shows the responses of different values of parameter g_1 with the present of exciter saturation (upper limit=2 & lower limit=0), parameter $t_2=1000$, parameter $g_2=900$, and all the other parameter of regulator are set to zero value.

From this study we observed the rest controller parameters (t_1 , t_0 , r_1 , and g_0) have no a valuable effect on the response. So they are not tuned and set to zero.

When the TMRAC examined with unit step input, second order reference model (0.7 damping ratio and 4 rad/second natural frequency), and exciter saturation (upper limit =2 & lower limit=0). The obtained results for different loads (heavy=1.9MVA, medium=1MVA, light=.1MVA) are according to the following cases:-

Case one with regulator parameters ($t_2=1000$, $g_2=900$, $g_1=250$, and $t_1=t_0=r_1=g_0=0$) and no adaptation (adaptation gain equal to zero) the obtained responses are depicted in figure (10), which shows good response only with medium load.

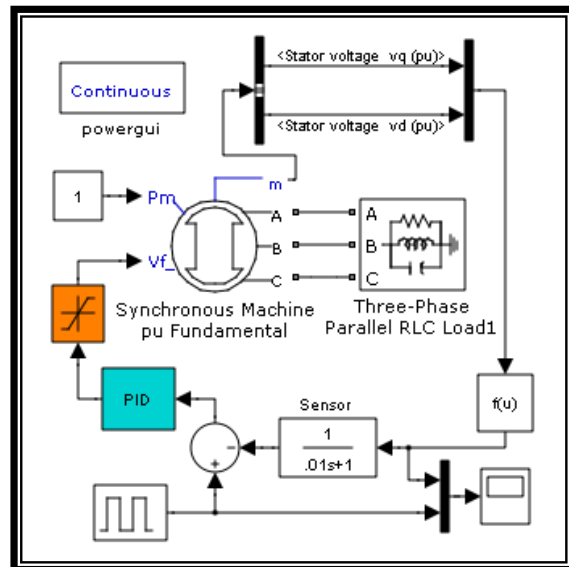
Case two with the same setting of regulator parameters as in case one and adaptation for dominant parameter g_2 (adaptation gain (γ) for parameter $g_2=120$ and the other parameters adaptation gain sated to zero). The obtained responses are shown in figure (11), which shows good responses for different loads. The adaptations of parameter g_2 for different loads are depicted in figure (12). It is clear from figure (12) the adaptation time approximately four second.

The conventional PID controller responses with same exciter saturation and loads are

shown in figure (13). The used gains for PID controller are (proportional =5, integral =4, derivative =0.001). Figure (13) shows high over shoot and large settling time compared with TMRAC for different loads.

Table (1) parameter of SG from Matlab R2008a

Rated Power	KVA	2000
Rated voltage	V(L-L)	400
Rated frequency	HZ	50
stator resistance	pu	.0095
Stator inductance	pu	0.05
Quadrature mutual ind.pu		1.51
direct mutual ind.pu		2.06
Field resistance	pu	.001971
Field inductance	pu	.3418
Damper resistance	pu	.2013
Damper inductance	pu	2.139
Inertia coefficient	pu	0.3072



Figure(5) PID simulink program for SG with exciter saturation

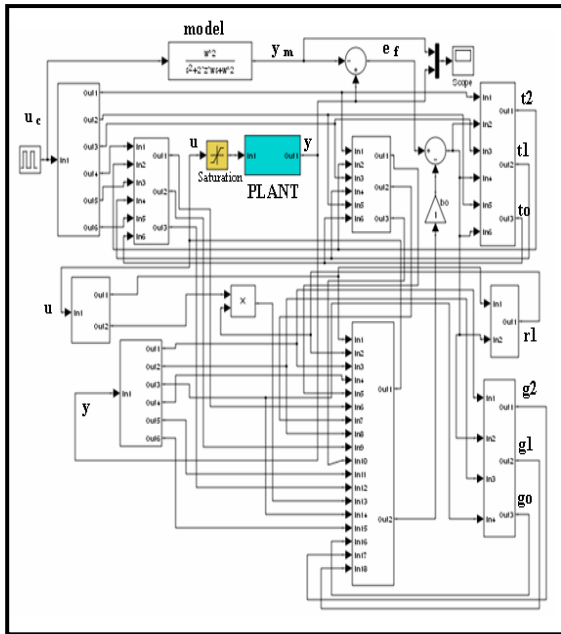


Figure (6): Simulink program of TMRAC for SG & saturation

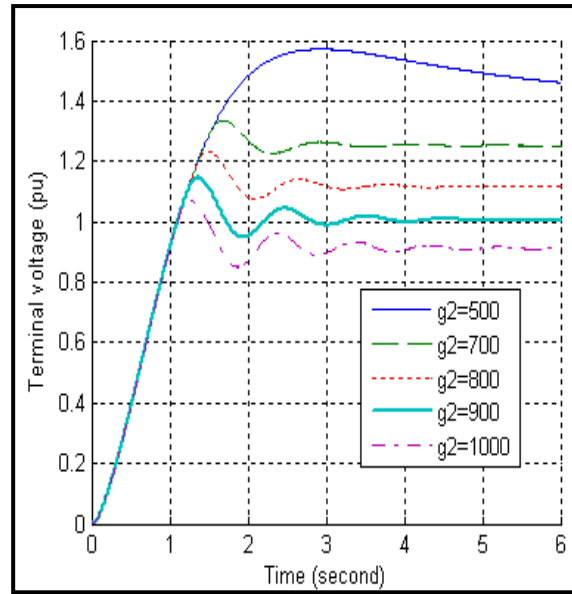


Figure (8): TMRAC response for parameters g_2 and $t_2=1000$

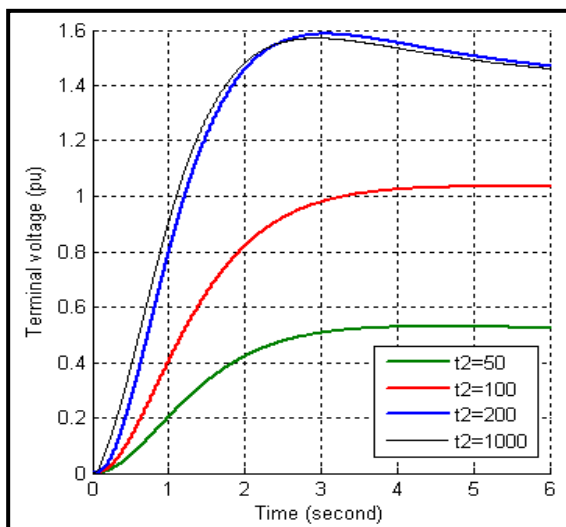


Figure (7): TMRAC response for t_2 parameter when other parameters are zero

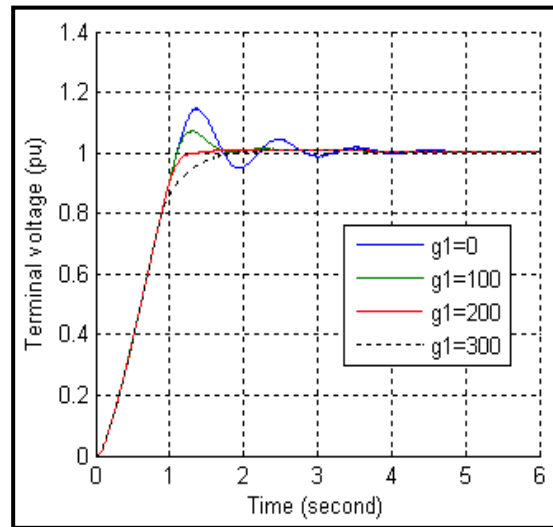


Figure (9): TMRAC responses for parameter g_1 , $g_2=900$ and $t_2=1000$

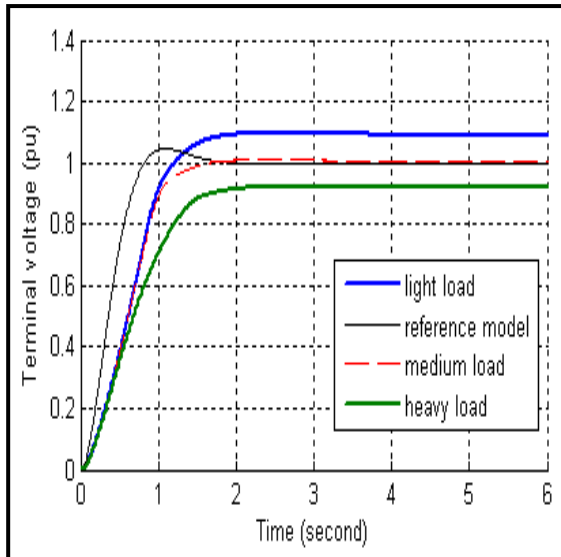


Figure (10): TMRAC response for different loads and adaptation gain=0 (no adaptation)

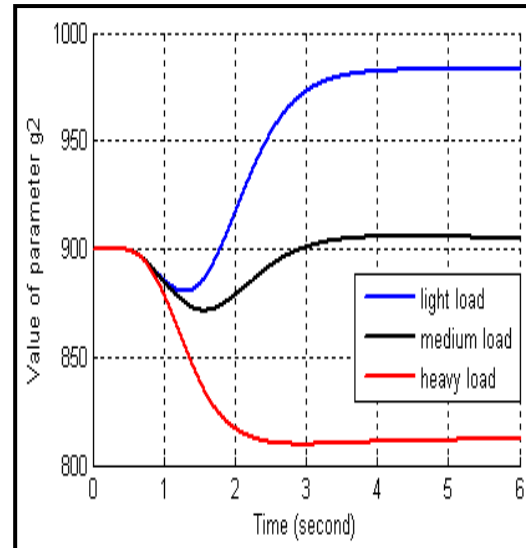


Figure (12): the adaptation of parameter g_2 for different loads

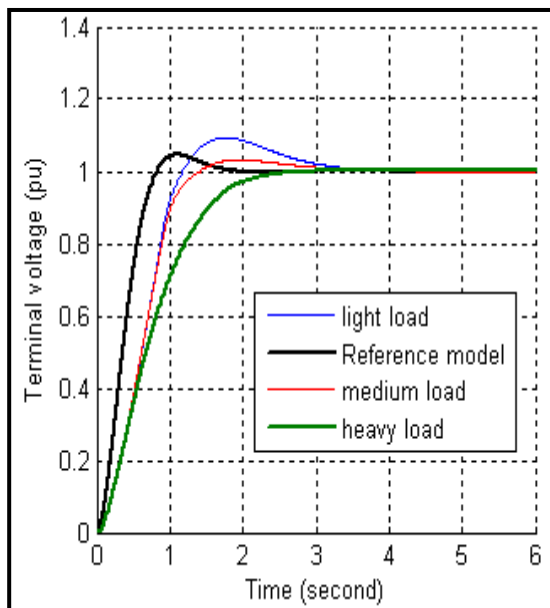


Figure (11): TMRAC response for different loads with adaptation gain of $g_2=120$

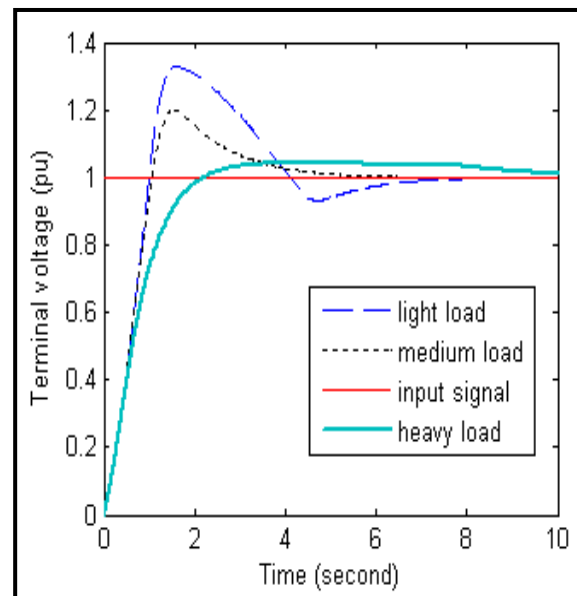


Figure (13): PID response for different loads

6. Conclusions

The design parameters of adaptive control have been investigated via several simulations. The results of this study can be summarized as follows:

1. With the novel approach, asymptotically stable response is achieved even though the plant with unknown dynamic equations of physical system.
2. The regulator parameters can be tuned without adaptation (adaptation gain =0) until the response approximately reach the reference model.
3. After adaptation mechanism works, the response will be very close to the reference model.
4. Only the dominant regulator parameters can be used.
5. The adaptation mechanism can be used for only one parameter.
6. The implementation of TMRAC used in this work is simple because of reduction in regulator parameters and the number of dominant parameters having adaptation.
7. The TMRAC has better response than conventional PID controller for the different loads.
8. The contributions obtained from this work are the adaptation mechanism for only one parameter and only the dominant regulator parameters can be used in the TMRAC.

References

- [1] Alireza S. (2006) "A PI Controller Based on Gain-Scheduling for Synchronous Generator" *Turk J ElecEngin*, VOL.14, NO.2.
- [2] Youping F., Yunping C., Shangsheng L., Dong L., and Yi. (2006) "Adaptive Control for Synchronous Generator Based on Pseudolinear Neural Networks" J. Wang et al. (Eds.): ISBN 2006, LNCS 3972, pp. 1348 – 1353. © Springer-Verlag Berlin Heidelberg 2006
- [3] Ndubisi S. N. (2008) "A Fuzzy Model Reference Learning Controller for Synchronous Generator Terminal Voltage Control" *European Journal of Scientific Research* ISSN 1450-216X Vol.24 No.3. (pp.378-386© EuroJournals Publishing, Inc. 2008 <http://www.eurojournals.com/ejsr.htm>)
- [4] Cirstea, M. N., Dinu ,A., Khor J. G., Cormick, M. M., (2002) "Neural and Fuzzy Logic Control of Drives and Power Systems", Linacre House, JordanHill,.
- [5] Jung-Wook P., Ronald G. H., and Ganesh K. V. (2003)"Adaptive-Critic-Based Optimal Neurocontrol for Synchronous Generators in a Power System Using MLP/RBF Neural Networks" *IEEE TRANSACTIONS ON INDUSTRY APPLICATIONS*, VOL. 39, NO. 5, SEPTEMBER/OCTOBER 1529.
- [6] Salem M. M., Zaki A. M., Malik O. P. (2002) " REAL-TIME IMPLEMENTATION OF A NEURO-AVR FOR SYNCHRONOUS GENERATOR" 15th Triennial World Congress, Barcelona, Spain , Copyright © 2002 IFAC
- [7] Humod A. T. and Ameen N. M. (2010) " Tuning Controller for Induction Motor using Model Reference Adaptive Control" *Eng & Tech. Journal*, Vol.28,No.11.
- [8] Astrom K. J., Wittenmark B. (2002) "Adaptive Control", India.

TRANSIENT VOLTAGE STABILITY ENHANCEMENT USING FUZZY LOGIC CONTROLLER TECHNIQUES

Dr. Majli Nema Hawas
College of Electrical & Electronic
Techniques
nmajli@yahoo.com

Abdullah Yaseen Abbas, B.Sc.
College of Electrical & Electronic
Techniques
techwsg@yahoo.com

Abstract

This paper discusses the transient voltage stability of a synchronous generator at its bus in a power system with a detailed transient modeling for the generator after being subjected to a three phase fault, and designed a Takagi-Sugeno first order fuzzy logic controller with center of area defuzzification algorithm as a fuzzy logic controller based exciter to stabilize the terminal voltage and to damp its oscillations so to keep the generator under balanced working conditions. The proposed exciter can be easily modified by changing the steady state field voltage value to be applied to any other synchronous generator. This paper also used the integral of square error as an indicator of the terminal voltage stability and monitors all of the generator variables specially the rotor angle to see whether the generator will maintain synchronism or not after the occurrence of the fault.

Keywords: *Voltage stability, Fuzzy controller, Exciter, Integral of square error.*

List of symbols:

dV_{err} Change in error voltage.
 E_f The field excitation voltage on the stator side.
 E'_q, E'_d The stator voltages behind the transient reactances.
 $[f_{abc}]$ Any three phase (AC) quantities.
 $[f_{qdo}]$ The equivalent two phase (DC) quantities.

H Inertia constant.
 i_q, i_d The stator windings currents.
 λ Flux linkage.
 mmf Magneto-motive force.
 r_s The stator winding resistance.
 r_e, x_e The external line resistance and reactance respectively.
 T_{acc} The rotor accelerating torque.
 T_{em} The electro-mechanical torque developed.
 T_{mech} The input mechanical torque.
 T'_{qo}, T'_{do} Transient time constants, which represent the change in the field currents in response to a change in the excitation voltage.
 $[T_{qdo}(\theta)]$ The Park's transformation matrix with respect to angle(θ).
 V_{err} Error voltage.
 V_{qi}^r, V_{di}^r Infinite bus voltages referred to the rotor synchronously rotating frame.
 V_{qi}^s, V_{di}^s Infinite bus voltages referred to the stator synchronously rotating frame.
 ω_b The base electrical angular frequency.
 x_q, x_d The synchronous steady state reactances.
 x'_q, x'_d The synchronous transient reactances.
 δ Rotor angle.

List of abbreviations:

COA Center of area.
FLC Fuzzy logic controller.
ISE Integral of square error

1. Introduction:

Voltage stability refers to the ability of a power system to maintain steady voltages at all buses in the system under normal operating conditions and after being subjected to a disturbance from a given initial operating condition. According to the time frame of interest there are two main types of voltage instability that the power system may suffer during its operation which are long term voltage instability and transient or short term voltage instability [1].

The long term voltage instability caused by the inability of the power system to meet the demand for reactive power which will lead to voltage collapse in one or more buses, while the transient voltage instability occurs after the system being subjected to a disturbance followed by either slow or inappropriate control action from the controlling device which will lead to oscillations in the voltage and therefore oscillation in the active, reactive power and the rotor angle and as a subsequence loose of synchronism; in other words improving the transient voltage stability will also improve the rotor angle stability [2] [3].

The controller which will be discussed in this paper is the field windings exciter of a synchronous generator, because it is directly control the voltage magnitude and the reactive power injected to the system by the generator which is the primary source of reactive power in the system and to great extent responsible for maintaining a good voltage profile across the power system [4].

2. Synchronous machine transient modeling:

The case study system is shown in fig. 1 below which consists of one synchronous generator connected to an infinite bus by a short transmission line with r_e and x_e .

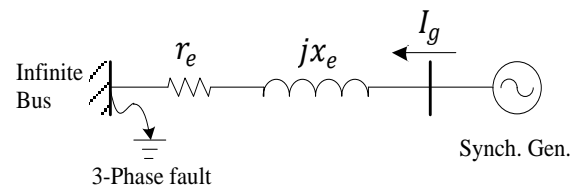


Fig. 1 Synchronous generator connected to infinite bus.

The Park's transformation or qdo transformation would be used to model the synchronous generator for two main reasons firstly to isolate the voltage control from the torque control and secondly is for sake of simplicity and reduction of calculations because it converts the three phase AC quantities into two phase DC equivalent quantities. The Park's transformation consists of two imaginary axes, the one to the north pole is the direct or d – axis, the quadrature or q – axis is defined in the direction 90 electrical degrees ahead of the direct axis. The field mmf will be along the d – axis, and the stator internal voltage, $d\lambda_{af}/dt$ will be along the q – axis. And it should be mentioned that the damping winding is not effective during the transient time interval therefore it won't be mentioned and also the changes in the stator $q d$ flux linkages will be neglected [5]; also the transient of x_q reactance will be ignored in equations 5.B, D_z eq., 6 and 8.B because its time constant is relatively small compared to x_d transient time constant, as an example for the simulated machine ($T'_{do} = 7.9 \text{ sec.}$) while ($T'_{qo} = 0.41 \text{ sec.}$; in which these times represent the effective time for each reactance [6].

The Park's transformation matrix and its inverse are shown below:

$$[T_{qdo}(\theta)] = \frac{2}{3} \begin{bmatrix} \cos \theta & \cos\left(\theta - \frac{2\pi}{3}\right) & \cos\left(\theta + \frac{2\pi}{3}\right) \\ \sin \theta & \sin\left(\theta - \frac{2\pi}{3}\right) & \sin\left(\theta + \frac{2\pi}{3}\right) \\ \frac{1}{2} & \frac{1}{2} & \frac{1}{2} \end{bmatrix} \quad (1.A)$$

$$[T_{qdo}(\theta)]^{-1} = \begin{bmatrix} \cos \theta & \sin \theta & 1 \\ \cos\left(\theta - \frac{2\pi}{3}\right) & \sin\left(\theta - \frac{2\pi}{3}\right) & 1 \\ \cos\left(\theta + \frac{2\pi}{3}\right) & \sin\left(\theta + \frac{2\pi}{3}\right) & 1 \end{bmatrix} \quad (1.B)$$

And they can be used to change the quantities from three phase to two phase representation and vice versa by using the following equations:

$$[f_{qdo}] = [T_{qdo}(\theta)] * [f_{abc}] \quad (2.A)$$

$$[f_{abc}] = [T_{qdo}(\theta)]^{-1} * [f_{qdo}] \quad (2.B)$$

Using the above equation (2) the infinite bus voltages will be referred to *qdo* axes of the stator synchronously rotating frame, then they will be transformed from the synchronously rotating frame of the stator to the one of the rotor by using the following equation (3):

$$\begin{bmatrix} V_{qi}^r \\ V_{di}^r \end{bmatrix} = \begin{bmatrix} \cos \delta & -\sin \delta \\ \sin \delta & \cos \delta \end{bmatrix} \begin{bmatrix} V_{qi}^s \\ V_{di}^s \end{bmatrix} \quad (3)$$

The synchronously rotating frame on the rotor will be the reference frame and all the variables will be transformed to it and calculated according to this assumption, and all the rotor quantities will be referred to the stator side by using the appropriate turns ratio [5]. By definition, the frequency of the infinite bus is constant at the synchronous value. With only one machine, it will be convenient for calculation purposes to select the phasor of the infinite bus voltage as the reference phasor and also the *q* – axis of the synchronously rotating reference frame. With this choice of synchronously rotating reference frame, V_{di}^r in the above equation will be identically zero.

The voltage behind the transient reactance (speed voltage) will be:

$$\frac{dE'_q}{dt} = \frac{1}{T_{do}} [E_f - (x_d - x'_d)i_d - E'_q] \quad (4.A)$$

$$\frac{dE'_d}{dt} = \frac{1}{T'_{qo}} [(x_q - x'_q)i_q - E'_d] \quad (4.B)$$

Thus the stator windings currents will be:

$$i_q = \frac{1}{D_z} [-(r_s + r_e)(V_{qi}^r - E'_q) - (x'_d + x_e)(V_{di}^r - E'_d)] \quad (5.A)$$

$$i_d = \frac{1}{D_z} [(x_q + x_e)(V_{qi}^r - E'_q) + (r_s + r_e)(V_{di}^r - E'_d)] \quad (5.B)$$

Where

$$D_z = (r_s + r_e)(r_s + r_e) + (x_q + x_e)(x'_d + x_e)$$

The electro-mechanical torque developed equation is:

$$T_{em} = E'_q i_q + E'_d i_d + i_d i_q (x_q - x'_d) \quad (6)$$

While the rotor accelerating torque equation will be:

$$T_{acc} = T_{mech} + T_{em} - Slip * Damp.Factor \quad (7)$$

Where

$$Slip = \frac{1}{2H} \int T_{acc} dt$$

Then the *qd* – axes components of the terminal voltage will be:

$$V_{qt} = E'_q - r_s i_q - x'_d i_d \quad (8.A)$$

$$V_{dt} = E'_d - r_s i_d + x_q i_q \quad (8.B)$$

Finally the terminal voltage, current, active and reactive power, and delta equations are:

$$|V_t| = \sqrt{V_{qt}^2 + V_{dt}^2} \quad (9)$$

$$|I| = \sqrt{i_q^2 + i_d^2} \quad (10)$$

$$P = V_{qt} i_q + V_{dt} i_d \quad (11)$$

$$Q = V_{qt} i_d - V_{dt} i_q \quad (12)$$

$$\delta = \omega_b \int Slip dt \quad (13)$$

3. Fuzzy Based proposed exciter:

The real problem which will face any researcher in this specific topic is the high non-linearity of the synchronous generator dynamics [7]. Some studies concerning FLC applications in excitation controller design using fuzzy set theory have been developed before [7], [8], [9] & [10].

3.1. Fuzzy logic controller structure:

In conventional control, the amount of control is determined in relation to a number of data inputs using a set of equations to express the entire control process. Expressing human experience in the form of a mathematical formula is a very difficult task, if not an impossible one. Fuzzy logic provides a simple tool to interpret this experience into reality. FLCs are rule-based controllers. The structure of the FLC resembles that of a knowledge-based controller except that the FLC utilizes the principles of fuzzy set theory in its data representation and its logic [11]. The basic configuration of the FLC can be simply represented in four parts, as shown in fig. 2 below:

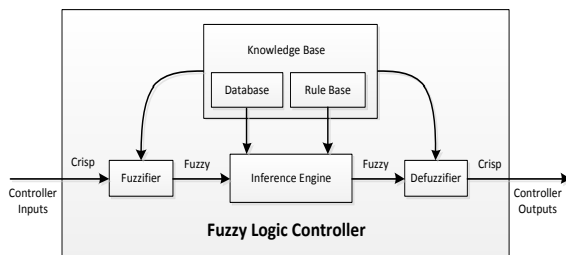


Fig. 2 Schematic diagram of the FLC [11].

Fuzzification module, the functions of which are, first, to read, measure, and scale the control variable (e.g. voltage, current) and, second, to transform the measured numerical values to the corresponding linguistic (fuzzy) variables with appropriate membership values.

Knowledge base, which includes the definitions of the fuzzy membership

functions defined for each control variable and the necessary rules that specify the control goals using linguistic variables.

Inference mechanism, which is the kernel of the FLC. It should be capable of simulating human decision making and influencing the control actions based on fuzzy logic.

Defuzzification module, which converts the inferred decision from the linguistic variables back to numerical values.

3.2. Fuzzy Based proposed exciter design:

There are mainly two types of FLC, Takagi-Sugeno FLC and Mamdani FLC, The Mamdani FLC used mainly for diagnosing, planning and for offline or slow speed systems because it involves the computation of a two dimensional shape by summing of the output memberships, which is a time consuming calculation; while the Takagi-Sugeno FLC ignores the output fuzziness and consider each output membership as a constant (singleton) resulting in a faster response of the system which makes the Takagi-Sugeno FLC superior on the Mamdani in the fast systems applications. Many researches showed that the structure of the Takagi-Sugeno FLC is more robust in the presence of noisy input data. Furthermore, when the sensitivity of both Takagi-Sugeno and Mamdani systems tested it would be observed that the Takagi-Sugeno FLC is more sensitive in areas where there is significant imprecision in the input representation, i.e. when the fuzzy sets overlap, and this point is very helpful in designing a FLC with relatively wide range of the input signal [12].

In order to keep the controller acting for the current and the upcoming instance the controller shall not ignore any gradient of the input variables and therefore the controller shall use COA defuzzification algorithm; it is the must used method although its computational complexity is relatively high [13]. The input and the output variables memberships are shown in fig. 3 below:

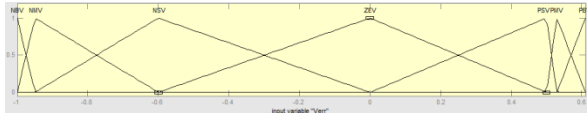


Fig. 3.a Error voltage (V_{err}) memberships (trigonometric).

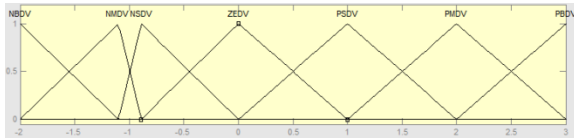


Fig. 3.b Change in error voltage (dV_{err}) memberships (trigonometric).

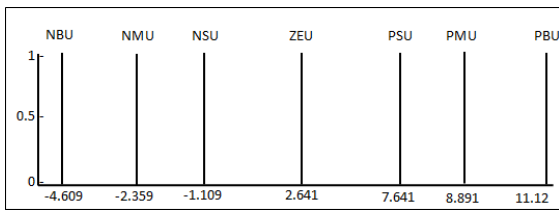


Fig. 3.c Field voltage (E_f) memberships (singleton).

Fig. 3 shows the input and the output variables memberships of the controller. Where: NB-Negative Big, NM-Negative Medium, NS-Negative Small, ZE-Zero, PS-Positive Small, PM-Positive Medium, and PB-Positive Big.

The fuzzy rules used in this controller are Takagi-Sugeno first order rules and they are given in table 1 below:

Table 1 the proposed FLC Rule Base.

dV_{err} \ V_{err}	PBDV	PMDV	PSDV	ZEDV	NSDV	NMDV	NBDV
PBV	PBU	PBU	PBU	PBU	PMU	PSU	ZEU
PMV	PBU	PBU	PMU	PMU	PSU	ZEU	NSU
PSV	PBU	PMU	PMU	PSU	ZEU	NSU	NMU
ZEV	PMU	PMU	PSU	ZEU	NSU	NMU	NMU
NSV	PMU	PSU	ZEU	NSU	NMU	NMU	NBU
NMV	PSU	ZEU	NSU	NMU	NMU	NBU	NBU
NB	ZE	NS	NM	NB	NB	NB	NB

The rules uses only the fuzzy (And) operator between the input variables memberships which are (Error Voltage) and (Change in Error Voltage) (shown in the clear cells) to form the incident and the output memberships (shown in the shaded cells) as the consequence [11]. The control surface of the proposed FLC based exciter is shown in fig.4.

For each instant the proposed FLC based exciter will act according to the flowchart shown in fig. 5.

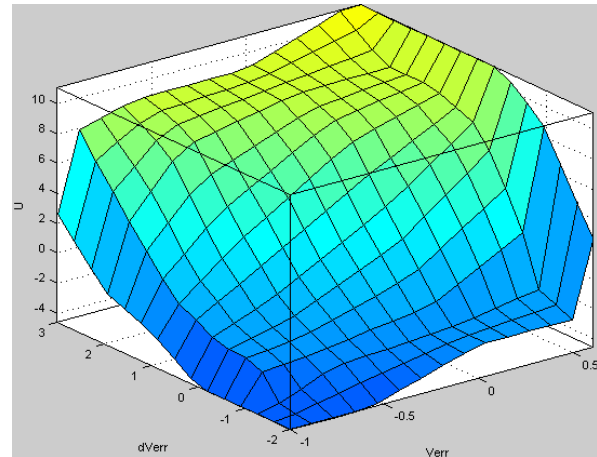


Fig. 4 The control surface of the proposed FLC based exciter.

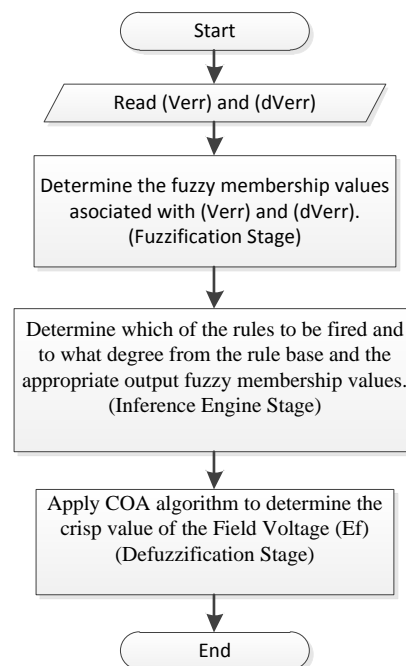


Fig. 5 Proposed FLC based exciter flow chart.

4. Simulation and results:

The above shown system in fig. 1 will be simulated by solving the equations in section 2 using MATLAB/Simulink, the disturbance subjected to the system is a three phase solid fault on the infinite bus which will reduce the infinite bus voltage to zero, the first run will be with the field windings of the generator being fed from a conventional DC1A

excitation system model [14] while the second one will be fed from the proposed fuzzy based exciter. The system will be re-subjected to the fault after 10 seconds in order to check the robustness of the exciter. The simulation also shows the ISE of the terminal voltage as an index of its stability. Simulink Signal Scopes were used to display and store the variables values, but in order to get clear graphs the data stored in the (Scopes) were plotted using the (plot) command in the (MATLAB) command window.

4.1. The first run results:

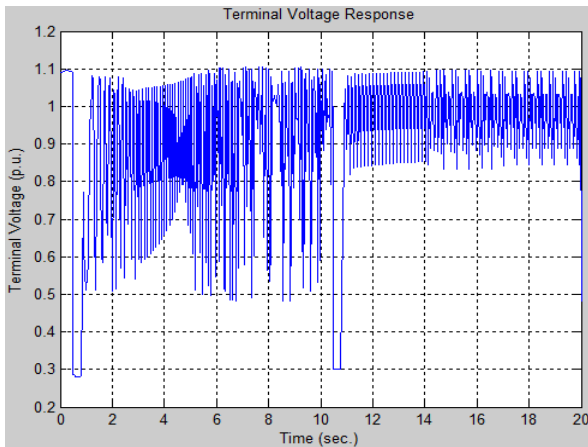


Fig. 6 The terminal voltage response of the generator.

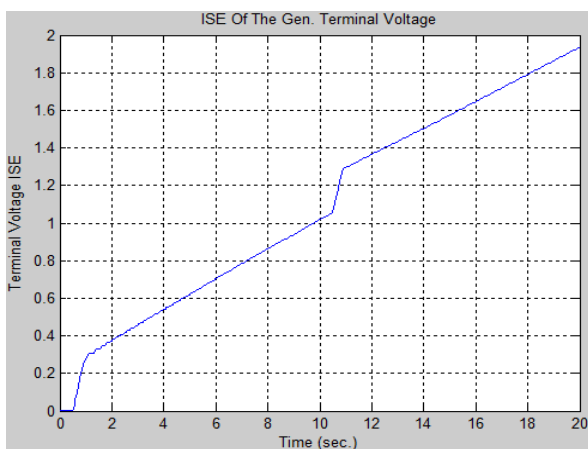


Fig. 7 The ISE of the terminal voltage response.

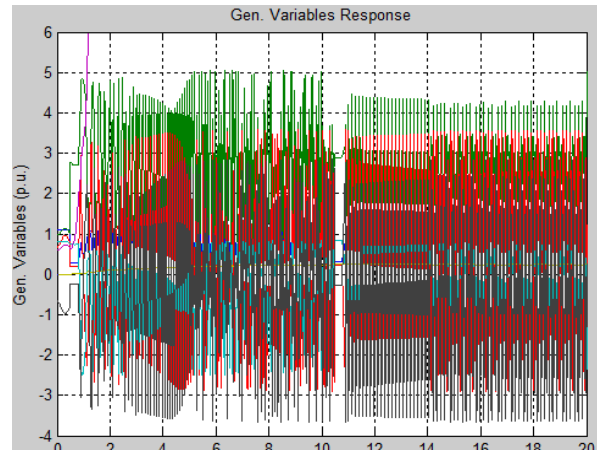


Fig. 8.a all of the generator parameters.

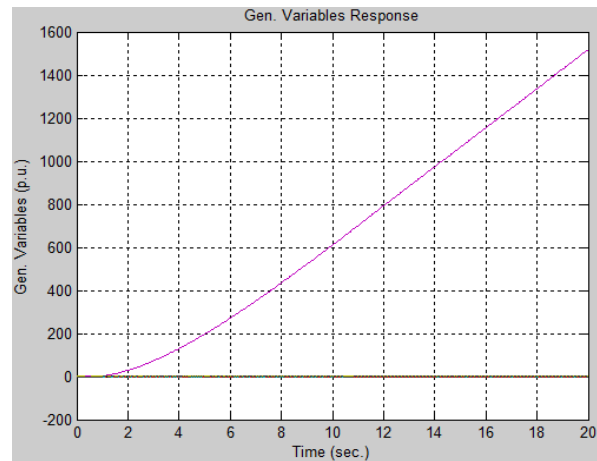


Fig. 8.b the rotor angle of the generator.

Fig. 8 shows the response of all the generator variables after being subjected to the fault.

4.2. The second run results:

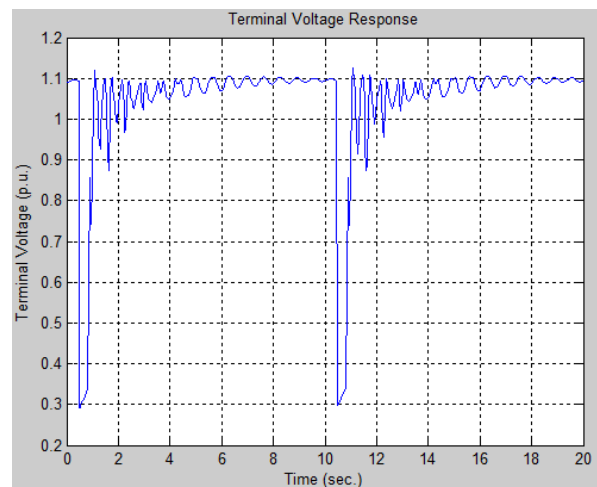


Fig. 9 The terminal voltage response of the generator.

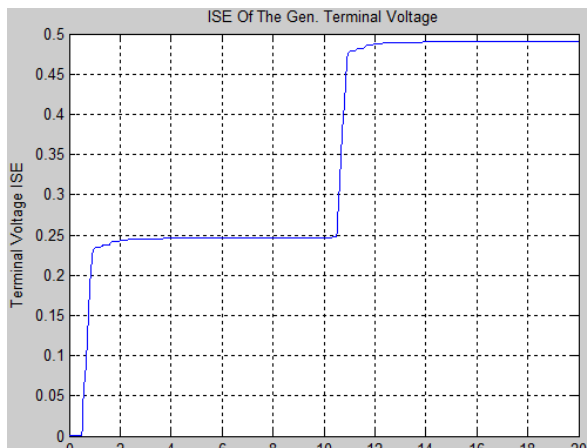


Fig. 10 The ISE of the terminal voltage response.

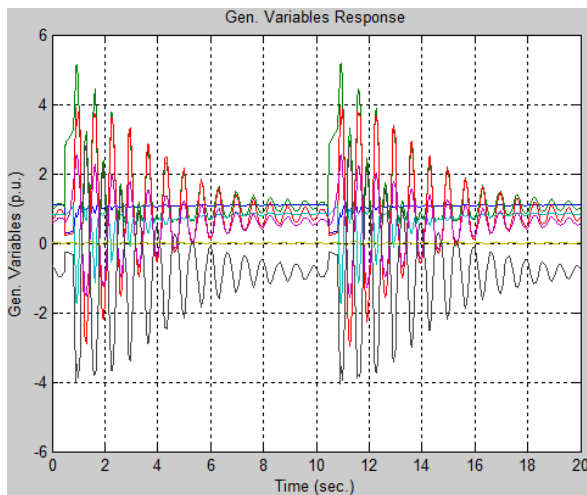


Fig. 11 Shows the response of all the generator variables after being subjected to the fault.

5. Discussion:

The first run shows clearly that the conventional DC1A exciter couldn't handle the fault which leads to large scale oscillations in the terminal voltage (fig. 6) which makes the terminal voltage had a progressive ISE (fig. 7), (fig. 8.a) shows that all of the generator variables active power, reactive power and the electro-mechanical torque are oscillating without damping, while (fig. 8.b) shows the rotor angle goes out of order indicating that, the machine had lost synchronism from the first occurrence of the fault.

The second run with the proposed exciter shows fast damping for the oscillations of the terminal voltage (fig. 9) and stable ISE after each occurrence of the fault (fig. 10), and (fig. 11) shows that all of the generator variables have been damped and stabilized due to the action of the proposed FLC based exciter.

6. Conclusion:

The conventional exciter in which its control action is very dependent on the generator response because of the built-in feedback control loops is unable to change the control action significantly from one distinct value to another with relatively large difference between them fast enough, i.e. has a slow controlling action and therefore it is incapable of handling many kinds of disturbances without additional assistance from stabilizing and protecting elements, while the fuzzy controller deals with current values of the input variables, in other words, it adapts itself to the current instant which makes it faster than the conventional control feedback strategies used in the conventional excitation systems in handling sever disturbances with fast and large scale fluctuations without relying on any other stabilizing or protecting elements.

References:

- [1] Kundur, P., S., Et All, 2004, "Definition and Classification of Power System Stability", IEEE Transactions on power systems, Vol. 19 Issue: 3, 15 pages.
- [2] Kundur, P., S., 1994, "Power system stability and control", McGraw-Hill, Inc., 1176 pages.
- [3] Anderson, P., M., and Fouad, A., A., 2003, "Power system control and stability", John Wiley & sons, Inc., 649 pages.
- [4] Cutsem, T., V., and Vournas, C., 1998, "Voltage stability of electric power systems", Springer, 378 pages.

[5] Ong, C., 1997, “Dynamic simulation of electrical machinery using MATLAB/Simulink”, Prentice Hall Ptr., 626 pages.

[6] Kothari, D., P., and Nagrath, I., J., 2008, “Modern power system analysis”, McGraw-Hill, 694pages.

[7] Karnavas, Y., L. , and Papadopoulos, D., P., 2004, “Excitation Control of A Synchronous Machine Using Polynomial Neural Networks”, Journal of Electrical Engineering, Vol. 55, 11 pages.

[8] Sumina, D., Erceg, G., Idzotic, T., 2006, “Excitation control of a synchronous generator using fuzzy logic stabilizing controller”, Proceedings of the 11th European Conference on Power Electronics and Applications (EPE 2005), Dresden, Germany, 6 pages.

[9] Idzotic T., Et all, 2005, “DSP Based Excitation Control System For Synchronous Generator”, International Conference on Electrical Drives and Power Electronics, Dubrovnik, Croatia, 5 pages.

[10] Sumina, D., Erceg, G., Idzotic, T., 2004, “Comparison of the Excitation Control of a Synchronous Generator with Fuzzy Logic Controller and PI Voltage Controller”, Proceedings of the 11th International PowerElectronicsandMotion Control Conference, Riga, Latvia, Vol.5, 5 pages.

[11] EL-Hawary, M., E., 1998, “Electric power applications of fuzzy systems”, IEEE Press, 343 pages.

[12] Jassbi, J., J., Serra, P., J., Ribeiro, R., A., and Donati, A., 2006, “A Comparison of mamdani and sugeno inference systems for a space fault detection application”, Proceeding of the 2006 World Automation Congress, 8 pages.

[13] Jantzen, J., 1998, “Design of fuzzy controllers”, Technical University of Denmark, Department of Automation,

Tech. report no 98-E 864 (design), 27pages.

[14] Hajagos, L., Et All, 2005 “IEEE recommended practice for excitation system models for power system stability studies”, IEEE Inc.,85 pages.

Appendix:

Simulink blocks for the simulated system:

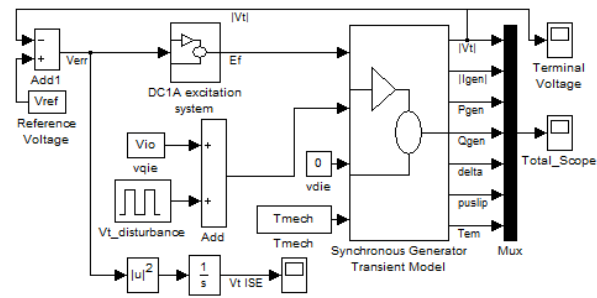


Fig.A.1 The total system with the DC1A excitation system.

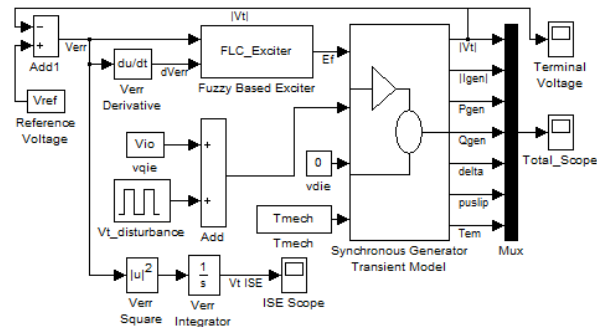


Fig. A.2 The total system with the proposed FLC based exciter.

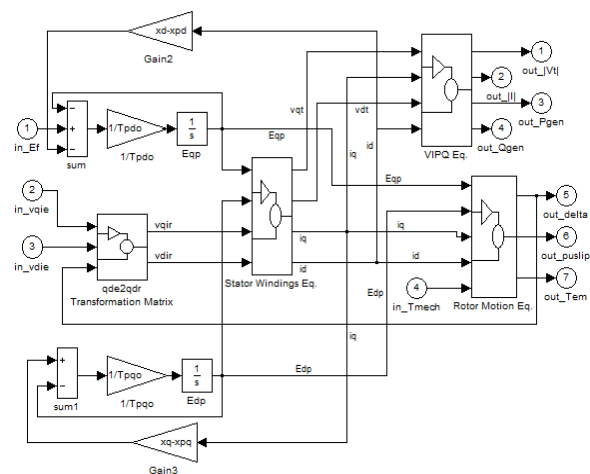


Fig. A3 inside the (Synchronous Generator Transient Model) subsystem

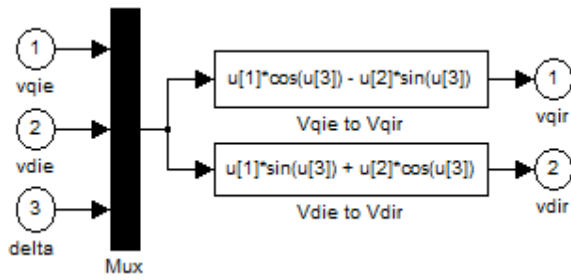


Fig. A4 inside the (qde2qdr Transformation Matrix) subsystem

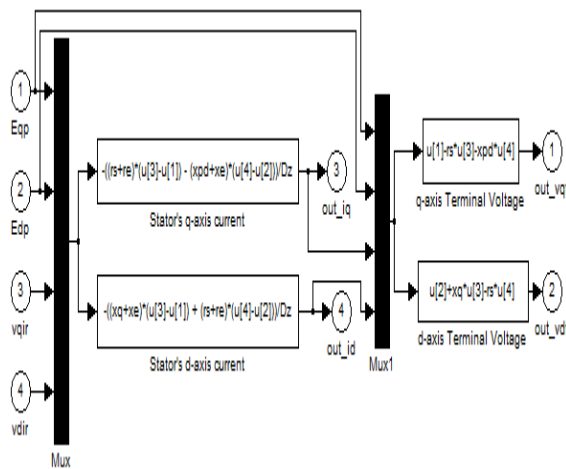


Fig. A5 inside the (Stator Windings Eq.) subsystem

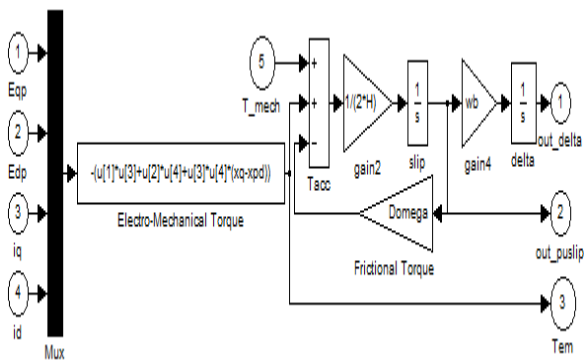


Fig. A6 inside the (Rotor Motion Eq.) subsystem

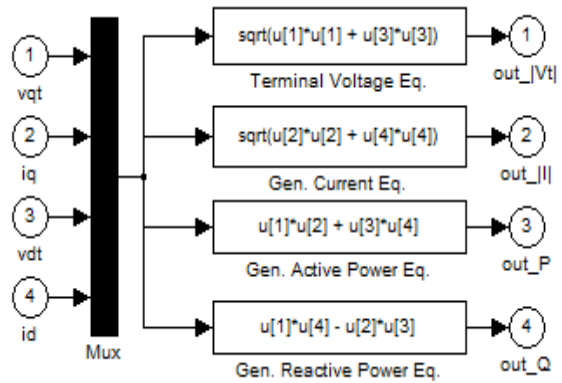


Fig. A7 inside the (VIPQ Eq.) subsystem

SENSORLESS FUZZY LOGIC-BASED SPEED CONTROL OF PERMANENT MAGNET STEPPER MOTOR

Dr. Farazdak Rafeek Yasein

Control and Systems Eng. Department
University of Technology
farazdakrafeek@yahoo.com

Abstract

Permanent Magnet Stepper Motors (PMSM) are widely used in systems that demand high accuracy with quick response. Their applications can be found in numerical control of machine tools (CNC), robotics, etc. The open-loop control scheme suffers from low-performance capability and lack of adaptability to load and system parameters variations. The closed-loop principle was introduced in order to increase the speed accuracy of the stepping motor while making it less sensitive to load disturbances. PMSMs are characterized by complexity of their dynamic model. The paper objective is initially concerned with the analysis and description of PMSM dynamic model. Then to increase measuring system reliability and save cost and weight, an estimator has been introduced to estimate both angular speed and angular position. These estimated measurements will be feedback to the controller to compensate actual measurements which is conventionally given by encoder or tachogenerator devices. The suggested estimator is based on Extended Kalman Filter (EKF) algorithm.

To obtain a prescribed dynamic performance, a controller is suggested to compensate the change of system parameters. Conventional Proportional and Integral (PI) controller could not intelligently compensate such parameter variation due to its fixed characteristics, unless its terms is repeatedly retuned. The fuzzy logic, based on uncertainty theory, can work as a good

intelligent controller for stepper motor. The significant feature of PI fuzzy controller is that it does not rely on the system complexity and model. The results showed that the PI fuzzy controller is more robust than the conventional PI controller.

Keywords: *Stepper Motor, PI Fuzzy Logic controller, Extended Kalman Filter*

1. Introduction:

The stepper motor is an electromagnetic device that converts digital pulses into mechanical shaft rotation. The shaft of a stepper motor rotates in discrete step increments when electrical command pulses are applied to it in the proper sequence. The sequence of the applied pulses is directly related to the direction of motor shafts rotation. The speed of the motor shafts rotation is directly related to the frequency of the input pulses. The step angle is the angle by which a stepper motor shaft rotates in response to an input signal pulse.

Many advantages are achieved using this kind of motors, such as [1]: the rotation angle of the motor is proportional to the input pulse, the motor has full torque at standstill (if the windings are energized), excellent response to starting/stopping/reversing, Very reliable since there are no contact brushes in the motor, a wide range of rotational speeds can be realized as the speed is proportional to the

Frequency of the input pulses. Disadvantages of SMs are resonances can occur if not properly controlled and not easy to operate at extremely high speeds. There are three basic stepper motor types. They are [1]:

- Variable-reluctance Stepper Motor (VRSM)
- Permanent-magnet Stepper Motor (PMSM)
- Hybrid Stepper Motor (HSM)

The VRSM consists of a soft iron multi-toothed rotor and a wound stator. When the stator windings are energized with DC current the poles become magnetized. Rotation occurs when the rotor teeth are attracted to the energized stator poles.

The PMSM rotor is magnetized with alternating north and south poles situated in a straight line parallel to the rotor shaft. These magnetized rotor poles provide an increased magnetic flux intensity and because of this the PMSM exhibits improved torque characteristics when compared with the VRSM type.

The HSM combines the best features of both the PMSM and VRSM type. The rotor is multi-toothed like the VRSM and contains an axially magnetized concentric magnet around its shaft. The teeth on the rotor provide an even better path which helps guide the magnetic flux to preferred locations in the air gap. This further increases the detent, holding and dynamic torque characteristics of the motor when compared with both the VRSM and PMSM types. The two most commonly used types of stepper motors are the PMSM and the HSM types [2].

2. Mathematical Model of PMSM:

The PMSM consists of a slotted stator with two phases and a permanent magnet rotor as shown in Fig. (1).

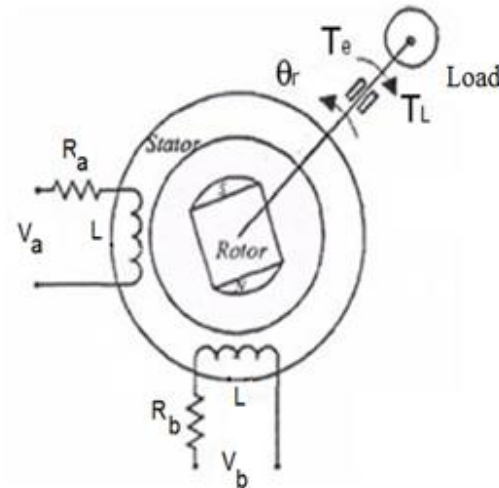


Figure (1) Two phase PMSM Configuration.

Using Kirchhoff's voltage law for PMSM we have

$$V_a = i_a R + \frac{d\phi_a}{dt} \quad (1)$$

Where V_a is the stator phase voltage, i_a is the stator current, R is the stator winding resistance, and ϕ_a is the flux linkages. Since the stator windings are displaced by 90 electrical degrees, hence the mutual inductances between the stator windings are zero. The flux linkages are functions of the number of rotor teeth N_r and the magnitude of the flux linkages produced by the permanent magnets ϕ_m . Then we have [3]

$$\phi_a = L i_a + \phi_m \cos(N_r \theta_r) \quad (2)$$

Where L is the stator winding inductance and θ_r is the rotor angular position. From Eq. (1) and (2)

$$V_a = i_a R + L \frac{di_a}{dt} - N_r \phi_m \omega_r \sin(N_r \theta_r) \quad (3)$$

Where ω_r is the rotor angular speed. Therefore, the stator current i_a is given by

$$\frac{di_a}{dt} = \frac{R}{L} i_a + \frac{N_r \phi_m \omega_r}{L} \sin(N_r \theta_r) + V_a/L \quad (4)$$

In the same way i_b is calculated as:

$$\frac{di_b}{dt} = -\frac{R}{L}i_b - \frac{N_r \varphi_m \omega_r}{L} \cos(N_r \theta_r) + \frac{V_b}{L} \quad (5)$$

The expression of the electromagnetic torque developed by PMSM can be obtained using the co-energy principle (w_c) [3]

$$w_c = \frac{1}{2}(Li_a^2 + Li_b^2) + \varphi_m i_a \sin(N_r \theta_r) + \varphi_m i_b \cos(N_r \theta_r) \quad (6)$$

Using Newton's second law

$$T_e - B_v \omega_r - T_L = J \frac{d^2 \theta_r}{dt^2} \quad (7)$$

Where T_e is the electrical torque, B_v is the viscous friction constant, and J is the rotor inertia. Hence

$$T_e = \frac{\partial w_c}{\partial \theta_r} = -N_r \varphi_m [i_a \sin(N_r \theta_r) - i_b \cos(N_r \theta_r)] \quad (8)$$

Then the differential equations of the rotor angular velocity and position are given by:

$$\begin{aligned} \frac{d\omega_r}{dt} &= -\frac{N_r}{J} \varphi_m [i_a \sin(N_r \theta_r) - i_b \cos(N_r \theta_r)] \\ &\quad - \frac{B_v}{J} \omega_r - \frac{1}{J} T_L \\ \frac{d\theta_r}{dt} &= \omega_r \end{aligned} \quad (9)$$

If the state variables of motor are set as $x = [i_a i_b \omega_r \theta_r]'$, then the PMSM model in state space can be shown as

$$\dot{x} = Ax + Bu \quad (10)$$

where

$$A = \begin{bmatrix} -\frac{R}{L} & 0 & \frac{k_m}{L} \sin(\theta_r) & 0 \\ 0 & -\frac{R}{L} & \frac{k_m}{L} \cos(\theta_r) & 0 \\ \frac{-k_m}{J} \sin(\theta_r) & \frac{k_m}{J} \cos(\theta_r) & -\frac{B_v}{J} & 0 \\ 0 & 0 & 1 & 0 \end{bmatrix}$$

$$B = \begin{bmatrix} \frac{1}{L} & 0 \\ 0 & \frac{1}{L} \\ 0 & 0 \\ 0 & 0 \end{bmatrix} \text{ and } u = \begin{bmatrix} V_a \\ V_b \end{bmatrix}$$

Where $k_m = N_r \varphi_m$. In the PMSM model, we neglect the slight coupling between the phases, the small change in L as a function of θ_r , the variation in L due to magnetic saturation and the detent torque.

At any constant speed, the direct-quadrature (d-q) transformation transforms the signal components of the currents i_a and i_b to the dc components of i_d and i_q as [4]

$$\begin{bmatrix} i_d \\ i_q \end{bmatrix} = \begin{bmatrix} \cos(N_r \theta_r) & \sin(N_r \theta_r) \\ -\sin(N_r \theta_r) & \cos(N_r \theta_r) \end{bmatrix} \begin{bmatrix} i_a \\ i_b \end{bmatrix} \quad (11)$$

The direct current i_d corresponds to the component of the stator magnetic field along the axis of the rotor magnetic field, while the quadrature current i_q corresponds to the orthogonal component.

3. The Continuous Extended Kalman Filter:

Since the sensors may not give enough resolution, and may have a high failure rate, therefore, using some kind of observer one can get the information of non-measured states. The Kalman filter (KF) technique is one of the good methods employed to identify the rotor speed and position based on measured quantities such as stator currents. For nonlinear motor model one can use the Extended Kalman Filter (EKF). The EKF is a recursive filter (based on the knowledge of statistics of both the state and measurement noise), which can be applied to non-linear time varying stochastic systems. The noisy corrupted process and observation models can be given by:

$$\begin{aligned} \dot{x} &= Ax + Bu + w = f(x, u) + w \\ v &= Zx + u + w \end{aligned} \quad (12)$$

where

$$H = \begin{bmatrix} 1 & 0 & 0 & 0 \\ 0 & 1 & 0 & 0 \end{bmatrix}$$

The process noise w is continuous time zero mean white noise (i.e. successive values for small intervals are essentially uncorrelated) with covariance Q . The measurement noise v is also continuous time zero mean white noise with covariance R_n , i.e., $cov(w) = E(w w^T) = Q$ and $cov(v) = E(v v^T) = R_n$

The Jacobean of the stepper motor model are described as follows:

$$F = \frac{\partial f(x, u)}{\partial x}$$

or

$$F = \begin{bmatrix} -\frac{R}{L} & 0 & \frac{k_m}{L} \sin(\theta_r) \omega_r & \frac{k_m}{L} \cos(\theta_r) \\ 0 & -\frac{R}{L} & \frac{k_m}{L} \cos(\theta_r) \omega_r & \frac{k_m}{L} \sin(\theta_r) \\ -\frac{k_m}{J} \sin(\theta_r) & \frac{k_m}{J} \cos(\theta_r) & -\frac{B}{J} - \frac{k_m}{J} (i_a \cos(\theta_r) + i_b \sin(\theta_r)) & 0 \\ 0 & 0 & 1 & 0 \end{bmatrix}$$

The Kalman gain K is calculated by [5,6]:

$$K = P H^T (H P H^T + R_n)^{-1} \quad (13)$$

Where P is the covariance error matrix and may be calculated as [5,6]:

$$\dot{P} = F P + P F^T + Q - P H^T (R_n)^{-1} H P \quad (14)$$

Then, the estimated states \hat{x} are given by:

$$\hat{x} = \hat{x} + K(Z - H\hat{x}) \quad (15)$$

4. Fuzzy Logic Controller (FLC):

FLCs are widely used to control the nonlinear systems. The control law is described by a knowledge-base and a fuzzy logic inference mechanism. The knowledge-base consists of a series of IF...THEN rules with vague predicates. The four principle components of a FLC are: a fuzzification interface, a knowledge-base, decision-

making logic, and a defuzzification interface [7].

The PI-like FLC, which shown in Fig. (2), is used to enhance the output response of the PMSM model by minimization of the steady state error. Tuning of k_1 and k_2 to match the input variables of the FLC to define universe of discourse, while k_3 is responsible for raising the level of changes in stator quadrature current Δi_q [7,8]. The output crisp Δi_q is based on Mamdani technique. The rules of the PI like FLC are designed and are shown in Table (1).

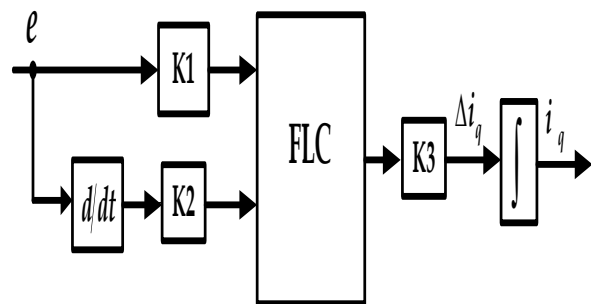


Figure (2) Structure of PI like FLC.

Table (1): Rules for Fuzzy Controller.

		e (pu)						
		NB	NM	NS	Z	PS	PM	PB
ė (pu)	NB	NB	NB	NB	NM	NS	NVS	Z
	NM	NB	NB	NM	NS	NVS	Z	PVS
	PS	NB	NM	NS	NVS	Z	PVS	PS
	Z	NM	NS	NVS	Z	PVS	PS	PM
	PS	NS	NVS	Z	PVS	PS	PM	PB
	PM	NVS	Z	PVS	PS	PM	PB	PB
	PB	Z	PVS	PS	PM	PB	PB	PB

5. Closed Loop System:

The direct fuzzy controller has seven fuzzy sets with membership functions uniformly distributed on each (normalized) universe of discourse. All membership

functions used in FLC are triangular type with a base-width of two, i.e., the input variables are set to per unit (pu) values with NB is negative big, NM is negative medium, NS is negative small, NVS is negative very small, Z is zero, PS is positive small, PM is positive medium, PB is positive big, and PVS is positive very big.

The speed control loop shown in Fig.(3) uses the fuzzy controller to observe the pattern of the speed loop error signal and correspondingly updates the output Δi_q so that the actual speed ω_r matches the reference speed ω_{ref} . The output of the fuzzy controller is integrated and then compared with the estimated i_q and fed to the conventional PI controller to obtain V_q . The error between the set value and the estimated i_d is fed to the conventional PI controller to obtain V_d . By using Inverse Park transformation the applied voltages of the PMSM are obtained. From measurements of noisy stator currents the continuous EKF can be used to estimate the angular speed and position of the rotor. The estimated values of stator currents are converted to the i_d and i_q by using the Park transformation. Tuning of parameters of conventional PI controller depends on Zeigler –Nichols Method.

6. Results:

The nominal values of PMSM parameters are listed in table (2). The process and measurement noise covariance matrices Q and R_n are shown below. Fig. (4) shows stator currents i_a and i_b . It is evident from figure that the nominal values of these currents settle at 0.54 Amp with no load application. The load is exerted one second later of motor startup with values $T_L=0.05$ Nm. This requires the machine absorbing greater current than no load situation, as the current becomes 0.7 Amp at this applied load.

Figure (5) shows the performance of EKF estimator. Two parameters have been shown;

angular speed and position. Figure shows that the estimator could successfully estimate these parameters. However, there is a considerable error at start of estimating. This can be attributed to covariance matrix initialization, as initially, the estimator has no confidence with initial values and no past values are available to give it a previous estimate. Then, the estimate finally could give approximate values of actual considered states. The above argument could be verified using Fig. (6). The trace of P is regarded as an indicator of the estimation goodness.

The robustness of suggested intelligent controller can be examined using a sudden disturbance to PMSM at settling operation. Firstly, the closed loop system with PI controller is excited with a step load at one second after motor starting up, see Fig. (7). This step load is applied to the system with FLC as shown in Fig. (8). One can argue from Fig. (7) and Fig (8) that the FLC could intelligently regain the speed before load exertion at lower time than its counterpart. Moreover, the height of dip with FLC is much lower than that with conventional PI controller. Therefore, one can deduce that the FLC is more robust than the conventional one.

Table (2): PMSM parameters.

Parameter	Value	Units
Ra	10	Ω
L	0.0011	H
B	0.001	N m /rad/s
J	5.7×10^{-6}	Kg m^2
Km	0.113	N m/ A
Nr	50	-

$$R_n = \begin{bmatrix} 0.012^2 & 0 \\ 0 & 0.012^2 \end{bmatrix}$$

$$Q = \begin{bmatrix} \frac{0.02^2}{L} & 0 & 0 & 0 \\ 0 & \frac{0.02^2}{L} & 0 & 0 \\ 0 & 0 & (0.5)^2 & 0 \\ 0 & 0 & 0 & 0 \end{bmatrix}$$

7. Conclusion:

From the simulated results, the following points can be highlighted and concluded:

1. The dynamic speed response based on FLC is faster than that with conventional PI controller.
2. FLC shows high load rejection capabilities than its counterpart.
3. The EKF could successively track the speed even with parameter variations. Therefore, a robust characteristic can be obtained with estimator.

References:

- [1] Acarnley P., "Stepping Motors: a guide to theory and practice", 4th Edition, Stevenage, U.K. 2007.
- [2] Morar A. "Stepper Motor Model for Dynamic Simulation" IEEE Transc. Automatic Control, Vol. 44, No. 2, 2003.
- [3] Bishop R., "The Mechatronics Handbook", Texas 2002.
- [4] Zribi M. and Chiasson J. " Position Control of a PM stepper Motor by exact linearization" IEEE Trans. Automatic Control, Vol. 36, No. 5, May 1991.
- [5] Simon D. " Optima State Estimation: Kalman, H ∞ , and Nonlinear Approaches", A John Wiley & Sons, Inc., 2006.
- [6] Shah C., "Sensorless Control of Stepper Motor Using Kalman Filter ", MSc Thesis, Cleveland state university, December 2004.
- [7] Reznik L. "Fuzzy Controllers", Biddles Ltd., UK 1997.
- [8] Martinez W., Parra L., and Perez L. " Software Simulation of a Fuzzy Logic controller Applied to a hybrid Stepper Motor", Journal of the Mexican Society of Instrumentation Vol. 3, No.7, 1997.

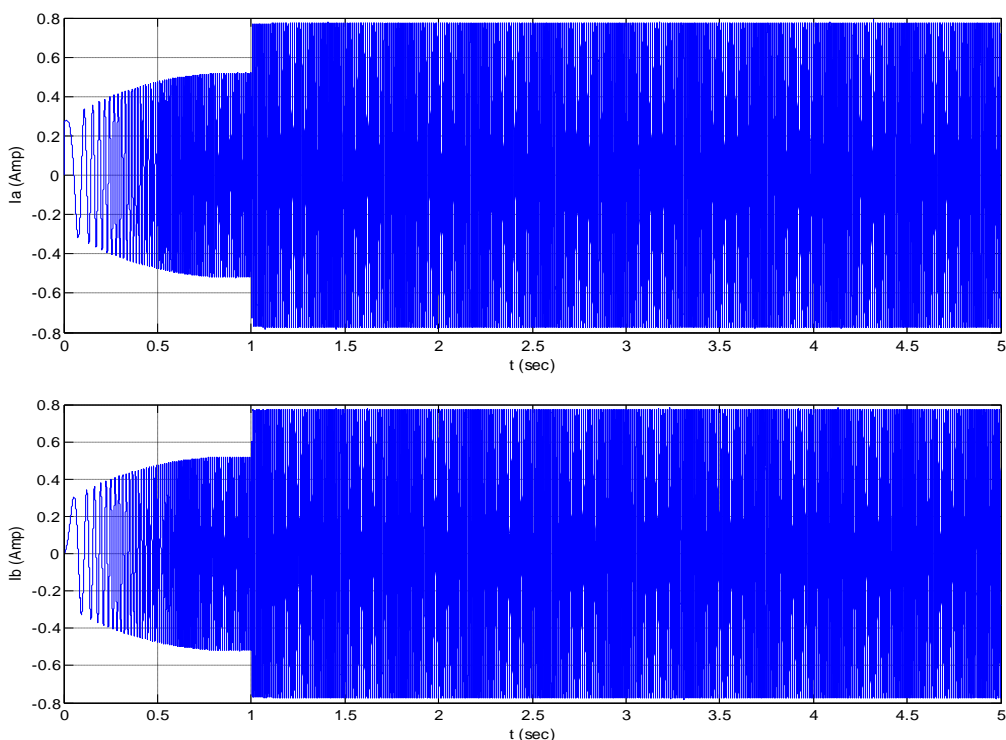


Figure (4) Stator Currents I_a and I_b .

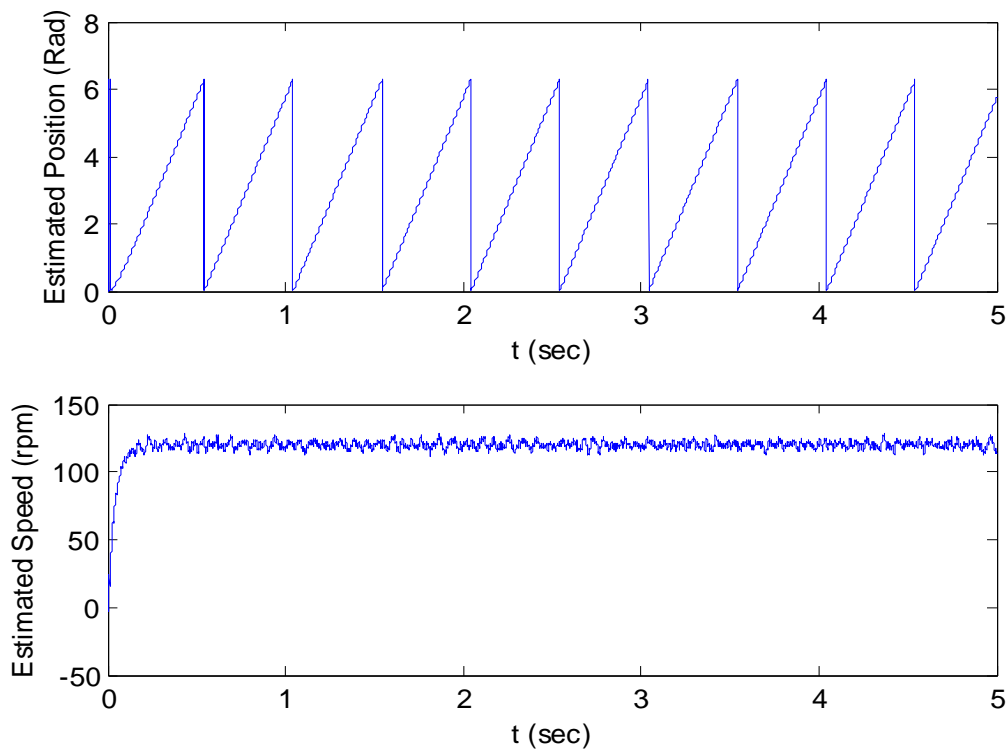


Figure (5) Estimation of Angular Position and Angular speed Using EKF.

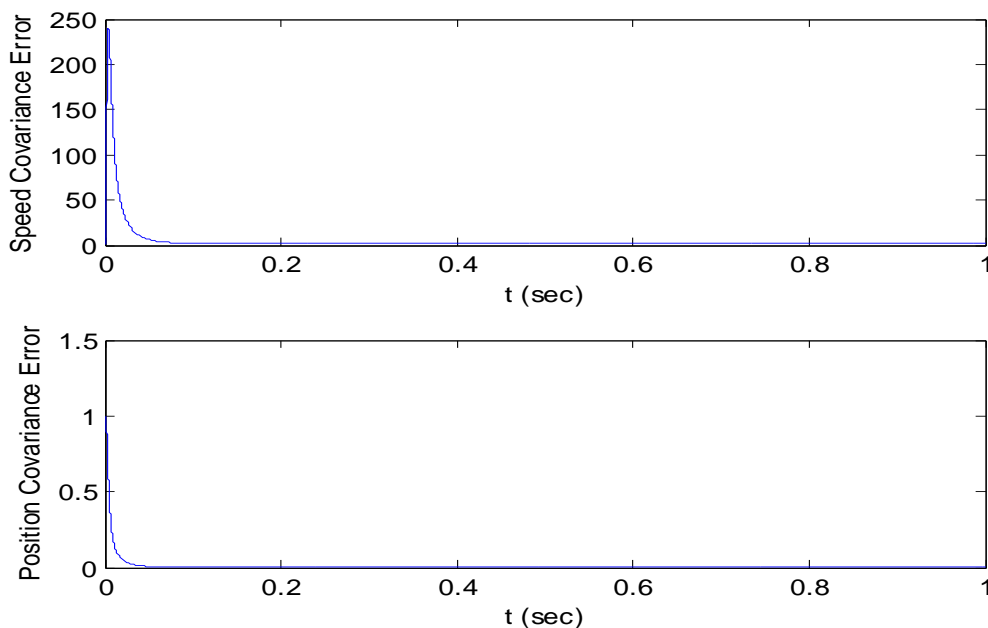


Figure (6) Zoomed Plot Shows the Trace (P) for PMSM.

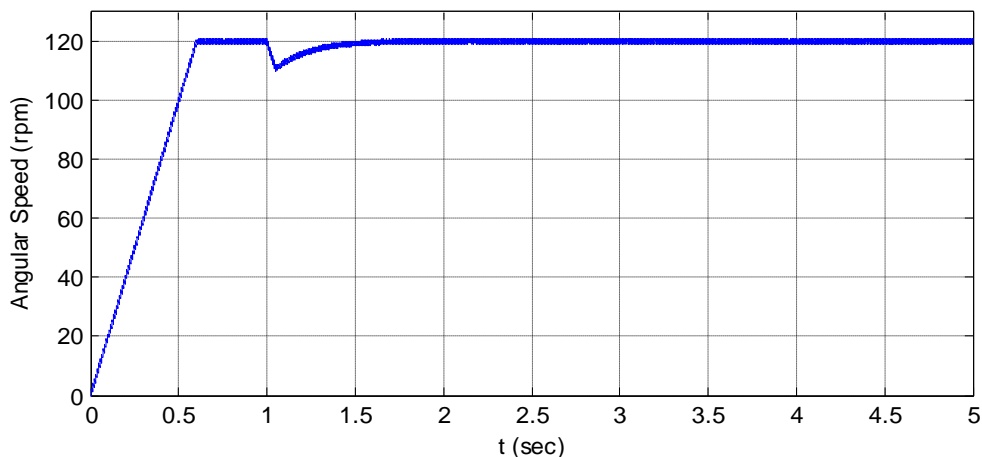


Figure (7) PMSM angular speed using classical PI controller.

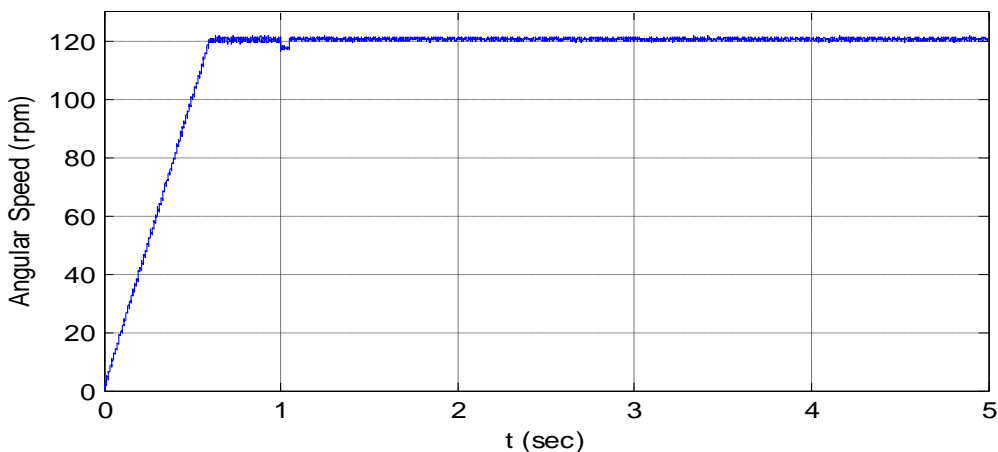


Figure (8) PMSM angular speed using PI like FLC.

INTEGRATED PID LIKE ADAPTIVE FUZZY NEURAL NETWORK FOR NONLINEAR SYSTEM CONTROL

Qusay Fadhil Hasan

Control and Systems Engineering Department
University of Technology
Qussay_74@yahoo.com

Abstract:

Fuzzy logic and neural network can be combined together to generate a fuzzy neural controller which can improve the output response of the controlled system. This mixture uses a neural network training ability to adjust the membership functions of the fuzzy logic controller.

The goal of the controller is to force the controlled system to behave like a reference model to reduce the response time with minimum overshoot. Fuzzy membership functions were tuned using the propagated error between the plant output and the desired one. The controller is designed to simulate the behavior of traditional PID controller in which both the PD and PI parts are merged together in the same fuzzy neural network.

The controller was tested using a nonlinear plant to demonstrate its ability to act as an adaptive PID controller.

Keywords: *Neural Network, Fuzzy Logic, PID Controller, Nonlinear Systems.*

1- Introduction:

The most widely used controller in industry is the famous Proportional Integral Derivative (PID) controller, but the problem of calculating the right values for such a controller is very tedious specially in nonlinear systems. Furthermore its robustness against environmental changes and disturbances is questionable [1,2].

During the last decades, the theory of intelligent control was improved and took its place in industry specially the use of neural network and fuzzy logic controllers. These theories have the power of designing the controller regardless of the plant, since they

look at it as a black box and their parameters do not depend on the plant parameters, hence becoming widely used in nonlinear control [2,3].

By combining both Fuzzy Logic and Neural network together, a robust controller is formed giving precise actions and learning to enhance its performance. The combination is called Fuzzy Neural Network (FNN) which consists of many specially designed fuzzy neurons that perform some kind of fuzzy operations [2,3].

The problem of tuning a PID controller using intelligent control has been discussed by many researchers specially using FNN in the process [3,4,5], but the main disadvantage of these algorithms is the complexity of the controller structure and the storage size needed for the neural network parameters.

In this paper introduces a new FNN structure that has three inputs instead of two (namely error, change of error, and sum of error). This structure can simplify the building of three dimensional fuzzy rule table and simulate at the same time the operation of a conventional PID controller along with the minimization of storage space by reducing the number of controllers used along with the number of rules.

2- Fuzzy Neural Network Design:

As mentioned above, the Fuzzy Neural Controller (FNC) consists of specially designed neurons that can simulate a designated fuzzy operation. The general structure of a PID FNC is the same as ordinary Fuzzy Logic Controller (FLC) but with the addition of a third input that

represents the sum of error as shown in figure 1

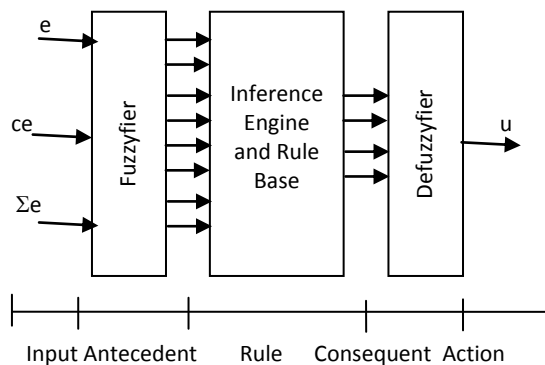


Fig.1 Fuzzy logic Controller Structure.

In this work, a Mamdani type FLC with three inputs and one output is used. The membership functions used to fuzzify the inputs are all bell shaped type with 7 memberships for each input. The overall number of rules will become $7*7*7$ that is 343 rules which can be reduced to only 7 by knowing that any input has some contribution to all of the fuzzy sets and it will always circle around the main diagonal of the fuzzy rule table and settle in the center of this table [6]. Hence the rules of the controller can be summarized as:

- a- IF e is PB AND ce is PB AND Σe is PB THEN u is NB.
- b- IF e is PM AND ce is PM AND Σe is PM THEN u is NM.
- c- IF e is PS AND ce is PS AND Σe is PS THEN u is NS.
- d- IF e is Z AND ce is Z AND Σe is Z THEN u is Z.
- e- IF e is NS AND ce is NS AND Σe is NS THEN u is PS.
- f- IF e is NM AND ce is NM AND Σe is NM THEN u is PM.
- g- IF e is NB AND ce is NB AND Σe is NB THEN u is PB.

The abbreviations for the fuzzy set are as follows:

PB: Positive Big, PM: Positive Medium, PS: Positive Small, Z: Zero, NS: Negative Small, NM: Negative Medium, and finally NB: Negative Big. Moreover, to insure smoothens

of the output, multiplication is used instead of AND operation in the rules. Finally, the method of the center of gravity is used as a defuzzyfier in this paper.

2-1 Fuzzy Neural Network Structure:

The NN used in this paper consists of five layers; each represents special fuzzy operations, and the parameters are updated using back propagation algorithm. Throughout this paper the subscript will represent the node number in the corresponding layer while the superscript represents the layer itself. The layers of FNN are:

a- *Input layer:* in the input layer, each node transmits the corresponding input to the antecedent layer as shown in figure 2

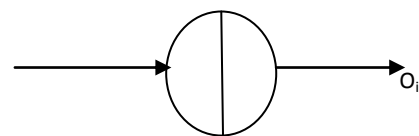


Fig.2 Input layer node.

The Feed Forward relations that govern this layer are:

$$X_1^I = e, X_2^I = ce, X_3^I = \Sigma e \dots \dots \dots 1$$

$$O_i^I = X_i^I, i = 1,2,3 \dots \dots \dots 2$$

I in the superscript stands for Input.

No parameters are updated in this layer.

b- *Layer 2 (Antecedent):* this layer will transmit each value of input to the corresponding linguistic set as shown in figure 3.

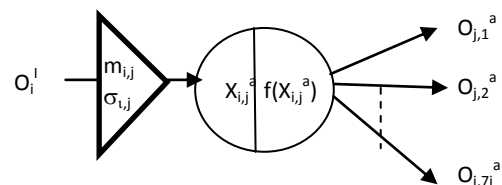


Fig. 3 Antecedent layer node.

The Feed Forward relations that govern this layer are:

$$X_{i,j}^a = -\frac{1}{2} \left(\frac{O_i^l - m_{i,j}}{\sigma_{i,j}} \right)^2 \dots\dots\dots 3$$

$$O_{i,j}^a = e^{X_{i,j}^a}, \quad i = 1,2,3, j = 1,2 \dots 7 \dots\dots\dots 4$$

a in the superscript stands for antecedent. When applying the steepest descent method on the antecedent layer to update both $m_{i,j}$ and $\sigma_{i,j}$ we get

$$\Delta m_{i,j} = \eta \cdot O_j^r (y_j - O_o) \cdot \frac{(O_d - O^o)}{O_2^o} \dots\dots\dots 5$$

$$\Delta \sigma_{i,j} = \eta \cdot O_j^r (O_o - y_j) \cdot \frac{(O_d - O^o)}{O_2^o} \dots\dots\dots 6$$

Where $i=1, 2, 3$. And $j= 1, 2, 3 \dots 7$, η is the learning rate, O^o is the action layer output, y_j is the weight between the rule layer and the consequent layer and O_d is the desired output.

c- *Layer 3(Rule layer):* this layer will determine the rule associated with each linguistic value calculated by the antecedent layer as shown in figure 4.

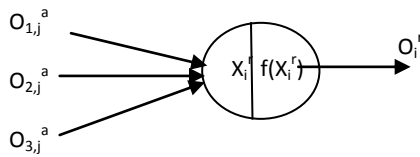


Fig. 4 Rule layer node.

The feed forward rule in this layer is

$$X_j^r = O_{1,j}^a \cdot O_{2,j}^a \cdot O_{3,j}^a \dots\dots\dots 7$$

$$O_j^r = X_j^r, j=1,2,3 \dots 7, \dots\dots\dots 8$$

r in the superscript represents rule. No parameter updating is done in this layer.

d- *Layer 4 (Consequent layer)* in this layer the first step of the center of gravity method is done and it consists of two nodes as shown in figure 5.

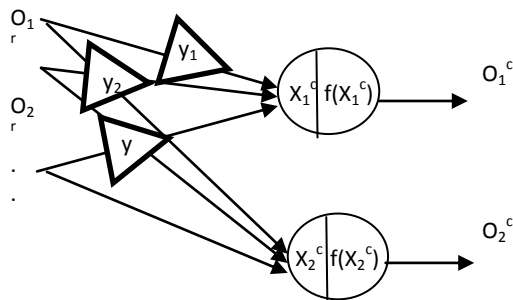


Fig. 5 consequent layer node

The output of this layer is described by

$$X_1^c = \sum_{j=1}^7 y_j \cdot O_j^r \dots\dots\dots 9$$

$$X_2^c = \sum_{j=1}^7 O_j^r \dots\dots\dots 10$$

$$O_k^c = X_k^c, k = 1,2 \dots\dots\dots 11$$

c in the superscript represents consequent. The update equation for y_j is given by

$$\Delta y_j = \eta \frac{(O_d - O^o)}{O_2^o} \cdot O_j^r \dots\dots\dots 12$$

e- *Layer 5 (Action layer):* the final step of the center of gravity method is done in this layer as shown in figure 6.

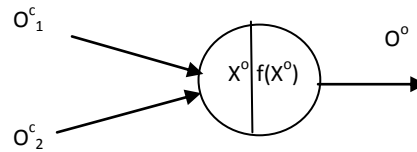


Fig. 6 output layer node.

The final output of FNC and this node is given by

$$X^o = \frac{O_1^c}{O_2^c} \dots\dots\dots 13$$

$$O^o = X^o \dots\dots\dots 14$$

O stands for output, and no update is needed in this layer

3-Simulation results:

The overall structure used to test the controller in this paper is shown in figure 7.

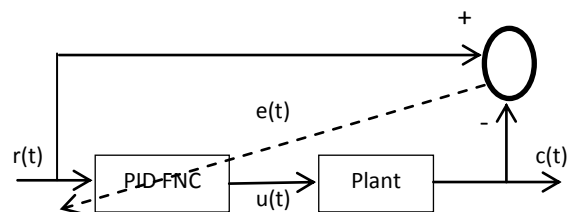


Fig. 7 General block diagram of the PID FNC controller system.

To test the system a nonlinear plant is used which is a simple magnetic levitation system. (figure 8)[7].

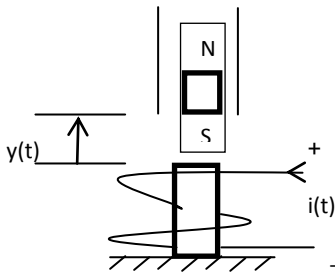


Fig. 8 Magnetic levitation system.

The motion equation of this system is:

$$\frac{d^2y(t)}{dt^2} = -g + \frac{\alpha \cdot i^2(t)}{M \cdot y(t)} - \frac{\beta}{M} \cdot \frac{dy(t)}{dt} \dots\dots\dots 15$$

y(t) is the distance of the magnet above the electromagnet, i(t) is the current flowing in the electromagnet, M is the mass of the magnet and g is the gravitational constant. β is the viscous friction coefficient determined by the material in which the magnet moves, and α is the field strength constant determined by the number of turns of wire on the electromagnet and the strength of the magnet [7].

The constants values are taken as in table 1.

Table 1 constant table used in the simulation.

Constant	M	g	β	α
Value	3	9.8	12	15
unit	Kg	m/sec ²	Kg/sec	N.m/Amp ²

Different step input values were injected to the closed loop system with the values of (3.5, 1, 2.5, 3 and 1.5) at the intervals of (0, 10, 20, 30, and 40) seconds to compare the proposed controller with that of [7]. For the purpose of simulation, it was taken that FNC will produce 1 amp to elevate the mass 1 meter of distance. The input and the output of the closed loop system is shown in figure 9

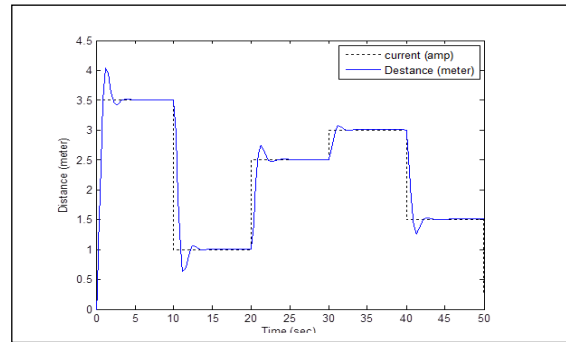


Fig. 9 closed loop response of the system corresponding to the input current.

The PID FNC action (u(t)) is shown in figure 10.

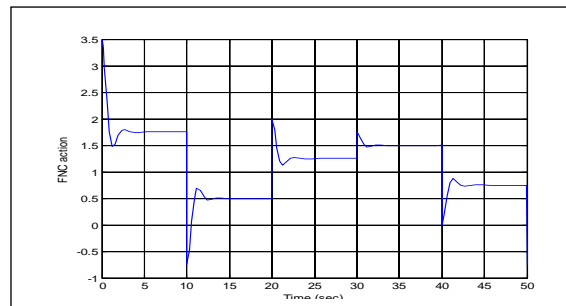


Fig. 10 PID FNC action.

4-Conclusions:

It is seen from the results that the controller met its desired goal by reducing the rise time to 0.9 sec and minimizing the overshoot to 17% and zero steady state error in deferent step changes. This controller is built with minimum number of rules (from 7*7*7 to only 7 rules) and it does not need to be separated into PI and PD FNC as in [3]. Instead, one controller is used which can act as full PID FNC. Furthermore, no neural network is needed to propagate the error to the controller. Hence the only learning to the controller is done online which simplifies the controlling task dramatically and reduces the time of calculation for the controller action. These features make this controller suitable for real time application and the learning ability makes the controller suitable to work in noisy environments with load and/or output disturbance.

References:

- [1] Kaya, A., and Schelb, T. J., July 1988 "tuning PID control of different structures", control engineering magazine, vol. 35, no. 7.
- [2] Kosko, B., 1992 "neural networks and fuzzy systems", prentice hall, Englewood cliffs, USA.
- [3] Mohammed Y., Qusay F., Jan. 2007," design of adaptive fuzzy neural pid like controller for nonlinear systems", Iraqi journal of computer, communication, control and systems engineering, vol 7 no.1
- [4] Samhouri, M., Raoufi, A., and surgenor, b., aug. 2005, " control of pneumatic robot for grinding: aneuro-fuzzy approach to PID tuning", proceedings 2005 of IEEE conference on control applications (cca), Toronto, Ontario, 28-31.
- [5] Yu, K. W., Hwang, R. C. and Hsien, J. G., 1998 "fuzzy PID controller gain scheduling by using neural network back – propagation algorithm", international conference of brain and neural network.
- [6] Chen, Y. M. and Gill K. F., April 1994 "application of fuzzy neural network to the control of an unstable system", imacs international symposium on signal processing, robotics and neural networks, France, pp 454-457.
- [7] Al-Rawi, Ammar, O., Jan 2002, "proposed novel neuro and fuzzy controllers", a thesis, computer engineering department, college of engineering, university of Baghdad.

DESIGN OF ON-LINE TUNED IDLE SPEED CONTROLLER FOR AN AUTOMOTIVE ENGINE

Ali Majeed Mahmood

Control and Systems Engineering Department
University of Technology
alimmj81@yahoo.com

Abstract:

This paper attempts to tune any controller without the knowledge of mathematical model for the system to be controlled. For that purpose, the optimization algorithm of MATLAB 7.0 / Nonlinear Control Design Blockset (NCD) is adapted for On-line tuning for controller parameters. To present the methodology, a PID controller is verified with the physical plant using Mean Value Engine Model (MVEM) of an Automotive Engine during Idle speed where the problem of maintaining the engine idle speed at a reference value with minimum overshoot, minimum undershoot, minimum settling time and minimum steady state error with the presence of load is studied. A Proportional Integral Derivative (PID) Controller is designed to solve this problem, but to get the best controller parameters the (NCD) Blockset is used for tuning the PID parameters. Simulation shows promising results in the idle speed response by comparing NCD tuning results with the trial and error results. The analytical results are carried out MATLAB / SIMULINK.

Keywords: PID controller, NCD Blockset, Automotive Engine, Idle speed.

1. Introduction

Most automotive machines that are used in every day's life are equipped with gasoline Port Fuel Injection (PFI) engines. Typically these engines are of four stroke type, Spark Ignited (SI), and Otto cycle based convert chemical energy of the fuel into mechanical work [1]. At idle operating mode, which is

characterized by low engine speed typically between (800-1500) RPM [1], the throttle valve is closed. This increases vacuum in the intake manifold. High vacuum and low engine speed results in overlap which creates poor combustion and leads to low produced torque. Poor combustion must be compensated by supplying rich mixture to the engine which contributes to high exhaust emissions and high fuel consumption [2]. According to low produced torque, the operation of any ancillary device, like air conditioning system which is powered by the engine, will lead to drop in the engine speed. Moreover, if all ancillaries are switched on simultaneously the engine speed dropping will be very high and may cause engine stalling [3]. Furthermore, Idle Speed Control (ISC) represents one of the generic and challenging problems in automotive engines, due to complexity, nonlinearity and time delays exhibited by the system. And such a typical challenge is confronted by automotive control researchers and practitioners. From this point of view, a controller that compensates for error in speed in the presence of disturbance load torque is needed. The controller has to provide fast and precise reach of target speed with improved fuel economy and reduced emissions as well as guaranteed combustion stability. Several control methodologies for idle speed problem have been proposed through the last decades. Kmap and Puskorius [4] described in 1993 a simulation based training of fuzzy controller using neural based procedure.

They found that training process proceeded more slowly than similarly executed training simpler plants. And a purely intuitive approach to fuzzy control would have much success in dealing with such model. Moreover, a control structure based on the analogy between a nonlinear control technique, which is chosen to be sliding mode, and the fuzzy control the engine speed was obtained compared with increasing exhaust residual gases due to valve technique was introduced by Boverie et al in 1994 [5]. This structure takes into account large dynamic variations in the processes. The designed controller controls the air valve only, while the developed algorithm had been implemented on a real time electronic controller and successfully tested on a car engine (Renault19, 16 valves). Furthermore, **Kruse et al.**, 1994 [6] developed a well founded generalized fuzzy controller for idle speed regulation of a car engine. The proposed fuzzy controller realizes a charge control only, the ignition adjustment is retained. The developed controller possesses a quite smooth control characteristic. In addition, fast and precise reach of the target rotation speed is achieved with great stability on slowly increasing load. **Balluchi et al.** [7], proposed in 2000 a hybrid controller where continuous and discrete variables retain their distinctive nature. The problem of maintaining the crankshaft speed within a given range has been formalized as safety specification for the closed loop system modeled as hybrid automation. **Albertoni et al.** [8] presented in 2003 a hybrid model of gasoline direct injection engine operating in stratified mode. The idle speed control problem is formulated as constrained optimal control problem where fuel consumption has to be minimized. **Panse** [1], developed in 2005 a dynamic control oriented MVEM of a PFI engine. Then a PID controller for idle mode is also developed that uses the throttle to adjust the speed. The developed PID controller successfully maintains the steady state idling speed in

simulated environment. **Santis et al.**, [9] formulated in 2005 the idle speed control as the problem of computing a maximal safe set for a hybrid system modeling of an SI engine. Finally, **Gibson et al.**, [10] presented in 2006 the analysis of lead compensation, feed-forward and disturbance observer design techniques for ISC system with minimal spark reserves levels. Simulation results show that a 30 percent reduction in the maximum drop of an ISC with no lead disturbance observer compensation

2. Nonlinear Control Design (NCD) Blockset [11]

The (NCD) is a MATLAB tool that helps to tune design parameters in a nonlinear Simulink model by optimizing time-based signals to meet user-defined constraints by graphically placing constraints within a time-domain window. The NCD Blockset automatically converts time domain constraints into a constrained optimization problem and then solves the problem using the optimization routines taken from the Optimization Toolbox. The constrained optimization problem formulated by the NCD Blockset iteratively calls for simulations of the Simulink system, compares the results of the simulations with the constraint objectives, and uses gradient methods to adjust tunable parameters to better meet the objectives. The NCD Blockset allows introducing uncertainty into plant dynamics, specify lower and upper limits on tunable parameters, and alter termination criterion. The progress of an optimization while the optimization is running can be followed from command window, and the final results are available in the MATLAB workspace when an optimization is complete. Intermediate results are plotted after each simulation. It allows the user to terminate the optimization before it has completed, to retrieve the intermediate result or change the design.

NCD uses optimization algorithms to find parameter values that allow a feasible solution to the given constraints. NCD automatically converts the constraint bound data and tunable variable information into a constrained optimization problem. Basically, the NCD Blockset attempts to minimize error and generates constraint errors at equally spaced time points (with spacing given by the Discretization interval defined in the Optimization Parameters dialog box) beginning at the simulation start time and ending at the simulation stop time. For upper bound constraints, it is defined the constraint error as the difference between the simulated output and the constraint boundary. For lower bound constraints, it is defined the constraint error as the difference between the constraint boundary and the simulated output.

Figure (1) shows an example usage of NCD Output block in a Simulink model of the sample plant including a PID controller.

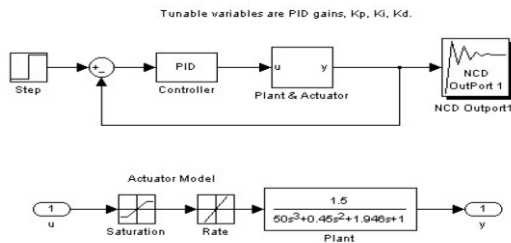


Figure (1): A Simulink model with NCD Output Block.[11]

3. Design of Idle Speed Controller

An idle speed ON-Line tuned PID controller is designed for automotive engine. The model used in this paper is a MVEM, the details of model are in an Appendix, [12]. The top level view of the model is shown in Figure (2) where the model is complex non-linear physical system and consists of many sub systems. The idle speed control is formalized as a control problem, where the engine stalling has to be prevented in spite of load acting and varying. So, the engine with the controller designed should get the idle rotational speed with minimum overshoot,

minimum undershoot, minimum steady state error and reach the target rotational speed as fast as possible. The idle speed controller designed in this paper uses the throttle angle only to compensate the drop in the rotational speed of the engine, by enlarging the area available for the air flow at the throttle valve. It is assumed that the air fuel ratio is held at the stoichiometric value and the spark timing is maintained to give Maximum Break Torque (MBT).

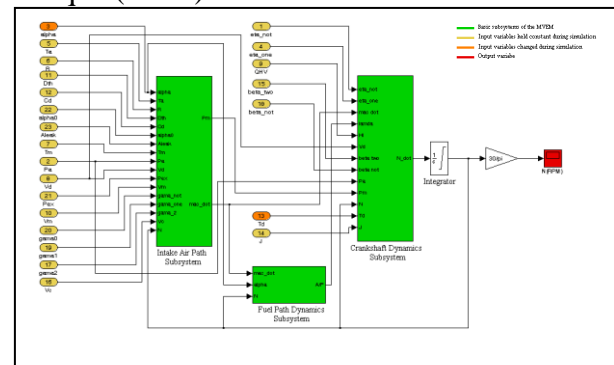


Figure (2): Top level view of the engine Simulink model.[12]

4. Controller Design

4.1 PID controller

The continuous-time PID controller is described by the following expression:

$$u(t) = K_p \times e(t) + K_i \times \int e(t)dt + K_d \times \frac{de(t)}{dt} \dots (1)$$

where, K_p and K_i are the proportional and the integral gain coefficients. A block diagram for a PID controller is shown in Figure (3). [13]

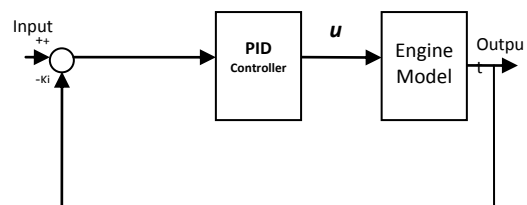


Figure (3): Block diagram of Engine Model with PID controller

4.2 PID controller with NCD Blockset

To use the NCD Blockset, it only requires to include a special block, the NCD output block, in Simulink diagram and to connect that block to any signal in the model to

signify that user wants to place some kind of constraint on the signal. NCD output block can be found under NCD within the Simulink Library Browser. Figure (4,5) shows the block diagram of Engine Model with PID controller and NCD blockset.

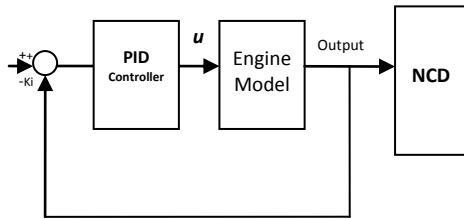


Figure (4): block diagram of Engine Model with PID controller and NCD blockset

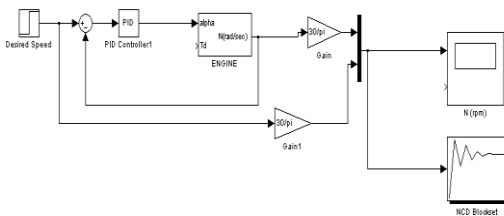


Figure (5): block diagram of Engine Model with PID controller and NCD blockset in MATLAB/SIMULINK

The closed loop system with PID is simulated with applying a variable value of a uniform load torque to the closed loop system, as shown in Figure (6).

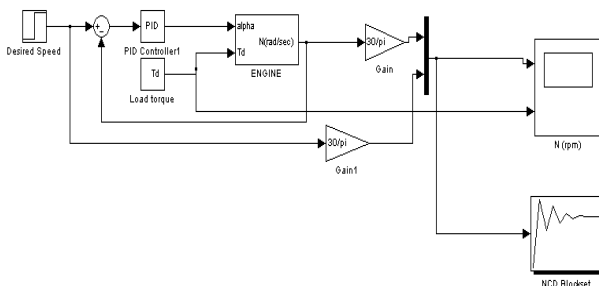
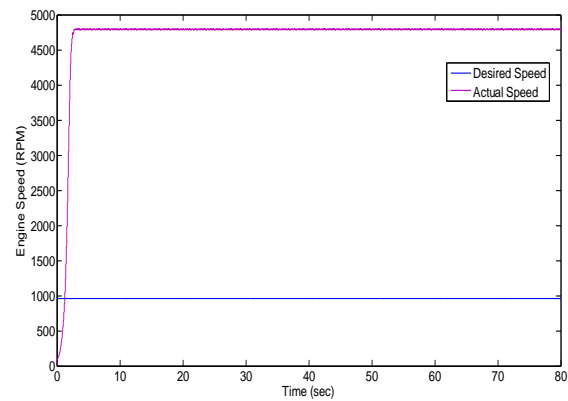


Figure (6): block diagram of Engine Model with PID controller and NCD blockset in MATLAB/SIMULINK with a uniform load torque

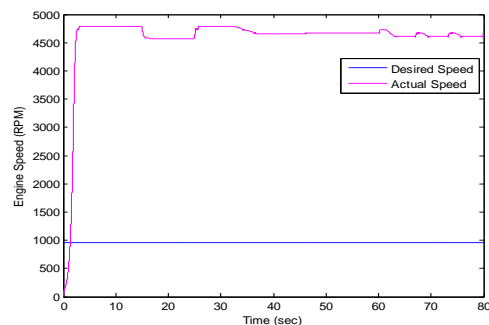
5. Simulation Results

Consider the desired engine speed is 955 rpm[14] and a variable value of a uniform load torque is applied, firstly the simulation is done without controller as shown in Figure(7,8), where it is shown that the system without controller is unable to track the desired Engine speed where the system goes

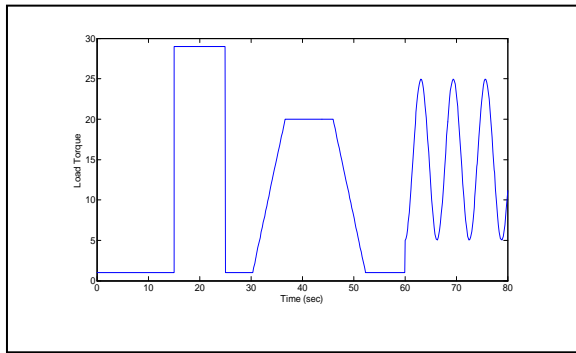
to high speed exceeding the desired level about (4750) rpm. In order to eliminate the error steady state and to get better tracking performance a PID controller is applied. As shown in Figure(9) where the system response with PID controller has the ability to get the desired performance. The PID controller parameters are selected by trial and error method. Thus the PID coefficients are $K_p=0.42 \times 10^{-2}$, $K_i=0.12 \times 10^{-2}$ and $K_d=0.04 \times 10^{-3}$ respectively. To enhance the system response and to get best parameters for PID controller, the NCD is used to on-line tuning for controller parameters with following parameters $K_p=0.9 \times 10^{-2}$, $K_i=0.18 \times 10^{-2}$ and $K_d=0.05 \times 10^{-3}$. As shown in Figure (10), it is noticed that the settling time and error steady state are reduced and the Peak Overshoot and Peak Undershoot are degraded too especially with high applied load Torque.



Figure(7): System Response without Controller and without Load Torque

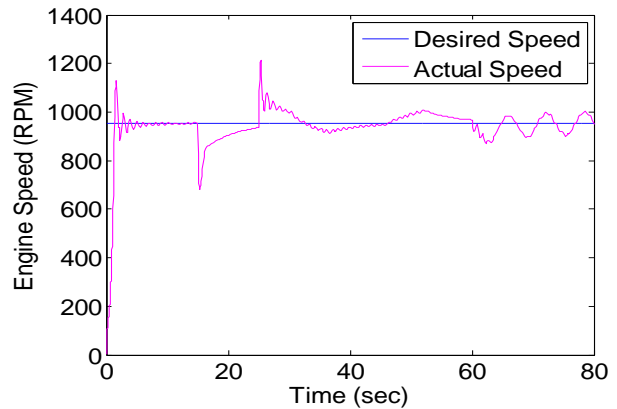


(a) Engine speed with load torque

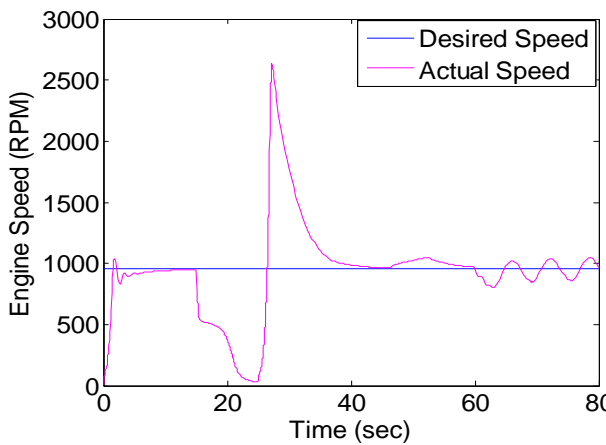


(b): Applied load torque

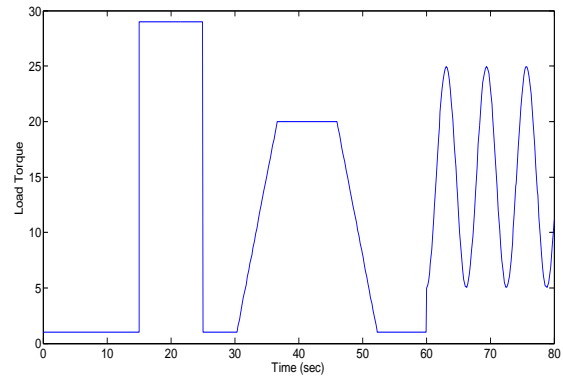
Figure(8): System Response without Controller and with Uniform Load Torque



(b): Engine speed with load torque

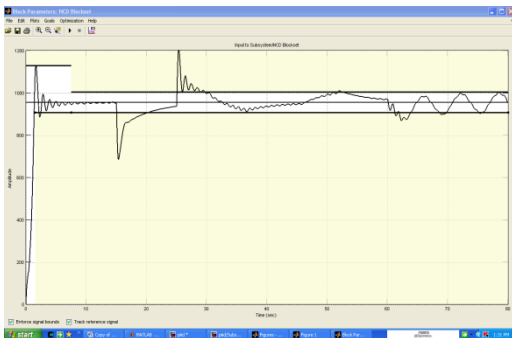


Figure(9): System Response with PID controller and Uniform Load Torque



(c): Applied load torque

Figure(10): System Response with PID controller and Uniform Load Torque Based NCD Blockset for tuning PID parameters



(a) NCD Blockset

6. Conclusions

- 1- When compared NCD with trial and error method, which is used widely in industry, this method offers a more scientific and logical approach to a difficult problem of tuning control systems. Also, when the control strategy is not well-known, unlike a PID controller, tuning by trial and error method will be a time-consuming process or almost insoluble.
- 2- NCD is adapted for real-time executions and it can tune any controller without the mathematical model knowledge of the system it is controlling.

- 3- Using PID controller with NCD achieve an improvement on the speed response by improving the steady state error.

References:

- [1] P. A. Panse, "Dynamic Modeling and Control of Port Fuel Injection Engines", Master Thesis, Indian Institute of Technology, 2005, India.
- [2] W. Pulkrabek, "Engineering Fundamentals of the Internal Combustion Engine", Prentice Hall, 1997, U.S.A.
- [3] D. Hrovat, and J. Sun, "Models and Control Methodologies for IC Engine Idle Speed Control Design", Control Engineering Practice, Vol. 5, No. 8, PP. 1093-1100, 1997, Britain.
- [4] L. A. Feldkamp, and G. V. Puskorius, "Trainable Fuzzy and Neural-Fuzzy Systems for Idle Speed Control", Proceeding of the 2nd IEEE International Conference on Fuzzy Systems, Vol. 1, PP. 45-51, 28 March-1 April 1993, U.S.A.
- [5] S. Boveie, P. Cerf, and J. M. L. Quellec, "Fuzzy Sliding Mode Control Application to Idle Speed Control", Proceeding of the 3rd IEEE Conference on Fuzzy Systems, Vol. 2, PP. 974-977, 26-29 June 1994, Orlando.
- [6] R. Kruse, J. Gebhardt, and F. Klawonn, "A Fuzzy Controller for Idle Speed Regulation", Proceedings of the ACM symposium symposium on Applied computing, 1994, U.S.A.
- [7] A. Balluchi, L. Benvenuti, M. D. D. Benedetto, T. Villa, H. Wong-Toi, and A. L. S. Vincentelli, "Hybrid Controller Synthesis for Idle Speed Management of an Automotive Engine", Proceeding of the American Control Conference, June 2000, Chicago, Illinois.
- [8] L. Albertoni, A. Balluchi, A. Asavola, C. Gambelli, E. Mosca, and A. L. S. Vincentelli, "Idle Speed Control for GDI Engines Using Robust Multirate Hybrid Command Governors", Proceeding of the IEEE Conference on Control Applications, Vol. 1, PP. 140-145, 23-25 July 2003, Istanbul, Turkey.
- [9] E. D. Santis, M. D. D. Benedetto, and G. Girasole, "Digital Idle Speed Control of Automotive Engines Using Hybrid Models", IFAC, 2005.
- [10] A. Gibson, I. Kolmanovsky, and D. Hrovat, "Application of Disturbance Observer to Automotive Engine Idle Speed Control for Fuel Economy Improvement", Proceedings of the IEEE American Control Conference, 14-16 June 2006, Minnesota, USA.
- [11] Math Works Inc., (2002), MATLAB® Nonlinear Control Design Blockset User's Guide, Version 1.1.6, July 2002
- [12] S. T. Al-Waysee "Fuzzy Logic Controller Design for an Automotive Engine", Master Thesis, 2007.
- [13] L. Reznik, "Fuzzy Controllers", Newnes, 1997.
- [14] A. I. Bhatti, S. K. Spurgeon, R. Dorey, and C. Edwards, "Sliding Mode Configurations for Automotive Engine Control", International Journal of Adaptive Control and Signal Processing, Vol. 13, Issue 2, PP. 49-69, March 1999.

Appendix
Engine Modeling:

It will be assumed that the model simulates a gasoline powered, four stroke, PFI, Spark Ignition (SI) engine. The model includes air, fuel and rotational dynamics as well as process delays inherent in the four stroke cycle engine. It is found that when modeling such a complex system, as the SI engine, it is beneficial to divide it into distinct subsystems [5].

The basic configuration of the engine model has three basic subsystems, describing the main phenomena take place in SI engine.

These subsystems are shown in fig (1):

- a- Intake air path subsystem.
- b- Fuel dynamics subsystem.
- c- Crankshaft dynamics subsystem.

a) Intake Air Path Dynamics

In this section a mean value model for the intake air path of SI engine is described. It is divided into three subsystems that have to be modeled, these are:

- 1) Throttle body
- 2) Intake manifold
- 3) Cylinder air induction

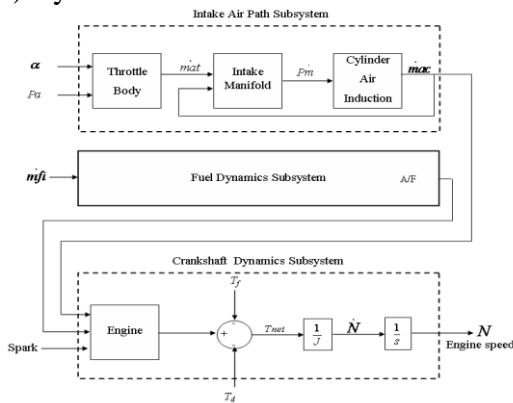


Figure (11): Block diagram of the engine model.

1) Static Model of the Throttle Body

The air mass flow into the cylinders, and thereby, the output power of the engine is controlled by the throttle valve. Its opening depends on the pedal position [6].

$$\dot{m}_{at}(t) = C_d \frac{P_a(t)}{\sqrt{RT_a}} \phi(R_p(t)) A(t) \quad (1)$$

Where:

$\dot{m}_{at}(t)$: is the air mass flow rate through the throttle valve.

C_d : is the discharge coefficient which is an experimentally determined constant and it relates the effective throat area to the actual throat area. It is roughly equals to 0.7 [1, 8].

P_a : ambient pressure (N/m^2).

R : ideal gas constant ($J/kg.K$).

T_a : ambient temperature (K)

$\phi(R_p(t))$: Function of pressure ratio across the throttle position, which depends on the flow conditions, where

under choked flow, $\phi(R_p)$ is constant and is calculated as follows [8, 9]:

$$\phi(R_p) = \sqrt{\gamma \left[\frac{2}{\gamma+1} \right]^{\frac{\gamma+1}{\gamma-1}}} \quad (2)$$

(2)

For $P_m(t) < P_c$

Where:

γ : denotes the ratio of specific heats of air which is assumed to be (1.35) [10].

Using this value of γ , equation (2) above is calculated to be equal to (0.6761).

R_p : represents the ratio of the manifold pressure (P_m) to the ambient pressure (P_a).

Moreover, during sonic flow $\phi(R_p)$ is a function of time and is calculated with the following equation [8, 9]:

$$\phi(R_p(t)) = (R_p(t))^{\frac{1}{\gamma}} \sqrt{\frac{2\gamma}{\gamma-1} \left[1 - (R_p(t))^{\frac{\gamma-1}{\gamma}} \right]} \quad (3)$$

(3)

For $P_m(t) \geq P_c(t)$

Where:

P_c : is the critical pressure where the flow reaches sonic condition in the narrowest part and is calculated as follows:

$$P_c = \left[\frac{2}{\gamma+1} \right]^{\frac{\gamma}{\gamma-1}} \cdot P_a \quad (4)$$

The area available for the flow ($A(t)$) equals the cross sectional area of the channel less the area blocked by the throttle plate. The blocked area depends on the throttle angle (α) measured from fully closed position in radian as shown in Figure (3) [10].

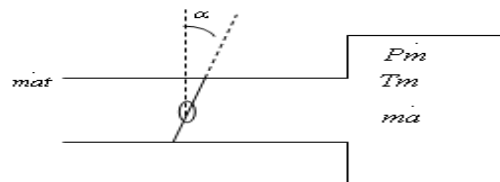


Figure (3): Air flow past the throttle plate If the channel and the throttle plate are assumed to be circular in shape with diameter (D_{th}), the available area for the flow can be expressed as [10]:

$$\dot{A}(t) = \frac{\pi}{4} D_{th}^2 (1 - \cos(\alpha(t))) \quad (5)$$

This equation is modified to the following form to account for the leakage mass flow rate. Deriving from the fact that when the engine throttle is fully closed, it holds $\alpha = \alpha_{leak}$ [10, 11, 12].

$$\dot{A}(t) = \frac{\pi}{4} D_{th}^2 \left(1 - \frac{\cos \alpha(t)}{\cos \alpha_{leak}}\right) + A_{leak} \quad (6)$$

where A_{leak} is the flow area when the throttle angle equals α_{leak} .

2) Dynamic Model of the Intake Manifold

The intake manifold dynamics can be described by a first order differential equation that is based on the mass conservation equation as given below [6, 10, 11]:

$$\dot{P}_m(t) = \frac{RT_m}{V_m} \dot{m}_a(t) \quad (7)$$

Where

$$\dot{m}_a(t) = \dot{m}_{at}(t) - \dot{m}_{ac}(t) \quad (8)$$

T_m : Manifold air temperature (K)

V_m : Manifold volume (m^3)

$\dot{m}_{ac}(t)$: Mass flow rate of the homogeneous mixture of air and exhaust gas.

$\dot{m}_{at}(t)$: Air mass flow through the throttle valve.

$\dot{m}_a(t)$: Intake manifold mass of air.

The dynamic pressure obtained by this model is not instantaneous value of the manifold pressure, but an averaged representation of the intake manifold filling dynamics [4].

In this paper, the fraction of EGR is assumed to be 0.1 of the air induced to the cylinder. The effect of engine speed and the manifold pressure on the volumetric efficiency is modeled separately in an individualistic manner as follows [10]:

$$\eta_v = \eta_N(N(t)) \cdot \eta_{P_m}(P_m(t)) \quad (11)$$

$$\eta_N(N(t)) = \gamma_0 + \gamma_1 \cdot N(t) + \gamma_2 \cdot (N(t))^2 \quad (12)$$

$$\eta_{P_m} = \frac{V_c + V_d}{V_d} - \frac{V_c}{V_d} \cdot \left(\frac{P_{ex}}{P_m(t)}\right)^{\frac{1}{\gamma}} \quad (13)$$

Where :

$\gamma_0, \gamma_1, \gamma_2$: are empirical constants related to specific engine.

V_c : clearance volume of the cylinder (m^3).

P_{ex} : the exhaust gas pressure (N/m^2).

b. Fuel Path Dynamics

Fueling dynamics are important for the in cylinder air-fuel ratio calculation. The fuel injector injects fuel as pulses when the intake valve is not open [10]. Fuel dynamics can be described by the following set of equations [4, 11, 14]:

models must be explained clearly in the crankshaft dynamics model. These are:

$$\dot{m}_{ff}(t) = x \cdot \dot{m}_{fi}(t) - \frac{1}{\tau_f} m_{ff}(t) \quad (14)$$

$$\dot{m}_{fv}(t) = (1-x) \dot{m}_{fi}(t) \quad (15)$$

$$\dot{m}_f(t) = \dot{m}_{fv}(t) + \frac{1}{\tau_f} m_{ff}(t) \quad (16)$$

where:

\dot{m}_{fi} : is the mass flow rate of the injected fuel (kg/sec).

\dot{m}_{ff} & m_{ff} : mass flow rate (kg/sec) and mass of the fuel film (kg) respectively.

\dot{m}_{fv} : mass flow rate of the fuel vapor (kg/sec)

\dot{m}_f : mass flow rate of fuel that enters the cylinder (kg/sec)

x : fraction of the injected fuel which is deposited on the manifold or intake port as fuel film, and is

calculated using the following equation [4]:

$$x = 0.3 + \frac{0.7}{90} \alpha(t) \quad (17)$$

τ_f : fuel evaporation time constant which is calculated as [14]:

$$\tau_f = 0.05 + \frac{2.25}{N(t)} \quad (18)$$

Ideal fuel delivery is assumed, i.e., the air fuel ratio is assumed to be kept at the stoichiometric value (14.67) [1]. The fuel injection \dot{m}_f is set according to the evolution of the air charge. The air charged to the cylinder is divided by stoichiometric A/F which denoted by (λ) in the Simulink model to provide the feed-forward fuel flow command.

b. Crankshaft Dynamics

The crankshaft variable of interest is the revolution speed expressed in revolution per minute (RPM) or rad. per second (r/s), which depends on the torque produced by cylinder during expansion stroke. Three important

- 1) Torque production.
- 2) Process delays.
- 3) Rotational dynamics of the engine.

1) Torque Production Model

The torque produced by the cylinder during expansion stroke depends in a nonlinear fashion on the mass of air loaded to the cylinder, air fuel ratio taken during the earlier intake stroke, spark timing and mass of residual gases left after the earlier exhaust stroke [4]. This can be expressed using the mean effective pressure (mep) notation as follows:

$$\eta_{i-t} = \frac{imep}{mep_{fe}} \quad (19)$$

$$bmep = imep - mep_{mec_losses} \quad (20)$$

$$bmep = mep_{fe} \cdot \eta_{i-t} - mep_{mec-losses}$$

Where (mep_{fe}) is the (bmep) that will be produced if the engine is fully efficient, as expressed mathematically in the following equations:

$$\begin{aligned} mep_{fe} &= \frac{\text{constant hypothetical forceacting on the piston if the engine is 100\% efficient}}{\text{piston area}} \\ &= \frac{\text{work produced during one cycle with 100\% efficiency}}{\text{piston displacement during expansion stroke}} \\ &= \frac{\text{piston area}}{\text{piston area}} \\ &= \frac{(\text{mass of fuel inducted during cycle } (M_f)) \times (\text{heating value of fuel } (Q_{HV}))}{\text{stroke volume } (V_d)} \end{aligned}$$

$$\text{So, } mep_{fe} = \frac{M_f \cdot Q_{HV}}{V_d} \quad (22)$$

The mass of fuel inducted during one cycle (M_f) is calculated as follows [4]:

$$A/F = \frac{\dot{m}_{ac}}{\dot{m}_f} \Rightarrow \dot{m}_f = \frac{\dot{m}_{ac}}{A/F}$$

and for one cycle: that is assumed to act on the piston during expansion stroke and produces the same amount of work that the real engine does in two crankshaft revolutions, as expressed mathematically below [10]:

$$M_f = \frac{mac \text{ (for one cycle)}}{A/F}$$

$$M_f = \frac{\dot{m}_{ac}(t) \cdot 4\pi}{A/F(t) \cdot N(t)} \quad (23)$$

Using equations (22) and (23), the final form of the (mep_{fe}) is found:

Using equations (22) and (23), the final form of the (mep_{fe}) is found:

$$mep_{fe}(t) = \frac{\dot{m}_{ac}(t) \cdot Q_{HV}}{A/F(t) \cdot V_d} \cdot \frac{4\pi}{N(t)} \quad (24)$$

The indicated thermal efficiency (η_{i-t}) is modeled as a function of the engine speed (N), air fuel ratio (A/F) and spark advance (δ) [10].

$$\eta_{i-t} = \varphi(N(t), A/F(t), \delta(t)) \quad (25)$$

By assuming that the air fuel ratio is held tightly around stoichiometric, and the spark timing maintained at MBT value [1], (η_{i-t}) is expressed as a function of engine speed only [10]:

$$\varphi(N(t)) = \eta_0 + \eta_1 \cdot N(t) \quad (26)$$

where (η_0, η_1) are empirical coefficient parameters of the function, related to a specific engine.

Finally, the mechanical losses which are denoted by ($mep_{mec-losses}$), are described by the following equation [10]:

$$mep_{mec-losses} = \psi(N(t), P_m(t)) \quad (27)$$

$$\psi(N(t), P_m(t)) = \beta_0 + \beta_1 N(t)^2 \cdot \frac{4\pi}{V_d} + (P_a - P_m(t)) \quad (28)$$

where the variables (β_0, β_1) are empirical constants related to a specific engine.

Now, by substituting equations (24), (25) and (27) in equation (21) the final form of the *b MEP* expression will be as follows [10]:

$$b MEP = \frac{m a c(P_m(t), N(t)) \cdot \varphi(N(t)) \cdot Q_{HV} \cdot 4\pi}{(A/F) \cdot N(t) \cdot V_d} - \psi(N(t), P_m(t)) \quad (29)$$

To get an expression that comprises only the *b MEP* and the break torque (T_b), the *b MEP* is defined as a constant hypothetical pressure

$$\begin{aligned} b MEP &= \frac{\text{constant hypothetical force acting on piston face}}{\text{piston area}} \\ &= \frac{\frac{\text{work produced during one cycle}}{\text{piston displacement during expansion stroke}}}{\text{piston area}} \\ &= \frac{(\text{brake torque } (T_b)) \cdot (\text{angular duration of one cycle})}{\text{stroke volume } (V_d)} \end{aligned}$$

$$\text{So, } b MEP = \frac{T_b \cdot 4\pi}{V_d}$$

By the substitution of equation (30) into (29) and making the suitable simplifications, an

expression for the break torque is produced as given below:

$$T_b = \frac{m a c(N(t), (P_m(t)) \cdot \varphi(N(t)))}{A/F(t) \cdot N(t)} \cdot Q_{HV}^{-\psi(N(t), P_m(t))} \cdot \frac{V_d}{4\pi} \quad (31)$$

2) Process Delays Model

The process of torque production is discrete depending on the engine speed. The model described here is continuous, two delays are included in the model [10, 15]:

a) Intake to torque production delay (T_{it}): this is the delay time between intake stroke to expansion stroke.

$$T_{it} = \frac{2\pi}{N(t)} \quad (32)$$

b) Spark to torque production delay (T_{st}): this is delay time from sparking to torque production.

$$T_{st} = \frac{\pi}{N(t)} \quad (33)$$

Incorporating the above delays in equation (31) gives:

$$T_b = \frac{m a c(t - T_{it}) \cdot \varphi(N(t))}{A/F(t) \cdot N(t)} \cdot Q_{HV}^{-\psi(N(t), P_m(t))} \cdot \frac{V_d}{4\pi} \quad (34)$$

3) Rotational Dynamics Model

The rotational dynamics of the engine crankshaft is obtained by applying Newton's second law for rotational motion [4].

$$T_{net} = J \dot{N} \quad (35)$$

where:

T_{net} : is the net torque used for vehicle acceleration (N.m).

J : the total inertia of the engine ($Kg \cdot m^2$).

and (\dot{N}) (rad/sec^2) represents the angular acceleration of the engine which will be integrated later to get angular speed of the engine. T_{net} is calculated from the difference between ⁽³⁰⁾ the torque produced by the cylinders during combustion process and the sum of all the load torques placed on the engine.

OPTIMAL CONTROLLER DESIGN FOR DYNAMIC SYSTEMS WITH PERTURBED TIME-VARYING DELAY

Dr. Abdulsalam H. Nafia

Ministry of Science and Technology
Baghdad, Iraq

Dr. Asmaa Q. Shareif

Computer Science Department
College of Science, University of Baghdad.
asama_sal@yahoo.com

Abstract:

In this work, a controller design is proposed to control systems subjected to uncertainties and perturbed time-varying delay. The proposed controller strategy is composed of three parts, the linear state feedback part is used for assigning the closed loop eigenvalues, and the nonlinear switching part of sliding mode and the adaptive part are used to achieve the robustness of globally stability. By using the stability theorem, the adaptive law is utilized for adapting the unknown bounds of the lumped perturbations so that the objective of asymptotical stability is achieved, and then to use the variable structure control method to enhance the robustness of stability of the controlled systems. Once the system goes inside of the sliding surface of the variable structure controller, the dynamics of the controlled systems are insensitive to effect of perturbations. The system and controller are simulated by using Matlab/Simulink. Finally, real numerical example is given for demonstrating the feasibility of the proposed controller.

Keywords: *Time-varying delay, uncertainty, Adaptive, Sliding Mode Controller*

1- Introduction:

The problem of stability for a class of uncertainties dynamic control systems with time-varying state delay is investigated in this work. An independent delay adaptive variable structure controller is designed to drive the states of the system to the equilibrium point (zero). The proposed controller strategy is composed of three parts, the linear state feedback part that is used to assign the closed

loop eigenvalues, the nonlinear switching part of sliding mode and the adaptive part that are used to achieve the robustness of globally stability. Variable structure controller (VSC) [1] with sliding mode (SM) has been traditionally recognized as a high gain control technique with outstanding robustness features for solving stabilization and tracking problem. The main feature of VSC is to employ a discontinuous control under the reaching law to drive the state from an arbitrary initial state in the state space toward a designed state along a pre-specified trajectory, i.e. switching hyperplane. The discontinuous high speed switching action maintains the state on this surface once the system enters the sliding hyperplane. Moreover, when the dynamics of the controlled system are in the switching hyperplane, it has been shown that VSC possesses several advantages, e.g., fast response, good transient performance, robustness of stability, insensitivity to the matching parameters variation and external disturbance [2].

1-1 Time-Varying Delay:

Due to the finite speed of information processing the transmission time-varying delay has been often encountered in various engineering systems, for example aircraft systems, microwave oscillator, rolling mill, chemical process, manual control and long transmission line in pneumatic, hydraulic systems. Since the existence of such delay is frequently a source of instability that cannot be ignored during the design of a control system, considerable attention has been paid to study of systems with delay [1]. In this work, a robust control scheme is proposed for a class of uncertain dynamical systems with

time-varying state delay. To increase the robust control efforts, one incorporate variable structure control with sliding mode to deal with the unknown parameters as well as the unknown gains in the bound of the delayed states. The uncertainties as well as the upper bound of the delayed states are dealt with by means of the well used robust control method.

1-2 System Description:

In this section, a class of systems that are subjected to time-varying state delays and perturbation are considered. The dynamic equation of these systems is governed by;

$$\dot{x}(t) = [A + \Delta A(t, x)]x(t) + [A_h + \Delta A_h(t, x)]x(t-h) + Bu(t) + D(t, x) \quad (1)$$

Where $x(t) \in R^n$ is the state vector, $u(t) \in R^m$ is the control input, $D(t) \in R^m$ is an uncertain external disturbance and/or unknown nonlinearity of the system. The constant $A \in R^{n \times n}$, $A_h \in R^{n \times n}$, $B \in R^{n \times m}$ are known, and B is full rank. The term $\Delta A(t, x)$ and $\Delta A_h(t, x)$ are unknown real function representing time-varying parameter uncertainties of system matrices A and A_h respectively. The unknown scalar $h(t)$ denotes bounded and continuous delay function satisfying the following,

$$0 \leq h(t) \leq \bar{h} < \infty; \quad \dot{h}(t) \leq \eta < 1 \quad (2)$$

Where \bar{h} an unknown constant, but is also η is a known constant. $x(t)$ is an arbitrary known continuous state vector for specifying initial condition.

The following assumptions are assumed to be valid:

Assume that, the system pair (A, B) is controllable, and all state variables are available for measurement. The Uncertain matrices and vector, ΔA , ΔA_h and D , that are continuously differentiable in x , and piecewise continuous in t . Then the objective is to design variable structure controller for

system in Eq.(1) subjected to the previous assumptions. It will be shown that, all the states of the controlled system will be asymptotically approach to zero in spite of the existence of perturbations, i.e.,

$$\lim_{t \rightarrow \infty} x(t) = 0 \quad (3)$$

Set all the uncertainties and perturbation to zero, i.e., $\Delta A = 0$, $\Delta A_h = 0$ and $D = 0$, the dynamic equation of Eq.(1) can be rewritten a nominal system,

$$\dot{x}(t) = Ax(t) + A_h x(t-h) + Bu(t) \quad (4)$$

Let a state feedback control be $u = Kx$, where $K \in R^{m \times n}$ is a constant matrix. Then one can rewrite the dynamic equation of the nominal system Eq.(4) as,

$$\dot{x}(t) = (A + BK)x(t) + A_h x(t-h) \quad (5)$$

In order to exam the stability of the nominal system which is represented by Eq.(5), a Lyapunov function is defined as

$$V(t) = x^T(t)Px(t) + \int_{t-h}^t x^T(\tau)Rx(\tau)d\tau \quad (6)$$

Where P and R are symmetric positive definite matrices.

The derivative of Lyapunov function in Eq.(6) corresponding to the nominal system which is represented in Eq.(5) is then given by,

$$\begin{aligned} \dot{V} &= \dot{x}^T(t)Px(t) + x^T(t)P\dot{x}(t) + x^T(t)Rx(t) - \\ &\quad (1 - \dot{h})x^T(t-h)Rx(t-h) \\ &= -\begin{bmatrix} x^T(t) & x^T(t-h) \end{bmatrix} Q \begin{bmatrix} x(t) \\ x(t-h) \end{bmatrix} \end{aligned} \quad (7)$$

Where

$$Q \cong \begin{bmatrix} -[(A + BK)^T P + P(A + BK) + R] & -PA_h \\ -A_h^T P & (1 - \dot{h})R \end{bmatrix} \quad (8)$$

According to the Lyapunov stability theorem, it is known that if $Q > 0$, the nominal system Eq.(4) will be uniformly asymptotically stable for all $x(t) \in R^n$.

It is well known that one can design the feedback gain matrix K by using pole

assignment method to obtain a set of pre-specified eigenvalues when (A, B) is controllable and nominal system, so that the desired system's performance can be achieved.

2- Propose Controller:

The design of variable structure controller with sliding, analysis of nominal system and then one can do the design and can apply to the original system then to take an example to show the simulation results for the designed controller.

2-1 Analysis of the Nominal System:

By setting all the uncertainties and perturbation to zero in Eq.(1), i.e. $\Delta A=0$, $\Delta A_h=0$ and $D=0$, from Eq.(1) one can obtain the dynamic equation of the nominal system as:

$$\dot{x}(t) = Ax(t) + A_h x(t-h) + Bu(t) \quad (9)$$

Let a feedback control u_{eq} be as:

$$u_{eq} = Kx \quad (10)$$

Where $k \in \mathfrak{R}^{m \times n}$ is a constant matrix, Then, one can rewrite the dynamic equation of the nominal system in Eq.(9) can be written as:

$$\dot{x}(t) = (A + BK)x(t) + A_h x(t-h) \quad (11)$$

In order to examine the stability of the nominal systems Eq.(11), a Lyapunov function in Eq.(6) is used. The nominal system in Eq.(11) is globally uniformly asymptotically stable if there are exist symmetric positive definite matrices P and R such as the following:

$$[(A + BK)^T P + P(A + BK) + R] > 0 \quad (12)$$

And

$$(1 - \dot{h})R + A_h^T P[(A + BK)^T P + P(A + BK) + R]^{-1} P A_h > 0 \quad (13)$$

The derivatives of Lyapunov function in Eq.(6) corresponding to the nominal system Eq.(11) can be given by:

$$\begin{aligned} \dot{V} &= \dot{x}^T(t)Px(t) + x^T(t)P\dot{x}(t) + x^T(t)R \\ &\quad x(t) - (1 - \dot{h})x^T(t-h)Rx(t-h) \quad (14) \\ &= \begin{bmatrix} x^T(t) & x^T(t-h) \end{bmatrix} Q \begin{bmatrix} x(t) \\ x(t-h) \end{bmatrix} \end{aligned}$$

Where

$$Q \cong \begin{bmatrix} -[(A + BK)^T P + P(A + BK) + R] & -PA_h \\ -A_h^T P & (1 - \dot{h})R \end{bmatrix} \quad (15)$$

According to the Lyapunov stability theorem, it is known that if $Q > 0$, then the nominal system that is represented by Eq.(10) will be uniformly asymptotically stable for all $x(t) \in \mathfrak{R}^n$, and it is also known that Q is positive definite if and only if Eq.(12) and (13) are fulfilled.

2.2 Switching hyperplane:

In order to stabilize the perturbed time-varying delay system in Eq.(1), the VSC technique is utilized. In general, the design procedure of VSC technique can be divided in to two phase. The first phase is to design a switching hyperplane for the system, so that once the controlled system enters the switching hyperplane, the desired dynamic performance can be generated. In this section the switching hyperplane of system in Eq.(1) is designed as:

$$\sigma = Cx - C \int_0^t (A + BK)x dt \quad (16)$$

Where $C \in \mathfrak{R}^{m \times n}$ is a constant full rank matrix and is chosen so that the matrix CB is non-singular $k \in \mathfrak{R}^{m \times n}$ also as a constant matrix that satisfies [3]:

$$\text{Re}[\lambda \max(A + BK)] < 0 \quad (17)$$

After designing the switching hyperpalne, the second phase of the VSC design is to design an appropriate control law so that the sliding condition $\sigma \dot{\sigma} < 0$ is satisfied. The satisfaction of the sliding condition ensures

that only the switching hyper plane will attract the trajectories of the controlled system and also the trajectories will stay thereafter. When the dynamics of the system in Eq.(1) are driven into the sliding phase, i.e.

$$\dot{\sigma}(x) = 0 \text{ And } \sigma(x) = 0$$

One can know that,

$$\dot{\sigma} = CA_h x_{(t-h)} + CBu - CBKx = 0$$

Therefore it is known that there exists an equivalent control, $u = u_{eq}$ as:

$$u_{eq} = -(CB)^{-1} CA_h x(t-h) + Kx \quad (18)$$

Such that $\dot{\sigma} = 0$. The closed-loop dynamic equation after system entering the switching hyperpalne can be obtained by substituting into Eq.(10) and the resulting equation is:

$$\dot{x} = (A + BK)x(t) + A_h x(t-h) - B(CB)^{-1} CA_h x(t-h) \quad (19)$$

$$= (A + BK)x(t) + A_h x(t-h) \quad (20)$$

3- Case Study:

Consider the dynamic model [4] with the following data:

$$A = \begin{bmatrix} -1 & 1 \\ -2 & -3 \end{bmatrix}$$

$$\Delta A = \begin{bmatrix} 0.1 \sin(2t) & -0.3 \sin(t) \\ -0.1 \sin(t) & -0.075 \sin(3t) \end{bmatrix}$$

$$A_h = \begin{bmatrix} 0 & 0.1 \\ 0.5 & 1 \end{bmatrix}$$

$$\Delta A_h = \begin{bmatrix} -0.2 \sin(2t) & 0.1 \sin(3t) \\ 0.1 \sin(t) & -0.175 \sin(t) \end{bmatrix}$$

$$D = \begin{bmatrix} 0.2 + 0.6 \sin(t) \\ 0.1 + 0.09 \sin(3t) \end{bmatrix}$$

$$B = \begin{bmatrix} 1 & 0 \\ 0 & 0.5 \end{bmatrix}$$

$$\Delta B = \begin{bmatrix} 0.25 \sin(t) & -0.15 \sin(2t) \\ -0.1 \sin(t) & 0.05 \sin(3t) \end{bmatrix}$$

$$h(t) = 0.1 |\cos(6t)|$$

It is clearly known that $0 < h(t) < \infty$, $\dot{h}(t) < 1$.

The main objective is to use the proposed control scheme of section two to design the controller to stabilize the system. According to Eq. (2-8) the switching function is designed as:

$$\sigma = \begin{bmatrix} 1 & 0 \\ 0 & 2 \end{bmatrix} \left\{ x - \int_0^t \left(\begin{bmatrix} -1 & 1 \\ -2 & -3 \end{bmatrix} + \begin{bmatrix} 1 & 0 \\ 0 & 0.5 \end{bmatrix} \right) x dt \right. \\ \left. \begin{bmatrix} 1 & 0 \\ -20 & -8 \end{bmatrix} \right\} \quad (21)$$

From Eq.(21), it is known that $C = \begin{bmatrix} 1 & 0 \\ 0 & 2 \end{bmatrix}$

and $CB = B^T C^T = 1$. Then the controller is designed as:

$$u = Kx$$

Where $K = \begin{bmatrix} 1 & 0 \\ -20 & -8 \end{bmatrix}$, and the sign function

is used as a saturation for removing the chattering problem.

The closed-loop dynamic response of computer simulation, using MATLAB/Simulink software is done, for this simulation; one can use the initial condition as $X_{(0)} = [4 \quad -2]^T$.

From this information, it is clearly shown that $0 < h(t) < \infty$, $\dot{h}(t) > 1$, the uncertain matrices and vector $\Delta A, \Delta A_h, D$ are continuously differentiable in x and piecewise continuous in t. Assume that there was existing an unknown continuous functions for an appropriate dimension G,E and F such as:

$$\Delta A = BG$$

$$\Delta A_h = BE$$

$$D = BF$$

These conditions are so called matching conditions [4] then, one can compute G, E and F as:

$$G = \begin{bmatrix} 0.1\sin(2t) & -0.3\sin(t) \\ -0.2\sin(t) & 0.1\sin(3t) \end{bmatrix}$$

$$E = \begin{bmatrix} -0.1\sin(2t) & 0.1\sin(3t) \\ 0.2\sin(t) & -0.35\sin(t) \end{bmatrix}$$

$$F = \begin{bmatrix} 0.2 + 0.6\sin(t) \\ 0.2 + 0.18\sin(3t) \end{bmatrix}$$

Then the controller is designed as:

$$U = u_{eq} + u_n$$

$$= Kx + L\sigma$$

Where $K = \begin{bmatrix} 1 & 0 \\ -20 & -8 \end{bmatrix}$, L is positive scalar.

Then the reachability condition can be given by:

$$\sigma \dot{\sigma} \leq u_n \leq -L\sigma^2$$

Then since $\sigma^2 \geq 0$ always, the reachability condition is satisfied for any positive value assigned to L.

The computer simulation of a nominal closed-loop system without uncertainty is given as shown in figure (1); and applying it under Matlab/Simulink as subsystem, figure (2) illustrates the simulink implementation of system delay, uncertainty for both (A, A_h) and disturbances also make a subsystem for using MATLAB/Simulink.

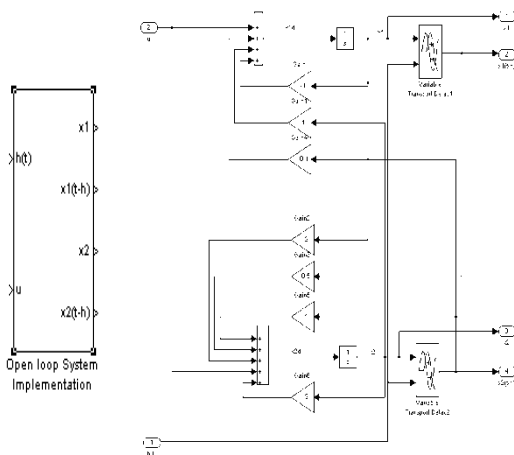


Fig.(1) The Simulink implementation of the open loop system

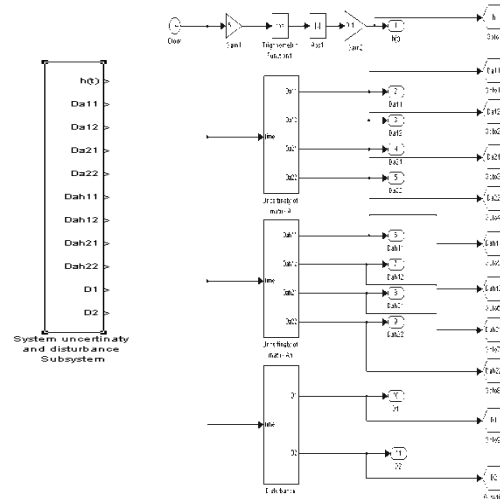


Fig.(2) The simulink implementation for system with uncertainty and disturbance.

The closed-loop dynamic trajectory of state variable X₁ (with and without delay) illustrated in figure (3).

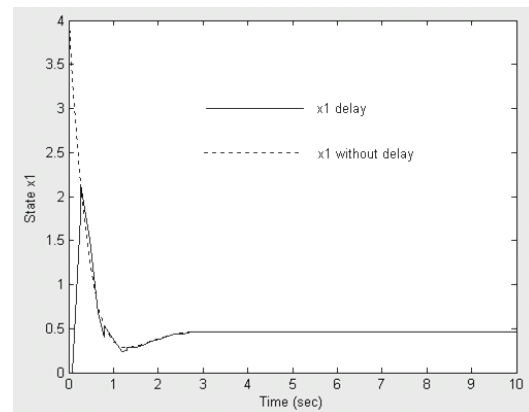


Fig.(3) State x1 response with initial condition =4.

And the same procedures for state X₂ are taken place the result is shown in figure (4).

Figure(5) illustrates the states trajectory (X₁ against X₂) without using the controller.

Note that: from figure (3) to figure (5) the initial conditions used is $X_{(0)} = [4 \ -2]^T$.

Figure (6) illustrates the Simulink implementation of the system with designed controller.

The state trajectory (X₁ and X₂ against time) is illustrated in Fig. (7) it is clear that the equilibrium value of both states goes to zero.

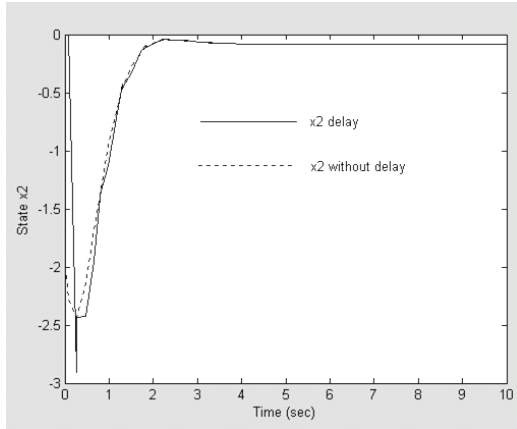


Fig.(4) State X_2 response with initial condition = -2.

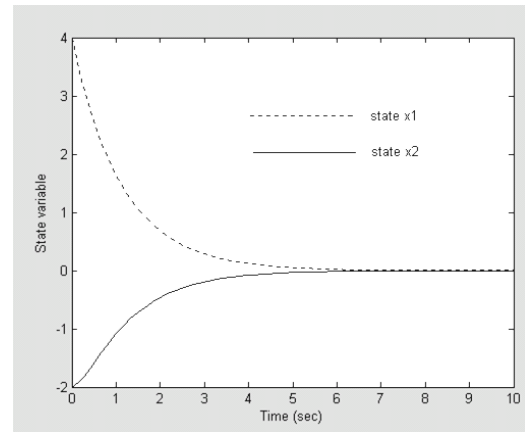


Fig.(7) State variable with controller.

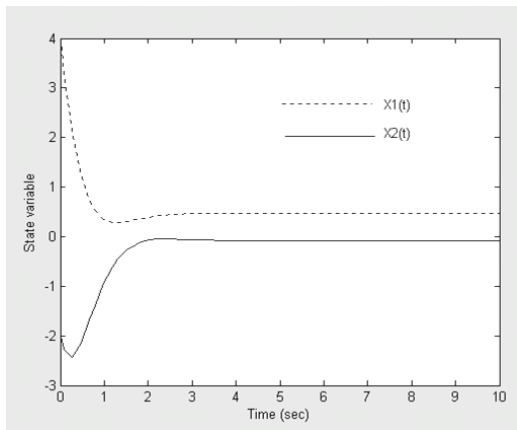


Fig.(5) State variable without controller.

Finally the phase plane plot of system without controller and with controller is illustrated in figure (8), it is clear the sliding phase when using the controller.

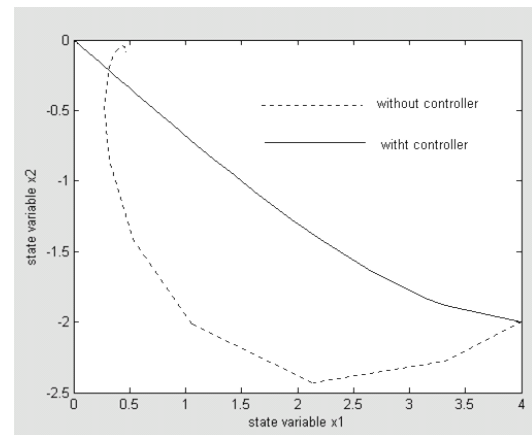


Fig.(8) Phase plane plot

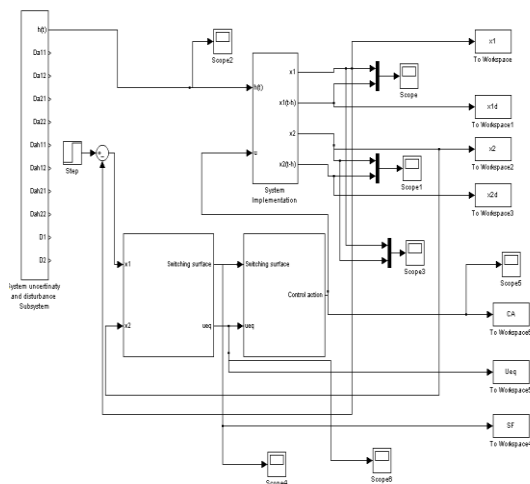


Fig.(6) the Simulink implementation of the system with controller.

4- Discussion and Conclusion:

The closed loop dynamic responses of the computer simulation are given from Fig.(3) to Fig.(5) with the initial conditions $X_{(0)} = [4 \ -2]^T$. It is clearly shown that each state variable approaches to a small bounded region in finite time as shown in Fig.(7) it is clear that the equilibrium value of both states goes to zero, note that the saturation function is adopted, and both switching function will enter a small bounded region. The case study

clearly demonstrates a very good advantage of the proposed control scheme.

In this work, variable structure with sliding mode controller is successfully designed for the system controlled with perturbed time-varying delays systems.

The VSC scheme is proposed for stabilizing a class of perturbed time-delay systems. Then by using the proposed control scheme, the controlled system is guaranteed to have the global asymptotically stable property.

Furthermore, the knowledge of the upper perturbations is not required and the desired systems performance is not required. Computer simulation results illustrated the design of variable structure with sliding mode controller and states trajectory for system performance are acceptable.

In general, the advantages of the proposed control are summarized as follows:

- The knowledge of the perturbation is not required.
- The perturbation adaptation strategy is simple to implement.
- The tracking accuracy is adjustable.
- The exact function of time-delay is not required.

References:

- [1] Xu J.-X., Jia Q.-X., and Lee T.-H., 2000, "Adaptive Robust Control of Uncertain Systems with Time-Varying State Delay", Vol.2, No. 1, PP.16-23.
- [2] DeCarlo R.A., Zak S.H. and Mathews G.P., 1988, "Variable Structure Control of Nonlinear Multivariable Systems: A Tutorial", Proceeding of IEEE, Vol.76, No.3, PP 212-232.
- [3] Hung J.Y., Gao W. and Hung J.C., 1993, "Variable Structure Control: A Survey", IEEE Yrans. Industrial Electronic, Vol. 40, PP. 2-22.
- [4] Slotine J.J.E and Coetsee J.A., 1986, "Adaptive Sliding Controller Synthesis for Nonlinear Systems", Int. J. Control, Vol. 43, PP. 1631-1651
- [5] Nilsson J., 1998, "Real-Time Control Systems with Delay", Sweden, Lunds Offset AB.
- [6] Jen W. and Karolos M.G., 2001, "LPV Systems with Parameter-Varying Time Delay and Control", Automatica, No. 37, PP. 221-229

LIMITATION & OPTIMIZATION OF GOVERNOR SPEED REGULATION FACTOR OF POWER SYSTEM STATION

Layth Tafwiq A. Ali

College of Engineering, Electrical Engineering Department
University of Al-Mustansiriya
Laith73a@yahoo.com

Abstract

For stable operation, the governors are designed to permit the speed to drop as the load increased. In the steady state characteristics of such a governor, the speed of the turbine will be decreased due a slop when the load increased. This slop is called the *speed regulation facto R*, which is the ratio of changing in the speed to the changing in the power for the same interval. The aim of this paper is to limit the speed regulation factor R and find the optimal value of its, where the speed regulation factor R is importance factor in the in the Load Frequency Control (LFC) and it is effected on the stability system. The programs that used in this paper are illustrated using Matlab package.

Keywords: *Load Frequency Control, Governor Speed Regulation Factor, Limit and Optimal.*

1. Introduction:

When the load is suddenly increased, the electrical power exceeds the mechanical input power. This power deficiency is supplied by the kinetic energy stored in the rotating system. The reduction in kinetic energy causes the turbine speed and, consequently, the generator frequency to fall. The change in the speed is sensed by turbine governor which acts to adjust the turbine input value to change the mechanical power output to bring the speed to a new steady-state. As the load is increased. The steady-state characteristics of this process of such governor is shown in figure(1)[1,2], where references [1,2] show how do governors with steady state speed regulation characteristic

interact when there are multiple generators in a power system. Also these references deals with the control of the system frequency after the increasing in the load which leads to decreasing in the system frequency as in the figure(1).Reference [3] also show as the load changes, the governors change the MW output of the units so that the steady-state total generation will equal the load. The actual frequency is the common value that will cause the total of the unit outputs to equal the system load. A change in unit MW output due to changes in system load is response to governor control. When actual frequency is not at the rated value, it can be changed to the rated value by supplemental control (Load Frequency Control LFC) that changes the set-points so that the sum of the set-points equals the system load. The change in unit MW output due to changes in the set-points is response to supplemental or LFC control. All the references in this paper deals with the steady state speed regulation characteristic as in the figure (1),but the work of this paper deals with dynamic response of the frequency deviation for the speed regulation factor R and from this way the paper found the limit & optimal value of R

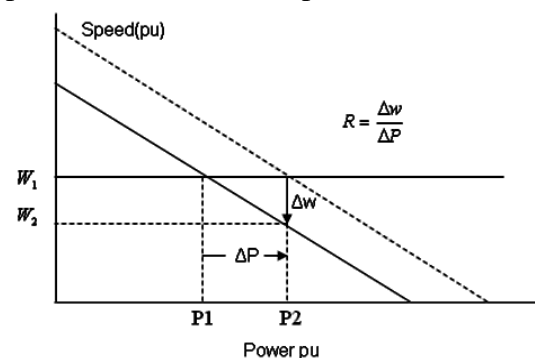


Figure (1): Governor steady-state speed power characteristics [1]

$P1$ is the per unit power at the steady state operation and it is equal to one per unit ($P1=1$ per unit).

$W1$ is the per unit speed at the steady state operation and it is equal to one per unit ($W1=1$ per unit).

$P2$ is the per unit power at the new steady state operation and it is equal to a value greater than $P1$.

$W2$ is the per unit speed at the new steady state operation and it should be less than $W1$.

R is the governor speed regulation factor and represent the slop of the curve in the figure (1) where [3]

$$R = \frac{\Delta w}{\Delta P} = \frac{w2 - w1}{P2 - P1} \quad (1)$$

2. The Power System Diagram:

The primary load frequency control (LFC) loop of the isolated power system is shown in figure (2) where each part of the power system is represent by its transfer function[4,5]

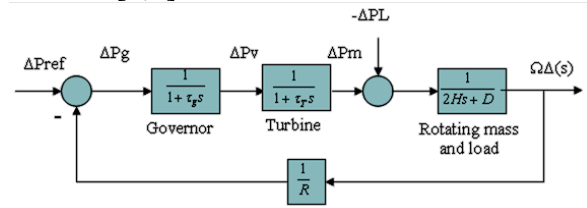


Figure (2): Load frequency control (LFC) of power station system [4].

Where:

ΔPm is the change in the mechanical power(output of the turbine)

$$\Delta Pm(s) = \frac{1}{1 + \tau_t s} \Delta P_v(s) \quad (2)$$

ΔP_v is the change in the steam value position (output of the governor).

$$\Delta P_v(s) = \frac{1}{1 + \tau_g s} \Delta P_g(s) \quad (3)$$

ΔP_g is the difference between the reference set power ΔP_{pref} and the power ($\frac{1}{R} \Delta w$) as

given from the governor speed characteristic, where

$$\Delta P_g(s) = \Delta P_{pref}(s) - \frac{1}{R} \Delta w(s) \quad (4)$$

Δf or $\Delta w(s)$ is frequency deviation of the station .

ΔPL is the change in the load.

ΔP_{pref} is the reference set power .

H is the inertia constant.

D is expressed as the percent change in load divided by the percent change in frequency.

For example if the load is change by 1.6 percent for 1 percent change in frequency, then $D=1.6$.

T_g is the governor time constant.

τt is the turbine time constant .

Also figure (2) can be simplified and represent as in the figure (3) [6][7].

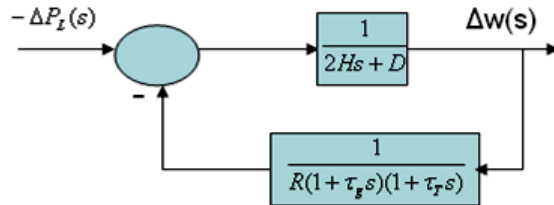


Figure (3): The equivalent block diagram LFC of figure(2) [6].

The open-loop transfer function of the block diagram in figure (3) is

$$KG(s)H(s) = \frac{1}{R(2Hs + D)(1 + \tau_g s)(1 + \tau_t s)} \quad (5)$$

and the closed-loop transfer function relating the load change ΔP_L to the frequency deviation Δw is :

$$T(s) = \frac{\Delta w(s)}{-\Delta P_L(s)} = \frac{(1 + \tau_g s)(1 + \tau_t s)}{(2Hs + D)(1 + \tau_g s)(1 + \tau_t s) + 1/R} \quad (6)$$

$$\Delta w(s) = -\Delta P_L(s) T(s) \quad (7)$$

The load change is a step input, i.e., $\Delta P_L(s) = \Delta P_L / s$.

Utilizing the final value theorem, the steady-state value of Δw is

$$\Delta w_{ss} = \lim_{s \rightarrow 0} s \Delta w(s) = (-\Delta P_L) \frac{1}{D + \frac{1}{R}} \quad (8)$$

It is clear that for the case with no frequency-sensitive load (i.e. with $D=0$), the steady-state deviation in frequency is

determined by the governor speed regulation, and is

$$\Delta w_{ss} = (-\Delta P_L)R \quad (9)$$

When several generator with governor speed regulations R_1, \dots, R_n are connected to the system, the steady state frequency deviation is given by[8]

$$\Delta w_{ss} = (-\Delta P_L) \frac{1}{D + \left(\frac{1}{R_1} + \frac{1}{R_2} + \dots + \frac{1}{R_n}\right)} \quad (10)$$

Now in order to find the range of the speed regulation factor (R) for control system stability, we use the Routh-Hurwitz array. This criterion provides a quick method for determining absolute stability that can be applied to an nth-order characteristic equation of the form:

$$a_n s^n + a_{n-1} s^{n-1} + \dots + a_1 s + a_0 = 0 \quad (11)$$

3. The calculation of the speed regulation factor R:

3.1 The data of the power system:

Consider the system in fig.(3), which have the following parameters:

Turbine time constant $\tau_T = 0.6$ sec .

Governor time constant $\tau_g = 0.3$ sec .

Generator inertia constant $H = 4$ sec .

If the load varies by 0.9 percent for a 1 percent change in the frequency (i.e. $D=0.9$). The output power (turbine rated power or mechanical power) is 250 MW at the nominal frequency of 50 Hz.

Let be assume that a sudden load change of 50 MW occurs ($\Delta PL = -0.2$ pu).

The following above parameters will be in figure (4) below due to figure (3)

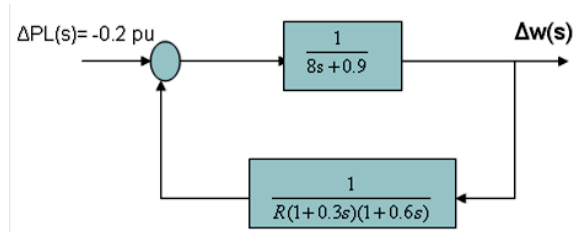


Figure (4): The block diagram of above system[4]

3.2 The critical value of the speed regulation factor R and the limitation of it:

Due to the above system in the figure(4). The first step is find the critical value of the speed regulation factor R which is show the ability of the system to be a stable or not stable by using the Routh-Hurwitz array, then find the limitation of R for a stable system as follow[7][9] .

The open loop transfer function of the above system as in the equation (5)

$$KG(s)H(s) = \frac{1}{R(8s + 0.9)(1 + 0.3s)(1 + 0.6s)} \quad (12)$$

$$= \frac{1}{R(1.44s^3 + 7.362s^2 + 8.81s + 0.9)} = \frac{1}{(8s + 0.9)(1 + 0.3s)(1 + 0.6s)} \quad (13)$$

Where

$$K = \frac{1}{R} \quad (14)$$

The characteristic equation is given by

$$1 + G(s)H(s) = \frac{k}{1.44s^3 + 7.36s^2 + 8.81s + 0.9} = 0 \quad (15)$$

Which result in the characteristic polynomial equation

$$1.44s^3 + 7.362s^2 + 8.81s + 0.9 + K = 0 \quad (16)$$

The Routh-Hurwitz array for this polynomial is then:

s^3	1.44	8.81
s^2	7.362	$0.9 + K$
s^1	$\frac{63.5632 - 1.44K}{7.362}$	0
s^0	$0.9 + K$	

Due to the Routh-Hurwitz array, and for a stable system,

$$\frac{63.5632 - 1.44K}{7.362} > 0 \dots \Rightarrow K < \frac{63.5632}{1.44} \Rightarrow K < 44.1411 \quad (17)$$

$$\text{Or } 0.9 + K > 0 \dots \Rightarrow K > -0.9 \quad (18)$$

Therefore K must be less than **44.1411** or greater than -0.9 which is neglected because K is a positive number .So that for stability system K must be less than **44.1411** and due to equation (14), the critical value of the speed regulation factor R is $1/K = 1/44.1411 = 0.0226$.

The limit of R for a stable system is: $R > 1/44.1411$ or $R > 0.0226$.

3.3 The Simulink method to find the limit & the optimal value of the governor speed regulation factor R:

The optimal value of the speed regulation factor R can be obtained due to the transient characteristic or dynamic state of the frequency deviation (Δw_{ss}) of the system where the best value of R will be at best response of the frequency deviation (Δw_{ss}). The response of the frequency deviation of the system in the figure(2) can be obtained by the Simulink method of Matlab package as in the figure(5) with the data in the section 3.1. Due to this Simulink and some of the Matlab commands, the parameters of the frequency deviation response (rise time, peak time, settling time, time of the frequency deviation, frequency deviation, peak amplitude and the percentage overshoot)[9] will be calculated in order to find the limit and optimal or best value of R as shown in table(1) and figures (6, 7, 8, 9, 10)

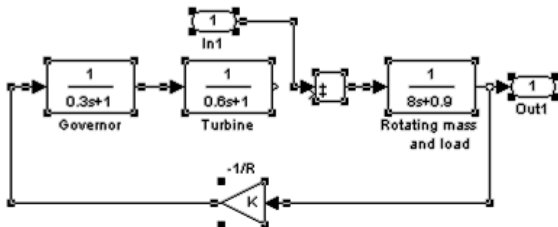


Figure (5) The Simulink of the power system of the figure (2)[9]

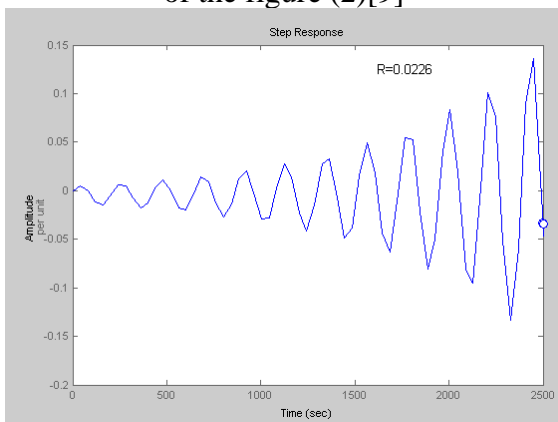


Figure (6) The frequency deviation of Simulink method with $R=0.0226$

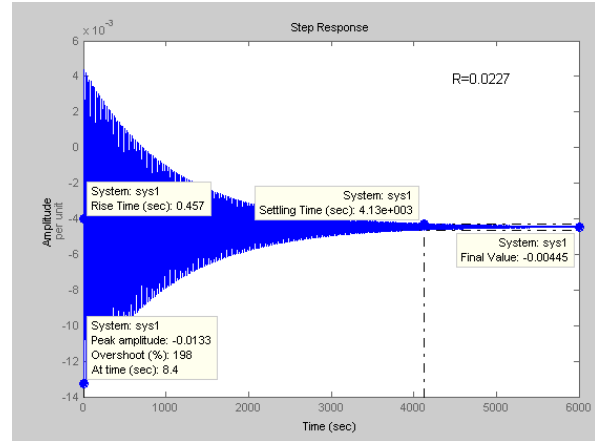


Figure (7) The frequency deviation of Simulink method with $R=0.0227$

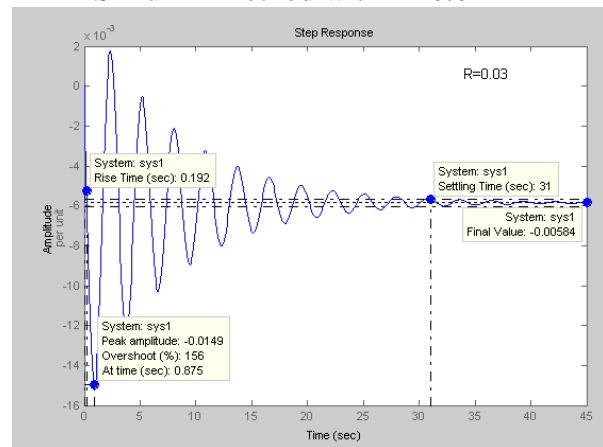


Figure (8) The frequency deviation of Simulink method with $R=0.03$

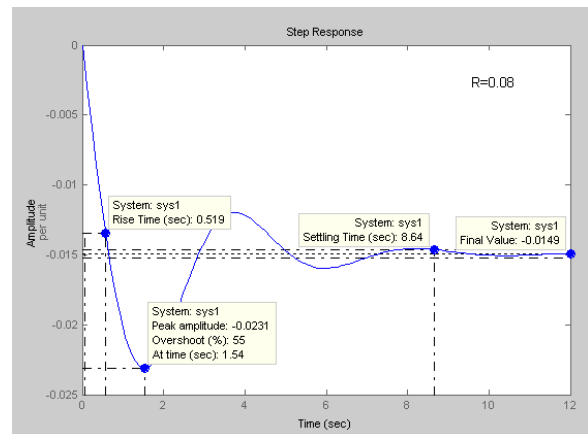


Figure (9) The Frequency deviation of Simulink method with $R=0.08$

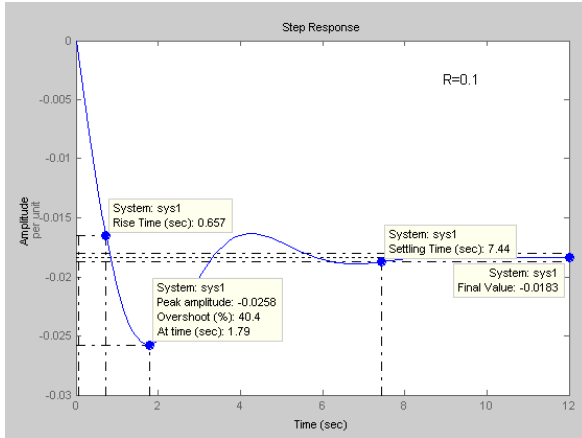


Figure (10) The Frequency deviation of Simulink method with **R=0.1**

R (pu)	Rise time (sec)	Peak time (sec)	Settling time (sec)	Time of (Δw_{ss}) sec	Steady state frequency deviation (Δw_{ss}) pu	Peak amplitude (pu)	Percent overshoot (%)
0.0226	Not stable	Not stable	Not stable	Not stable	Not stable	Not stable	Not stable
0.0227	0.457	8.4	4130	6000	-0.00445	-0.0133	198
0.026	0.166	0.854	61.4	90	-0.00508	-0.0141	178
0.03	0.192	0.875	31	45	-0.00584	-0.0149	156
0.04	0.255	1.05	17.3	25	-0.00772	-0.0169	119
0.05	0.32	1.23	12.3	18	-0.00957	-0.0186	94.6
0.06	0.386	1.32	9.71	15	-0.0114	-0.0202	77.8
0.07	0.452	1.41	8.4	15	-0.0132	-0.0217	64.9
0.08	0.519	1.54	8.64	12	-0.0149	-0.0231	55
0.09	0.588	1.67	7.28	12	-0.0167	-0.0245	47
0.1	0.657	1.79	7.44	12	-0.0183	-0.0258	40.4
0.11	0.728	1.92	5.8	12	-0.02	-0.027	34.9
0.12	0.8	2.05	6.02	10	-0.0217	-0.0282	30.3
0.13	0.874	2.08	6.19	10	-0.0233	-0.0294	26.4
0.14	0.95	2.21	6.31	10	-0.0244	-0.0306	23
0.15	1.03	2.34	6.34	9	-0.0264	-0.0317	20.1
0.2	1.43	3.07	5.07	9	-0.0339	-0.0373	10

Table (1) The parameters of the frequency deviation response due to the Simulink method in the figure (5)

The figures(6,7,8,9,10) represent the response of the frequency deviation due to the Simulink method in the figure(5) for different speed regulation factor R (0.0226, 0.0227, 0.03, 0.06 and ,0.1) respectively and it is chosen arbitrary from table(1) .Due to this table when the speed regulation factor R increase from (0.0227 to 0.2) for a stable system, the steady state frequency deviation Δw_{ss} will be increase as shown in the figure(11) also the rise time ,peak time and the peak amplitude will be increase , this is

from side but from the other side the time of the steady state frequency deviation (time of Δw_{ss}) will be decrease as in the figure(12) also the settling time ,and the percentage overshoot will be decrease .In general form and for optimization stable system ,the steady state frequency deviation (Δw_{ss}) and the time of Δw_{ss} , rise time, peak time, settling time, and peak amplitude should be at lesser values as possible as, but it is impossible in this case because as example for lesser value of steady state frequency deviation (Δw_{ss}), there will be a higher value of time of Δw_{ss} . Also for a higher value of steady state frequency deviation (Δw_{ss}), there will be a lesser value of time of Δw_{ss} . So that in order to solve this problem ,the speed regulation factor R should be chosen as a middle case between the two above cases (Δw_{ss} and time of Δw_{ss}), unless the designer or the system assume some assumption such as the system need a very small rise time or need a very small steady state frequency deviation (Δw_{ss}) in spite of the higher value of the time of the frequency deviation therefore in this case the designer should be choose a small value of R as in table(1) .Now for a stable system and without any assumption and for a middle case, the optimal value of the speed regulation factor is **R=0.08**, for the same data in section 3 .1

Therefore the parameters of the frequency deviation response for R=0.08 are:

The per unit steady state frequency deviation $\Delta w_{ss} = -0.0149$.

The steady state frequency deviation Δw_{ss} in Hz is $\Delta w_{ss} = -0.0149 * 50 = 0.745$ Hz (assume that the frequency is 50 Hz).The system frequency = $50 - 0.745 = 49.255$ Hz

The time of the steady state frequency deviation $\Delta w_{ss} = 12$ sec.

The peak amplitude = -0.0231 per unit.

The overshoot = 55% .

The rise time = 0.519 sec.

The peak time = 1.54 sec.

The settling time = 8.64 sec

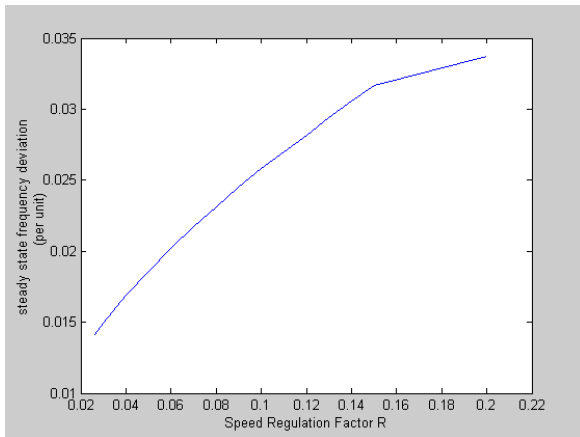


Figure (11) Variation of the steady state frequency deviation with the speed regulation factor **R**

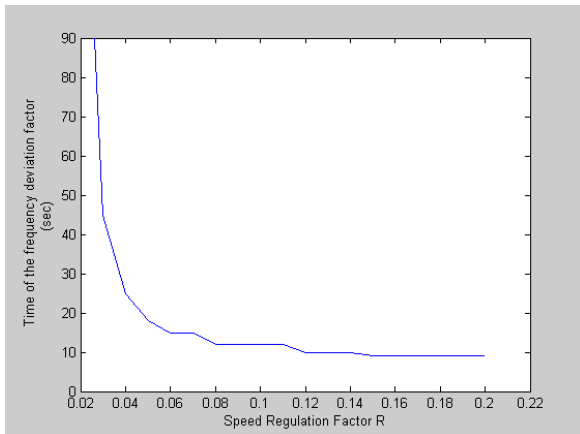


Figure (12) Variation of the time of the steady state frequency deviation with the speed regulation factor **R**

4. The Steady State Characteristic of the Governor Speed Regulation Factor **R**:

There is no way to find the optimal value of the speed regulation factor **R** due to the steady state characteristic of **R** (static state) as in the figure(13), because there is no parameters can be depend on it to choose the best value of **R**, instead of the transient characteristic (dynamic state), as in table(1) and the figures(6,7,8,9,10) where best value of **R** will be due to the best response of the frequency deviation and this depend on the parameters of the frequency deviation response (rise time, peak time, settling time, the time of the steady state frequency deviation, the steady state frequency

deviation, the peak amplitude and the percentage overshoot).

The figure (13) represent many specific values of the speed regulation factor **R** (0.0226546, 0.05, 0.07, 0.1, 0.15, 0.2) choosing arbitrary from table(1). These lines represent the slope of the relation between the frequency and the power after the steady state as in the figure(1)

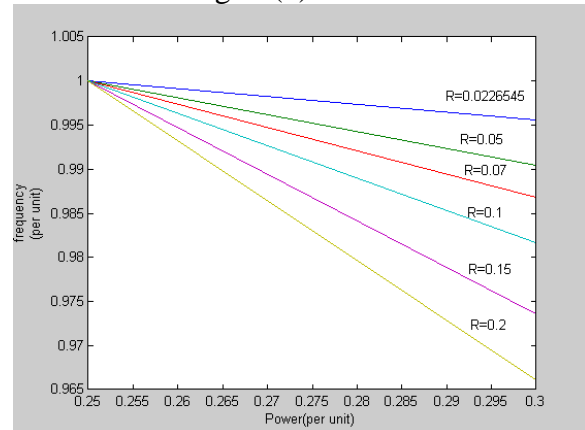


Figure (13) Governor steady state frequency power characteristic for different values of the speed regulation factor **R**

5. Checking the Result:

5.1 First check:

From table(1), and in order to make a first *check* for the solution of the method of the Simulink that used in section 3.3 to find the limitation and optimization of the speed regulation factor **R**.

Figures (6,7,8,9,10) represent the frequency deviation response at **R** equal to (0.0226, 0.0227, 0.03, 0.08 and 0.1) respectively and due to these figures, the system is unstable for **R**=0.0226 and stable for **R**(0.0227, 0.03, 0.08 and 0.1). Therefore the critical value of speed regulation factor **R** is **0.0226** and the system is stable for **R**>**0.0226** which is the same result that got it from section 3.2 due to the Routh-Hurwitz method.

5.2 Second check:

Now in order to make a *second check* for the solution of the method of the Simulink of Matlab package that used in section 3.3, let

take as example $R=0.0227$, $R=0.08$ and $R=0.1$.

Due to the data in the section 3.1, $\Delta PL=0.2$, $D=0.8$ and from equation (8)

The steady state frequency deviation (Δw_{ss}) will be:

$$\Delta w_{ss} = \lim_{s \rightarrow 0} s \Delta w(s) = (-\Delta P_L) \frac{1}{D + \frac{1}{R}} = -0.2 * \frac{1}{0.8 + \frac{1}{0.0227}} = -0.00445 \text{ pu}$$

$$\Delta w_{ss} = \lim_{s \rightarrow 0} s \Delta w(s) = (-\Delta P_L) \frac{1}{D + \frac{1}{R}} = -0.2 * \frac{1}{0.8 + \frac{1}{0.08}} = -0.01503 \approx 0.0149 \text{ pu}$$

$$\Delta w_{ss} = \lim_{s \rightarrow 0} s \Delta w(s) = (-\Delta P_L) \frac{1}{D + \frac{1}{R}} = -0.2 * \frac{1}{0.8 + \frac{1}{0.1}} = 0.0185 \approx 0.0183 \text{ pu}$$

Which is the same result that got it from table (1) for $R=0.0227$, $R=0.08$ and $R=0.1$ as in the figures (7,9,10).

6. Conclusion:

The aim of this paper is to find the limit and the optimal value of the governor speed regulation factor R . The limit of R can be calculated due to the Routh-Hurwitz or due to the Simulink method of Matlab package as in the section 3.3 and due to the data in section 3.1, the limit of the governor speed regulation factor R for a stable system is $R > 0.0226$, but it is very difficult to find the optimal value of the governor speed regulation factor R due to the Routh-Hurwitz or other calculation methods or even from the steady state frequency power characteristic (static response) as in the figure(13). It must be find the dynamic response of the system, that's mean find the transient response of the frequency deviation in order to find the optimal value of R , where best value of R will be due to the best response of the frequency deviation depending on the parameters of this response (rise time, peak time, settling time, time of the frequency deviation, steady state frequency deviation, peak amplitude and the overshoot). The Simulink method of the Matlab package in section 3.3 can be find the dynamic response

(frequency deviation response) of the system as in the table(1) and the figures(6,7,8,9,10).

Due to this table, the optimal or the best value of the governor speed regulation factor R for a stable system is $R=0.08$ without any assumption from the designer where the designer can be choose any value of R for a stable system depending on the parameters of the response of the frequency deviation (rise time, peak time,.....etc) as in the section 3.3. A two check are applied on the Simulink method in section 5.1 and 5.2 to vary the result and it is found applicable.

References:

- [1] Green, B., 2009, "Governor and AGC control of system frequency", TRE Technical workshop.
- [2] Bian, J., "Generator frequency response", NERC, North American electric reliability corporation, 2009.
- [3] RKG, 2008, "Governor/AGC model with and without governor deadbands".
- [4] Saccomanno, F., 2003, "Electrical Power System Analysis and Control", John wily & sons, publication.
- [5] Glover, J.D & Saram, M., 2002, "Power System Analysis and Design", BROOKS/COLE : THOMSON LEARNING
- [6] Hoa D. Vu & J. C. Agee, 2002, "WECC Tutorial on Speed Governors", WECC control work group.
- [7] Ogata, K., 2002, "Modern Control Engineering", Prentice Hall.
- [8] Weedy, B.M & Cory, B. J, 2004, "Electrical Power System", Johnwiley & sons.
- [9] Benjamin, C. & Golnaraghi, F., 2003, "Automatic Control Systems", John wiley & sons, Inc.

Topic 2

Robots and Their Applications

HUMAN ARM SIMULATION BASED ON MATLAB WITH VIRTUAL ENVIRONMENT

Dr. Mohammed Z. Al-Faiz, MIEEE
Computer Engineering Department
Al-Nahrain University
mzalfaiz@ieee.org

Dr. Abduladhem A. Ali
Computer Engineering Department
Basrah University
abduladem1@yahoo.com

Abbas H. Miry
Electrical Engineering Department
Al-Mustansiriyah University
abbasmiry83@yahoo.com

Abstract

This work presents a novel simulation methodology applied to a human arm. It is aimed to allow the robotic system to perform complex movement operations of human arm. The human arm is represented by using virtual reality (VR). The work includes mathematical modeling of the direct kinematics, inverse kinematic and the dynamics of the human arm. The model permits direct forward dynamics simulation, which accurately predicts hand position, also presents a solution to the inverse problem of determining set of joints angle to achieve a given position or motion. The method implements in the 3D space and uses the Simulink/ MATLAB Ver.2009a approach. This methodology can be used with different robots to test the behavior and control laws.

Keywords: *Human Arm, Inverse Kinematic, Levenbrge marquite, Virtual Reality.*

1. Introduction

Robotics is one of the main disciplines in the industry which can be used in the development of new technologies. The synergy of robotics with the different applications like submarine task, car assembly operation, vision systems and artificial intelligence allows the innovation and reduces the manufacture costs. For this purpose, it is important that the robot programmers are able to visualize and test the behavior of the robots

in different circumstances and with different parameters [1].

Motion is one of the most natural and important activities that a human being can practice, even before birth. Thus, one of the major difficulties by those who are fitted with prosthetic devices is the great mental effort needed during the first training stages. This makes it very difficult to precisely detect the spatial position as well as the forces done by the prosthesis in replacement of the muscle. This problem is still more complicated when working with upper limb prosthesis, whose function is to simulate its biological equivalents (shoulder, arm, forearm, elbow, and wrist). All these mechanisms present a very efficient system with a lot of information (degrees of freedom, speed, angles etc) to be simulated and absorbed by brain commands to help professionals dedicated to special physical needs patient rehabilitation [2].

Some other works only make a 3D virtual that deal with the use of Matlab for systems simulations, M. Z. Al-Faiz[3] presents architecture for posture learning of an anthropomorphic robotic arm using Matlab/Simulink with virtual reality. The approach was aimed to allow the robotic system to perform complex movement operations of human arm; in this paper only forward kinematic is used in the simulation. B. Lee et al [4] presents the simulation of humanoid walking pattern using 3D simulator with Virtual Reality Toolbox. By using the Virtual Reality Toolbox incorporated with MATLAB, The simulator was composed of

three modules, namely, waking pattern code, kinematics code and display code. V. Sanchez et al [1] simulated methodology of the 5-DOF includes mathematical modeling of the direct, inverse and differential kinematics as well as the dynamics of the manipulator. This method was applied to test the robot CATALYST 5 by using a project in Simulink and Matlab. The method implements the path following in the 3D space and uses the Matlab-Simulink approach.

The main objective of the present work is to show a complete simulation of human arm, where, the combination of Matlab/Simulink and virtual reality is proposed. The method allows to manipulate the human arm system and to visualize the robot's behavior from different perspectives.

2. Human Arm Modeling

The modeling of a manipulator robot with n degree of freedom (DOF.) can be divided in three steps: Direct Kinematics, Inverse Kinematics, and Dynamics.

2.1. Kinematics of Human Arm Based Levenberg-Marquardt Algorithm

Kinematics is the study of motion without regard to the forces that create it. The representation of the robot's end-effector position and orientation through the geometries of robots (joint and link parameters) are called forward Kinematics. The forward kinematics is a set of equations that calculates the position and orientation of the end-effectors in terms of given joint angles. This set of equations is generated by using the D-H parameters obtained from the frame assignation [5]. The inverse kinematics problem (IKP) for a robotic manipulator involves obtaining the required manipulator joint values for a given desired end-point position and orientation. It is usually complex due to lack of a unique solution and closed-form direct expression for the inverse kinematics mapping [6].

2.2 Structure and Kinematics of Human Arm

The development of a high-DOF, kinematic is discusses human arm model that can be used to predict realistic human arm postures. One may deal with human arm by 7-DOF and assume the origin at shoulder joint. The first joint is the shoulder joint s with 3 DOFs.

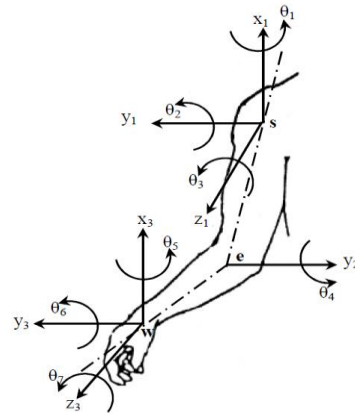


Fig.1. Kinematic chain of human arm

The elbow joint e has only one DOF. The wrist joint w is of the same type as the shoulder joint s and also has 3 DOFs. Note that the arrow at the end of the chain indicates the end effectors orientation and is not another link. It can be focused on a kinematic chain that is formed after a human arm. This means the kinematic chain has 3 joints with spherical joints as shoulder and wrist joint and a hinge joint as the elbow joint. The spherical joints have 3 DOFS while the hinge joint has only one DOF, giving a total of 7 DOFs for this kinematic chain, see Fig.1. The homogeneous transformation matrices for the frame transitions are set up with D-H parameters.

Table 1. D-H Parameters of human arm

Frame (joint)	q_i (rad)	d_i (cm)	a_i (cm)	α_i (rad)
1	q_1	0	0	$\pi/2$
2	q_2	0	0	$\pi/2$
3	q_3	0	20	$-\pi/2$
4	q_4	0	25	$\pi/2$
5	q_5	0	0	$-\pi/2$
6	q_6	0	0	$\pi/2$
7	q_7	0	0	$-\pi/2$

It has following transformation matrices

$$A_1 = \begin{bmatrix} c_1 & -s_1 & 0 & 0 \\ 0 & 0 & -1 & 0 \\ s_1 & c_1 & 0 & 0 \\ 0 & 0 & 0 & 1 \end{bmatrix},$$

$$A_2 = \begin{bmatrix} c_2 & -s_2 & 0 & 0 \\ 0 & 0 & -1 & 0 \\ s_2 & c_2 & 0 & 0 \\ 0 & 0 & 0 & 1 \end{bmatrix}$$

$$A_3 = \begin{bmatrix} c_3 & -s_3 & 0 & a_3 \\ 0 & 0 & 1 & 0 \\ s_3 & -c_3 & 0 & 0 \\ 0 & 0 & 0 & 1 \end{bmatrix}$$

$$A_4 = \begin{bmatrix} c_4 & -s_4 & 0 & a_4 \\ 0 & 0 & -1 & 0 \\ s_4 & c_4 & 0 & 0 \\ 0 & 0 & 0 & 1 \end{bmatrix}$$

$$A_5 = \begin{bmatrix} c_5 & -s_5 & 0 & 0 \\ 0 & 0 & 1 & 0 \\ s_5 & -c_5 & 0 & 0 \\ 0 & 0 & 0 & 1 \end{bmatrix}$$

$$A_6 = \begin{bmatrix} c_6 & -s_6 & 0 & 0 \\ 0 & 0 & -1 & 0 \\ s_6 & c_6 & 0 & 0 \\ 0 & 0 & 0 & 1 \end{bmatrix}$$

$$A_7 = \begin{bmatrix} c_7 & -s_7 & 0 & 0 \\ 0 & 0 & 1 & 0 \\ -s_7 & -c_7 & 0 & 0 \\ 0 & 0 & 0 & 1 \end{bmatrix}$$

Where 'c' is cosine of theta and 's' is sin of theta, the forward kinematic represents by T

$$T = A_1 * A_2 * A_3 * A_4 * A_5 * A_6 * A_7$$

$$A_7 \begin{bmatrix} nx & ox & ax & dx \\ ny & oy & ay & dy \\ nz & oz & az & dz \\ 0 & 0 & 0 & 1 \end{bmatrix} \quad (1)$$

2.3 Dynamic of Human Arm Based Genetic Algorithm

Decentralized control has been widely accepted by the robotics industry due to ease of implementation and tolerance to failure. Conventional controllers for industrial robots are based on independent joint control schemes in which each joint is controlled separately by a simple position servo loop with predefined constant gains [7]. In this paper, the proposed scheme is based on the principle of treating each joint as a subsystem in which the joint dynamics are modeled by a third order system plus a disturbance torque. By a simple disturbance cancellation procedure, the disturbance in the joint dynamic equation is directly rejected so that simple fixed linear joint controllers can be readily designed. Fig. 1 shows the structure of Human arm which has 7 Degree Of Freedom(DOF), this mean seven motor are used to represent movement of human arm with independent joint control. The equation describing the dynamic behavior of the DC motor is given by the following equations:

$$G(s) = \frac{K_b}{[JLaS^3 + (RaJ + BLa)S^2 + (K_bK_T + RaB)S]} \quad (2)$$

As PID controller has simple structure, easy to understand, the tuning technique provides adequate performance in the vast majority of applications, the PID controller is widely used in most industrial processes, despite continual advances in control theory it cannot Effectively control complicated or fast system such as motor controlled systems, however, because the response of a plant depends on three parameters (P, I, and D) and gain must be manually tuned by trial and

error. Most PID tuning rules use conventional methods. This requires considerable technical experience to apply tuning formulas to determine PID controller parameters.

GA is a stochastic global adaptive search optimization technique based on the mechanisms of natural selection. Recently, GA has been recognized as an effective and efficient technique to solve optimization problems. As a mathematical means for optimization, GAs can naturally be applied to the optimal-tuning of PID controllers. With reference to a step input signal, the entire system will generate an output step response. The role of the PID controller is to drive this output response within the user's specifications. Obviously, the parameter settings of the PID controller should be fine tuned so as to meet as high requirements as possible. In this paper, genetic algorithm is operated with following: number of population =20, probability of crossover is 0.8, probability of mutation is 0.01.

The most crucial step in applying GA is to choose the objective functions that are used to evaluate fitness of each chromosome. Some works use performance indices as the objective functions. The objective functions are Integral of Time multiplied by Squared Error (ITSE), Integral of Time multiplied by Absolute Error (ITAE), Integral of Absolute Magnitude of the Error (IAE), and Integral of the Squared Error (ISE), integral term become summation in the discrete time.

The PID controller is used to minimize the error signals, or we can define more rigorously, in the term of error criteria: to minimize the value of performance indices mentioned above. And because the smaller the value of performance indices of the corresponding chromosomes the fitter the chromosomes will be, and vice versa, we define the fitness of the chromosomes as

$$fitnessvalue = \frac{1}{Objectivefunction} \quad (3)$$

In this paper a multi objective is introduced to get better time response by replacing fitness value in Eq (4) by

$$= \frac{1}{w*t_s + w*ov + Objectivefunction} \quad (4)$$

Where

Objective function is taken from Eq (3).

$w \gg 1$ since the value of performance index is very large with respect to the settling time and overshoot.

3. Inverse Kinematics Solution Using Optimization Method

The problem of inverse kinematics is not linear, as rotations are involved. This means that analytical solutions are only available in limited situations. In all other cases, alternative methods will have to be employed. The most-used alternative is numerical solutions. Analytical solutions are the best option to use when available, as they are the fastest and most reliable inverse kinematics solvers. The problem of analytically solving inverse kinematics is that it does not scale to more complex bone sets and is therefore only an option for simple situations, like robot arms with few joints, or a single human leg. The numerical solution that can be utilized to solve the inverse kinematics problem is through the use of existing optimization algorithms. For optimization of a reference joint angle configuration regarding the similarity measure, one can use the Levenberg-Marquardt algorithm. The algorithm provides a standard technique for solving nonlinear least squares problems by iteratively converging to a minimum of function expressed as sum of squares. Combining the Gauss-Newton and the steepest descent method, the algorithm unites the advantages of both methods. Hence, using the LM method, a more robust convergence behavior is achieved at points far from a local minimum, while a faster convergence is gained close to a minimum. Due to its numerical stability, the LM method has also become a popular tool for solving inverse kinematics problems as demonstrated in [8]. The LM algorithm is an iterative technique that locates a local minimum of a multivariate function that is expressed as the sum of squares of several non-linear, real-

valued functions. It has become a standard technique for nonlinear least-squares problems, widely adopted in various disciplines for dealing with data-fitting applications. LM can be thought of as a combination of steepest descent and the Gauss-Newton method. When the current solution is far from a local minimum, the algorithm behaves like a steepest descent method: slow, but guaranteed to converge.

$$E(x) = \frac{1}{2} \sum e^T(x)e(x) \quad (5)$$

The Gauss-Newton method can be written as $x^{k+1} = x^k - [J(x^k).J(x^k)]^{-1}.J(x^k).e(x^k)$ (6)

LM method can be expressed with the scaling factor

$$x^{k+1} = x^k - [J(x^k).J(x^k)\lambda.I]^{-1}.J(x^k).e(x^k) \quad (7)$$

Where I is the identity matrix[9].

It required minimizing the error between the target transformation matrix and calculated transformation matrix, the problem can be formularizing as optimization problem as following:

$$\text{Minimize } e(q) = \begin{bmatrix} |P_x^d - dx| \\ |P_y^d - dy| \\ |P_z^d - dz| \end{bmatrix} \quad (8)$$

Subject to

$$q_i^l \leq q_i \leq q_i^u \quad i=1 \dots 7$$

$$q^l = \left[-\frac{\pi}{2} - \frac{11\pi}{2} - \frac{\pi}{2} \frac{\pi}{12} - \frac{\pi}{3} - \frac{\pi}{9} - \pi \right]$$

$$, q^u = \left[\frac{\pi}{2} \frac{2\pi}{3} \frac{\pi}{2} \frac{5\pi}{6} \frac{\pi}{3} \frac{\pi}{9} \quad 0 \right]$$

Where p^d Target position in the space. These constrain become

$$q_i^l - q_i \leq 0, q_i - q_i^u \leq 0 \quad i=1 \dots 7$$

By convert this constrained problem to unconstrained problem using penalty function [10], the problem become

$$e(q) = \begin{bmatrix} |P_x^d - dx| \\ |P_y^d - dy| \\ |P_z^d - dz| \\ G_{1i} \\ G_{2i} \end{bmatrix} \quad (9)$$

$$G_{1i} = \max(0, (q_i^l - q_i)),$$

$$, G_{2i} = \max(0, (q_i - q_i^u)) \quad i=1 \dots 7,$$

Eq (9) becomes unconstrained objective function to be minimized.

4. Virtual Reality

With the advent of high-resolution graphics, high-speed computing, and user interaction devices, virtual reality (VR) has emerged as a major new technology in recent years. An important new concept introduced by many VR systems is immersion, which refers to the feeling of complete immersion in a three-dimensional computer-generated environment by means of user-centered perspective achieved through tracking the user. This is a huge step forward compared to classical modeling and CAD/CAM packages, VR technology is currently used in a broad range of applications, the best known being flight simulators, walkthroughs, video games, and medicine (virtual surgery). From a manufacturing standpoint, some of the attractive applications include training, collaborative product and process design, facility monitoring, and management. Moreover, recent advances in broadband networks are also opening up new applications for virtual environments in these areas [11].

5. Proposed Model and VR Simulation for a Human Arm

The simulator was built using MATLAB with Virtual Reality Toolbox. MATLAB provides powerful engineering tool including frequently used mathematical functions. It is easy to implement control algorithm including visualization of data used in the algorithm. In addition, by using Virtual Reality Toolbox, it is convenient to treat 3D objects defined with

VRML (Virtual Reality Modeling Language). Thus, it is possible to build a simulator within a relatively short period. Virtual Reality (VR) is a system which allows one or more users to move and react in a computer generated environment. The basic VR systems allow the user to visual information using computer screens. The simulation contain two part ,first, building model for human arm in VRML, second, constitution the Simulink model in MATLAB then call and run the model of human arm using virtual reality toolbox.

5.1. The VRML Model for Human Arm

To realize the VRML model for Human arm save the file as All.wrl file, which is the file format for Virtual Reality software, the VRML model of the Human arm was designed in V-Realm Builder 2.0 .In Fig.2 is presented the VRML model of the Human arm. In V-Realm Builder 2.0 program it was defined the viewpoints, the background properties, the properties for each element, its position and orientation, etc. In Fig.3 is presented the V-Realm Builder 2.0 captured screen with all the views of the VRML model of the Human arm.

5.2 The Simulink Model for Human Arm

The VRML model represents a Human arm. It is manipulated by a simple Simulink model as it can be seen in Fig.4. As it can be seen from Fig.4 the Human arm is represented by several blocks: the first one named Target position which is represent the desired target ,the second block calculate the inverse kinematics of desired target to produce desired angle, the third block is dynamic part which contain PID controller and fourth part is simulation part using virtual reality.

6. Simulation Results

The implemented simulation of human arm which built in VR technique, the solution of inverse kinematic equations and control of joints are achieved by MATLAB Ver.R2009a. Fig.4 represents the connection between MATLAB\Simulink, which solve the

kinematic equations, and VR model of human arm. The moving commands for this model are calculated in MATLAB and then they implement in VR. Different cases of PID control are studied and illustrated in Fig. 5,6,7,8 and 9 From Fig.7,8,9 it can be seen the ability of performed GA based PID tuning with our fitness function ,that remove the overshoot and reduce the settling time with lower error, finally the trajectory of human arm using the proposed fitness function has better motion . As inputs sources for the block that represent the target positioning kinematics part ,joint angle of human arm are calculated using optimization method (Levenberg-Marquardt algorithm).In dynamic part two methods of controlling are used, first using proportional gain equal to one, second using PID control tuning by genetic algorithm.

7. Conclusion

This paper presents the mechanical analysis of human arm joints (shoulder, elbow and wrist).The modeling of the human arm includes direct and inverse kinematics as well as dynamics. This method was applied to test the human arm control by using a project in Simulink/Matlab with virtual reality. A proposed method was represented in the 3D space the simulation show the good performance of the proposed methodology. From the obtained results, it can be concluded that, The Virtual Reality is useful to test the viability of designs before the implementation phase on a virtual reality prototype, the ability of performing of GA based PID tuning for human arm .The system is of flexibility due to the easy program language. So it is really useful before lab experiment and hardware design for human arm. It gives a clear direction to the design of human arm control system and the entire optimum design.

Appendix: Dynamic of DC Motor

The equations describing the dynamic behavior of the DC motor are given by the following equations;

$$v = Ri + L \frac{di}{dt} + e_b \quad (10)$$

$$T_m = K_T * i_a(t) \quad (11)$$

$$T_m = J \frac{d^2\theta(t)}{dt^2} + B \frac{d\theta(t)}{dt} \quad (12)$$

$$e_b = e_b(t) = K_b \frac{d\theta(t)}{dt} \quad (13)$$

After simplification and taking the ratio of $\theta(s)/v(s)$ we will get the transfer function as below,

$$G(s) = \frac{\theta(s)}{v(s)} = \frac{K_b}{[JLaS^3 + (RaJ + BLa)S^2 + (K_bK_T + RaB)S]} \quad (14)$$

When an industrial robot transfers objects of different masses, the dynamics of DC motor will be changed, also, for disturbance rejection it is more efficient PID control system which it is well known as a simple and useful method to control manipulators. Many industrial robots use a form of so called PID control law [12] as

$$\ddot{q}_d + k_p e + k_d \dot{e} + k_i \int e dt = u \quad (15)$$

Where u is the control law vector, $e = q_d - q$ is the position error vector, q_d is the desired joint angle vector, q is the joint angle vector, k_p , k_d and k_i are the coefficient of PID controller.

References

- [1] Sanchez .V, Gutierrez .R, Valdovinos .G and Ortega .P,2010 “5-DOF manipulator simulation based on MATLAB-Simulink methodology “, 20th International Conference on Electronics, Communications and Computer (CONIELECOMP, pp: 295 - 300 .
- [2] Grecu.V, Grecu.L, Demian.M and Demian.G, 2009,”A Virtual System for Simulation of Human Upper Limb “, Proceedings of the World Congress on Engineering London, U.K., Vol. 2, pp: 1474-1478.
- [3] Al-Faiz, M. Z., 2009,” A Posture Human Robotic Arm by Inverse Kinematic With Virtual Environment”, MASAUM Journal of Basic and Applied Sciences, Vol.1, No. 4,
- [4] Lee. B, Kim .Y, Yoo. J, Park .I and Kim .J, 2008,”Walking Pattern Simulation based on Virtual Reality Toolbox”.
- [5] Xu, D., and Acosta .A, 2005,” An Analysis of the Inverse Kinematics for a 5-DOF Manipulator”, International Journal of Automation and Computing Vol. 2 , pp :114-124 .
- [6] Hua. Cand shan.W.,2006 , “Wavelet network solution for the inverse kinematics problem in robotic manipulator”, Chen Zhejiang Univ Science , Vol. 7 ,No. 4 PP: 525-529.
- [7] Hsia .T. C, Lasky T. A, andGuo.Y, 1988 “Robust Independent Robot joint control: design and Simulation”, 1988 IEEE International Conference on Robotics and Automation, vol.3 pp: 1329-1334.
- [8] Wampler.C. W, 1986”Manipulator inverse kinematic solutions based on vector formulations and damped least-squares methods”, IEEE Transactions on Systems, Man and Cybernetics, no 1 pp 93–101.
- [9] Endisch .C and Kennel .R, 2009” Levenberg-marquardt-based BS algorithm using adaptive pruning interval for system identification with dynamic neural networks”, IEEE International Conference on Systems, Man, and Cybernetics , San Antonio, TX, USA, pp 3402 - 3408.
- [10] Rao. S. S, 1996”Engineering Optimization Theory and Practice”, Third Edition John Wiley & Sons, Inc.
- [11] Tachi, S., 1998,” Virtual Reality in Robotics” In: Proceedings of the 8th International Symposium on Measurement and Control in Robotics ISMCR '98. Prague, pp. 29-34.
- [12] Craig.J. J,2009,” Introduction to Robotics, Mechanics and Control”, Addison-Wesley.

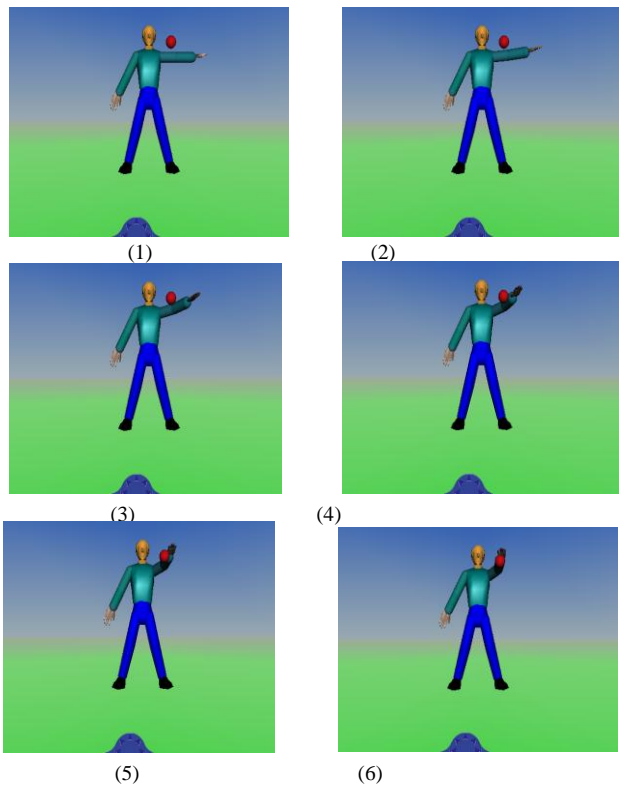


Fig. 5 Human arm movements with proposed PID

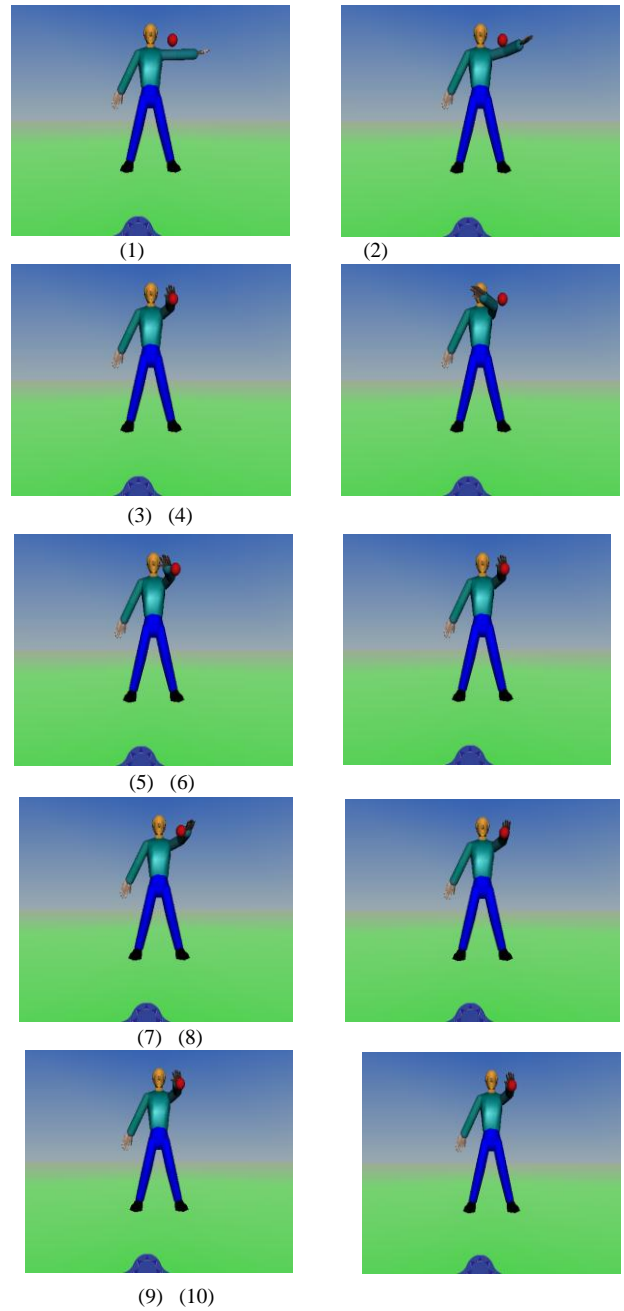


Fig.6. Human arm movements with unity feedback

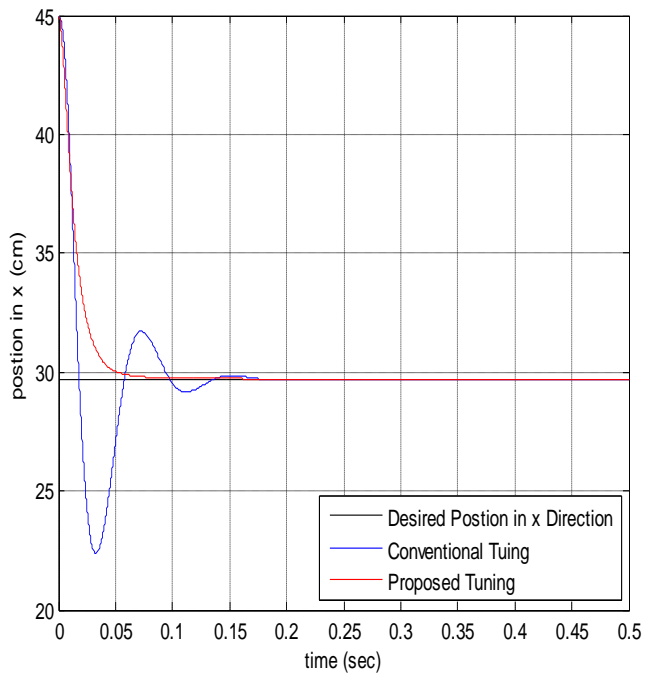


Fig .7 Position Responses in X Direction

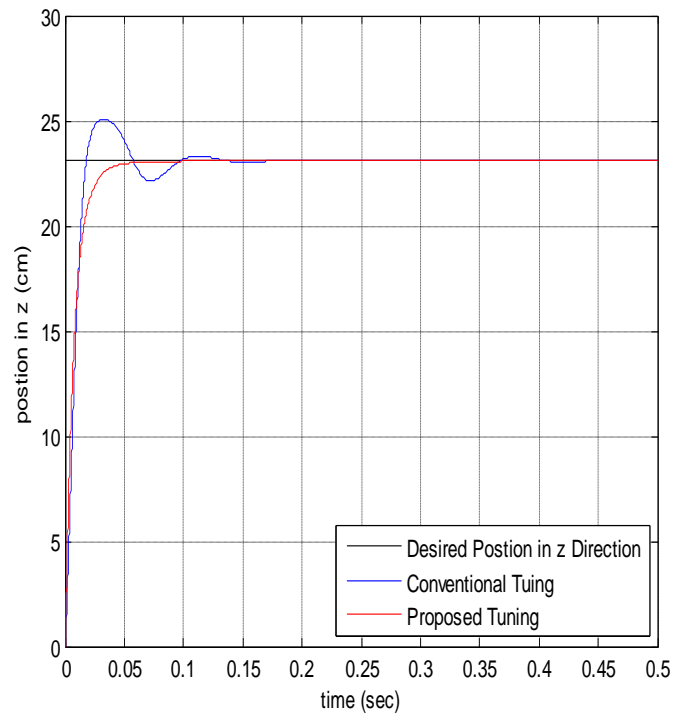


Fig.9 Position Responses in Z Direction

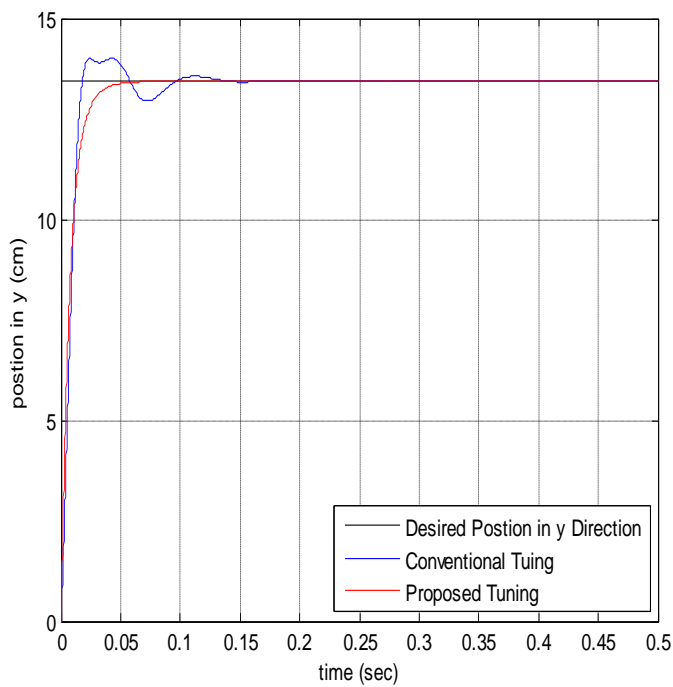


Fig .8 Position Responses in Y Direction

MEASUREMENT OF HUMAN LEG JOINT ANGLE THROUGH MOTION BASED ON ELECTROMYOGRAPHY (EMG) SIGNAL

Dr. Yousif I. Al-Mashhadany, MIEEE

Electrical Engineering Department

College of Engineering

University of Anbar

yousif_phd@hotmail.com

Abstract:

Surface electromyography (SEMG) measurement technique for the signal was produced through the contraction of muscle in human body. The surface electrode is connected on the skin of the muscle. This paper presents off-line design for estimation of the actual joint angle of human leg was obtained in performing flexion-extension of the leg at slow and high speeds movement. The design is composed of two phases. The first is measured of real EMG signal of human leg performance by using SEMG technique and processing this signal with filtering, amplification and then normalized with maximum amplitude. The second phase is artificial neural network (ANN) design was trained to predict the joint angle from the parameters were extracted from the SEMG signal. Three main parameters of EMG signal are used in prediction process: Number of turns in specific time period, duration of signal repetition and amplitude of signal. The design of ANN is included the identification of performance human leg EMG signal with two speed level (slow-fast) and estimation of knee joint angle by recognition process depended on the parameters of real measured EMG signal. The real EMG signal is measured from full leg-extension to full leg-flexion by (3 sec) with slow motion and (1 sec) at fast motion. Root mean square (RMS) errors were calculated between the actual angle (measured by the trigonometric formula was applied with any human leg gives real EMG signal measurement) and the angle predicted by the neural network design. This design is simulated by using MATLAB Ver. R2010a,

and satisfied results are obtained, that explains the ability of estimation of joint angle for human leg, where the RMS errors are obtained from (0.065) to (0.015) at fast speed leg flexion -extension and from (0.018) to (0.0026) at slow speed leg flexion-extension.

Keywords: *Surface Electromyography (SEMG), Artificial Neural Network (ANN).*

1- Introduction

Surface electromyography (SEMG) signals provide a non-invasive tool for investigating the properties of skeletal muscles. The bandwidth of the recorded potentials are relatively narrow (50-500 Hz), and their amplitude is low (50 μ V - 5 mV). These signals have been used not only for monitoring muscle behavior during rehabilitation programs, but also for the mechanical control of prostheses. In this context, it is important to be able to correctly predict which movement is intended by the user. The SEMG signal is very convenient for such application, because it is noninvasive simple to use, and intrinsically related to the user's intention. However, there are other useful variables, especially those related to proprioception, for example: the angle of a joint, the position of the limb, and the force being exerted [1,2].

Specifically, for the development of an active leg prosthesis that also possesses ankle and foot axes, it is necessary to use other sources of information besides SEMG. Thus, the use of myoelectric signals combined with other variables related to

proprioception may improve the reliability in closed-loop control systems. Fig.1. presents the typical main components of general myoelectric pattern recognition. The SEMG signals are acquired by surface electrodes placed on the skin over muscle(s) of the user. The signals originating from the electrodes are pre-amplified to differentiate the small signals of interest, and then are amplified, filtered and digitized. Finally, the information is transferred to a myoelectric controller[3].

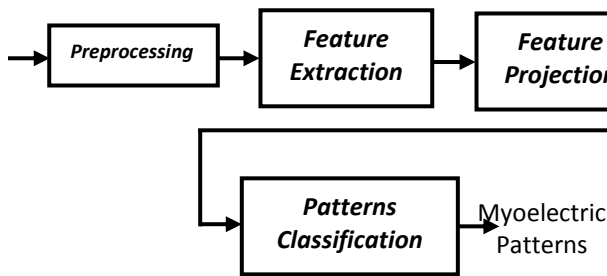


Fig.1. Typical main components of a general myoelectric controller based on pattern recognition.

The knee joint is one of the most complex synovial joints that exist in the human body, whose main functions are: to permit the movement during the locomotion, and to allow the static stability. The mobility associated with the knee joint is indispensable to human locomotion and it helps the correct foot orientation and positioning in order to overcome the possible ground irregularities. In the knee articulation, there are three types of motion, namely, flexion, rotation, and sliding of the patella. The knee joint includes three functional compartments, medial, lateral, and patello-femoral, which make the knee quite susceptible to injuries and chronic disease, such as displacement, arthritis, ligaments rupture, and menisci separation. In fact, the greatest number of human ligament injuries occurs in ligaments of the knee. The knee joint is surrounded by a joint capsule with ligaments strapping the inside and outside of the joint (collateral ligaments) as well as crossing within the joint (cruciate ligaments). [4].

The muscles of the lower limbs are larger and more powerful than those of the upper limbs. These muscles can be divided into three groups and they are shown in Fig.2. [5,6]:

- Muscles that move the thigh.
- Muscles that move the leg.
- Muscles that move the foot and toes.

Movements of the knee:

The principal knee movements are flexion and extension, but note on The *capsule* is attached to the margins of these articular surfaces but communicates above with the *suprapatellar bursa* (between the lower femoral shaft and the quadriceps), posteriorly with the bursa under the medial head of gastrocnemius and often, through it, with the bursa under semimembranosus. It may also communicate with the bursa under the lateral head of gastrocnemius. The capsule is also perforated posteriorly by popliteus, which emerges from it in much the same way that the long head of biceps bursts out of the shoulder joint.

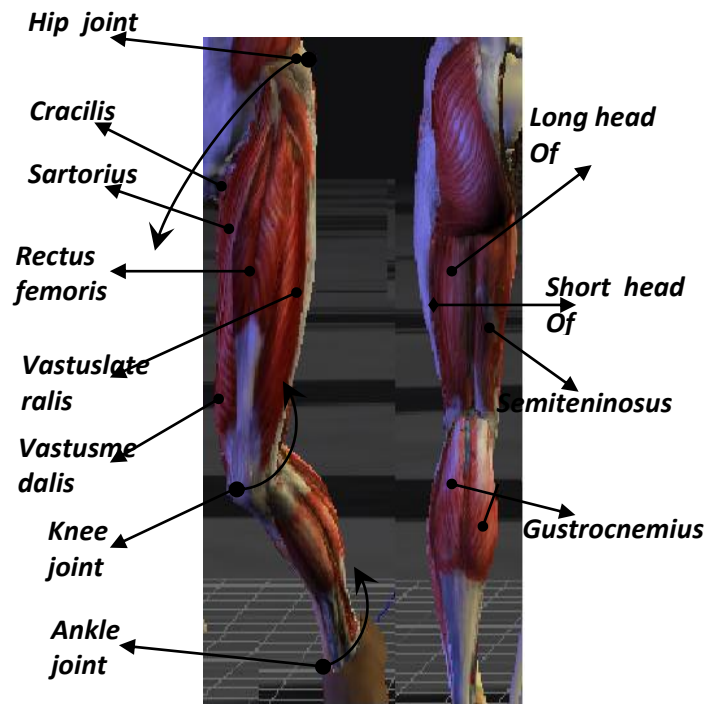


Fig.2. The Human leg muscles that caused flexion / extension knee joint [7].

The capsule of the knee joint is reinforced on each side by the *medial* and *lateral collateral ligaments*, the latter passing to the head of the fibula and lying free from the capsule. Anteriorly, the capsule is considerably strengthened by the *ligamentum patellae*, and, on each side of the patella, by the *medial* and *lateral patellar retinacula*, which are expansions from vastusmedialis and lateralis. Posteriorly, the tough *oblique ligament* arises as an expansion from the insertion of semimembranosus and blends with the joint capsule [7,8].

2- EMG Characteristics

A motor unit action potential, or MUAPs, is a summated action potential as detected from all the muscle fibers in the same motor unit. It is the summation of all the MFAPs produced by fibers of the MU. The shape and characteristics of a MUAP are shown in Fig.3. Now can be summarized the characteristics of EMG or the O/P from MUAP where. It will cover the following characteristics are: Duration / Amplitude / Area / Area- Amplitude, the Area to Amplitude Ratio (AAR) [Thickness] / Size Index Firing Rate / Firing Rate per Motor Unit (FR/MU) / # of Phases / % Polyphasic MUAPs / # of Turns [8].

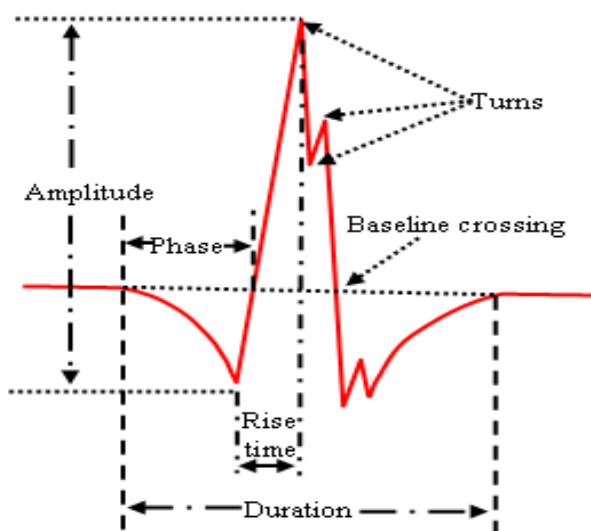


Fig.3. Characteristics of a EMG signal [9].

Now the simple explanation of them will present classification, the amplitude is consistently reduced or normal (5 to 850 mV) in myopathic cases, but can vary between reduced and very high for neuropathic cases. Amplitude also has correlations with other characteristics that may make it valuable to graph it on a two dimensional scatter plot with another characteristic. Amplitude and Duration are positively correlated. Amplitude and AAR are negatively correlated which leads to more separable data distributions when the two are plotted together. [8,9].

2- Real EMG Signal Measurement

There are many important parameters must be take under consideration in the measurement process. The most important parameter in the measurement process is selecting of position for electrodes and clinical information of the job.

A. position of electrodes:

There are nine muscles up and down of knee joint are affecting in the movements of knee. From the clinical information and practice experiential, the best position of electrodes to recognize the maximum amplitude for flexion/extension knee joint. Fig.4 (a&b).represent practice experiment to select the position for two electrode to get the EMG signal at the movements of joint. In this paper I used four muscles that have min effect for flexion/extension knee joint. The EMG signal recorded by using SEMG electrodes therefore must be used four electrodes at the same moment (i.e. four channels recorded) this property don't available practically in my country therefore we used off-line technique for estimation of joint angle by using EMG signal[10,11].

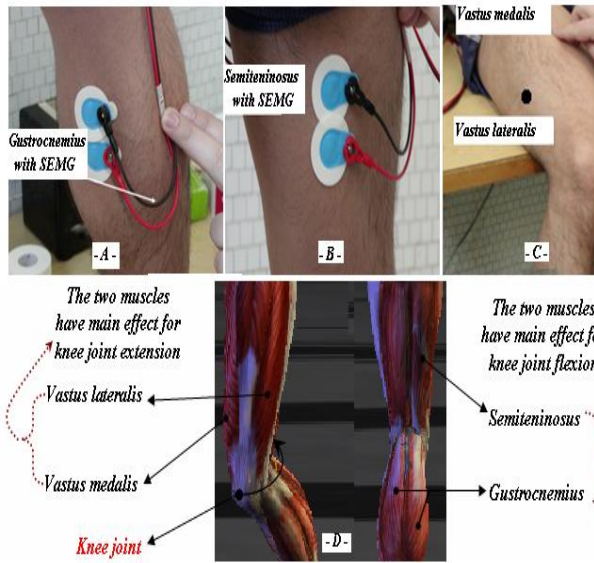


Fig.4. Location of SEMG on human leg.

B. Recording SEMG Data:

In this paper the real SEMG signals were recorded by the following procedure:

- Record the signal with relax and no movement in the knee joint (spontaneous case).
- Record the signal from full extension to full flexion of knee joint with time (3 sec) (i.e. slow motion of leg).
- Record the signal from full extension to full flexion of knee joint with time (1 sec) (i.e. fast motion of leg).
- Repeated the items 2&3 with angle of flexion about 45° , 90° , 135° or max angle implement from human.

Fig.5(a-d) represents the photos of SEMG signal for main leg muscles that caused flexion /extension knee joint and these processing achieved by using the instruments in AL Yarmook, Education Hospital in Baghdad.

The data for this experiential is recording with single channel, this problem caused the design is achieved off line where for each movement must take four runs to get full data.

Fig.6. represent example for SEMG signal was made preparing the signal by using filtering and amplification and these processing was achieved by used EMG Lab software where, it has ability for processing with real data recorded from Micromed

company instrumentation that has the data format (.TRC).

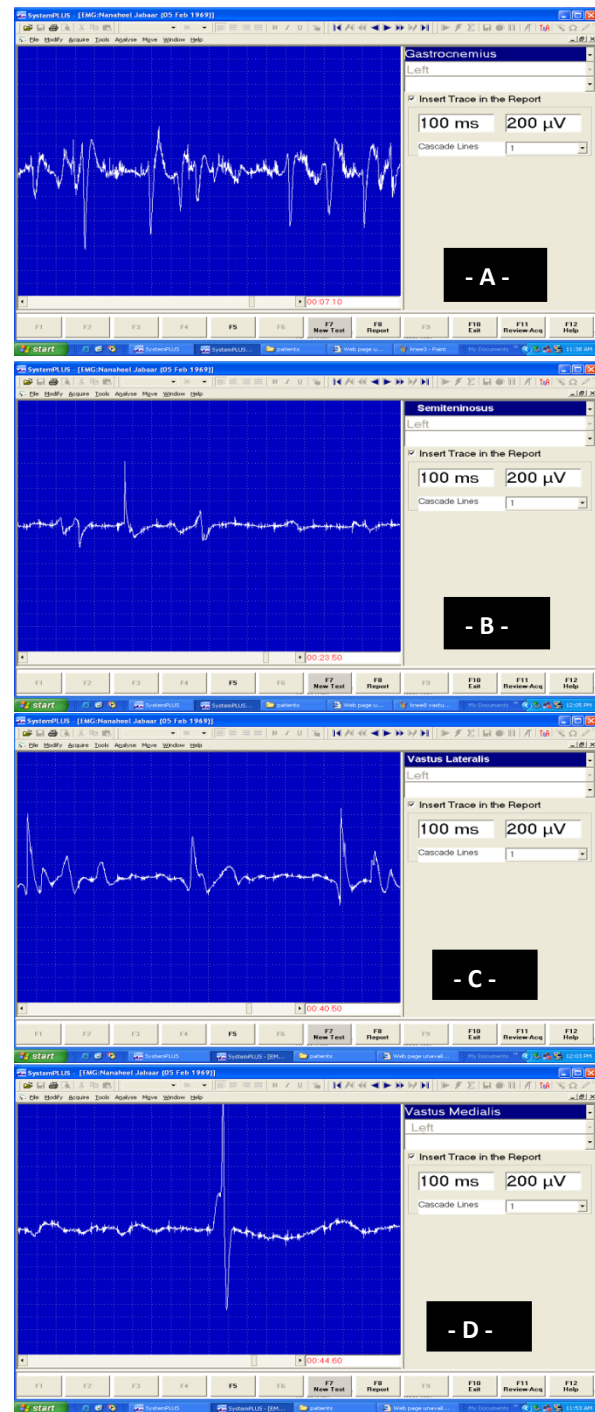


Fig.5. Photo of real SEMG signal from Micromed measurement model.

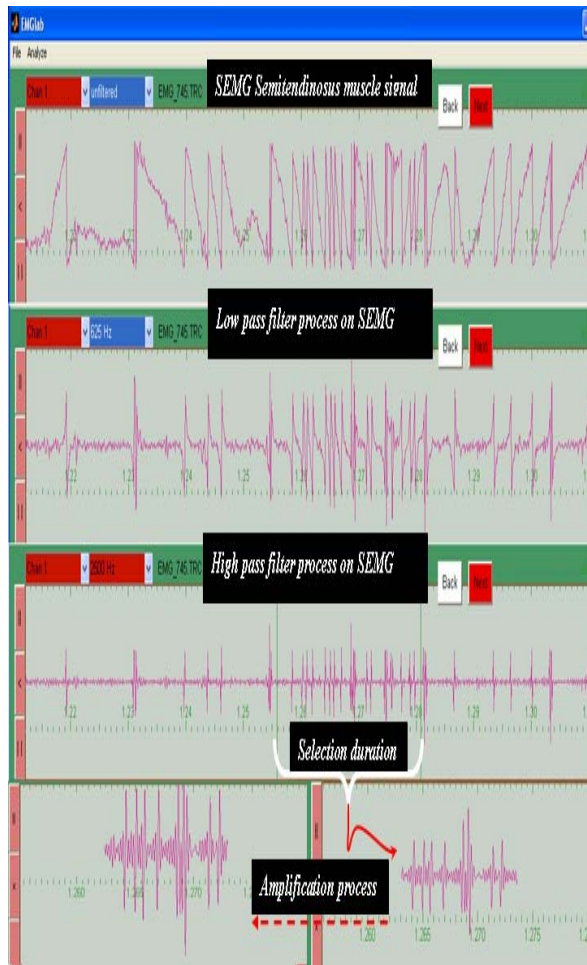


Fig.6. Real SEMG signal represent by EMG Lab software.

4. Design of Estimation Joint Angle

The angle of Knee joint in this paper is calculating by two methods as follow: the first practice method by using trigonometric relationship with the posture of human leg to get angle of knee joint before measurement the real SEMG that is using in the second design for estimation the joint angle. Fig.7. explain the geometry for human leg that used the trigonometric form to calculate angle joint, these calculation is achieved with assumption that the radius of cross section area of normal human leg with age 25 years is ($r = 13 \text{ cm}$) [12,13] :

$$S=R\theta, \quad \theta=\frac{S}{R}; \quad \theta \text{ in rad}, \quad \theta = \frac{\theta_{\text{rad}} * 180}{\pi} \quad (1)$$

Where (R) is represent the length of lower leg (from knee joint to ankle joint) and (S) is represents the length of arc from initial

position of ankle joint to its second position, while (θ) is the angle of flexion/extension knee joint.

The second method for estimation angle of joint is designing by using ANN approach, Fig.8 explain the diagram of design. The design is consists to two main stages:

The identification stage: From the explanation of movement knee joint, there are nine muscles in the human leg consists the movement of the joint but there is four main muscles caused the angle joint of flexion/extension joint as follows (Vastusmedialis, Vastuslateralis for extension and Semitendinosus, Gastrocnemius for flexion). The SEMG signals of the four muscles will be used in estimation of the angle at the human leg movement.

In this paper used the Recurrent Multilayer Perception (RMLP) Neural Network (NN) used in identification of the SEMG signals for the main four muscles. The block diagram in Fig.9.explain the details of identification stage [14].

The NN structure ($3 \times 2_R \times 2$) is shown in Fig.10 i.e. three units in layer 1 (this is input layer), two recurrent units in layer 2, and 2 units in layer 3. This network has external feedback with 2 unit delays. Sigmoidal activation functions were used for all units in both hidden and output layers. The error function which measures the difference between the neural net approximation and the desired trajectory [14]:

$$E(w) = \frac{1}{2} \sum_{n=1}^M \sum_{l=1}^L [d_l(n) - y_l(n)]^2 \quad (2)$$

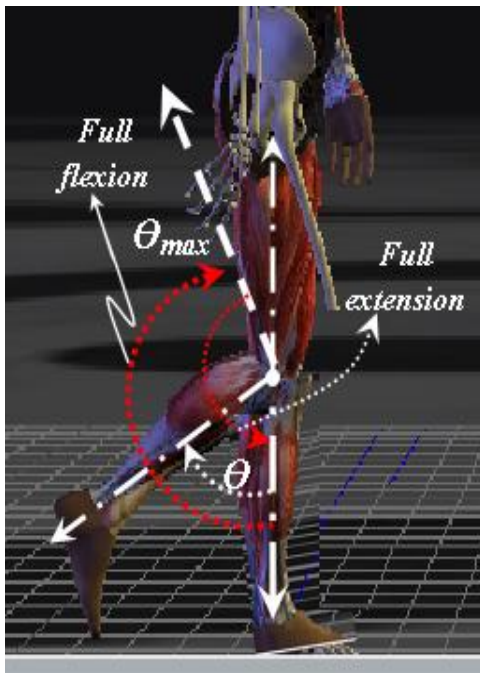
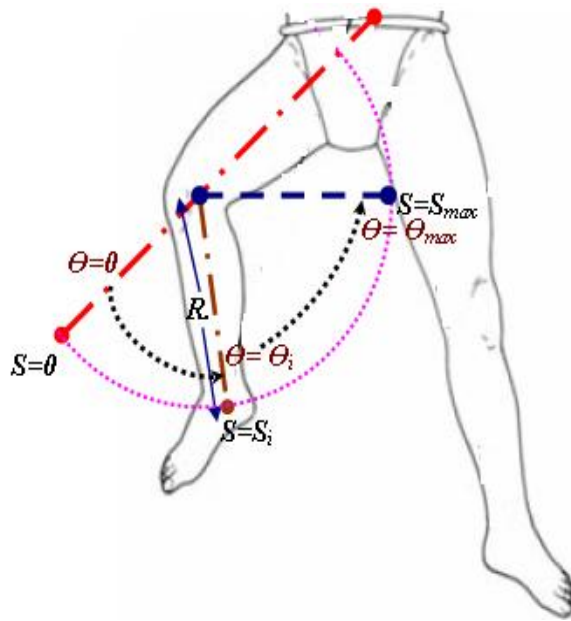


Fig.7. Geometry calculation of Knee joint angle.

The error function given here is called the *batch error*, because it contains the sum of the errors over the entire training set; that is, the error over all time steps. The training algorithm used in this paper is backpropagation-through-time (BPTT)[14, 15].

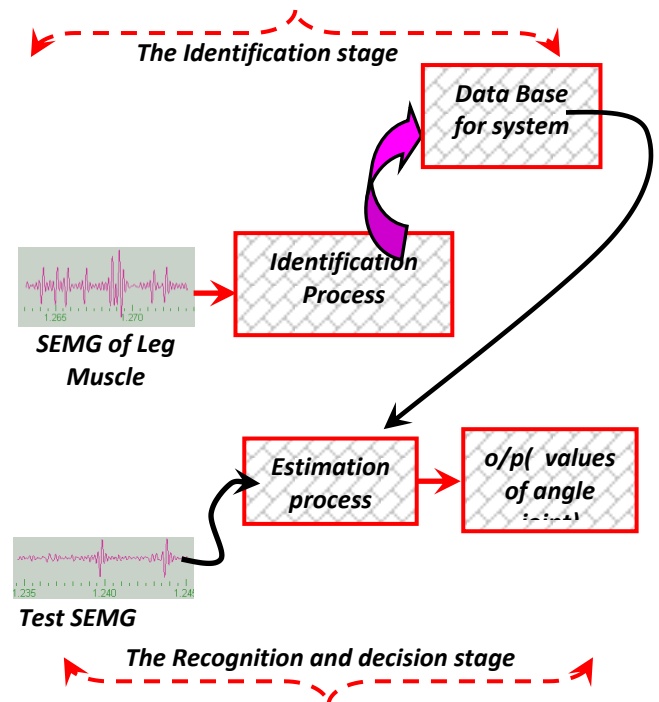
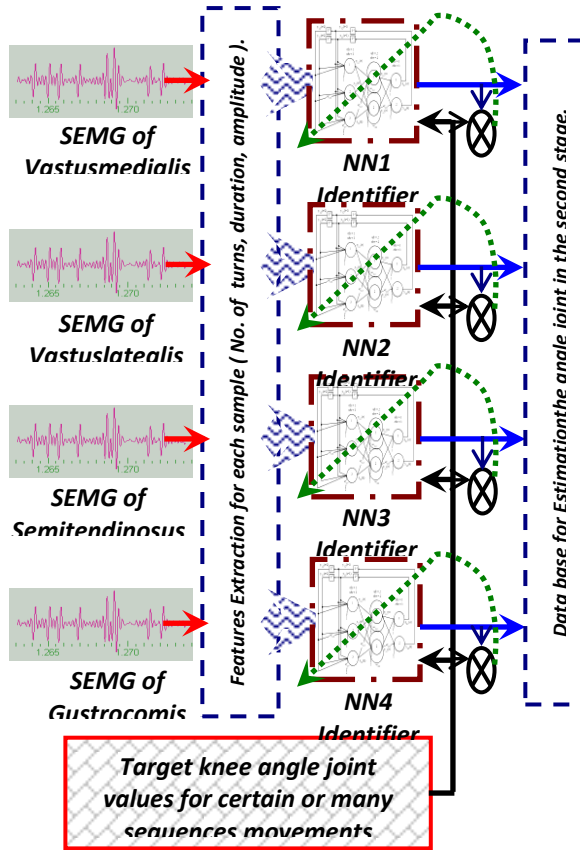


Fig.8. NN design for estimation knee joint angle.

The Recognition and Decision Stage:
 The test signal that is recording from the same type of muscles will be used to estimate the angle of joint where the data base is formatting by recorded the SEMG of muscles with values of joint angle (0(no command from brain), $\pi/4$, $\pi/2$, and $3\pi/4$ (max movement)). After reconstructed the same features for test signal will be entered to the same structure of RMLP-NN with identification data base by feed forward training only the output of these networks is recognizing the muscles and the amplitude of SEMG with each sample. By using the following relation with amplitude of SEMG signal with time and take the average between results of Vastusmedialis, Vastuslateralis for extension and Semitendinosus, Gstrocomis for flexion will be get the angle of joint at flexion and then the complement angle (extension angle). Fig.11. explains the second stage of design for estimation of knee joint angle.



$$\left. \begin{aligned} \theta_{f_{1,2}} &= \frac{A_i * \theta_{f \max}}{A_{\max}} \\ \theta_{flexion} &= \frac{\theta_{f_1} + \theta_{f_2}}{2} \\ \theta_{E_{1,2}} &= \frac{A_i * \theta_{E \max}}{A_{\max}} \\ \theta_{Extension} &= \frac{\theta_{E_1} + \theta_{E_2}}{2} \end{aligned} \right\} (3)$$

Fig.9. NN Identification of SEMG signal for human leg muscles.

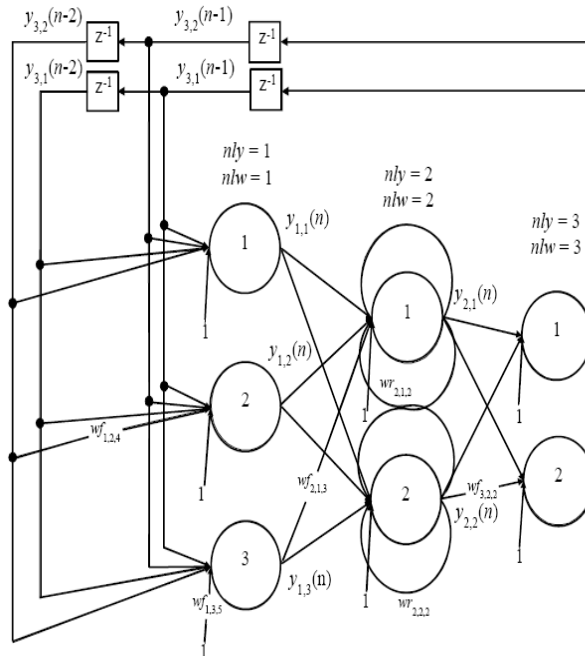


Fig.10. Recurrent Multilayer Perception Neural Network with structure $(3 \times 2_R \times 2(2))$ [14].

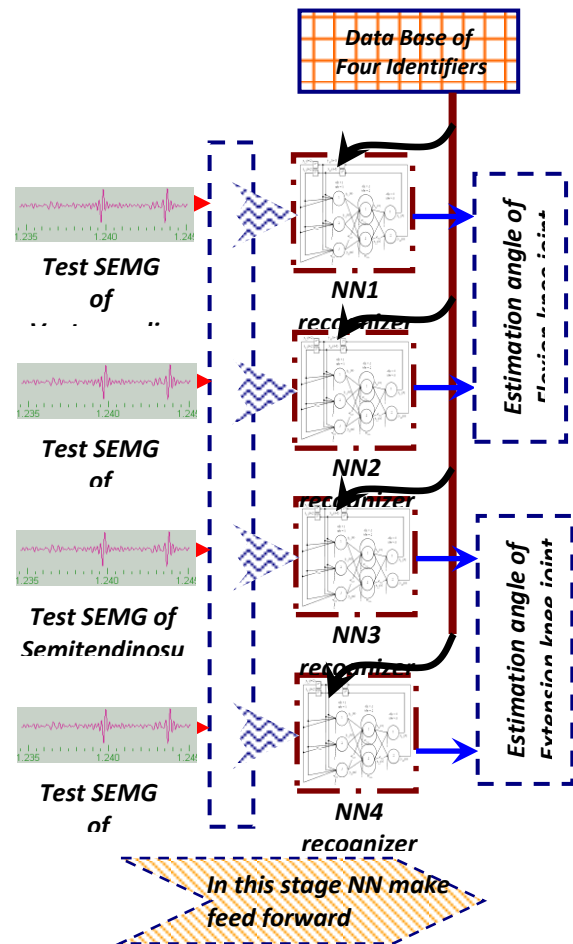


Fig.11. Estimation of knee joint angle.

5. Simulation Results

The simulation of the estimation design is achieved by MATLAB Var.R2010a. Fig.12. presents the identification of SEMG signals of human leg that related to knee joint flexion/extension movement and from this figure can be seen that the error approach to zero after about nine iteration and after that no local minimum or increasing in error therefore; this best results for identification after some trial to adjustment the learning rate and momentum term.

Two type of human leg movement according to speed of leg are used in simulation:

Low speed: the human leg in this simulation was moving from full extension to full flexion with speed about 3sec/cycle. Fig.13. represents the estimated values of knee flexion/extension joint angle. The calculation of the accuracy of joint angle is achieved by calculate the RMS error between estimated values and practice value that measured in first stage of the design. The RMS error has the value from (0.065) to (0.015).

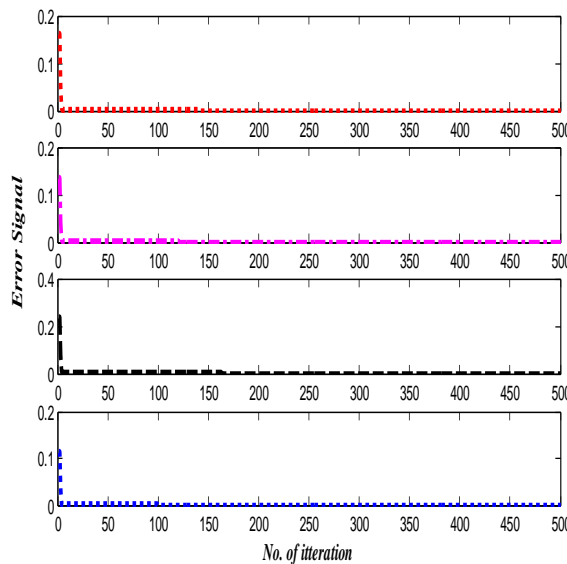


Fig. 12. Error signal for identification of four muscles SEMG signal

High speed: the same procedure in low speed was implemented here and the results explains in Fig.14 and the RMS errors are obtained from (0.018) to (0.0026) at fast speed leg flexion –extension. Fig.15. explain the RMS values in two speed of movement (low and high) with recorded time (180 sec, 60 sec) for low and high speed respectively.

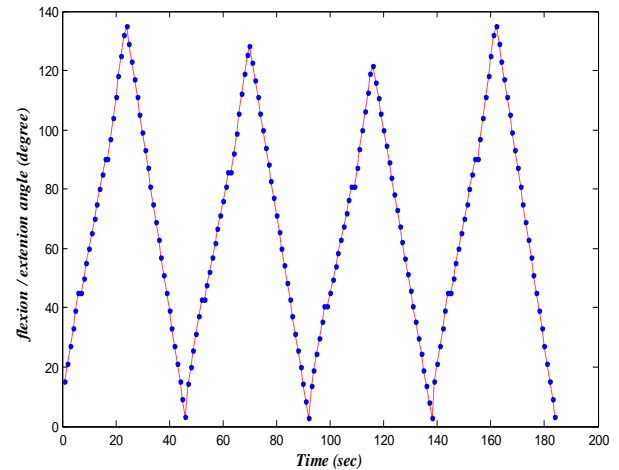


Fig.13. Estimation of knee joint angle with low speed movement.

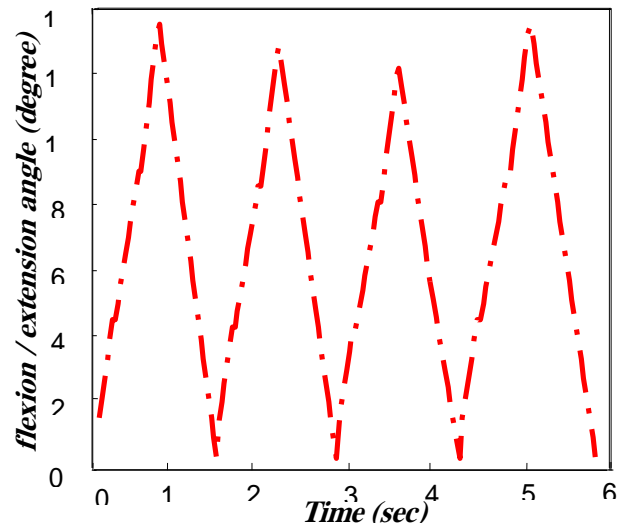


Fig.14. Estimation of knee joint angle with low speed movement.

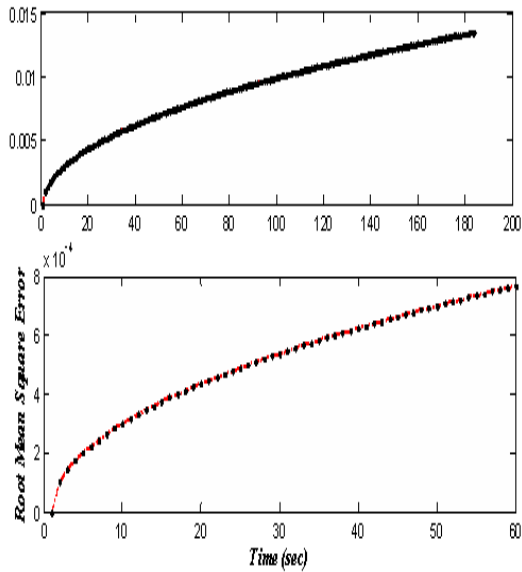


Fig.15. RMS values for two speed of human leg movement.

Conclusion:

From the obtained results, it can be concluded that the ability of RMLP-NN to identify and solve the IK of human leg with high accuracy and simplicity. The ability of estimation of angle knee joint based on SEMG with high accuracy and can be used with many applications. There are many critical coefficient in the movement knee joint must be under consideration in the estimation of angle joint. The obtained results are off-line because there is no SEMG multi-channel recorded therefore must record the data of SEMG for each muscle alone and return the same command to record the another muscle. If available measurements and saving of SEMG muscles signal can be implement this design on-line and it can be implemented as portable unit to used with many application.

References:

[1] Alberto L. Delis, J. L. Azevedo, F. Rocha, "Development of A Myoelectric Controller Based on Knee Angle Estimation", BIODEVICES - International Conference on Biomedical Electronics and Devices, 2009.

[2] Hartmut Geyer, Hugh Herr, "A Muscle-Reflex Model that Encodes Principles of Legged Mechanics Produces Human Walking Dynamics and Muscle Activities", IEEE Transactions on Neural Systems and Rehabilitation Engineering, 2010.

[3] M. Machado, P. Flores, J.C. Claro, J. Ambrósio, M. Silva, A. Completo, "Development of a planar multibody model of the human knee joint", Nonlinear Dyn 60: 459–478, DOI 10.1007/s11071-009-9608-7, 2010.

[4] H. ELLIS, "Clinical Anatomy Arevision and applied anatomy for clinical students", Eleventh edition 2006.

[5] Frederic M. Michael, Timmons R. Tallitsch, "Human Anatomy", Fifth Edition, 2000.

[6] Mader, "Understanding Human Anatomy & Physiology", Fifth Edition Front Matter Preface © The McGraw–Hill Companies, 2004.

[7] EMGLAB software Version 0.9 User's Guide, "The MathWorks, at www.mathworks.com, May 2008.

[8] N. BU, "EMG-Based Motion Discrimination Using a Novel Recurrent Neural Network", Journal of Intelligent Information Systems, 21:2, 113–126, 2003.

[9] O. Bida, "Influence of Electromyogram (EMG) Amplitude Processing in EMG-Torque Estimation", M.Sc Thesis, WORCESTER POLYTECHNIC INSTITUTE, Electrical Engineering, January 2005.

[10] I. Reichl, W. Auzinger, H. B. Schmiedmayer, "Reconstructing the Knee Joint Mechanism from Kinematic Data", ASC Report No. 48/2009.

- [11] R. Tarlochan, S. Ramesh, B. M. Hillberry, “ Dynamic Analysis of the Human Knee”, *Vol. 14 No. 3 June 2002*.
- [12] J. Goodfellow, J. Oconnor, “ The Mechanics of the Knee and Prosthesis Design”, *The Journal of Bone and Joint surgery*, 1999.
- [13] R. Kulpa, F. Multon, “ Fast inverse kinematics and kinetics solver for human-like figures”, *Proceedings of 5th IEEE-RAS International Conference on Humanoid Robots*, 2005.
- [14] L.R. Medsker, L.C. Jain, “Recurrent Neural Networks”, 2001.
- [15] N. A. Shirao, N. arender, P, Reddy, “ Neural network committees for finger joint angle estimation from surface EMG signals”, *Biomedical Engineering Online* 8 :2, 2009.

THE USE OF VIRTUAL REALITY TO DEMONSTRATE TRAJECTORY PLANNING AND CONTROL OF A 3-DOF UNDERACTUATED ROBOT IN A HORIZONTAL PLANE IN REAL-TIME

Dr. Waladin K. Sa'id
waladinsky@yahoo.com

Mohammed Y. Algailany
malgailany@yahoo.com

Control and Systems Engineering Department
University of Technology
Baghdad-IRAQ

Abstract

Real-Time 3D animation and Real-Time Simulation results are reported for a 3R underactuated robot moving in a horizontal plane using Virtual Reality Toolbox™, Real-Time Windows Target™, Real-Time Workshop®, and interfaced to Simulink® under the MATLAB® environment. The reason behind Real-time 3D animation and Real-Time simulation is to provide animated real-time tools in a realistic fashion to demonstrate the effectiveness of the controllers in tracking the desired trajectory and to provide a tool for researchers to test their proposed controllers and observe their behavior using 3-DOF underactuated manipulator in real-time.

Key-words: *Virtual-Reality, Underactuated Robot, Nonholonomic Constraint, Real-Time.*

1- Introduction

Virtual Reality (VR) is a field of study that aims to create a system that provides a synthetic experience for its user(s). The experience is dubbed “synthetic,” “illusory,” or “virtual” because the sensory stimulation to the user is simulated and generated by the system. The term Virtual Reality is used to describe a computer-generated, highly-realistic artificial world or environment (called a Virtual environment), allowing the user to interact with it in real-time by interfacing some of his actions in the real world back into the virtual environment and providing visual, acoustical and, sometimes, haptic feedback [1]. VR allows

people to get the experience of things that would otherwise be very difficult or even impossible to attain in real life. VR may provide invaluable tools to engineers seeking rapid and inexpensive development for their prototypes.

The aim of this work is to demonstrate trajectory planning and control of a 3-degrees of freedom (3DOF) *underactuated* planar robot with a passive rotational last joint using the Dynamic Feedback Linearization (DFL) method, utilizing the VR toolbox under the MATLAB and Simulink in real time.

Underactuated mechanical systems are mechanical systems with fewer actuators than DOFs [2]. For a conventional robot manipulator, the number of joints is equal to the number of actuators, or actuated joints; such a fully driven serial mechanism is called a full-actuated system. If the total number of joints is greater than the number of actuators in the mechanism, the system is referred to as an underactuated system. Underactuated mechanical systems may arise from intentional design as in the pendubot [3], and the Acrobot [4]. Mobile robot systems are considered to be underactuated. For example, when a manipulator arm is attached to a mobile platform or an undersea vehicle [5] also underactuation arise due to the mathematical model used for control design as, for example, when joint flexibility is included in the model [6]. It is also interesting to note that certain control problems for fully actuated redundant robots are similar to those for underactuated robots [2].

The class of underactuated systems is composed of variety of mechanical as well as biological systems. A biological system which can be considered underactuated is the human body [7]. When for example; gymnasts perform acrobatic maneuvers on a high bar; they are able to rotate about their wrist by actuating the muscles on their hip and knees. The wrist is therefore a joint kept unactuated, whose displacement can be controlled by the actuation of other joints.

There are a number of advantages to the use of the underactuated systems. First, reducing the number of actuators for a robot manipulator will minimize energy consumption, and will be potentially attractive to the applications where energy efficiency is a major concern, such as for space robots [8]. Second, eliminating some actuators will allow more compact design leading to both overall size and total weight reductions. This will ultimately reduce the manufacturing cost and running power. Not only the underactuated system is useful in practice but also the concept is important in analysis of a class of systems that can be considered as virtual underactuated systems. For example, a free-flying space robot system [8] is useful in maintenance tasks in space stations and/or satellites. The concept of underactuated systems provides an approach to modeling dynamic systems with either free bases, or free joints. Some of these mechanisms can be potentially utilized in space and underwater applications.

In this paper, section II describes the mathematical model of the passive link dynamics, section III presents motion planning and trajectory control using DFL. Section IV utilizes Simulink software under MATLAB environment to simulate numerical results of an example, where the trajectory motion of the passive link is controlled. Also in section IV a 3D animation is provided for the 3R robot using Virtual Reality Tool box, Real-Time Windows Target, Real-Time Workshop, and interfaced to Simulink all under the MATLAB

environment. Finally, the conclusions are provided in section V.

2- Modeling of an Underactuated 3-Link Planar Robot in a horizontal plane

A manipulator with three degrees of freedom in horizontal plane is considered in Fig. 1. The first and second joints are actively controlled and are used to control the position of the passive joint in 2D plane. The passive joint is a revolute joint around a vertical axis.

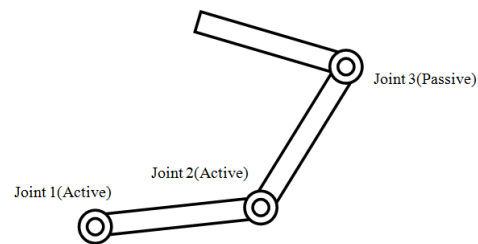


Fig. 1. Three-DOF planar underactuated manipulator.

To simplify the model, the dynamics of the first and second joint are neglected, except that the translational acceleration of the passive joint is assumed to be finite. The work space limit and singularity of the first and second joint are ignored too. The dynamics can be modeled with regard to only the free link as shown in Fig.2, where the generalized coordinates which represent the configuration of the manipulator are (x, y, θ) . The equations of motion with respect to the link is written as [9]

$$\begin{aligned} f_x &= m\ddot{x} - ml\ddot{\theta}\sin\theta - ml\dot{\theta}^2\cos\theta \\ f_y &= m\ddot{y} + ml\ddot{\theta}\cos\theta - ml\dot{\theta}^2\sin\theta \\ \tau_\theta &= -m\ddot{x}\sin\theta + m\ddot{y}\cos\theta + (I_G + ml^2)\ddot{\theta} \end{aligned} \quad (1)$$

Where

- m mass of link;
- I_G moment of inertia of the link around G;
- l distance $|OG|$, between the joint and the center of mass;

(f_x, f_y) translational force at the joint O;
 τ_θ torque around the joint O.

As the joint O is passive, $\tau_\theta = 0$. Where $l \neq 0$ and $k \equiv I_G/ml$, is equivalent to the distance of the mechanical property, *center of percussion* (CP) [10], [11]. Center of percussion play an important role in the dynamics of rigid pendulums. In fact, the motion of an oscillating pendulum of a mass m can be described by the equation of motion of a point mass all concentrated in the center of percussion [12]

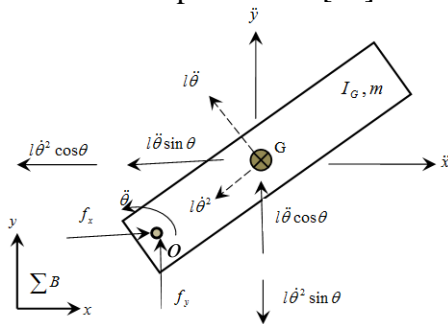


Fig. 2. Acceleration components of the free link.

The constraint on the system is represented in the form of a 2nd order nonholonomic differential equation as [9]

$$-\ddot{x}\sin\theta + \ddot{y}\cos\theta + k\ddot{\theta} = 0 \quad (2)$$

from equation (1), the translational acceleration (\ddot{x}, \ddot{y}) , of the passive joint can be treated as inputs to the system. The state equations of the system is written as [9]

$$\frac{d}{dt} \begin{bmatrix} x \\ y \\ \theta \\ \dot{x} \\ \dot{y} \\ \dot{\theta} \end{bmatrix} = \begin{bmatrix} \dot{x} \\ \dot{y} \\ \dot{\theta} \\ 0 \\ 0 \\ 0 \end{bmatrix} + \begin{bmatrix} 0 \\ 0 \\ 0 \\ 1 \\ 0 \\ \sin\theta/k \end{bmatrix} \ddot{x} + \begin{bmatrix} 0 \\ 0 \\ 0 \\ 0 \\ 1 \\ -\cos\theta/k \end{bmatrix} \ddot{y} \quad (3)$$

It should be noted that the linear approximation of this system is not controllable since no gravity is applied on the passive joint [9].

We may write the dynamic equations in the Euler-Lagrange form for a mechanical system with n degrees of freedom and $m = n - 1$ control inputs, denote by $q \in \mathcal{R}^n$ the generalized coordinates and by $\tau \in \mathcal{R}^m$ the control input. The dynamics is written as [13]

$$B(q)\ddot{q} + h(q, \dot{q}) + g(q) = F(q)\tau \quad (4)$$

where $B > 0$ is the $n \times n$ symmetric inertia matrix, h is the centrifugal and Coriolis vector, $g = (\partial U / \partial q)^T$ is the vector of potential terms, and F is the $n \times m$ input matrix assumed of full rank.

Substituting the link parameters into equation (4), with $g(q) = 0$ (zero gravity), equation (4) is written as

$$\begin{bmatrix} m & 0 & -ml\sin\theta \\ 0 & m & ml\cos\theta \\ -ml\sin\theta & ml\cos\theta & I_G + ml^2 \end{bmatrix} \begin{bmatrix} \ddot{x} \\ \ddot{y} \\ \ddot{\theta} \end{bmatrix} + \begin{bmatrix} -ml\dot{\theta}^2 \cos\theta \\ -ml\dot{\theta}^2 \sin\theta \\ 0 \end{bmatrix} = \begin{bmatrix} f_x \\ f_y \\ 0 \end{bmatrix} \quad (5)$$

3-Motion Planning and Trajectory Control via Dynamic Feedback Linearization

One effective technique to solve the motion planning and control for 2nd order nonholonomic mechanical system is *Dynamic Feedback Linearization* (DFL). In this methodology, the exact state linearization is based on changing the coordinates of the states and finding a control law such that, in the new coordinates, the closed-loop system is linear and controllable [13],[14]. In robotics, dynamic feedback has been used for the exact linearization of manipulators with elastic joints and of nonholonomic wheeled mobile robots [15] (and the references therein).

The trajectory motion of the 3rd passive link considered here were controlled using DFL. Under an appropriate regularity assumption; the robot can be transformed into a fully linear, input-output decoupled system by using a second-order dynamic feedback compensator. As a result of dynamic feedback linearization, each coordinate of the CP is driven independently by an auxiliary input through a chain of integrators. Therefore, it is sufficient to solve an interpolation problem for the CP point to generate a feasible point-to-point trajectory and the associated nominal inputs. As a byproduct of this approach, global exponential tracking of the generated trajectory is guaranteed by adding a linear feedback (in the linearizing coordinates) to the feedforward command. To make the analysis independent from the nature of the first $n - 1$ joints, we preliminarily perform a partial linearization of equation (5) via static feedback. The idea is to reduce the dynamics of the active joints to $n - 1$ chains of double integrators, so that they can be controlled via acceleration inputs. The partially linearizing static feedback is obtained in the form

$$\begin{bmatrix} f_x \\ f_y \end{bmatrix} = \begin{bmatrix} m - \frac{ml\sin^2\theta}{k} & \frac{ml\sin\theta\cos\theta}{k} \\ \frac{ml\sin\theta\cos\theta}{k} & m - \frac{ml\cos^2\theta}{k} \end{bmatrix} \begin{bmatrix} a_x \\ a_y \end{bmatrix} - \begin{bmatrix} ml\dot{\theta}^2\cos\theta \\ ml\dot{\theta}^2\sin\theta \end{bmatrix} \quad (6)$$

putting together equations (5) and (6), the complete closed-loop system becomes

$$\begin{aligned} \ddot{x} &= a_x \\ \ddot{y} &= a_y \\ \ddot{\theta} &= \frac{\sin\theta}{k} a_x - \frac{\cos\theta}{k} a_y \end{aligned} \quad (7)$$

where, $k = (I_3 + m_3 l_3^2) / m_3 l_3$ is precisely the distance of the CP of the last link from its base. If a uniform mass distribution is assumed, then $k = 2l_3 / 3$ (l_3 is the length of the third link). Define the Cartesian position

of the CP of the last link as output (see Fig 3),

$$\begin{bmatrix} y_1 \\ y_2 \end{bmatrix} = \begin{bmatrix} x \\ y \end{bmatrix} + k \begin{bmatrix} \cos\theta \\ \sin\theta \end{bmatrix} \quad (8)$$

1st and 2nd differentiation of equation (8) and substitution of equation (7) yields

$$\begin{bmatrix} \ddot{y}_1 \\ \ddot{y}_2 \end{bmatrix} = \begin{bmatrix} \cos^2\theta & \sin\theta\cos\theta \\ \sin\theta\cos\theta & \sin^2\theta \end{bmatrix} \begin{bmatrix} a_x \\ a_y \end{bmatrix} + k\dot{\theta}^2 \begin{bmatrix} -\cos\theta \\ -\sin\theta \end{bmatrix} \quad (9)$$

since the matrix multiplying the acceleration vector (a_x, a_y) is singular, the invertible feedback transformation defined as

$$\begin{bmatrix} a_x \\ a_y \end{bmatrix} = \begin{bmatrix} \cos\theta & -\sin\theta \\ \sin\theta & \cos\theta \end{bmatrix} \begin{bmatrix} \xi + k\dot{\theta}^2 \\ \sigma_2 \end{bmatrix} \quad (10)$$

where ξ and σ_2 are two auxiliary input variables. As a result of equation (10), equation (9) is written as

$$\begin{bmatrix} \ddot{y}_1 \\ \ddot{y}_2 \end{bmatrix} = \xi \begin{bmatrix} \cos\theta \\ \sin\theta \end{bmatrix} \quad (11)$$

proceeding with differentiation and defining new auxiliary input variables as necessary, 3rd and 4th derivatives become as

$$\begin{bmatrix} \ddot{y}_1 \\ \ddot{y}_2 \end{bmatrix} = R(\theta) \begin{bmatrix} \eta \\ \xi\dot{\theta} \end{bmatrix} \quad (12)$$

where, $R(\theta) = \begin{bmatrix} \cos\theta & -\sin\theta \\ \sin\theta & \cos\theta \end{bmatrix}$. And avoiding

differentiating the input ξ , by adding two integrators on the first channel as

$$\begin{aligned} \dot{\xi} &= \eta \\ \dot{\eta} &= \sigma_1 \end{aligned} \quad (13)$$

with σ_1 the new auxiliary input in place of ξ .

$$\begin{bmatrix} y_1^{[4]} \\ y_2^{[4]} \end{bmatrix} = \begin{bmatrix} v_1 \\ v_2 \end{bmatrix} \quad (14)$$

With (v_1, v_2) as the new input vector, and the inversion based control is expressed by

$$\begin{bmatrix} \sigma_1 \\ \sigma_2 \end{bmatrix} = \begin{bmatrix} 1 & 0 \\ 0 & -k/\xi \end{bmatrix} R^T(\theta) \begin{bmatrix} v_1 \\ v_2 \end{bmatrix} + \begin{bmatrix} \xi \dot{\theta}^2 \\ 2k\dot{\theta}\eta/\xi \end{bmatrix} \quad (15)$$

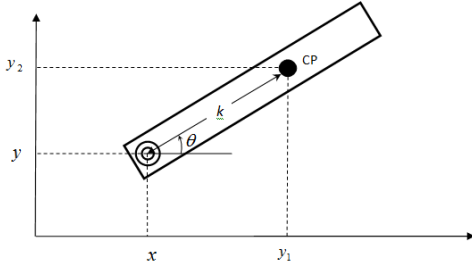


Fig. 3. Cartesian position of the CP of the last link.

under the regularity assumption, the matrix multiplying the inputs is nonsingular or, equivalently, that $\xi \neq 0$. The initialization of the compensator state at time $t = 0$, i.e., $(\xi(0), \eta(0))$, is arbitrary. As a byproduct of the linearization, a new set of state coordinates can be defined consisting of the output function and its derivatives up to the 3rd order (i.e. $y_1, y_2, \dot{y}_1, \dot{y}_2, \ddot{y}_1, \ddot{y}_2, \dddot{y}_1, \dddot{y}_2$). The inverse transformation from these linearizing coordinates are written as

$$\theta = \text{ATAN2}\{\text{sign}(\xi)\ddot{y}_2, \text{sign}(\xi)\ddot{y}_1\} \quad (16)$$

$$\xi = \ddot{y}_1 \cos \theta + \ddot{y}_2 \sin \theta \quad (17)$$

$$\begin{bmatrix} \eta \\ \dot{\theta} \end{bmatrix} = \begin{bmatrix} \cos \theta & \sin \theta \\ -\sin \theta / \xi & \cos \theta / \xi \end{bmatrix} \begin{bmatrix} \ddot{y}_1 \\ \ddot{y}_2 \end{bmatrix} \quad (18)$$

$$\begin{bmatrix} x \\ y \end{bmatrix} = \begin{bmatrix} y_1 \\ y_2 \end{bmatrix} - k \begin{bmatrix} \cos \theta \\ \sin \theta \end{bmatrix} \quad (19)$$

$$\begin{bmatrix} \dot{x} \\ \dot{y} \end{bmatrix} = \begin{bmatrix} \dot{y}_1 \\ \dot{y}_2 \end{bmatrix} - k\dot{\theta} \begin{bmatrix} -\sin \theta \\ \cos \theta \end{bmatrix} \quad (20)$$

The problem of trajectory planning can be formulated as an *interpolation* problem using smooth parametric functions $y_1(r)$ and $y_2(r)$, with a timing law $r = r(t)$. For simplicity, one can directly generate trajectories $y_1(t)$ and

$y_2(t)$. In particular, assume that at time $t = 0$ the robot starts from a generic state $(q_s, \dot{q}_s) = (x_s, y_s, \theta_s, \dot{x}_s, \dot{y}_s, \dot{\theta}_s)$ to reach a goal state $(q_g, \dot{q}_g) = (x_g, y_g, \theta_g, \dot{x}_g, \dot{y}_g, \dot{\theta}_g)$ at time $t = T$. The appropriate boundary conditions for the new state variables, i.e., y_1, y_2 and their derivatives up to the third order are,

at time $t=0$

$$\begin{bmatrix} y_1(0) \\ \dot{y}_1(0) \\ \ddot{y}_1(0) \\ \dddot{y}_1(0) \end{bmatrix} = \begin{bmatrix} y_{1s} \\ \dot{y}_{1s} \\ \ddot{y}_{1s} \\ \dddot{y}_{1s} \end{bmatrix}, \quad \begin{bmatrix} y_2(0) \\ \dot{y}_2(0) \\ \ddot{y}_2(0) \\ \dddot{y}_2(0) \end{bmatrix} = \begin{bmatrix} y_{2s} \\ \dot{y}_{2s} \\ \ddot{y}_{2s} \\ \dddot{y}_{2s} \end{bmatrix}$$

at time $t=T$

$$\begin{bmatrix} y_1(T) \\ \dot{y}_1(T) \\ \ddot{y}_1(T) \\ \dddot{y}_1(T) \end{bmatrix} = \begin{bmatrix} y_{1g} \\ \dot{y}_{1g} \\ \ddot{y}_{1g} \\ \dddot{y}_{1g} \end{bmatrix}, \quad \begin{bmatrix} y_2(T) \\ \dot{y}_2(T) \\ \ddot{y}_2(T) \\ \dddot{y}_2(T) \end{bmatrix} = \begin{bmatrix} y_{2g} \\ \dot{y}_{2g} \\ \ddot{y}_{2g} \\ \dddot{y}_{2g} \end{bmatrix}$$

a straightforward solution to the interpolation problem is to generate trajectories as polynomials of seventh degree:

$$y_i(t) = \sum_{j=0}^7 a_{ij} t^j, \quad i=1,2, \quad (21)$$

An expression for the coefficients a_j where $j=0, \dots, 3$, is straight forward and for $j=4, \dots, 7$ may be written in matrix form as

$$\begin{bmatrix} a_4 \\ a_5 \\ a_6 \\ a_7 \end{bmatrix} = \begin{bmatrix} T^4 & T^5 & T^6 & T^7 \\ 4T^3 & 5T^4 & 6T^5 & 7T^6 \\ 12T^2 & 20T^3 & 30T^4 & 42T^5 \\ 24T & 60T^2 & 120T^3 & 210T^4 \end{bmatrix}^{-1} \times \begin{bmatrix} y_g - y_s - T \dot{y}_s - \frac{T^2}{2} \ddot{y}_s - \frac{T^3}{6} \dddot{y}_s \\ \dot{y}_g - \dot{y}_s - T \ddot{y}_s - \frac{T^2}{2} \dddot{y}_s \\ \ddot{y}_g - \ddot{y}_s - T \dddot{y}_s \\ \dddot{y}_g - \dddot{y}_s \end{bmatrix} \quad (22)$$

the open-loop commands that realize this trajectory are

$$v_i(t) = 840a_{i7}t^3 + 360a_{i6}t^2 + 120a_{i5}t + 24a_{i4}, \quad i=1,2 \quad (23)$$

The selection of initial and final compensator states (ξ_s, η_s) and (ξ_g, η_g) affects the boundary conditions, and thus the generated motion inside the chosen class of interpolating functions. In particular, the compensator states should be chosen so as to avoid the singularity $\xi = 0$ during the motion. The problem of *tracking* the generated trajectories will now be discussed. The feedforward commands resulting from a trajectory planning algorithm yield the desired robot reconfiguration only in nominal conditions, i.e., initial state matched with the desired reference trajectory and absence of disturbances during motion. Feedback control must be used to alleviate the effects of an initial state error and of different kinds of perturbations. The linearizing controller and the feedback control is shown in Fig. 10.

Link	Length (m)	Mass (kg)	K (CP) in (m)
1	1.5	Not specified	not required
2	1.5	Not specified	not required
3	1	1	2/3*

* Uniform mass distribution is assumed

Table 1.3R robot parameters.

4-Simulation and 3D Animation Results

The robot parameters that will be considered is presented in table 1. Initial states of the passive link are assumed to be as

$$\begin{aligned} x_{start} &= 0.5m & \dot{x}_{start} &= 0 \text{ m/s} \\ y_{start} &= 1m & \dot{y}_{start} &= 0 \text{ m/s} \\ \phi_{start} &= 90^\circ & \dot{\phi}_{start} &= 0 \text{ rad/s} \end{aligned} \quad (24)$$

goal states are planned to be as

$$\begin{aligned} x_{goal} &= 0.5m & \dot{x}_{goal} &= 0 \text{ m/s} \\ y_{goal} &= 1m & \dot{y}_{goal} &= 0 \text{ m/s} \\ \phi_{goal} &= 0^\circ & \dot{\phi}_{goal} &= 0 \text{ rad/s} \end{aligned} \quad (25)$$

The controller states are assumed to be as

$$\xi_{start} = -0.1 \text{ m/s}^2 \quad (26)$$

$$\xi_{goal} = -0.1 \text{ m/s}^2$$

See Fig. 4. Trajectory time is T=10 seconds.

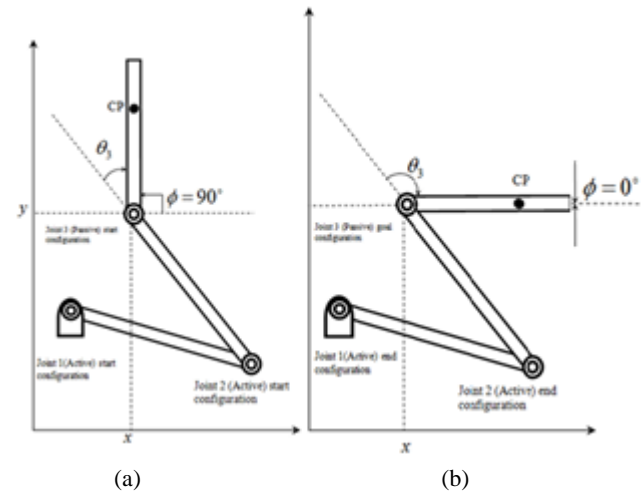


Fig. 4. Start (a) and End (b) configuration for the 3R planar underactuated robot.

A series of experimental tests were carried out and Figs. 5 to 9 summarize the results. Figure 5 shows the reset-to-reset path of the CP of the 3rd link. The figure also presents the path of the passive joint necessary to achieve this target. Figure 6 displays the evolution of the CP in terms of y_1 and y_2 and Fig.7 indicates the high-quality performance of the controller. The required torque to achieve this end is shown in Fig. 8. Figure 9 displays the stroboscopic motion of the 3R robot. Figures 11 and 12 are snap shots of the animated results with their real time stamps [16]. The builder environment of the robot model that was developed for this purpose is shown in Fig. 13.

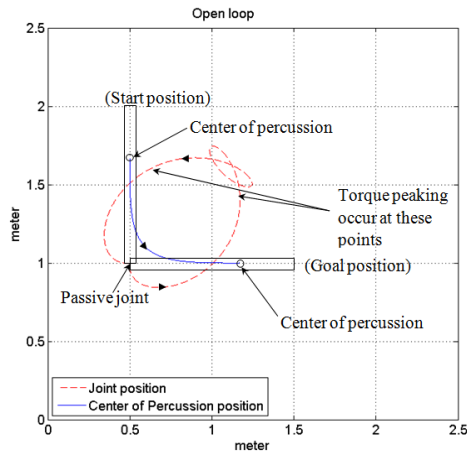


Fig. 5. Rest-to-rest planning for the third link.

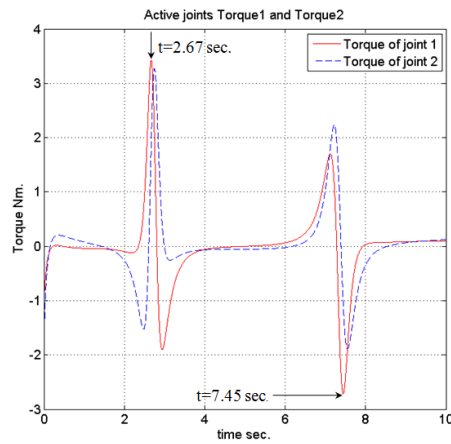


Fig. 8. Torques of the active joints, 1 and 2.

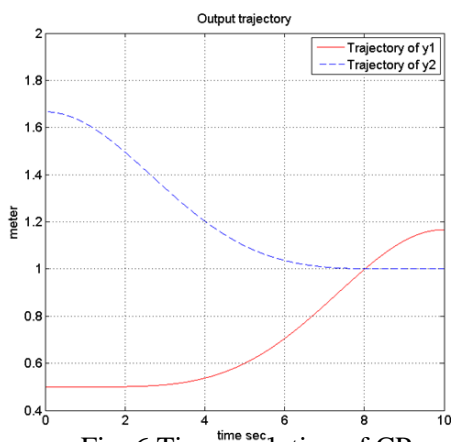


Fig. 6. Time evolution of CP.

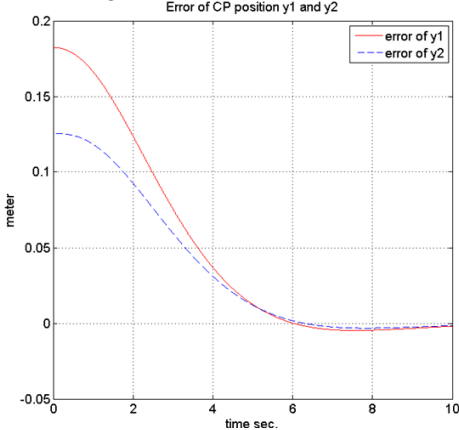


Fig. 7. Trajectory tracking error.

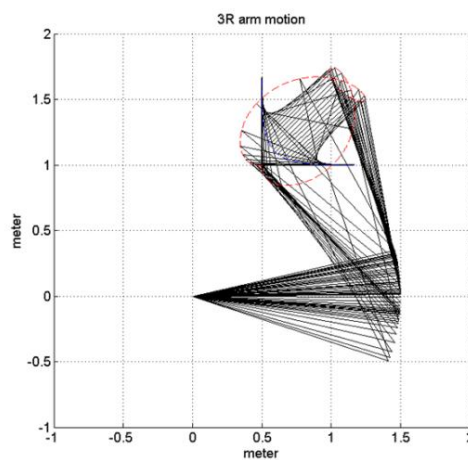


Fig. 9. Stroboscopic motion of the 3R robot.

5-Conclusion

An interactive tool for analysis was presented and exemplified on the trajectory planning and control in VR environment for a 3-DOF underactuated robot. VR was chosen to create a simulation because it was faster, cheaper, and safer than actually programming the real robot in real time. Results of using this methodology for training before interaction with a physical robot shows that the use of the virtual environment for learning to control a robotic device provides sufficient training to allow a user to become more effective in implementing a new task in a novel situation.

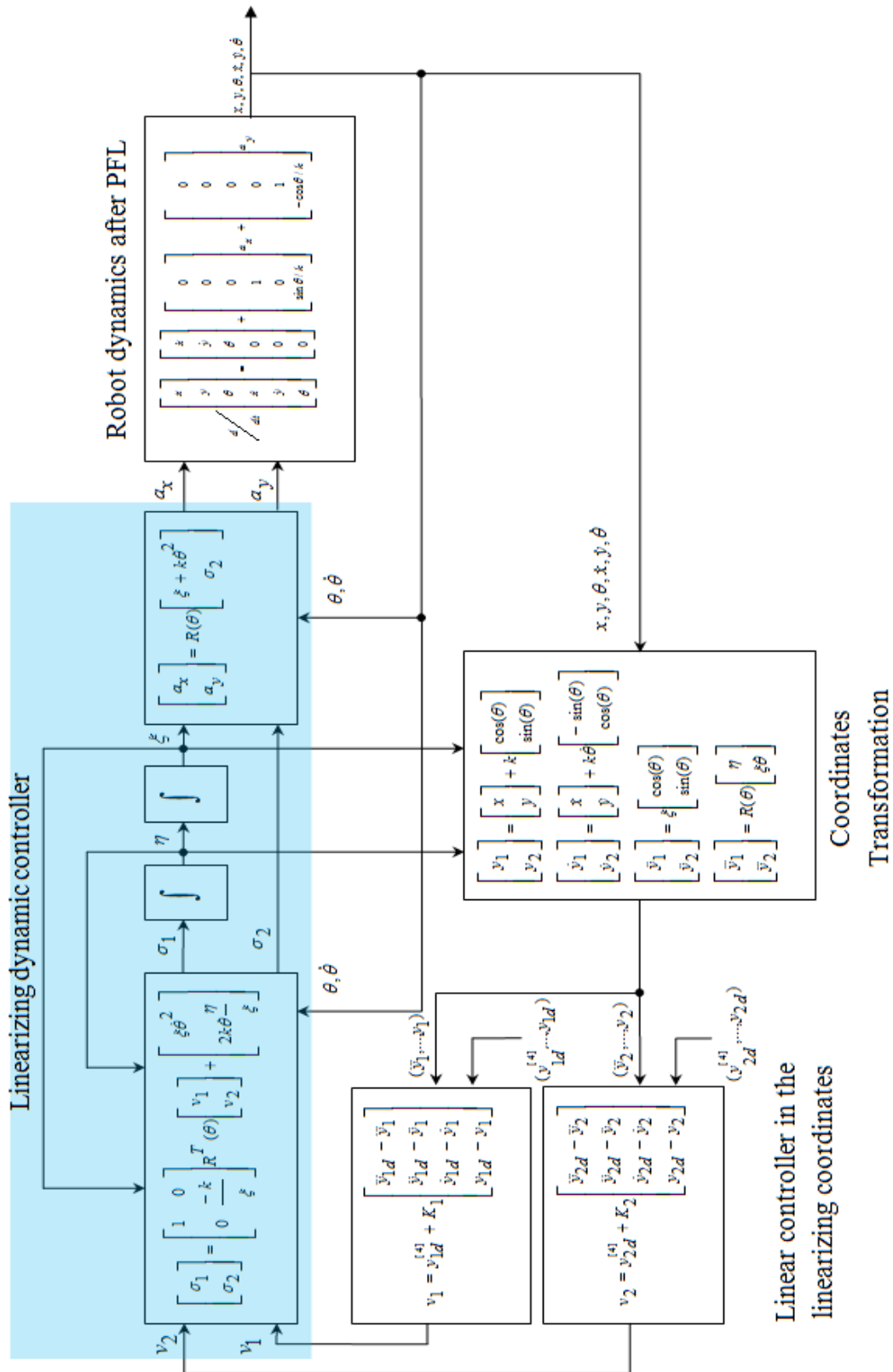


Fig. 10. Linearizing dynamic controller and tracking controller acting on the robot dynamics.

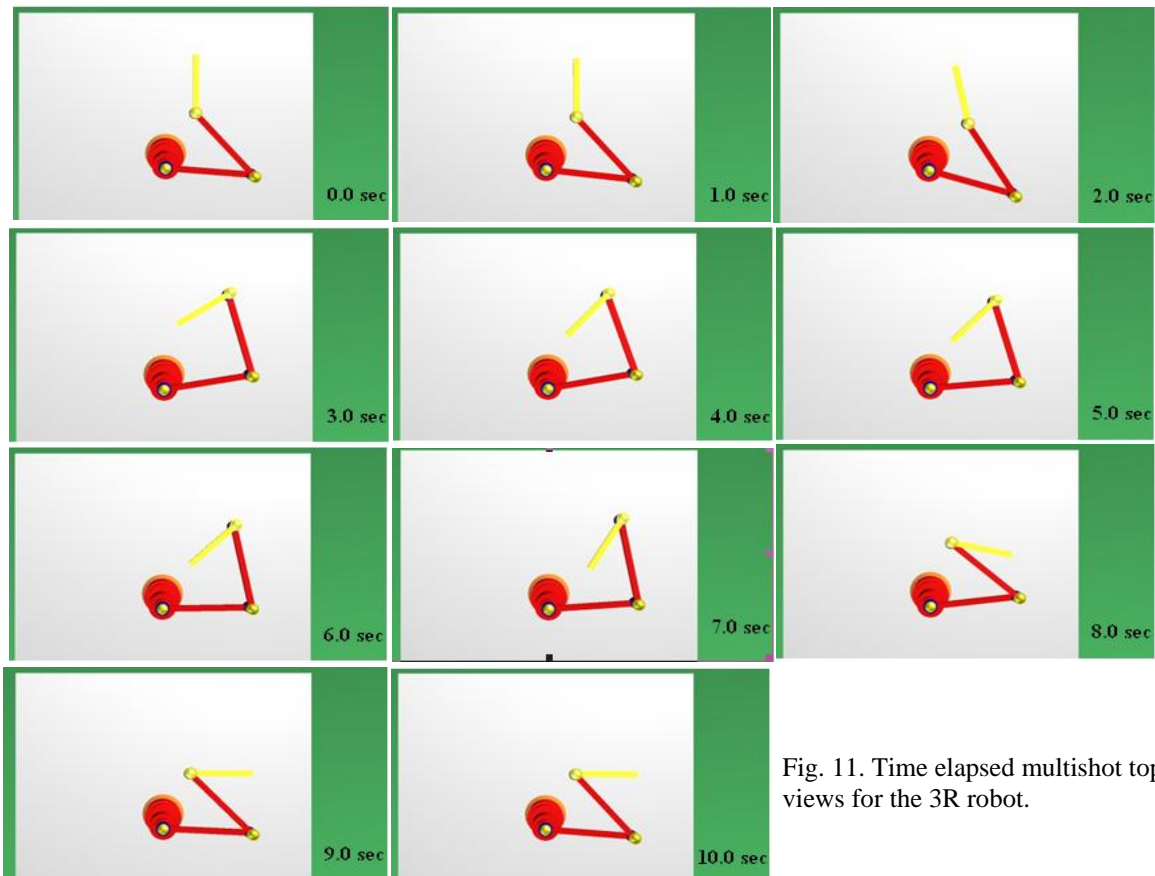


Fig. 11. Time elapsed multishot top views for the 3R robot.

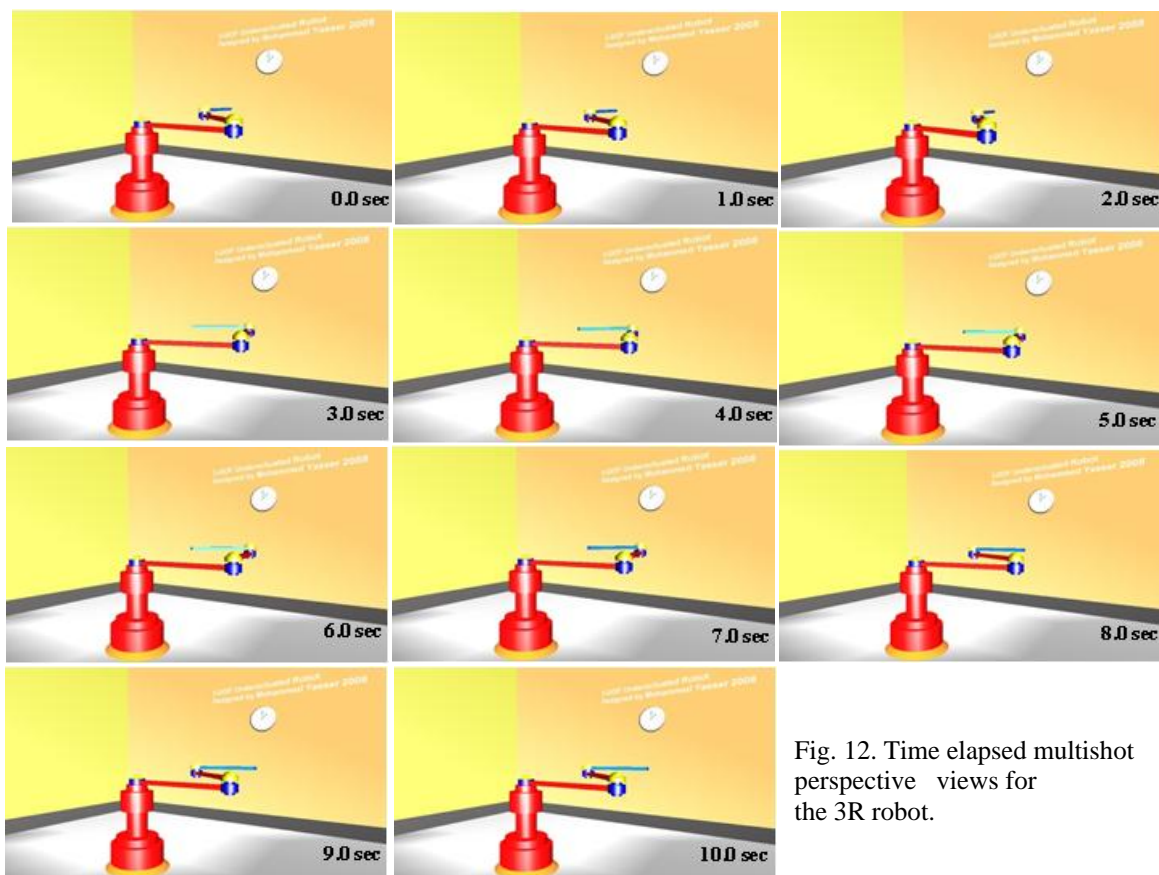


Fig. 12. Time elapsed multishot perspective views for the 3R robot.

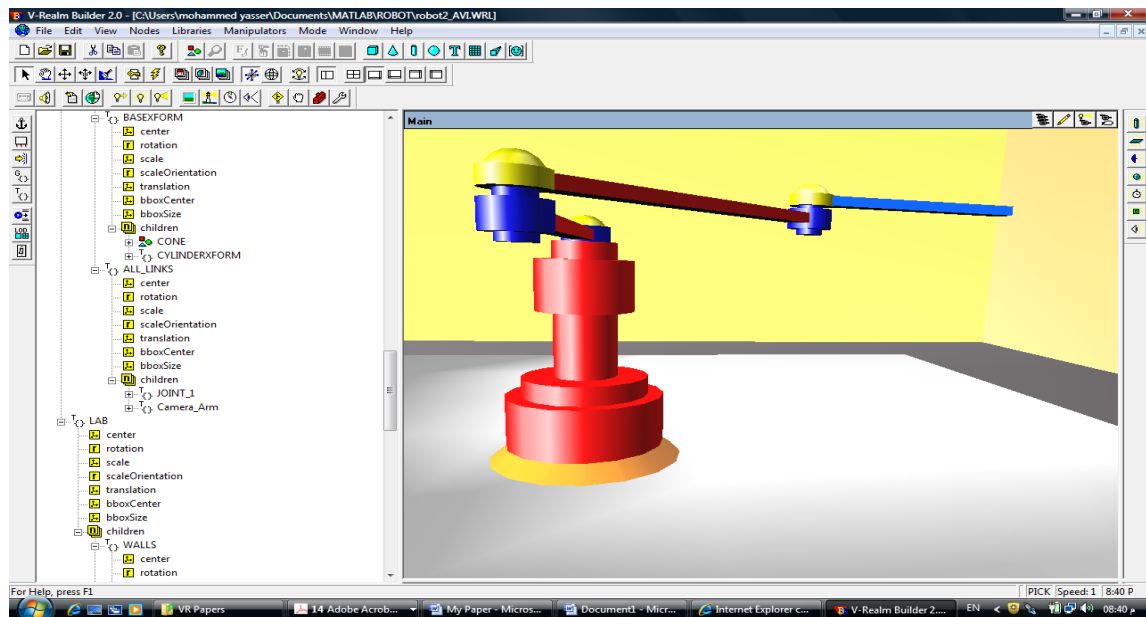


Fig. 13. Vrealm builder environment.

References:

- [1] Kharitonov V. Y., 2008 “An Approach to Consistent Displaying of Virtual Reality Moving Objects,” 3rd International Conference on Dependability of Computer Systems DepCoS-RELCOMEX.
- [2] Spong M. W., 1998 “Underactuated mechanical systems,” in Control Problems in Robotics and Automation, B. Siciliano and K. P. Valavanis (Eds.), LNCIS, vol. 230, Springer Verlag, pp. 135–150.
- [3] Spong M. W. and Block D., December 1995 “The pendubot: A mechatronic systems for control research and education,” In IEEE Conference on Decision and Control, New Orleans, LA, pages 555-557.
- [4] Bortoff S.A., May 1992 “Pseudolinearization using Spline Functions with application to the Acrobot,” PhD thesis, University of Illinois at Urbana-Champaign, Dept. of Electrical and Computer Engineering.
- [5] Wichlund K. Y., Sordalen O. J., and Egeland O., 1995 “Control of vehicles with second-order nonholonomic constraints: Underactuated vehicles,” In Proceedings of the European Control Conference, Rome, Italy, pages 3086-3091.
- [6] Spong M.W., Dec. 1987 “Modeling and control of elastic joint robots,” Transactions of the ASME, J. Dynamic Systems, Measurement and Control, 109:310-319.
- [7] Bergerman M., December, 1996 “Dynamics and Control of Underactuated Manipulators,” Ph.D. thesis; Electrical and Computer Engineering Department, Carnegie Mellon University Pennsylvania.
- [8] GU Y. L. and Xu Y., 1994 “Underactuated Robot Systems: Dynamic Interaction and Adaptive Control,” IEEE International Conference on Systems, Man, and Cybernetics, pp.958-963.
- [9] Arai H., Tanie K., and Shiroma N., 1998 “Nonholonomic control of a three-dof planar underactuated manipulator,” IEEE Trans. on Robotics and Automation, Vol. 14, No. 5, pp. 681–695.
- [10] Sears F.W. 1966, Zemansky M.W., “College Physics,” Addison-Wesley Publishing company, Inc.
- [11] Meriam J.L., Kraige L.G., 1998 “Engineering Mechanics Dynamics,”

- JOHN WILEY & SONS, INC., 4th edition.
- [12] Iannitti S., Dec. 2001 "Motion Planning and Control of a Class of Underactuated Robots," Ph.D. thesis, Dipartimento di Informatica e Sistemistica, Università di Roma "La Sapienza".
- [13] Spong M. W., Hutchinson S., and Vidyasagar M., 2006 "Robot Modeling and Control," JOHN WILEY & SONS, INC.
- [14] Lecture notes, June 2008 "Control of Nonlinear Dynamic Systems," University of California at Berkeley Mechanical Engineering, ME 237, at: <http://www.me.berkeley.edu/ME237/syllabus.html>.
- [15] De Luca A. and Oriolo G., 2002 "Trajectory planning and control for planar robots with passive last joint," Int. J. of Robotics Research, vol. 21, no. 5-6, pp. 575–590.
- [16] Algailany M. Y., November 2008 "Trajectory planning and control of a three-DOF manipulator with a passive joint under nonholonomic constraint with real-time animation," MSc. thesis, University of Technology, Dept. of control and Systems Engineering.

DESIGN AND SIMULATION OF FUZZY LIKE PD CONTROLLER FOR AUTONOMOUS MOBILE ROBOT

Dr. Muna H. Saleh
University of Baghdad
drmhsa@yahoo.com

Dr. Mazin Z. Othman
Mosul University
mzothman60@yahoo.com

Dr. Arif A. Al-Qassar
University of Technology
arifqassar@yahoo.com

Abstract:

Mobile robot is a mechanical device capable of moving in an environment with a certain degree of autonomy. The main goal of this work is to design, and simulate an intelligent controller for autonomous mobile robot named Fuzzy like PD Controller, as the test bed for future development of an intelligent vehicle. The fuzzy algorithm was implemented using a combination of three different units of fuzzy logic system. That controls two identical DC servo motors to implement the requirements of the safety navigation of the mobile robot. The paper implies computer simulations in MATLAB platform with using a step input to demonstrate the ability of each controller to accommodate the sudden changes along the motion of the mobile robot.

Keywords: *Autonomous system, intelligent control, Soft Computing (SC), Fuzzy like PD Controller, Mobile Robot.*

1- Introduction

Autonomous systems have the capability to independently perform complex tasks with higher degree of success. "Intelligent control" techniques offer alternatives to conventional approaches by borrowing ideas from intelligent biological systems. Such ideas can either come from humans who are, e.g., experts at manually solving the control problem, or by observing how a biological system operates and using analogous techniques in the solution of represented in a mathematical

model or may heavily rely on heuristics on how best to control the process, [Oga 97, Hoo 03].

There is a wide range of industrial and commercial problems that require the analysis of uncertain and imprecise information. Usually, an incomplete understanding of the problem domain further complicates the problem of generating models used to explain past behaviors or predict future ones. These problems present a great opportunity for the application of soft computing (SC) technologies, [Kac 03]. In the industrial world, it is increasingly common for companies to provide diagnostic and intuitive services for expensive machinery. Many manufacturing companies are trying to shift their operations to the service field, where they expect to find higher margins. This has been accomplished by using a tool that measures the state of the system and indicates any early failures. Such a tool must have a high level of sophistication that incorporates monitoring, and decision making about possible preventive or corrective action, and monitoring of its execution. A second industrial challenge is to provide intelligent automated controllers for complex dynamic systems, which have currently been controlled by human operators such as mobile robot control. Due to the complexity of these tasks, Artificial Intelligence (AI), and in particular SC, is called upon for help, [Sat 00, Fra 03]. Additionally, human thinking has logical,

intuitive and subjective sides. The logical thinking side has been developed and utilized. This resulted in the present advance in the expert systems known as hard computing. However, it has been found that, hard computing could not give solutions for very complicated problems. In order to cope with this difficulty, the human mind using intuitive and subjective thinking is realized as SC, which offers machine intelligence. SC is extended to include computing not only from human thinking aspects (mind and brain), but also from artificial engineering systems [Don 00, Chr 00]. An intelligent machine such as mobile robot that must adapt to the changes of its environment must also be equipped with a vision system so that it can collect visual information and use this information to adapt to its environment [Hac 09].

Fuzzy logic has been found to be very suitable for embedded control applications. Several manufacturers in the automotive industry are using fuzzy technology to improve quality and reduce development time; fuzzy logic enables very complex real time problems to be tackled using a simple approach. The concept of Fuzzy Logic (FL) presented as a way of processing data by allowing partial set membership rather than crisp set membership or non-membership [Pas 98, Hof 01]. There are many attempts to solve the problems related to mobile robot in both known and unknown environments.

In 1998, a fuzzy collision avoidance system for a fixed obstacle was designed and tested by [Kru 98]; this work describes a fuzzy trajectory controller with over 300 rules that is used with a specially designed car-driving robot. The rules were created based on the trajectories various drivers used to avoid a fixed obstacle. In 2004, Riid, Pahhomov and Rustern[Rii 04] have designed a fuzzy logic enhanced car navigation and collision avoidance system. Essentially, the control of a car in this system is based on the flexible use of a

fuzzy trajectory mapping unit that enables smooth trajectory management independent of car's initial position or position of the destination. This was done with a fuzzy controller consisting of 28 rules and a state machine containing 4 states. In 2005, Aniket, Joseph and Benjamin [Ani 05] has developed an intelligent wheelchair, to be useful as a mobility assistant for a human driver, an intelligent robotic wheelchair must be able to distinguish between safe and hazardous regions in its immediate environment. They presented a hybrid method using laser rangefinders and vision for building local (2-Dimension) metrical maps that incorporate safety information (called local safety maps). In this research, a fuzzy controller which incorporates fuzzy logic have been designed and evaluated. This controller named fuzzy like PD.

2- Mobile Robot and Control System Modeling

The proposed mobile robot in this paper is assumed to be using two set of sensors which are a camera and a laser sensor. The camera captures images of the ceiling of the environment (corridor) and makes calibration and correction for the heading of the mobile robot, and the laser sensor detects objects in the nearby vicinity providing the orientation and the distance of the nearest obstacles. The mobile robots has number of specialties, the following are two major characteristics of the mobile robots [Rol 04]:

❖ Mobility

Real robots always have moving parts. With mobile robots it means robots that can locomotive, (i.e. move in its entirety in space). On the ordinary ground this usually means the robot has wheels, legs or tracks. If the robot acts in the air or underwater, surely other methods of transport are used.

❖ **Autonomy**

Another degree of freedom is autonomy which describes how independent from humans a robot can operate. At one end is a robot that is fully controlled by a human operator. At the other extreme, the robot is totally autonomous. To be autonomous, the robot needs to be able to adapt reasonably well to unexpected changes in the environment. In order to achieve a level of autonomy, awareness of the world surrounding is necessary.

2.1 Wheeled Mobile Robot

The wheel has been by far the most popular navigation mechanism in mobile robotics; it can achieve very good efficiencies, and does so with a relatively simple mechanical implementation. In addition, balance is not usually a research problem in wheeled robot designs, because wheeled robots are almost always designed so that all wheels are in ground contact at all times. Thus, three wheels are sufficient to guarantee stable balance, although two wheeled robots can also be stable. There is a very large space of possible wheel configurations when one considers possible techniques for mobile robot. The wheel design will be discussed first as there are a number of different wheel types with specific strengths and weaknesses. There are four major wheel classes, they differ widely in their kinematics, and therefore the choice of wheel type has a large effect on the overall kinematics of the mobile robot. The four basic wheel types are [Rol 04]:

- ❖ Standard wheel: two degrees of freedom.
- ❖ Castor wheel: two degrees of freedom; rotation around an offset steering joint.
- ❖ Swedish wheel: three degrees of freedom; rotation around the (motorized) wheel axle, around the rollers, and around the contact point.
- ❖ Ball or spherical wheel: realization technically difficult. The choice of wheel types for a mobile robot is strongly linked to the choice of wheel arrangement, or wheel configuration.

Three fundamental characteristics of a robot are governed by these choices: maneuverability, controllability, and stability [Mar 89].

In order to specify the position of the robot on the plane a relationship is established between the global reference frame of the plane and the local reference frame of the robot, as in Figure (1). The axes (X_I) and (Y_I) define an arbitrary inertial basis on the plane as the global reference frame from some origin: $\{X_I, Y_I\}$. To specify the position of the robot, a point (P) on the robot chassis is chosen as its position reference point. The basis $\{X_R, Y_R\}$ defines two axes relative to (P) on the robot chassis and is thus the robot's local reference frame. The position of (P) in the global reference frame is specified by coordinates (x) and (y), and the angular difference between the global and local reference frames is given by (θ) [Rol 04].

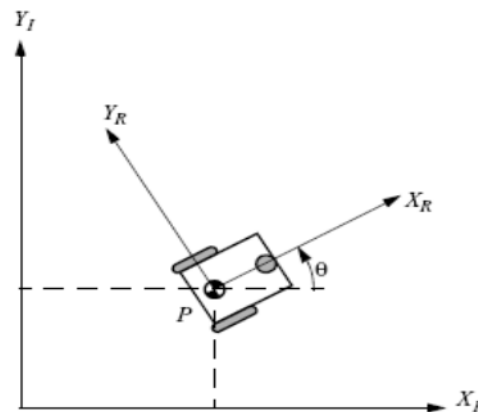


Figure (1): The global reference frame and the robot local reference frame

The pose of the robot can be described as a vector with these three elements [Rol 04].

$$\xi_1 = \begin{bmatrix} X \\ Y \\ \theta \end{bmatrix} \text{-----(1)}$$

Where: (X) is the x-axis of robot position while (Y) is a y-axis of robot position, and θ

is an angular difference between the global and local reference frames. To describe robot motion in terms of component motions, it will be necessary to map motion along the axes of the global reference frame to motion along the axes of the robot's local reference frame. Of course, the mapping is a function of the current pose of the robot.

$$R(\theta) = \begin{bmatrix} \cos\theta & \sin\theta & 0 \\ -\sin\theta & \cos\theta & 0 \\ 0 & 0 & 1 \end{bmatrix} \text{-----} (2)$$

This matrix can be used to map motion in the global reference frame $\{X_I, Y_I\}$ to motion in the local reference frame $\{X_R, Y_R\}$. This operation is denoted by $R(\theta)\zeta_I$ because the computation of this operation depends on the value of (θ) .

$$\xi'_R = R(\theta)\xi'_I \text{-----} (3)$$

Where ξ'_R and ξ'_I are the derivatives of ξ_R and ξ_I , respectively in which ξ_R is the robot position in respect to the local reference frame and ξ_I is the robot position in respect to the global reference frame. The process of understanding the motions of a robot begins with the process of describing the contribution each wheel provides for motion. Each wheel has a role in enabling the whole robot to move. By the same token, each wheel also imposes constraints on the robot's motion.

3-Designing the PD like Fuzzy Controller

As mentioned before the sole core of the proposed mobile robot is the DC servo motor in which two identical DC servo motor each attached to a wheel to achieve the movement of the robot in different directions, controlling the velocities of these two motors could control the position

of the mobile robot in the world coordinates. Intelligent controller was applied to the DC motor transfer function; this is the Fuzzy like PD controller. Fuzzy Logic Controller could be used as an analogy to classical PD (Proportional-Derivative) controller, and overcome the disadvantages of the PD-Controller, to do this it is necessary to choose the input and output variables and the rules of the controller properly, the equation giving a conventional PD-Controller is [Oga 97]:

$$u(t) = K_p * E(t) + K_d * CE(t) \text{-----} (4)$$

Where K_p and K_d are proportional and differential gain factors, $E(t)$ is the error and $CE(t)$ is the change in error. The fuzzy controller should do the same thing. For any pair of the values of the error and the change of the error, and it should workout to control signal. The rule base for "Fuzzy Logic Controller Like PD (FLC-PD)" a implements a static nonlinear input-output map between its inputs, error $E(t)$ and change of error $CE(t)$ and control action $Uc(t)$.

Assuming that there are seven membership functions on each input of the universe of discourse (NB stands for negative big, NM stands for negative medium, NS for negative small, Z for Zero, PS for positive small, PM for positive medium and PB stands for positive big).

Usually fuzzy sets are specified as a function with parameters that have to be adapted according to the problem. A widely used function is the so called triangular membership functions. From the number of the membership functions on the universe of discourse that there are forty nine possible rules that can be put in the rule-base [Leo 97, Pas 98]. The complete set of rules is given in table (1).

Table (1): The complete set rules of FLC-PD

Control Action (Uc)		Error (E)						
		NB	NM	NS	Z	PS	PM	PB
Change of Error (CE)	NB	NB	NB	NM	NM	NS	NS	Z
	NM	NB	NB	NM	NS	NS	Z	PS
	NS	NB	NM	NS	NS	Z	PS	PM
	Z	NB	NM	NS	Z	PS	PM	PB
	PS	NM	NS	Z	PS	PS	PM	PB
	PM	NS	Z	PS	PM	PM	PM	PB
	PB	Z	PS	PS	PM	PB	PB	PB

4 – Simulations Results

Through many various examinations of FLC-PD, it was noticed that it is produced good response, but the main drawback for all kind of fuzzy control is that they have a high sensitivity to the variations in the parameters of the input and output gains and control action gain (G_e , G_{ce} and G_u), figure (2) represents the FLC-PD applied to a DC servo motor.

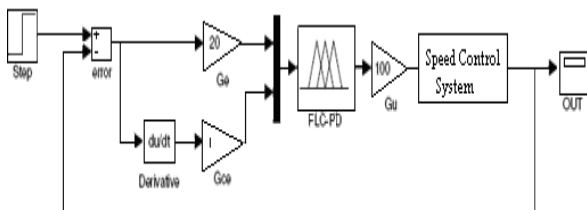


Figure (2): The fuzzy control system

Three different ranges on Universe of Discourse (UoD) were used in the simulation in the MATLAB [Mat 01] as follows:

- UoD₁: the inputs and output ranges between (-1, 1).
- UoD₂: the inputs range between (-5, 5), while the outputs range (-10, 10).
- UoD₃: the inputs and output ranges between (-10, 10).

The system were tested with wide range of scaling gains, with varying the range of universe of discourse for the inputs and output, figure (3) shows the simulation results of applying FLC-PD of a UoD₁ with different gains. Figure (4) illustrates the

simulation results of applying FLC-PD of a UoD₂ with different gains, while figure (5) shown the simulation results of applying FLC-PD of a UoD₃. Table (2) lists the experimental results of the simulation of the FLC-PD control system of all these conditions.

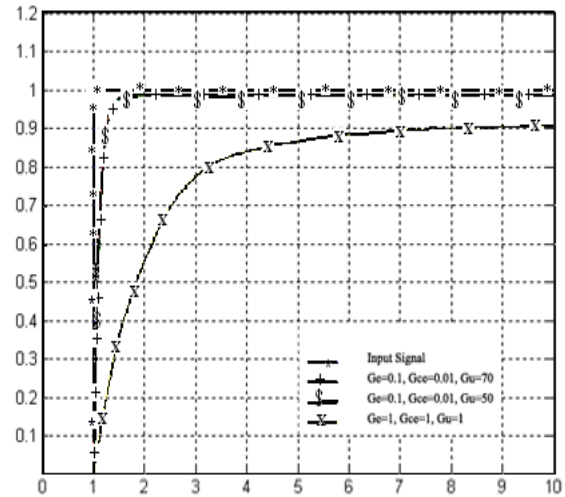


Figure (3): Motor step response controlled by FLC-PD with UoD₁

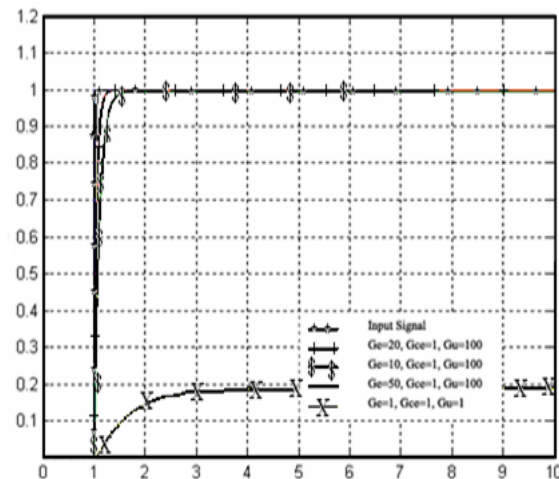


Figure (4): Motor step response controlled by FLC-PD with UoD₂

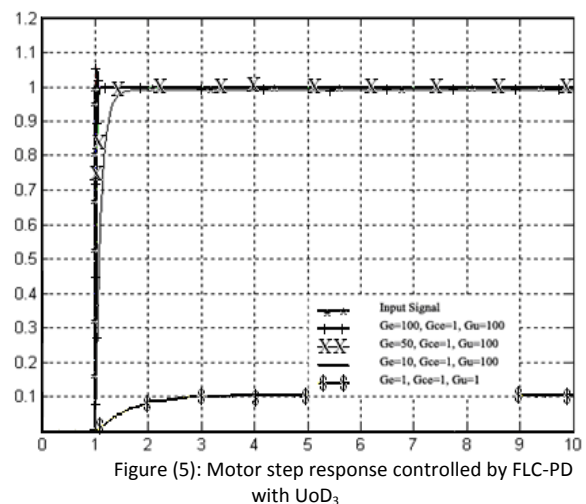


Figure (5): Motor step response controlled by FLC-PD with UoD₃

5- Conclusions

The theoretical study, simulation, and the experimental implementation based on FLC-PD controller had been presented. Several conclusions are presented as follows:

- ❖ FLC-PD provides good response to a step input controlling the DC servo motor in which is the sole of the mobile robot.
- ❖ From the simulation results obtained, it is noticeable that the desired output for a step response when using UoD₃ and scaling parameters of (Ge=100, Gce=1 and Gu=100).

References

- [1] [Oga 97] Ogata K., "Modern Control Engineering", University Of Minnesota, 1997.
- [2] [Hoo 03] Hoogsteden, R. Babuška, H.C. and A.F.M. Verbraak, "Computer-Controlled Mechanical Simulation of the Artificially Ventilated Human Respiratory System," IEEE Transactions on Biomedical Engineering, Vol. 50, No. 6, 2003.
- [3] [Kac 03] Kacprzyk, J., "Studies in Fuzziness and Soft Computing," ISSN: Physica-Verlag Heidelberg, New York, 2003.
- [4] [Sat 00] Sathish K. Shanmugasundaram, "Control System Design for an Autonomous Mobile Robot", University of Cincinnati, 2000.
- [5] [Fra 03] Franz R., "Representations for Genetic and Evolutionary Algorithms, Studies in Fuzziness and Soft Computing," Internet Article, 2003.
- [6] [Don 00] Dong-Oh Kang and Z. Bien, "Design of Multi objective Satisfactory Fuzzy Logic Controller Using Reinforcement Learning," International Journal of Fuzzy Systems, Vol. 2, No. 2, June 2000.
- [7] [Hac 09] O. Hachour, "The proposed Fuzzy Logic Navigation approach of Autonomous Mobile robots in unknown environments," International journal of mathematical models and methods in applied sciences, Vol .3, 2009.
- [8] [Pas 98] Passino Kevin M., "Fuzzy Control", Addison Wesley Longman, 1998.
- [9] [Hof 01] Hoffmann F., "Evolutionary Algorithms for Fuzzy Control System Design," Proceedings of the IEEE, Special Issue on Industrial Application of Soft Computing, Oct. 2001.
- [10] [Kru 98] Kruse, E. Wahl, F.M., "Camera-based Monitoring System for Mobile Robot Guidance", Victoria, Can, IEEE/RSJ International Conference on Intelligent Robots and Systems, Oct 1998.
- [11] [Rii 04] Riid, Andri, Pahhomov, Dmitri and Rustern, Ennu, "Car Navigation and Collision Avoidance with Fuzzy Logic," Fuzzy Systems IEEE International Conference, 2004.
- [12] [Ani 05] Aniket Murarka, Joseph Modayil, and Benjamin Kuipers Building Local Safety Maps for a Wheelchair Robot using Vision and Lasers University of Texas at Austin, 2005.
- [13] [Rol 04] Roland Siegwart and Illah R. Nourbakhsh, "Introduction to autonomous mobile robots", the MIT press, Cambridge, Massachusetts, 2004.
- [14] [Mar 89] Mark W. Spong and M. Vidyasgar, "Robot Dynamics Control," John Wiley SONS, 1989.
- [15] [Leo 97] Leonid R., "Fuzzy Controllers," Newnes, First Published, 1997.

Table (2): The results of applying FLC-PD								
	Parameters			Peak Response		Rise Time (sec)	Steady State	
	Ge	Gce	Gu	Voltage (Volt)	Time (sec)	Time (sec)	Voltage (Volt)	Time (sec)
UoD ₁	1	1	1	0.91	9.6	3.53	0.91	10
	10	1	10	0	0	0	0	0
	10	1	100	0	0	0	0	0
	0.1	0.1	10	0.92	7	3.2898	0.92	7.15
	0.1	0.1	50	0.98	8	3.273	0.982	8.42
UoD ₂	1	1	1	0.1868	4.95	2.5	0.186	5.2
	10	1	10	0.958	1.95	1.283	0.958	4.03
	10	1	100	0.995	1.88	1.23	0.996	2.4
	50	1	100	1	2	1.04	0.999	2.3
	20	1	100	1	1.674	1.11	1	1.8
UoD ₃	1	1	10	0.103	4.19	2.4	0.103	4.06
	10	1	10	0.92	2.52	1.312	0.92	3.3
	10	1	100	0.99	1.69	1.23	0.99	1.72
	50	1	100	0.999	1.19	1.04	0.998	1.22
	100	1	100	1.05	1.032	1.02	1	1.08

Topic 3

Modeling And Measurements

TEXTURE IDENTIFICATION BY USING NEURO-WAVELET TECHNIQUE

Dr. Waleed A. Mahmoud
College of Engineering
University of Baghdad
profwaleed54@yahoo.com

Dr. Asmaa Q. Shareif
College of Science
University of Baghdad
asama_sal@yahoo.com

Qaswaa K. Abood
Collage of Science
University of Baghdad
kaswaaa@yahoo.com

Abstract:

Artificial neural networks (ANNs) are massively parallel distributed processing systems that improve their performance through dynamic learning. The main feature of ANN, that is weight adaptation, is used effectively to identify the texture, here wavelet transform was used as a first step to identify the texture from the spatial domain (i.e. image), then it was implemented under the transform domain (i.e. frequency), the resultant was used to find the energy, which became the actual inputs to the multi-layered feed forward ANN. The desired output represents the original texture under the identification process.

Keywords: *wavelet transform, texture identification, artificial neural network, energy calculation.*

1. Introduction

Neuro-Wavelet(NW) have recently attracted great interest, because of their advantages over multi-layer feed forward neural network as they are identification networks, and achieve fast convergence, also are capable of dealing with learning process by the training procedure. In addition, NW are generalized multilayer feed forward neural networks. (MLFN). However, the generalization performance of NW trained by back propagation (BP) generalized algorithm.

Texture provide important characteristics for surface and object identification from aerial or satellite photographs, biomedical

images and many other types of images. Texture analysis is fundamental to many applications such as automated visual inspection, biomedical image processing.

In this paper, we propose a robust Neuro-Wavelet based on the theory of robust feedback for dealing with target in the framework of multilayer neural networks. The number of training data involved during training was adaptively adjusted. Simulation results are demonstrated to validate the generalization ability and efficiency of the proposed network.

The characteristic features of energy to the texture signals have been used as inputs to the artificial neural network (ANN) named as multiplayer feed forward that consists of one input, one hidden and one-output layers. The ANN is trained using back propagation algorithm. In this technique, the ANN is used for texture identification: so combining the wavelet transform (WT) and MLFN for texture identification that is applied in three phases:

First: To compute the discrete transform of 3-Dim. Daubechies wavelet (Db4) [1], then to calculate the energy for the chosen texture [2], and finally to apply the calculated energy into the MLFN with Bp algorithm [3].

The task of training NW involves estimating parameters in the network by minimizing some cost function (in our case the calculated energy for the WT), a measure reflecting the approximation quality performed by the network over the parameter space in the network. The generalized delta rule is the most popularly used in estimating the weights which provides optimal results.

The advantage of the used method is demonstrated by computer simulations.

This paper is organized as follows:

Section 2 presents the Wavelet transform that is used in this study. Section 3 illustrates the computation of the energy; Section 4 demonstrates the reason why a robust NW is needed; Section 5 demonstrates the simulation results. Section 6 is the conclusion; the paper ends with references.

The following will present a literature survey; in [4] they propose a robust wavelet neural network based on the theory of robust regression for dealing with outliers in the framework of function approximation. By adaptively adjusting the number of training data involved during training, the efficiency loss in the presence of Gaussian noise is accommodated.

In [5] a novel technique is presented for restoring a blurred noisy image without any prior knowledge of the blurring function and the statistics of noise. The technique combines wavelet transform with radial basis function (RBF) neural network to restore the given image which is degraded by Gaussian blur and additive noise. and the wavelet transform is adopted to decompose the degraded image into high frequency parts and low frequency part. Then the RBF neural network based technique is used to restore the underlying image from the given image. The inverse principal element method (IPEM) is applied to speed up the computation.

In [6] an algorithm for texture feature extraction was described that uses wavelet decomposed coefficients of an image and its complement. Four different approaches to color texture analysis are tested on the classification of images from the VisTex database.

In [7] a research on a prototype software system that automatically classifies an image as having hidden information or not was considered, it uses a sophisticated artificial neural network (ANN) system that is trained

on a selection of image features that distinguish between stego and nonstego images. The novelty of this ANN is that it is a blind classifier that gives more accurate results than previous systems. It can detect messages hidden using a variety of different types of embedding algorithms.

In [8] researchers introduced an approach to protect the ownership by hiding the iris data into a digital image for authentication purposes. The idea is to secretly embed an iris code data into the content of the image, which identifies the owner. Algorithms based on biologically inspired Spiking Neural Networks, called Pulse Coupled Neural Network (PCNN) are first applied to increase the contrast of the human iris image and adjust the intensity with the median filter. It is followed by the PCNN segmentation algorithm to determine the boundaries of the human iris image by locating the pupillary boundary and limbus boundary of the human iris for further processing. A texture segmentation algorithm for isolating the iris from the human eye in a more accurate and efficient manner is presented.

2. Wavelet Transform

Wavelets mean small waves that segments data into different frequency components and transfer each component with different resolution that is matched to its scale. The main idea of wavelet analysis is to see both coarse and detail data without heavy computational penalty. The goal of most modern wavelet researches is to create a set of basis functions and transform them in order to give information. The fundamental idea behind wavelets is to analyze the signal at different scales or resolutions, which is called multi-resolution.

Wavelets are a class of functions used to localize a given signal in both space and scaling domains. A family of wavelets can be constructed from a mother wavelet. Compared to Windowed Fourier analysis, a mother wavelet is stretched or compressed to

change the size of the window. In this way, big wavelets give an approximate image of the signal, while smaller and smaller wavelets zoom in on details. Therefore, wavelets automatically adapt to both the high-frequency and the low-frequency components of a signal by different sizes of windows. Any small change in the wavelet representation produces a correspondingly small change in the original signal, which means local mistakes will not influence the entire transform. The wavelet transform is suited for un-stationary signals, such as very brief signals and signals with interesting components at different scales [9].

We use the Daubechies filter in this paper because of its excellent performance. The wavelet coefficients are often organized as a spatial-orientation tree, as shown in Fig.(1) that demonstrates an example for the tested image "woman". The coefficients from the highest to the lowest levels of wavelet subbands depict a coarse-to-fine variation in scales (resolutions). We have thus determined to construct by its accumulated significance. Let H_i , V_i , and D_i denote the wavelet coefficients of horizontal, vertical, and diagonal subbands at level i respectively. (A larger value of i indicates a coarser resolution.) The map is organized into the smallest-scale detail subbands $H1$, $V1$, and $D1$ (excluding the approximation subband), and the value of its entry is obtained by adding the magnitude of the corresponding wavelet coefficient.

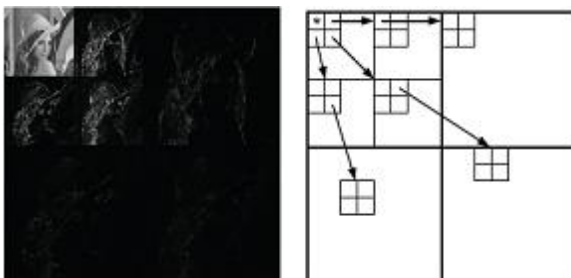


Fig.(1) (a) Wavelet transform (b) spatial-orientation trees [9].

The wavelet transform (WT) decomposes a signal $f(t)$ by performing inner products with a collection of analysis function $\psi(a, b)$, which are scaled and translated version of the wavelet ψ . It refers to the degree of similarity between the basis functions (wavelet) and the original signal at the current scale. The amplitude of the WT therefore tends to be maximum at those scales and locations where the signal most resembles the analysis template.

When the scale (a) varies, the filter ψ is only reduced or dilated, while keeping the same pattern. The reconstruction is only possible if $C\psi$ is defined by admissibility condition, which restricts the class of functions that can be wavelet [8].

3. Energy Computation

The calculation of energy for the texture will be performed as shown in the following formulas [2]

$$E = 10 \log(P_e)^2 \quad (1)$$

$$P = 1/8 * 8 \sum_k P_e(k)^2 \quad (2)$$

This is done by calculating the energy that belongs to the texture. The energy of the texture will be represented as a column. This column will be the input data to the designed ANN, which represents the second phase of the work.

4. Neuro-Wavelet Technique

The neural network with back-propagation feed forward has been used; the feeded back is for updating the weights of the connection between the layer and the layer before it and so on. The weight update uses the

generalized delta rule (GDR) learning algorithm for training the net; this is based on comparing the output of the MLFN with the target value and updated the weights between the output layer and the hidden layer before the output layer. In addition, the output of the hidden layer is compared with that of input layer and the error- correction term is calculated which is used to update the weights [3].

Wavelets occur in family of functions and each is defined by dilation a_i which control the scaling parameter and translation t_i which controls the position of a single function, named the mother wavelet $\psi(x)$. Mapping functions to a time-frequency phase space, NW can reflect the time-frequency properties of function more accurately than the MLP. Given an n -element training set, the overall response of a NW is:

$$\hat{y}(\mathbf{w}) = w_0 + \sum_{i=1}^{Np} w_i \psi_i\left(\frac{x-t_i}{a_i}\right) \quad (3)$$

Where Np is the number of wavelet nodes in the hidden layer and w_i is the synaptic weight of NW. A NW can be regarded as a function approximate which estimates an unknown functional mapping:

$$y = f(x) + \varepsilon \quad (4)$$

Here f is the regression function and the error term is a zero-mean random variable of disturbance [4].

5. Simulation Results

The data we used for training and testing the NW was provided from [9]. The image data was originally formatted in Matlab function, which was grayscale image, the image scenes in these images include natural scenes, digitized photographs, maps, computer graphics images. We excluded one image due to its overly large size. We used

Matlab for coding the feature values and to run the identification algorithms as is represented in Fig. (3).

The BP training approach provides an asymptotically optimal solution with minimum variance, which assumes that the error distribution is identically independent. Fig.(4) gives a comparison for the test data set.



Fig. (3) Simulation results for texture identification

A) original texture, b) after wavelet, c) after NW

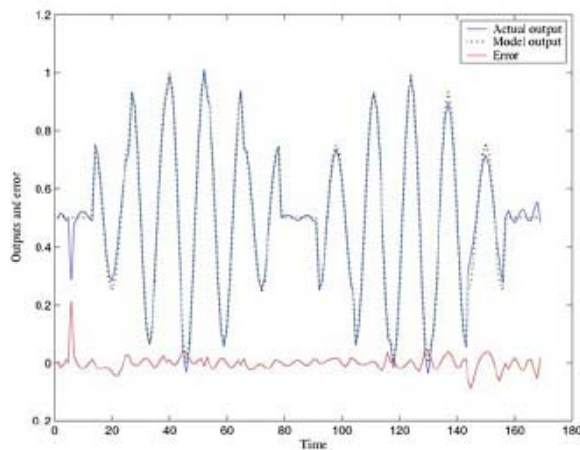


Fig.(4) Comparison of the model output, dynamic system output and identification error for test data set.

6. Conclusion

In this paper, a Neuro-wavelet network was proposed. The working process of the proposed network can be viewed as to decompose the wavelet, nonlinear system represented by the artificial neural network into an active network, then the energy of the wavelet to be entered as inputs to the artificial neural network. One advantage of the proposed method is that it needs the calculation of the wavelet's energy for a given problem to be entered into neural networks. A training algorithm, generalized delta rule, was also introduced for training the neural network. Simulation results for identified image approximation and the original image shows the effectiveness of the proposed technique.

The proposed technique for texture identification based image processing by using the wavelet transform together with the feed forward neural network. This paper presents an efficient learning algorithm based on the back propagation.

References

[1] Aboud Q. K., 2005 "Speech Scrambling using Multi-wavelet Transform", M.Sc. Dissertation.

- [2] Naser M. A., 2009"Texture Classification using a proposed Mix Transform",M.Sc. Dissertation.
- [3] Shareif A. Q., 1995" Neural networks for System Identification", M.Sc. Dissertation.
- [4] Sheng-Tun L. and Shu-Ching Ch., 2007,"Function Approximation using Robust Wavelet Neural Networks" Taiwan supported in part by NSC89-2213-E-327-007.
- [5] Ping G., Hongzhai Li, Michael R. L., 2006, "Blind Image Restoration by Combining Wavelet Transform and RBF Neural Network", International Journal of wavelets, Multiresolution and Information Processing, World Scientific Publishing Company.
- [6] Hiremath P.S., Shivashankar S., and Pujari J., 2006."Wavelet Based Features for Color Texture Classification with Application to CBIR", IJCSNS International Journal of Computer Science and Network Security, VOL.6 No.9A, pp.124-133,
- [7] Jennifer D., Clifford B., Eric B. 2005 "An artificial neural network for wavelet steganalysis", Proceedings of SPIE - The International Society for Optical Engineering, vol. 5916, Mathematical Methods in Pattern and Image Analysis, pp. 1-10.
- [8] Hassanien Ab., Abraham A., and Grosan C., 2008, "Spiking Neural network and Wavelets for Hiding Iris data in Digital Images",Soft Computing DOI 10.1007/s00500-008-0324-x.
- [9] Al-Taee H. N., 2005 "Optical Flow Estimation using DSP Technique", Ph.D Thesis, University of Technology.

PERFORMANCE COMPARISON OF TWO NEURAL NETWORK IDENTIFIERS FOR SPACE VECTOR MODULATION

Dr. Sabah N. Al-Ubaidi
Electrical and Electronic
Engineering
Commission of Higher
Education

Dr. Amjad J. Humaidi
Control and Systems Dept.
University of Technology
aaacontrol2010@yahoo.com

Jamal A. Ali A. Alradh, B.Sc.
Electrical and Electronic
Engineering
Commission of Higher Education
gamalal_84@yahoo.com

Abstract

The space-vector PWM (SVM) method is an advanced computation-intensive PWM method and is possibly the best among all the PWM techniques for variable-frequency drive application because of its superior performance characteristics. Use of Artificial Neural Network (ANN)-based technique avoids the direct computation of trigonometric function used in conventional SVM implementation. In this work, the implementation of SVM based on ANN for a voltage-sourced inverter has been studied. Two neural scheme structures have been suggested to identify and approximate the conventional SVM; backpropagation and radial basis structures. Then, the trained structures are utilized to drive three phase induction motor. Performance comparisons have been made between these two structures under different modulator parameters and conditions. The results have been simulated using MATLAB package (R 2010a).

Keywords: *Induction machine, space vector modulation, neural network*

1. Introduction

High power electronic devices are being used increasingly to control and facilitate flow of electric power, while meeting stringent operating conditions of today's heavily-loaded networks. These devices are able to enhance the voltage profile of the power system, control the flow of real and reactive power, and improve the dynamic

performance and stability of the system. One of such devices is voltage-sourced converter (VSC) that acts as a controlled voltage source, converting a DC voltage to an ac voltage with desired frequency, phase and magnitude [1,2].

Two aspects of operation of a VSC are of primary importance: (i) the operation under PWM typically results in large switching losses, and (ii) the resulting output wave form contains harmonics, largest of which occur around the switching frequency. Using a high switching frequency improves the harmonic spectrum by drifting the harmonics towards higher orders, which would have less adverse impact on the network. However, it also increases the switching losses [3].

Pulse width modulation (PWM) has been studied extensively during the past decades. Many different PWM methods have been developed to achieve the following aims: wide linear modulation range; less switching loss; less total harmonic distortion (THD) in the spectrum of switching waveform; and easy implementation and less computation time [4].

The space-vector PWM (SVM) method is an advanced, computation-intensive PWM method and is possibly the best among all the PWM techniques for variable-frequency drive application. Because of its superior performance characteristics, it has been

finding widespread application in recent years [5].

The main disadvantages with conventional implementation are the use of a look-up table and the need to interpolation of non-linear functions. The use of any look-up table implies the need for additional memory; while interpolation of non-linear functions lead to poor accuracy and thus to increased harmonics in the PWM waveforms. Moreover, the interpolation demands additional computing time that limits the maximum inverter switching frequency [6].

A neural network has the advantage of very fast implementation of an SVM algorithm, particularly when a dedicated application-specific IC chip is used instead of a digital signal processor (DSP). A neural network based implementation of space vector modulation of a voltage-sourced inverter has been proposed in this paper. Use of ANN based technique avoids the direct computation of trigonometric function (e. g. sine function) as in conventional space vector modulation implementation. The proposed scheme is simple and straight forward and avoids the direct computation of non-linear functions. This scheme is evaluated under simulation for a variety of operating conditions of the drive system and comparison is made with the conventional method of implementation [6,7].

Figure (1) shows the block diagram of induction motor driven by ANN-based space-vector PWM. At identification mode, the switches (a, b and c) are closed and the switches (a', b' and c') are open. The induction motor is driven by the conventional SV modulator. The neural network receives the voltage (V_{ref}) and (θ) signal at the input of actual modulator and the timing sequences (T_a , T_b and T_c) generated at the output of actual space vector

modulator. Based on this information, the N.N identifier would try to identify the actual space vector modulator and generate an approximate command signals (T'_a , T'_b and T'_c).

If the induction motor is to be driven by N.N.-based space-vector modulator, the switches (a, b and c) are opened and at the same time the switches (a', b' and c') are closed. This would disconnect the actual SV modulator and replace the N.N-based SV modulator for driving the induction machine.

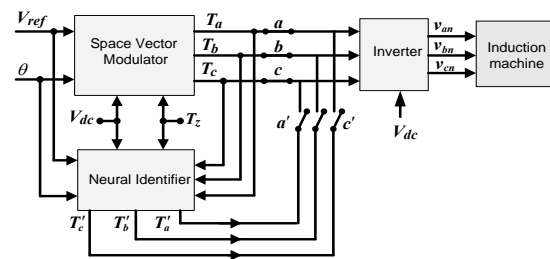


Figure (1) connection of neural identifier with actual space vector modulator

2. Analysis of Space Vector Modulator

In conventional sinusoidal PWM, for instant, is an analog domain method, duration of each pulse is found through *comparison* of a sinusoidal reference waveform and a triangular carrier waveform. A digital domain variation of PWM, space vector modulation (SVM), on the other hand, directly *computes* the duration of voltage pulses using the amplitude and angular location of the reference vector [3].

Space vector employs the concept of converter states to generate firing pulse. The states are determined by the status of switches of three legs of the converter. In a three-phase, two level VSC, the output voltage of a leg can be either $+V_{dc}/2$ or $-V_{dc}/2$ and as such the VSC can be placed in eight states depending on the ON/OFF status of its six switches (switches on the same leg have complementary states). Figure (2) shows a

three phase bridge inverter induction motor drive and the eight switch states S_i where $i = 0, 1, \dots, 7$ are shown in Fig.3. There are eight voltage vectors $V_0 \dots V_7$ corresponding to the switch states $S_0 \dots S_7$ respectively. The lengths of vectors $V_1 \dots V_6$ are unity and the length of V_0 and V_7 are zero.

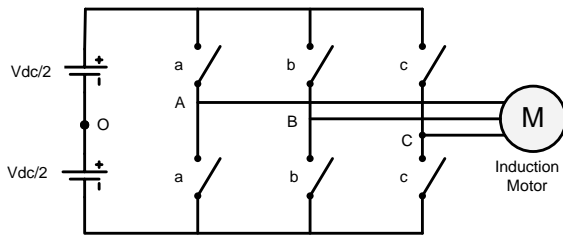


Figure (2) Three phase voltage source inverter

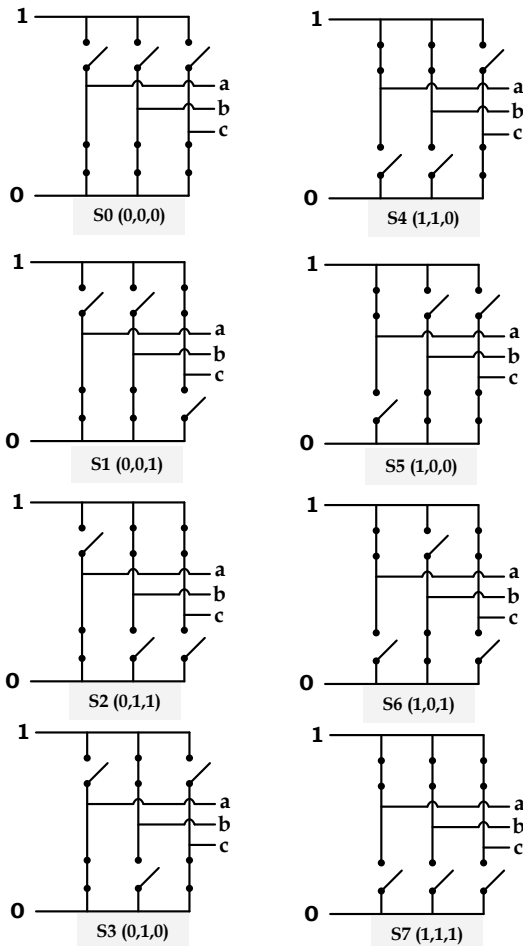
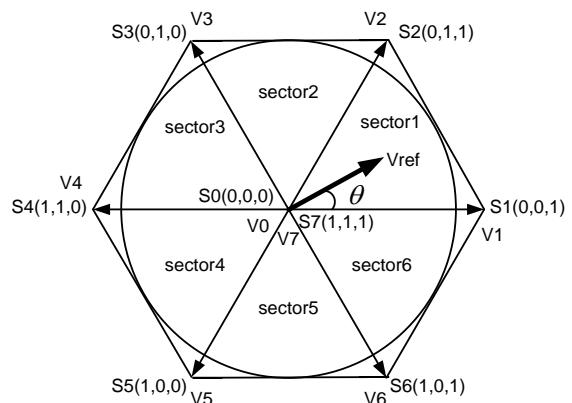


Figure (3) Eight switching states of voltage source inverter

The voltages corresponding to each state can be transformed to a space vector using Eq.(1).

$$V = \frac{2}{3} (v_a + v_b e^{j2\pi/3} + v_c e^{-j2\pi/3}) \quad (1)$$

Figure (4) shows the space vectors and composition of a reference vector. The voltages are synthesized by placing the converter in respective states for designated time shares within each sampling period. Six of these space vectors, denoted by V_1 to V_6 in Fig. 4, point to the vertices of a hexagon; two of the states translate to space vectors with zero length and are denoted by zero vectors V_0 and V_7 located at the origin. Similarly, any set of balanced reference phase voltages v_a , v_b , and v_c can be represented as a corresponding reference space vector V in two dimensions using Eq.(1). Any reference vector that lies entirely within the hexagon can be decomposed to space vectors V_0 and V_7 , as depicted in Fig.(4), for a V_{ref} in the first sector of the hexagon. This is achieved by constructing voltages that average to the reference vector, which is sampled at a rate determined by a given sampling frequency F_z ($1/T_z$).



Figure(4) Voltage space vector

The time shares are proportional to the length of the projected vectors. The rest of the sampling period is filled with zero space

vectors \mathbf{V}_0 and \mathbf{V}_7 . Time shares are calculated as [3,5]:

$$T_1 = \frac{\sqrt{3} T_z |V_{ref}|}{V_{dc}} \left[\sin\left(\frac{n\pi}{3}\right) \cos(\theta) - \cos\left(\frac{n\pi}{3}\right) \sin(\theta) \right] \quad (2)$$

$$T_2 = \frac{\sqrt{3} T_z |V_{ref}|}{V_{dc}} \left[-\sin\left(\frac{(n-1)\pi}{3}\right) \cos(\theta) + \cos\left(\frac{(n-1)\pi}{3}\right) \sin(\theta) \right] \quad (3)$$

$$T_o = T_z - (T_1 + T_2) \quad (4)$$

Where $n=1$ through 6 (that is sector 1 to 6) and $0 \leq \theta \leq \pi/3$, while T_1 , T_2 and T_o are the time shares of respective voltage vectors, T_z is the sampling period, and θ is the angle between the reference vector and the space vector. The reference voltage V_{ref} in Eq.(2) and (3) is defined in terms of modulation index m as $V_{ref} = (2/3)m V_{dc}$.

It is worth to note that the SVM strategy only determines the time shares of space vectors and does not identify the order in which they are applied. Moreover, the individual time shares of T_o and T_7 are not specified. Fig.5 shows the switching patterns at sector 1.

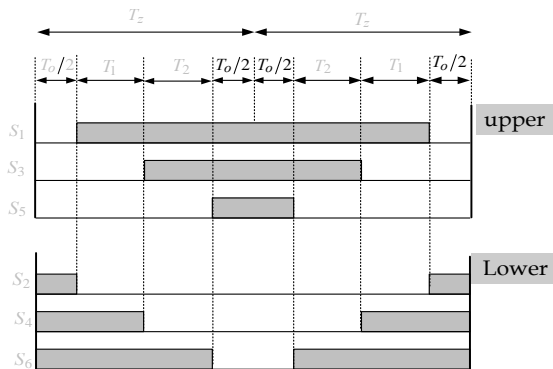


Figure (5) shows space vector PWM switching patterns at sector 1

3. Neural network identification structure

The main advantage of ANN implementation as a SVM is its high speed when implemented on the IC's chip.

The back propagation neural network structure for the model system is shown in the Fig.(6). It consists from three layers; the

input layer, the hidden layer and the output layer. The input layer consists of two inputs ($x_1 = V_{ref}$) and ($x_2 = \theta$), hidden layers of N -nodes and the output layer of three outputs ($y_1 = T_a$), ($y_2 = T_b$) and ($y_3 = T_c$). The sigmoid activation functions are assigned equally to both hidden and output layer neurons. Equation (5) shows the relationship between the hidden layer responses. Also, Eq. (6) shows the output layer equations

$$net_j = \sum_{i=1}^2 w_{ij} x_i, \quad O_j = \sum_{i=1}^N f(net_j) \quad (5)$$

$$net_k = \sum_{j=1}^3 w_{jk} O_j, \quad y = \sum_{i=1}^3 f(net_k) \quad (6)$$

where

$i = 1, \dots, 3$ (Number of input),

$j = 1, \dots, N$ (Number of node in the hidden layer),

$k = 1, \dots, 3$ (Number of output),

$x_i =$ input value, $O_j =$ output hidden layer,

, and $y_k =$ output value.

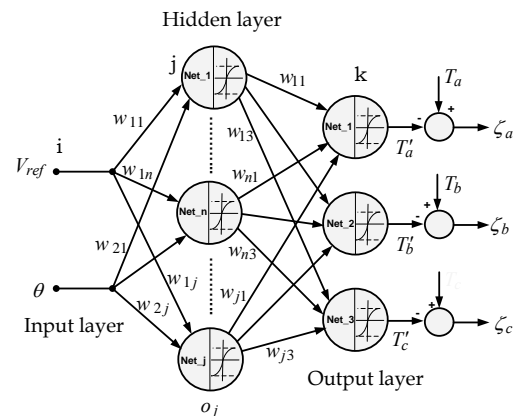


Figure (6) Modified back propagation layer based implement of the space vector modulation technique for VSI

A radial basis network is a feed-forward neural network using the radial basis activation function. RBFs can be used for discrete pattern classification, function approximation, signal processing, control, or any other application which requires a mapping from an input to an output [8,9].

The Radial-basis network can be regarded as a feed-forward neural network and it consists of three layers. The input layer accepts input signals hidden layer is used for radial-basis activation function and the output layer for linear activation function.

Fig.7 shows the RBF structure used in the present work. An RBF consists of the 2-dimensional input x ($x_1 = V_{ref}$ and $x_2 = \theta$) being passed directly to a hidden layer. Suppose there are c neurons in the hidden layer. Each of the c neurons in the hidden layer applies an activation function of the Gaussian form,

$$R_i(x) = \exp\left(-\frac{(x - \mu_i)^2}{(\sigma_i)^2}\right) \quad (7)$$

where μ_i and σ_i are the mean and spread of the i th activation function. The output of each hidden neuron is then weighted and passed to the output layer. The outputs of the network consist of sums of the weighted hidden layer neurons. The three output of RBF are the inverter time durations T'_a , T'_b , and T'_c .

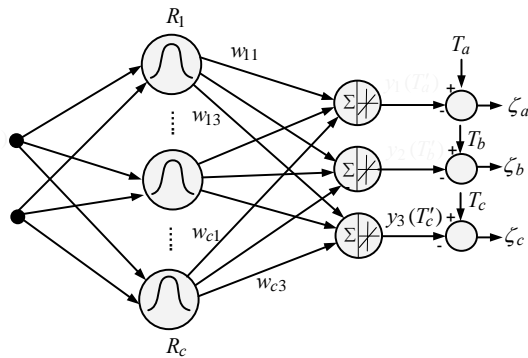


Figure (7) Structure of Radial Basis Function

The performance of an RBF network depends on the number and location (in the input space) of the centers, the shape of the RBF functions at the hidden units, and the method used for determining the network weights [10].

Training a neural network is, in general, a challenging nonlinear optimization problem.

Various derivative-based methods have been used to train neural networks, including gradient descent, conjugate gradients, quasi-Newton, Levenberg and Marquardt method, Kalman filtering, and the well-known back propagation. Derivative-free methods, including genetic algorithms, learning automata and simulated annealing have also been used to train neural networks [10, 11].

In the present work, the Levenberg and Marquardt optimization method has been used, which specifically adapted the minimization of an error function that arises from a squared error criterion of the form

$$E = \frac{1}{2}(\zeta_a^2 + \zeta_b^2 + \zeta_c^2) \quad (8)$$

A neural network can be trained in two different modes: online and batch modes. The batch mode is used here and the data used for training the both ANN structures have been collected from the simulation of conventional SV modulator.

4. Induction Machine Model

Generalized Machine theory provides the induction motor model in the form of twin axis equations in the stator reference frame [12]:

$$\begin{bmatrix} \dot{i}_d \\ \dot{i}_q \\ \dot{\varphi}_d \\ \dot{\varphi}_q \end{bmatrix} = \begin{bmatrix} a_{11} & 0 & a_{13} & a_{14} w_r \\ 0 & a_{22} & -a_{23} w_r & a_{24} \\ a_{31} & 0 & a_{33} & -w_r \\ 0 & a_{24} & w_r & a_{44} \end{bmatrix} \begin{bmatrix} i_d \\ i_q \\ \varphi_d \\ \varphi_q \end{bmatrix} + \begin{bmatrix} b_{11} & 0 \\ 0 & b_{22} \\ 0 & 0 \\ 0 & 0 \end{bmatrix} \begin{bmatrix} v_d \\ v_q \end{bmatrix} \quad (9)$$

where,

$$a_{11} = a_{22} = -\left(\frac{R_s}{\sigma L_s} + \frac{1 - \sigma}{\sigma \tau_r}\right); \quad a_{13} = a_{24} = \left(\frac{L_m}{\sigma \tau_r L_s L_r}\right)$$

$$a_{14} = a_{23} = \frac{L_m}{\sigma L_s L_r}; \quad a_{31} = a_{42} = \left(\frac{L_m}{\tau_r}\right) \quad a_{33} = a_{44} = -\left(\frac{1}{\tau_r}\right)$$

$$b_{11} = b_{22} = \frac{1}{\sigma L_s}; \quad \sigma = 1 - \frac{L_m^2}{L_r L_s}; \quad \tau_r = \frac{L_r}{R_r}$$

v_d, v_q : d -axis and q -axis stator voltages in stationary frame respectively.

i_d, i_q : d -axis and q -axis stator currents in stationary frame respectively

φ_d, φ_q : *d*-axis and *q*-axis stator currents in stationary frame respectively

R_s, R_r : stator and rotor resistances

L_s, L_r : stator and rotor self-inductances

L_m : mutual inductance of stator and rotor

ω_r : electrical rotor angular velocity

5. Simulink Implementation

Figure (8) shows the Simulink model of sector generator. The subsystem receives three input values V_{ref} , V_{dc} and T_z to produce $\sqrt{3}V_{ref}T_z/V_{dc}$, which is later necessary to generate the switching times. Also, this block is responsible for determining the sector number at which the reference vector lies. First, the clock block generates time as set by the simulation parameters. The mod function is used to generate a triangular wave of height and width 2π , as shown in Fig.(9).

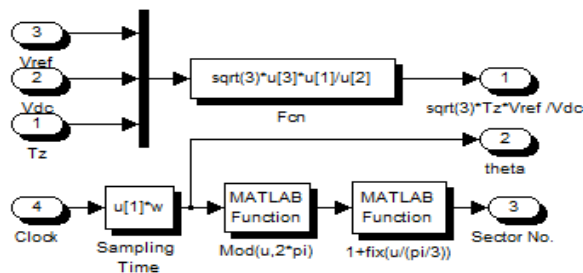


Figure (8) Inside subsystem of sector generator

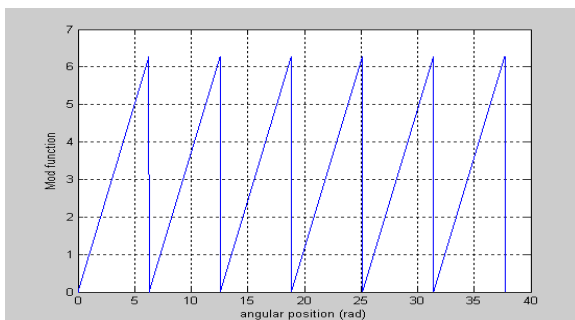


Figure (9) The output of mod-function

The other Matlab function receive the output of mod function and uses the built-in fix

function to generate the sector at each $\pi/3$, as illustrated by Fig.(10).

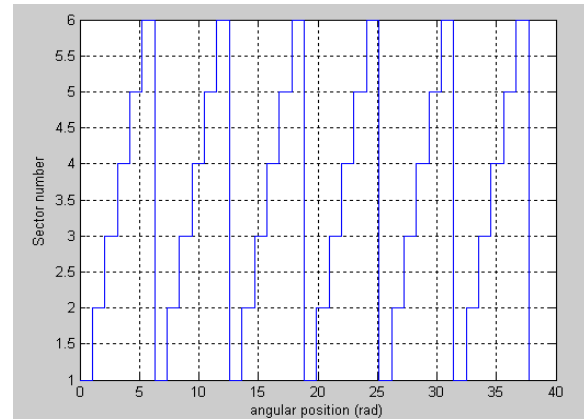


Figure (10) Sector generation

Figure (11) shows the blocks responsible for generating the time intervals T_1, T_2, T_a, T_b and T_c . Functions, assigned T_1 and T_2 in Fig.(11), calculate time intervals T_1 and T_1 based on Eq.s (2) and (3). These can be written in Matlab code as follows:

$$T1 = u[1] * (\sin(u[3] * \pi/3) * \cos(u[2]) - \cos(u[3] * \pi/3) * \sin(u[2]))$$

$$T2 = u[1] * (\cos((u[3]-1) * (\pi/3)) * \sin(u[2]) - \sin((u[3]-1) * (\pi/3)) * \cos(u[2]))$$

Based on Fig.(5), the time intervals (T_a, T_b and T_c) required to control each leg of inverter can also be coded in Matlab as;

$$T_a = (u[4]==1) * (u[1]+u[2]+u[3]) + (u[4]==2) * \dots \\ (u[1]+u[2]+u[3]) + (u[4]==3) * (u[1]+u[3]) \dots \\ + (u[4]==4) * (u[1]) + (u[4]==5) * (u[1]) + \dots \\ (u[4]==6) * (u[1]+u[2])$$

$$T_b = (u[4]==1) * (u[1]) + (u[4]==2) * (u[1]+u[2]) \\ + (u[4]==3) * (u[1]+u[2]+u[3]) + \dots \\ + (u[4]==4) * (u[1]+u[2]+u[3]) + (u[4]==5) * (u[1]+u \\ [3]) + (u[4]==6) * (u[1])$$

$$T_c = (u[4]==1)*(u[1]+u[3]) + (u[4]==2)*(u[1]) + (u[4]==3)*(u[1]) + (u[4]==4)*(u[1]+u[2]) + (u[4]==5)*(u[1]+u[2]+u[3]) + (u[4]==6)*(u[1]+u[2]+u[3])$$

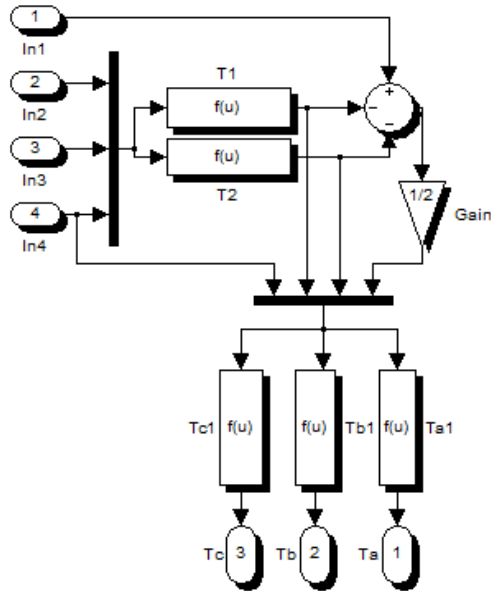


Figure (11) Inside switching time generator block

In Fig.(12), the values of time intervals output from “Switching Time Generator” block are compared with a triangular signal generated from a block contains a built-in “rem-function”. The output of this block is shown in Fig.(13).

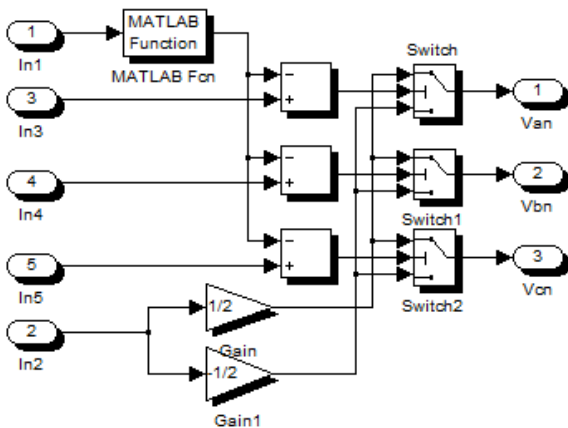


Figure (12) Simulink modeling of inverter

The inverter is represented by three ideal switches. The line voltages are obtained by comparing the outputs of switches, which are DC levels of height $\pm 0.5V_{dc}$.

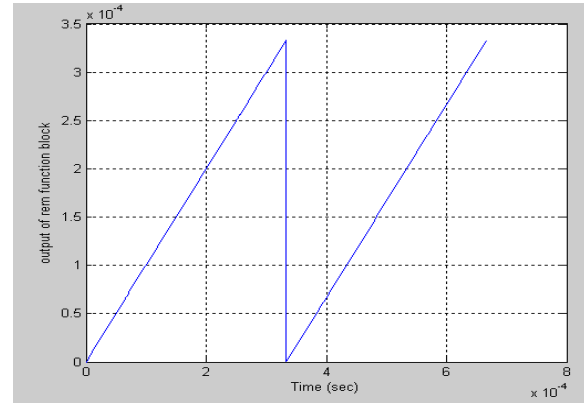


Figure (13) The output of rem-function

The three phase line voltages (v_{an} , v_{bn} and v_{cn}) are converted to quadrature voltages v_q and v_d via abc2dq block shown in Fig.(14).

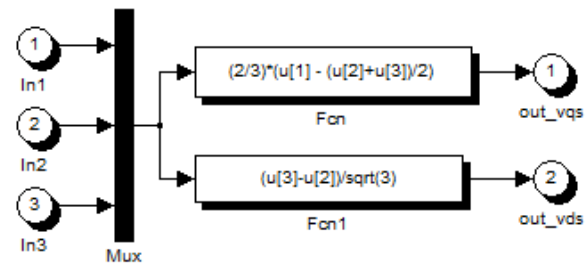


Figure (14) abc2dq block

The quadrature voltages (v_q and v_d) are used to actuate the three phase induction machine. Figure (15) shows the complete Simulink portrait of the SV-actuated induction machine. The figure also shows the interconnection of N.N-based modulator with the conventional SV block. The switches at the input of the inverter will connect the actual SV modulator to induction motor at training mode and then divert the actuating

action to neural-based modulator when the learning process has been accomplished.

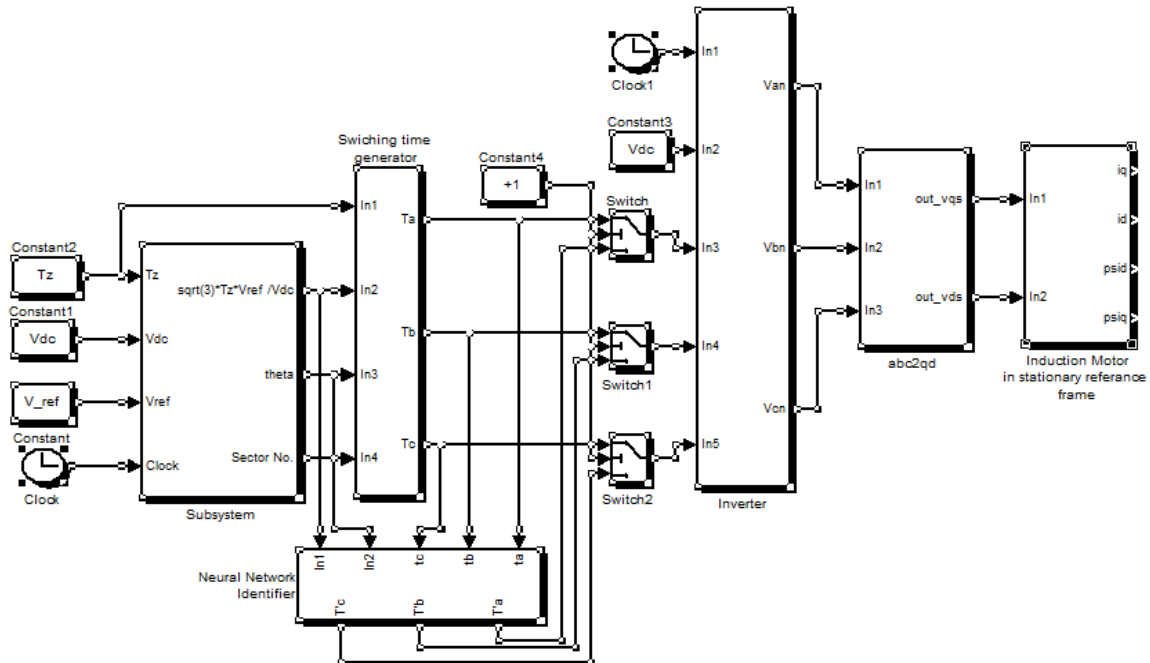


Figure (15) Simulink model of Neural Network-based Space Vector Modulation

6. Simulated Results:

A simulated MATLAB-based space vector modulator is used to generate the data required to train the network using back propagation and radial basis algorithms. In the training mode stage, the N.N modulator is fed by the same excitation input to the actual SVM scheme (V_{ref} , θ) and with the same timing sequence generated from actual space vector modulator (T_a , T_b and T_c).

These algorithms has been built utilized the MATLAB N.N Toolbox. The performance space vector modulator-based induction machine has evaluated based on harmonics level and the capabilities of both modulators to work properly under variations of converter dc voltage. The system parameters are list in Table (1).

Table (1): Definition of system parameters and their values

Parameters	Definition	Value
P_r	Power rated	746Kw
V_n	Voltage rated	380V
N_n	RPM and pole	1500rpm,
R_s	Stator resistance	3.35Ω
R_r	Rotor resistance	1.99Ω
L_s	Stator inductance	6.94mH
L_r	Rotor inductance	6.94mH
L_m	Mutual inductance	163.73mH
f	Frequency	50Hz
F_z	Switching frequency	3KHz
m	Modulation index	0.6
P	Numberof pole	4

Figure (16) and (17) show the speed response and switching time due to actual and learned SVMs. It is worthy to mention that

for these simulations the value of DC voltage has been set to $V_{dc}=400$ V (i.e., V_{ref} would equal to 160 V.). It is clear from Fig. (16) that how well the speed response based on BP learning tracks the actual speed, while there is a small deviation in case of application of RB-based SVM, especially is the machine startup. This argument can be clearly seen using the switching time plot (Fig.(17)). The switching time based on the BP learning is approximately coincident with those of actual switching times, while that with RB learning is much deviated from the actual one.

To account for variation of voltage source due to load changes, the actual SVM has been fed with a random noise of 160 V mean and variance 42.42 V as depicted in Fig.(18). Then, the two neural schemes are allowed to be learned under such noisy input.

The noise-learned identifiers are allowed to excite the induction machine with different values of source voltages ($V_{dc}=400, 375, 350$ and 325 V). Based on Eq.(2), the reference voltage will be (160, 150, 140, 130 V), respectively.

It is evident from Fig.(19) and (20) that both schemes could successfully drive the induction machine under $V_{dc}=375$ ($V_{ref}=150$). However, a little degradation in both speed responses of neural-driven motor. But, the RB-based scheme shows speed characteristics closer to actual system than its counterpart.

At a further decrease in source voltage ($V_{dc}=350$ or $V_{ref}=140$), the BP-based identifier would lack the ability to drive motor. Meanwhile, the other identifier still gives a good switching time and speed response characteristics (see Fig. (21) and Fig. (22)).

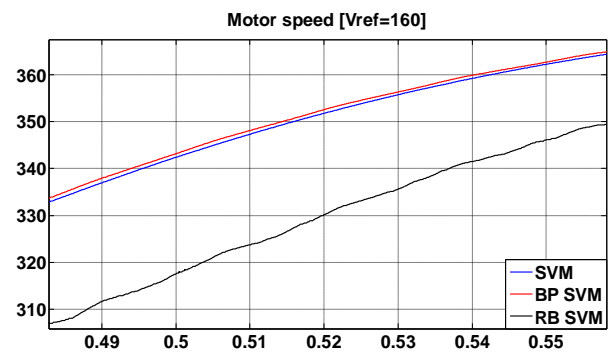
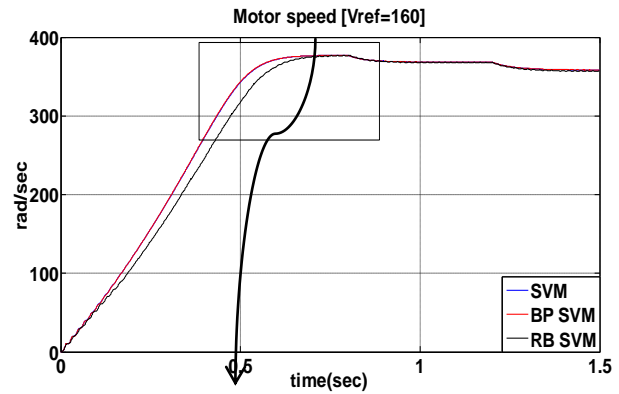


Figure (16) motor speed for three types of SVM

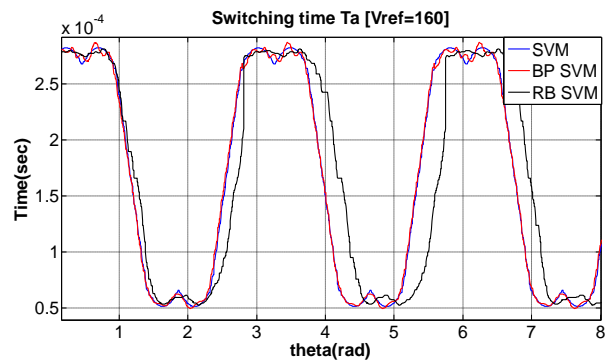


Figure (17) Switching time T_a for three types of SVM at $V_{ref} = 160$.

If the source voltage is decreased to a level of $V_{dc}=325$ ($V_{ref}=130$), one can see from Fig.(23) and Fig.(24) that the RB-identifier cannot drive the system at all. In other words, the neural-learned modulator cannot supply the motor with sufficient actuating voltage to rise up its speed.

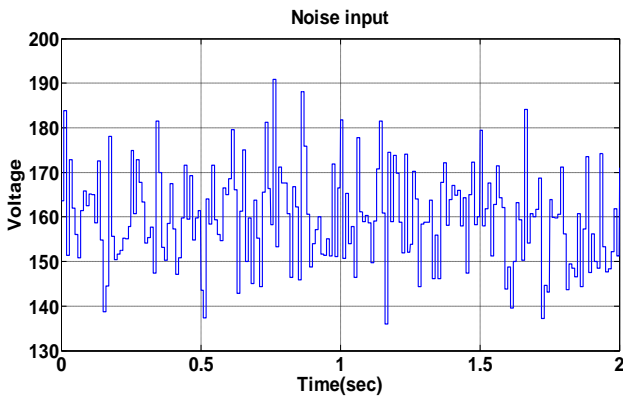


Figure (18) Learning of neural schemes under random noise input

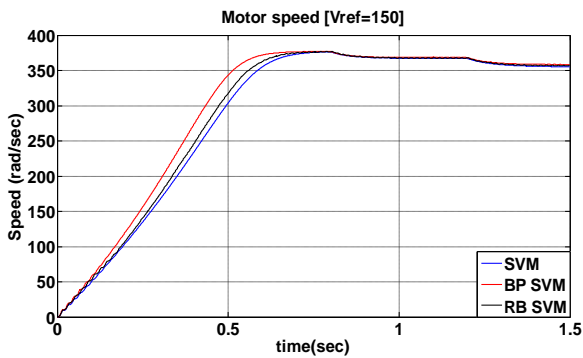


Figure (19) motor speed for three types of SVM at $V_{ref} = 15$

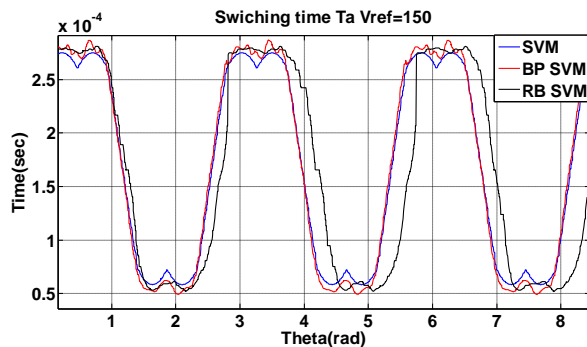


Figure (20) Switching time T_a for three types of SVM at $V_{ref} = 150$.

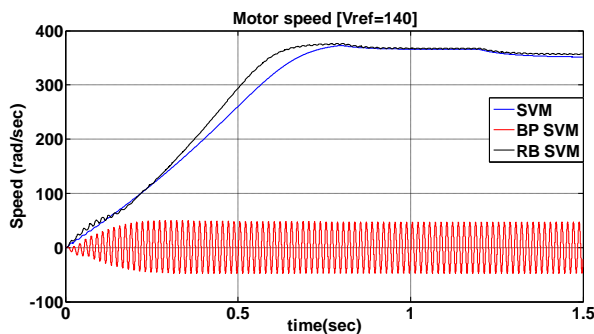


Figure (21) motor speed for three types of SVM at $V_{ref} = 140$



Figure (22) Switching time T_a for three types of SVM at $V_{ref} = 140$.

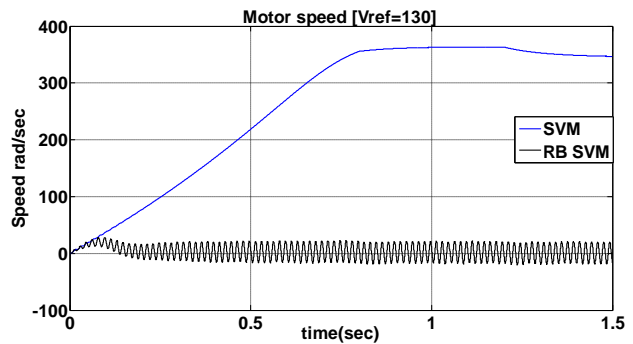


Figure (23) motor speed for three types of SVM at $V_{ref} = 130$

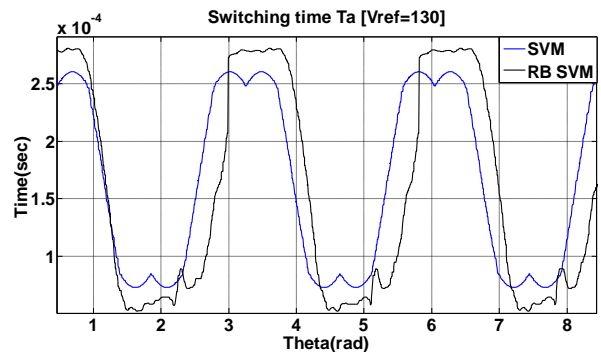


Figure (24) Switching time T_a for three types of SVM at $V_{ref} = 130$.

7. Conclusion: One can conclude from the above results that both neural space vector modulation could successfully represent the actual SV modulator. Moreover, the RB-based modulator can outperform its BP counterpart and it shows more robust characteristics when the system parameter change far from nominal value.

References

- [1] S. R. Bowes and D. Holliday, "Optimal regular-sampled PWM inverter control techniques," *IEEE Trans. Ind. Electron.*, vol. 54, no. 3, pp. 1547–1559, June 2007.
- [2] H. W. van der Broeck, H. C. Skudelny, and G. Stanke, "Analysis and realization of a pulsewidth modulator based on voltage space vectors," *IEEE Trans. Ind. Applicat.*, vol. 24, no. 1, pp. 142–150, Jan./Feb. 1988.
- [3] A. Mehrizi-Sani, S. Filizadeh "An Optimized Space Vector Modulation Sequence for Improved Harmonic Performance" *IEEE Proc.-Electr.PowerAppl.*, pp. 1-10 January 2009.
- [4] K. Zhou and D. Wang, "Relationship between space-vector modulation and three phase carrier-based PWM a comprehensive analysis" *IEEE Trans. Ind. Applicat.*, vol. 49, no. 1, pp. 186–196, Feb. 2002.
- [5] Bimal K. Bose, "Power Electronics and Motor Drives," Elsevier Inc, 2006.
- [6] R. Kumar, R. A. Gupta, R. S. Surjuse, "A Vector Controlled Induction Motor Drive With neural Network Based Space Vector Pulse Width Modulator," *JATIT Elec. Engineer* pp. 577-584 2005.
- [7] S. K. Mondal, J. O. P. Pinto, B. K. Bose "A Neural-Network-Based Space-Vector PWM Controller for a Three-Level Voltage-Fed Inverter Induction Motor Drive," *IEEE Proc.-Electr.Power Appl.*, vol. 38, no. 3 pp. 660-669 May 2002.
- [8] G. Narayanan and V. T. Ranganathan, "Synchronized PWM strategies based on space vector approach: I. Principles of waveform generation," *IEEE Proc.-Electr. Power Appl.*, vol. 146, no. 3, pp. 267–275, May 1999.
- [9] A. H. Fakher "Gaussian Noise Reduction using Artificial Neural Networks" M.Sc. thesis in electrical engineering, Technology University 2004.
- [10] Dan Simon, "Training radial basis neural networks with the extended Kalman filter," Elsevier Science Ltd, 2001.
- [11] Ajith Abraham, "Artificial Neural Networks," Oklahoma State University, Stillwater, OK, USA.
- [12] Q. Ge, Z. Feng "Speed Estimated for Vector Control of Induction Motor Using Reduced-order Extended Kalman Filter" Institute of Electrical Engineering, Academia Sinica, Beijing 100080, P. R. China.
- [13] Ong.C "Dynamic simulation of electrical machinery using MATLAB/SIMULINK", Prentice Hall PTR, 1997.

MULTIWAVELET TRANSFORM AND MULTIDIMENSION-TWO ACTIVATION FUNCTION WAVELET NETWORK USING FOR PERSON IDENTIFICATION

Dr. Waleed A. Mahmoud
College of Engineering
University of Baghdad
profwaleed54@yahoo.com

Dr. Majed E. Alneby
College of Engineering
University of Basrah

Wael H. Zayer
College of Engineering
University of Basrah
wael_zayer@yahoo.com

Abstract:

The relatively new field of Multiwavelets shows promise in removing some of limitation of wavelets. This paper introduces a new human face recognition using the combination of Multiwavelet transform (MWT) and multidimension-Two Activation Function Wavelet Network (MD-TAFWN). After taking the MWT of the image it is required to divide the approximate quarter into four parts and rearrange them in 3D form. Next, this 3D data will be feed into a proposed MD-Two Activation Function Wavelet Network, this is for face image. For fingerprint image is required to divide the approximate quarter into four parts and rearrange them in 3D form. Next, this 3D data will be feed into a proposed MD-Two Activation Function Wavelet Network. The proposed transform is considered as a feature extractor of the decomposed reference images with different frequency sub bands, and amid-range frequency sub band for data image to the representation of the given image. Evaluations have generally shown that the technique of the combination for Discrete Multi-wavelet Transform (DMWT) and the Two Activation Function Wavelet Network (MD-TAFWN) is interesting and promising. The results obtained showed that the combination technique outperform. Other conventional method that use a given transform with neural Network (NN). It results in a perfect recognition of 100% to a data base consists of 100 human face images.

Keywords: *Biometric, Multiwavelet, Wavelet Network, Face Identification, Fingerprint Identification.*

1. Introduction

Face and fingerprint tracking and recognition are important parts of our daily lives. Tracking an object under time varying position and orientation is a basic ability of the human visual system [1]. Studies [1] show that infants are, in some way, preprogrammed to recognize and pay attention to faces more than other objects. Throughout our lives people present their face as a form of recognition in person and through the use of photo recognition cards such as a driver's license or passport. Since face and fingerprint recognition are so pervasive in the natural world, it is reasonable to consider faces and fingerprint as a means for recognition using machines.

So far, robust algorithms to perform automated face and fingerprint tracking and recognition in unconstrained environments have not been achieved. To further complicate matters, psychology suggests that the principal means of recognition used by humans changes from a primarily feature-based method in childhood to a primarily holistic-based method in adulthood [1]. Which method, if either, will work best in an automated recognition system? A great

wealth of research has been done in many fields to determine how to best track and recognize faces, how to simulate (or surpass) human face tracking and recognition performance [2], and how to overcome difficulties that hinder the development of automated face tracking and recognition. There are several imaging modalities: video, infrared, and three dimensional (3D) scanning. Although there has been tremendous research in video, other modalities deserve attention [4]. Many issues hinder research efforts in the field of face and fingerprint recognition. Variation exists in every imaging modality used, and finding fast, simple algorithms that are robust to variation is difficult (as evidenced by years of research). Categorizing the variation may be helpful in the development of effective face and fingerprint recognition algorithms. Intrinsic sources of variation include identity, facial expression, speech, gender, and age [1].

Extrinsic sources of variation include viewing geometry, illumination, imaging processes, and other objects. Viewing geometry includes pose changes, either by the observer or the object to be recognized; illumination changes include shading, color, self-shadowing, and specular highlights; imaging process variations include resolution, focus, imaging noise, sampling technique, and perspective distortion effects; variation from other objects include occlusions, shadowing, and indirect illumination. These sources of variation may or may not hinder the recognition process depending on which algorithm is used. It is possible that the variation due to factors such as facial expression, lighting, occlusions, and pose is larger than the variation due to identity [1,3]. That makes identification under such varying environments a difficult task. However, human proficiency at face recognition [5] has motivated enormous research in this area despite these challenges. (The ability of humans to recognize faces is

also an actively researched field with widely varying results depending on numerous factors. Many reviews of face recognition are available [6, 7, 8, 9, 10]. Samal and Iyengar (1992) [8] describe several techniques they refer to as nonconnectionist. Most of these techniques operate on 2D images and are concerned with finding intra-feature distances, angles, and areas.

A complementary survey by Valentin et al. (1994) [9] covers connectionist (statistical) methods of face processing. Connectionist methods of face processing usually take 2D image data and work with pixel values of entire face images (instead of extracting features from a subset of the total pixels for an image as is done in nonconnectionist approaches). Because full images are used in these techniques, the relationships between features within the image, texture, and shape information are preserved. Nonconnectionist and connectionist techniques are also called geometrical and statistical respectively [7,10, 11]. Chellappa et al. (1995) [6] draw the following conclusions: 1) The upper parts of the face should play a dominant role in recognition, 2) Eigenface and feature point based methods are currently the most developed and should undergo additional testing in realistic situations with thousands of faces, 3) Neural approaches should be developed further and should be tested on much larger databases. The approaches cited in this survey use between 16 and 80 faces.

2. Proposed method for Multi-biometric Identification

2.1 Training Method

1. Input seven images for each person (three face images, two right thumb fingerprint images and two left thumb fingerprint images) figure (1).

2. Take the multiwavelet transform (MWT) using (GHM) for each image.

3. Take (L2L2) only of the (MWT) for each image.

4. Segment (L2L2) to four segments for each image.

5. Take the first segment of the first person and entered to (TAFWN) using the following algorithm (figures (2,3,4,5,6):

a) Given an initial value of $(a_{1,1}, a_{1,2}, a_{1,3}, b_{1,1}, b_{1,2}, b_{1,3}, w_{1,1}, w_{1,2}, w_{1,3}, a_{2,1}, a_{2,2}, a_{2,3}, b_{2,1}, b_{2,2}, b_{2,3}, w_{2,1}, w_{2,2}, w_{2,3})$ and given an accepted error ($E=0.001$).

b) Take the first row of the first segment and entered it to (MD-TAFWN) where the input neurons (n) equal to the number of the row and the column of the segments ($n*n$) and the hidden neurons is three and the output neuron is one where the output equal to the number of the person.

c) Since the images to the first person then the output ($Y=1$) then find the error (E_1).

d) Update the parameters (a, b, w) using there update equations, then entered the second row of the first segment and find the error (E_2) where the output also equal to one ($Y=1$).

e) Update the parameters (a, b, w) using there update equations, then entered the third row of the first segment and find the error (E_3) where the output also equal to one ($Y=1$).

f) Continue the above procedure until reach to the last row then find (E_n).

g) Find the summation of error ($E_{sum}=E_1+E_2+E_3+E_4+\dots+E_n$). then find the mean of the error where ($E_{mean}=0.5*E_{sum}$).

h) If ($E_{mean} > E_{th}$) then the above procedure return until ($E_{mean} < E_{th}$) at this point finishing

and take the last parameters (a, b, w) (vector $18*1$) as an initial to the second segment of the same image.

i) Apply the above procedure on the second segment and then third and then fourth segment where the last value of parameters used as an initial for the next segment until finished the fourth segment then the final parameters (a, b, w) (vector $18*1$) used an initial for first segment of the second image of the person one ($N=1$ and $Y=1$).

6. Take (L2L2) of the second image of person one ($N=1$) and applied step (5) on it then the last parameters (a, b, w) used as an initial to the third image of person and applied also step (5) on it then the last parameters $(a_{1,1}, a_{1,2}, a_{1,3}, b_{1,1}, b_{1,2}, b_{1,3}, w_{1,1}, w_{1,2}, w_{1,3}, a_{2,1}, a_{2,2}, a_{2,3}, b_{2,1}, b_{2,2}, b_{2,3}, w_{2,1}, w_{2,2}, w_{2,3})$ (vector $18*1$) used as a represented to the person one, this mean that three image of one person can be represented only by vector ($18*1$).

7. Applied steps (5,6) on the four images of the fingerprint of the person one where also used the output ($Y=1$) where the result the person number one can be represented by two vectors ($18*1$) one for the face of the person and the other represented the fingerprint (right and left thumbs) of the person therefore person one represented by vector ($36*1$) then save it in database matrix.

8. Take seven images of the second person and applied steps (5,6, and 7) on it then save it's vector ($36*1$) where the output become ($Y=2$).

9. Completed the images of each persons and applied the above procedure on it where the output ($Y=3, 4, 5, \dots, M$) where (M) represented number of persons, at the end a database matrix ($36*M$) saved.

2.2 Testing Method

1) Input seven images (three images for face and four images for fingerprint (two for the right thumbs and two for the left thumbs)) for the person.

2) Taking (MWT) using (GHM) method for each image.

3) Taking (L2L2) only and segment it for four segment for the face image and for sixteen segments for the fingerprint images.

4) Select randomly one row from each segment and entered it to (TAWN) where used the parameters of the database matrix of training method then find the error with each person the minimum error which or less than threshold value (t) then the image represented this person, this result represented score one ($S1$) (for face identification), and score two ($S2$) (for fingerprint identification).

5) If ($S1$ =person N) and ($S2$ =person N) then the result is person N but if ($S1$ =person N) and ($S2$ =person M) then if the percentage of $S1$ more than $S2$ then the person is N but if the percentage of $S2$ more than $S1$ then the person is M . (figure (7)).

6) The above procedure is for identification, in case of verification the same procedure can be done but in step four used the column of parameters of the database which

represented the claimed person then if ($S1$ =claimed person) and ($S2$ =claim person) then the result is this person but if ($S1$ =claimed person) and ($S2$ =unclaimed person) and used **AND** configuration then the result is failure.(figure (8))

3. Evaluation Tests

To perform recognition experiments we first need to create two sets of images: training and testing. Training images are used to generate a data base matrix saved to recognition the test images where in proposed method used three face images and four fingerprint image for each thumb for each person for training, test images are a set of range images of faces we wish to identify. Any subject we wish to identify must have at least one facial range image in the training data set. The faces and fingerprint in the test range images need not have the same facial expressions as those in the training data set. Each test image is then reshaped as a column vector where in proposed method used vector ($18*1$) to represented all the three face images of the same person and other vector ($18*1$) to represented the four fingerprint images of the same person therefore each person can be represent only by vector ($36*1$) also the database matrix will be ($36*M$) where (M) is the number of identification person. Any input test image applied the same procedure on it then make a correlation with the data base matrix in order to get on the maximum value of this matrix means that the test face and fingerprint images represented the person who the maximum value lied in his column where each column in the data base matrix represented one person.

Cumulative Match Characteristic (CMC) curve shown in figure (9) for identification and the receiver operating characteristic (ROC) curve shown in figure (10) for verification where the same procedure used but the comparison made with the column of the claimed person.

Table (1) and table (2) using the **OR** and **AND** configuration respectively to identification

4. Conclusions

It was shown throughout this paper that proposed combination had a great impact on the capabilities of all image techniques. Method of person identification was implemented and tested based upon the proposed combination. This paper introduced a combining of the Discrete Multi-wavelet Transform (2D-DMWT) of Repeated Row Algorithm (RRA) and the Multi-dimension Two Activation Function Wavelet Network (MD-TAFWN) the advantage of this method can be summarized as follows:

- 1) The combined technique achieved an excellent result of 100%.
- 2) This method can give an excellent representation of the data images as well as reduce the huge information obtained as a matrix to a vector one.
- 3) This proposed combination is important in many applications particularly when the high data rate is required and when a limited bandwidth or small memory is available.

This achieved by the excellent combination between Multiwavelet Transform and Two Activation Function Wavelet Network where (MWT) given a

good image with reduced any external effect such as noise or illustration and with minimum size and without loss any information from the image also (TAFWN) given an excellent feature extraction vector represented the input image where an image (128*128) can be represented by (18*1) vector only. Also the segmentation of the image before entered to the (TAFWN) reduced the effect of the facial expression.

References

- [1] Gong, Shaogang, Stephen J. McKenna, Alexandra Psarrou. *Dynamic Vision: From Images to Face Recognition*. Imperial College Press, 2000.
- [2] Zhao, W. Y., Rama Chellappa, A. Rosenfeld, P. J. Phillips. *Face Recognition: A Literature Survey*. UMD CfAR Technical Report, CAR-TR-948, 2000.
- [3] Howell, A. Jonathan, Hilary Buxton. *Towards Unconstrained Face Recognition from Image Sequences*. *Proceedings of the International Conference on Automatic Face and Gesture Recognition*, Killington, VT, pp. 224-229, 1996.
- [4] Daugman, John. *Face and Gesture Recognition: Overview*. *IEEE Transactions on Pattern Analysis and Machine Intelligence*, vol. 19, issue 7, July 1997.
- [5] Srivastava, Anuj, Xiuwen Liu, Brian Thomasson, Curt Heshner. *Spectral Probability Models for IR Images and their Applications to Face Recognition*. *Proc. of Computer Vision and Pattern Recognition workshop on Beyond Visual Spectrum*, Hawaii, 2001.
- [6] Barrett, William A. *A Survey of Face Recognition Algorithms and Testing*

- Results Conference Record of the Thirty-First Asilomar Conference on Signals, Systems, and Computers, pp. 301-305, 1998.
- [7] Chellappa, Rama, Charles L. Wilson, SaadSirohey. Human and Machine Recognition of Faces: A Survey. Proc. IEEE, vol. 83, no. 5, pp. 705 - 740, May 1995.
- [8] Fromherz, Thomas. Face Recognition: A Summary of 1995-1997. Technical Report ICSI TR-98-027, International Computer Science Institute, Berkeley, 1998.
- [9] Samal, A., P. A. Iyengar. Automatic Recognition and Analysis of Human Faces and Facial Expressions: A Survey. Pattern Recognition, vol. 25, no. 1, pp. 65-77, 1992.
- [10] Valentin, Dominique, Herv_eAbdi, Alice J. O'Toole, Garrison W. Cottrell. Connectionist Models of Face Processing: A Survey. Pattern Recognition, Vol. 27, no. 9, pp. 1209-1230,1994.
- [11] Turk, Matthew, Alex Pentland. Face Recognition using Eigenfaces. Proc. IEEE Conference on Computer Vision and Pattern Recognition, pp. 586-591, Maui, Hawaii,1991.
- [9] Samal, A., P. A. Iyengar. Automatic Recognition and Analysis of Human

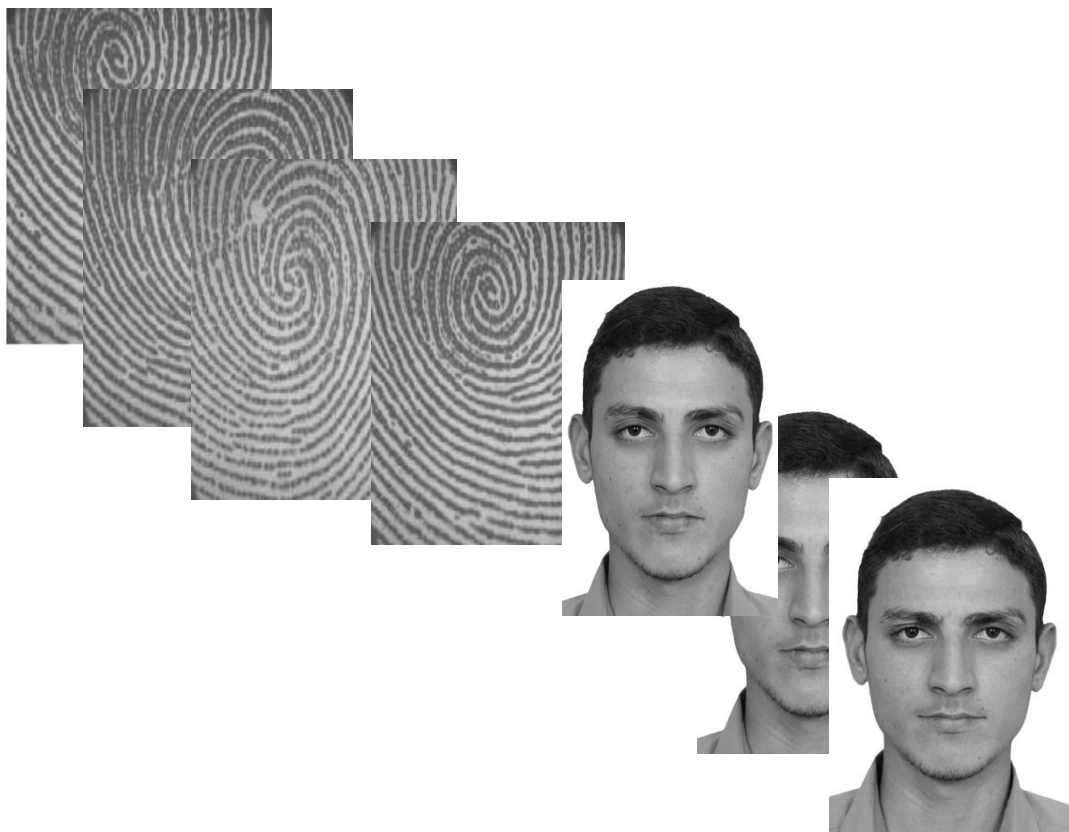


Figure (1) Seven Input images.

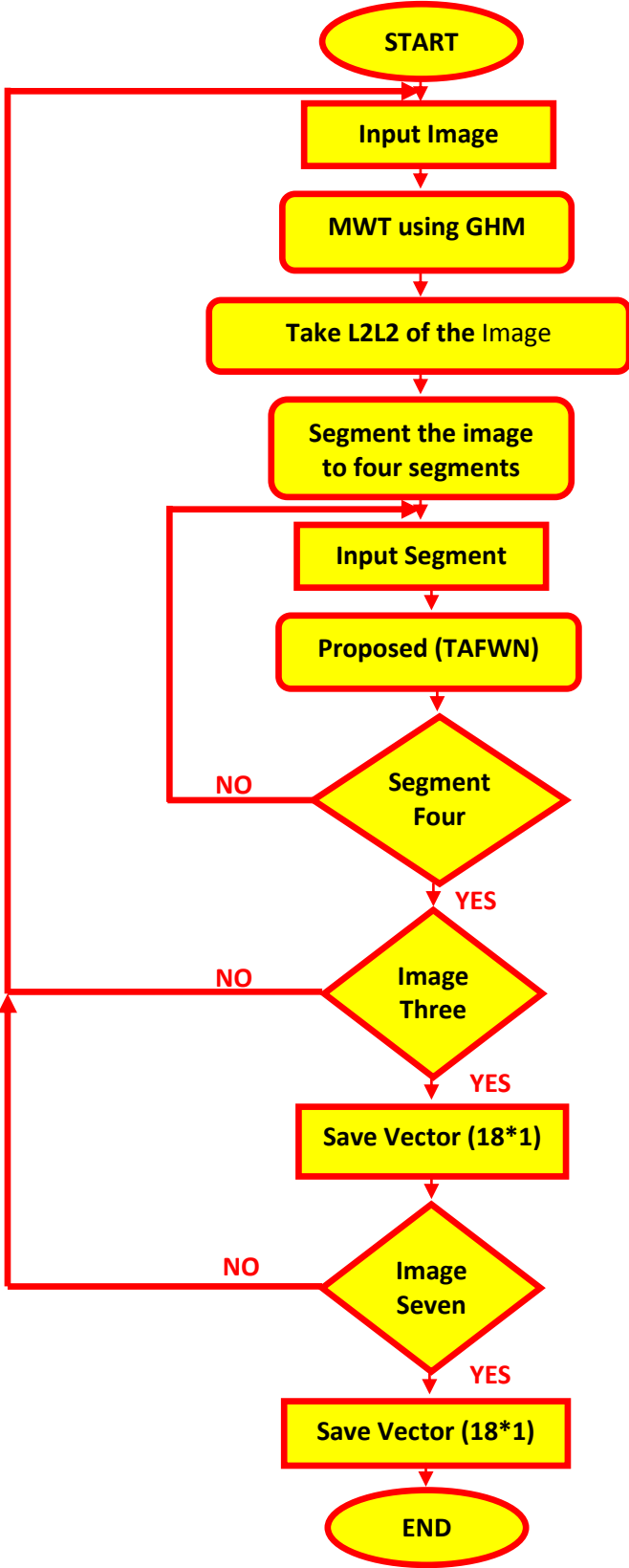


Figure (2) The Mechanization of the Proposed Algorithm for face identification.

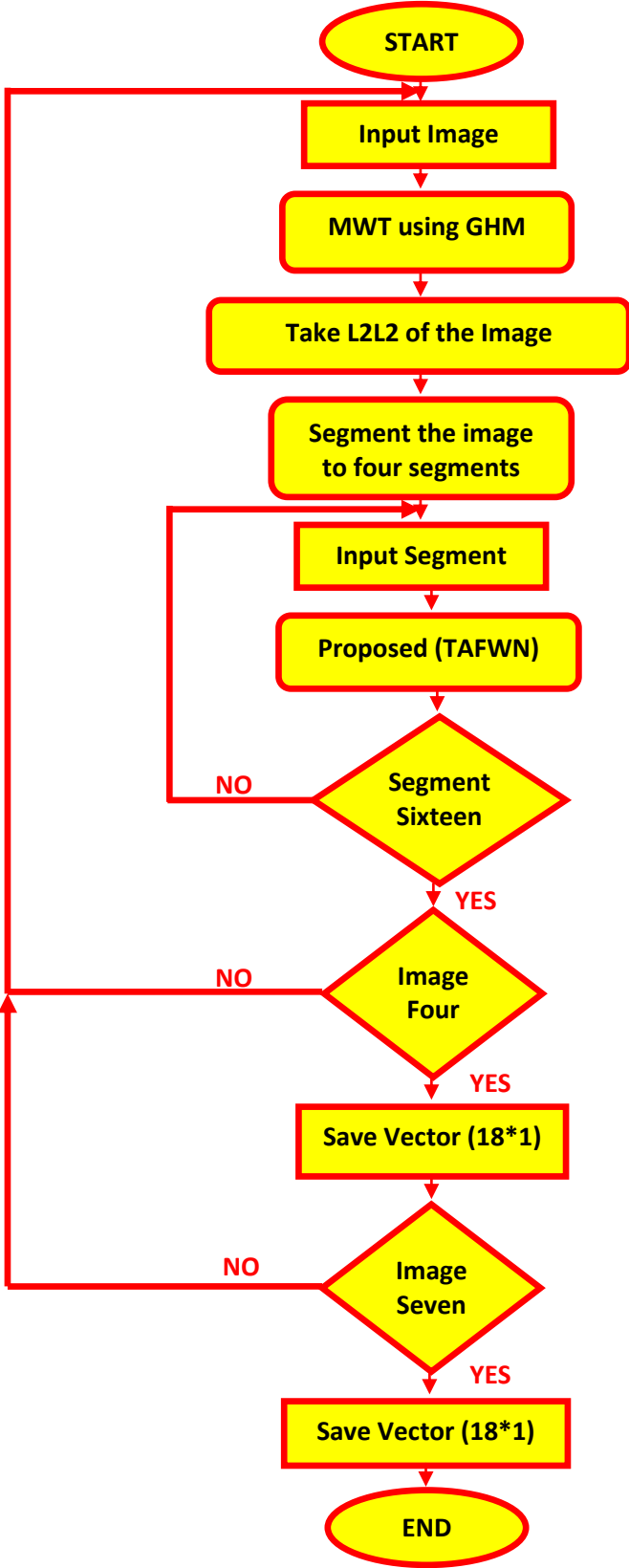


Figure (3) The Mechanization of the Proposed Algorithm for fingerprint identification.

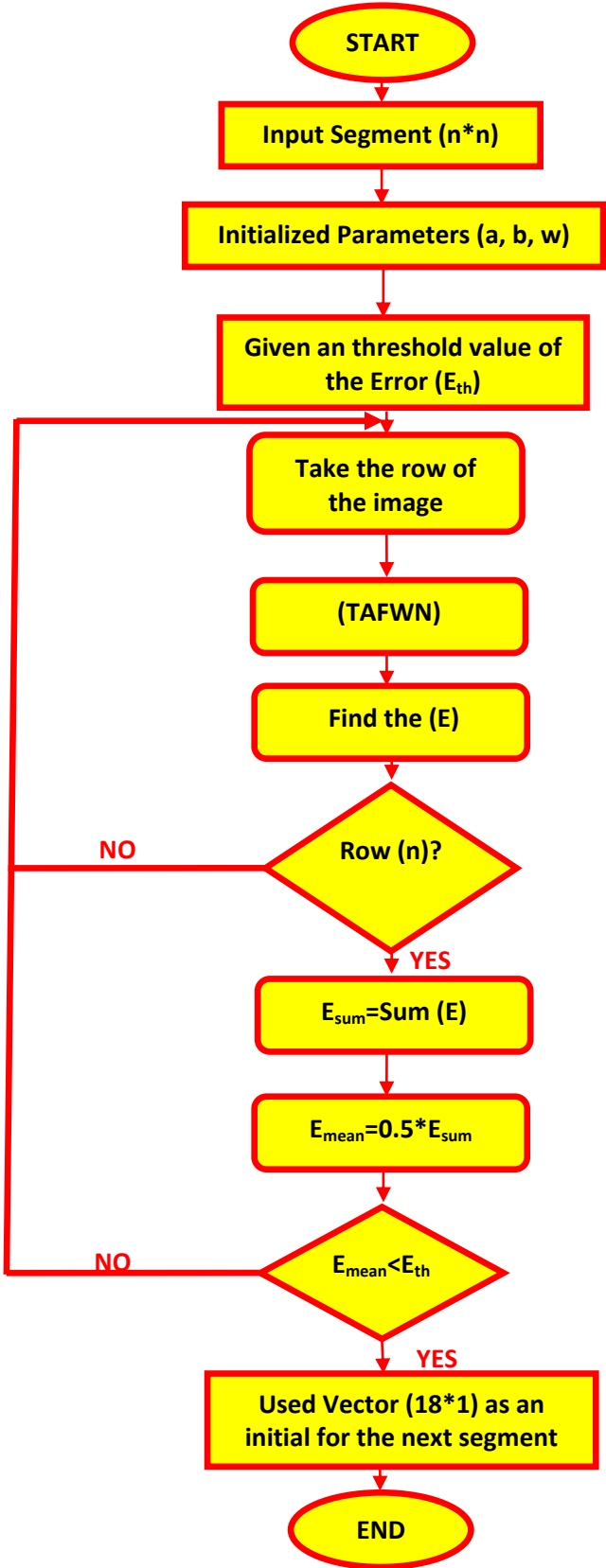


Figure (4) The Mechanization of the Proposed Algorithm of TAFWN.

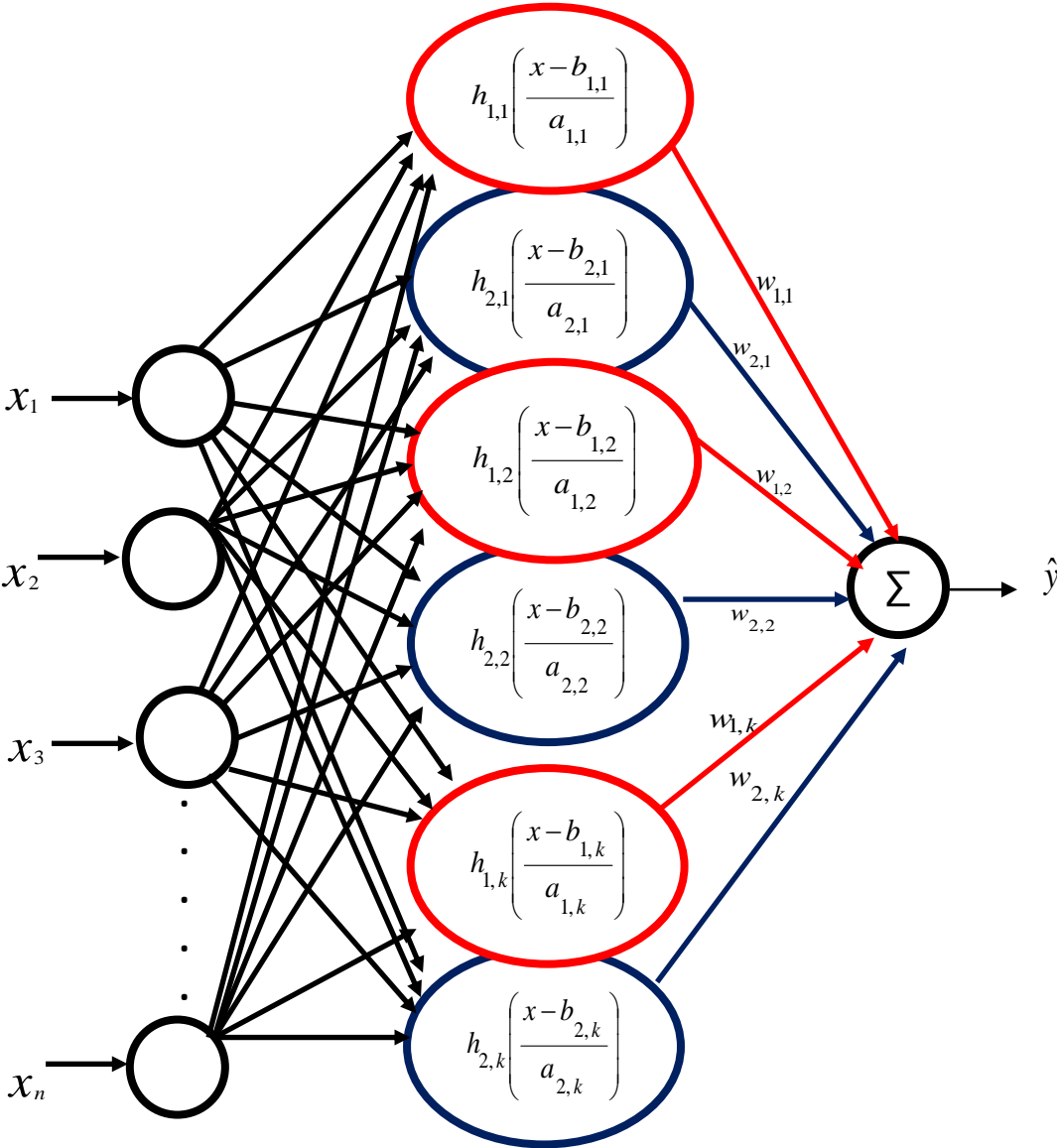


Figure (5) The block diagram of the Proposed Algorithm of TAFWN.

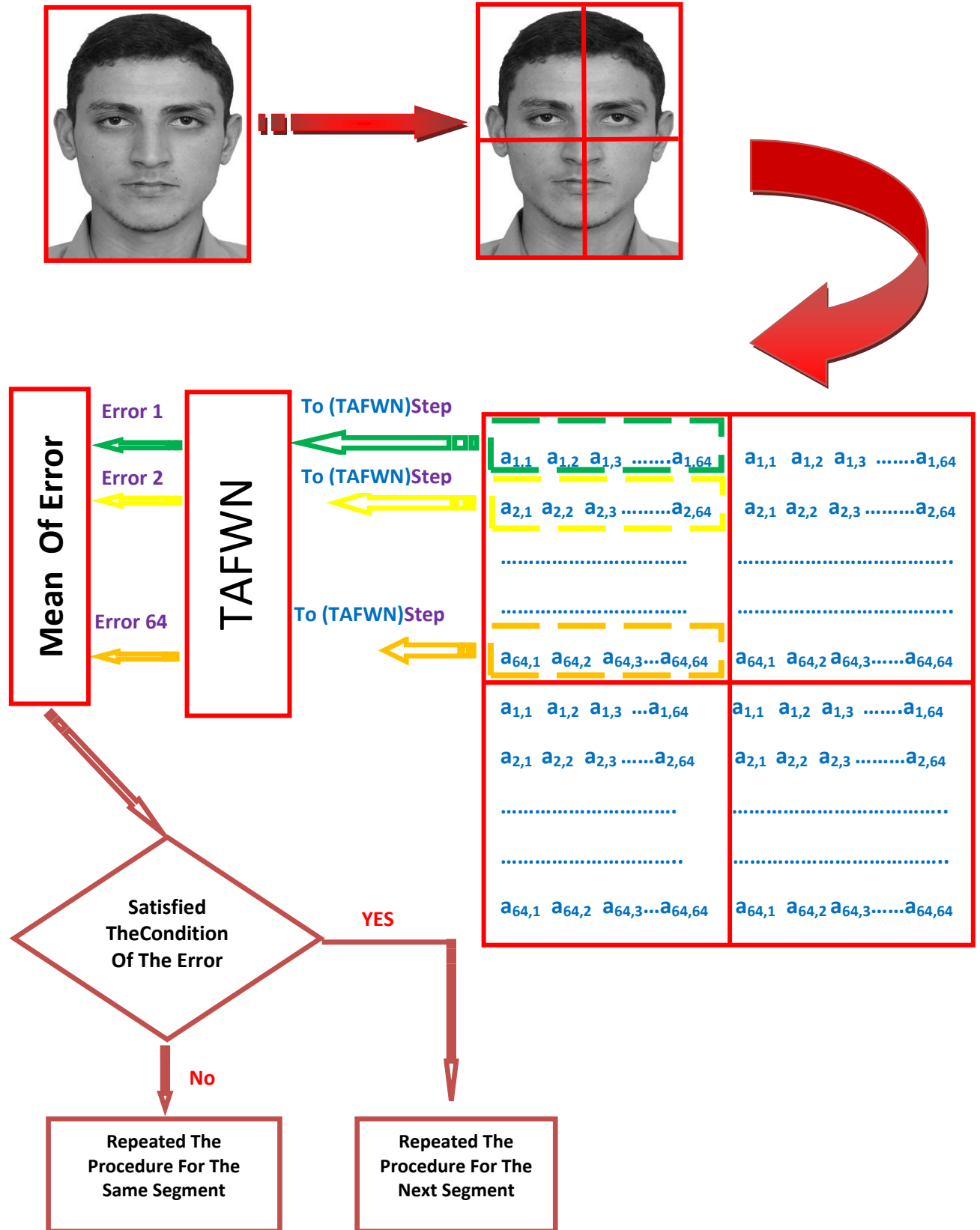


Figure (6) The block diagram of the Proposed Algorithm.

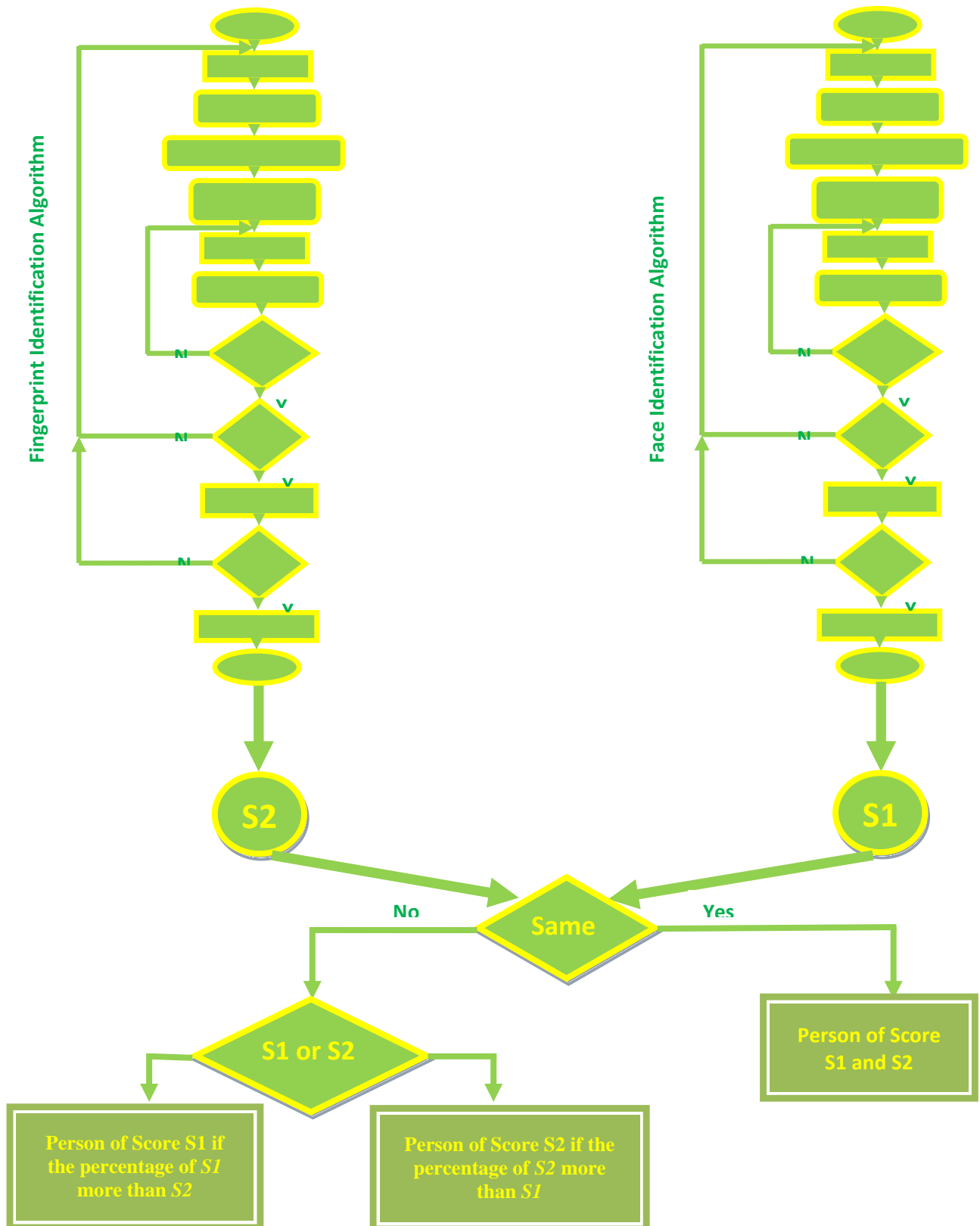


Figure (7) The block diagram of the test identification Proposed Algorithm.

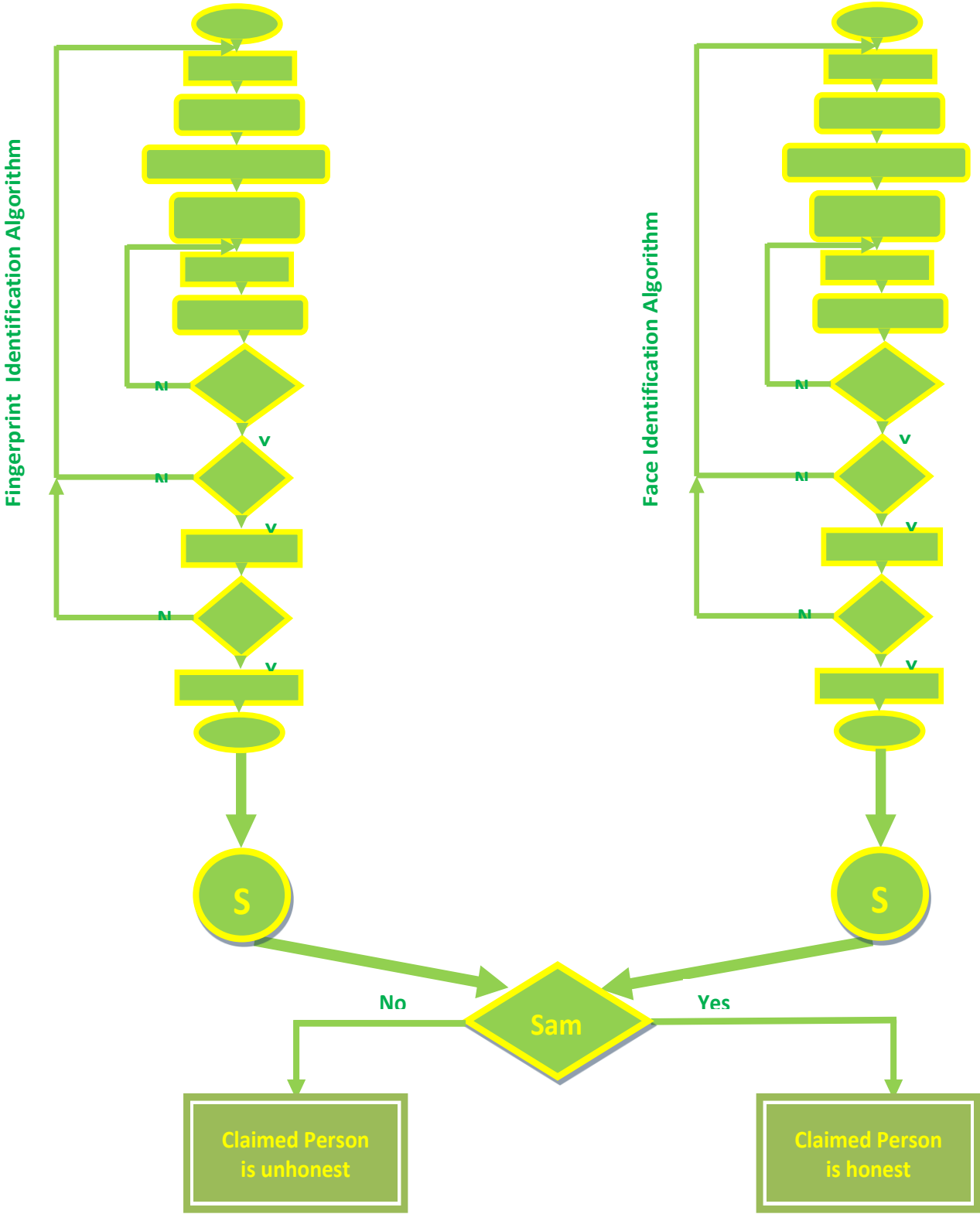


Figure (8) The block diagram of the test verification Proposed Algorithm.

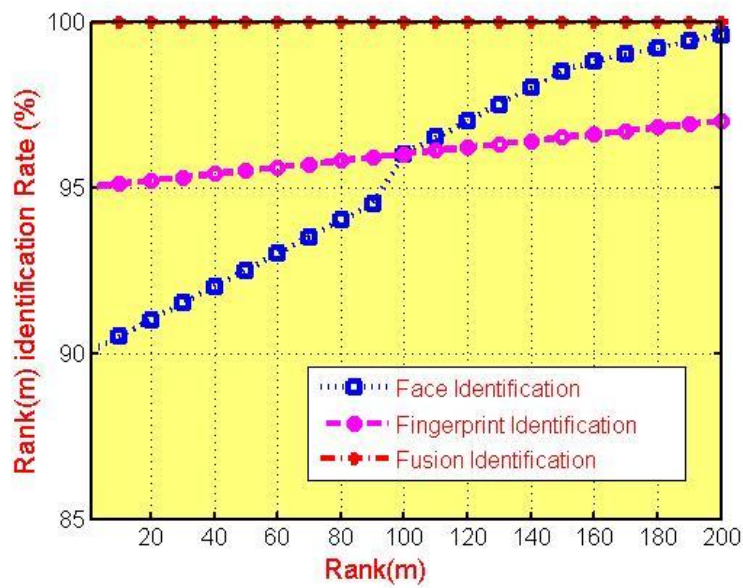


Figure (9) Cumulative Match Characteristic (CMC) curve.

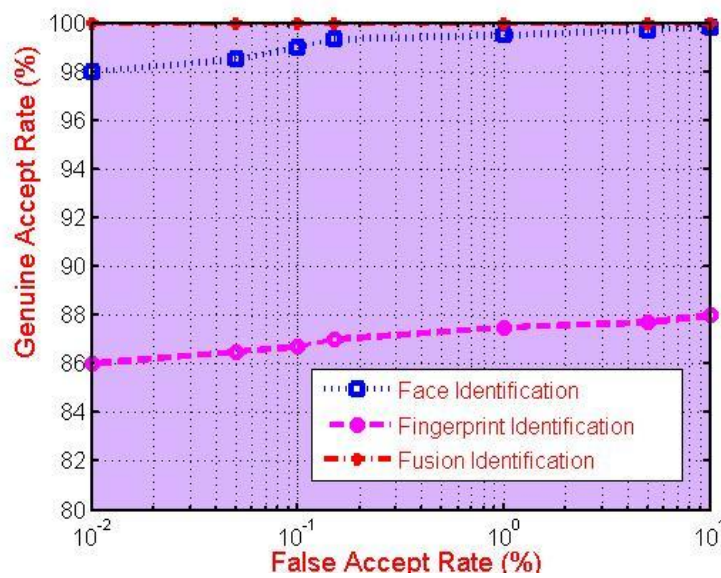


Figure (10) The receiver operating characteristic (ROC) curve.

Training Images	Test Images	Input FPI confirmation	Input FI confirmation	% Correctly identification
150	800	4	3	100%
60	480	4	3	100%
150	800	3	2	87.3%
40	200	3	2	89.2%
150	800	2	1	83.4%
60	480	2	1	84.7%
150	800	4	2	97.4%
40	200	4	1	99.1%
60	480	3	3	95.6%
40	200	3	3	96.2%

Table (1) Training and Test images with correctly identification using the OR configuration.

Training Images	Test Images	Input FPI confirmation	Input FI confirmation	% Correctly identification
150	800	4	3	100%
40	200	4	3	100%
150	800	3	2	83.6%
40	200	3	2	85.3%
150	800	2	1	80.1%
60	480	2	1	82.4%
40	200	4	2	87.4%
150	800	4	1	84.9%
40	200	4	1	86.2%
60	480	3	3	86.6%

Table(2) Training and Test images with correctly identification using the AND configuration.

MODELING AND DESIGN OF A SUBOPTIMAL CONTROLLER FOR A HYDRAULIC SYSTEM

Dr. Rami A. Maher

Electrical Engineering Department
Al-Isra Private University
Amman-Jordan
ramimahir@yahoo.com

Dr. Eman S. Kareem

Electromechanical Department
University of Technology
dr_esk_71@yahoo.com

Abstract

Practical hydraulic control systems are nonlinear, high-order and parameters sensitive systems. On the other hand, usually the customer demands are difficult to achieve without some type of tradeoffs among these demands. Therefore, the burden of designing an optimal controller will be so complicated, and a suboptimal controller seems to be preferable. However, the validation of such design requires a detailed mathematical model of the hydraulic system and actual values of parameters. In this paper, a mathematical model of a hypothetical hydraulic system is derived first. Then after, for the linearized model, a suboptimal controller is designed based on the LQR techniques. A Simulink model of the overall controlled system is utilized to simulate the closed-loop performance.

The stable very fast response indicates the validity of the proposed procedure of design.

Keyword: *LQR Linear quadratic regulator, EHS Electro hydraulic system*

1. Introduction:

In solving problems of optimal control systems, one may have the goal of finding a rule for determining the present control decision, subjected to certain constraints, which will minimize some measure of a deviation from ideal behavior. Such a measure is usually provided by a criterion of optimization, or performance index.

A performance index is a number, which indicates the “goodness” of system performance. The performance index is important because it, to a large degree, determines the nature of the resulting optimal control. In other words, the resulting control may be linear, nonlinear, stationary, or time-varying, depending on the form of the performance index. [1]

Electrohydraulic systems (EHS), have been used in industry in a large number of applications, due to their size-to-power ratio, and the ability to apply very large force and torque. However, the dynamics of hydraulic systems are highly nonlinear. The system may be subjected to non-smooth and discontinuous, nonlinearities due to control input saturation. Moreover, directional change of valve opening, friction, and valve overlap are affecting the operation [2]. Therefore, it is necessary to simulate the hydraulic actual-like system using its representative mathematical model. This should describe the dynamic of the hydraulic directional proportional valve and the cylinder unit of the hydraulic driver. A conventional controller has been designed using suboptimal control theory; as the results were within the required accuracy.

2. Mathematical Modeling of Electrohydraulic System:

The position electrohydraulic servomechanism consists of two parts [3]; the electro hydraulic proportional valve (proportional solenoid with stroke-to-

current relationship), and a hydraulic driven unit cylinder. The output signal of this system is the position of the hydraulic cylinder piston, while the control signal is the output current of an electrical amplifier unit. Figure (1) shows the schematic of the proposed hydraulic system. The directional proportional valve converts the electrical signal to a translation motion, which in turn directs the position of the controlled sliding lever of the valve to control the fluid flow in a hydraulic cylinder. As a result, the hydraulic piston moves to translate the cylinders to the required position. With such description, if this control chain is closed through any type of position sensors, then a servo hydraulic system is obtained. However, the degree of complexity of the system is deliberately chosen to be near enough to practical systems.

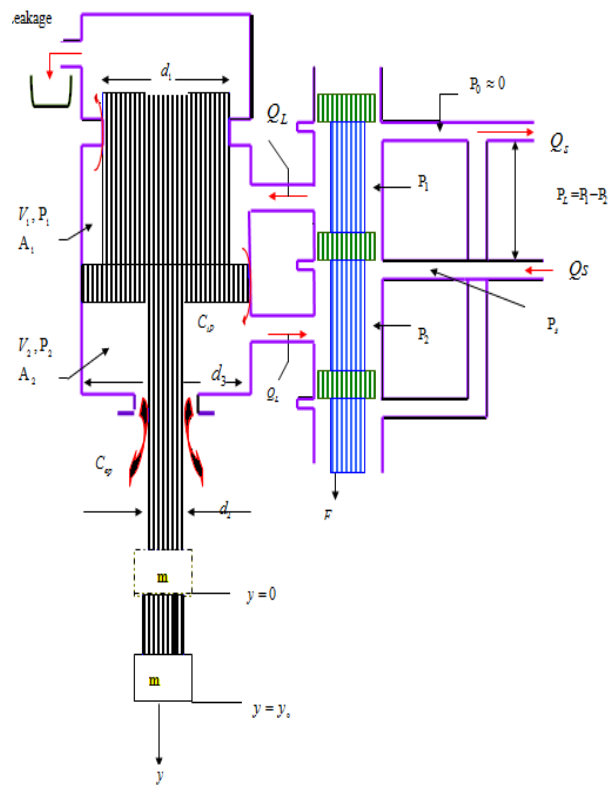


Figure (1) schematic diagram of hydraulic system

2.1 Proportional Directional Valve Modeling

A proportional directional valve with electric feedback consists of the housing, two proportional solenoids, and inductive positional transducer. An electrical amplifier of a linear gain K_a characteristic is used. It is defined by the ratio of the electrical output current (solenoid current) $i(\text{mA})$ to the input voltage signal $u_r(\text{volt})$ for given load. Moreover, it is supposed that the current has no ripples, and the amplifier output signal u is the system control input. It is constrained as $u \in \langle -U_{\max}; +U_{\max} \rangle$, which actuates the hydraulic system. The value U_{\max} is the maximum permissible value of the signal before saturation occurs. This means that the amplifier model will be as a nonlinear saturation element of gain K_a and $\pm U_{\max}$ (volt) cutoff values.

In the solenoid unit, the fixed solenoid performs magnetic field of constant boosting, while the movable solenoid represents an electrical load of the electronic amplifier. The position of the moveable solenoid $d_s(\text{mm})$ is a function of the current passing through it. A first order lag transfer function for the solenoid circuit can be used to model this electrical circuit, i.e.

$$\frac{i(s)}{u(s)} = \frac{1}{(T_s s + 1)} \quad (1)$$

Where T_s is the solenoid time constant.

The translation motion of the solenoid together with the mechanical part in the proportional valve can be represented by the following transfer function.

$$\frac{d_s(s)}{i(s)} = \frac{K_m}{(T_1 s + 1)(T_2 s + 1)} \quad (2)$$

Where K_m is the proportional valve gain T_1 and T_2 are two time constants.

If the position of the sliding lever $d(mm)$ is proportional to the movement of the movable Solenoid then the total transfer function for the proportional valve with mechanical constraints on the sliding lever movement for $\pm \delta d(mm)$ becomes

$$G_p(S) = \frac{K_m}{(T_3s+1)(T_1s+1)(T_2s+1)(T_3s+1)} \quad (3)$$

However, due to the shelter of the sliding lever and the passive resistivity of sealing an overlap is expected as shown in figure 2.

Such overlap can be simply modeled by a dead-zone with saturation nonlinearity of 2δ Sensitivity bandwidth and of a gain K_n , [2]. Therefore, the output of this hydraulic proportional valve will be defined as

$$f(d) = \begin{cases} 0 & ; |d| < \delta \\ dK_n & ; |d| > \delta \end{cases} \quad (4)$$

2.2 Hydraulic Cylinder Modeling

It is known that the hydraulic cylinder can be represented in general by a third order differential equation [4, 5, and 6]. However, the nature of this equation (linear or nonlinear) and its coefficients depend on the piston shape and dimensions, fluid properties, the used pressure and sealing performance.

In this paper, a hydraulic cylinder of non-equal piston chambers will be considered; see figure 1. As it can be seen the piston area of the controlled pressure chamber, is greater than the area of the uncontrolled pressure chamber. For the considered piston chambers (the subscript 1 is used for uncontrolled pressure chamber, and the subscript 2 is used for controlled pressure chamber) the continuity relations are

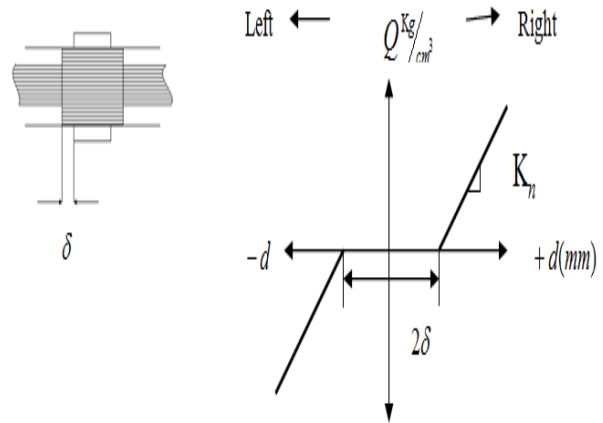


Figure 2 Overlap model [2]

$$Q_1 - C_{ip}(P_1 - P_2) - C_{ep}P_1 = \frac{dV_1}{dt} + \frac{V_1}{\beta_e} \frac{dP_1}{dt} \quad (5)$$

$$-Q_2 - C_{ip}(P_1 - P_2) - C_{ep}P_2 = \frac{dV_2}{dt} + \frac{V_2}{\beta_e} \frac{dP_2}{dt} \quad (6)$$

where:

- Q, Q_2 are the volumetric flow rates. (m^3/sec)

- P_1, P_2 are the pressure. (N/m^2)

- V_1, V_2 are the volumes. (m^3)

- C_{ip} is the internal cross part leakage coefficient of piston. ($m^3 \cdot sec^{-1} \cdot pa^{-1}$)

- C_{ep} is the external leakage coefficient of piston. ($m^3 \cdot sec^{-1} \cdot pa^{-1}$)

- β_e is the effective bulk modulus. (N/m^2)

If the initial volumes for the two chambers are denoted by V_{o1} and V_{o2} , then the instantaneous volumes as a function of the piston movement y are given by

$$\begin{aligned} V_1(y) &= V_{o1} + A_2 y \\ V_2(y) &= V_{o2} + A_1 y \end{aligned} \quad (7)$$

where chambers effective area are given by

$$A_1 = \frac{\pi}{4}[d_3^2 - d_1^2]$$

$$A_2 = \frac{\pi}{4}[d_3^2 - d_2^2] \quad (8)$$

where d_1, d_2 , and d_3 are piston diameters as shown in Figure 1. The rates of change for the chambers volume are

$$\frac{dV_1}{dt} = A_2 \frac{dy}{dt}$$

$$\frac{dV_2}{dt} = -A_1 \frac{dy}{dt} \quad (9)$$

By subtracting equation (6) from equation (5) and substituting for the volumes of the chambers, the following equation is obtained

$$Q_1 + Q_2 - 2C_{ip}(P_1 - P_2) - C_{ep}(P_1 - P_2)$$

$$= (A_1 + A_2) \frac{dy}{dt} + \frac{V_{o1}}{\beta_e} \frac{dP_1}{dt} - \frac{A_2}{\beta_e} y \frac{dP_1}{dt}$$

$$- \frac{V_{o2}}{\beta_e} \frac{dP_2}{dt} + \frac{A_1}{\beta_e} y \frac{dP_2}{dt} \quad (10)$$

Since we have,

$$P_0 \approx 0, \quad P_L = P_1 - P_2, \quad P_s = P_1 + P_2$$

Then,

$$Q_L = \frac{1}{2}(Q_1 + Q_2) = \frac{K_\mu}{\sqrt{\rho}} [\sqrt{P_s - P_L} - \sqrt{P_s + P_L}] f(d) \quad (11)$$

Where K_μ is the coefficient including orifice geometry and discharge coefficient, ρ is the oil density and $f(d)$ is the hydraulic valve output given by equation (4). Also,

$$\frac{dP_1}{dt} = \frac{1}{2} \frac{dP_L}{dt} \quad \text{and} \quad \frac{dP_2}{dt} = -\frac{1}{2} \frac{dP_L}{dt} \quad (12)$$

If a leakage constant C is defined by

$$C = C_{ip} + \frac{1}{2} C_{ep} \quad (13)$$

then a final equation can be written

$$Q_L = CP_1 + A \frac{dy}{dt} + \frac{V_o + ay}{4\beta_e} \frac{dP_L}{dt} \quad (14)$$

where

$$A = \frac{A_1 + A_2}{2}, \quad a = A_2 - A_1, \quad V_o = V_{o1} + V_{o2}$$

For certain constant load force F_L , the load pressure can be calculated from the principle equation

$$P_L = \frac{F_L}{A} \quad (15)$$

Applying Newton's law to the forces acting on the piston yields

$$m \frac{d^2 y}{dt^2} + b \frac{dy}{dt} = AP_L \quad (16)$$

where

- y is the piston displacement (mm).
- m is the total mass of piston & the load referred to piston (kg).
- b is the viscous damping coefficient of piston to the load ($N \cdot \text{sec} \cdot m^{-1}$).

Arranging both of equation (14) and equation (16) in one relation by eliminating the load pressure P_L , yields

$$\frac{V_o + ay}{4\beta A} m \frac{d^3 y}{dt^3} + \left[\frac{V_o + ay}{4\beta A} b + \frac{Cm}{A} \right] \frac{d^2 y}{dt^2} + \left[A + \frac{Cb}{A} \right] \frac{dy}{dt} = Q_L \quad (17)$$

Next, we define the following eight coefficients; only two of them c_2, c_3 are function of the piston displacement y .

$$c_1 = \frac{1}{2} \frac{K_\mu}{\sqrt{\rho}} [\sqrt{P_s - P_L} + \sqrt{P_s + P_L}]$$

$$c_2 = \frac{4\beta A}{m(V_o + ay)}, \quad c_3 = \frac{1}{mc_2} = \frac{V_o + ay}{4\beta A}$$

$$c_4 = \frac{m}{A}, \quad c_5 = \frac{b}{A}, \quad c_6 = A, \quad c_7 = C, \quad c_8 = b \quad (18)$$

The specified 3rd-order nonlinear differential equation governs the piston translation movement (displacement y) will have the form

$$\frac{d^3 y}{dt^3} + c_2 [c_3 c_8 + c_7 c_4] \frac{d^2 y}{dt^2} + c_2 [c_6 + c_7 c_5] \frac{dy}{dt} = c_1 c_2 f(d) \quad (19)$$

The 4th order transfer function of equation (3) and the 3rd-order differential equation of equation 19 represent the complete model of the electrohydraulic system.

3. Linearized Model

In order to design the controller via the optimal LQR theory, we have to determine first a linear state space model. A state vector $X(t)$ representing the electrohydraulic system will have seven states, and are selected as follows:

- The current of the movable solenoid, $x_1(t) = i(\text{mA})$.
- The velocity of the movable solenoid, $x_2(t) = \dot{d}_s (\text{mm}.\text{sec}^{-1})$.
- The position of the movable solenoid, $x_3(t) = d_s (\text{mm})$.
- The position of the sliding lever, $x_4(t) = d (\text{mm})$.
- The dynamic load pressure, $x_5(t) = P_L (\text{Pa})$
- The velocity of piston $x_6(t) = y' (\text{mm}.\text{sec}^{-1})$
- The position of piston, $x_7(t) = y (\text{mm})$

As it is mentioned in section (2.1) the proportional value has been linearized by a transfer function of four lags constants $T_s, T_1, T_2, \& T_3$ and total gain K_m , while the hydraulic cylinder has not yet been linearized. For constant F_L and assumed initial position of the piston y_0 (the piston is moved before any control but only due to pressure balance), the two nonlinear coefficient functions c_2 and c_3 can be calculated at $y = y_0$ to obtain constant values \bar{c}_2 and \bar{c}_3 . In this way, it is possible to

represent the differential equation (21) by a transfer function of the form

$$G_c(s) = \frac{K_c}{s(s^2 + as + b)} \quad (20)$$

where

$$\begin{aligned} K_c &= c_1 \bar{c}_2 K_n \\ a &= \bar{c}_2 (\bar{c}_3 c_8 + c_7 c_4) \\ b &= \bar{c}_2 (c_6 + c_7 c_5) \end{aligned}$$

With the above definition for state variable and the two transfer functions given in equation (3) and equation (22), the linearized model can be represented by the state equation

$$X' = \begin{bmatrix} -\frac{1}{T_s} & 0 & 0 & 0 & 0 & 0 & 0 \\ \frac{K_m}{T_1 T_2} & -\frac{(T_1 + T_2)}{T_1 T_2} & -\frac{1}{T_1 T_2} & 0 & 0 & 0 & 0 \\ 0 & 1 & 0 & 0 & 0 & 0 & 0 \\ 0 & 0 & \frac{1}{T_3} & -\frac{1}{T_3} & 0 & 0 & 0 \\ 0 & 0 & 0 & c_4 K_c & -\bar{c}_2 c_4 c_7 & -\bar{c}_2 c_4 c_6 & 0 \\ 0 & 0 & 0 & 0 & \frac{1}{k} & -\frac{c_5}{c_4} & 0 \\ 0 & 0 & 0 & 0 & 0 & \frac{c_4}{k} & 0 \end{bmatrix} X + \begin{bmatrix} 1/T_s \\ 0 \\ 0 \\ 0 \\ 0 \\ 0 \\ 0 \end{bmatrix} u \quad (21)$$

Where k is equal to 10 (1cm = 10mm). Finally, the nonlinear elements are modeled in the linearized model only by their gain K_a and K_n ; however it is expected that the dead zone with saturation element may cause unstable limit cycle or at least long regulating time and unaccepted overshoot. Therefore, a sort of compensation is necessary to be included. A standard technique is to use a dither signal.

Due to the expected sensitivity problem of the considered hydraulic system, the system simulation has to be carefully carried. This in turn requires that the system parameters must be correct to physical point of view. To overcome such circumstances, the numerical model is readjusted several times based on the suitable literatures [5, 6, and 7] to reach a final physical meaningful

model. The final numerical values taken to construct the hydraulic system model are listed in Table (1) of the appendix. The hydraulic cylinder parameters and coefficients c_i are calculated and listed in Table (2) of the appendix. For the linearized model, the coefficient matrix, A and the input matrix, B are calculated, see the appendix.

The eigenvalues set of the A matrix contain one zero. Theoretically, if there is zero eigenvalue in the linearized model, then the stability of the nonlinear system (according to second Lyapunov theory) cannot be deduced from the linearized model. However, as expected the simulation of the open loop nonlinear electrohydraulic system shows unstable response for arbitrary step input.

4. Suboptimal Controller Design

For the linearized model, the linear optimal control theory is invoked; specifically, the infinite horizon LQR. Therefore, for this SISO constrained system, the problem is stated as,

$$\min_{|u| \leq U} \{J(u) = \int_0^{\infty} (X^T Q X + r u^2) dt\}, \quad r = 1$$

subjected to:

$$X'(t) = AX + Bu, \quad X(0) = 0_{7 \times 1} \quad (22)$$

Accordingly, a state feedback gain can be obtained to perform this task using the Matlab function *lqr*. However, first the weight matrix Q has to be determined. Since in this system, only the piston position of interest, the Q matrix should have only one non zero element q , i.e. Q has the form

$$Q = \begin{bmatrix} 0_{6 \times 6} & 0_{6 \times 1} \\ 0_{1 \times 6} & q \end{bmatrix}$$

Using the known thumb of rules of selecting q , it could be possible to set a range of values $[q_{min}, q_{max}]$ and based on the system performance (the regulating time, settling time and the maximum overshoot) one specified value could be obtained. To reduce the effort of such ad hoc searching, a SIMULINK model of the system as shown in figure (3) is set (see the appendix for the

complete electrohydraulic model), in which a direct measure of the regulating time and settling time is recorded for different values of input q in the stable operation range of values. Moreover, a Matlab m. program is running simultaneously as a function block in the Simulink set up to solve the LQR problem and supplies the model with the state feedback gain vector K . For $2 \times 10^7 \leq q < 2 \times 10^8$, the simulation reveals that one can choose the value $q = 2.5 \times 10^7$ as an optimal value, for which the step response has a compatibly good response. Figure (4) illustrates the idea of how to select specific q , where the vertical lines represent the crossing of 1 ± 0.01 value. The regulating settling time is read at the first and last vertical lines respectively. The gain matrix k for $q = 2.5 \times 10^7$ is

$$K = [0.1029 \quad 0.1642 \quad 141.8653 \quad 263514 \quad 0.0007 \quad 0.2598 \quad 192307]$$

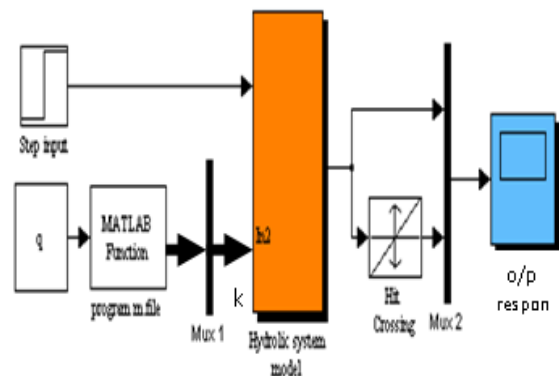


Figure (3) The Simulink Model illustrates how to reach the optimal value of Output

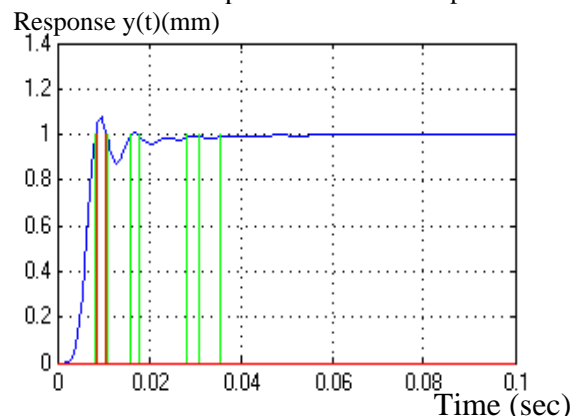


Figure (4) Step response for values of $q = 2.5 \times 10^7$

For implementing the optimal state feedback control law, the position and velocity of the movable solenoid ($x_2(t)$, $x_3(t)$) are not measurable while the other states are all measurable. Therefore, a certain type of reduced-order state estimator should be incorporated. The general theory of design reduced-order Luenberger observer will be utilized [8]. The estimator uses states $x_1(t)$, and $x_4(t)$ to estimate $x_2(t)$, and $x_3(t)$. The design of the estimator is performed such to have a fast response with minimal possible estimation errors [9]. The result is shown by the dynamic system in figure (5), where,

$$A = \begin{bmatrix} -525 & 84761 \\ 1 & -214.8 \end{bmatrix},$$

$$B = \begin{bmatrix} 586.3339 & -40071 \\ 0 & 92.12 \end{bmatrix},$$

$$C = \begin{bmatrix} 1 & 0 \\ 1 & 1 \end{bmatrix}, \quad D = 0_{2 \times 2}$$

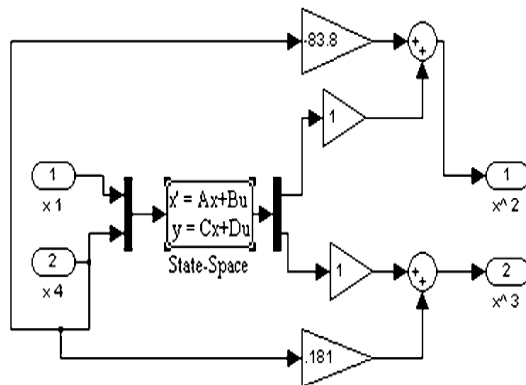


Figure (5) Block diagram of reduced order Luenberger observer

Running the simulation of the complete design electrohydraulic with state estimator and state feedback control, we can determine the system response. Figure (6) depicts the

output response for different input set with the optimal value of q ; the simulation time is 0.1 second. In all three cases, the output reaches the required position within a settling time less than approximately 0.02 second. However, the dither signal is experimentally decided to be with amplitude 17, and frequency ($2 \cdot \pi \cdot 100$); these values give the smallest amplitude of the existing limit cycle.

Output $y(t)$ (mm)

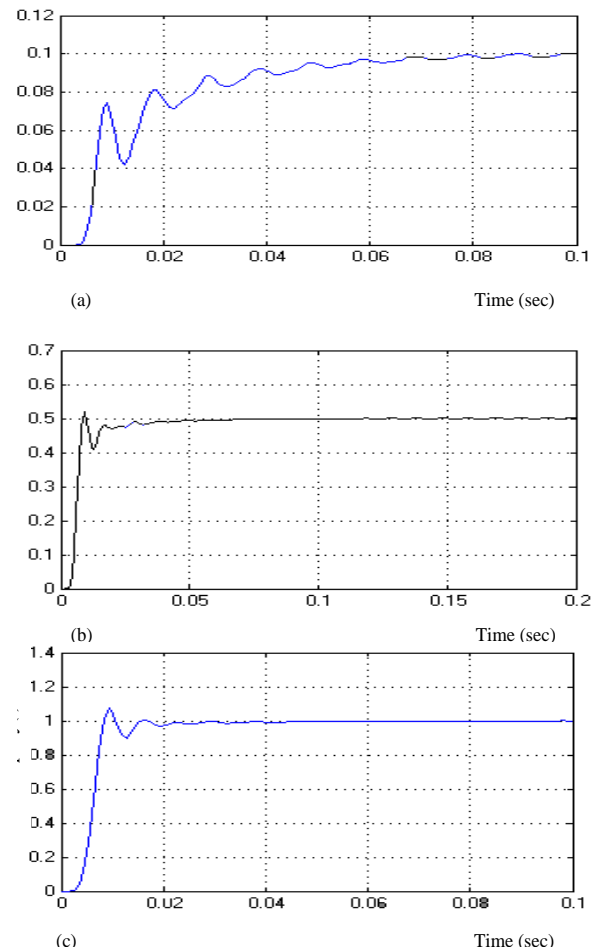


Figure (6) the output response for different input set with the optimal value of q ;
 a) $p=0.1$ unit step b) $p=0.5$ unit step c) $p=1$ unit step

5. Conclusions

The following points summarize the main conclusions drawn from this research:

- 1) The mathematical modeling of both of the proportional valve and the hydraulic cylinder and hence transfer functions are presented, however the degree of complexity of the system is deliberately chosen to be near enough to practical systems; hydraulic cylinder of non-equal piston chambers is considered.
- 2) A suboptimal controller can be designed for nonlinear system by applying linear quadratic regulator (LQR) technique to a linearized model and adjusting the controller parameters based on nonlinear system performance.
- 3) The dead zone element causes unstable limit cycle, long regulating time and unaccepted overshoot, therefore a conventional technique dither signal is used.

References:

- [1] Yousif R.N., "Design of Suboptimal Controller for Industrial Application", M.Sc.Thesis, Control Engineering Department, Technology University, Oct. 1994.
- [2] Merritt H. E., "Hydraulic Control system", Wily and Sonse, 1967.
- [3] DÖrr H.:EwaldR., "The Hydraulic Trainer Volume 2 –Propotional and Sewo Valve Technology", Mannesmann Rexroth GmbH, 1986.
- [4] Vilenius M.J., "The Application of Sensitivity Analysis to Electrohydraulic Position Control Servos", Journal of Dynamic Systems, Measurement, and Control, Vol. 105, June 1983.
- [5] Zheng-jin H. Yu. andXu-yongW., "Nonlinear Control for A Class of Hydraulic Servo System", Journal of Zhejiang University Science, <http://www.zju.edu.cn/jzus>, 2003.
- [6] BoltonW., "Pneumatic and Hydraulic System", Butterworth –Heinemann, 1997.
- [7] Akers S. J. Lin "Optimal Control Theory Applied to A Pump with Single- Stage Electrohydraulic Servo valve" Transaction of the ASME Vol. 110, June 1988, pp120 -125.
- [8] William L. Brogan, "Modern Control Theory", 3 rd –Edition, Prentice-Hall International, Inc., 1991.
- [9] Al-Ghabban,E.S. "Neural Network controller for a hydraulic system", PhD thesis, University of Technology, 2007

Appendix:- Table (1 & 2) Numerical values of parameters and coefficients

Table (1) Numerical values of parameters for an electrohydraulic system

symbol	value	Unit
K_a	26	$mA.v^{-1}$
U_{max}	300	volt
T_s	2.5×10^{-3}	sec.
K_m	0.04	$mm.A^{-1}$
T_1	2.018×10^{-3}	sec.
T_2	3.3806×10^{-2}	sec.
T_3	8.424×10^{-4}	sec.
δ	0.1	mm
δ_d	4	mm
K_n	0.2	$mm.v^{-1}$
V_o	500	cm^3
C	10^{-8}	$m^3.sec^{-1}.Pa^{-1}$
d_1	100	mm
d_2	25	mm
d_3	136	mm
P_s	12	M Pa
β	2.73×10^5	M Pa
$\frac{K_m}{\sqrt{\rho}}$	2.57×10^{-4}	$m^2.sec^{-1}.Pa^{-0.5}$
m	297	kg
b	1.66×10^6	$N.sec.m^{-1}$
F_L	70	kN
y_o	55	mm

Table (2) the hydraulic cylinder parameters & coefficients

Parameters & coefficients	Values and units	Parameters & coefficients	Values and units
A_1	66 cm^2	c_3	$4.48 \times 10^{-8} + 6.64 \times 10^{-9} y$
A_2	140 cm^2	\bar{c}_3	$4.1 \times 10^{-7} \text{ cm}^3 \cdot \text{N}^{-1}$
A	103 cm^2	c_4	$2.88 \text{ Kg} \cdot \text{cm}^{-2}$
a	74 cm^2	c_5	$161 \text{ N} \cdot \text{sec} \cdot \text{cm}^3$
P_L	6.8 MPa	c_6	103 cm^2
c_1	$8500 \text{ cm}^2 \cdot \text{sec}^{-1}$	c_7	$0.01 \text{ cm}^3 \cdot \text{sec}^{-1} \cdot \text{Pa}^{-1}$
c_2	$5.22 \times 10^6 (69.5 + 10.3y)^{-1}$	c_8	$1.66 \times 10^4 \text{ N} \cdot \text{sec} \cdot \text{cm}^{-1}$
\bar{c}_2	$8207 \text{ cm}^{-2} \cdot \text{sec}^{-2}$		

- The matrices A and B

$$A = \begin{bmatrix} -400 & 0 & 0 & 0 & 0 & 0 & 0 \\ 586.3339 & -525.1 & -14658 & 0 & 0 & 0 & 0 \\ 0 & 1 & 0 & 0 & 0 & 0 & 0 \\ 0 & 0 & 1187 & -1187 & 0 & 0 & 0 \\ 0 & 0 & 0 & 4 \times 10^7 & -236.4 & -2.43 \times 10^6 & 0 \\ 0 & 0 & 0 & 0 & 0.347 & 55.9 & 0 \\ 0 & 0 & 0 & 0 & 0 & 10 & 0 \end{bmatrix}, \quad B = \begin{bmatrix} 400 \\ 0 \\ 0 \\ 0 \\ 0 \\ 0 \\ 0 \end{bmatrix}$$

SIMULATION OF BOILER DRUM WALL TEMPERATURE DIFFERENTIAL AND ITS ESTIMATION

Dr. Waladin K. Sa'id

Control and Systems Eng. Dept.
University of Technology
waladinsky@yahoo.com

Bashra Kadhim Oliewe

Control and Systems Eng. Dept.
University of Technology
bushrakad@yahoo.com

Abstract

This paper is concerned with the problem of boiler drum wall temperature estimation to limit thermal stresses. The boiler drum of AL-Mussiab thermal power station is taken as a case study. It deals with the fundamental issue that must be considered when applying a linear theory (i.e the Kalman filter) to practical non-linear problems. The Kalman filter is applied to estimate boiler drum wall temperature using outer surface temperature of boiler drum wall (measurable) variable. The classical estimator (Kalman filter) is simple but it requires a good dynamic model to give reliable results. The numerical test results showed that the estimator is efficient and works well and it converges to the correct conditions (to within $\pm 1^\circ\text{C}$) in time about half an hour from boiler heating start up. The estimator is robust where 100% error in initial conditions did not seriously influence the transient time to produce correct estimated output.

Keywords: *Boiler Drum, Kalman Filter, temperature estimation*

1- Introduction

The boiler is a major part in thermal power stations and since the boiler is the slowest responding part in the plant especially at starting up, the plant response is highly influenced by the boiler response. The procedure of starting up and shutting down the power station is limited by following the procedure of starting and shutting the boiler to prevent high thermal stresses [1,2].

Stresses in boiler equipment particularly those of the drum during transients limit the time taken for starting up of thermal power

plants. Short starting up time is desired to meet energy demand requirements. Furthermore boiler drum working environment is harsh, thus the probability of failure in the measurement system is high. Therefore, it is necessary to develop a state space model and optimal estimation of states, which would gradually improve the current state estimates by making use of the available on-line measurements for the drum wall temperature. This approach can make use of the Kalman filter procedure for observable systems, as it is for this case.

Kalman filter represents the most widely applied and demonstrably useful results to emerge from the state variable approach of "modern control theory"[3]. The Kalman filter has been the subject of extensive research and application, hence, orbit determination, tracking and navigation problems, represent probably, the first major applications of the Kalman filter. Estimation and control problems in industrial processes and power systems utilized Kalman filter extensively. It has been applied to the estimation of temperature and prediction of the ingot temperature in the soaking pit operations based on other available measurements Lumelsky [4]. A bank of Kalman filters (one for each instrument) in the design of an instrument failure detection system for a pressurized water reactor (PWR) pressurizer was applied by Tylee [5]. A Kalman filter with extended models to estimate state variables (unmeasured temperatures in the glass melting furnace) was used by Huisman, *et. al.* [6]. A regular Kalman filter for continuous monitoring of induction furnace charge temperature based on a single furnace lining temperature

measurement was developed by Sa'id and AL-Kubaissy[7]. Fluerasu and Sutton[8] designed and implemented a computer-controlled temperature tracking system which combines standard Proportional-Integral-Derivative (PID), thermal modeling and Kalman filtering of the temperature reading in order to reduce the noise.

This paper is concerned with the development of a practically feasible dynamic estimator (Kalman filter) which can be used to limit thermal stresses during power station boiler start up. In the following sections a mathematical model for the boiler drum temperature is derived for the starting up mode and the Kalman filter estimator is developed and evaluated numerically.

2. System Description

The drum of the boiler is a thick wall cylinder used for separating the steam from steam-water mixture, as shown in figure (1). It is located at the top of the boiler and it is hanged by four hinges, two at each side and it is manufactured from steel alloy (SA 299). The steam-water mixture coming from riser tubes enter the drum via a number of cyclonics, which are used for increasing the rate of separation process as shown in figure (1). The separated steam is conveyed from the drum to the super heater through a set of pipelines. The intake points of these pipelines are uniformly distributed along the longitudinal direction at the top of the drum [2].

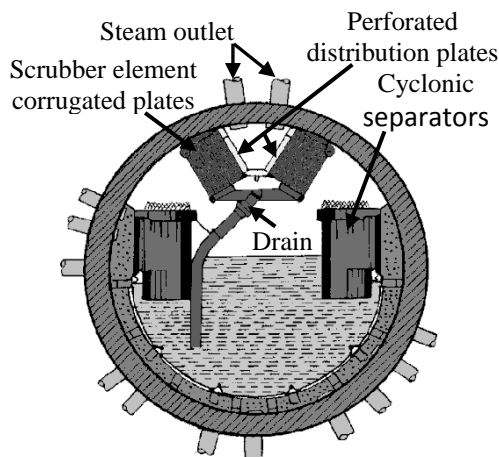


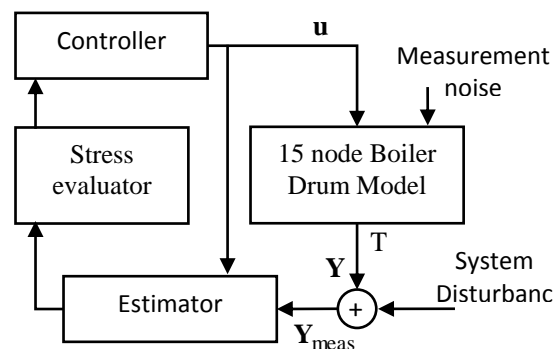
Figure (1) Cross section of Al-Mussiab boiler drum.

The boiler drum is subjected to thermal stresses due to the temperature difference between the inner and outer surfaces of the drum wall during starting up. Hence, the working speed of thermal power stations is limited by the maximum amount of permissible thermal stresses. There are “24” thermocouples located at different points on the drum wall used to monitor the stresses. The drum dimensions used in this work are detailed in Table (1).

The structure of the proposed thermal stress control system to be developed is shown in figure (2). The control loop includes the estimator which produces the estimated values of the states and outputs for the next moment based on the measured values of the outputs at the current moment and the control effort at the previous moment.

Table (1): Drum dimensions used in this work [2].

Item	Dimension
Length	15 m
Inner Radius	0.9144 m
Outer Radius	1.0964 m
Thickness	0.182 m
Volume	42.3 m ³
Weight	172 ton



State T = Drum node temperature, and
 Output Y =Outer surface temperature,
 Control u =Input vector.

Figure (2) Boiler drum control system structure.

3. Boiler Drum Simulation Requirements

The coming sections are devoted to the simulation and the realization of the system shown in figure (2). The simulation is based on Matlab software.

A. Boiler Drum Wall Temperature Rise Modeling

For practical monitoring applications, the thermal system can be approximately represented by a lumped parameter system that can be described by ordinary differential equations. Such a set of linearised ordinary differential equations are much easier and faster to solve numerically. The lumped thermal model assumes that heat storage in a material can be represented by an effective thermal capacitance, C , and that the resistance to heat flow between two points can be represented by an effective thermal resistance, R , [9].

The lumped model approach results in first order dynamics in the temperature response to heat input at a given point or “node “. For a single node, the heat balance equation is simply given by [9].

$$q_i(t) = \frac{T(t) - T_a(t)}{R} + C \cdot \frac{dT(t)}{dt} \quad (1)$$

where T_a is the adjacent node temperature. Equation (1) may be put in state variable form, anticipating the construction of a set of dynamic equations describing temperature distribution in the drum wall, i.e.,

$$\dot{T} = \frac{1}{RC}(T_a(t) - T(t)) + \frac{q_i(t)}{C} \quad (2)$$

To obtain a set of linearized differential equations for the lumped parameter model, the single node described by equation (2) will be used.

The transient temperature variation in the shell material of the boiler drum is a two-dimensional case and the boundary conditions are dictated by the drum water level and temperature. The latter is, of course, dependent on the steam pressure. This assumes that there is no temperature gradient along the 15 m long boiler drum. Figure (3) shows one way in which the basic thermal network may be set on the drum wall.

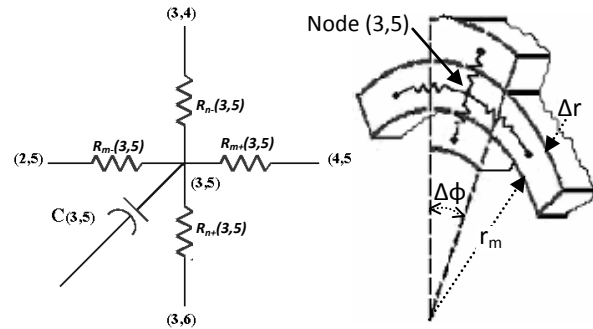


Figure (3) Equivalent R-C simulation for the boiler drum shell.

B. Boiler Drum Wall Thermal Dynamic Equations

For a two dimensional heat flow, and using the node (m, n) shown in figure (3), equation (2) takes the following form [10,11,12];

$$\dot{T}_{m,n} = (\psi_{m,n} + q_{m,n}) / C_{m,n} \quad (3)$$

Where m and n designate radial and circumferential number of nodes, and;

$$\psi_{m,n} = \sum_{i=+1 \& -1} ((T_{m+i,n} - T_{m,n}) / R_{m+i,n} + \beta_{m,n}),$$

where;

$$\beta_{m,n} = (T_{m,n+i} - T_{m,n}) / R_{m,n+i}.$$

$R_{m\pm i,n}$ = Radial thermal resistance.

$R_{m,n\pm i}$ = Circumferential thermal resistance.

$C_{m,n}$ = Node thermal capacitance

Writing equation (3) for each of the specified nodes leads to a system of first order dynamic equations. A computer program using MATLAB software was written to solve the set of first order differential equation using fourth order RungeKutta method.

C. State Space and Measurement Equations of Boiler Drum

The system representations given by equation (3) are based on input and output variables and it is a linear model. It is convenient to obtain a simplified boiler drum model using state variables.

To derive the state space model, the number of states must be first determined. Equation (3) clearly shows that the states are the temperature of the nodes of the drum wall. The number of nodes depends on whether the problem is a one dimensional

heat flow (radial heat flow) or a two dimensional heat flow (radial and circumferential heat flow). Increasing the number of nodes will improve the accuracy of the mathematical model of the boiler drum. We shall first divide the drumwall radially into three nodes and assume radial heat flow only. Equation (3) will take the following equivalent state space model (general form);

$$\dot{\mathbf{T}}(t) = \mathbf{A} \mathbf{T}(t) + \mathbf{B} \mathbf{u}(t) \quad (4)$$

Where \mathbf{T} is the drum wall temperature node state vector and \mathbf{u} is the input vector.

Using the drum dimension of AL-Mussiab boiler drum as given in Table (1) and the definition of R and C for 3 radial nodes and 20 circumferential nodes, equation (4) becomes;

$$\begin{bmatrix} \dot{T}_1 \\ \dot{T}_2 \\ \dot{T}_3 \end{bmatrix} = 10^{-3} \begin{bmatrix} -1594 & 0.75 & 0 \\ 0.7 & -1445 & 0.745 \\ 0 & 0.7 & -0.744 \end{bmatrix} \begin{bmatrix} T_1 \\ T_2 \\ T_3 \end{bmatrix} + \begin{bmatrix} 0.844 & 0 \\ 0 & 0 \\ 0 & 0.044 \end{bmatrix} \begin{bmatrix} T_d \\ T_{air} \end{bmatrix} \quad (5)$$

Where T_d and T_{air} represent temperature of fluid inside drum and temperature of air outside drum (state input), respectively.

The discrete form of equation (4) is;

$$\mathbf{T}_k = \boldsymbol{\Phi}_{k-1} \mathbf{T}_{k-1} + \mathbf{B}_{k-1} \mathbf{u}_{k-1} \quad (6)$$

$$\mathbf{Y}_k = \mathbf{H} \mathbf{T}_k \quad (7)$$

where;

$\mathbf{T}_{k-1}, \mathbf{T}_k$ = Plant state vectors at moments $k-1$ and k , respectively.

\mathbf{u}_{k-1} = Control variable vector at the moment $k-1$.

\mathbf{Y}_k = Output vector at moment k ,

k = Time index.

(Note: Along this paper $\mathbf{T}(k) = \mathbf{T}_k$, $\mathbf{Y}(k) = \mathbf{Y}_k$, $\mathbf{u}(k) = \mathbf{u}_k$).

For a sampling time of 1 second, the elements of equation (6) are;

$$\boldsymbol{\Phi}_k = \begin{bmatrix} 0.9984 & 0.0007 & 0 \\ 0.0007 & 0.9986 & 0.0007 \\ 0 & 0.0007 & 0.9993 \end{bmatrix}, \quad \text{and}$$

$$\mathbf{B}_k = 10^{-3} \begin{bmatrix} 0.8429 & 0 \\ 0.0003 & 0 \\ 0 & 0.0438 \end{bmatrix}$$

To select the number of nodes for the drum wall in radial and circumferential directions, a set of numerical tests were made to examine the dynamic wall temperature response with various number of nodes in both directions (radial and circumferential).

The above study was concluded to adopt a mathematical model with 5 rings in radial direction and 20 sections in circumferential direction. Figure (4) shows the temperature time response of boiler drum wall. It illustrates the dynamic behavior of 5 nodes along the thickness of the drum wall at the starting up of the boiler with inner surface temperature gradient of “0.54 °C/min”. This model was used as the mathematical model for Kalman filter design.

A fifteen nodes state apace model was also derived and used as a reference model for estimator’s performance. A set of models describing the dynamic behavior of the drum wall temperature for two dimensional heat flow case (radial and circumferential heat flow) were derived and are given in reference [12].

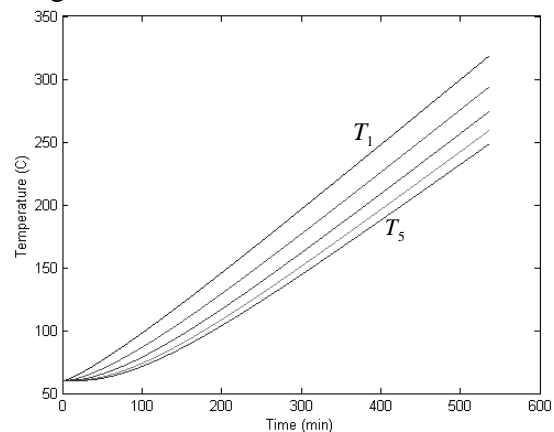


Figure (4) Temperature distribution for 5 nodes on the drum wall with inner surface temperature gradient of “0.54°C/min” at starting up mode.

4. Kalman Filter

The Kalman filter is essentially a set of mathematical equations that implement a predictor-corrector type estimator. It is optimal in the sense that it minimizes the estimated error covariance [13]. Hence, it is the best linear estimator, which can produce an optimal estimate of the state of a linear

dynamic system, subject to the disturbances having Gaussian distribution. The function of a filter is to separate the signal or information from the noise- corrupted data and it can be used to compute the optimal estimate of the signal [14].

The filter is initialized with an initial estimate of the signal and its error covariance. Then as each measurement becomes available in real time, it is used to update or refine the filter's previous estimate. Thus, the initial estimate is successively improved until, eventually; a steady state condition is reached where no further improvements are obtained [15].

In the implementation of a Kalman filter, a mathematical model of the signals to be estimated is described by means of linear stochastic difference equations. Equation (6) will assume the following form:

$$\mathbf{T}_k = \boldsymbol{\Phi}_{k-1} \mathbf{T}_{k-1} + \mathbf{B}_{k-1} \mathbf{u}_{k-1} + \mathbf{w}_{k-1} \quad (8)$$

The observation (measurement) of the process is assumed to occur at discrete points in time in accordance with the relationship.

$$\mathbf{Y}_k = \mathbf{H} \mathbf{T}_k + \mathbf{v}_k \quad (9)$$

Where \mathbf{w}_k and \mathbf{v}_k represent the process noise and measurement noise, respectively. They are assumed to be uncorrelated zero-mean, white noise sequences with known statistics whose properties are described by:

$$E[\mathbf{w}_k] = E[\mathbf{v}_k] = 0 \quad (10)$$

And joint covariance matrix;

$$E\left[\begin{pmatrix} \mathbf{w}_k \\ \mathbf{v}_k \end{pmatrix} \begin{pmatrix} \mathbf{w}_k^T & \mathbf{v}_k^T \end{pmatrix}\right] = E\left[\begin{bmatrix} \mathbf{Q}_k & 0 \\ 0 & \mathbf{R}_k \end{bmatrix}\right] \quad (11)$$

Where; \mathbf{Q} and \mathbf{R} are the process and measurement noise covariances and they are assumed constant [15].

The equations for the Kalman filter fall into two groups: time update equations and measurement update equations. The time update equations are responsible for projecting forward (in time) the current state and error covariance estimates to obtain the a priori estimates for the next time step. The measurement update equations are responsible for the feedback, i.e., for incorporating a new measurement into a

priori estimate to obtain an improved a posteriori estimate. The time update equations can also be thought of as predictor equations, while the measurement update equations can be thought of as corrector equations. Indeed the final estimation algorithm resembles that of a predictor-corrector algorithm for solving numerical problems. The time and measurement update equations are given below [13];

i-) *Discrete Kalman filter time update equations*

$$\hat{\mathbf{T}}_k^- = \boldsymbol{\Phi} \hat{\mathbf{T}}_{k-1} + \mathbf{B} \mathbf{u}_{k-1} \quad (12)$$

$$\mathbf{P}_k^- = \boldsymbol{\Phi} \mathbf{P}_{k-1} \boldsymbol{\Phi}^T + \mathbf{Q} \quad (13)$$

ii-) *Discrete Kalman filter measurement update equations*

$$\mathbf{K}_k = \mathbf{P}_k^- \mathbf{H}^T (\mathbf{H} \mathbf{P}_k^- \mathbf{H}^T + \mathbf{R})^{-1} \quad (14)$$

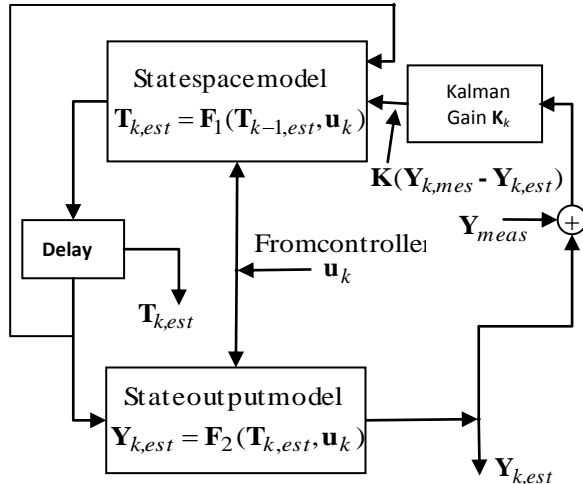
$$\hat{\mathbf{T}}_k = \hat{\mathbf{T}}_k^- + \mathbf{K}_k (\mathbf{Y}_k - \mathbf{H} \hat{\mathbf{T}}_k^-) \quad (15)$$

$$\mathbf{P}_k = (\mathbf{I} - \mathbf{K}_k \mathbf{H}) \mathbf{P}_k^- \quad (16)$$

Having an initial estimate $\hat{\mathbf{T}}_0$ and the initial estimation error (noise) covariance \mathbf{P}_0 and a model for the system and measurement, the recursive Kalman filter equations can be solved next (equations (12) to (16)). As can be seen from time update equations (12) and (13) the state and covariance estimates are projected forward from time step $k-1$ to k . However, the first task during the measurement update is to compute the Kalman gain, \mathbf{K}_k using equation (14). The next step is to actually measure the process to obtain \mathbf{Y}_k , and then to generate a posteriori state estimate by incorporating the measurement (equation (15)). The final step is to obtain a posteriori error covariance estimate via equation (16).

After each time and measurement update pair, the process is repeated with the previous a posteriori estimates used to project or predict the new a priori estimates. This recursive nature is one of the very appealing features of the Kalman filter, it makes practical implementations much more feasible than (for example) the Wiener filter. The Kalman filter recursively conditions the current estimate on all of the past

measurements. A MATLAB program is designed to solve the problem and figure (5) gives a pictorial overall structure of the computation scheme.



State \mathbf{T} = Drum wall node temperature,
 Output \mathbf{Y} = Outersurface temperature,
 \mathbf{u} = Input vector.

Estimation equations

$$\mathbf{T}_{k,est} = \mathbf{A}\mathbf{T}_{k-1,est} + \mathbf{B}\mathbf{u}_k + \mathbf{K}(\mathbf{Y}_{k,meas} - \mathbf{Y}_{k,est})$$

$$\mathbf{Y}_{k,est} = \mathbf{H}\mathbf{T}_{k,est}$$

Figure (5) The overall structure of the estimator computation scheme.

5. Simulation

The Kalman filter scheme shown in figure (5) estimates the temperature difference between inner and outer surface during boiler starting up. F_1 and F_2 are given by equations (8) and (9), respectively.

The current work is concerned with the estimation of temperature difference between inner and outer surfaces using the 5 node model. The temperature measurement is taken from the 15 node model which is taken as the reference. Figure (6) clearly defines the symbols used where nodes (2) and (14) of the 15 node model correspond to nodes (1) and (5) of the 5 node model. That is temperatures T_2 and T_{14} of the 15 node model correspond to temperatures T_1 and T_5 of the 5 node model, respectively. For simplicity, the symbols *T_1 and *T_5 will be used instead of T_2 and T_{14} for the 15 node

model. Also, the drum wall temperature difference Δ^*T_w , the reference, represents (${}^*T_1 - {}^*T_5$) whilst the estimated wall temperature difference is ΔT_w or $(T_1 - T_5)$. Finally, Gaussian noise is added to the drum wall temperature measurement “ *T_1 and/or *T_5 ” to simulate measurement noise.

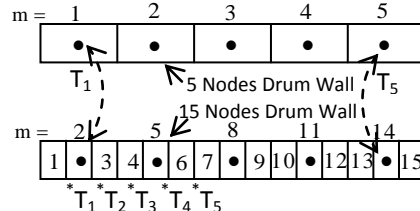


Figure (6) A comparative correspondence between 5 and 15 nodes models.

6. Boiler Drum Performance with Kalman Filter

A series of numerical experimental tests were carried out and figures (7) to (15) summarize the results. Figure (7a) shows the temperature difference behavior of the estimator using the 5 nodes model and the data obtained from the 15 nodes dynamic model. As was discussed above, the temperatures of the latter model are considered as real system temperatures. Hence, the field temperature measurement is taken using the outer node, i.e., *T_5 . Gaussian noise is added to *T_5 to simulate real temperature measurements. Based on this temperature measurement, the estimator estimates the wall temperature difference where the estimator initial conditions are $[60 \ 60 \ 60 \ 60 \ 60]^T$ °C. The figure shows very good tracking after about half an hour from boiler heating start up. The temperature difference between that estimated by the Kalman filter (ΔT_w) and the reference model (Δ^*T_w) is shown in figure (7b), where the peak error deviation is +3 and -5.2°C. From the results shown in figure (7b), the estimator performance is close to reference performance.

Figure (8a) shows the performance of the estimator using measurements of the inner drum wall temperature (*T_1 plus Gaussian noise). The difference between the reference

temperature, Δ^*T_w , and estimated temperature, ΔT_w , is illustrated in figure (8b). The peak deviation (error) is +12.5 and -4°C . Figure (8b) also shows that the performance of the estimator to follow the desired wall temperature differential is very good. A comparison between figures (7b) and (8b) reveals that the performance of the Kalman filter using outer drum wall temperature measurement (*T_5) is superior to that when inner drum wall temperature measurement (*T_1) is used. The former filter shows 50% reduction in maximum temperature deviation. A better estimator performance is expected if both temperatures *T_1 and *T_5 are used.

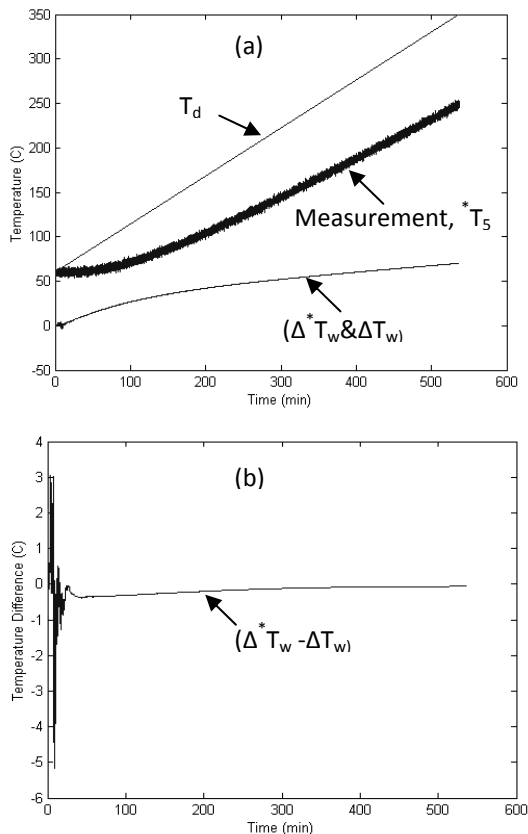


Figure (7) a) Estimator performance with *T_5 node measurement. b) Estimated (Δ^*T_w) and drum wall differential (ΔT_w) difference.

The performance of the estimator using inner and outer wall temperature measurements is shown in figure (9a). The difference between the estimator and actual model wall

temperature differentials ($\Delta^*T_w - \Delta T_w$) is shown in figure (9b). It can be clearly seen that the maximum error is 0.42°C which shows a marked improvement in performance. A comparison between the three cases above shows that the tracking is now faster due to the availability of more information by the measurement of *T_1 and *T_5 .

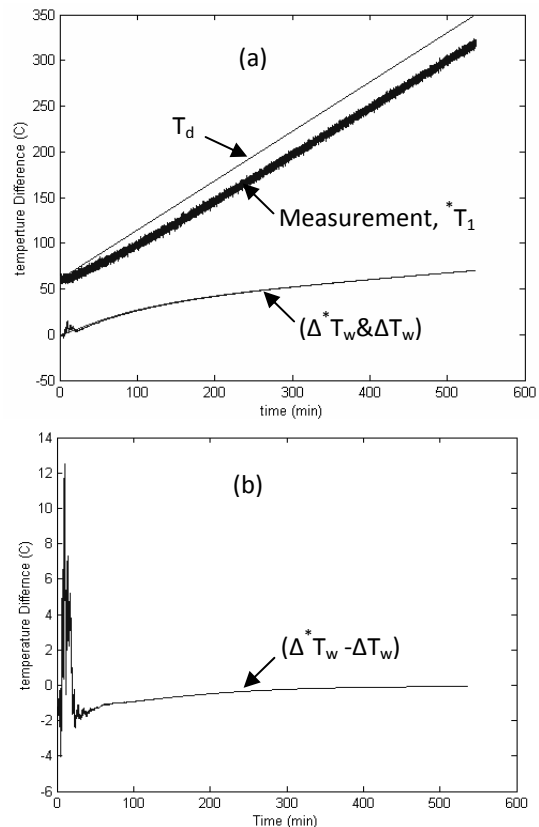


Figure (8) a) Estimator performance with *T_1 node measurement. b) Estimated (Δ^*T_w) and drum wall differential (ΔT_w) difference.

The performance of the three types of estimators can best be evaluated by using the performance index (J_i), which is defined as [7];

$$J_i = \frac{1}{n} \sum_{i=1}^n |T_{\text{est}}(i) - T_{\text{real}}(i)| \quad (17)$$

where, $T_{\text{est}}(i)$ is the estimated temperature value at the i^{th} time point. $T_{\text{real}}(i)$ is the actual value of the temperature and n is the number of time points. The performance of the estimator is the average absolute

deviation of the estimated temperature from the actual temperature. For initial estimator conditions of $[60\ 60\ 60\ 60\ 60]^T$, the estimator performance is rather poor at the beginning of the heating process and the quality of the estimation improves at the end of the heating process, as shown in figures (7), (8) and (9).

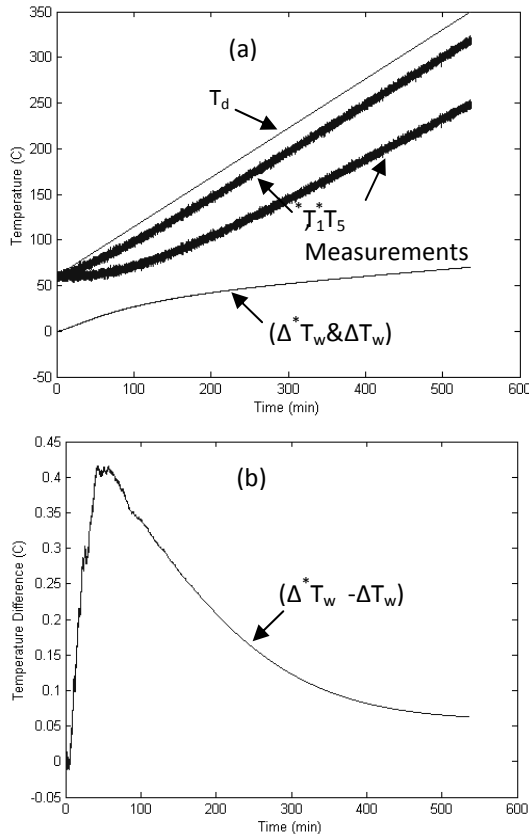


Figure (9) a) Estimator performance with T_1^* and T_5^* measurements. b) Estimated (ΔT_w^*) and drum wall differential (ΔT_w) difference.

The behavior of the estimator is investigated by evaluating the index (J_i) for three time intervals. The test results are summarized in Table (2). The first interval is defined by the period “0-50 min” from start up. The second interval is defined by the remaining run time. Finally, the third interval covers overall run time. For the first interval, Table (2) clearly shows that the estimator with T_1^* and T_5^* measurements ($J_i=0.24$) is better than the other two estimators. Also, the estimator with T_5^* measurement ($J_i= 0.59$) is better than that with T_1^* measurement ($J_i=1.75$). Columns two and three of Table (2) show a similar

trend in behavior. Column three clearly demonstrates that using one outer drum wall temperature sensor is justifiable.

Table (2) Performance index (J_i) of the three estimators for the intervals (0-50), (50-487) and (0-537) min.

Measured Variables	J_i		
	50 min	487 min	537 min
T_1^*	1.7501	0.3495	0.4799
T_5^*	0.5938	0.161	0.2013
T_1^* & T_5^*	0.2397	0.1752	0.1812

The tests shown in figures (10) and (7) are similar but with estimator initial conditions of $[100\ 100\ 100\ 100\ 100]^T$. The temperature error response (case I) indicates very good tracking and the estimator follows the input in less than 30 minutes. The figure also shows (case II) that the estimator is capable of estimating the drum wall temperature and tracks the reference temperature even when random and unequal initial conditions of $[100\ 60\ 60\ 60\ 30]^T$ are used.

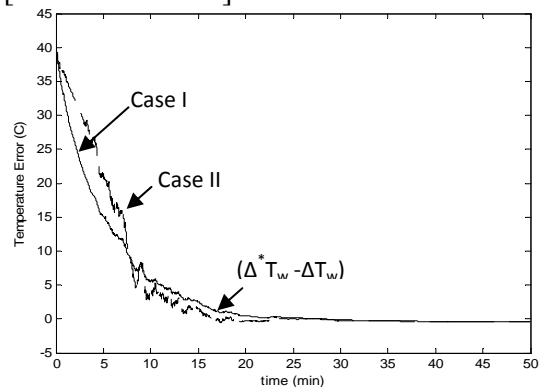


Figure (10) Temperature error response with two different initial conditions.

To demonstrate the performance of the estimator under other operating conditions, three cases were considered. The first case is that of a boiler shut-down after about 5 hours from heating start up. The estimator behavior is shown in figure (11). Such a case may arise if a decision is taken by the power station engineers to shut-down

the boiler due to a failure alarm in any one of the plant's units. The estimator is based on the *T_5 measurement with estimator initial conditions of $[60 \ 60 \ 60 \ 60 \ 60]^T$. The second case study is shown in figure (12) where for some reason or another estimator is started after 2.5 hours from boiler start up. The estimator uses *T_5 as temperature measurement and with initial conditions of $[60 \ 60 \ 60 \ 60 \ 60]^T$.

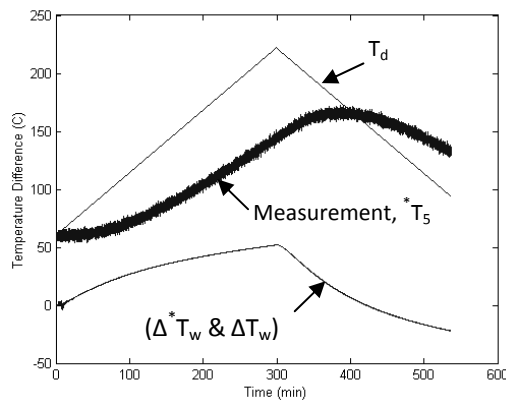


Figure (11) As in figure (7a) but with boiler shut-down after about 5 hours from heating start up.

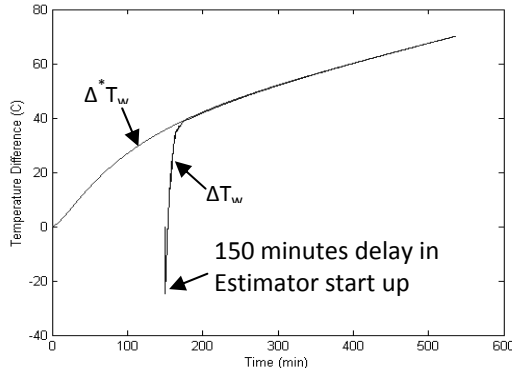


Figure (12) As in figure (7a) but the estimator is initiated 2.5 hours after boiler start up.

Finally, the estimator performance is examined with the presence of process noise in the plant dynamic model. Using uncertainty (w_k) in the dynamic model (equation (8)), two sets of numerical tests were carried out as shown in figures (13) to (15) with uncertainty of 0.1 and 0.01. The temperature noise (v_k) was ± 2 °C in *T_5 for all tests. Figure (13) shows that the estimator estimates the drum wall temperature difference and tracks the reference

temperature closely. Figure (14) shows that the maximum wall temperature difference between the estimated and the reference model temperatures is -7 and 13 °C. Since the plant noise is of a random nature, a series of tests were conducted and the maximum deviation in all these tests was within 30 °C temperature range for the first 15 minutes of the run time. In all these tests the estimator output is within 7% of the true value after 30 minutes from the start up. Reducing the plant noise uncertainty leads to reduces the estimation error. Figure (15) is a repeat the test shown in figure (14) but with plant model noise uncertainty of 0.01. The temperature difference error is within ± 4 °C.

7. Conclusions

A classical estimator (Kalman filter) was designed to estimate boiler drum temperature wall differential, a crucial issue in limiting drum's thermal stresses especially at the start up. The proposed system is simple in the sense that it requires a single thermocouple located at the outer surface of the drum and a software estimator. The model should be accurate enough to get good estimation in reasonably short time. The quality of the model affects the estimation. Many sets of initial conditions were used in the numerical experiments of the estimator. The estimator performance was as expected, rather slow at the beginning of the estimation. It takes about 30 minutes to estimate wall temperature difference with an accuracy of ± 1 °C. The quality of the estimation increases from start up to finish. The results indicated robust estimator performance with regard to the variation in initial conditions. The performance of the estimator was not seriously influenced even with 100% error in initial conditions. Temperature estimation using software solution is simple and cheap as compared with hardware solution. Thus, attention must be paid to the application of the estimation techniques, which can provide solutions to many engineering problems especially those

where the operating environment is harsh such as those of power station boiler drums. Future work is to be directed to improve the boiler drum model by including inner and outer surfaces heat transfer conditions.

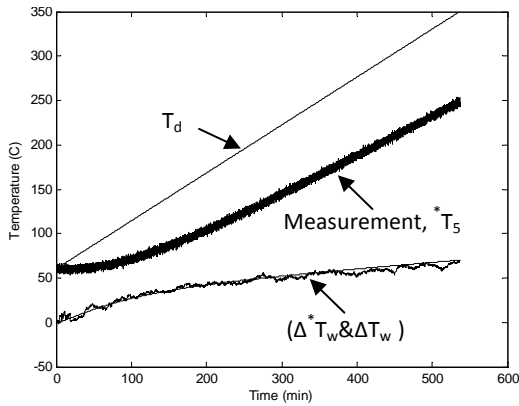


Figure (13) Estimator performance with 0.1 plant model noise uncertainty.

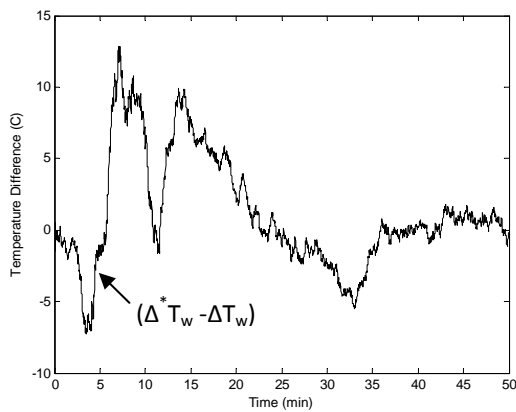


Figure (14) Typical temperature error response with 0.1 plant noise uncertainty.

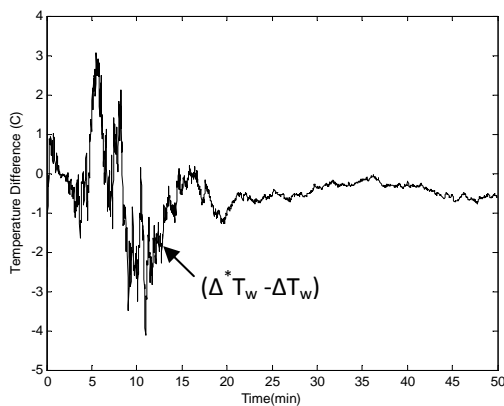


Figure (15) Typical temperature error response with 0.01 plant noise uncertainty.

References

- [1] Weisman, J. and Eckart, R., 1984, "Modern Power Plant Engineering", Prentice-Hall, Englewood Cliffs.
- [2] "AL-Mussiab Power Station Document", AL-Mussaib Thermal Power Plant Engineering Department, Ministry of Electricity, Baghdad, IRAQ.
- [3] Sorenson, H. W., 1985, "Kalman Filtering: Theory and Application", IEEE Press, New York.
- [4] Lumelsky, V. J., March 1983, "Estimation and Prediction of Unmeasurable Variables in the Steel Mill Soaking Pit Control System", IEEE-Transactions on Automatic Control, Vol. AC-28, pp. 388-400.
- [5] Tylee, J. L., March 1983, "On-Line Failure Detection in Nuclear Power Plant Instrumentation", IEEE Transactions on Automatic Control, Vol. AC-28, pp. 406-415.
- [6] Huisman, L., Beerkens, R. and Backx, T., 2001, "Estimation of Process Variables in a Glass Melting Furnace", http://www.tno.nl/Docs/DMP/glass-group2001/Posterleo_2001.pdf.
- [7] Sa'id, W. K. and AL-Kubaissy, O. F., 2002, "Estimation of Unmeasurable Molten Metal Temperature of Induction Furnaces by Kalman Filtering Technique", 3rd National Conference on Computers, Control and Systems Eng. (CCSE), UOT.
- [8] Fluerasu, A. and Sutton, M., September 2003, "Kalman-Predictive-Proportional-Integral-Derivative (KPPID) Temperature Control", AIP Conference Proceeding, Vol. 684, No. 1, pp. 933-938.
- [9] Ben-Yaacov, G. Z. and Bohn, J. G., December 1982 "Methodology for Real-time Calculation of Temperature Rise and Dynamic Rating for Distribution System Duct Banks", IEEE-Transactions on Power Apparatus and Systems, Vol. PAS-101, No.12, pp. 4604-4610.

- [10] Holman, J. P., 1989, "Heat Transfer", McGraw-Hill, Inc.
- [11] Al-Ubaidy, M. A., 1994, "Charge Temperature Estimation of an Induction Furnace", M.Sc., Thesis, Al-Nahrain University.
- [12] Oliewi, B. K., 2005, "Kalman Estimator Design for the Boiler Drum Wall Temperature Differentials during Start Up", M.Sc., Thesis, University of Technology.
- [13] Welch, G. and Bishop, G., 2006 "An Introduction to the Kalman Filter", ACM, Inc.
- [14] Kanjilal, P. P., 1995, "Adaptive Prediction and Predictive Control", IEE Control Engineering Series 52.
- [15] Girgis, A. A. and Brown, R. G., July 1981 "Application of Kalman Filter in Computer Relaying", IEEE-Transactions on Power Apparatus and Systems, Vol. PAS-100, No. 7, pp. 3387-3397.

DEVELOPING A 3-D MATHEMATICAL MODEL FOR NETWORK TOPOLOGY BASED ON GRAPH THEORY

Dr. Laith Jasim Saud
Control and Systems Eng. Dept.
University of Technology
Baghdad-IRAQ
laith_js@yahoo.com

Abstract

Communication networks efficiency depends upon many factors among which is the “Topology”, which makes topology optimization an important issue to care for. One important thing in optimization problems is the formulation of objective functions. For the case of topology design it is not a straightforward matter to develop an efficient topology model as well as objective functions to be used in the optimization process, and an effective unconventional approach is needed. This paper is concerned with enhancing the already existing set of formulas, relating topology and topology properties modeling and topology design objectives, by proposing a 3-dimensions way of modeling that can serve network analysis, design, and optimization. The approach is based on graph theory. The proposed model and formulas can be easily programmed.

Keywords: *Network topology, Modeling, Graph theory.*

1- Introduction

One of the very important matters in engineering analysis and design is how to model the given problem as all. By the problem it is meant the system under consideration as well as the design targets or objectives. The problem representative model should reflect fairly the features of interest in the given system besides the

design objectives, and should be suitable for the following analysis and design work [1,2]. For this to happen, the representation adopted must suits a sufficient and efficient analysis, design, and optimization methods and tools, whether those already existing in the first place, or those that could be developed. When optimization methods are judged their suitability, time it consumes, difficulty, implementation robustness, and accuracy, are among the things to be considered and the objective function is one of things affecting these points [3]

Different modeling ways do exist among which and the most important is the mathematical one. The model must be as much as possible direct, simple, general, reasonable mathematically, and practical for computation and programming purposes. Model generality implies that it could serve a lot of work purposes or targets and flexible to cover different features of interest in representation, analysis purposes, and design features and targets [1].

Graph Theory (G.T.) is very useful for the purposes mentioned above when it comes to modeling, analysis, and design of communication network topology, noticing that topology itself is a structure [4]. Topology design optimization is a very important issue as it affects cost, survivability, and efficiency of the communication network [5]. Routing is just an example of network related matter that is affected by topology [6].

This work proposes a 3-dimensional way for modeling the topology. The approach of

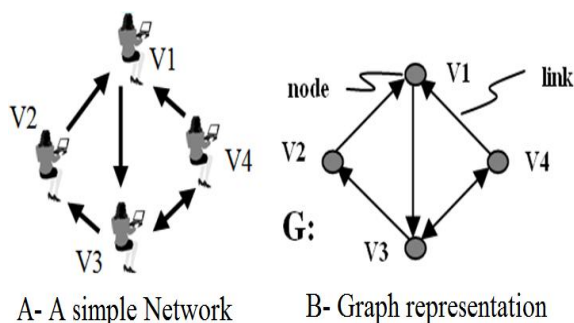
developing the proposed model makes use of G.T. ideas, tools, and theorems.

2- Modeling Network Topology and Its Properties with Graph Theory

Graph theory is a branch of mathematics concerned mainly about structures. This theory is concerned with patterns of relationships among pairs of abstract elements [2]. Graph theory has many practical applications in various disciplines like engineering, biology, computer science, economics, mathematics, medicine, and social science [7].

Graphs are excellent modeling tools, and graph theory is quite useful when the main interest is in the structural properties of any empirical system as it provides concepts, theorems, and methods appropriate to the analysis of structures [7,4].

Graph theory represents structures as graphs which in turn will be represented as matrices. These matrices of the way nodes are connected in the graph are called adjacency matrices. Graph theory could be used to model network topologies, keeping in mind that the topology of a network is in reality a structure, as well as many topology properties and measures [1]. Figure (1) shows a simple network with its corresponding graph and adjacency matrix.



$$A(G) = \begin{matrix} & V1 & V2 & V3 & V4 \\ \begin{matrix} V1 \\ V2 \\ V3 \\ V4 \end{matrix} & \begin{bmatrix} 0 & 0 & 1 & 0 \\ 1 & 0 & 0 & 0 \\ 0 & 1 & 0 & 1 \\ 1 & 0 & 1 & 0 \end{bmatrix} \end{matrix}$$

C- Adjacency matrix representation
(Note: Diagonal elements are considered zeros)

Figure (1): A sample network topology with its representative graph and adjacency matrix.

With graph theory many useful topology properties could be computed. Figure (2) shows a 10 nodes sample network with its adjacency matrix and two properties, the first of which, the distance (geodesic) matrix, gives the shortest paths length between nodes while the other, reachability matrix, shows what a given node can reach of the other nodes [1].

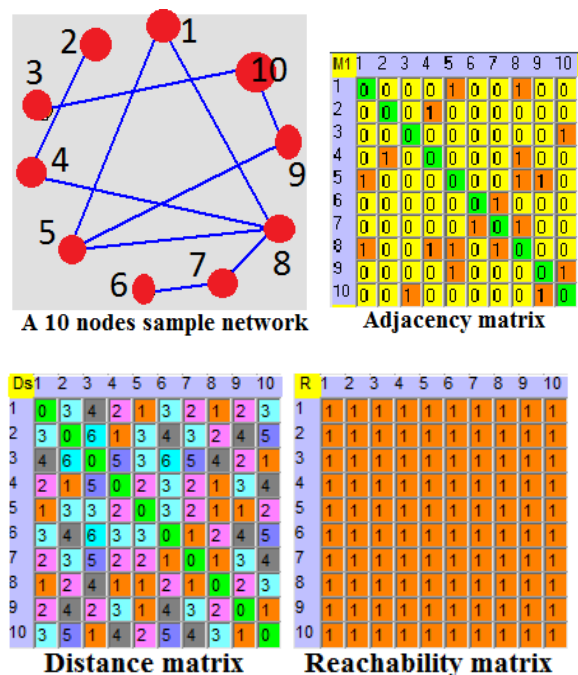


Figure (2): A 10 nodes sample network with its adjacency matrix and two properties.

Another important matrix is the number of geodesics matrix which gives the number of geodesics between each pair of nodes. Figure (3) shows an example for this matrix [1].

All of the matrices given so far are two dimensional arrays. Finding the distance matrix involves in part of it repetitive logic multiplication of the adjacency matrix [2]. Each stage of multiplication reveals paths of certain length.

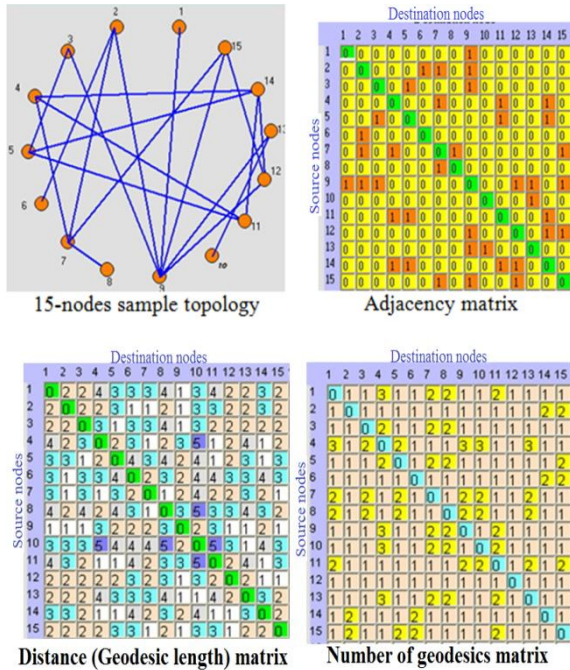


Figure (3): A 15 nodes sample network with its adjacency and geodesics matrices.

For example, logic multiplication of adjacency matrix (A) by itself, i.e. $A^2 \#$, results in a matrix indicating the paths of two links length, and $A^3 \#$ indicates the paths of three links length, and so on. But one of the disadvantages with this approach is that it results in invalid paths. For example in Figure (4), $A^4 \#$ indicates that there is a path of length four between node 1 and node 4 which moves through nodes this way, 1,5,4,3,4. Of course such a path is not acceptable as part of the path which passes from node 4 to 3 and back to 4 is not needed at all.

Moreover, the matrices produced with the given approach do not tell the nodes through which the path travels through. Also two matrices are needed to indicate the geodesics length and the number of geodesics.

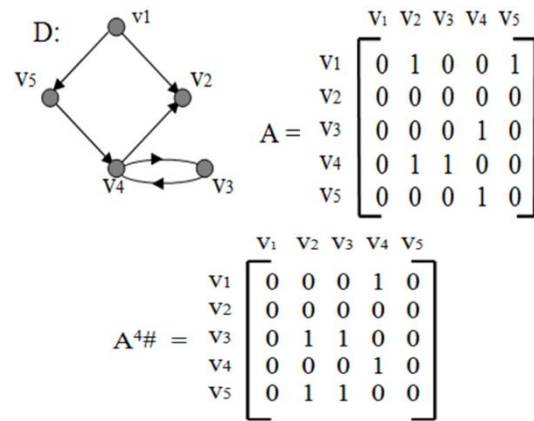
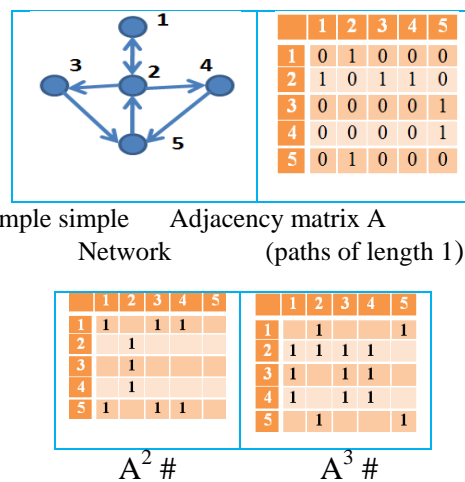


Figure (4): A 5 nodes network with the adjacency matrix and the matrix of Paths of length four ($A^4 \#$).

3- A Proposed 3-Dimensional Modeling Array.

To avoid some limitations of the two dimensional matrix approach mentioned earlier, here a three dimensional array is proposed. To explain the difference between the two cases, the sample network of Figure (5) will be used to apply the proposed modeling approach.

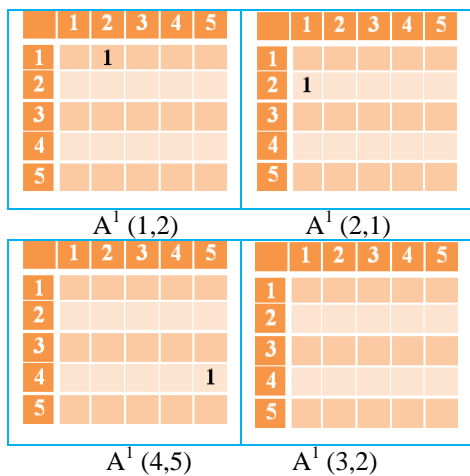


A sample simple Network Adjacency matrix A (paths of length 1)

Figure (5): A sample network with the adjacency matrix and its logic powers of 2, and 3.

The proposed method adopts the idea of modeling paths rather than links. But of course the links are still contained within the

paths models. It also adopts the concept of levels. So $A^1(3,2)$ (or $A(1,3,2)$) means paths from node 3 to node 2 of level or length 1, and $A^4(1,5)$ (or $A(4,1,5)$) means paths from node 1 to node 5 of length 4, and so on. As it is seen, this is a three dimensional representation of paths. For each level, i.e. path length, each path will be represented by a two dimensional array. Figure (6) gives some examples of paths representation regarding the sample network of Figure (5).



Note: empty cells here mean 0 and states for no link existence.

Figure (6): Representation of some sample paths for the network in Fig.(5).

The proposed approach could be used to represent topology and to compute its properties and goodness measures. Also the model could be used to compute path weights depending on links weights. A sample for such a model for a 5 nodes network is shown in figure (7). The shown array is of size $(4 \times 5 \times 5)$. For such a network the maximum path length will be 4, and in general the maximum path length equals the number of nodes in the network minus one. Such an array gives the following information:

- Direct links between nodes (i.e. paths of length 1). This means that the adjacency matrix will be included in this model.

- Paths existence between nodes and length of such paths and the number of such paths.
- The nodes through which a given path travels.

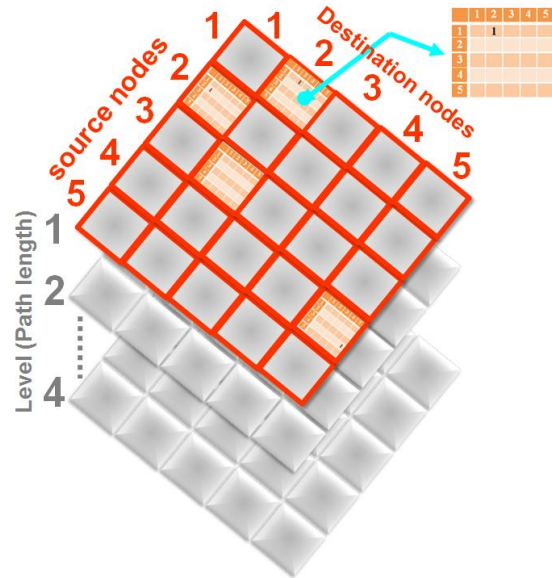


Figure (7): A 3-dimensions array which models topology for a 5 nodes network.

To fill the whole cells of such an array with a network of n nodes, the following algorithm is used:

- Do a loop for $k=2$ to $n-1$
- Do a loop for $s=1$ to n
- Do a loop for $d=1$ to $n, s \neq d$
- Find:

$$A^k(s,d) = \sum_{i=1}^n (A^1(s,i) + A^{k-1}(i,d)) \times (PE(A^1(s,i))) \times (PE(A^{k-1}(i,d))) \dots \dots \dots (1)$$

Where:

- n = number of nodes in the network.
- S,d : source and destination nodes.
- PE = Path Existence
- $PE A^z(v,w)$ means path existence between node v and w with length z and is found using the following formula:

$$\bigcup_{m=1}^n \bigcup_{l=1}^n a_{A^z(v,w)}(m,l)$$
 Where $a_{A^z(v,w)}(m,l)$ is an element of the matrix $A^z(v,w)$ defined by row m and column l , and \cup stands for the OR function.
- Path length from a node to itself is zero.

- v. Eliminate possibility that the target path from s to d contains a link from s to d:

$$A^k(s, d) = (a_{A^k(s,d)}(s, d) \text{ NAND } a_{A^1(s,d)}(s, d)) \times A^k(s, d) \dots\dots\dots (2)$$

- vi. Eliminate possibility of link repetition in a path:

$$A^k(s, d) = [\prod_{i=2}^n (\prod_{j=1}^{i-1} a_{A^k(s,d)}(i, j) \text{ NAND } a_{A^k(s,d)}(j, i))] \times A^k(s, d) \dots\dots\dots (3)$$

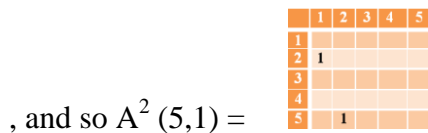
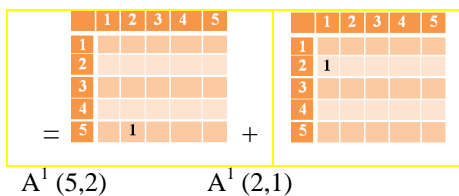
- vii. Back to loop iii.
- viii. Back to loop ii.
- ix. Back to loop i.
- x. End.

In what follows the procedure above will be used to find paths of levels (length) other than 1 for some sample cases.

Example ((1)): finding $A^2(5,1)$.

Step 1: Find preliminary $A^2(5,1)$:
 $A^2(5,1) = \sum_{i=1}^n (A^1(5, i) + A^1(i, 1)) \times (PE(A^1(5, i))) \times (PE(A^1(i, 1))) \dots\dots (4)$

Equation 4 then yields:
 $A^2(5,1) = 0 + A^1(5,2) + A^1(2,1) + 0 + 0 + 0$



, and so $A^2(5,1) =$

The result is very indicative and it indicates that there is single path of length 2 links from node 5 to node 1.

Step 2: Eliminate the possibility that the path contains link 5,1:

$$A^2(5,1) = (a_{A^2(5,1)}(5,1) \text{ NAND } a_{A^1(5,1)}(5,1)) \times A^2(5,1) \dots\dots\dots (5)$$

So: $A^2(5,1) = (0 \text{ NAND } 0) \times A^2(5,1) = A^2(5,1)$

Step 3: Eliminate possibility of link repetition in the path:

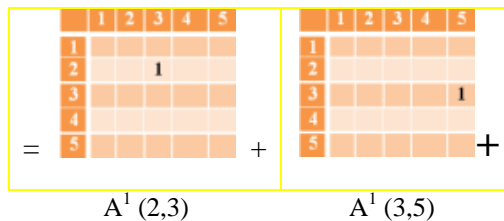
$$A^2(5,1) = [\prod_{i=2}^n (\prod_{j=1}^{i-1} a_{A^2(5,1)}(i, j) \text{ NAND } a_{A^2(5,1)}(j, i))] \times A^2(5,1) \dots\dots\dots (6)$$

And so: $A^2(5,1) = 1 \times A^2(5,1) = A^2(5,1)$

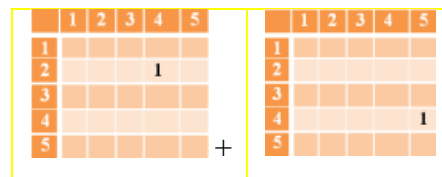
Example ((2)): finding $A^2(2,5)$:

Step 1: Find preliminary $A^2(2,5)$:

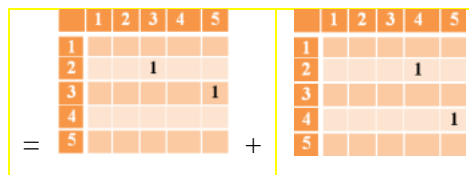
$$A^2(2,5) = \sum_{i=1}^n (A^1(2, i) + A^1(i, 5)) \times (PE(A^1(2, i))) \times (PE(A^1(i, 5))) = 0 + 0 + A^1(2,3) + A^1(3,5) + A^1(2,4) + A^1(4,5) + 0$$



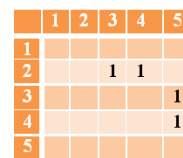
$A^1(2,3)$ $A^1(3,5)$



$A^1(2,4)$ $A^1(4,5)$



and so $A^2(2,5) =$



The next steps could be checked as well and still the result will be as it is as there are no eliminations. The result indicates that there are two paths of length 2 links from node 2 to node 5. The first is 2,3,5 and the second is 2,4,5.

Example ((3)): finding $A^3(2,4)$:
Following the same procedure as above we get:

$$A^3(2,4) = A^1(2,1) + A^2(1,4)$$

	1	2	3	4	5
1					
2	1				
3					
4					
5					

	1	2	3	4	5
1		1			
2				1	
3					
4					
5					

$$= A^1(2,1) + A^2(1,4)$$

	1	2	3	4	5
1		1			
2	1			1	
3					
4					
5					

With applying the elimination step $A^3(2,4)$ will be 0 which means that it does not exist as a valid path.

4- Assessments of Results and Conclusions

A three dimensional model has been proposed to model network topology. The model has been developed based on graph theory ideas and theorems. The proposed model adds some important features to The proposed model can provide the following information about topology:

- The adjacency matrix of the network topology which defines the direct links and direction between the network nodes.
- The existence of paths between any nodes pair, and the number of such paths.
- The length of the existence paths.
- The nodes through which a given path could travel starting from a given source node towards a given destination node.

In addition to the features just mentioned, the new model excludes any invalid paths in which a link is traversed more than once.

The introduced model can serve computing topology properties and topology measure as well. The model can be used to compute paths weights depending on links weights when they are defined. The formulas developed in the work suits programming purposes, and could be used to develop objective functions for network topology optimization approaches and programs.

References

- [1] Saud L. J., 2006, "Topology Design Optimization Using GA.", PhD Thesis, Control and Systems Engineering Department, University of Technology.
- [2] Harary F., 1965, "Structural Models: An Introduction to the Theory of Directed Graphs", John Wiley & Sons.
- [3] Coello C. A., 1998, "An Updated Survey of GA_BasedMultiobjective Optimization Techniques", Technical report (Lania-RD-98-08), Laboratorio Nacional de Informatica Avanzada (LANIA), Xalapa, Veracruz, Mexico. (ACM computing Surveys- <http://citeseer.ist.psu.edu/coello98updated.html>).
- [4] Freeman, L., 1978/79, "Centrality in Social Networks Conceptual Clarification", Social Network Journal, No 1.
- [5] Nazrul,S., 1998, "Survivability Analysis of Two Specific 16-Node, 24-Link communication Networks", Master's Thesis, Electrical and Computer Engineering, Virginia Polytechnic Institute and State University.
- [6] Streenstrup,M., 1995, "Routing in Communication Networks", Prentice-Hall Inc.
- [7] Agnarsson, G., Greenlaw, R., 2007, "Graph Theory: Modeling, Applications, and Algorithms", Pearson Education Inc.

A SIMULATION MODEL FOR IRRIGATION SCHEDULING TO MAIZE CROP IN MOSUL AREA

Ahmed Azhor Thanoon

Technical Institute of Mosul

aazhor@yahoo.com

Abstract

This study aims to determining the irrigation scheduling for maize crop during autumn season in Mosul area with a computerized simulation model and applied this results in experiment carried out in field of Technical Institute of Mosul for season 2009 .The simulation was based on 16 years of climatologically data for the period1985-2000for Mosul station , which include average daily maximum and minimum temperatures , maximum and minimum relative humidity, wind speed , and sunshine hours, and were used to calculate daily reference evapotranspiration with Penman-Monteith equation and crop evapotranspiration with dual crop coefficient .The results of simulation model were compared with measured using correlation coefficient r and it gave a good relation for this results to four irrigation levels.

Keywords: *Simulation model, Irrigation scheduling, Maize crop, Mosul area .*

1- Introduction :

The computer models are essential for management of irrigation system and also have an important role to mitigate lack water resources problems in dry and semidry regions. Many computer models were developed and written in different languages to simulate the soil water balance for irrigation scheduling such as CROPWAT (Smith 1992) , DSS (Abdullah and Munir 2003), ISIAMod (Igbadun et al 2006) .Irrigation scheduling is defined as the process of determining when to irrigate and how much water to apply (Hill and Allen 1996).How much and how often water has to be given depends on the irrigation water need

of the crop. The irrigation water need is defined as the crop water need minus the effective rainfall. It is usually expressed in mm/day or mm/month (Brouwer et al 1989). The importance of irrigation scheduling is magnified when water supply is short and costs are high or when soil conditions exist which restrict water movement or root development (Jensen et al 1970). Therefore it is the primary tool to improve water use efficiency and raise yields, and in turn will lead to higher incomes and greater availability of water resources, and provoke a positive effect on the quality of soils and groundwater (Smith et al 1996). There are several common irrigation scheduling approaches include (Hill and Allen 1996):

1. Irrigating on fixed intervals or following a simple calendar, i.e., when a water turn occurs or according to a predetermined schedule;
2. Irrigating when one's neighbour irrigates;
3. Observation of visual plant stress indicators;
4. Measuring (or estimating) soil water by use of instruments or sampling techniques such as feel, gravimetric, electrical resistance (gypsum) blocks, tensiometers or neutron probes;
5. By following a soil water budget based on weather data and/or pan evaporation;
6. Some combination of the above

The objective from this study is to determining irrigation scheduling for maize crop during autumn season in Mosul area with a computerized simulation model and applied this results in experiment in Mosul area in north of Iraq .

2-Evapotranspiration (ET):

Evaporation and transpiration occur simultaneously and there is no easy way of distinguishing between the two processes. Apart from the water availability in the topsoil, the evaporation from a cropped soil is mainly determined by the fraction of the solar radiation reaching the soil surface. This fraction decreases over the growing period as the crop develops and the crop canopy shades more and more of the ground area. When the crop is small, water is predominately lost by soil evaporation, but once the crop is well developed and completely covers the soil, transpiration becomes the main process. The ET from crop surfaces under standard conditions is determined by crop coefficients (Kc) that relate ETc to ETo. The ET from crop surfaces under non-standard conditions is adjusted by a water stress coefficient (Ks) and/or by modifying the crop coefficient (Allen et al 1998).The crop evapotranspiration , ETc, is calculated by multiplying the reference crop evapotranspiration, ETo, by a crop coefficient , Kc (Allen et al 1998) :

$$ET_c = K_c E_{T_o} \text{ -----(1)}$$

Where

ETc : crop evapotranspiration [mm day⁻¹],

Kc :crop coefficient [dimensionless],

ETo: reference crop evapotranspiration [mm day⁻¹].

The reference evapotranspiration (ETo) is defined as the rate of evapotranspiration from a hypothetical crop with an assumed crop height (12 cm) and a fixed canopy resistance (70) [s m⁻¹], and albedo (0.23) which would closely resemble evapotranspiration from an extensive surface of green grass cover of uniform height, actively growing, completely shading the ground and not short of water (Smith et al 1992). The measurement or estimation of grass-reference evapotranspiration ETo is one of the critical components of irrigation scheduling and water management (Irmak et al 2005).It can be computed from meteorological data

(radiation or sunshine hours , air temperature, air humidity and wind speed data) with FAO Penman-Monteith equation (Allen et al 1998). The FAO Penman-Monteith equation is used in this model , see Fig.1 in Appendix1.

The crop coefficient, Kc, is basically the ratio of ETc to the reference ETo, and it represents an integration of the effects of major characteristics that distinguish the crop from the reference. These characteristics are crop height, crop-soil surface resistance, and albedo of the crop-soil surface. Kc is defined for pristine conditions having no water or other ET reducing stresses (Allen et al 2000). Allen et al (1998) classified Kc to two types : the single crop coefficient and the dual crop coefficient (the basal crop coefficient Kcb to describe plant transpiration , and the soil evaporation coefficient Ke to describe evaporation from the soil surface) . Kc varies during the growing season as plants develop , as the fraction of ground covered by vegetation changes, and as plants age and mature (Allen et al 2005).The dual crop coefficient is used in this model , see Fig 1 in Appendix 1.

3-Soil water balance:

The calculation of the scheduling program is based on a soil water balance, Where the soil moisture status is determined based on a daily accounting of all ingoing and outgoing water in the root zone (Smith 1992). This is expressed in term of depletion at the end of the day by equation of Allen et al (1998):

$$D_{r,i} = D_{r,i-1} - (P - RO)_i - I_i - CR_i + ET_c + DP_i \text{ --(2)}$$

where

D_{r, i} : root zone depletion at the end of day i [mm],

D_{r,i-1} : water content in the root zone at the end of the previous day, i-1 [mm],

P_i : precipitation on day i [mm],

RO_i : runoff from the soil surface on day i [mm],

I_i : net irrigation depth on day i that infiltrates the soil [mm],

CR_i: capillary rise from the groundwater table on day i [mm],
 ET_c: crop evapotranspiration on day i [mm],
 DP_i: water loss out of the root zone by deep percolation on day i [mm].

The values of precipitation, runoff, deep percolation and capillary rise from the groundwater table were assumed equal zero in this model.

4-Readily available water RAW:

Allen et al (1998) defined RAW as the fraction of TAW that a crop can extract from the root zone without suffering water stress:

$$RAW = p \text{ TAW} \text{ -----(3)}$$

where

RAW: the readily available soil water in the root zone [mm],

p : average fraction of total available soil water (TAW) that can be depleted from the root zone before moisture stress (reduction in ET) occurs [0 - 1],

The depletion p are assumed 0.45 , 0.55 , 0.65 and 0.75 in this model .

TAW : the total available soil water in the root zone [mm] .

TAW is the amount of water that a crop can extract from its root zone, and its magnitude depends on the type of soil and the rooting depth (Allen et al 1998) :

$$TAW = 1000 (\theta_{FC} - \theta_{WP}) Z_r \text{ ----- (4)}$$

where

θ_{FC}: the water content at field capacity [m³ m⁻³],

θ_{WP} :the water content at wilting point [m³ m⁻³],

Z_r : the rooting depth [m].

The depth of effective root zone can be estimate from (Allen et al 1998) ,see Fig 1 in Appendix 1 . In this model (θ_{FC} - θ_{WP}) is assumed 0.15 m³ m⁻³ from the typical values of silty clay loam soil (Allen et al 1996).

5-The simulation model:

The simulation model is shown in Fig 1 in Appendix 1, it can be written with any languages in computer, and was design to estimate:

1. Daily reference crop evapotranspiration (ET_o) with FAO Penman-Monteith equation .
2. Daily dual crop coefficient K_c=K_{cb}+K_e.
3. Daily crop evapotranspiration (ET_c) .
4. Daily soil water depletion in the root zone Dr_i.
5. Irrigation date when Dr_i reaches RAW and the how much from the value of Dr_i .

6-Materials and Methods:

6-1 Experiment:

The experiment was carried out at Institute Technology of Mosul which located in north of Iraq and raised 247 m above sea level during autumn season of 2009 in 16th July , the experiment was designed to 4 plots with size 2 m² and 2 replications and irrigated using bucket .The soil texture is silty clay loam and water content at field capacity was 36 m³ m⁻³ and bulk density was 1.5 gm cm⁻³,the soil properties were given in Table 1 in Appendix 2.

6-2 Climate area of study:

Average daily maximum and minimum air temperature , maximum and minimum relative air humidity, wind speed , and sunshine hours data for five months (July to November) to 16-year period 1985-2000 were obtained from Mosul station which located at latitude 36° 19' in North of Iraq , used to estimate the daily reference crop evapotranspiration (ET_o) using FAO Penman-Monteith equation .

6-3 Basal crop coefficient:

The values of the basal crop coefficient K_{cb} for maize were obtained from (Allen et al 1998) to standard climate then adjusted to climate of Mosul.

7- Results:

7-1 Model results:

7-1-1 Irrigation water applied:

The weather, soil and crop data were used in this model to calculate the net irrigation depth water which used later in experiment for four depletion values (0.45,0.55,0.65,and 0.75). The depth and time of irrigation are listed in Table 2 in Appendix 2.

7-1-2 Water content:

The simulated water content by equation of Pereira and Allen (1999) see Fig 1 in Appendix 1 , are compared with measured water content which measured with drying at 105 °C after the samples were taken from soil at depths 15 , 30 , 50 and 75 cm using auger soil for four treatment then multiplying by bulk density. The results are plotted for the four treatments in the Fig 2 , Fig 3 , Fig 4 and Fig 5 in Appendix 3. The water content measured at depths 30 , 50 and 75 cm closed from simulated water content for the 0.45 and 0.55 depletion levels because the irrigation interval is minimal.

7-1-3 The consumptive crop water use:

The consumptive crop water use (CWU) defined as the depth of water (mm) utilized by a crop through ET and cultivated under given farming conditions in a given growing environment (Pereira and Allen 1999).It can be measured from soil moisture studies .In this research the CWU was measured by multiplying the change in mean moisture content of soil profile on base volumetric (before and after irrigation) , $\Delta\theta$, by the rooting depth for each irrigation , and before harvest .The Fig 6 in Appendix 3 shows the simulated and measured the consumptive crop water use .The correlation coefficient r between simulated and measured the consumptive crop water use is 0.98 .

7-2 Results of experiment:

7-2-1 The crop properties:

The crop properties were measured for five plants elected to each treatment, and listed in Table 3 in Appendix 2. From the Table 3 concluded that the maximum yield of crop gave treatment 1 under depletion 0.45 because it received maximum water applied.

8- Conclusion:

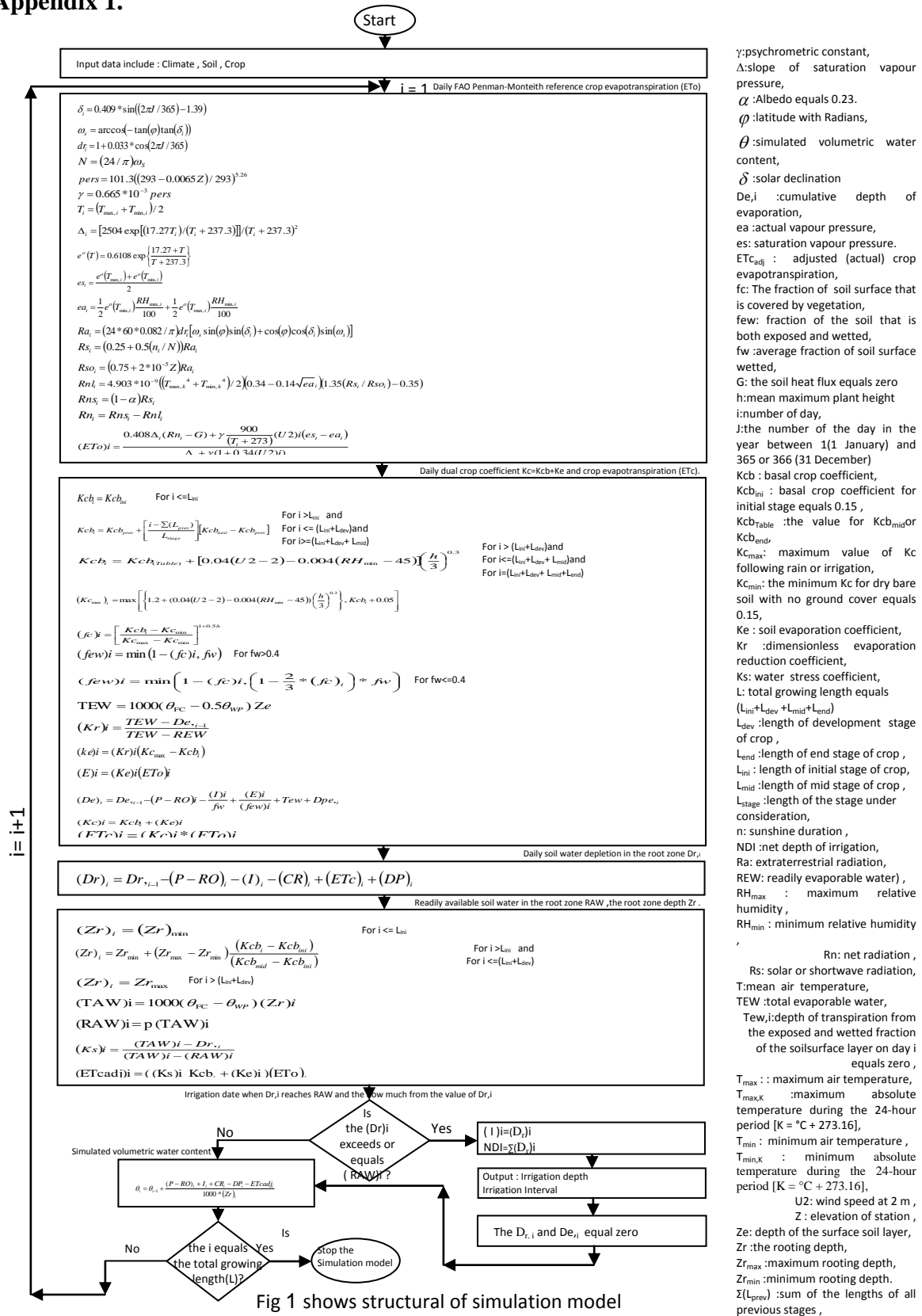
Irrigation scheduling is contributed in reducing water losses and improving production of yield. The simulation model is used to estimate how much and when irrigated for maize crop during autumn season in Mosul area. It depend on Penman-Monteith equation and dual crop coefficient for calculation irrigation scheduling .The results are showed that irrigation scheduling at 0.45 depletion gave maximum the net irrigation depth, number of irrigations and yield .

References:

- [1] Abdullah, M, N, and Munir , A, 2003, "decision support system (DSS) for irrigation water management in sugarcane plantation", J. Sains&Teknologi , Vol.3 , No.1:34-42.
- [2] Allen, R,G, Pereira L,S, Raes D, and Smith M, 1998," Crop evapotranspiration. Guidelines for computing crop water requirements" FAO Irrigation and Drainage Paper, 56, Rome, Italy, 300 pp.
- [3] Allen, R, G, M, Smith, L, S, Pereira, D, Raes, and J, L,Wright, 2000," Revised FAO Procedures for Calculating Evapotranspiration: Irrigation and Drainage Paper No,56 for testing in Idaho" , In Proc. Watershed Management and Operations Management, June 20-24, Fort Collins, CO.
- [4] Allen, R, G, Pereira, L, S, Smith, M, Raes, D, and Wright, J, L, 2005," The

- FAO-56 dual crop coefficient method for predicting evaporation from soil and application extensions " , J. Irrig. Drain. Eng., Div, (ASCE), 131(1),2–13.
- [5] Allen, R, G, Pruitt, W, O, Businger, J, A, Fritschen, L, J, Jensen, M, E, and Quinn, F, H, 1996, Evaporation and Transpiration, "ASCE handbook of hydrology" , Wootton et al, eds, Chap. 4, New York ,125–252.
- [6] Brouwer , C, Prins , K, and Heibloem , M, 1989, " Irrigation Water Management: Irrigation Scheduling ",FAO Training manual no. 4, Rome, Italy.
- [7] Hill, R,W, and Allen, R,G, 1996, "Simple irrigation calendars: a foundation for water management, In: Irrigation Scheduling: From Theory to Practice " , eds . Smith ,M, et al ,FAO Water Reports , Vol. 8 ,pp.69-74, International Commission on Irrigation and Drainage and FAO , Rome,Italy.
- [8] Igbadun, H, Mahoo H, Tarimo A, and Salim B, 2006, "Irrigation Scheduling Scenarios Studies for a Maize Crop in Tanzania Using a Computer-based Simulation Model" , Manuscript LW 06 007, Vol. VIII, November.
- [9] Irmak, S, M, Dukes, M, D, and Jacobs , J,M , 2005, " Using Modified Bellani Plate Evapotranspiration Gauges to Estimate Short Canopy Reference Evapotranspiration " , J. Irrig. Drain. Eng., Div, (ASCE) 131(2),164–175.
- [10] Jensen, M , E, Robb, D,C, and Franzoy C, E, 1970, "Scheduling irrigations using climate-crop-soil data " , J. Irrig. and Drain. Div, (ASCE), 96(IR1):25-38.
- [11] Pereira, L, S, and Allen, R, G, 1999, Crop Water Requirements , " CIGR (International Association of Agricultural Engineers) handbook of agricultural engineering " , Vol. I, Sec. 1.5.1, ASAE, St, Joseph, Mich., 213–262.
- [12] Smith , M , Pereia , L, S , Berengena , J, Itier, B , Goussard, J, Ragab, R, Tollefson, L, and P, van Hoffwegen (eds),1996, " Irrigation Scheduling: From Theory to Practice " , FAO Water Reports , Vol. 8 , p.69-74 International Commission on Irrigation and Drainage and FAO , Rome , Italy .
- [13] Smith M., 1992, "CROPWAT-A computer program for irrigation planning and management " , FAO Irrigation and Drainage Paper, 46, Rome, Italy ,126 pp.
- [14] Smith, M , Allen, R, Monteith , J, L, Pereira, L, S , Perrier, A, and Segeren , A, 1992, "Report on the Expert Consultation for the Revision of FAO methodologies for crop water requirements" , FAO-AGL, Rome, Italy .

Appendix 1.



γ : psychrometric constant,
 Δ : slope of saturation vapour pressure,
 α : Albedo equals 0.23.
 ϕ : latitude with Radians,
 θ : simulated volumetric water content,
 δ : solar declination
 De_i : cumulative depth of evaporation,
 ea : actual vapour pressure,
 es : saturation vapour pressure.
 ET_{cadj} : adjusted (actual) crop evapotranspiration,
 fc : The fraction of soil surface that is covered by vegetation,
 f_w : fraction of the soil that is both exposed and wetted,
 f_w : average fraction of soil surface wetted,
 G : the soil heat flux equals zero
 h : mean maximum plant height
 i : number of day,
 J : the number of the day in the year between 1(1 January) and 365 or 366 (31 December)
 Kc_b : basal crop coefficient,
 $Kc_{b_{ini}}$: basal crop coefficient for initial stage equals 0.15,
 $Kc_{b_{table}}$: the value for $Kc_{b_{mid}}$ or $Kc_{b_{end}}$
 Kc_{max} : maximum value of Kc following rain or irrigation,
 Kc_{min} : the minimum Kc for dry bare soil with no ground cover equals 0.15,
 Ke : soil evaporation coefficient,
 Kr : dimensionless evaporation reduction coefficient,
 Ks : water stress coefficient,
 L : total growing length equals $(L_{ini} + L_{dev} + L_{mid} + L_{end})$
 L_{dev} : length of development stage of crop,
 L_{end} : length of end stage of crop,
 L_{ini} : length of initial stage of crop,
 L_{mid} : length of mid stage of crop,
 L_{stage} : length of the stage under consideration,
 n : sunshine duration,
 NDI : net depth of irrigation,
 Ra : extraterrestrial radiation,
 REW : readily evaporable water),
 RH_{max} : maximum relative humidity,
 RH_{min} : minimum relative humidity
 Rn : net radiation,
 Rs : solar or shortwave radiation,
 T : mean air temperature,
 TEW : total evaporable water,
 Tew_i : depth of transpiration from the exposed and wetted fraction of the soil surface layer on day i equals zero,
 T_{max} : maximum air temperature,
 $T_{max,K}$: maximum absolute temperature during the 24-hour period [K = °C + 273.16],
 T_{min} : minimum air temperature,
 $T_{min,K}$: minimum absolute temperature during the 24-hour period [K = °C + 273.16],
 $U2$: wind speed at 2 m,
 Z : elevation of station,
 Ze : depth of the surface soil layer,
 Zr : the rooting depth,
 Zr_{max} : maximum rooting depth,
 Zr_{min} : minimum rooting depth.
 $\Sigma(L_{prev})$: sum of the lengths of all previous stages,

Appendix 2.

Table 1 shows the soil properties of experiment.

Depths	0-25 cm	25-50 cm	50-75 cm
Clay %	24.775	40	40
Silt %	32.275	44.625	44.7
Sand %	42.95	15.375	15.3
Texture	loam	Silty clay loam	Silty clay loam
Electric conductivity (ds m ⁻¹)	0.1	0.1	0.2
PH	7.94	7.8	7.32
Sodium Na (ppm)	10	15	15
Potassium K (ppm)	2	3	1

Table 2 shows model results the depth and time of irrigation which used in experiment.

Treatment 1(0.45p)		Treatment 2(0.55p)		Treatment 3(0.65p)		Treatment 4(0.75p)	
Time	Depth mm						
16/7	31	16/7	31	16/7	31	16/7	31
19/7	22	19/7	22	20/7	26	21/7	29
21/7	17	22/7	23	24/7	26	26/7	30
23/7	18	25/7	24	28/7	27	31/7	29
25/7	18	28/7	24	1/8	27	5/8	30
27/7	18	31/7	24	5/8	29	18/8	60
29/7	18	3/8	24	13/8	42	2/9	98
31/7	18	6/8	24	23/8	62	18/9	113
2/8	18	11/8	33	5/9	91	7/10	116
4/8	18	18/8	45	18/9	99		
7/8	23	27/8	63	5/10	98		
10/8	25	2/9	83				
14/8	30	19/9	84				
19/8	39	31/9	84				
26/8	50	26/10	84				
4/9	65						
14/9	70						
23/9	70						
6/10	70						
26/10	70						
Sum	708		672		558		536

Appendix 2 continued.

Table 3 shows the yield of average five plants elected to each treatment.

Treatment	T1	T2	T3	T4
Grain (g/plant)	72	48	33	0
Number of ears in plant	1.2	1.2	1	1
Weight of ear (g)	214	132	115	50
Length of ear (cm)	24	22	20	10
Number of rows in ear	32	32	19	-
Weight of leaves and stem (g/plant)	256	184	153	135
Length of leaf (cm)	77	69	59	49
Width of leaf (cm)	10	8	6	5

Appendix 3.

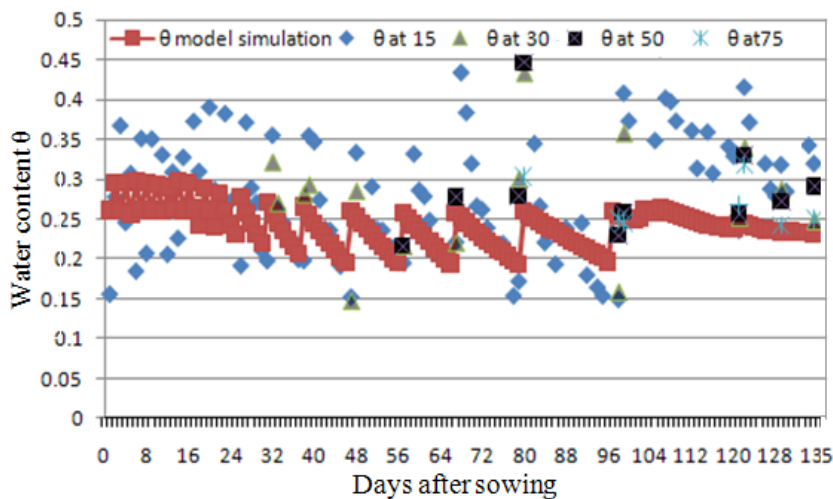


Fig 2 shows the simulated and measured water content for treatment 1

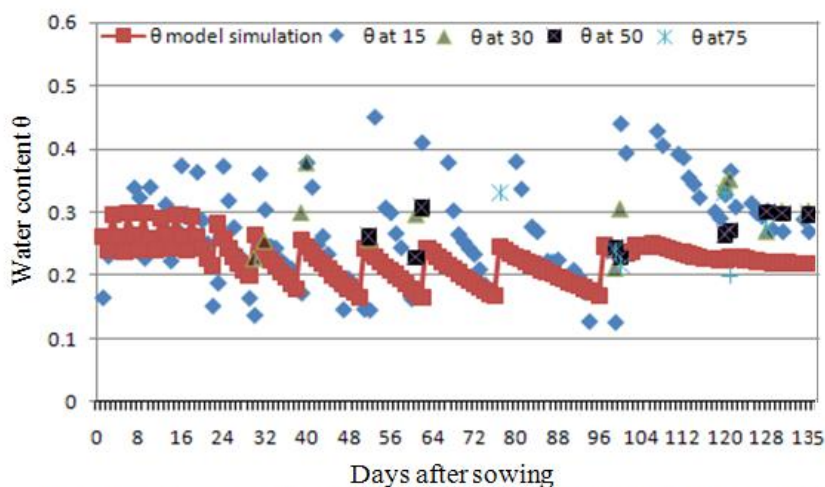


Fig 3 shows the simulated and measured water content for treatment 2

Appendix 3 continued .

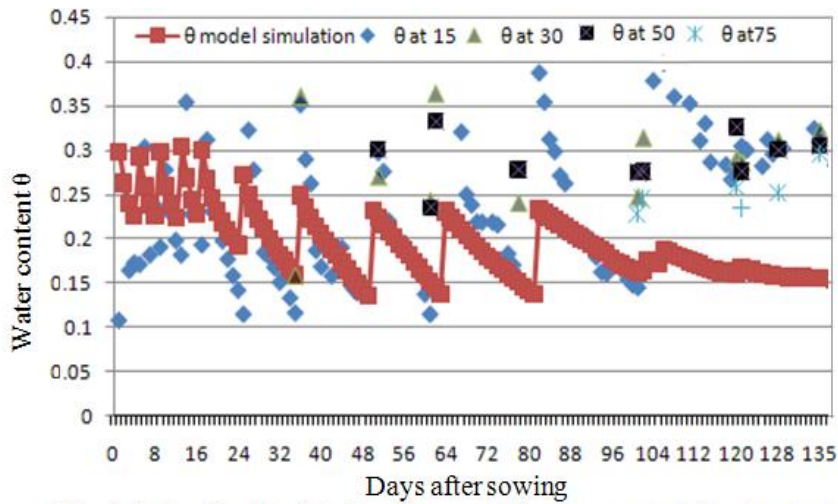


Fig 4 shows the simulated and measured water content for treatment 3

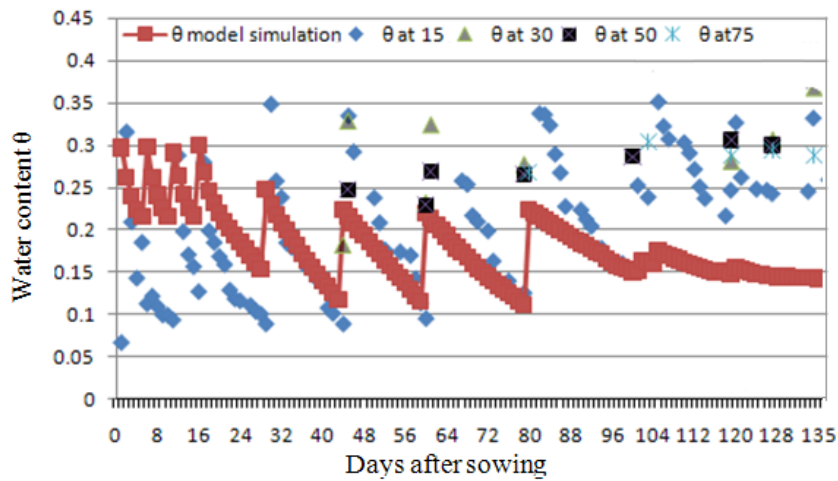


Fig 5 shows the simulated and measured water content for treatment 4

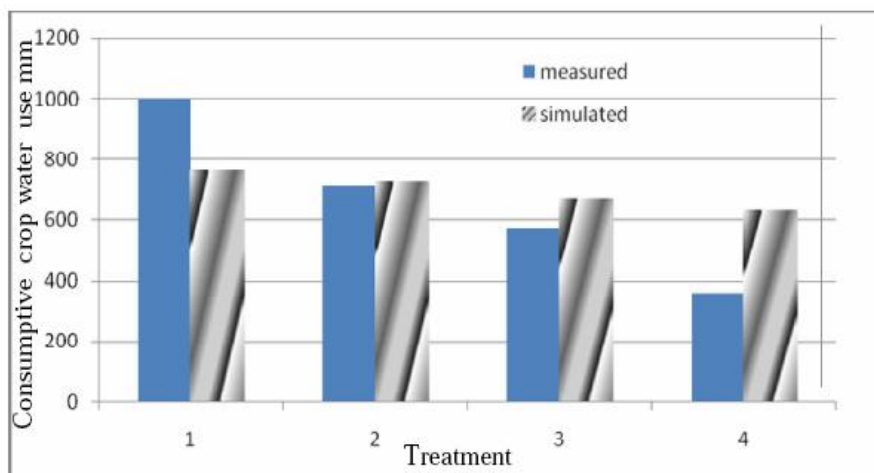


Fig 6 shows the simulated and measured the consumptive crop water use for all treatment

Topic 4

Computer Networks

INDOOR PROPAGATION MODELING FOR WIRELESS LOCAL AREA NETWORK (WLAN)

Samir M. Hameed

Iraqi Commission for Computers and Informatics (ICCI)

engsamir74@yahoo.com

Abstract

This paper presents indoor propagation modeling for wireless area network at 2.4GHz. Different propagation path loss models are simulated such as the International Telecommunication Union (ITU) and the log-distance path loss models. ITU model is tested in residential or office environments, and is examined; whatever the position of the Access Point (AP) and the WLAN cards on the same floor or in other floors. Log-distance path loss model is tested and simulated; from this model the effects of the shadowing deviation can be seen. Practical measurements will be taken by using a laptop equipped with the NETSTUMBLER 0.40 software to see the impression of walls and doors. Different charts are illustrated to view the responses of ITU and log-distance path loss models versus distances, path loss, transmitting power and receiving power. Practical data are also plotted in different cases, for open area between AP and mobile user and in randomly positions case.

Keywords: *WLAN, Indoor Propagation Models, ITU and Log Distance Path Loss Models*

1-Introduction

Today, wireless area networks WLANs based on the IEEE 802.11 standard constitute a practical and interesting solution of network connection offering mobility, flexibility, low cost of deployment and use [1,2]. The number of people using wireless networks in an indoor environment increases very rapidly. Therefore, an efficient planning and developing for indoor communication is definitely essential. The indoor environment is considerably different from the typical

outdoor environment and in many ways is more hostile. Modeling indoor propagation is complicated by the large variability in building layout and construction materials. In addition, the environment can change radically by the simple movement of people, closing of doors, and so on [3-6]. There are several causes of signal corruption in an indoor wireless channel; the primary causes are signal attenuation due to distance, penetration losses through walls or floors and multipath propagation. Signal attenuation over distance is observed when the mean received signal power is attenuated as a function of the distance from the transmitter. Thus, the received signal arrives as an unpredictable set of reflections or direct waves or both, each with its own degree of attenuation and delay.

The modeling of the propagation path needs to take into account a number of effects. These include the following [3-7]:

Path loss: The signal gets reduced in power with the distance it traverses following an inverse square law. So, ITU and log-distance path loss models are presented in this paper for understanding the affecting parameters in the path loss for WLAN.

Shadowing: Scattering environments along various propagation paths will be different, causing variations with respect to the nominal value given by the path loss. Some paths will suffer increased loss; while others will be less obstructed and have increased signal strength. The log-distance path loss model is a modified power law with a log-normal variability, similar to log-normal shadowing. Some "typical" values from Ref [3,4] are given in Table 3. This phenomenon is called shadowing or slow fading and is said to follow log-normal fading statistics.

Multipath: These effects are caused by the local scattering environment around the access point (AP). Fig. (1) shows a representation of multiple signal paths in an indoor wireless implementation, where the signal lines intersect are points of likely multipath reception problems and negative effects on wireless network signal integrity [8]. The solution of this problem is to get an access point closer to the users, or increasing the transmitted power.

This paper is organized as follow: Section 2 presents the ITU indoor path loss model and its expression. Log-distance path loss model is presented in Section 3. Section 4 presents calculations and measurements results for the following cases: single floor scenario based ITU model for both home and office conditions, multi floors scenario based ITU model, shadowing deviation effects scenario based log distance path model and finally the practical measurements. The last Section summarizes the paper and discusses the results.

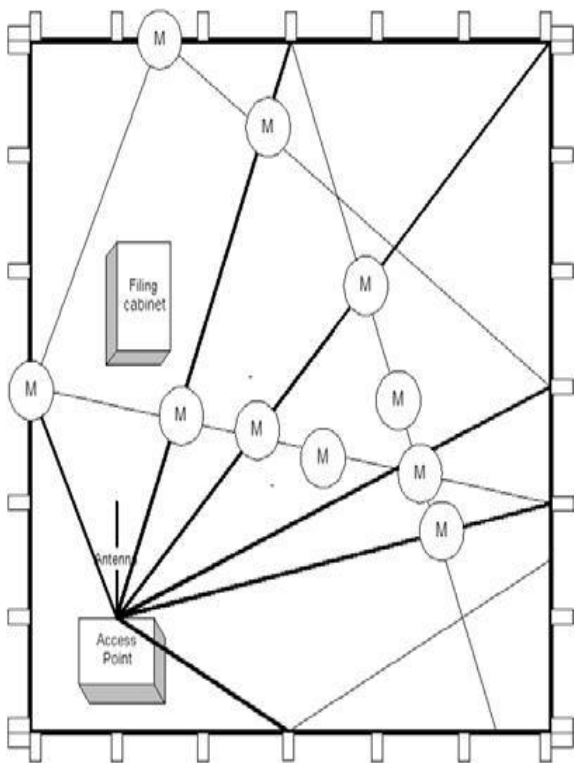


Fig. (1) A representation of multiple signal paths in an indoor wireless network.

2-The ITU Indoor Path Loss Model

The indoor propagation path loss prediction for ITU model in dB is [4,5,9] :

$$L_{total} = 20\text{Log}(f) + N\text{Log}(d) + Lf(n) - 28 \quad (1)$$

Where, N is the distance power loss coefficient, f is frequency of transmission in MHz, d is the distance in meter between AP and WLAN adapter card, $Lf(n)$ is the floor penetration loss factor and n is the number of floors between the transmitter and the receiver.

The distance power loss coefficient, N is the quantity that expresses the loss of signal power with distance. This coefficient is an empirical one, some values are provided in Table 1. The floor penetration loss factor is an empirical constant dependent on the number of floors the waves need to penetrate; some values are tabulated in Table 2.

Table 1 Power Loss Coefficient Values, N , for the ITU Model

Frequency Band	Residential Area	Office Area	Commercial Area
900 MHz	N/A	33	20
1.2-1.3 GHz	N/A	32	22
1.8 – 2 GHz	28	30	22
4 GHz	N/A	28	22
5.2 GHz	N/A	31	N/A

Table 2 Floor Penetration Loss Factor, $Lf(n)$, for the ITU Model

Frequency Band	No. of Floors	Residential Area	Office Area	Commercial Area
900 MHz	1	N/A	9	N/A
900 MHz	2	N/A	19	N/A
900 MHz	3	N/A	24	N/A
1.8 – 2.0 GHz	1-3	$4n$	$15+4(n-1)$	$6 + 3(n-1)$
5.2 GHz	1	N/A	16	N/A

3-Log-Distance Path Loss Model

The Log-Distance Path Loss model for indoor propagation path loss prediction in dB is [4,6,10] :

$$L_{total} = PL(d_0) + N \text{Log}\left(\frac{d}{d_0}\right) + X_s \quad (2)$$

Where, $PL(d_0)$ is the path loss at the reference distance in dB, N is the path loss distance exponent, d is the path distance in meter, d_0 is the reference distance 1m, X_s is a Gaussian random variable with zero mean and standard deviation of σ in dB.

The free-space loss is expressed as:

$$PL(d_0) = -20 \text{Log}\left(\frac{\lambda}{4\pi d_0}\right) \quad (3)$$

The log-distance path loss model is a modified power law with a log-normal variability, similar to log-normal shadowing. Some empirical measurements of coefficients N and σ in dB have shown the following values for a number of indoor wave propagation cases from References [3,4,10] are given in Table3.

Table 3, Typical Log-Distance Path Model Parameter Measurements

Building Type	Frequency of Transmission	N	σ (dB)
Vacuum, infinite space		20	0
Retail store	914 MHz	22	8.7
Grocery store	914 MHz	18	5.2
Office with hard partition	1.5 GHz	30	7.0
Office with soft partition	900 MHz	24	9.6
Office with soft partition	1.9 GHz	26	14.1
Textile or chemical	1.3 GHz	20	3.0
Textile or chemical	4 GHz	21	7.0/ 9.7
Paper or cereals	1.3 GHz	18	6.0
Metalworking	1.3 GHz	16/ 33	5.8/ 6.8

4-Calculations and Measurements Results 4.1-Single Floor Scenario Based ITU Model

In this section, single floor scenario is simulated based on ITU model, it has been tried in an environment of residential area and office area by considering application of WLAN using IEEE 802.11b standard with AP transmission frequency of 2.4 GHz. Let $L_f(n) = 0$ on the same floor, by substituting these values in eq.(1), the path loss expression for these values is:

$$L_{total} = 39.6 + N \text{Log}(d) \quad (4)$$

From the power loss coefficient values given in Table 1, for an office building the value of N is found to be 30 and 28 for home area. After simulation of Eq.(4), the response of path loss versus distance between the AP and WLAN cards can be obtained as shown in fig.(2). Consider the transmitted output power from AP is 1w or 30 dBm with 6 dBi antenna gain, so, the effective radiated power (EIRP) is 36dBm or 4w, neglecting the receiver antenna gain, the received power for these values is:

$$Pr = -3.6 - N \text{Log}(d) \quad (\text{dBm}) \quad (5)$$

The response of ITU model for the received power vs. distance is characterized in fig. (3).

4.2-Multi Floors Scenario Based ITU Model

In multi floors scenario, the floor penetration loss factor is $15+4(n-1)$ as mentioned in Table 2, so the path loss expression for 2.4 GHz for multiple floor is:

$$L_{total} = 39.6 + N \text{Log}(d) + 15 + 4(n-1) \quad (6)$$

A graph of the ITU model response shows the path loss for multi floors between AP and WLAN cards or users as illustrated in fig.(4) for office area environment, where $N=30$.

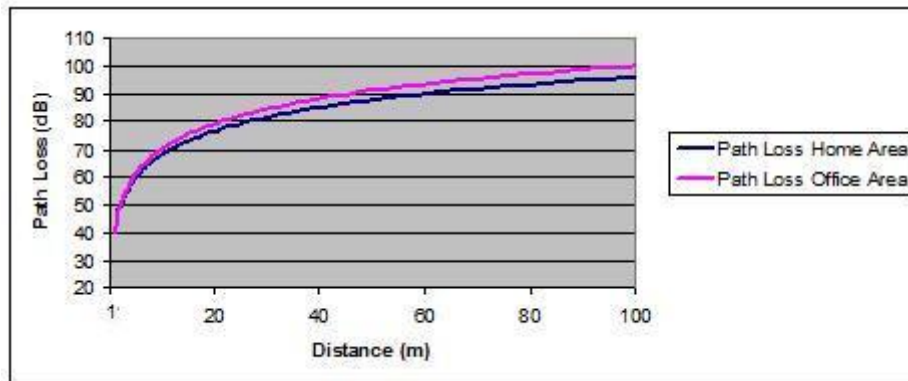


Fig. (2) Response of the path loss for single floor scenario based ITU model for home area compared to office area.

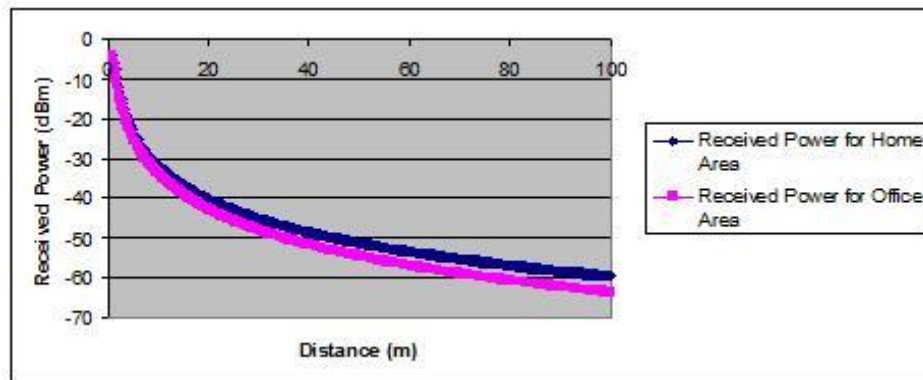


Fig. (3) Response of the received power for single floor scenario based ITU model for home area compared to office area.

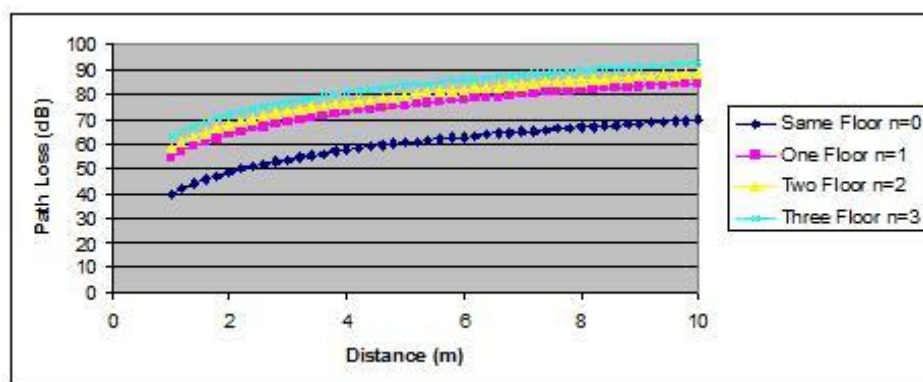


Fig. (4) Response of the path loss in multiple floors scenario based ITU model for office area.

4.3-Shadowing Deviation Effects Scenario Based Log Distance Path Model

To study the modeling of wireless indoor propagation, it is important to use log-distance path loss model where the shadowing deviation comes into play as a significant parameter [6]. The mathematical expression of this model is given in eq. (2). From eq. (3) the free space loss $PL(d_0)$ for 2.4GHz system is 40 dB, so the eq. (2) become as:

$$L_{total} = 40 + N \text{Log}(d) + X_s \quad (7)$$

For our simulation, the appropriate power decay index was assumed to be 30 [6]. The standard deviation σ was assigned of value 7 dB.

The standard normal pdf has a mean of zero and a standard deviation of unity. Any Gaussian random variable can be converted to an equivalent standard normal random variable using the transformation [4]:

$$z = \frac{X_s}{\sigma} \quad (8)$$

So, the probability of exceeding any particular value can be looked up in Table A.1 in Ref. [4] for complementary error function:

$$Q(z) = \int_z^{\infty} \frac{1}{\sqrt{2\pi}} \exp\left(-\frac{u^2}{2}\right) du \quad (9)$$

Consider the coverage area is %90 so from the Q function table (Table A.1) [4], $p = 0.1$ occurs when $z \cong 1.286$. By using eq.(8), X_s is 9 dB.

Now, eq.(7) become as:

$$L_{total} = 49 + 30 \text{Log}(d) \quad (10)$$

The expression of received power in dBm is represented in eq.(11), by assuming (EIRP) 36 dBm and neglecting receiving antenna gain.

$$Pr = -13 - 30 \text{Log}(d) \quad (11)$$

Fig. (5) Shows the response of the path loss versus path distance for log distance model. Where the received power in the WLAN cards or users for log-distance model is shown in Fig.(6).

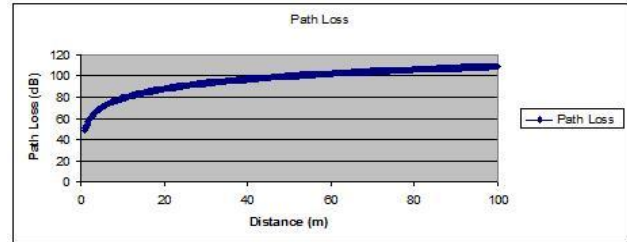


Fig. (5) Response of the path loss for the log-distance model.

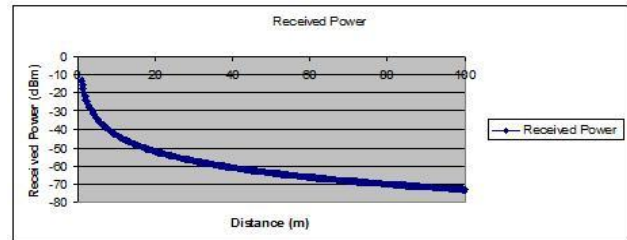


Fig. (6) Response of the received power for the log-distance model.

4.4-Practical Measurements

A laptop equipped with the NETSTUMBLER 0.40 software was used as the receiver detector, operated by a moving user [6,8]. The NETSTUMBLER software calculates the instantaneous signal strength based on a ray-tracing incorporated technique of arriving signal components as shown in fig. (7). In technical terms, different measurement locations were recorded with 30 dBm transmitting power. Fig (8) shows a practical graph for different distances for open area between AP and the laptop inside the building. Fig (9) shows a practical graph but the measurements were taken in different locations randomly through the walls to examine the building layout and understand the obstacles to propagation that are present. This experiment was done in home area which the approximately sketch as shown in fig.(10) with typical dimensions about 200 m².

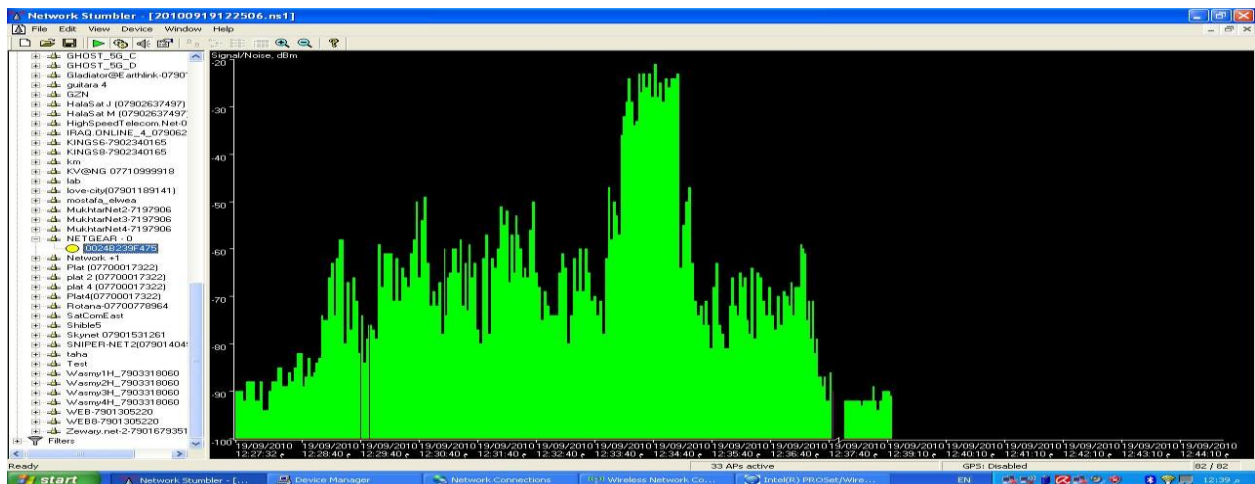


Fig. (7) The NETSTUMBLER0.40 program.

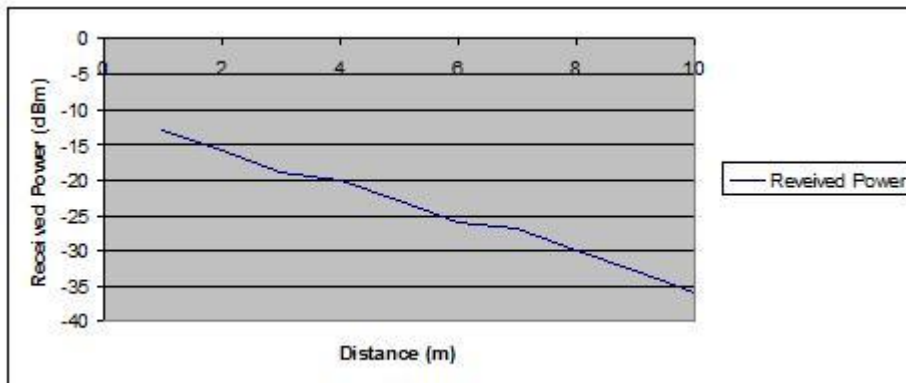


Fig. (8) Response of the received power for open area between AP and the laptop.

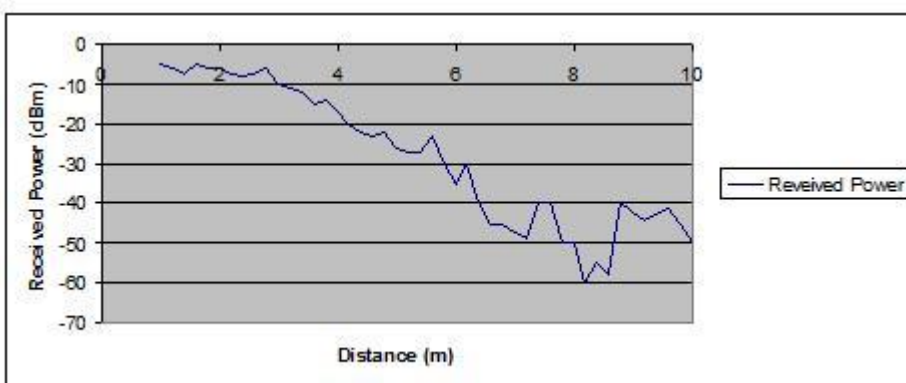


Fig. (9) Response of the received power for randomly locations between AP and the laptop.

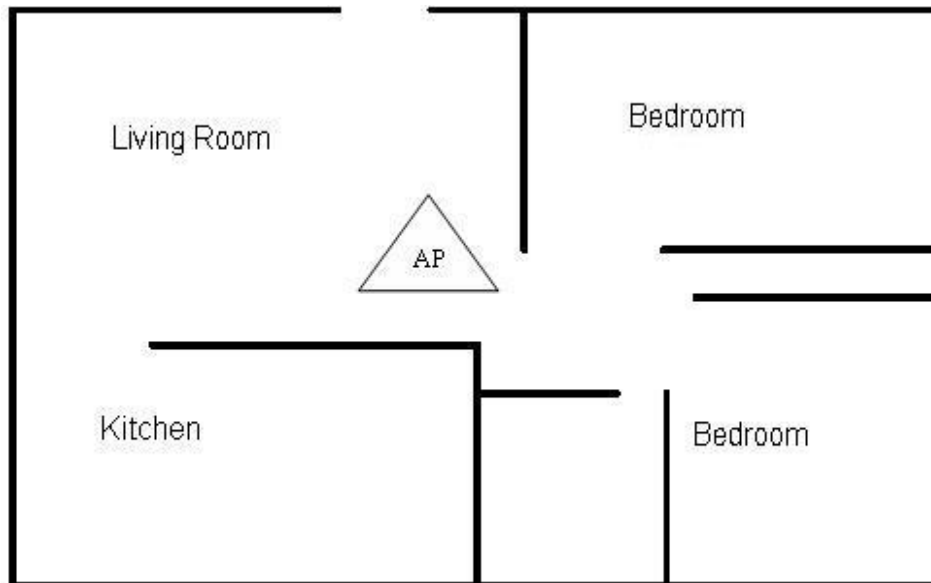


Fig. (10) A typical home layout.

5-Conclusions

The indoor propagation modeling for WLAN had been addressed in this paper. Different cases and models were simulated and technical requirements were also taken in considerations. The simulations of ITU model shows the response of the path loss via the distance between the AP and the mobile users and it had tried in the same floor and in multi floors system as illustrated in fig. (4), from this figure we can deduce that it is better to have the AP site in the same floor with the users to avoid the extra path loss. The ITU model had tested in residential area and also in office area which is more complicated by the frequent movement of people and the quantity of partitions as shown in fig.(2), there is a little difference of path loss in small distances and it increases with respect to distances, fig.(3) verifies the received power (dBm) at the user site versus distances by considering EIRP 36 dBm and ignoring receiver antenna gain. Log distance path loss model had been tested and simulated. It is important when study indoor propagation modeling to highlight the log distance, because this model notifies the shadowing deviation effects. The response of log distance model were plotted as in fig.(5)

and fig.(6), by considering %90 coverage. Practical measurements were taken in different positions and distances in house area using 802.11b standard wireless network. In this work, the used AP as transmitter with EIRP 36dBm and using laptop equipped with the NETSTUMBLER software as receiver. The tested results were illustrated as shown in fig. (8) for open area between transmitter and receiver and in fig.(9) for randomly positions between AP and laptop. From these results there is a little drift between practical and calculated results. It is important to model the indoor environments which are useful in design WLAN to study the coverage area of AP and also to select the transmitting power, transmitting antenna gain, receiver antenna gain but in the range of Federal Communications Commission (FCC) conditions [8]. Wireless networking is perfect for home and office networking but one of the most common problems is to select the optimum location for AP to allowed either desktop PC or laptop to connect by the wireless network. If the building area is more than 200m^2 it is better to use more than AP and it is optimum to put access points in the center location of floor.

Finally the empirical models that presented in this work it is not limited to 802.11b standards, but it could be used for 802.11g with transmitting frequency about 5.2 GHz.

References

- [1] Chandra P., Dobkin D. M., 2008, "Wireless Networking", Elsevier Inc., 573/pages.
- [2] Labiod H., Afifi H., 2007, "Wi-Fi-Bluetooth -ZigBee and WiMAX", Springer, Netherlands, 327/pages.
- [3] Rappaport T., 2002, "Wireless Communications Principles and Practice", 2nd ed., Prentice-Hall, Upper Saddle River, NJ, 640/pages.
- [4] Seybold J. S., 2005, "Introduction to RF Propagation", John Wiley & Sons New Jersey Inc., USA, 349/pages.
- [5] Chrysikos T., Georgopoulos G., Kotsopoulos S., 2009, "Site-Specific Validation of ITU Indoor Path Loss Model at 2.4 GHz", IEEE Int. Sym. on World of Wireless, Mobile and Multimedia Networks & Workshops, pp.1-6.
- [6] Chrysikos T., Georgopoulos G., Kotsopoulos S., 2009, "Empirical Calculation of Shadowing Deviation for Complex Indoor Propagation Topologies at 2.4 GHz", Int. Conf. on Ultra Modern Telecommunications & Workshops (ICUMT '09), pp. 1-6.
- [7] Mukherjee A., Bandyopadhyay S., Saha D., 2003, "Location Management and Routing in Mobile Wireless Networks", Artech House, Norwood-USA, 233/pages.
- [8] Aspinwall J., 2003, "Installing, Troubleshooting and Repairing Wireless Networks", McGraw-Hill inc., USA, 418/pages.
- [9] http://en.wikipedia.org/wiki/ITU_Model_for_Indoor_Attenuation
- [10] http://en.wikipedia.org/wiki/Log-distance_path_loss_model

FUZZY-GENETIC CONTROLLER FOR CONGESTION AVOIDANCE IN COMPUTER NETWORKS

Dr. Mohammed Z. Al-Faiz
Computer Engineering Dept.
Al-Nahrain University
mzalfaiz@ieee.org

Ali Majeed Mahmood
Control and Systems Eng. Dept.
University of Technology
alimmj81@yahoo.com

Abstract

In this paper a fuzzy proportional-Integral (FPI) controller is designed as an Active Queue Management (AQM) in internet routers to improve the performance of PI controller for congestion avoidance in computer networks. Firstly the parameters of FPI controller are selected by trial and error method, but to get the best controller parameters the Genetic Algorithm (GA) is used as an optimization method for tuning the FPI parameters. The analytical results for linearized TCP/AQM model are presented in MATLAB version 7.0. From the obtained results, a faster response time as well as the regulation of the output to a constant value by the designed FPI controller is clearly observed and it is noted that the FPI controller provides good tracking performance under different circumstances for congestion avoidance in computer networks.

Keywords: *Active Queue Management, fuzzy logic controller, Genetic Algorithm, computer networks.*

1. Introduction

Congestion can be defined as filled to excess, or overcrowded; for example, highway congestion. Although, the best solution of congestion is to simply avoid situations where and when congestion is likely to occur, this strategy isn't always possible. Unfortunately, congestion occurs in many real world networking environments because there is always a bottleneck of some sort a slow computer, a low-speed link, or an intermediate node with low throughput [1]. Congestion in a computer network is a state

in which performance degrades due to the saturation of network resources such as communication links, processor cycles, and memory buffers. Network congestion has well recognized as a resource-sharing problem. When too many packets are contending for the same link, the queue overflows and packets have to be dropped. When such drops become common events, the network is said to be congested. It is anticipated that this results in better response compared to linear controllers due to the nonlinear nature of NNPI.

Several researches have been done in the field of congestion avoidance in traffic of computer networks. A brief description of these researches is submitted in the following paragraphs. In the last 80's Jacobson and Karels [2] proposed the end-to-end congestion control is algorithms which forms the basic for the TCP congestion control. Its content that a TCP sender keeps a sending window (packets) rate according to the rate of dropped packets when a buffer becomes full in the router queue.

In the last 90's, Floyd and Jacobson [3] presented the RED. Its mechanism is that packets are randomly dropped before the buffer of queue overflows. And, Braden et al. [4] proposed the enhanced end-to-end congestion control for AQM.

Misra et al.[5] developed a methodology to model and obtain numerically expected transient behavior of networks with AQM routers supporting TCP flows. The solution methodology scales well to a large number of flows. This modeling/solution methodology has a great potential in analyzing and understanding various network congestion

control algorithms. Hollot et al. [6] used linearization to analyze a previously developed Non-linear model of the TCP/AQM. They linearized the model by using small-signal linearization about an operating point to gain insight for the purpose of feedback control to analyze a combined TCP and AQM model from a control theoretic standpoint and ability to present design guidelines for choosing parameters that lead to stable operation of the linear feedback control system.

Hollot et al. [7] proposed PI controller based on the linear control theory. The main contribution is to convert the congestion control Algorithm into the controller design problem within the framework of control theory in AQM system by studying a previously developed linearized model of TCP and AQM. The controller showed better theoretical properties than the well known RED controller.

Waskasi et al. [8] developed a new AQM algorithm based on neural networks. PI controller based on Artificial Neural Networks (ANN) is applied to AQM for the objective of congestion avoidance and control in middle nodes. The proposed controller is simple and can be easily implemented in high-speed routers. Neural Network PI (NNPI) dynamically adapts its parameters with respect to changes in the system.

Yann et al. [9] proposed an AQM based on the Lyapunov theory for time delay systems. With the help of Lyapunov-Krasovskii functional and using a state space representation of a linearized fluid model of TCP/AQM which is extended to the robust case where the delay in the loop is unknown. Al-Hammouri [10] developed analytical characterization of the complete stability region of the PI controller for TCP/ AQM model .The analytical challenge is the presence of time-delays in the TCP-AQM feedback loop. The complete stability region provides an in-depth understanding of the

performance of PI controller under different network parameters.

Kang et al. [11] proposed the LQ-Servo controller for AQM routers. The proposed controller structure is made by taking a traditional servo mechanism based on Linear Quadratic (LQ) approach. The proposed LQ-Servo controller can deal with a good tracking performance comparing with PI controller.

Kang et al. [12] developed the LQ-Servo controller based on loop shaping method for TCP/AQM router in order to meet such frequency domain design specifications as good disturbance rejection. The simulation results show that the proposed controller is more effective in getting the good tracking responses than PI controller for the varying reference queue size in AQM routers.

2. TCP/AQM Model

AQM has been extensively analyzed using control-theoretical methods. Control-theoretical approaches lead to stable, effective, and robust congestion control operation. In [5], the non-linear dynamic model for multiple TCP flows control has been developed based on fluid-flow theory to model the interactions of a set of TCP flows and AQM routers in computer networks which consist of a system of nonlinear differential equations. For the control theoretical analysis, it was approximated as a linearized constant model by small signal linearization about an operating point(W_0, q_0, p_0), see [6] for linearization details, which leads to the following :

$$\begin{aligned} \dot{\delta W}(t) &= -\frac{2N}{R_0^2 C} \delta W(t) - \frac{R_0 C^2}{2N^2} \delta p(t - R_0) \\ \dot{\delta q}(t) &= \frac{N}{R_0} \delta W(t) - \frac{1}{R_0} \delta q(t) \end{aligned} \quad (1)$$

where $\delta W(t) \approx W - W_0$, $\delta q(t) \approx q - q_0$, $\delta p(t) \approx p - p_0$,

$\dot{W}(t)$ denotes the time-derivative of $W(t)$,
 $\dot{q}(t)$ denotes the time derivative of $q(t)$, and

W : Expected TCP window size (packets)

q : Expected queue length (packets)

R_0 : Round-trip time (seconds)

C : Link capacity (packets/second)

N : Load factor (number of TCP sessions)

p : Probability of packet mark/drop

t : Time

The expected queue length q and the expected TCP window size W are positive value and bounded quantities. And also, the probability of packet (mark /drop) p takes value only in $[0, 1]$.

Taking the Laplace transform of equation (1) and rearranging the following transfer Taking the Laplace transform of equation (1) and rearranging the following transfer functions are obtained:

$$P_{tcp}(s) = \frac{W(s)}{p(s)} = \frac{R_0 C^2}{s + \frac{2N}{R_0^2 C}} \quad (2)$$

$$P_{queue}(s) = \frac{q(s)}{W(s)} = \frac{R_0}{s + \frac{1}{R_0}} \quad (3)$$

So, the overall plant transfer function becomes:

$$P(s) = P_{tcp}(s)P_{queue}(s)e^{-sR_0} \quad (4)$$

And can be expressed as:

$$P(s) = \frac{\delta q(s)}{\delta p(s)} = \frac{\frac{C^2}{2N} e^{-sR_0}}{(s + \frac{2N}{R_0^2 C})(s + \frac{1}{R_0})} \quad (5)$$

Thus, the block diagram of linearized AQM control system is shown in Fig.1. In this diagram $P_{tcp}(s)$ denotes the transfer

function from loss probability $\delta p(t)$ to window size $\delta W(t)$, $P_{queue}(s)$ denotes the transfer function from $\delta W(t)$ to queue length $\delta q(t)$, and $C(s)$ denotes the transfer function of controller. Taking the Z-transform to Eq.(5), the designed plant transfer function is obtained after considering the sampling time half of R_0 . Precisely and for consider the case study with $N=60$, $C=3750$ packets/sec and $R_0=0.253$ sec the following discrete transfer function are obtained.

$$P(z) = \frac{q(z)}{p(z)} = \frac{11252.46 z^{-3}}{1 - 1.545 z^{-1} + 0.569 z^{-2}} \quad (6)$$

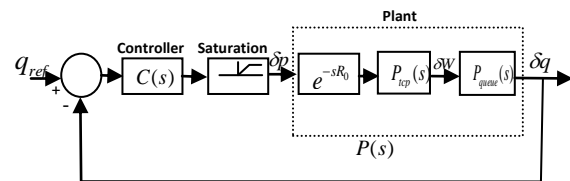


Fig.1:Block diagram of a linearized AQM as feedback control.

3. Controller Design

3.1. Conventional PI controller

The continuous-time PI controller is described by the following expression:

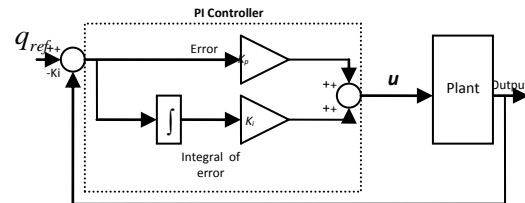


Fig.2: Block diagram of PI controller.

3.2. Fuzzy PI (FPI) Controller

The previous equation (6) gives a conventional PI-controller .To provide a formal methodology for representing, and implementing a human's heuristic knowledge about how to control a system, which may provide a new paradigm for non-linear systems and to get more robust controller that can cover a much wider range of operating conditions than PI controller and can operate with noise and disturbances of different nature, a fuzzy PI controller is designed as an intelligent controller for congestion avoidance in AQM routers. A block diagram of a fuzzy PI controller system looks like Fig.3.

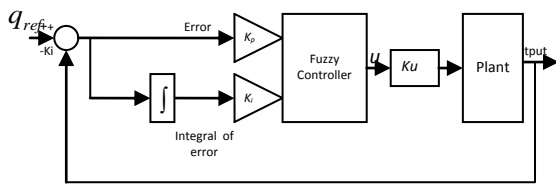


Fig.3: Block Diagram of FPI Controller with (e & e-dot).

From Fig3 it is noted that the formulation of control rules is difficult with the input variable sum-of-error ($\sum e$) because its steady-state value is unknown for most control problems, because it may have the very wide universe of discourse [13]. So another configuration gaining more popular utilization by the designers which depends on the inputs (e, \dot{e}) which is used by moving the integration from the part preceding to a fuzzy controller to part following it, and integrate the output of a controller not the input. When the derivative, with respect to time, of the Equation (6) is taken, it is transformed into the following equivalent expression:

$$u(t) = K_p \times e(t) + K_i \times \int e(t)dt \quad (7)$$

where, K_p and K_i are the proportional and the integral gain coefficients. A block diagram for a PI controller is shown in Fig.2.

the control signal it needs to integrate the output of controller as shown in Fig.4

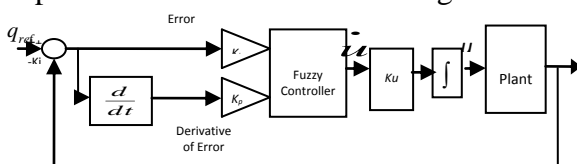


Fig.4: Block Diagram of FPI Controller with (e, e-dot).

3.3. Specifications of Fuzzy PI Controller

a) The (Universe of Discourse) UOD Partitions and Membership Type

The UOD of each input control variable (e, \dot{e}) is decomposed into five fuzzy sets .The linguistic values of these inputs are: (Negative Big) NB, (Negative Small) NS, (Zero) Z, (Positive Small) PS, (Positive Big) PB and the control Signal of output variable (u) is decomposed into seven fuzzy

sets that have the linguistic values: (Negative Big) NB, (Negative Medium) NM, (Negative Small) NS, (Zero) Z, (Medium) NM, (Negative Small) NS, (Zero) Z, (Positive Small) PS, (Positive Medium) PM, (Positive Big) PB. The UOD for inputs (e, \dot{e}) and output control variable (u) are normalized between (-1,1) and for simplicity and effectiveness, triangular and trapezoidal shapes are chosen as membership functions for inputs (e, \dot{e}) and Singleton for output (u) as shown in Fig.5.

b) Formation of Rule Bases and Defuzzification Method

The proposed rule base contains 25 rules, with a linguistic description of domain expert knowledge in the “if-then” form. The FPI controller rules are obtained by expertise and the trial-and-error method. The rule base of the designed FPI controller is shown in Table (1), where Mamdani fuzzy rules are used to perform the fuzzy rules with Mamdani

$$du(t)/dt = K_p \times \frac{de}{dt} + K_i \times e(t) \quad (8)$$

So the controller output is not a control signal, but as a derivative of a control signal. To get

and the above ever mentioned sets give the better response. The first rule is outlined below, Rule 1:

If (e) is NB AND (\dot{e}) is NB THEN u is NB

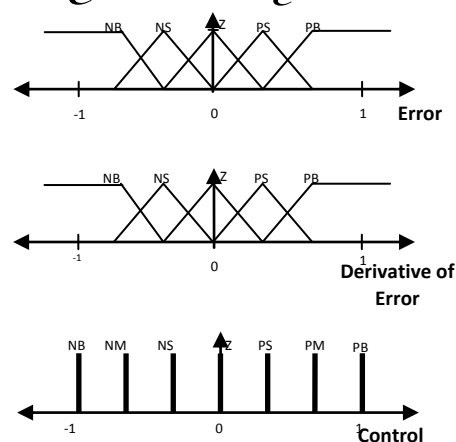


Fig.5: Fuzzy Input and Output Memberships with Normalized UOD.

Table (1): Fuzzy Rule Base.

u		e				
		NB	NS	Z	PS	PB
e	NB	NB	NB	NM	NS	Z
	NS	NB	NM	NM	Z	PS
	Z	NM	NM	Z	PM	PM
	PS	NS	Z	PM	PM	PB
	PB	Z	PS	PM	PB	PB

3.4. FPI Based Genetic Algorithm

GA method is used as alternative to trial and error method since it is a suitable optimization method to find best FPI parameters (K_i , K_p , K_u) according to minimization of the criterion ITAE set in equation (8) to get the maximized fitness of minimum inference method that is used in a fuzzy rule to determine the rule outcome from the given rule input information. The center of gravity method is used in defuzzification to convert fuzzy sets to a real number. It worth mentioning that other sets of input and output membership function and fuzzy rules are used is achieved or the value of fitness is fixed for next generations.

$$ITAE = \int_0^{t_f} t|e|dt \quad (9)$$

where, t_f : the final time of simulation.

$$\text{Fitness} = 1/(1+ITAE) \quad (10)$$

4. Network Topology Scenario

Fig.6. shows the network case study taken, where the simulation is conducted for a single link (Bottleneck link) that has a bandwidth capacity $C=3750$ packets/sec (corresponds to a 15 Mbps with packet size 500 bytes), and the same bandwidth capacity is used at other links, the Round Trip Time (R_0) is 0.253 second where the desired queue size is 200 packets and the propagation delay is 0.2 second. The number of TCP sessions

(N) is 60 for source and destination, where applying the above parameters in equation (3.17) gets the overall TCP/AQM system transfer function as shown in equation (10). The maximum queue length in the AQM router Router1 is 800 packets. The AQM mechanism (PI or FPI) is configured at Router1, and drop Tail is used at other gateways.

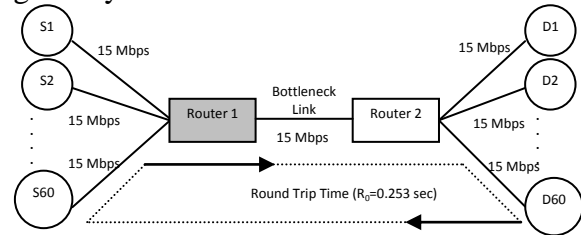


Fig.6: Network Topology Case Study.

5.Linearized TCP/AQM Model Simulation Results

The simulation of the linearized TCP/AQM model was done in MATLAB 7.0. Consider the TCP/AQM model with network parameters as set in pervious section and the reference input (queue size) which has rectangular form changes every 50 seconds as shown in equation (4.2). First the simulation is done for the system without controller as shown Fig.7.

$$q_{ref} = \begin{cases} 300 & 0 < t < 50; \\ 200 & 50 < t < 100; \\ 400 & 100 < t < 150; \\ 200 & 150 < t < 200; \end{cases} \quad (11)$$

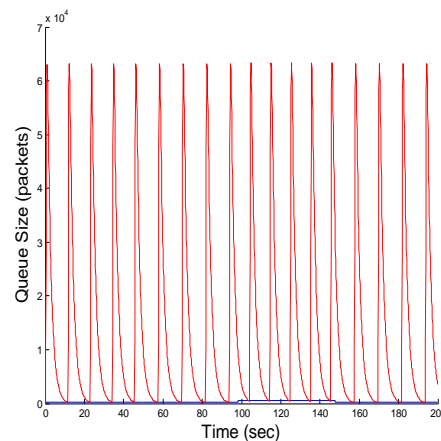


Fig.7: System Response without Controller.

From Fig.7 it is shown that the system without controller is unable to track the queue length around the queue length to the desired level, where the system goes into a sustained oscillation with high congestion exceeding the maximum buffer size. In order to eliminate this sustained oscillation and get better tracking performance a classical control (PI-controller) is applied. As it is shown in Fig.8. The PI controller parameters are selected by trial and error method. Thus the PI coefficients are $K_p=0.3 \times 10^{-5}$ and $K_i=0.1 \times 10^{-5}$ respectively. Although the PI controller shows good performance the system response is slow, so to overcome this drawback a FPI controller is designed to speed up the system response. Fig.9 shows the system response with PI and FPI

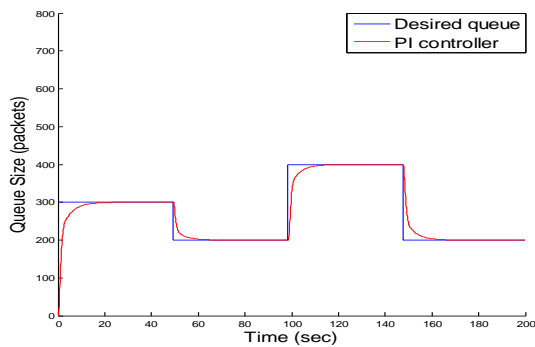


Fig.8: System Response with PI Controller.

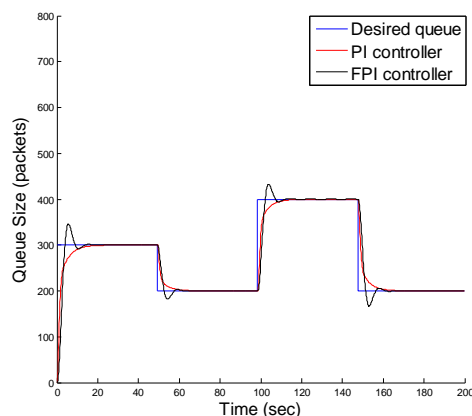


Fig.9: System Response with PI and FPI Controllers.

From Fig.9 above it is shown that the FPI controller speeds up the response comparing with PI controller, where the FPI controller

parameters are selected by trial and error method as follows $K_p=0.5 \times 10^{-3}$, $K_i=0.9 \times 10^{-3}$, $K_u=0.2 \times 10^{-2}$, so to get the best parameters to controller and to enhance the system response the Genetic Algorithm (GA) is used as a suitable optimization method for tuning FPI Parameters, where the population size is 100, crossover probability $pc=0.9$, mutation probability $pm=0.05$, for varying queue size in AQM the system response enhanced especially in decreasing the rising time and the settling time which means that the FPI with GA could speed up the system response, as a result it gives better congestion avoidance compared with FPI and classical PI controllers, as shown in Table (2) and Figure (10). It is worth mentioning that other sets of GA parameters

Table (2): TCP/QAM System Response Performance of PI, FPI and FPI

Based GA with error criteria 5%.

Controller	Rise Time (t_r) (sec)	Overshoot M_p %	Peak Time (t_p) (sec)	Settling Time (t_s) (sec)
PI	18	-	-	20
FPI	4	15	5	8
FPI based GA	2.5	7	3	4

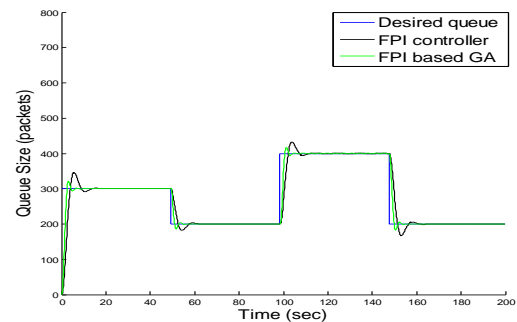


Fig.10: System Response with FPI and FPI Based GA.

6. Conclusions

From the design and the simulation results, it can be concluded that:

1- The designed FPI controller can deal with congestion problem with a good tracking performance about the desired queue size

with high link utilization and faster system response observed as compared with routers.

2- By using the GA to optimally select the best FPI parameters the system response is improved as shown in table (2) which prove the efficiency of GA as suitable optimization method

3- the modeling and linearization of window and queue dynamics of the TCP/AQM model about an operating point to gain insight for the purpose of feedback control in design and analysis of AQM schemes.

References

- [1] D. E. Mcdysan and D.Paw, "ATM & MPLS Theory & Application: Foundations of Multi-Service Networking", McGraw-Hill, 2002.
- [2] V. Jacobson and M. J. Karels, "Congestion Avoidance and Control", *In SIGCOMM'ss*, 1988.
- [3] S. Floyd and V. Jacobson, "Random early detection gateway for congestion avoidance", *IEEE/ACM Transactions on Networking* Vol.1, No. 4, August 1993.
- [4] B. Braden, D. Clark and J. Crowcroft, "Recommendations on Queue Management and Congestion Avoidance in the Internet", Network Working Group ,Request for Comments: 2309 (*RFC2309*), April 1998.
- [5] V. Misra, W.-B. Gong, and D. Towsley, "Fluid-Based Analysis of a Network of AQM Routers Supporting TCP Flows with an Application to RED", in *Proc. ACM SIGCOMM*, 2000. pp. 151-160.
- [6] C. V. Hollot, V. Misra, D. Towsley, and W. B. Gong, "A Control Theoretic Analysis of RED", *In Proceedings of IEEE INFOCOM*, 2001.
- [7] C. V. Hollot, V. Misra, D. Towsley, and W. B. Gong, "On Designing Improved Controllers for AQM Routers Supporting TCP Flows". *In Proceedings of IEEE INFOCOM*, pages 1726–1734, 2001.
- [8] M. Y. Waskasi, M. J. Yazdanpanah and N. Yazdani, "a New Active Queue Management Algorithm Based On Neural Networks PI", *Control and Intelligent Processing Center of Excellence Electrical and Computer Engineering Department University of Tehran*, 2005
- [9] Y. Labit, Y. Ariba and Gouaisbaut, "On Designing Lyapunov-Krasovskii Based AQM for Routers Supporting TCP Flows", UPS, 118 Route de Narbonne, F-31062 Toulouse, France, December, 2007.
- [10] A. T. Al-Hammouri "Internet Congestion Control Complete Stability Region for PI AQM and Bandwidth Allocation in Networked Control". Ph.D. Thesis, January, 2008.
- [11] K. M. Lee, J. H. Yang and B. S. Suh, "Congestion Control of Active Queue Management Routers Based on LQ-Servo Control", *Engineering Letters*, July, Korea, 2008, 332-338.
- [12] K. M. Lee, J. H. Yang and B. S. Suh, "Lq-Servo Control Design Based On Loop-Shaping Method For TCP/AQM Router" International Conference Modeling , Identification, and Control MIC February 16 -18 ,2009 Innsbruck ,Austria
- [13] L. Reznik, "*Fuzzy Controllers*", Newnes, first edition, 1993

DESIGN OF A TELEMEDICINE NETWORK FOR IRAQ

Haider Tarish Haider

Computer and Software Dept.

Engineering College, Al-Mustansiriya University.

hth.1977@yahoo.com

Abstract

Telemedicine is the use of electronic communications and information technologies to provide clinical services when participants are at different locations, information technologies are used to support healthcare services like videoconferencing, transmission of still images,

Telemedicine does not represent a separate medical specialty rather it is a tool that can be used by health providers to extend the traditional practice of medicine outside the walls of the typical medical practice. Telemedicine networks should take a pioneer role in the national health care plans because it's powerful tools for health care, cost effectiveness also to get the tele-consultation from the Iraqi physicians living abroad.

The propose design will connects all clinics, health centers and hospitals in Iraq for the purpose of data transmission in the form of text, images, and video as well as instantaneous access to patient information and learning. The system consist from hardware components that referred to the LAN and WAN network design in additional to software that manage the resources of Telemedicine system, the software based using a web based Graphical User Interface (GUI) specifically designed for telemedicine system to store and retrieve patient information, to write referrals and give feedback to referrals, Also provides basic services for medical tele-consultation. The Proposed network design of current study includes a hierarchical standard model based LAN architecture that enables design of the network devices in layers and a hybrid WAN architecture. The network model of the LAN is expandability and improved fault isolation characteristics.

Keywords: *Telecommunication; WAN, LAN; Information Technology; VLAN; SSL;*

1. Introduction

Telemedicine is the combined use of telecommunications and computer technologies to improve the efficiency and effectiveness of health care service by liberating caregivers from traditional constraints of place and time. It's transfer of electronic medical data (that is, images, sounds, live video and patient records) from one location to another. It includes the use of electronic information and telecommunications technologies to support long-distance clinical health care, patient and professional health-related education, public health, and health administration. The terms telemedicine and telehealth are often used interchangeably [1,2].

Information Technology (IT) is a best choice to offering access to health care service to the expectation of people, both the health care providers and patient can benefit from those networks [3]. Such communication is possible by implementing a nationwide Telemedicine network, based on affordable telecommunications infrastructure. The network should connect all clinics and health centers to hospitals for the purpose of: [4]

1. Improved access: Telemedicine can provide an improved access to health care in unserved or under-served geographical areas.
2. Reduced cost: The travel cost of the patients for specialty care, the travel cost of the health care professionals for continuing education or consulting, the personnel/equipment cost for not having to keep specialty care facility in rural hospitals, and other costs can either be eliminated or reduced.

3. Reduced isolation: Telemedicine provides a peer and specialist contact for patient consultations and continuing education. Full-motion video is critical to the health professionals for simulating face-to-face communication between colleagues in consultations and between patients and physicians.

4. Improved quality of care: Telemedicine allows the consultation among the referring physician, the consulting physician, the patient, and the patient's family through interactive video with critical information of the patient available on-line. Also, the physicians or other personnel at remote locations can be educated during the consultations with specialty physicians and other experts, increasing their ability to treat other similar cases in the future. It helps the doctors to be better prepared for incoming patients.

The successful implementation of a telemedicine system depend on the following factors: [2]

- What telehealth applications are proposed (e.g., diagnosis and treatment, consultations to other providers, home health monitoring, dispensing prescriptions, continuing medical education)
- Where services are provided (e.g., in-house, within a medical system, regionally, across state borders, or internationally)
- How the model operates

2 Telemedicine Network Considerations

The telemedicine system goal is to implements connectivity among rural clinics and urban area hospitals to be used mainly for tele-consultation, and maintaining patient information [3]. The network should be expandable, secure and interoperable

2.1. Expandability

Many telemedicine networks have required multiple independent entities to work together toward a common goal of providing healthcare [5]. Expandable system is one in

which additional inputs and outputs (such as the number of incoming data, the number of simultaneous users served, the number of clinics to get connected, etc.) can be added without a major reworking of the network design. So the design should consider the network's ability to continue to function well as it is changed in size or volume to meet new traffic or application requirements. In this regard expandability is a concern in the telemedicine network design for the following reasons [3]:

- The number of hospitals built will be increased. However there are more clinics being added to the health system.
- There is also a chance to incorporate private hospitals in the nationwide telemedicine network as necessary, which will ultimately increases the number of sites to be connected in the future.
- The area of telemedicine applications will not be limited to some specific diseases, but will be expected to increase in type and number in the future.
- The network should also support advanced applications, which require real time connectivity such as video conferencing.

2.2. Security

This is extremely important topic as security that protects the confidentiality of the patient's electronic health record. Security options need to be planned and tested well in advance of the implementation of application. There are many types of security protection and authentication programs that are available [6]. For a secure communication, protocols such as Secure Socket Layer (SSL) could be used. SSL permits users to conduct secure communication over web-based applications. This provides the ability to safely exchange patient information across the network. In addition to these, the network hardware can be protected by firewall against external invader. Firewalls could be software or hardware for the sole purpose of keeping digital pests such as viruses, worms, and hackers out of the network [3].

2.3. Interoperability

A key to interoperability is the use and adoption of standards. Interoperability is the ability to “talk” from one information system to another and to share data. As more and more clinical information systems are installed in healthcare organizations across the health centers, it will be necessary for these systems to talk to one another and to share data to provide the best in patient care [6]. In many cases there may be several vendors involved. This requires that interfaces be developed. Many systems today support industry standards such as HL7 that make interface development easier than in past years. In essence what this means is having a standard dictionary for all computers so that the terms are defined and communicated back and forth from computer to computer in a manner that makes it easy to use and pass data between systems. An interface engine is another tool that is often effective. It allows the provider to control and develop the interfaces [6].

3. Design of Proposed System

The Designed network requires hardware components for LAN and WAN connections among the clinics, health centers and hospitals to make one network for the purpose of data exchange in different types such as text, images, video as well as instantaneous access to patient information, also the system has software applications to manage the patients information by using a web based Graphical User Interface (GUI) specifically designed for Telemedicine.

3.1 Hardware network design

3.1.1 Proposed LAN:

For the LAN Connections for each hospital, a typical site should be taken as a sample for standard LAN design for all other locations, The Medicine City in Baghdad Specialized Group of Hospitals as a sample also it's considered as a central site. It's clearly each hospital is organized into

departments. Each department will have units as necessary. For instance, the Internal Medicine department has units such as Renal Unit, Cardiology Unit, etc. The physicians in these departments/units need to communicate whenever a patient visits more than one of the units. The proposed LAN will follow the hierarchical standard LAN structure of the hospital. a sample hospital which is taken from Medicine city Group of Hospitals in Baghdad, it's composed of many floors (from A to Z). The hospital is physically separated. All the departments and offices are located in either of the blocks. Each floor Having router and switches in each of the departments is ideal to design a high speed and expandable LAN.

The rate of the hospital LAN growth depends on the level of computerization. The switches/routers selected in this design should have many free ports to help cascade the growing number of connections in the future. The designed LAN will be divided in three standard layers [7] as shown in Fig.(1). It enables us to design and arrange the device in layers. Its ease of understanding, expandability and improved fault isolation characteristics.

3.1.1.1 The Core layer:

The core layer is responsible for transporting large amounts of traffic both reliably and quickly. The only purpose of the network's core layer is to switch traffic as fast as possible. The traffic transported across the core is common to a majority of users [7]. The Core layer have high performance devices like switches, Routers, Core server and firewalls, that is putted in central location in the hospital, this layer represent the backbone LAN of this hospital so it's connect all floors in the building, for this design the minimum servers that will be found are web server for web applications and database server to store the telemedicine information, the firewall hardware will protect the LAN from outside attack. Also this layer will connect to the outside WAN and to Distributed layer

3.1.1.2 The Distribution layer:

The primary functions of the distribution layer are to provide routing, filtering, and to determine how packets can access the core, if needed. The distribution layer must determine the fastest way that network service requests are handled. It's the communication point between the access layer and the core [7]. For this network the switches/routers will be putted for each building depend on the LAN traffic.

3.1.1.3 The Access layer:

The access layer controls user and workgroup access to internetwork resources. The access layer is sometimes referred to as the desktop layer. The network resources most users need will be available locally [7]. This layer contains switches to connect PCs, medical devices, printers etc., in each department so one or more switches will be putted in each department with VLAN configuration for network separation,

3.1.2 Proposed WAN Design:

WAN connectivity are differ from LAN because it's depends on the available solutions of WAN infrastructure in the country and for the applications bandwidth that is needed, Table (1) illustrates a sampling of several of the more common digital medical devices used in telemedicine associated with data rate required. Fig.(2) illustrates the image sizing determination for the devices listed in Table 1. Except for the last few items contained in the table (starting with ultrasounds and running through full motion video), the majority of vital sign medical devices require relatively low data transmission rates. Capabilities currently offered by these systems, even 1G and 2G wireless and basic telephone connections, would support the transfer of information provided error free or as "error detecting and correcting" processes [8].

Tradeoff must be considered when choosing a telecommunications system for

high data intensive services, as illustrated in Table 1. For example assumes digital radiography requiring 2048 X 2048 pixels for quality and 12 bits per pixel. In this example, it would take almost 30 minutes to complete the transfer of a single image when using a modem and a speed of 28.8 kbps. This is clearly unacceptable given that several views of a single patient must be transmitted in a single episode. However, the newest telecommunications offerings reduce the time per view to less than a second per view [8].

For Current design, a hybrid WAN network proposed depend on the available infrastructures for each site, such as Wireless network 1G, 2 G or 2.4 G Band, or telephone lines this is proposed between the Telemedicine sites in the local Iraqi conservative, this will be reduces the effective cost design, for the connection between constrictive and the other, a VSAT connection will be established as shown in Fig. (3). The VSAT service with on demand network that is make the bandwidth controlled, any site need high bandwidth will get the high priority, after finish the band will be balanced over the other site this will make good WAN design and saving VSAT bandwidth.

4. ITS Prototype Software Applications

ITS are based on two servers. It is a web-based application server, which will have a web server to provide the interfaces of the system and database server to store the information required in the system. The prototype is constructed with a combination of open source products and freely available software components. The web server have used is the Abyss web server [9].

The user interface and text of web pages are implemented by using PHP languages. The database have been used is the open source MySql to back up database driven application. MySql works on many different operating system platforms and is known for its speed of data retrieval.

4.1. ITS Interfaces

The home web page of the ITS system contain a login screen for registered users to put username and password as in Fig.(4). The user types are defined in the database when the user registered, the page corresponding to the specific user type will be opened upon successful login. Here the defined users are administrator, physician and Editors.

4.1.1. Administrator's Main page

The administrator's user will manage the registration functions for all user types, it's contains register new user and search user by either or a combination of user name, Name, and secret number as shown in Fig. (5). The button add new user, opens up a user registration form where the administrator can put the information necessary about the user and define the user type. Fig. (6) Shows the user registration page.

4.1.2. Editor Main page

The editors will manage the patient's information, the main page of editors contains searching for previously registered patient for editing his/her information. Also has button to register new patients as shown in fig. (7), from the new patient registration can add the patient information associated with medical images, laboratory test and other test that are available as shown in fig. (8).

4.1.3. Physician's Main page

The Physician that has been register, can access his own main page just by putting the user name and password this page have:

- 1-Searching the specific patients by using combinations of name, and/or patient number,
- 2-Read the current referrals for physicians and select any patient's card,
- 3-Write patients card for any selected patient,

Fig. (9) Shows the Physician man page

The options provided to the physician are to see referrals forwarded to her/his department. They can select any patient referrals and clicking the patient card button lead to the patient's card page, from this form the physicians can check the patient medical images, laboratory test, and other test then write his/ her diagnosis and add any other notes as shown in fig. (10),

4.1.4. Medical eLearning page

The ITS eLearning will help the physician to update his/her knowledge for the current technology in medical fields also for online lectures, and Online medical operation, figure (11) shows the ITS eLearning page

4.1.5. Patient Search

The home page contains the patient search to follow his/her case and the date of treatments defined by the health centers as shown in Fig. (12)

5. Conclusion

This paper proposed a telemedicine system for Iraq, this system contains a hardware LAN with hierarchical standard model to keep the system update for any additional sites or applications, for WAN connections a hybrid technologies has been used in local connection in the city depend on the infrastructures available in each site, and using VSAT connection for cities connections. The band of this VSAT will be on demand to keep the band under control, also a prototype software was proposed for control the ITS service, where is control patient information (registration, referrals, patient card, etc.), physician issues like (registration, patients diagnosis, write notes for patients cases, eLearning etc.) also the software make the administrator to register the physician, Editor and other admin or editing the previously registered,

The ITS system will convert the old medical operations to one click operation, also this system will make us updated for the Iraqi patient's database and the types of deices in the country, in additional to the fast operation that is very important in the medical operations.

References

- [1] Ari T. A., May 2000 "A Cost-Effective Portable Telemedicine Kit for Use in Developing Countries" M.Sc. thesis Massachusetts Institute of Technology, 95
- [2] Louis A. K. and Anne M. C., February 2005 "Planning and Implementing a Statewide Telehealth Program in New Hampshire" NH Telehealth Planning/ Advisory Committee, [www.unh.edu/chi/media/documents/D-NHTelehealth WhitePaper.pdf](http://www.unh.edu/chi/media/documents/D-NHTelehealthWhitePaper.pdf)
- [3] Fikreyohannes L., S. A. and Samuel K. K., 2006 "Design of Architecture for a Terrestrial LAN & VSAT- Based National Telemedicine Network in Ethiopia"
http://www.digitaladdis.com/sk/TeleMedicine_Ethiopia_Paper2.pdf
- [4] Abhijeet S B., 1998 "Intelligent Network Based Wireless" M.Sc thesis, Faculty of the Graduate School of the University of Maryland, 84
- [5] The American Telemedicine Association, May 2006 "Telemedicine, Telehealth, and Health Information Technology" Journal and e-Health, an ATA Paper, www.americantelemed.org/files/public/policy/HIT_Paper.pdf
- [6] Joseph T., 2004 "A Guide to Getting Started in Telemedicine ", Office for the Advancement of Telehealth, University of Missouri Health Care, 405
- [7] Todd L. 2004 "Cisco Certified Network Associate " SYBEX Publisher, 706
- [8] Gary S., Thomas N. and Richard B. and others 2002 "Organizational Models of Telemedicine and Regional Telemedicine Networks" telemedicine journal and e - health volume 8, Number 1, 10
- [9] Abyss Web ServerTM For Windows, 2007 Aprelium Technologies, accessed on September, <http://www.aprelium.com>

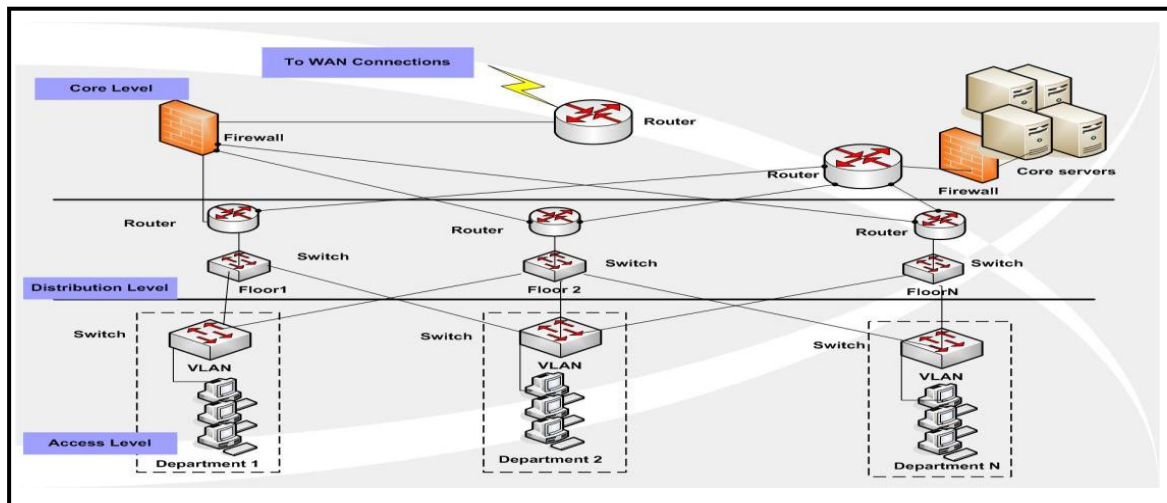


Fig. (1) LAN design

Table 1 Data rate of typical devices used in telemedicine

Digital device	Data rate required
Digital Blood Pressure Monitor (sphygmomanometer) ,	10 kb of data (required transmission rates)
Digital thermometer	10 kb of data (required transmission rates)
Digital audio stethoscope and integrated electrocardiogram	10 kb of data (required transmission rates)
Ultrasound, Angiogram	256 kilobytes (KB) (image size)
Magnetic resonance image	384 KB (image size)
Scanned x-ray	1.8 megabytes (MB) (image size)
Digital radiography	6 MB (image size)
Mammogram	24 MB (image size)
Compressed and full motion video (e.g., nasopharyngoscope, ophthalmoscope, proctoscope, episcope, ENT scope)	384 kbps to 1.544 Mb/s (speed)

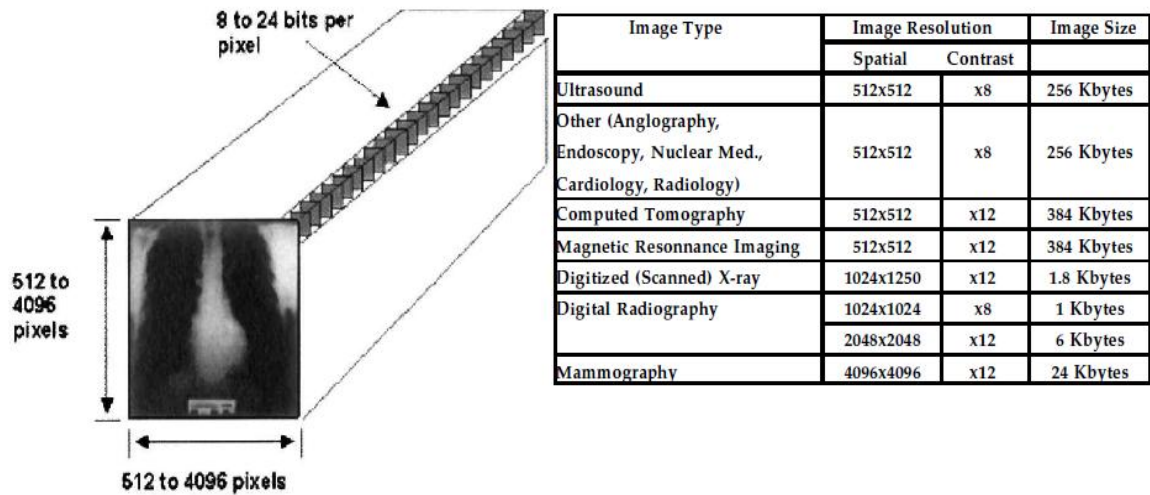


Fig.(2) Teleradiology imaging applications

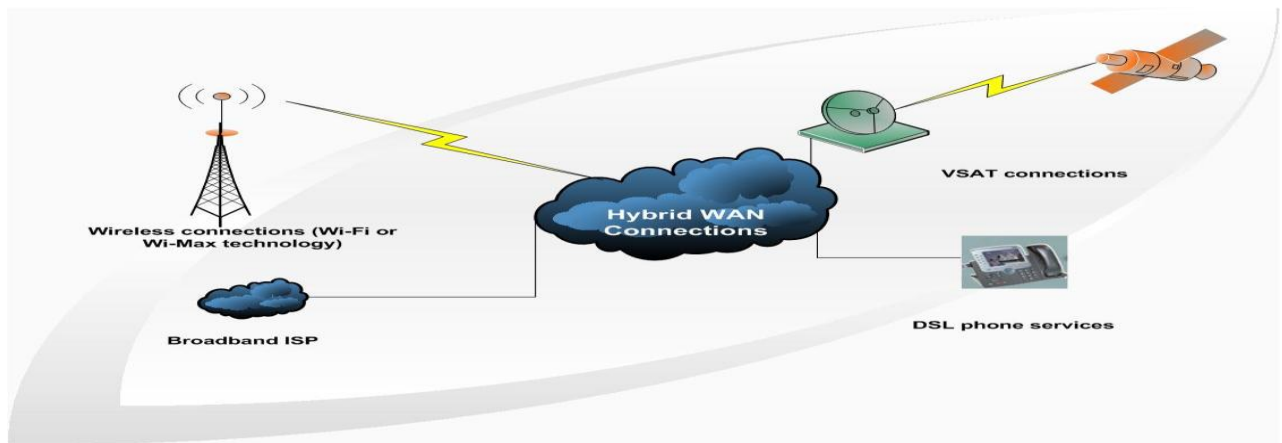


Fig.(3) Hybrid WAN Connections

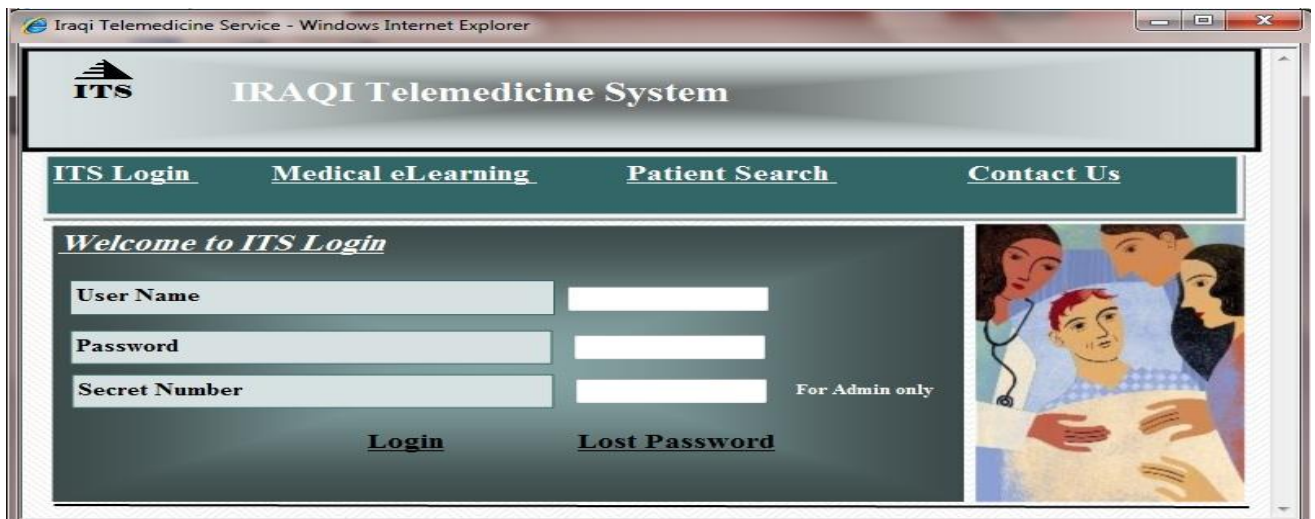


Fig. (4) ITS Home Page

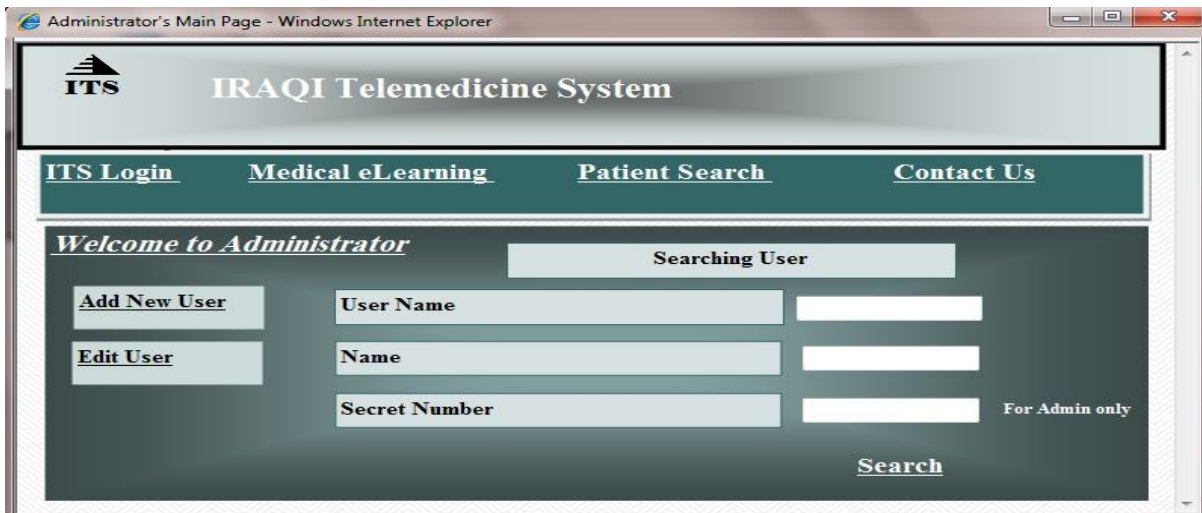


Fig. (5) Administrator's main page of ITS

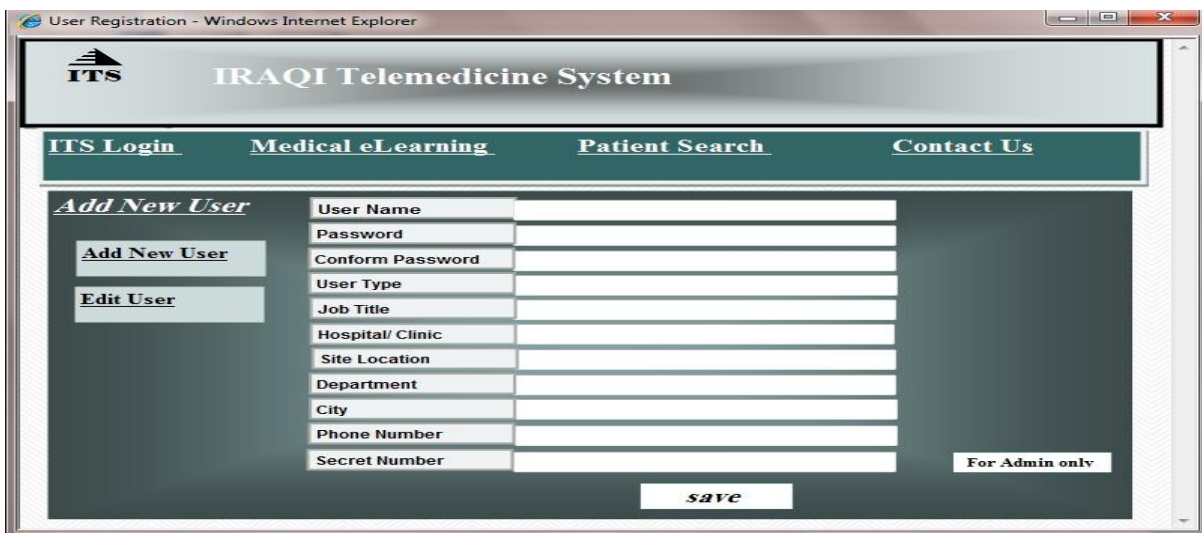


Fig. (6) User registration page



Fig. (7) Patient Editors Page

Fig. (8) Patient Registration main page

Fig. (9) Physician's main page

Patient Name	Ahmed Ahmed Ahmed
Patient Number	0012
Age	45
Gender	M
Marital status	Marid
Hospital	Kendi
Address	Baghdad H\20 St\15 Qrt\ 720
Phone Number	+974 5555555555

Fig. (10) patient Card page

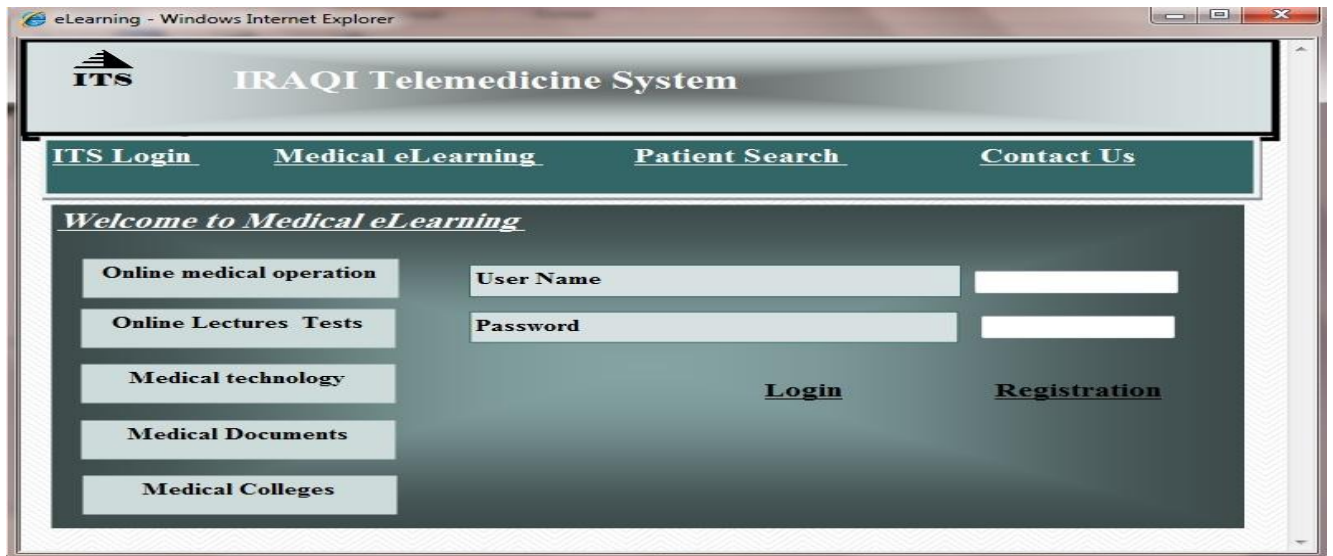


Fig. (11) ITS eLearning page

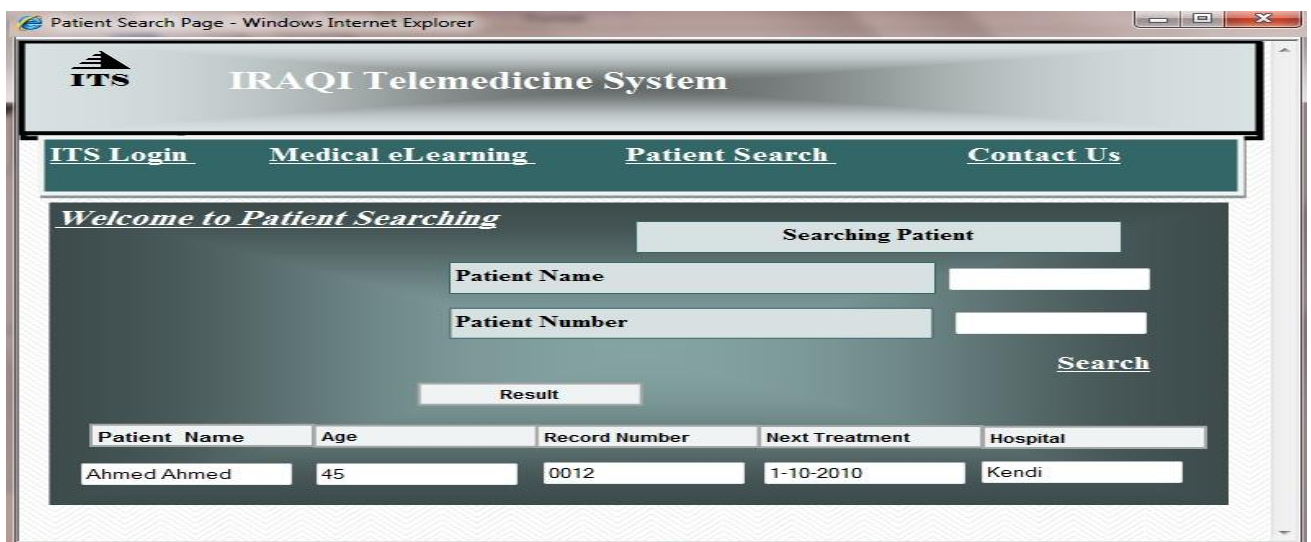


Fig. (12) Patient Search page of ITS

WEB BASED MULTITHREADING SYSTEM

Husam Ali Abdul Muhsin
Computer Science Department
College of Science
University of Baghdad
husamex@yahoo.com

Abstract

Web based (database installed in the web server) functionally combine globally distributed computers and information systems for creating a universal source of information. Web based server is a very large scale, generalized distributed network information system that can scale to Internet-size environments with machines distributed across multiple organizations and administrative domains. The variety of O.S and new applications demand support efficient data management mechanisms where java comes in, this paper used to provide application level multithreading platform independent system for individual parallel jobs for data, implemented by using Borland JBuilder 7 Enterprise - WebLogic Edition as shown in appendix A.

Keywords: *web based, Application Level, Multithreading, Platform Independent.*

1. Introduction

A fundamental concept in computer programming is the idea of handling more than one task at a time. Many programming problems require that the program be able to stop what it's doing, deal with some other problem and return to the main process. The solution has been approached in many ways. Initially, programmers with low-level knowledge of the machine wrote interrupt service routines and the suspension of the main process was initiated through a hardware interrupt. Although this worked

well, it was difficult and non-portable, so it made moving a program to a new type of machine slow and expensive. Sometimes interrupts are necessary for handling time-critical tasks, but there's a large class of problems that are partitioned into separate-running pieces so that the whole program can be more responsive [1]. Within a program, these separately-running pieces are called threads and the general concept is called multithreading [1][2]. A common example of multithreading is the user interface. By using threads, a user can press a button and get a quick response rather than being forced to wait until the program finishes its current task. Ordinarily, threads are just a way to allocate the time of a single processor. But if the operating system supports multiple processors, each thread can be assigned to a different processor and they can truly run in parallel. One of the convenient features of multithreading at the language level is that the programmer doesn't need to worry about whether there are many processors or just one. The program is logically divided into threads and if the machine has more than one processor then the program runs faster, without any.

The basic concept of client/server computing, then, is not so complicated. The problems arise because you have a single server trying to serve many clients at once. As client software changes, it must be built, debugged and installed on the client machines, which turns out to be more complicated and expensive than you might think. It's especially problematic to support

multiple types of computers and operating systems. Finally, there's the all-important performance issue: you might have hundreds of clients making requests of your server at any one time, and so any small delay is crucial. To minimize latency, programmers work hard to offload processing tasks, often to the client machine but sometimes to other machines at the server site using so-called middleware. (Middleware is also used to improve maintainability). So the simple idea of distributing information to people has so many layers of complexity in implementing it that the whole problem can seem hopelessly enigmatic. What we've come up with in the past is individual solutions to individual problems, inventing a new solution each time. These were hard to create and hard to use and the user had to learn a new interface for each one. The entire client/server problem was solved by the platform independent Java programming language [1].

In this paper, we propose a program that uses Multithreading technology to implement job parallelism in a scalable information system environments, as shown in appendix A, because workload management is an essential function provided at the service level of the Web based infrastructure. To improve the performance of such systems, effective and efficient load distributing algorithms are fundamentally important. Most strategies were developed in mind, assuming homogeneous set of resources linked with homogeneous and fast networks. There for addressing main new challenges, like heterogeneity, scalability and adaptability had to be.

This paper addresses the issue of multithreading web based information in a reliable Java Code program. Sections 2,3 and 4 describe the background and propose an effective architecture and related works in this approach. In sections 5 and 6 we describe the future works and conclusion.

2. Related Work

Multithreading in SQLJ depends on the multithreading support in the underlying JDBC driver. In Oracle JDBC, methods are synchronized on the connection (i.e., the driver sends a command to the server on behalf of a thread and then waits for its completion before the connection/socket can be used by another thread. Simultaneous multithreading is possible when threads are not sharing the same connection [3].

The Java Native Interface (JNI) is a native programming interface that is part of the Java Software Development Kit (SDK). JNI lets Java code use code and code libraries written in other languages, such as C and C++. The Invocation API, which is part of JNI, can be used to embed a Java virtual machine (JVM) into native applications, thereby allowing programmers to call Java code from within native code. One of the more advanced issues you'll face when working with JNI is multithreading with native methods. The Java platform is implemented as a multithreaded system, even when running on platforms that don't necessarily support multithreading; so the onus is on you to ensure that your native functions are thread safe. In Java programs, you can implement thread-safe code by using synchronized statements. The syntax of the synchronized statements allows you to obtain a lock on an object. As long as you're in the synchronized block, you can perform whatever data manipulation you like without fear that another thread may sneak in and access the object for which you have the lock. JNI provides a similar structure using the MonitorEnter() and MonitorExit() functions. You obtain a monitor (lock) on the object you pass into the MonitorEnter() function and you keep this lock until you release it with the MonitorExit() function. All of the code between the MonitorEnter() and MonitorExit() functions is guaranteed to be thread safe for the object you locked[5].

3. Threads Concept

Threads are a control mechanism that enables you to write concurrent programs. You can think of a thread in an object-oriented language as a special kind of “system object” that contains information about the state of execution of a sequence of function calls that are said to “execute as a thread”. Usually, a special “run” or “start” procedure starts a separate thread of control. Normally, when you call a function or procedure, the compiler sets-up a stack frame (also called an activation frame) on the run-time procedure call stack, pushes arguments (or puts them into registers), and calls the function. The stack is also used as temporary storage for locally allocated objects declared in the scope of a procedure. In a sequential program, there is only one run-time stack and all activation frames are allocated in a nested fashion on the same run-time stack,

Corresponding to each nested procedure call. In a multithreaded application, each “thread” represents a separate run-time stack, so you can have multiple procedure call chains running at the same time, possibly on multiple processors. Java on Solaris supports multi-processor threads. In a sequential program, the main run-time stack is allocated at program start and all procedure calls, including the initial call to “main” are made on this single run-time stack. In a multi-threaded program, a program starts on the system run-time stack where the main procedures run. Any Function / procedure called by the main procedure have their activation frames allocated on this run-time stack. If the main procedure creates a new thread for run some procedure (usually calling a special “thread creation or construction” procedure/method), then a new run-time stack is dynamically allocated from the heap and the activation frames for the procedures are allocated on this new stack[4].

4. Connecting To Databases With JDBC

It has been estimated that half of all software development involves client/server operations. A great promise of Java has been the ability to build platform-independent client/server database applications. In Java 1.1 this has come to fruition with Java DataBase Connectivity (JDBC). One of the major problems with databases has been the feature wars between the database companies. JDBC is designed to be platform-independent, so you don’t need to worry about the database you’re using while you’re programming. However, it’s still possible to make vendor-specific calls from JDBC so you aren’t restricted from doing what you must. JDBC, like many of the APIs in Java, is designed for simplicity. The method calls you make correspond to the logical operations you’d think of doing when gathering data from a database: connect to the database, create a statement and execute the query, and look at the result set. To allow this platform independence, JDBC provides a driver manager that dynamically maintains all the driver objects that your database queries will need. So if you have three different kinds of vendor databases to connect to, you’ll need three different driver objects. The driver objects register themselves with the driver manager at the time of loading, and you can force the loading using `Class.forName()`. To open a database, you must create a “database URL” that specifies:

1. That you’re using JDBC with “jdbc”.
2. The “subprotocol”: the name of the driver or the name of a database connectivity mechanism. Since the design of JDBC was inspired by ODBC, the first sub protocol available is the “jdbc-odbc bridge,” specified by “odbc”.
3. The database identifier. This varies with the database driver used, but it generally provides a logical name that is mapped by the database administration software to a physical directory where the database

tables are located. For your database identifier to have any meaning, you must register the name using your database administration software. (The process of registration varies from platform to platform.) All this information is combined into one string, the “database URL.” For example, to connect through the ODBC subprotocol to a database identified as “people,” the database URL could be: `String dbUrl = "jdbc:odbc:people";` If you’re connecting across a network, the database URL will also contain the information identifying the remote machine. When you’re ready to connect to the database, you call the static `DriverManager.getConnection()` method, passing it the database URL, the user name, and a password to get into the database. You get back a `Connection` object that you can then use to query and manipulate the database [1].

5. Conclusions

A system was presented to design Web Based system. A Multithreading algorithm was also proposed, which minimizes the overall tasks response time by the effective usage of multithreading, a thread for each client accessing the database, and maximizes the web Database utilization by using the internet explorer and the java platform independent, this increase the scalability, and also the heterogeneity of our system supported by JAVA2 compiler that increase the platform Independents in our system.

6. Future works

There are, of course, several open issues that need to be addressed in database multithreading system like as:

1. The performance of our web based database strategy in sharing the data with every client knowing the username and password of the database can be strengthened by supporting each client with his own username and password or any other information.
2. The global usage of storage and other resources depends to some extent on no. of clients. Reducing this resource usage by client data movements can ultimately improve performance of the server, by sending a copy of the executable code to the client to use its resources.
3. Designing a backup filing system to avoid data loses caused by any system collapses.

References

- [1] Eckel B. J., 1998, “Thinking in Java”, MindView Inc., www.mindview.net/books.
- [2] DeveloperWorks, 2004, “Introduction to Java Threads”, your source for great tutorials, ibm.com/developerWorks, 490.
- [3] Mensah K. A. , 2006, “Oracle Database Programming Using Java And Web Services”, Elsevier, Inc., 566.
- [4] Lavender G. G., 1999, “Concurrent Programming using Threads”, Kasper Inc., 890.
- [5] Stricker S. K., 2002, “Java programming with JNI”, Developer IBM, 390, (sstricke@us.ibm.com).


```
BufferedReader in = null;
Printwriter out = null;
System.out.println(Accepted Client : ID _ " + m_cid + "Accrose_" + m_cs.GetInetAddress().GetHostName());
Try{
    In = new bufferedreader( new InputStreamReader( m_cs.GetInputStream()));
    out = new PrintWriter( new OutputStreamWriter( m_cs.GetOutputStream()));
    String cc = in.readline();
    StringTokenizer st = new Stringtokenizer(cc, "/");
    st.Nexttoken();
    StringTokenizer st1 = new Stringtokenizer(st.NextToken()," ");
    cc = st1.NextToken();
    Static Final String db = "Jdbc:Odbc:Airline";
    Static Final String user = "USER NAME";
    Static Final String password = "PassWord";
    Calss.forName("Sun.Jdbc.Odbc.JdbcOdbcDriver");
    Connection con = DriverManager.GetConnection(db,User,PassWord);
    Statement stmt = con.CreatStatement();
    ResultSet rs = stmt.ExecuteQuery(cc);
    Out.Write("<html>".GetBytes());
    Out.Write("<head>".GetBytes());
    Out.Write("<title> This Is The Table That You Requested</title>".GetBytes());
    Out.Write("<head>".GetBytes());
    Out.Write("<body>".GetBytes());
    ResultSetMetaData rsmd = rs.GetMetaData();
    int noc = rsmd.GetColumnCount();
    For (i=1 ; i<= noc ; i++)
    { string cn = rsmd.GetColumnName(i);
      Out.Write(cn.GetBytes + " , ".GetBytes);
    }
    Out.Write("\n".GetBytes);
    While (rs.Next())
    For (int i = 1 ; i <= nc ; i++)
    Out.Write(rs.GetString(i).GetBytes() + " , ".GetBytes());
    Out.Write("\n".GetBytes());
    Out.Write("</body>".GetBytes());
    Out.Write("</html>".GetBytes());
    In.Close();
    Out.Close();
    m_cs.Close();
    Stmt.Close();
}Catch(Exception ex)
{System.Out.Println(ex);
}
} //Class Server
```

REMOTE USER AUTHENTICATION SCHEME USING HIDING INFORMATION IN IMAGE BASED ON LSB STEGNOGRAPHY

Amer Kais Obaid

Control and Systems Engineering Department
University of Technology
amerkais2010@yahoo.com

Abstract

Remote User Authentication Scheme using Hiding Information in Image is the best practical solution for remote accessing. To authenticate the legitimacy of a remote user over insecure channel, password based remote user authentication scheme is widely used, but may be vulnerable to interception from attackers, so needing to another approach to supporting the process of authentication. In this paper we propose a new remote mutual authentication scheme using hiding information in Image based on LSB (Least Significant Bit) Stenography. It provides high security and mutual authentication at a reasonable computational cost. Furthermore it restricts most of the current attacking mechanisms.

Keywords: *Web security, User authentication, confidentiality, Hiding Information, Steganography.*

1. Introduction

To access resources from a remote system, users should have proper access rights. One of the simpler and more efficient mechanisms is the use of a password authentication scheme. To access the resources, each user should have an identity and a password [1], thus information in transmission may be vulnerable to

interception by attackers because of the Internet as a whole is unsecure transmission media, thus information in transmission may be vulnerable to interception by attackers. The important of reducing a chance of the information being detected during the transmission. Some solutions to be discussed are how to passing information in a manner that the very existence of the message is unknown in order to repel attention of the potential attacker. We can use Steganography to hide this information in a digital image. We focus on the Least Significant Bit (LSB) technique in hiding secret information in a digital image [2].

2. User authentication

Remote user authentication using password is the most widely used scheme for a valid user to login to a remote server and to access the services provided by the server over insecure channels [3].

In remotely accessed computer systems, a user identifies himself to the system by sending a secret password. There are many ways an intruder could learn the user's secret password and then impersonate him when interacting with the system; one of these by intercepting the user's communication with the system, e.g., eavesdropping on the line connecting the user's terminal with the system, or observing the execution of the password checking program [4]. The password-based authentication scheme with

steganography is the important parts of security for accessing remote servers [5].

4. Steganography

Steganography is the process of hiding one file inside another such that others can neither identify the meaning of the embedded object, nor even recognize its existence. Current trends favor using digital image files as the cover file to hide another digital file that contains the secret message or information. One of the most common methods of implementation is Least Significant Bit Insertion, in which the least significant bit of every byte is altered to form the bit-string representing the embedded file. Altering the LSB will only cause minor changes in color, and thus is usually not noticeable to the human eye. While this technique works well for 24-bit color image files, steganography has not been as successful when using an 8-bit color image file, due to limitations in color variations and the use of a color map [6].

4. Least Significant Bit Insertion

One of the most common techniques used in steganography today is called least significant bit (LSB) insertion. This method is exactly what it sounds like; the least significant bits of the cover-image are altered so that they form the embedded information as shown in figure 1. The following example shows how the letter B can be hidden in the first eight bytes of three pixels in a 24-bit image [6].

Pixels: (00100101 11111001 10001001)
 (00100110 11001001 11001001)
 (11001000 00100110)

B: 01000010

Result: (00100100 11111001 10001000)
 (00100110 11001000 11101000)
 (11001001 00100110)

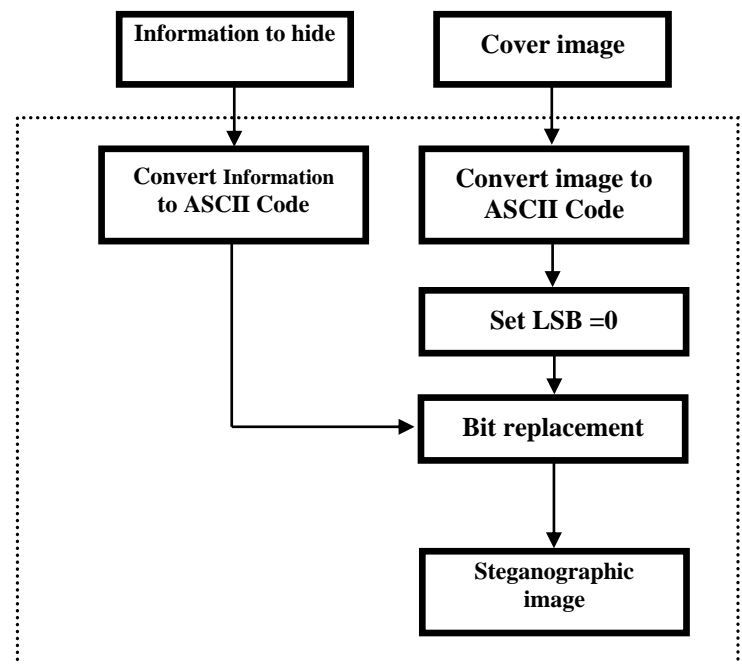


Figure 1 The structure of the algorithm LSB.

5. Information Hiding System.

An information hiding system has been developed for confidentiality. However, in this paper, we use an image file as a carrier to hide secret information. Therefore, the carrier will be known as cover-image, while the stego-object known as stego-image. The implementation of the system will only focus on Least Significant Bit (LSB) as one of the steganography techniques as mentioned in section 4 above.

For embedding the data into an image, we require two important files. The first is the original image so called cover-image. The image in Figure 2, will hold the hidden information. The second file is the message itself, which is the information to be hidden in the image. In this process, we decided to use a plaintext as the message.

The advantages of LSB are its simplicity to embed the bits of the message directly into the LSB plane of cover-image and many techniques use this method. Modulating the LSB does not result in a human-perceptible

difference because the amplitude of the change is small. Therefore, to the human eye, the resulting stego-image will look identical to the original image. This allows high perceptual transparency of LSB [2].

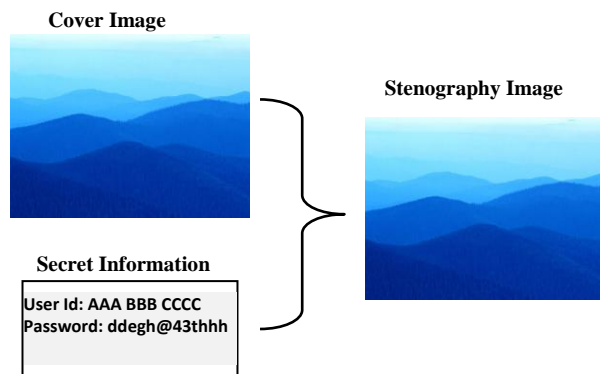


Figure 2 Stenography Image Process

6. The Proposed System

In this paper, we propose a new remote user authentication system using hiding information based on stenography. Our proposed system is composed of an initial phase, a login phase and an authentication phase. When the user wants to access the remote server, he firstly requests a connection with the server. The server authenticates the user identity in the authentication phase. Figure 3 shows the structure of the proposed System.

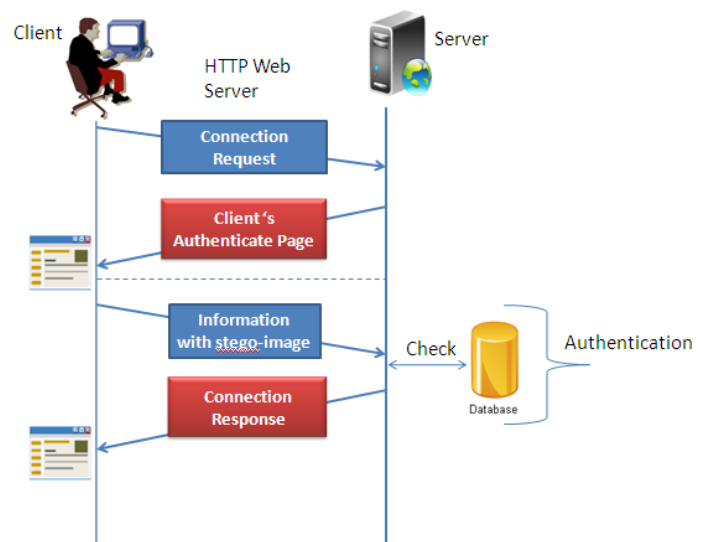


Figure 3 The general structure of the proposed system.

6.1 Initial Phase

First the Remote user and Authentication Server have the same idea about stenography and the transmission of secret information must be done by using hiding information based on stenography.

6.2 Login Phase

When the user requests to the web server services, the server sends a page to authenticate from user's identity. The user will perform the following operations:

1. Loading Digital Image.
2. Writing User ID and Password.
3. Generating Stenography Image.
4. Uploading Steno-Image and sending it to the server.

6.3 Authentication Phase

After the server receives the Steno-Image, it will perform the following operations:

1. Checking the format of Steno-Image.
2. Extracting the secret information (User ID and Password).
3. Checking this secret information with authorized user in its database.
4. If the identity is correct, then server will accept the login request. Otherwise, the request will be rejected.

7. Conclusions

In this paper, we have proposed a new password authentication scheme over insecure networks based on hiding user identity and password. It can enhance confidentiality of information and provides a means of communicating privately and mutual user authentication between the user and the server is provided.

References

- [1] Rajaram R., Amutha P. M., 2009, "New Remote Mutual Authentication Scheme using Smart Cards", Thiagarajar College of Engineering, Madurai, India, p-12.
- [2] Muhalim M. A., Subariah I., Mazleena S., Mohd R., 2003, "Information Hiding Using Steganography", University Technology Malaysia.
- [3] Sung W. L., Hyuck J. K., and Hyun S. K., 2008, "Cryptanalysis on Improved Remote User Authentication Scheme Preserving User Anonymity", International Journal of Computer Science and Network Security, VOL.8 No.10.
- [4] Anita K. Jones, 1981, "Password Authentication with Insecure

Communication", Leslie Lamport SRI International, VOL.24 No.11.

- [5] GiriD., and Srivastava P. D., 2006, "An Improved Remote User Authentication Scheme with Smart Cards using Bilinear Pairings.", Indian Institute of Technology, Kharagpur, India, p-11.
- [6] Mamta J., Parvinder S., and Ekta W., 2009, "Application of LSB Based Steganographic Technique for 8-bit Color Images", World Academy of Science, Engineering and Technology.

Appendix A

This appendix explains the steps for embedding the information into an image, as the following steps:

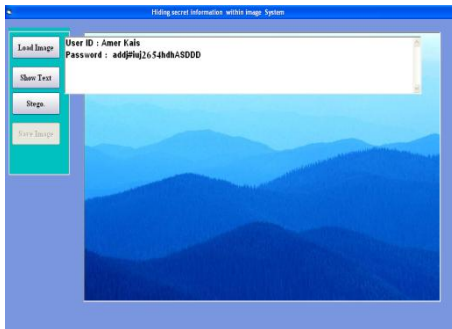
1. The first step loading the original image as *cover-image*.
2. Writing User ID and Password in text-box.
3. Generating Steganography Image, by embedding the information in the text-box into loaded image.
4. Saving stego-image, and sending it to server by uploading this image by the authentication web-page.



a. Main Form of Steganography Program



b. Loading the original image as cover-image.



c. Generating Stenography Image

Figure A.1 Embedding the information into an image.

COMPUTING NODES AND LINKS APPEARANCES ON GEODESICS IN NETWORK TOPOLOGIES USING GRAPH THEORY

Dr. Siddeeq Yousif Ameen
College of Engineering
Gulf University
BAHRAIN

Dr. Laith Jasim Saud
Control and Systems Eng. Dept.
University of Technology
Baghdad-IRAQ
laith_js@yahoo.com

Abstract

There are many issues to consider when analyzing, designing, or optimizing a communication network. Network topology is one of these issues. Most of the analysis, design, and optimization methods need modeling the system or case of concern and preparing the necessary related mathematical basis. This paper proposes two important topology properties models and provides the necessary formulas for computing them using graph theory approach. The first of these two properties is related to routes reliance on links and the other is related to routes reliance on nodes. These properties could be used in support with other topology properties to develop important topology design objectives necessary for topology analysis, design, and optimization.

Keywords: Network topology, Graph theory, Topology modeling and properties, Node and link utilization.

1- Introduction

One of the important issues in communication in a network is the traffic distribution over links and nodes in the network. It is an important matter that the network utilizes its nodes and links as uniformly as possible. Unfortunately, determining the traffic distribution in a communication network is a very complex process and in many cases is unpredictable

which makes some use statistical methods to help in predicting to some extent the nature of the traffic or load in the network. The traffic distribution and link and node utilization is a function of many parameters among which are the topology, the relative positions and number of the source and destination nodes, and the presence of high, medium or low traffic carrying source-destination node pairs [1].

Here, it is suggested to adopt an approach which helps in link and node utilization estimation which is only topology dependent, and so avoiding the uncertainty and unpredictability of other factors. This will, at least, help in designing a topology which provides a fair ground for uniform use of nodes and links. Any such approach will need computing the number of appearances of nodes and links on all possible routes. Two important topology properties regarding computing link and node appearances on routes are proposed here. These properties could be used to develop topology objectives for topology optimization purpose. The two properties are developed using graph theory approach.

2- Definition of Nodes and Links Utilization

In general, the amount of traffic between a source-sink pair is the amount of information carried between them. The

measure of traffic is dependent on the switching strategy followed by the system. If a packet switched network is considered then the minimum packet size may be defined as one unit of traffic. If a circuit switched network is considered, an arbitrary small amount of time can be considered as the amount of traffic. But for either of the cases it will be assumed that a direct or virtual connection has been established between the source-sink pair prior to initiation of the information transfer. So while routing the information through the pre-established path some specific links and nodes will be utilized. When a unit amount of traffic is routed through a link or a node, it is said that, that particular link or node has been utilized once [2].

2- Modeling Network Topology with Graph Theory

Graph theory is a branch of mathematics concerned mainly about structures. This theory is concerned with patterns of relationships among pairs of abstract elements [3].

Graph theory is quite useful when the main interest is in the structural properties of any empirical system as it provides concepts, theorems, and methods appropriate to the analysis of structures [4].

Graph theory represents structures as graphs which in turn will be represented as matrices. These matrices of the way nodes are connected in the graph are called adjacency matrices. Graph theory will be used here for two main purposes the first of which is to model the network topology in question, keeping in mind that the topology of a network is in reality a structure, and the second will be in computing topology properties. Figure (1) shows a simple network with its corresponding graph and adjacency matrix.

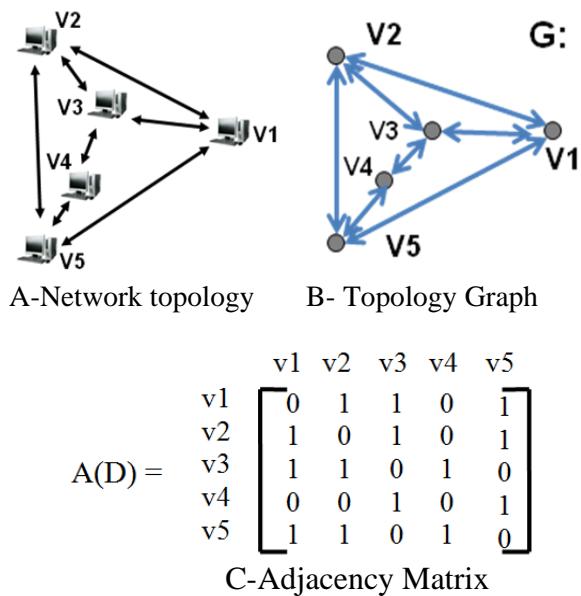


Figure (1): A sample network topology with its representative graph and adjacency matrix.

4- Computing the “Number of Appearances of Links and Nodes on Geodesics” Properties

There are different strategies of data movement over the network through the links and nodes. One well known and used strategy is the shortest distance path (geodesic) strategy [5]. This strategy will be depended when developing the properties here.

A- Developing the “Number of Appearances of Nodes on Geodesics” Array

The first property to be developed is the number of appearances of nodes on geodesics (NAG(D)) array. This array shows the number of times a given node is on the geodesics between a given connected nodes pair in a given graph D. Here a formula (F_1) is derived to support finding the array ($NAG_{ij}(N_k)$), which is a three dimension array and stands for the number of times node k is on the geodesics from node i to node j. The NAG array is found as follows:

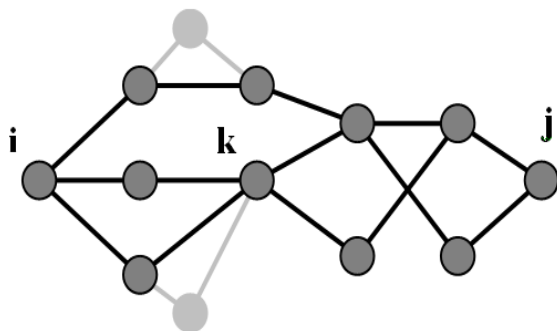
a- Find the distance matrix. (Refer to appendix A for how to find the distance matrix)

b- For a given i, j, k (where: $1 \leq i, j, k \leq n$ and $k \neq i \neq j$, n =number of nodes in the given network or graph), check if the node k is on the geodesics from node i to node j . This is done by checking if the distance from node i to node k plus the distance from node k to node j is equal to the distance from node i to node j . If this is true then apply formula (F_1) which states:

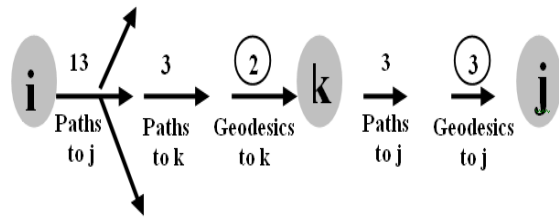
"If node k is on one or more of the geodesics from node i to node j , then the number of times node k is on the geodesics from node i to node j is equal to the number of geodesics from node i to node k multiplied by the number of geodesics from node k to node j ".

Figure (2) illustrates this formula which is to be proved as follows:

i- Since it is assumed that k is on (one or more) of the geodesics from node i to node j , then all geodesics from node i to node k and all geodesics from node k to node j are part of these geodesics. This is obtained from the theorem which states that a point k is on a geodesic from point i to point j if and only if $d_{ik} + d_{kj} = d_{ij}$, and the converse is right [3].



A- Part of a sample topology showing all possible paths from node i to node j .

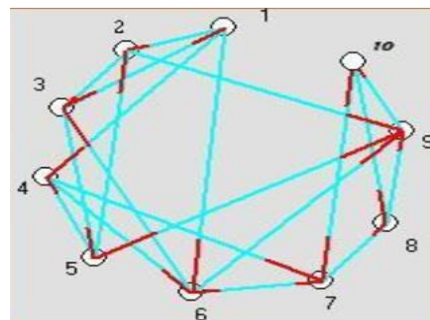


B- Details of the paths from node i to node j through node k . Number of times node k is on the geodesics from node i to node $j = 2 \times 3 = 6$.

Figure (2): Illustration of the formula (F_1).

ii- Each geodesic from node i to node k can be completed by any of the geodesics from node k to node j to form a geodesic from node i to node j . This is obtained from the theorem which states that every subpath of a geodesic is a geodesic, then the number of times k will appear on the geodesics from node i to node j is equal to the number of geodesics from node i to node k multiplied by the number of geodesics from node k to node j [3].

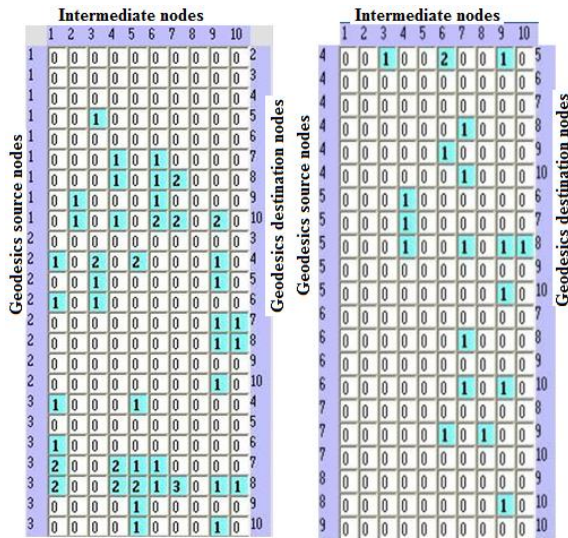
Figure (3) shows a 10-nodes sample topology with its adjacency Matrix and the number of appearances of nodes on geodesics.



A- A 10 nodes network

A	1	2	3	4	5	6	7	8	9	10
1	0	1	1	1	0	1	0	0	0	0
2	0	0	1	0	0	0	0	0	1	0
3	1	0	0	0	1	0	0	0	0	0
4	0	0	0	0	0	1	1	0	0	0
5	0	1	0	1	0	0	0	0	1	0
6	0	0	1	0	0	0	1	0	1	0
7	0	0	0	0	0	1	0	1	0	1
8	0	0	0	0	0	0	0	0	1	0
9	0	0	0	0	1	0	0	0	0	1
10	0	0	0	0	0	0	1	1	0	0

B- Adjacency matrix



C- Number of times a given node is on the geodesics between 2 connected nodes

Figure (3): Number of appearances of nodes on geodesics.

B- Developing the “Number of Appearances of Links on Geodesics” Matrix

The second property to be developed is the number of appearances of links on geodesics (LAG(D)) matrix. This matrix shows the number of times a given link is on the geodesics between a given linked nodes pair. To form LAG(D) means finding the number of times a given link (ab) is on the geodesics from node i to node j, for all i's and j's (where $i \neq j$). A formula is derived here for this purpose and is given below:

$$LAG_{ab} = \sum_{i=1}^n \sum_{j=1(j \neq i)}^n LAG_{ab}(i, j) \dots (1)$$

where;

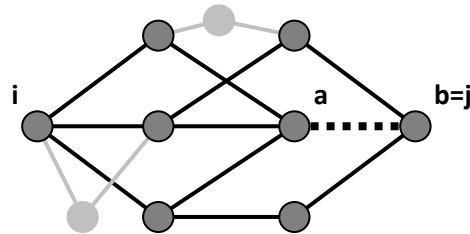
$$LAG_{ab}(i, j)_{i \neq j} = \begin{cases} NAG(i, j, a) & ; b=j, a \neq i \\ NAG(i, j, b) & ; a=i, b \neq j \\ (NAG(i, b, a)) \times (NAG(a, j, b)) & ; a \neq i, b \neq j \\ 1 & ; a=i, b=j \end{cases}$$

where;

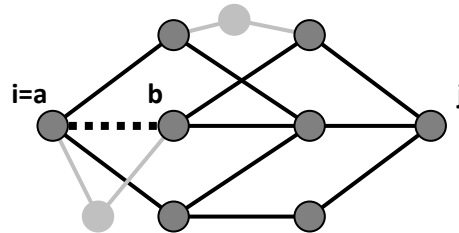
- LAG_{ab} : number of times link (ab) appears on network's geodesics.
- $LAG_{ab}(i,j)$: number of times link (ab) is on the geodesics from node i to node j.
- n: number of nodes in the network.

- $NAG(i,j,b)$: number of times node b is on the geodesics from node i to node j, and similarly for the other NAGs.

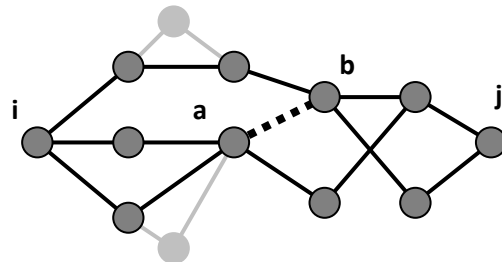
Examples for the four cases or possibilities covered by this formula are shown in Figure (4).



Case 1
(There are 5 geodesics from i to j.)(There are 8 paths from i to j.)(a is 3 times on the geodesics from i to j.)(The link ab is 3 times on the geodesics from i to j.)



Case 2
(There are 5 geodesics from i to j.)(There are 8 paths from i to j.)(b is 2 times on the geodesics from i to j.)(The link ab is 2 times on the geodesics from i to j.)



Case 3:
(There are 8 geodesics from i to j.)(There are 13 paths from i to j.)(There are 2 geodesics from i to a.)(There are 2 geodesics from b to j.)(The link ab is $2 \times 2 = 4$ times on the geodesics from i to j.)



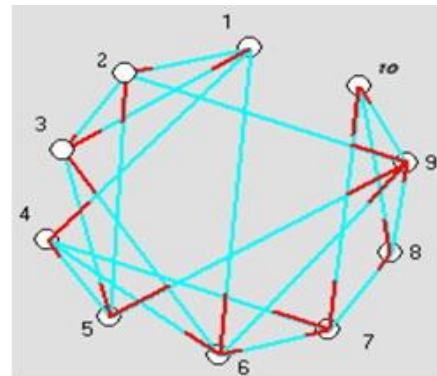
Case 4: (There is 1 geodesic from i to j.)(There is 1 path from i to j.)(The link ab is 1 time on the geodesic from i to j.)

Figure (4): The four possible cases for link ab appearance on the geodesics between nodes i and j.

The LAG formula (equation 1) could be proved as follows:

- i- If $b=j$, this means that node a is directly linked to node j (i.e. distance from node a to node j is 1), and so the link ab will appear on the geodesics from i to j as much as node a appears on these geodesics because all the geodesics passing from node i to node j through node a have to pass through the unique geodesic of length one, namely link ab . This is given by: $NAG(i, j, a)$.
- ii- If $a=i$ and $b=j$, then ab is a unique geodesic of length one between node i and node j . Hence, the link ab appears once whenever node i approaches node j .
- iii- If $a \neq i$ and $b \neq j$, then for the link ab to appear on the geodesics from node i to node j , each of these geodesics must pass through nodes a and b simultaneously. Hence, the number of appearances of link ab depends on the number of times node a appears on the geodesics from node i to node j with the condition of passing through node b , and on the number of times node b appears on the geodesics from node i to node j with the condition of passing through node a . Based on this mutual dependability, the number of times link ab appears on the geodesics from node i to node j is given by the number of appearances of node a on the geodesics between node i and node b , multiplied by the number of appearances of node b on the geodesics between node a and node j , or: $NAG(i,b,a) \times NAG(a,j,b)$.
- iv- If $a=i$, this means that node b is directly linked to node i (i.e. distance from node b to node i is 1), and so the link ab will appear on the geodesics from i to j as much as node b appears on these geodesics, because all the geodesics passing from node i to node j through node b have to pass through the unique geodesic of length one, namely link ab . This is given by: $NAG(i, j, b)$.

Figure (5-b) shows the links number of appearances on geodesics matrix for the network of Figure (5-a).



5-a

		Link destination node									
		1	2	3	4	5	6	7	8	9	10
Link source node	1		5	2	8			10			
	2			5						8	
	3	8				11					
	4						5	12			
	5		3		9					6	
	6			4				8		6	
	7						8		10		5
	8									8	
	9						7				8
	10							5	4		

Matrix showing links appearances on geodesics

5-b

Figure (5): A 10 nodes network with a matrix showing the number of appearances of each link on the geodesics for the network.

5- Assessment and Conclusions

Two new topology properties have been introduced here relating computing nodes and links appearances on geodesics in a given communication network. The two properties are quite useful when considering load distribution on nodes and links, and so can help in designing topologies with fair distribution of load on nodes and links. The properties have been developed using graph theory approach and are quite suitable for programming purposes. The properties are useful for analysis, design, and optimization purposes when it comes to loading considerations.

References

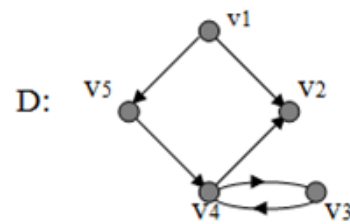
- [1] Nazrul,S., 1998, “Survivability Analysis of Two Specific 16-Node, 24-Link communication Networks”, Master's Thesis, Electrical and Computer Engineering, Virginia Polytechnic Institute and State University.
- [2] Streenstrup,M., 1995, “Routing in Communication Networks”, Prentice-Hall Inc.
- [3] Harary F., 1965, "Structural Models: An Introduction to the Theory of Directed Graphs", John Wiley & Sons.
- [4] Freeman, L., 1978/79, "Centrality in Social Networks Conceptual Clarification", Social Network Journal, No 1.
- [5] Saud L. J., 2006, “Topology Design Optimization Using GA.”, PhD Thesis, Control and Systems Engineering Department, University of Technology.

Appendix “A” Finding the Distance Matrix [3]

Let $N(D) = [d_{ij}]$ be the distance matrix of a given graph D, where $i = 1,2,\dots,n$, and $j = 1,2,\dots,n$. Then;

1. Every diagonal entry d_{ij} is 0,
2. $d_{ij} = \infty$ if there is no path from i to j and so i cannot reach j , and otherwise, d_{ij} is the smallest power y to which A must be raised so that $a^y_{ij} > 0$, that is, so that the i,j entry of $A^y_{\#}$ is 1. (Note: The $A^y_{\#}$ stands for the y^{th} logic power of the adjacency matrix A . The logic power is made by logic multiplication rather than arithmetic multiplication, and as an example: $1 \times 1 + 1 \times 0 + 1 \times 1 = 1$).
3. $N(D)$ only tells the length of the geodesic between two points, and does not tell how many geodesics are there between any given two points.

The procedure for constructing the distance matrix $N(D)$ from the adjacency matrix will be illustrated for the graph of Figure (6).



$$A = \begin{matrix} & \begin{matrix} v_1 & v_2 & v_3 & v_4 & v_5 \end{matrix} \\ \begin{matrix} v_1 \\ v_2 \\ v_3 \\ v_4 \\ v_5 \end{matrix} & \begin{bmatrix} 0 & 1 & 0 & 0 & 1 \\ 0 & 0 & 0 & 0 & 0 \\ 0 & 0 & 0 & 1 & 0 \\ 0 & 1 & 1 & 0 & 0 \\ 0 & 0 & 0 & 1 & 0 \end{bmatrix} \end{matrix}$$

$$A^{2\#} = \begin{matrix} & \begin{matrix} v_1 & v_2 & v_3 & v_4 & v_5 \end{matrix} \\ \begin{matrix} v_1 \\ v_2 \\ v_3 \\ v_4 \\ v_5 \end{matrix} & \begin{bmatrix} 0 & 0 & 0 & 1 & 0 \\ 0 & 0 & 0 & 0 & 0 \\ 0 & 1 & 1 & 0 & 0 \\ 0 & 0 & 0 & 1 & 0 \\ 0 & 1 & 1 & 0 & 0 \end{bmatrix} \end{matrix}$$

$$A^{3\#} = \begin{matrix} & \begin{matrix} v_1 & v_2 & v_3 & v_4 & v_5 \end{matrix} \\ \begin{matrix} v_1 \\ v_2 \\ v_3 \\ v_4 \\ v_5 \end{matrix} & \begin{bmatrix} 0 & 1 & 1 & 0 & 0 \\ 0 & 0 & 0 & 0 & 0 \\ 0 & 0 & 0 & 1 & 0 \\ 0 & 1 & 1 & 0 & 0 \\ 0 & 0 & 0 & 1 & 0 \end{bmatrix} \end{matrix}$$

$$A^{4\#} = \begin{matrix} & \begin{matrix} v_1 & v_2 & v_3 & v_4 & v_5 \end{matrix} \\ \begin{matrix} v_1 \\ v_2 \\ v_3 \\ v_4 \\ v_5 \end{matrix} & \begin{bmatrix} 0 & 0 & 0 & 1 & 0 \\ 0 & 0 & 0 & 0 & 0 \\ 0 & 1 & 1 & 0 & 0 \\ 0 & 0 & 0 & 1 & 0 \\ 0 & 1 & 1 & 0 & 0 \end{bmatrix} \end{matrix}$$

$$N(D) = \begin{matrix} & \begin{matrix} v_1 & v_2 & v_3 & v_4 & v_5 \end{matrix} \\ \begin{matrix} v_1 \\ v_2 \\ v_3 \\ v_4 \\ v_5 \end{matrix} & \begin{bmatrix} 0 & 1 & 3 & 2 & 1 \\ \infty & 0 & \infty & \infty & \infty \\ \infty & 2 & 0 & 1 & \infty \\ \infty & 1 & 1 & 0 & \infty \\ \infty & 2 & 2 & 1 & 0 \end{bmatrix} \end{matrix}$$

Figure (6): Constructing the distance matrix $N(D)$ for graph D.

RSA SECURITY ENHANCEMENT

Qaswaa K. Abood **Manal F. Younis** **Mahmoud A. Othman**
kaswaaa@yahoo.com manal_fadel2@yahoo.com maomk72@yahoo.com

Computer Department, Collage of Science,
University of Baghdad.

Abstract

The RSA cryptosystem is the most widely deployed public key cryptosystem and is used for both encryption and digital signature. It is commonly used in securing e-commerce and e-mail, implementing virtual private network and providing authenticity of electronic documents. RSA security depends on the difficulty of the factoring large numbers. However if one could factor large number n into primes number, then one could obtain the private key. This paper presents RSA an approach to increase RSA security key size of RSA by adding a large prime number to the modulus. The proposal approach result was compared with the standard RSA. This work approach was applied on local area network (LAN).

Keywords: *Public key cryptosystem, RSA, RSA enhancement*

1. Introduction

Today even small businesses have more than one computer; at a minimum they have several personal computers. More realistically, most organizations are taking advantage of computer networks by installing portion of applications on more than one computer. As companies open offices in new location, they need to share data across a larger distance; companies are finding it useful and necessary to share data with people around the world. Unfortunate, the data going across the internet may not be as secure as we would like to think, it is not especially difficult for a person with the

right technical skill to intercept the data going from one computer to another, but fortunately, there are several mechanisms that can protect any information that need to be send over a network [1], one of these algorithms that are used for this is RSA algorithm [2].

In cryptography, a **key** is a piece of information (a parameter) that determines the functional output of a cryptographic algorithm. Without a key, the algorithm would have no result. In encryption, a key specifies the particular transformation of plaintext into cipher text, or vice versa during decryption. Keys are also used in other cryptographic algorithms, such as digital signature schemes and message authentication codes [3]. RSA is a public key cryptography: that includes a pair of cryptography keys (a public key and a private key) [1]. The private key is kept secret, while the public key may be widely distributed, incoming messages would have been encrypt with the recipients public key and can only be decrypt with his corresponding private key. The keys are related mathematically, but the private key cannot be practically derived from the public keys as RSA algorithm [1]. A Fast implementation on the RSA algorithm using A GNU MP library the application is executed, the existence of the key files are checked and if they do not exist, the RSA keys are generated [4]. On the Security of Multi prime RSA collect the strongest known algebraic attacks on multi-prime RSA these include factoring, small private exponent, small CRT exponent and partial key exposure attacks [5]. Both 2-prime and multi-prime implementations require squaring reduction

and multiplication reduction of multi-precision integers proposed as An efficient implementation of multi-prime RSA on DSP processor[6]

This paper is organized as follows. Section 2 illustrates the proposal algorithm. Section 3 computation complexity of the proposal algorithm. Section 4 implementation. In section 5 the simulation results followed by conclusion in section6.

2. The proposal algorithm:

This paper presents a method to increase the key size of RSA modulus by adding another large prime numbers to this algorithm. The proposed approach involves two main processes RSA key generation process and encryption ,decryption process:-

2.1. RSA key generation process

The keys of RSA algorithm are generated using following steps:

- Choose (4-6) distinct large number random prime p,q,r,s,x,y.
- Compute $n=p*q*r*s*x*y$ n is used as modulus for both public and private key.
- Compute Euler totient of n, which is the number of positive integer less than n and relatively prime to n.
 $\Phi(n)=(p-1)*(q-1)*(r-1)*(s-1)*(x-1)*(y-1)$
- Choose the integer e such that $1 < e < \Phi(n)$, e is released as the public key exponent.
- Compute d that represents the private key and satisfy the congruence relation

$$d = e^{\phi(n)-1} \bmod \phi(n)$$

2.2. Encryption and decryption process

To Encrypt the M message, M is divided into blocks such that $M < n$ then using the formula $M^e \bmod n$ to produce the cipher text.

$$c = M^e \bmod n \text{ Cipher text}$$

Decrypting the cipher text to recover the plaintext the following formula is used.

$$M = c^d \bmod n$$

3. Computation complexity of the proposal algorithm:

In the following algorithms the $\Phi(n)$ become complex according the following computations Computing $\Phi(n)$ without Factoring n with p, q keys.

Assume that $n = p \times q, p < q$.

Since $(p + q)^2 - (q - p)^2 = 4pq = 4n$, then

$$(p+q)^2 = 4n + (q - p)^2 \text{ so}$$

$$q + p = \sqrt{4n + (q - p)^2} \text{ and then}$$

$$\Phi(n) = n - (p + q) + 1$$

q - p	$(q - p)^2 + 4n$	$q + p = \sqrt{4n + (q - p)^2}$
1	885	29.7489...
2	888	29.7993...
3	893	29.8831...
4	900	30

Example:

$$n = 221 (4n=884)$$

So, $q - p = 4$ and $q + p = 30$, then $\Phi(n) = 221 - (30) + 1 = 192$ and $p = 13, q = 17, n = 13 \times 17$.

Therefore breaking RSA system by computing $\Phi(n)$ is not easier than breaking RSA system by factoring n. (This is why n must be composite; $\Phi(n)$ is easy to compute if n is prime.)

a) Computing $\Phi(n)$ without Factoring n with p,q keys, assume that

$$n = p \times q \times r, p < q, q < r.$$

$$\text{Since } (p + q)^2 + (q - r)^2 - (q - p)^2 - (r - q)^2 = 4n(1/r + 1/q + 1/p)$$

So to compute $\Phi(n)$ we must at least know one prime key

Therefore braking it will be more complicated and degree of complexity increase according to increase key size of RSA when $n=pqrsxy$

4. Implementation

This work concerns implementation of RSA enhancement on network. The suggested system is designed by connecting two computers as a network client/server model.

Then the sending message is encrypted by this algorithm in one computer when the other computer receives the message and decrypts it. Consider a situation where takao wants to send database transaction to makiko across the internet. Takao looks up makiko's public key in a directory. Once the message is encrypted with makiko's public key, only her private key can decrypt no one else can read or change the transaction message. However, someone might be able to destroy the message before makiko receives it.

There is a second use of dual- key system called authentication. Let's say that takao wants to send a message to makiko. To make sure that only she can read it, he encrypts it with her public key; however, he is worried that someone has been sending false message to makiko using his name. takao wants to make sure that makiko knows the message came from him. If takao also encrypts the message with his private key, it can be decrypted only with takao's public key. When makiko receives the message, she applies her private key and takao's public key. If the message is readable, then it must have been sent by takao. This situation is depicted in figure (1).

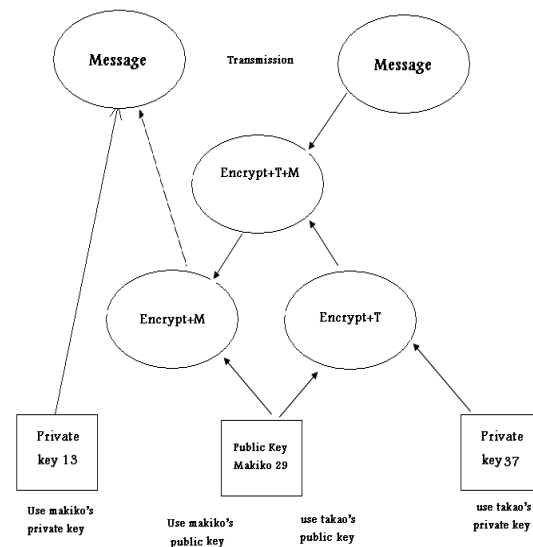


Figure (1)

5. Simulation results:

RSA security depends on factoring large number (N). The security of RSA approach relies on factoring huge numbers (128 digits or more), which would take many years to factor with current technology.

Factoring n would enable an enemy cryptanalyst to break out method. The factors of n enable him to compute $\Phi(n)$ and thus d. fortunately; factoring a number seems to be much more difficult than determining whether it is prime or composite [7].

There are several methods to factor number, but the fastest factoring algorithm developed by Pollard [8] is the general number field sieve (GNFS) is a general purpose algorithm for either factoring large integers or for solving an ordinary discrete logarithm problem. Its run time depends only on the size of the number being factored, or the size of the underlying field for the discrete logarithm problem. The time required to factor N using the general number field sieve is [9]:

$$L(N) = \exp(c (\ln N)^{1/3} (\ln \ln N)^{2/3}).$$

This function combines the time to do the sieving and the time to solve the matrix. Theoretically each takes an equal amount of time. This fraction has been increased as the number get large.

The space required scales with SQRT (L (N))the proposed method more common for increased efficiency of encryption due to the hardware speedups has enabled keys to easily scale up to the dominant size of 1024 bits[9,10]

Tables (1-3) demonstrate the compare between RSA and the proposed methods in term of time, operation and space.

Table 1:RSA operation verses the proposed method operation.

Digit	pq	pqr	Pqrs	Pqrsx	pqrsxy
100	8.7×10^{12}	3.5×10^{15}	5.08×10^{17}	3.4×10^{19}	1.4×10^{21}
150	3.5×10^{15}	4.4×10^{18}	1.4×10^{21}	2×10^{23}	2.3×10^{26}
200	5.1×10^{17}	1.4×10^{21}	9.1×10^{23}	2.3×10^{26}	3.1×10^{28}
250	3.4×10^{19}	1.9×10^{23}	2.3×10^{26}	1×10^{29}	2×10^{31}
300	2×10^{23}	1.6×10^{25}	3.18×10^{28}	2×10^{31}	6.8×10^{33}
350	4.1×10^{22}	8.4×10^{26}	2.6×10^{30}	2.7×10^{33}	1.25×10^{36}

Table 2: RSA time in years verses the proposed method time.

Digit	Pq	pqr	pqrs	pqrsx	Pqrsxy
100	2.7×10^5	1.1×10^8	1.6×10^{10}	1.1×10^{12}	4.4×10^{13}
150	1.1×10^8	1.3×10^{11}	4.4×10^{13}	6.4×10^{15}	7.2×10^{18}
200	1.6×10^{10}	4.4×10^{13}	2.9×10^{16}	7.2×10^{18}	9.8×10^{20}
250	1.1×10^{12}	6.4×10^{15}	7.2×10^{18}	3.1×10^{21}	6.3×10^{23}
300	6.4×10^{15}	5×10^{17}	9.8×10^{20}	6.3×10^{23}	2.1×10^{26}
350	1.3×10^{15}	2.6×10^{19}	8.2×10^{22}	8.5×10^{25}	4×10^{29}

Table 3: RSA space in Giga byte and the proposed method space.

Digit	pq	pqr	Pqrs	pqrsx	Pqrsxy
100	400	1×10^4	1.2×10^5	1×10^6	6.6×10^6
150	1×10^4	3.6×10^5	6.6×10^6	8×10^7	2.6×10^9
200	1.2×10^5	6.6×10^6	1.7×10^8	2.6×10^9	3.1×10^{10}
250	1×10^6	8×10^7	2.6×10^9	5.5×10^{10}	7.9×10^{11}
300	8×10^7	7×10^8	3.1×10^{10}	7.9×10^{11}	1.5×10^{13}
350	3.6×10^7	5×10^9	2.8×10^{11}	9.2×10^{12}	6.3×10^{14}

Table (1) shows the difference in number of operation between the standard RSA and the proposed method, in different ways when each prime digits=50 the number of operation of pq= 8.7×10^{12} , pqr= 3.5×10^{15} , pqrs= 5.08×10^{17} , pqrsx= 3.4×10^{19} and pqrsxy= 1.4×10^{21} also, the number of operation to factor n is increased then the attacker to break this factor will be more difficult due the increase in prime number and its coefficient.

The table (1) gives the number of operations needed to factor n with GNFS method, and Table (2) illustrates the time required if each operation uses one microsecond, for various lengths of the number n (in decimal digits) and the difference between the standard RSA and the proposed RSA method.

Table (3) shows the space is increased according to increasing the prime numbers.

6. Conclusion

This paper was implemented on LAN as a practical application during RSA appearance there was a limitation in speed, size and time of factoring keys. So, two prime numbers for securing key are used at that time. A practical reason for using an extended keys make possibility of cryptanalyst to the key is difficult. This paper proposed a method to extend the RSA key. Increasing RSA key to increase the time of factoring n and the number of operations, an extending in RSA

key is required so the cryptanalyst encounter face difficulties to factor the number n . On the other hand, the space needed for the proposed method increases as was represented in the simulation results tables.

References

- [1] Gerald V., 1999, "Database Management System", McGraw/Hill.
- [2] Stallings W., 2003, "Cryptography and Network Security principles and practice", U.S.
- [3] "Encryption and network security", U.S.,21-Sep-2000, www.en.wikipedia.org/wiki/RSA.
- [4] Rajorshi B.,Shibdas B.,Anirban B., 2003, "A Fast Implementation of the RSA Algorithm using the GNU MP Library", India, at Anna University, Chennai.
- [5] Hinek M. J., David R., 2006, "On the Security of Multi-prime RSA", University of Waterloo Ontario, N2L 3G1, Canada, mjhinek@alumni.uwaterloo.ca
- [6] Krishnamurthy A., Tang Y.,2003, "An efficient implementation of multi-prime RSA on DSP processor", *Multimedia and Expo, IEEE International Conference on*, vol. 3, pp. 437-440.
- [7] Pollard, J.M., 1974, "Theorems on factorization and primality testing", 512-528.
- [8] Montgomery P., 2000, "Parallel Implementation of the Block_Lanczos Method RSA".
- [9] Rivest R.L., Shamir A., and Adleman L., 2009, "A Method for Obtaining Digital Signatures and Publickey Cryptosystems".
- [10] Carlos F., 2003, "Cryptoanalysis of RSA", SANS institute.

Topic 5

Computer Software in Engineering Applications

PROPOSED DESIGN AND IMPLEMENTATION OF A SCHEMATIC FPGA-BASED BINARY ARITHMETIC MULTIPLIER

Dr. Yazen A. Khalil

College of Engineering - University of Koya

yazen_ad@yahoo.com

Abstract

Programmable logic requires both hardware and software. Programmable logic devices can be programmed to perform specified logic functions by the manufacturer or by the user. This paper presents a proposed design and implementation of an 8-bit Arithmetic Multiplier based on FPGA (Field Programmable Gate Array). The design is implemented by using a schematic FPGA way using CPLD (Complex Programmable Logic Device) development board SN-PLDE2. The development board contains an FPGA device EPF8282ALC4-4 (5000 gates account) of *Altera* FLEX8000 family (Flexible Logic Element MatriX) with the other necessary peripherals. The proposed design is achieved under MAXplus2 V10.1 software for FPGA programming. The designed arithmetic multiplier is tested using an experiment board (SN-PLDE3A). The results show both efficient usage and high performance including the accuracy and the fast operation.

consideration for the differing numerical significance of each digit of the multiplier. Each partial product is either identically zero or equal to the multiplicand, depending on whether the multiplier digit is 0 or 1 respectively [1, 2].

				d ₃	d ₂	d ₁	d ₀	
				1	0	1	0	Multiplicand
	x			1	1	0	1	Multiplier
	0	0	0	0	0	0	0	Partial product initially
								d ₀ =
				1	0	1	0	1
Shif				0	0	0	0	d ₁ =
Shif				1	0	1	0	0
Shif	+			1	0	1	0	d ₂ =
t								1
				1	0	0	0	d ₃ =
								1
				1	0	0	0	Final Product
				0	0	1	0	

Figure (1) Binary Multiplication Example

Keywords

Arithmetic Multiplier, FPGA, FLEX

1. Introduction

The process of a binary multiplication with paper and pencil is illustrated in Figure (1). The multiplicand is multiplied in turn by each digit of the multiplier. These partial products are then added with due

2. The Proposed Design

As shown in Figure (1), the binary arithmetic multiplication process needs binary multiplication, shifting, and addition processes. Therefore; the main parts of the proposed design should involves an 8-bit full adder (8ADD), an 8-bit multiplier shift register constructed with two 4-bit shift registers, an accumulator (MUL8ACC)

constructed with four PIPO shift registers, pulse generator and a control pulse generator. All above parts will be detailed in the following sub-sections. The complete proposed design is shown in Figure (2).

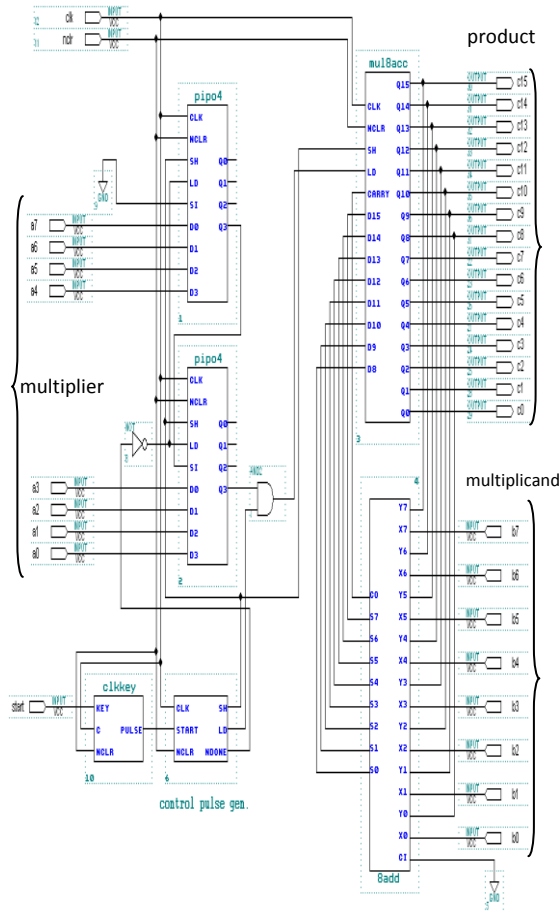


Figure (2) The Proposed 8-bit Multiplier

The 8-bit multiplicand (b0-b7) is fed to the adder input (X0-X7). The accumulator output (Q8-Q15) is fed to the adder input (Y0-Y7). With the LD control signal, the adder output (S0-S7) and its carry out are loaded to the inputs (D8-D15) of the accumulator (MUL8ACC). The 8-bit multiplier (a0-a7) is

parallel-loaded into the multiplier shift register.

The pulse generator (clkkey) generates a starting pulse to drive the 8-bit multiplier. The control pulse generator is used to generate the control pulses for the multiplication process. The following sections will give the details of each part mentioned above.

2.1 Multiplier Shift Register

This part constructed with two 4-bit shift registers as shown in Figure (2). Its main job is the serial shift process of the multiplier bits to determine whether the load signal to the LD input of MUL8ACC is generated or not according to the following AND process.

$$LD(acc) = \text{Multiplier bit} \bullet LD(\text{control signal})$$

For 1 multiplier bit leads to pass the LD signal to load adder output into the accumulator.

2.2 8-bit Full Adder (8ADD)

This part is constructed with two 4-bit adders. Each one of these 4-bit adders involves four ordinary full adders as shown in Figure (3). Its job is to implement the required addition process of the partial products till reach the final product.

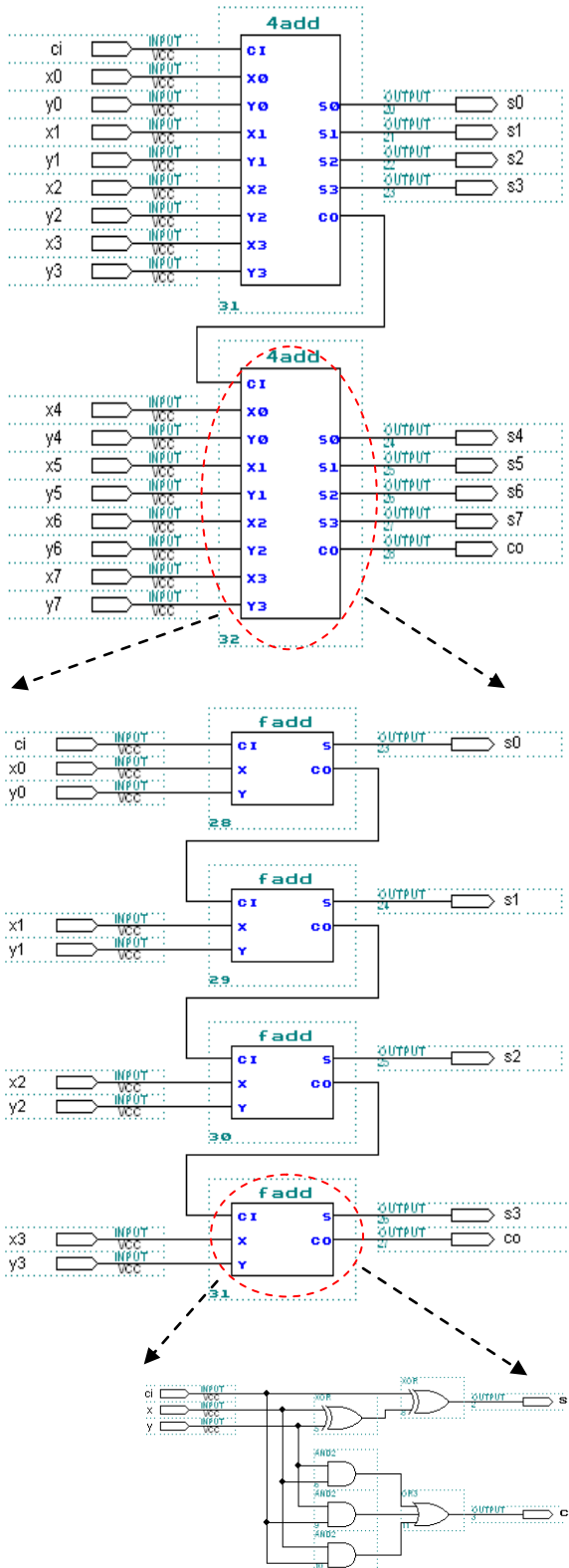


Figure (3) 8-bit full adder (8ADD)

2.3 Accumulator (MUL8ACC)

The accumulator part of this design consists of four 4-bit PIPO shift registers and its control logic circuit as shown in Figure (4). It has two main jobs; the first one is to accumulate (temporary storage) of the partial products after each the multiplication process with the multiplier bit. The second one is the one bit shifting process that is required after each multiplication process as described in Figure (1), [1, 3].

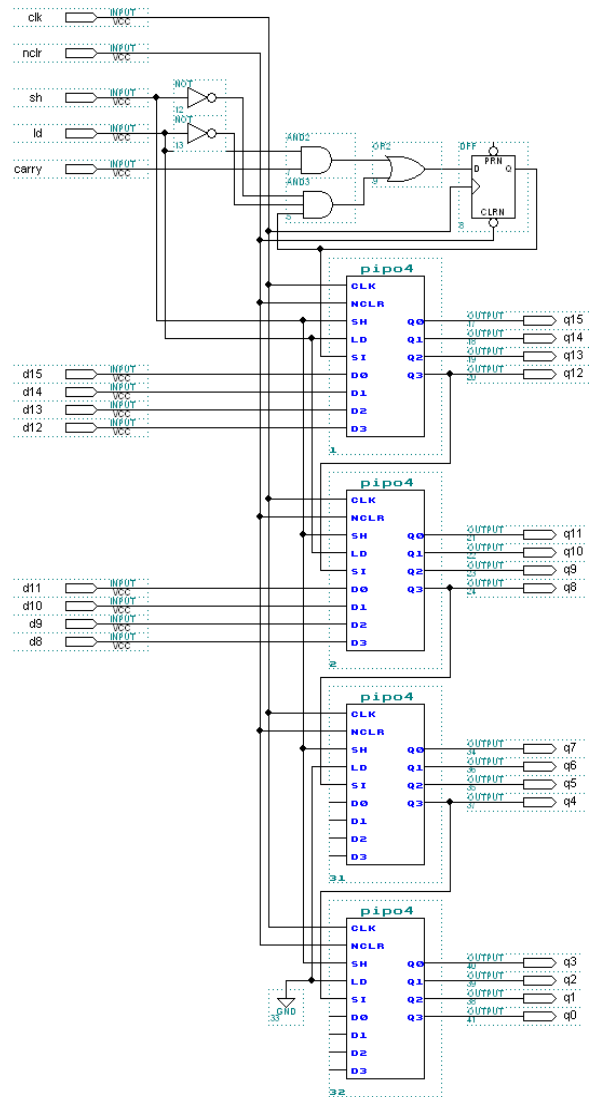


Figure (4) Accumulator

The 4-bit shift register (pip04) that is used in the accumulator is shown in Figure (5)

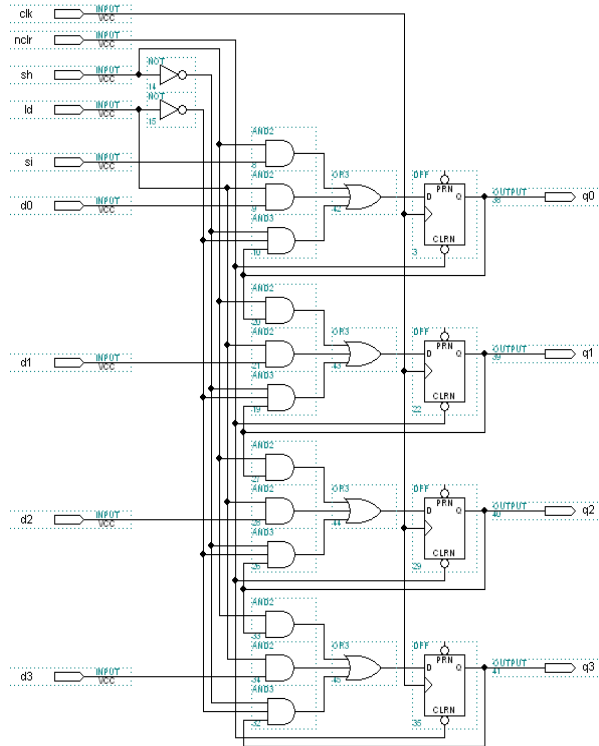


Figure (5) 4-bit Shift register

2.4 The Pulse Generator (clkkey)

Figure (6) shows the pulse generator (clkkey) that generates a starting pulse to drive the 8-bit multiplier. Figure (7) shows its timing diagram. Initially, all flip-flop outputs are cleared. If a START signal (logic 1) is applied to the KEY input, the flip-flop outputs $Q1=1$ and $Q2=D2=\overline{Q1}$. $KEY=1$ on the rising edge of clock pulse no. 1. On the rising edge of clock pulse no. 2, the $Q1$ output remains at 1 and the $Q2$ output returns to 0 because $D2= \overline{Q1}$. $KEY=0$. Hence, a pulse appears at the $Q2$ output.

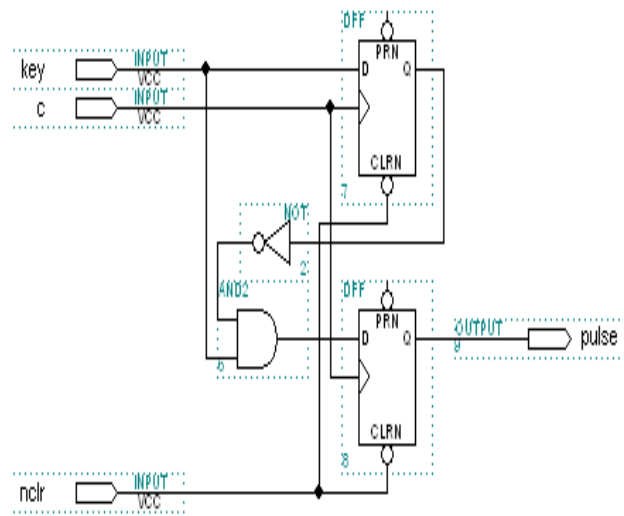


Figure (6) Start pulse generator

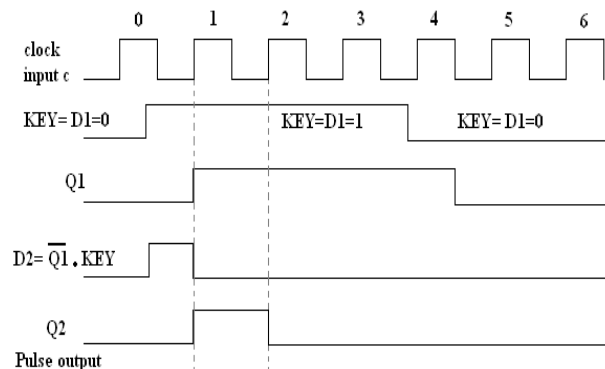


Figure (7) Timing diagram of clkkey

2.5 The Control Pulse Generator

The control pulse generator shown in Figure (8) is used to generate the control pulses for the multiplication process. The START pulse comes from the PULSE output of clkkey. On the rising edge of the third clock pulse, a logical high appears at the DONE output and flip-flop output, and arrives at the EN and CLRN (clear) inputs

of the divide-by-16 counter to start counting. The DONE output holds at high for the succeeding clock pulses until the 17th clock pulse arrives. During this counting period, the counter output changes from 0000 to 1111; load operation (LD=1) performs at every even-numbered clock pulse, and shift operation (SH=1) performs at every odd-numbered clock pulse. Therefore, 16 clock pulses are needed for an 8-bit multiplication.

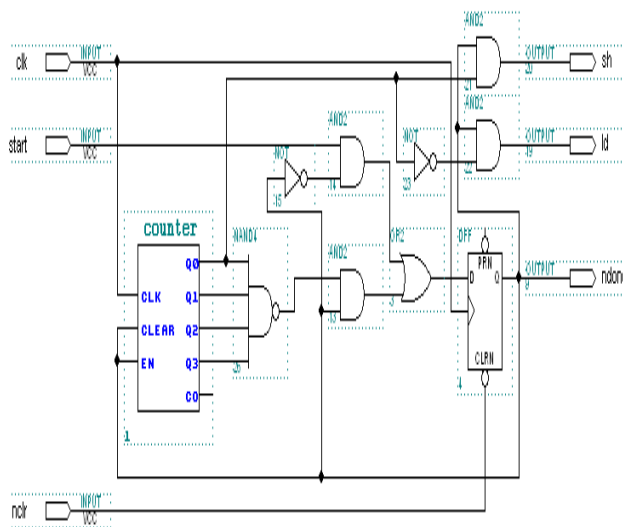


Figure (8) Control pulse generator

From the logic diagram shown in Figure (8), the Boolean equations for SH and D are given by:

$$D = \text{START} \& \bar{Q} + Q \& \overline{Q0 \& Q1 \& Q2 \& Q3}$$

$$SH = Q \& Q0$$

$$LD = Q \& \bar{Q0}$$

When the START pulse appears at the start input, the Q output is clocked to a logical 1, which drives the 4-bit synchronous binary counter to counting up: After 16 clock pulses,

$$Y = \overline{Q0 \& Q1 \& Q2 \& Q3} = 0. \text{ The Q output}$$

returns to 0 to terminate the counting. The timing diagram of the control pulse generator is shown in Figure (9).

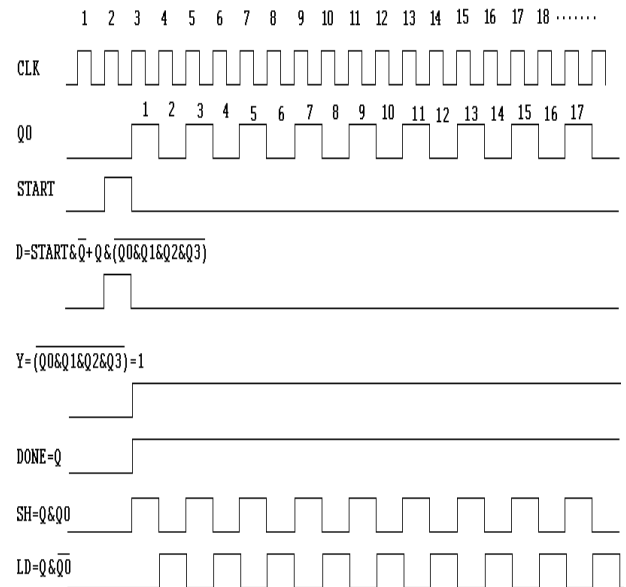


Figure (9) Timing diagram of the Pulse generator

The 8-bit multiplier has eight shift-and-add cycles. Each cycle is divided into shift and addition operations [4]. During shift operation, both the multiplier a0-a7 and the partial product Q0-Q15- are shifted by one position. If the multiplier bit at D0 is 1, addition operation is then performed. The shift operation is performed at every odd-numbered clock pulse when Q0=1 and SH=1, the addition operation is performed at every even-numbered clock pulse when Q0=0 and LD=1. During this operation, the adder output S7-S0 is loaded into the accumulator D8-D15.

3. Experimental Test

- Implementing the proposed design with the software MAXPlus2 V10.1, as shown in Figure (10) and save it as graphic editor file format (.gdf).

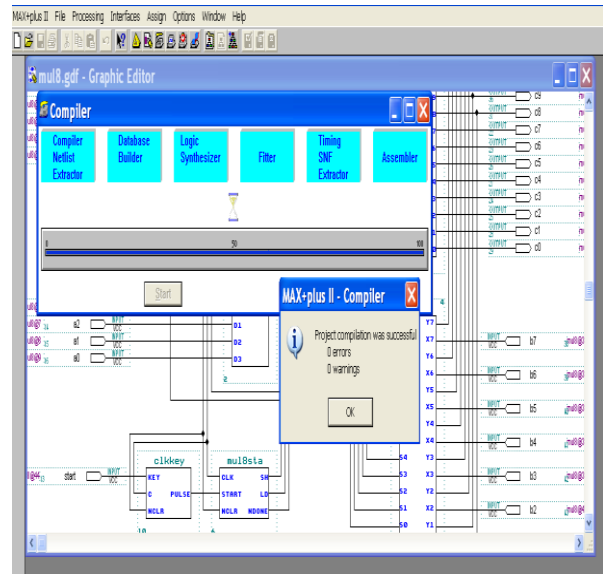
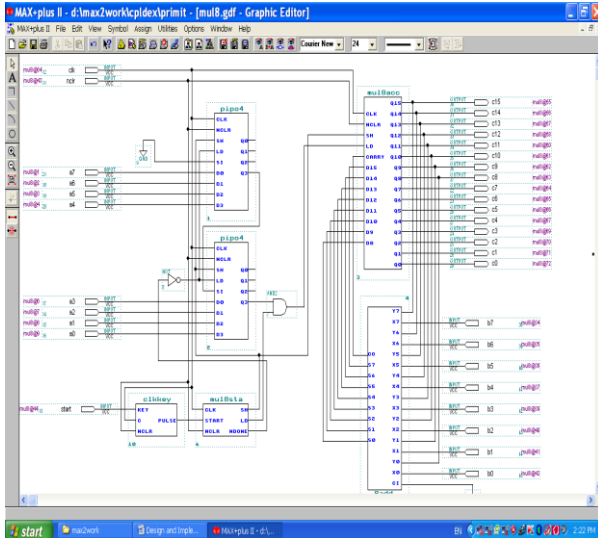


Figure (11) Compiler window

Figure (10) the proposed Design as appear in maxplus2 software

- Compile the design and assign FPGA pins to I/O devices. As shown in Figure (11).
- Download the design into the CPLD / FPGA development system CIC-310 with appropriate downloader software (DNLD82.exe) by using the RS-232 COM Port as shown in Figure (12), this done by the aid of the *Altera* applications note for FPGA devices [5].
- Set the input values of the multiplicand a7-a0 and the multiplier b7-b0. Apply clock pulses by pushing and releasing the pulse generator equipped with the development system and recording the partial products and the final product and checking its validity.

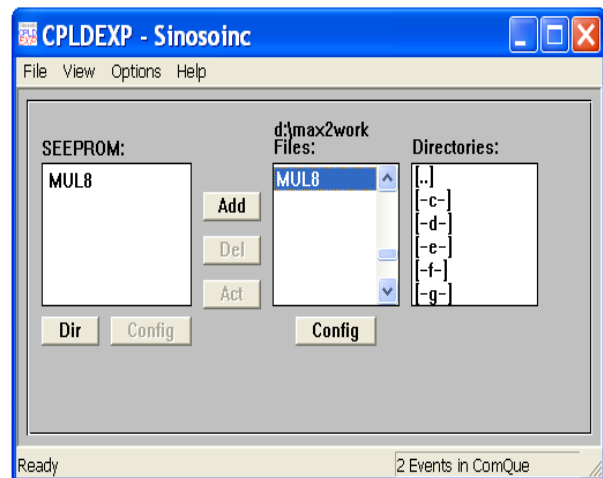


Figure (12) Downloader window

4. Conclusions

Arithmetic Binary Multipliers can be implemented in FPGAs, providing both efficient usage and high performance. The Altera FLEX8000 family is particularly well suited for this application. There is a range of options available to the user when designing multipliers: speed, area, accuracy and the design method.

During this design and implementation, the following points can be concluded:

- The Altera development tools and the FLEX8000 devices can effectively create multipliers to meet the individual requirements.
- The advantage of the programmable logic over fixed-function logic is that the devices use much less board space for an equivalent amount of logic.
- With programmable logic, designs can be readily changed without rewiring or replacing components.
- A logic design can generally be implemented faster and with less cost with programmable logic than with fixed-function ICs.
- The proposed design can be used to build the decimal multipliers.

References

- [1] Floyd T. L. , 2006, “Digital Fundamentals”, ninth edition, Pearson Prentice Hall, Page(s) 628-648.
- [2] Neto H. C. and Vestias M. P. ,2008 “Decimal Multiplier On FPGA Using Embedded Binary Multipliers”, Field Programmable Logic and Applications International Conference,Page(s): 197 – 202.
- [3] Beuchat J. L. and Muller J. M. , 2008, “Automatic Generation of Modular Multipliers for FPGA Applications”, IEEE Transactions On Computers, Vol. 57, No. 12, Page(s): 1600 – 1613.
- [4] Beuchat J. L. and Muller J. M., 2004, “Modulo m Multiplication-Addition: Algorithms and FPGA Implementation,” Electronics Letters, vol. 40, no. 11, pp. 654-655.
- [5] Altera Application Note 306, for FPGA devices, July, 2004.

PROPOSAL OF CREATING ENTITY-RELATIONSHIP TABLE FROM ENGLISH SENTENCES GROUPS

Maitham Ali Naji

College of Electrical and Electronic Techniques

maithamnaji@yahoo.com

Abstract:

The aim of this research is to provide a computerized technique to built Entity Relationship Table (ERT) instead of Entity Relationship Diagram (ERD). The ERT contains Source Node Type (SNT) and Destination Node Type (DNT) which either Entity or Attribute. Also contain source and destination node and their relationship type; Source Node Relationship Type (SNRT) and Destination Node Relationship Type (DNRT); the verb presents the relationship name between nodes. The program in this research is splitting the relationship from subject item then the relation will map to relationships dictionary to get real word presentation to the corresponding relationship words. The same process is repeated with Complement group.

Keywords: *Natural Language Processing (NLP), Entity-Relationship Model (E-R), Visual Basic.*

1-Introduction:

ERD is a simple graphical technique, which is used to decide which database tables, fields and relationships will be needed in any database no matter what Data Base Management System (DBMS) you are going to implement your database application. The technique can be used as the first step in database design [1].

A relationship is an association between entities. The relationship name is an active or passive verb. For example, a STUDENT takes

a CLASS, a PROFESSOR teaches a CLASS [2].

Most previous papers and researches use *Semantic Network* (SN) [3]. In [3], the author uses the SN to represent the E-R Model using Prolog language.

In [4], the Inference Rules for Functional Dependencies (FD) (*Reflexivity, Augmentation, Transitivity, Pseudo Transitivity, Union, and Decomposition*) are used by the authors to get *Closure*.

For a set H of dependencies, the inference rules above can be used to drive all dependencies implied by H. H^+ should be used to refer to as the Closure of H to denote the set of all dependencies that are drivable from H it is called *Cover* of H and it is a non redundant cover if no proper subset of it is a cover of H [5].

The system has been implemented in Visual Basic language. The results that obtained in this paper validate the truth that the next stages of normalization are to simply be implemented.

1-1 Entities:

Entity at the modeling level actually refers to the entity set and not to a single entity occurrence. In other word Entity in the E-R model corresponding to a table and not a row in the relational environment [6]. The relationship lines represent relationships between entities. The relationship can be classified into four types [1].

- 1- One to one (1:1).
- 2- One to many (1: M).
- 3- Many to one (M: 1).
- 4- Many to many (M: N).

In Chen models, an entity is represented by a rectangle containing the entity's name. The entity name, a noun, is usually written in capital letters. The Chen model places the relationship names with a diamond. The diamond is connected to the entity rectangles through a so-called relationship line [7]. For example "A CLASS is enrolled in one or more COURSES" is represented in Chen Model as shown in Figure (1). The result of the example as an ERT is shown in Figure (15).

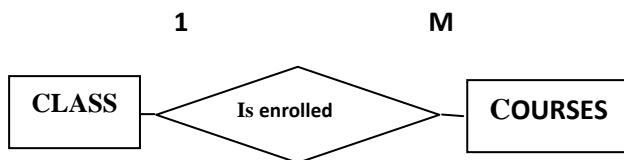


Figure (1): The ERD between Class and Courses Entities

1-2 Attributes:

Attributes are characteristics of entities [8]. In the Chen model, attributes are represented by ovals and are connected to the entity rectangle with a line. Each oval contains the name of the attribute. Attribute can be classified in two types [7]:

- 1- A Single-valued attribute is an attribute that can have only a single value. For example "A COURSE has a number, a day and an hour" is represented in Chen model as shown in Figure (2). The result of the example as an ERT is shown in Figure (16).

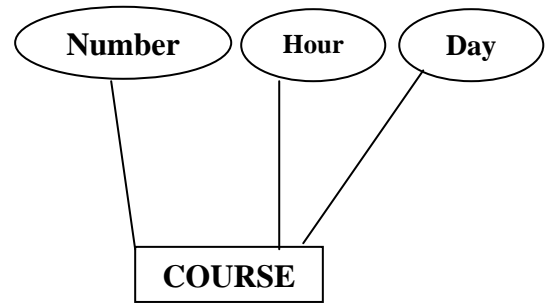


Figure (2): The Attribute of the Course Entity in Chen Model

- 2- Multi-valued attribute are attributes that can have many values. For instance a Student may have name, age and several addresses, College address and Home address. In the Chen E-R model, multi-valued attributes are shown by double line connecting the attribute to the entity. The E-R diagram for "STUDENTS have a name, an age and one or several addresses" is shown in Figure (3).

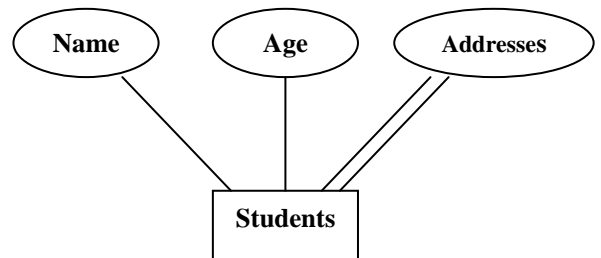


Figure (3): Multi-value for Students Entity

- Within the original entity, create several new attributes, one for each of the original multi-valued attribute's components. For example, we can split the Students entity's attribute addresses to create the new attributes College address and Home address as shown in Figure (4).

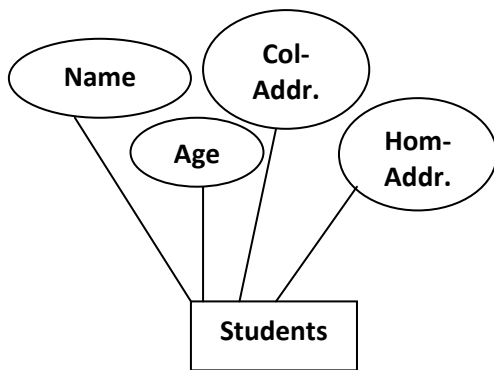


Figure (4): splitting the multi-valued attribute into new attributes

- Create a new entity composed of the original multi-valued attribute's components as shown in Figure (5). The new (independent) Address entity is then related to the original Students in a 1: M relationship. This step can be applied in ERT as shown in Figure (17).

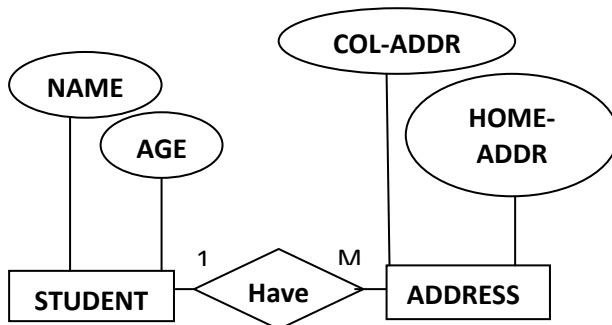


Figure (5): A New Entity Set Composed of a Multi-Valued Attributes

2-Proposal System:

The system that has been implemented previously was "Sentence Analysis via Verb", the system gets sentence as input, the sentence has syntax <Subject Group><Verb Group><Complement Group>. Subject group is everything before verb group while Complement group is everything after verb group. The system divides sentence by verb into Subject Group list, Verb Group and Complement Group list.

For example:

STUDENTS HAVE A NAME , AN AGE AND ONE OR SEVERAL ADDRESSES

Subject Group list:

Sub1-list (0) = STUDENTS

Verb Group: HAVE

Complement Group list:

Comp1-list (0) = A NAME

Comp1-list (1) = AN AGE

Comp1-list (2) =ONE OR SEVERAL ADDRESSES

The output will be an input to the current system. The program has six main stages to create ERT. As shown in Figure (6).

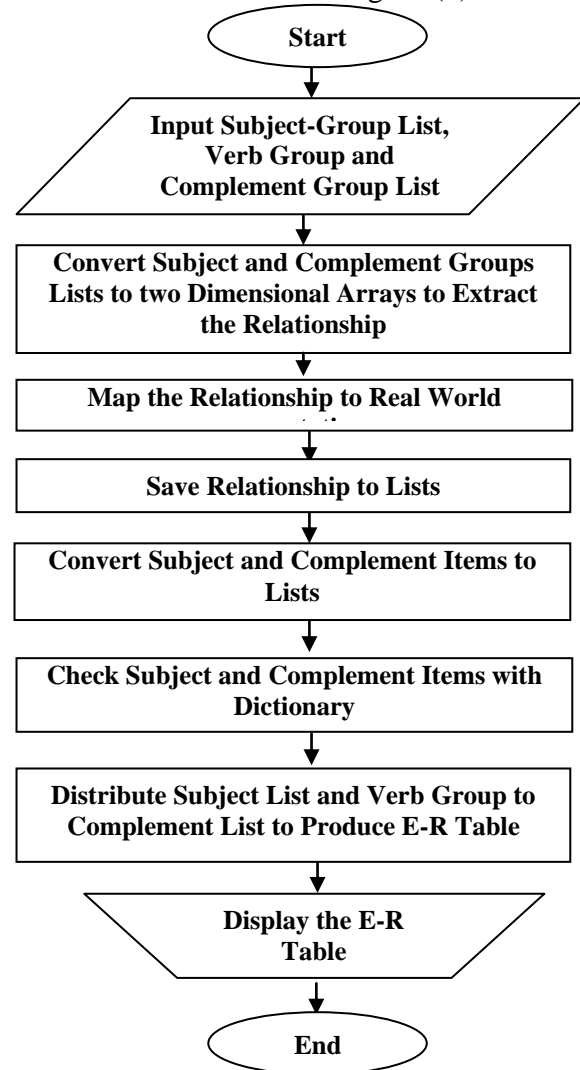


Figure (6): Block Diagram for ERT

The flowchart has nested loops; the first loop will take a row from complement group list to convert it to one dimensional array, by using *split* instruction which store each word in single location. The second loop will convert one dimensional array to two dimensional array. This process will continue until complement group list stores in two dimensional array. As shown in Figure (7). The result of the flowchart is shown in Table (1). The same process is done to subject group.

Table (1): Two Dimensional Array of Complement Group

	Comp(1)	Comp(2)	Comp(3)	Comp(4)
1	A	NAME		
2	AN	AGE		
.	ONE	OR	SEVERAL	ADDRESSES
9				

The major point to convert complement list in two dimensional array, in order to deal with relationship and present it in real world presentation i.e. (1, M) as shown in Table (2). The program first try to find relationship that consist of four words. These words are then compared with relationship dictionary. If the relationship is found, the program will change the default flag value from *false* to *true* and took the relationship type i.e. (1, M) from dictionary and store it in first location in the array while the other words are deleted from the array as shown in Figure (8); otherwise if the flag is remain *false* the program execute another codes to find relationship that consist of three or two or one words.

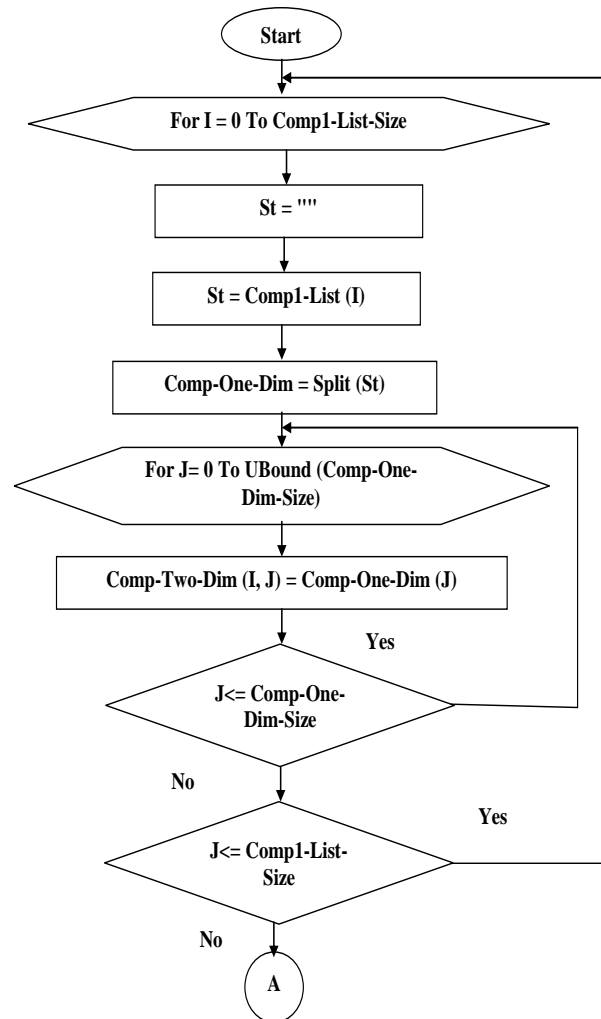


Figure (7): Convert Complement Group to Two Dimensional Array

Table (2): Convert Relationship to Real Word Presentation

	Comp(1)	Comp(2)	Comp(3)	Comp(4)
1	1	NAME		
2	1	AGE		
.	M			ADDRESSES
9				

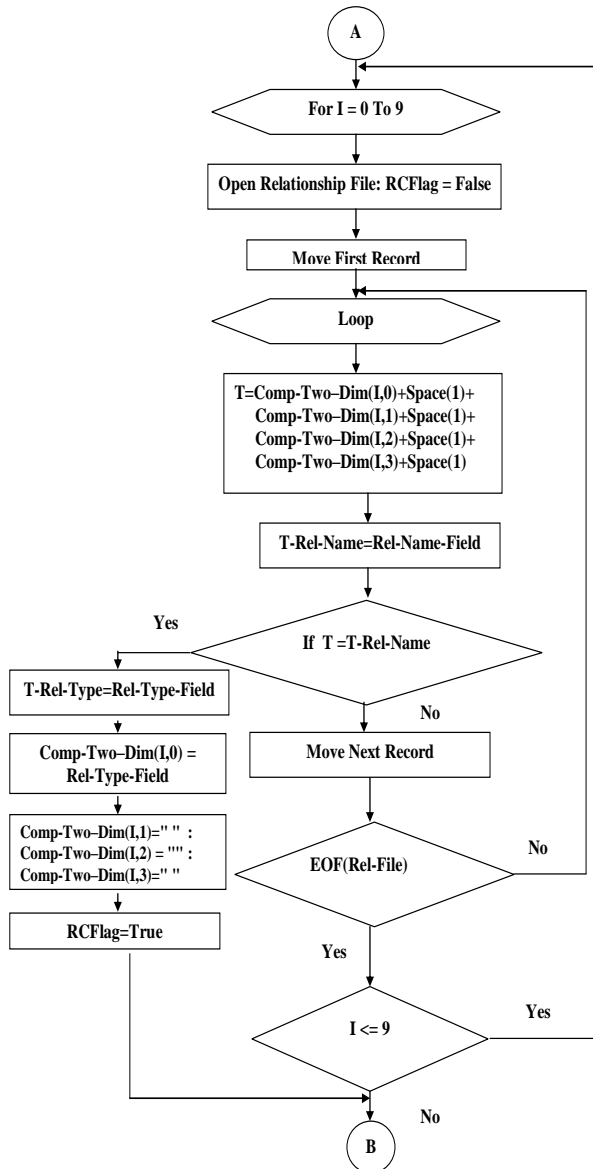


Figure (8): Convert Relationship to Real World Presentation

The first location of two dimensional array that contain the type of relationship is stored in complement relationship list and the relationship type will be deleted from the array, as shown in table (3), in case if the first location of each row does not has data, the program will add "1" to complement list. As shown in Figure (9).

Table (3): Delete Relationship from Array

	Comp(1)	Comp(2)	Comp(3)	Comp(4)
1		NAME		
2		AGE		
.				ADDRESSES
9				

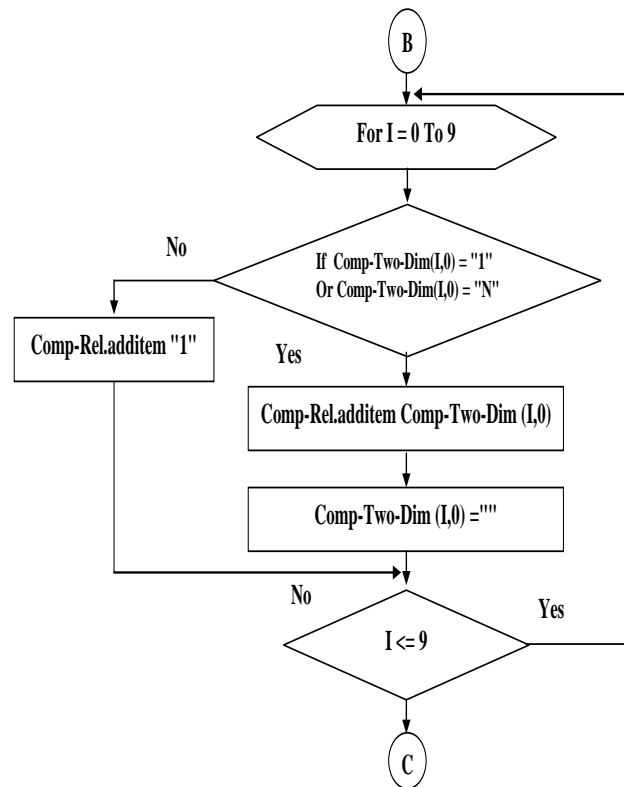


Figure (9): Convert Relation to Complement List

As shown in Table (3) each complement item consists from one word but in some case the complement item may contain two or more words, for example if the item "AGE" is replaced with "SOCIAL SECURITY NUMBER" that mean will take three location

in the array. Therefore the job of the program collects these words and stores it in complement list. As shown in Figure (10).

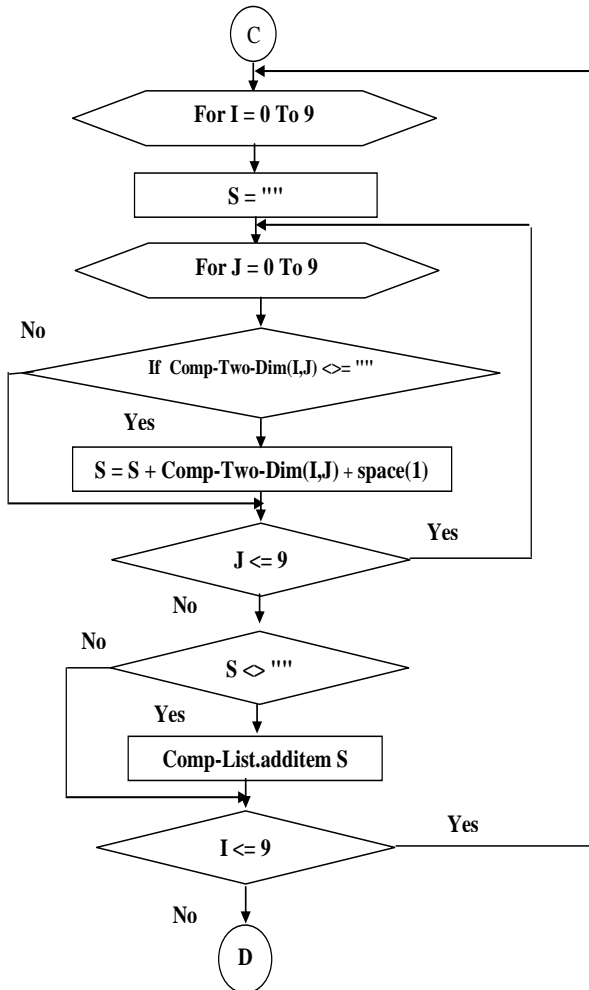


Figure (10): Store Complement Item in Complement List

The next process the program take each complement item from the list complement and call the check complement item with dictionary as shown in Figure (11).

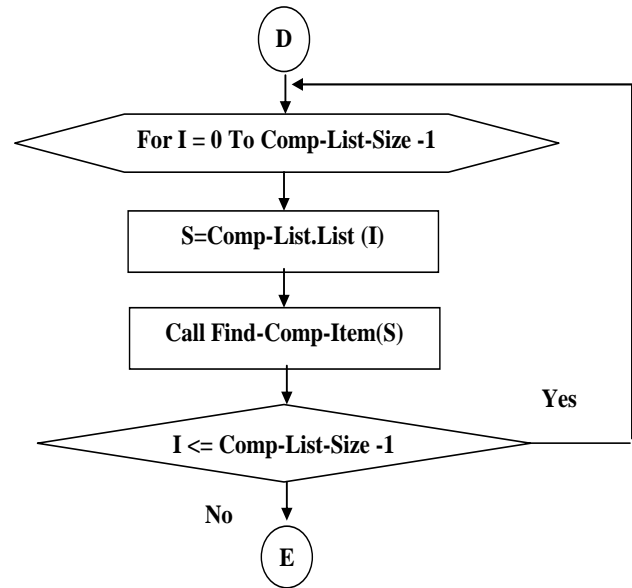


Figure (11): Calling Check Complement Item Procedure

The following program take a complement item to compare with Subject-complement dictionary that has two fields (Node Name and Node Type) for example "STUDENT" present Node Name while Node Type either "E or A" which mean Entity or Attribute. If the complement item is found the flag will be converted from *False* to *True* and the node type will store in complement list type then the program will exit from the sub routine. While if the search is failed to find word in dictionary that mean the flag remain *false* and the program will display message to inform the user that Node Name does not exist in the dictionary, and should entered it and specify the node type may an Entity (E) or Attribute (A). The system will add node name to the list as shown in Figure (12).

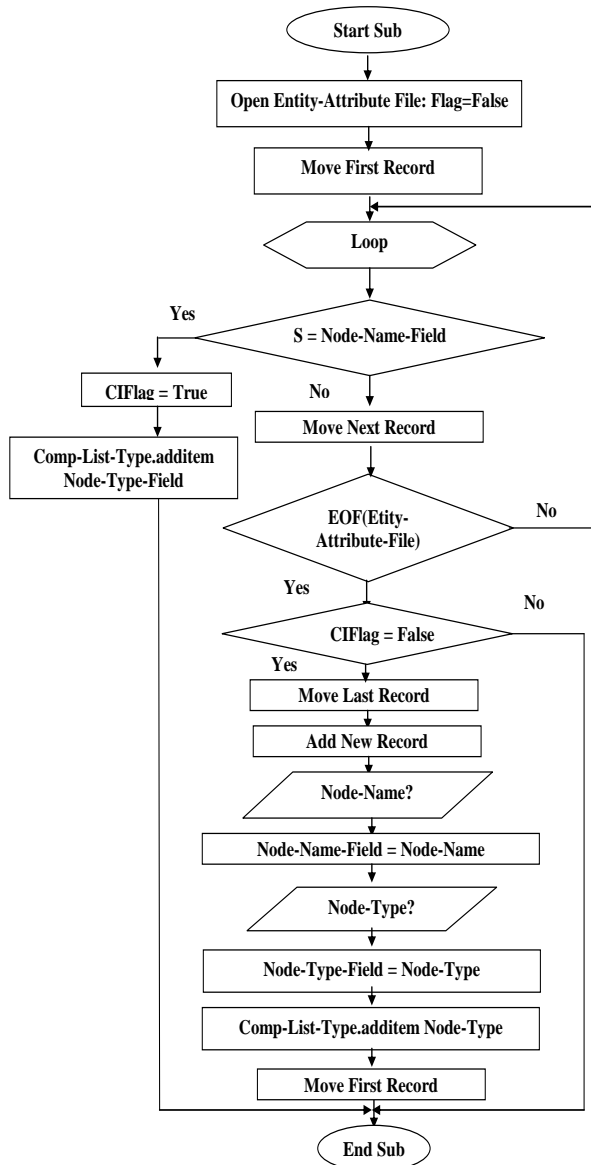


Figure (12): Complement Item Procedure

The last flowchart has nested loop, the first one for Subject list while the second loop for complement list and verb group. The complement list and verb group is distributed among subject list to produce ERT. As shown in Figure (13).

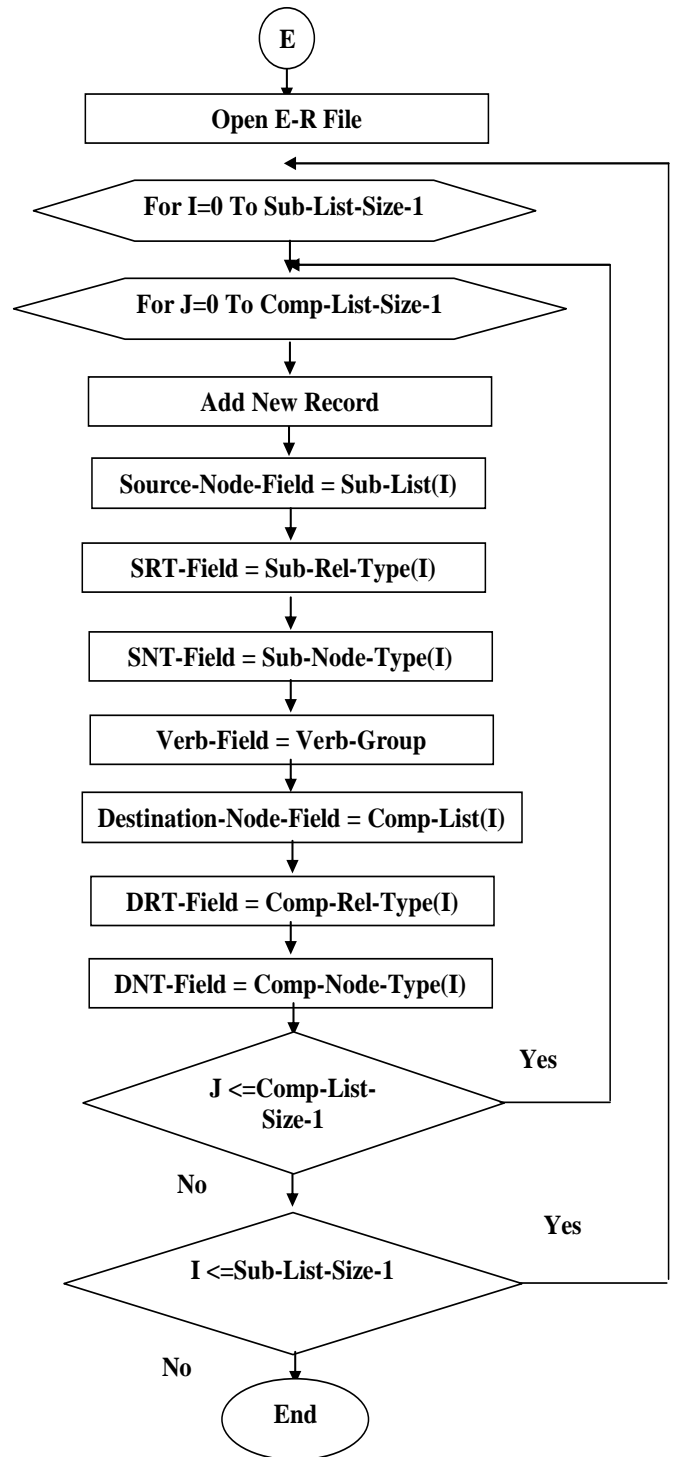


Figure (13): Create Entity Relationship Table

3-The Implementation:

The system has been implemented in Visual Basic language; the main window consists of three main buttons, the first one is "Create New ERT" which create new Entity relationship Table (ERT) when the user click on it a message will appears to alarm the user that "all data will be deleted?" The second button "Modify Old ERT" will add new data to the existing data, the third button "Exit" to exit from the system as shown in Figure (14). The second window allow the user to enter sentence, this window contain two buttons, "Sentence Analysis": this button has two actions; the first one will analyzed sentence to three groups, the second action; will create ERT from sentence groups, the result will be display on DB-grid. The second button is "New Sentence" is used to clear the text box from previous sentence and all other lists and variables will be cleared from data of previous execution.

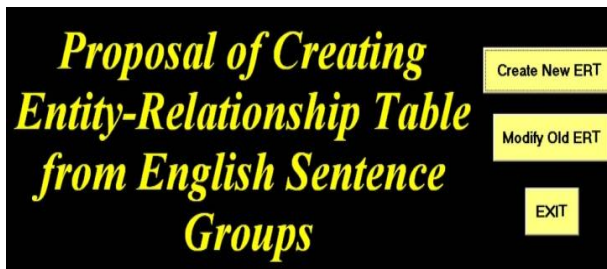


Figure (14) Main Window

In the implemented system, the entity and attribute is written in capital letters. The following example shows the ERT between two entities.

Input Sentence: A CLASS IS ENROLLED IN ONE OR MORE COURSES

Output ERT:

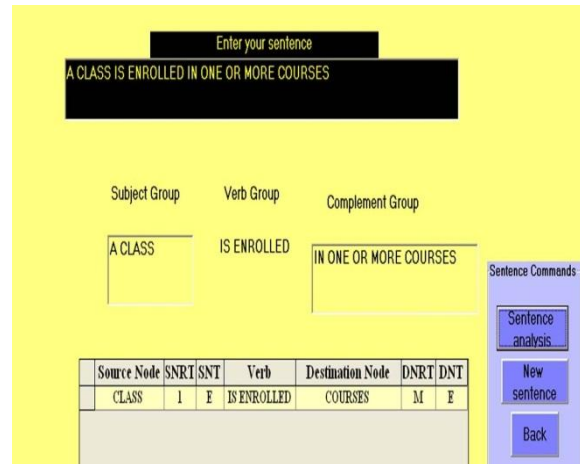


Figure (15): The Relationship Between Class and Course Entities

The following example shows the single value attributes of COURSE entity.

Input Sentence: A COURSE HAS A NUMBER , A DAY AND AN HOUR

Output ERT:

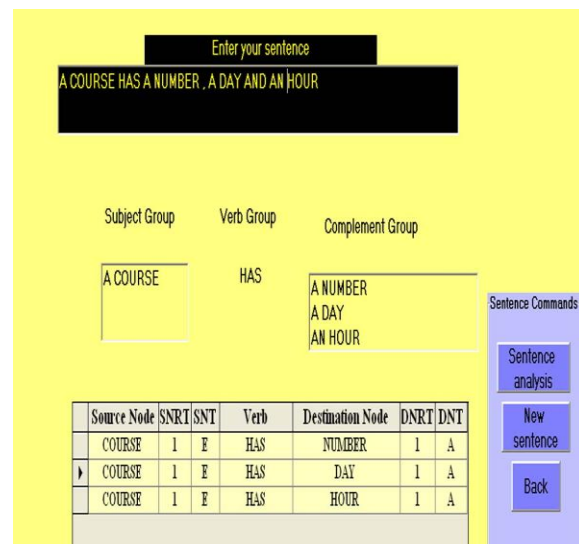


Figure (16): Single Value Attributes for Course Entity

The following example shows the multi-value attributes of STUDENTS entity.

Input Sentence1: STUDENTS HAVE A NAME , AN AGE AND ONE OR SEVERAL ADDRESSES

Input Sentence2: ONE OR SEVERAL ADDRESSES HAVE COLLEGE ADDRESS AND HOME ADDRESS

Output ERT:

Source Node	SNRT	SNT	Verb	Destination Node	DNRT	DNT
STUDENTS	1	E	HAVE	NAME	1	A
STUDENTS	1	E	HAVE	AGE	1	A
STUDENTS	1	E	HAVE	ADDRESSES	M	E
ADDRESSES	M	E	HAVE	COLLEGE ADDRESS	1	A
ADDRESSES	M	E	HAVE	HOME ADDRESS	1	A

Figure (17): Multi-Valued Attributes for Students Entity

4- Conclusion:

Many points are concluded in this paper. First, Computer Aided techniques can be successfully applied to the database design problem. When used with appropriate interface they can help the Data Base Administrator (DBA) produce more quickly a better quality design with this assistance. Second, The ERT can be use as a learning application to describe the E-R model. Third, the ERT can be used to makes the programming of Inference Rules for Functional Dependencies easy to process to get well design.

References:

- [1] Carter, J, 2000, "Database Design and Programming with Access, SQL and Visual Basic", McGraw-Hill Publishing Company, 483.
- [2] Atzeni, Ceri, Parabosche, Torlone, 1999, "Database systems, conceptual languages and architecture", McGraw- Hill Edition, 477.
- [3] Taha, S, A, 1994, "Tools to Aid for Database Design and Development", Cairo University,102,63.
- [4] "Theory of Relational Database Design and Normalization"; on line document at www.ec.gatech.edu/classes/AY2002/C36400-spring/normalize_revised.pdf
- [5] Date, C, J, 1999, "An Introduction to Database system"; Addison – Wesley,647.
- [6] Anderson, V, 2001, "How to Do Everything with Access 2002", McGraw-Hill Edition, 639.
- [7] Rob, P, Coronel, C, 2002, "Database Systems: Design, Implementation, and Management", McGraw- Hill Edition,751
- [8] Carter, J, 1995, "The Relational Database", McGraw- Hill Edition,502

CONVERSION OF ENGLISH CHARACTERS INTO BRAILLE USING NEURAL NETWORK

Dr. Mohammed Yousif Hassan
Control and Systems Engineering Dept.
University of Technology
myhazawy@yahoo.com

Ahmed G. Mohammed, B. Sc.
Rimal Medical Services Company
ahmed87exe@yahoo.com

Abstract:

The Braille system is a method that is widely used by blind people to read and write. Braille generally consists of cells of raised dots arranged in a grid. The presence or absence of dots can be sensed by the blind people's fingertips to give them the coding for the symbol.

The electronic revolution is changing the way Braille is produced, stored and retrieved, making it easier to use in the work place. All kinds of materials can be put into Braille, from bank statements to bus timetables, maps to music. But it is still difficult to produce an error-free Braille for complex materials. In this paper, the ability of the neural networks will be tested to be used for translating scanned text pages, books or lectures from English language into Grade I Braille; so that blind people can deal with it.

An artificial neural network is designed with minimum structure and tested to convert the English characters into grade I literary Braille code. English characters will be assumed to be affected by noise of mean variant between 0 and 0.4. The output of the

N.N can be stored in a data file that can be sent into a Braille printer or a Braille display.

Keywords: *Neural Network, conversion, Braille, English characters.*

1- Introduction:

The Braille system is a method that is widely used by blind people to read and write; Figure (1). Braille generally consists of cells of six raised dots arranged in a grid of two dots horizontally by three dots vertically. The dots are conventionally numbered 1, 2, and 3 from the top of the left column and 4, 5, and 6 from the top of the right column, as shown in figure (2). The presence or absence of dots gives the coding for the symbol [1]. Today, different Braille codes (or code pages) are used to map character sets of different languages to the six bit cells. Different Braille codes are also used for different uses like mathematics and music. In addition to simple encoding, modern Braille transcription uses contractions to increase reading speed; therefore; Braille method is classified as a nonlinear writing [1].



Figure (2): Braille cell.



Figure (1): Picture of reading Braille.

Many authors dealt with the use of Neural Networks for handprint OCR and character recognition using Neural Network [2][3][4]. These researches includes the recognition of Arabic Hand Written Characters [5][6]. Furthermore, many authors discussed detailed description of methods for converting English letters into Braille and display characters on display terminals [7] [8]. Also, the quality testing of Braille printed paper was also investigated [9].

2- Braille System:

Braille system was presented by Louis Braille in 1834. Common Braille characters are based on a 6-dot cell having two columns of three dots. Dot height is approximately 0.02 inches (0.5 mm). The horizontal and vertical spacing between dot centers within a cell is approximately 0.1 in (2.5 mm). The blank space between dots on adjacent cells is approximately 0.15 in (3.75 mm) horizontally and 0.2 in (5.0 mm) vertically. A standard US Braille page is 11.5 by 11 inches and typically has a maximum of 40 to 42 Braille cells per line and 25 lines [1].

Some 6 dot Braille cells have numerous meanings. Numbers, capital letters, and many symbols require more than one cell to produce 6 dot Braille data. There are four Braille codes currently used in the United States. The four U.S. Braille codes are the Literary Braille Code, the Nemeth Braille Code, Computer Braille Code (CBC), and the Music Braille Code. There are differences in the Braille alphabet codes used in various English-speaking countries, which prevent the exchange of Braille materials. Other Braille codes are presently under development, some require the use of 8 dots or other raised symbols [10].

2.1 Types of Braille Codes:

A- Literary Braille Code: [11]

1) Grade I Braille

The basic code is called grade I Braille; it is a direct substitution of normal print letters for letters from the Braille alphabet which can be read by all Braille users, and it is the first stage of learning to read Braille.

2) Grade II Braille

Grade II is a shorter form which makes reading and writing Braille much faster. Grade II Braille consists of contractions added to the combinations to represent letter groups such as 'the' and 'for'. The contractions are too numerous to list here. Grade II should be used for longer signs i.e. an opening plaque or site description. Grade II is also used widely in books, magazines and leaflets. It occupies less space than Grade I Braille but all Braille is bulky. For example, one A4 printed page would need approximately two and a half pages to reproduce in Braille.

B- Nemeth Braille Code

It is used for mathematics and science material which contains symbols not available in Literary Braille. The Nemeth Braille Code is not an expanded version of the Literary Braille Code [10].

C- Computer Braille Code (CBC)

Computer Braille Code was developed in order to transcribe materials relating to computers. It uses some symbols from Literary Braille, some from Nemeth Code, and some symbols of its own. Computer Braille Code requires file names, the exact count of blank spaces, and other details that are required for computer programming and the use of computers [10].

D- Music Braille Code

Music Braille Code is a completely different Braille code. An extensive

knowledge of music is necessary for the accurate transcription of music into Braille. [10].

2.2 Braille Letters and Characters:

In this paper, the literary grade I Braille code will be considered. The first ten letters of the alphabet and the numbers 1 through 0 are formed using only the top four dots (1, 2, 4, and 5). Adding dot 3 forms the next ten letters, and adding dot 6 forms the last five letters (except w) and the words: (and, for, of, the, and with). Omitting dot 3 from the letters U-Z and the five word symbols forms nine digraphs (ch, gh, sh, th, wh, ed, er, ou, and ow) and the letter w [1]. The numbers (1, 2... 0) are announced by a sign using dots 3, 4, 5, and 6 before the letters (A, B... J). The use of dot 6 just before a letter indicates a capital letter as shown in the figure (3) [1] [12].

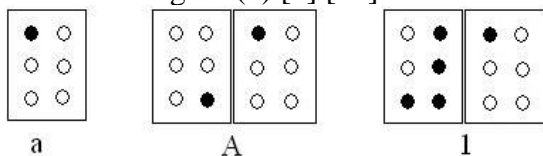


Figure (3): The use of two cells to express capital letters and numbers.

3- Neural Networks:

An Artificial Neural Network (ANN), often just called a "Neural Network" (NN), is a mathematical model or computational model composed of simple elements operating in parallel. These elements are inspired by biological nervous systems. It consists of an interconnected group of artificial neurons and processes information using a connectionist approach to computation. In most cases an ANN is an adaptive system that changes its structure

based on external or internal information that flows through the network during the learning phase.

In more practical terms neural networks are non-linear statistical data modeling tools. They can be used to model complex relationships between inputs and outputs or to find patterns in data. [13] [14].

The universal approximation theorem for neural networks states that: "every continuous function that maps intervals of real numbers to some output interval of real numbers can be approximated arbitrarily closely by a multi-layer perceptron with just one hidden layer". This result holds only for restricted classes of activation functions, e.g. for the sigmoidal functions.

4- Design of English to Braille converter using Neural Networks:

Using MATLAB programming; a neural network will be designed to recognize and to convert English characters into Braille characters. The neural network should be able to classify noisy characters as well as noise free characters.

A page that is scanned by an imaging device is converted into matrices of 400 element columns that represent a 20*20 grid for each character. The matrix should have the values of 1's to represent black, and 0's elsewhere. Sometimes, the imaging device is not perfect and the letters may suffer from noise. Here the neural network should be able to recognize the true characters and generate an output according to each character. However, the method of scanning and converting the image into matrices is out of the scope of this paper.

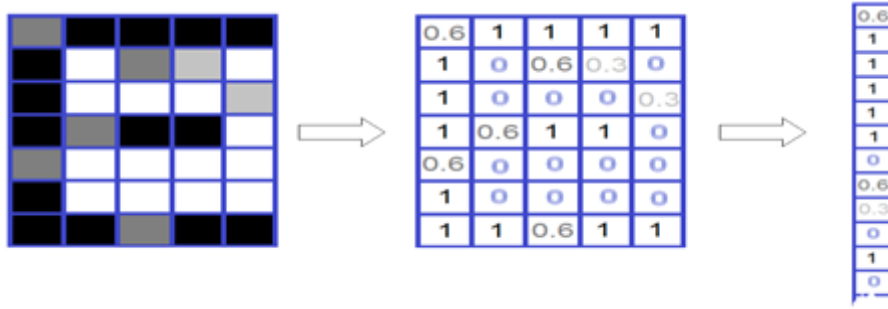


Figure (4): Converting noisy E character into 35 element array.

The output of the network is used to generate the corresponding Braille character according to the Braille rules. The generated Braille characters are saved as a matrix of 2*6 elements for each character. As in English representation; each Braille dot is represented by 1 in its corresponding place in the output matrix, and zero elsewhere.

In this paper, the artificial neural network will be designed and trained to recognize 63 characters :(52 English capital and small letters, 10 numbers and the space) using back-propagation training algorithm. The network is trained using the patterns of the input matrix (English_char). This matrix has a size of 400*63 elements, each column of this matrix contain the data of a perfect character. Capital letters (A-Z) are placed in the columns (1-26) and then the small letters, followed by numbers and the (space). The output of the network is represented by the identity matrix (Targets) that has 63*63 elements. The steps of the algorithm are shown in the figure (5). The neural network needs 400 inputs in the input layer and 63 outputs in its output layer. The output of the network should be 1 in the position of the detected character and 0 elsewhere. For example; if character (B) is the input then the output should have 1 in the 2nd element in the output vector and 0 elsewhere. Finally, the MATLAB program is used to generate Braille characters according to the output of the neural network.

4.1- Initialization of the Data Characters:

In order to design and train the neural network, data characters should be initialized and the following steps should be made:

- Load Perfect characters images.
- Resize and reshape the characters into a column matrix.
- Arrange characters' columns side by side in the matrix (English_char).
- Create each Braille character as a 6*2 array.
- Arrange the arrays of the Braille characters in the matrix (braille) so that it contains all of the Braille characters (side by side).
- Create the matrices (capital_next) and (number_next) as 6*2 for each.
- Create the matrix (Targets) which is the identity matrix of 63*63.

4.2- Creating the Neural Network:

In order to create and train the Neural Network, a feed-forward one is created with 400 inputs in the input layer, different number of hidden layers and 63 outputs in its output layer. Sigmoid activation functions are used in hidden layers and bipolar linear activation functions are used in the nodes of output layer. The resilient back-propagation algorithm (trainrp) is used to train this Neural Network. This method supports training with validation and test vectors.

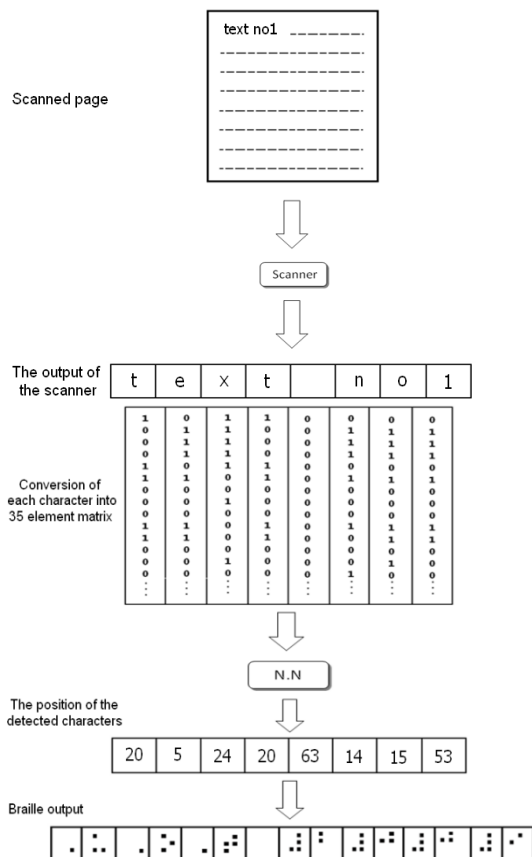


Figure (5): conversion steps of English characters into Braille.

After several trials, using the following steps to get minimum structure of the designed network it was found that the best structure is achieved with 190 neurons in the hidden layer.

4.3- Training the Neural Network:

1- Training without noise:

First, the network was trained to recognize the noise free characters with the learning rate of 10^{-3} and an error goal of 10^{-6} .

2- Training with noise:

Second, after the weights updated to recognize the ideal inputs with a very small error, the network was forced to recognize noisy input characters. The noise is created by generating random numbers with mean of 0 and standard deviation (std) of 0.2. This

learning was repeated 35 times; for each time it was trained, with 14 copies of the input; half of these copies have a noise of std 0.2 added to them. More error was expected because more input vectors (some with noise) are used; therefore; the error goal was reduced to 10^{-3} .

3- Training without noise:

Third, to make sure that the network always responds correctly to the ideal inputs, the network was trained once more with ideal inputs. The mean square error goal was decreased to 10^{-3} .

5. Simulation of the Neural Network as a Converter:

To simulate the variable noise from the scanner; a random noise was added to the input signal with std of 0.05 and the detected English characters as well as the corresponding Braille characters were drawn as in Figure (6).

Using noise of 0.1 std resulted in no mistakes during the detection and conversion, shown in Figure (7). Increasing the noise into 0.2 resulted in (0-2) mistakes for each trial as shown in Figure (8).

Conclusions:

It can be concluded that:

A feed forward artificial neural network was designed and tested to convert English characters into grade I literary Braille code, taking into account the nonlinearity of the conversion because of Braille rules. The network was designed with minimum structure including number of layers, and number of neurons in each layer. Noisy input patterns were introduced to the network including the addition of a noise of std 0.2 to all characters which resulted in one or two characters to be detected wrong for each time running the program. A pattern of characters without and with noise were tested using the designed N.N and the results were satisfying.

abCdEf gHi j k l m nOpqrSt UVWXYZ ABCDE
FGHI JKLMNOPQRS TUVWXYZ1 234567890

Figure (6-a): Noisy input characters with 5% noise.

abCdEf gHi j k l m nOpqrSt UVWXYZ ABCDE
FGHI JKLMNOPQRS TUVWXYZ1 234567890

Figure (6-b): Detected characters using the N.N.



Figure (6-c): Corresponding output Braille characters

abCdEf gHi j k l m nOpqrSt UVWXYZ ABCDE
FGHI JKLMNOPQRS TUVWXYZ1 234567890

Figure (7-a): Noisy input characters with 10% noise.

abCdEf gHi j k l m nOpqrSt UVWXYZ ABCDE
FGHI JKLMNOPQRS TUVWXYZ1 234567890

Figure (7-b): Detected characters using the N.N.



Figure (7-c): Corresponding output Braille characters.

abCdEf gHi j k l m nOpqrSt UVWXYZ ABCDE
FGHI JKLMNOPQRS TUVWXYZ1 234567890

Figure (8-a): Noisy input characters with 20% noise.

abCdEf gHi j k **i** m nOpqrSt UVWXYZ ABCDE
FGHI JKLMNOPQRS TUVWXYZ1 234567890

Figure (8-b): Detected characters using the N.N.



Figure (8-c): Corresponding output Braille characters.

Finally, it can be concluded that conversion of English to Braille using Neural Network is a fast and accurate method of conversion. It can be assumed as a general method for any script written in English language.

References:

- [1] Wikipedia the free encyclopedia, 2008 <http://en.wikipedia.org/wiki/Braille>
- [2] Avi-Itzhak H. I., Diep T. A., and Garland H., Feb 1995, "High Accuracy Optical Character Recognition Using Neural Networks with Centroid Dithering", IEEE Transaction on Pattern Analysis and Machine Intelligence, Vol. 17, No. 2, PP. 218-224.
- [3] Oh S., Suen C. Y., 1998, "Distance features for neural network-based recognition of handwritten characters", International Journal on Document Analysis and Recognition (IJ DAR), c Springer-Verlag, Vol. 1, PP. 73-88.
- [4] Garris M. D., Wilson C. L., and Blue J. L., Aug. 1998, "Neural Network-Based Systems for Handprint OCR Applications", IEEE Transaction on Image Processing, Vol. 7, No. 8, PP. 1097-1112.
- [5] Khatatneh K., El Emary I. M. M. and Al-Rifai B., 2006, "Probabilistic Artificial Neural Network For Recognizing the Arabic Hand Written Characters", Journal of Computer Science, Vol. 3, No. 12, PP. 881-886.
- [6] Shilbayeh N. F. and Iskandarani M. Z., 2008, "Effect of Hidden Layer Neurons on the Classification of Optical Character Recognition Typed Arabic Numerals", Journal of Computer Science, Vol. 4, No. 7, PP. 578-584.
- [7] Sriskanthan N. and Subramanian K. R., May 1990, "Braille Display Terminal for Personal Computers", IEEE Transactions on Consumer Electronics, Vol. 36, No. 2, PP. 121-128.
- [8] Blenkhorn P., June 1995, "A System for Converting Braille into Print", IEEE Transaction on Rehabilitation Engineering, Vol. 3, No. 2, 215-221.
- [9] Karmakar S., Chatterjee R. P. and Dutta U., 2010, "Improvement in quality testing of Braille printer output with Euclidean distance measurement using camera calibration", International Journal of Engineering, Science and Technology Vol. 2, No. 1, pp. 35-48.
- [10] Alternative Method Research, www.braillefont.com/index.html
- [11] MK Design, 2004, "The Professional Sign Consultancy Service".
- [12] www.mkdesign.free-online.co.uk/braille.htm
- [13] www.cnib.ca/en/living/braille/braille
- [14] Peter A., Burgsteiner H., Maass W., 2008, "A learning rule for very simple universal approximators consisting of a single layer of perceptrons", Neural Networks, Vol. 21, No. 5, PP. 786–795.
- [15] Zurada J. M., 1996, "Introduction to Artificial Neural Networks", 2nd Edition, India.

HARDWARE IMPLEMENTATION OF ANN TRAINED BY GA AND PSO BASED ON FPGA

Dr. Hanan A. R. Akkar

hnn_aaa@yahoo.com

Sundus Dhamad Hasan

sun2007dusdamad@yahoo.com

Department of Electrical and Electronic Engineering
University of Technology
Baghdad-IRAQ

Abstract:

In this paper, Particle Swarm Optimization-feedforward Neural Network (PSO-FFNN) and Genetic Algorithm-Neural Network (GANN) are proposed to enhance the learning process of ANN in term of convergence rate and classification accuracy. They have been tested and compared the results applied in pattern classification. The experiments show that both algorithms produce feasible results in terms of convergence time and classification percentage. At the end of the evolutionary process of GANN for optimal structure, not only the best network structure for a particular application but also the trained network with few numbers of epochs is provided. A Hardware Design of ANN platform (HDANN) is proposed to evolve the architecture of ANN circuits using FPGA-spartan3 board (XSA-3S1000 Board). The HDANN design platform creates ANN design files using WebPACK™ ISE 9.2i, and converted into device-dependent programming files for eventual downloading into an FPGA device by using GXSLD program from the XSTOOLS programs.

Keywords: *Neural Network, Genetic Algorithm, Particle Swarm Optimization and FPGA*

1-Introduction

Artificial Neural Networks (ANNs) exhibited remarkable properties, such as: adaptability, capability of learning by examples, and ability to generalize. One of

the most used ANN models is the well-known Multi-Layer Perceptrons (MLPs). The training process of MLPs for pattern classification problems consists of two tasks, the first one is the selection of an appropriate architecture for the problem, and the second is the adjustment of the network connection weights. Extensive research work has been conducted to tackle this issue. Global search techniques, with the ability to broaden the search space in attempt to avoid local minima, has been used for connection weights adjustment or architecture optimization of MLPs, namely Particle Swarm Optimization (PSO), Evolutionary Algorithms (EA), and Genetic Algorithm (GA) [1].

Reprogrammable systems have provided significant performance improvements for many types of applications. Many modern FPGAs have the ability to be reprogrammed in-system, in whole or in part. This has led some researchers to create dynamically reconfigurable computing applications within one or more FPGAs in order to create extremely high-performance computing systems. The technology of reconfigurable computing is still in its infancy, however, due in large part to the high cost, in terms of power and configuration time, of dynamically reprogramming an FPGA [2].

Thus, there is great interest in implementing neural networks in reprogrammable systems, both because of the speed benefits, as well as because the reprogrammability of the FPGAs can support the reconfiguration necessary to program a neural network [3].

2-Artificial Intelligent Systems

The Artificial Neural Network (ANN), Genetic Algorithm (GA) and Particle Swarm Optimization (PSO) are examples of AI techniques [4]. Each of these techniques has demonstrated some success at solving simple AI problems [3]. An Artificial Neural Network (ANN) is an information processing paradigm that is inspired by the way biological nervous systems process information. The Backpropagation (Bp) algorithm is commonly used learning algorithm for training ANN. Bp algorithm is used in ANN learning process for supervised or associative learning. During training, the network tries to match the outputs with the desired target values [5].

The intelligent techniques, such as Genetic algorithm (GA) and Particle Swarm Optimization (PSO), have been developed rapidly [4]. Genetic algorithm was introduced by John H. Holland in 1960's where GA was a probabilistic optimization algorithm. GA is a family of computational model inspired by evolution. The original idea came from biological evolution process in chromosomes. GA exploits idea of the survival of fittest where best solutions are recombined with each other to form new better solutions. There are three processes in GA which are selection, crossover and mutation [6].

PSO is a simple concept adapted from nature decentralized and self-organized systems such as bird flock and fish schooling [7]. The PSO was introduced by Kennedy and Eberhart 1995 as a population based stochastic search and optimization process. It's a population-based algorithm in which individual particles work together to solve a given problem.

The population (or swarm) and the member called particle is initialized by assigning random positions and velocities then the potential solutions are flown through the hyperspace [8].

3- Programmable Logic Devices (PLDs)

Programmable Logic Devices PLDs (Programmable Modules) are modules that have been developed to be customizable for particular functions at the last stage of fabrication. PLD can be programmed, erased, and reprogrammed many times, allowing easier prototyping and design modification [2]. In the mid 1980s a new technology for implementing digital logic was introduced, the Field Programmable Gate Array (FPGA). FPGAs were capable of implementing significantly more logic than PLDs, especially because they could implement multi-level logic, while most PLDs were optimized for two-level logic. One common use of the FPGA is the prototyping of a piece of hardware that will eventually be implemented later into an ASIC. FPGAs have been increasingly used as the final product platforms. Their use depends, for a given project, on the relative weights of desired performances, development, and production costs [9].

4- Design and Implementation of ANN using GA and PSO

One of the more intriguing possibilities is that of combining a neural network with other AI systems, like GA and PSO, to enhance the learning process in terms of convergence rate and classification accuracy.

Genetic Algorithm (GA) has been used to determine optimal value for BP parameters such as learning rate and momentum rate and also for weight optimization. Particle Swarm Optimization (PSO) is chosen and applied in feedforward neural network to enhance the learning process in terms of convergence rate and classification accuracy. Two programs called Particle Swarm Optimization feedforward Neural Network (PSO-NN) and Genetic Algorithm Neural Network (GANN) have been proposed.

5- The Proposed Genetic Algorithm-Neural Network (GANN)

To guide ANN learning, GA is employed to determine the best number of hidden layers and nodes, learning rate, momentum rate and weight optimization. With GA, it is proven that the learning becomes faster and effective.

The flowchart of GANN for weight optimization is shown in Figure (1). The first step, weights are encoded into chromosome format and the second step is to define a fitness function for evaluating the chromosome's performance. This function must estimate the performance of a given neural network. The function usually use is the Mean Squared Errors (MSE). The error can be transformed by using one of the two equations below as fitness value.

$$Fitness = \frac{1}{MSE} \dots (1)$$

or

$$Fitness = \frac{1}{1 + MSE} \dots (2)$$

In GANN for optimum topology, the neural network is defined by a "genetic encoding" in which the genotype is the encoding of the different characteristics of the MLP and the phenotype is the MLP itself. Therefore, the genotype contains the parameters related to the network architecture, i.e. number of hidden layers (**H**), number of neurons in each hidden layer (**N_H**), and other genes representing the Bp parameters. The most common parameters to be optimized are the learning rate (**η**) and the momentum (**α**). They are encoded as binary numbers. The parameter, which seems to best describe the goodness of a network configuration is the number of epochs (ep) needed for the learning. The goal is to minimize the ep. The fitness function is:

$$Fitness = \frac{1}{ep} \dots (3)$$

or

$$Fitness = \frac{1}{1 + ep} \dots (4)$$

The flowchart of GANN for optimum network architecture is shown in Figure (2).

3-layer ANN is used to do the classification of three examples as shown in Figure (3). The parameters of GANN training algorithm are a one-point crossover with probability $P_c=0.8$ and mutation operator with probability $P_m=0.05$. The MSE is equal to 10^{-6} and the maximum number of generations (epochs) equal to 50. The fitness function is defined by equation (2). After several runs the genetic search returns approximately the same result each time as the best solution despite use of different random generated populations and different population size (for each example). Figures (4), (5), and (6) show the curves of MSE against the number of iterations of training for both GANN and Bp algorithms for each example respectively. These Figures show the training of the network by using GANN training algorithm for each example, reaching the lowest value of MSE with a very few number of generations as compared with the results from using Bp algorithm. The learning by using GANN algorithm is independent of the value of η and α . Conversely, Bp algorithm fails if unsuitable values of η and α are chosen. GANN training algorithm avoids local minima by searching in several regions. It has no restrictions on the network structure because it doesn't require backward propagation of an error signal.

In GANN for optimal structure, the initial population is evaluated, which includes a certain number of Bp training cycles. The maximum number of training cycles may be set relative to the size of the network. The fitness of an individual is defined by equation (4). The number of individuals in the population has been fixed equal to 10. The operators are the crossover with $P_c=0.8$ and mutation with $P_m=0.05$. The value of the minimum error (MSE) has been set to 10^{-6} . it has been necessary to train the neural networks for 100, 100, 1000 epoch for each example respectively. The results of this algorithm for the three examples are

summarized in Table (1). It can be seen that, the best network for each example can be obtained in a small number of generations with low number of epoch for training with Bp as compared with the old networks. At the end of the evolutionary process, not only the optimal network architecture for a particular application but also the trained network is provided.

6- The Proposed Particle Swarm Optimization - Feedforward Neural Network (PSOINN)

PSO is one of the latest techniques that can be fitted into ANN. A swarm is made up of particles, where each particle has a position and a velocity. The idea of PSO in ANN is to get the best set of weight (or particle position) where several particles (problem solution) are trying to move or fly to get the best solution [10].

In PSOINN, the position of each particle in swarm represents a set of weights for the current epoch or iteration. The dimensionality of each particle is the number of weights associated with the network. The particle moves within the weight space attempting to minimize learning error (or Mean Squared Error-MSE or Sum of Squared Error-SSE). Changing the position means updating the weight of the network in order to reduce the error of the current epoch. In each epoch, all the particles update their position by calculating the new velocity, which they use to move to the new position. The flowchart of PSOINN algorithm is shown in Figure (7).

The acceleration constants C_1 and C_2 are set equal to 2, the number of particles is equal to 15, and the MSE is equal to 10^{-6} . $r_1=0.8$, $r_2=0.2$, $\Phi=0.9$ and the maximum number of iterations (epochs) equal to 6000. Figures (8), (9), and (10) show the curves of MSE against the number of iterations for PSOINN training algorithm for each example respectively. It has been noticed that the training of the network by using PSOINN algorithm reaches the lowest value of MSE with less number of iteration (epoch) as compared with the results

from using Bp algorithm. The PSO can avoid getting into the local optimal solutions because PSO has the probabilistic mechanism and multi-starting points (it's a global optimizer).

On the other hand, GANN is faster than PSOINN with less accuracy for each example as shown in Table (2). Both algorithms are converged using the minimum error criteria.

For the correct classification percentage, it shows that PSOINN result is better than GANN. GANN significantly reduce the error at small number of iteration compared to PSOINN. For overall performance, the experiments show that both algorithms produce feasible results in terms of convergence time and classification percentage.

7-The Proposal Hardware Design of ANN platform (HDANN)

Hardware implemented ANNs have an important advantage over computer simulation ANNs because they fully exploit the parallel operation of the neurons, thereby achieving a very high speed of information processing. The proposed Hardware Design of ANN platform (HDANN) is a circuit design platform built to evolve the architecture ANN circuits using FPGA hardware. Therefore, the system must have software that can be downloaded into an FPGA.

The basic hardware and software components of the proposed HDANN are shown in Figure (11). It consists of a computer and FPGA-spartan3 board (XSA-3S1000 Board).

After down-loading the design into the board, a Dc function generator has been applied to the input-pins of the ANN design while the output has been measured by an oscilloscope. Figure (12) shows these output data when the input to the network is applied. It shows that the experimental result is the same as the simulation result that is shown in Figure (13) for example2.

8-Conclusions

Based on the experiments performed in this study, it can be concluded that, GANN for training has proved to be superior to Bp algorithm in both accuracy and speed of learning because GAs avoid local minima by searching in several regions. GANN for training is independent of the parameters that the Bp depends on. Tests show that GAs obtain best weight vectors quickly for each example at the same efficiency.

The optimal structure, including number of neuron in the hidden layer, learning rate, and momentum rate is found by using GANN for designing an optimal ANN structure. It is used GA to find a network structure that is best able to classify data from a specific situation with a small number of epochs.

PSO is a simple optimization algorithm with less mathematical equations that can be effectively applied in ANN. The results of PSO have been shown that the PSO is an efficient alternative to ANN training as compared with Bp algorithm. On the other hand, GANN is faster than PSO with less accuracy for each example.

PSO is similar to GA in the sense that they are both population-based search approaches and they both depend on information sharing among their population members to enhance their search processes using a combination of deterministic and probabilistic rules. Both are Global optimizer algorithms. PSO is more computationally efficient (uses less number of function evaluations) than GA. The results show that equal effectiveness but superior efficiency for PSO over GA.

HDANN platform has the ease of reimplementing due to the parameterized modules as well as the state of the art for the chosen FPGA platform. It possesses the speed of hardware while retaining the flexibility of the software implementation due to the reprogramming ability of FPGA. It has the potential to create ANN circuitry for AI applications.

References

- [1] Conforth M. and Meg Y., September 21-23, 2008, "Reinforcement Learning for Neural Networks using Swarm Intelligence", IEEE Swarm Intelligence Symposium, St. Louis Mo USA, pages(7).
- [2] Pellerin D. and Thibault S., 22 April, 2005, "Practical FPGA Programming in C", Prentice Hall PTR, pages (464).
- [3] Earl D. D., May, 2004, "Development of an FPGA-Based Hardware Evaluation System for Use with GA-Designed Artificial Neural Networks", PhD thesis, University of Tennessee, Knoxville, pages (147).
- [4] Engelbrecht A. P., 2007, "Computational Intelligence, an Introduction", J. Wiley & Sons, Ltd, USA, pages (288).
- [5] Picton P., 2000, "Neural Networks", Antony Rowe Ltd, Chippenham, Wilts, Great Britain.
- [6] Goldberg D. E., 1989, "Genetic Algorithms in Search Optimization and Machine Learning", Addison-Wesley Publishing Company.
- [7] Lazinica A., 2009, "Particle Swarm Optimization", Published by In-Tech, Vienna, pages (476).
- [8] Kiranyaz S., Ince T., Yildirim A., and Gabbouj M., 31 May, 2009, "Evolutionary Artificial Neural Networks by Multi-Dimensional Particle Swarm Optimization", Journal Neural Network, pages (15).
- [9] Deschamps J. P., Bioul G. J. and Sutter G. D., 2006, "Synthesis of Arithmetic Circuits FPGA, ASIC", and Embedded Systems, J. Wiley & Sons, pages (556) .
- [10] Kuok K. K., Harun S., and Shamsuddin S. M., 2010, "Particle Swarm Optimization feedforward Neural Network for Modeling Runoff", International Journal of Environmental Science of Technology, Volume 7, No. 1, pp. (67-78).

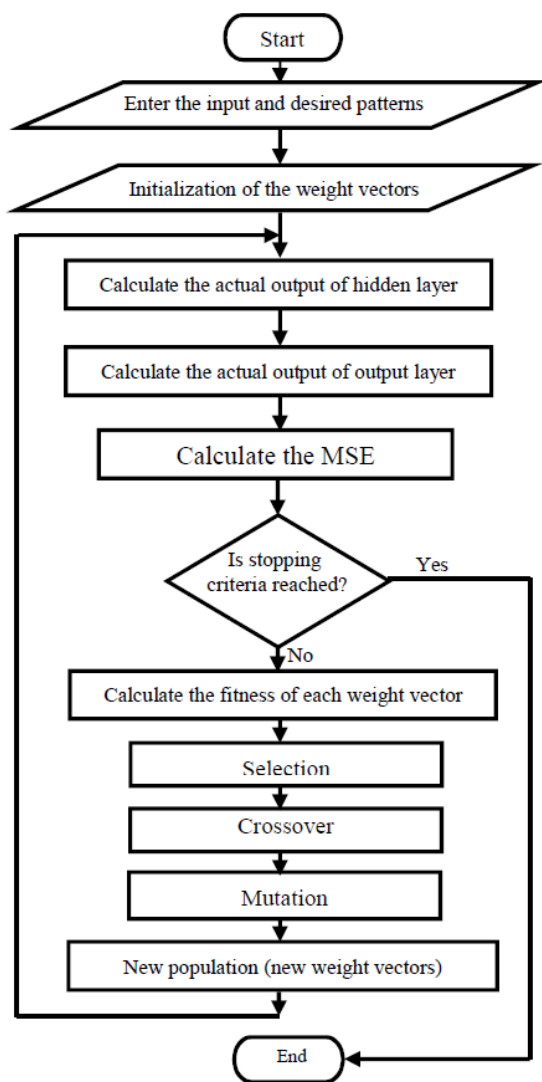


Figure (1) Flowchart of GANN weight optimization.

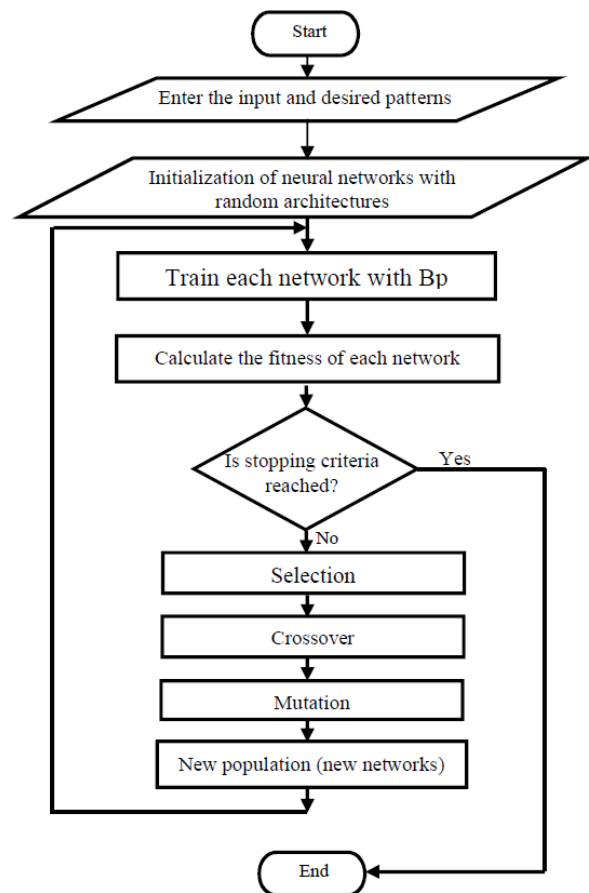


Figure (2) Flowchart of GANN for optimum network architecture.

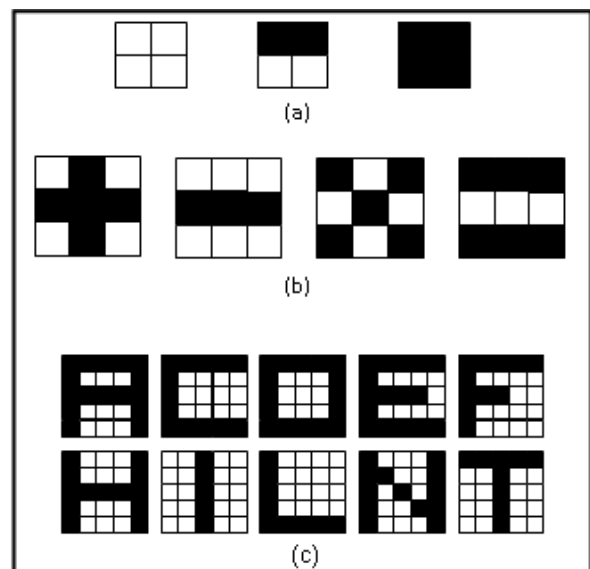
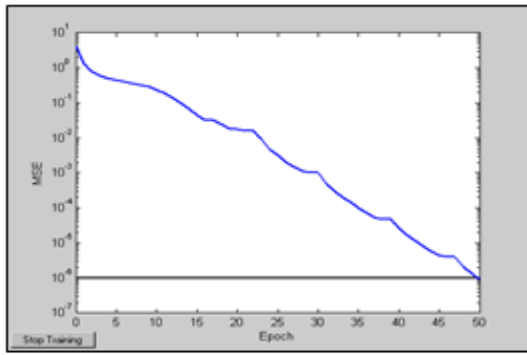
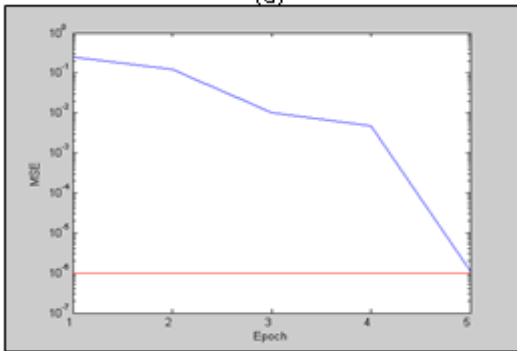


Figure (3) The tested examples: (a) example 1 (3 patterns of 2x2 pixels). (b) example 2: 4-patterns of 3x3 pixels). (c) example 3: 10-patterns of 5x5 pixels.)

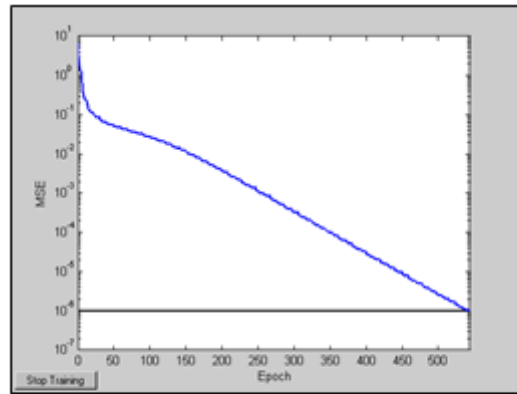


(a)

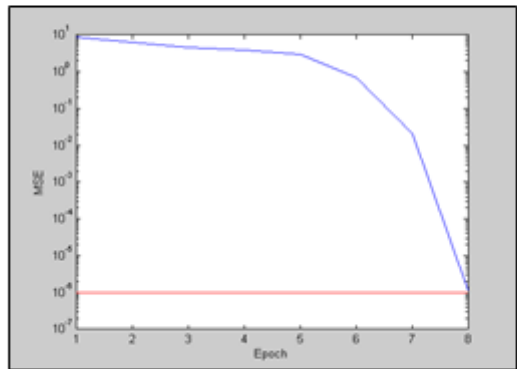


(b)

Figure (4) Training MSE with epoch for example1: (a) With Bp algorithm. (b) With GANN.

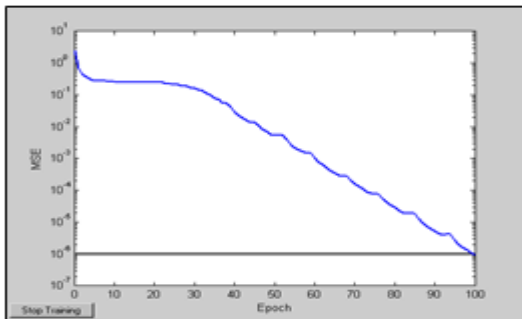


(a)

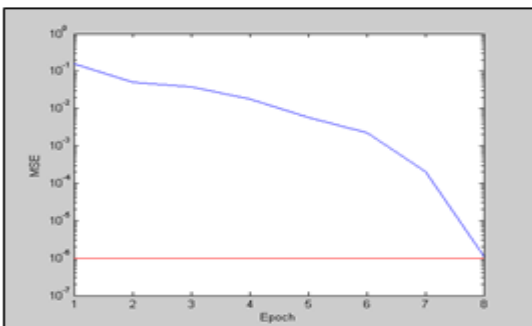


(b)

Figure (6) Training MSE with epoch for example3: (a) with Bp algorithm. (b) With GANN.



(a)



(b)

Figure (5) Training MSE with epoch for example2: (a) with Bp algorithm. (b) with GANN.

Table (1) The results of GANN for optimum structure for each example.

Examples	Example1	Example2	Example3
No. of generation	5	5	8
No. of epoch for old network	50	100	544
No. of epoch for new network	20	52	50
η	0.11	0.59	0.74
α	0.63	0.62	0.83
No. of neurons in the hidden layer (old)	3	4	20
No. of neurons in the hidden layer (new)	5	8	16

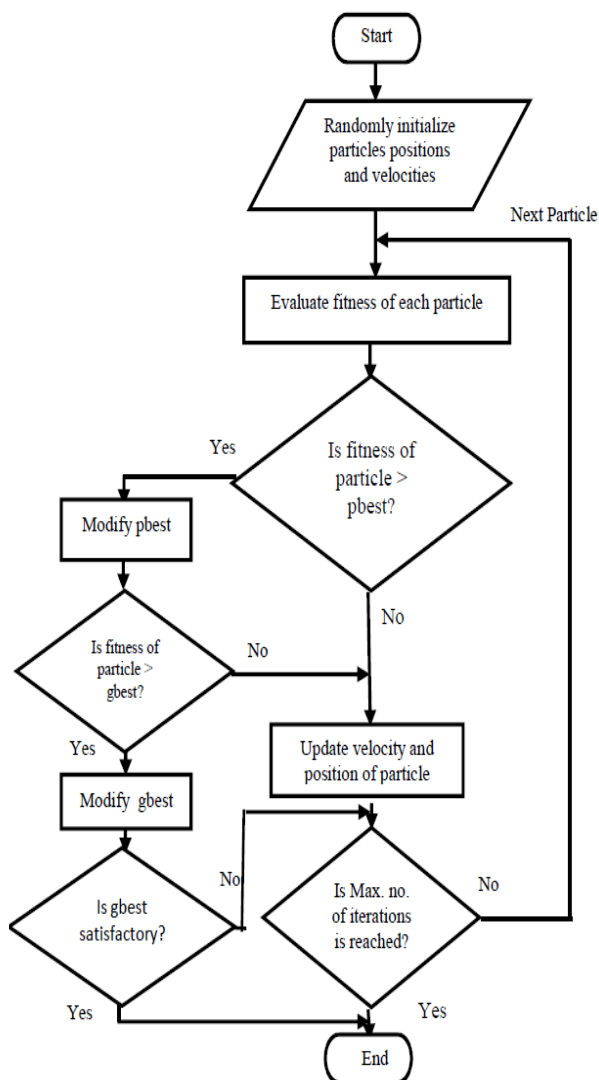


Figure (7) The flowchart of PSO algorithm.

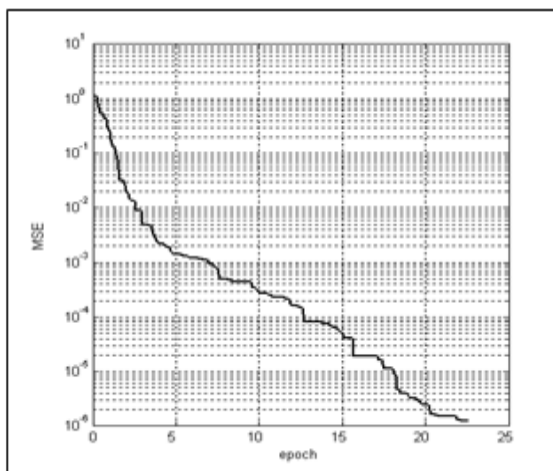


Figure (8) Training MSE with epoch for example1 by using PSO algorithm.

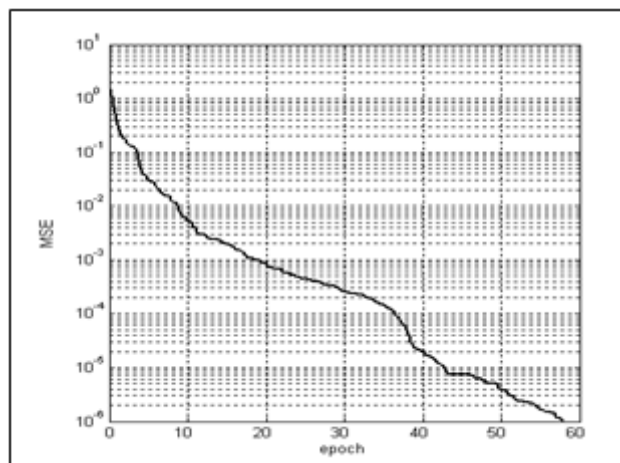


Figure (9) Training MSE with epoch for example2 by using PSO algorithm.

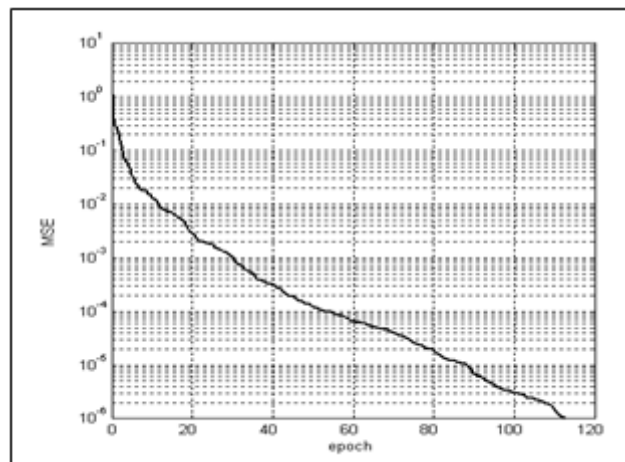
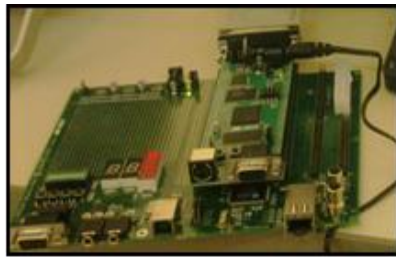


Figure (10) Training MSE with epoch for example3 by using PSO algorithm.

Table (2) the comparison results between GANN and PSO algorithms.

	GANN			PSO		
	a	b	c	a	b	c
Examples						
Learning iteration	5	8	8	23	58	116
Error Convergence	$4.008 e^{-6}$	$1.0001 e^{-6}$	$3.0009e^{-6}$	$9.75e^{-7}$	$7.86 e^{-7}$	$9.95e^{-7}$
Classification (%)	93.2 %	96.24 %	92.83 %	99.98 %	99.99 %	98.42 %



(a)

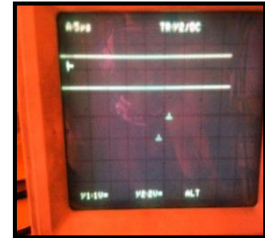


(b)

Figure (11) The Hardware Design of ANN platform (HDANN) system: (a)FPGA board (b)HDANN system.



(a)



(b)



(c)



(d)

Figure (12) the output data when the input to the ANN is applied: (a) Nu0 (b)

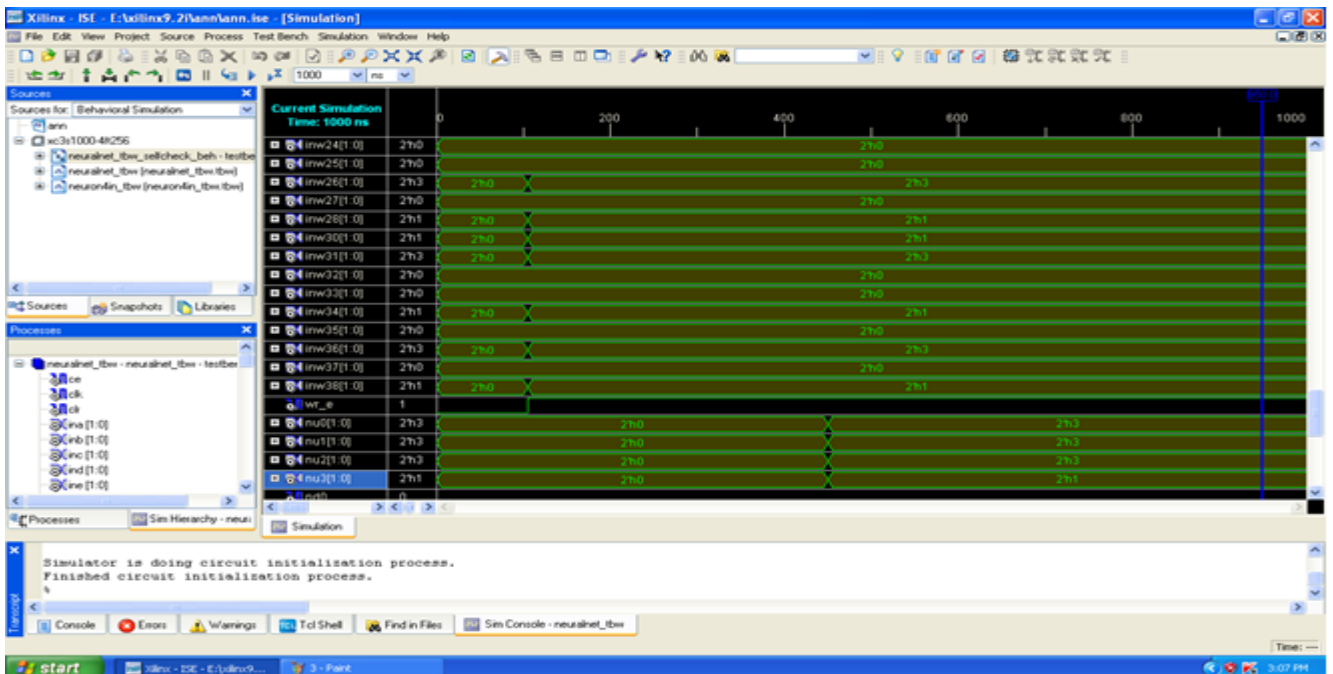


Figure (13) The simulation results of the ANN circuit of example2.

MODIFIED METHOD OF INFORMATION HIDING BASED ON HYBRID ENCRYPTION AND STEGANOGRAPHY

Baedaa H. Helal

Control and Systems Engineering Dept.

University of Technology

baedaa_hashim@yahoo.co.uk

Abstract

Hiding information by embedding secret data into an innocuous medium is often referred to as steganography. Steganography can be applied electronically by taking a message (a binary file) and some sort of cover (often a sound or image file) and combining both to obtain a “stego-object”. The stego-object is essentially the cover with its redundant information replaced with the message. Unfortunately, replacing the redundant information with structured message data often results in the stego-object being an augmented version of the cover “marked” by the hidden data—and this makes it easy to suspect the presence of steganography.

This paper produces a development method based on steganography techniques to prevent intruders to obtain the transmitted information. This work is based on a combination of steganography and cryptography techniques to increase the level of security and to make the system more complex to be defeated by attackers.

The algorithm that is used for encryption is the RC6 algorithm. RC6 is a block cipher submitted to NIST for consideration as the Advanced Encryption Standard (AES). RC6 is 128 bits block size work with four 32-bit registers A;B;C;D which contain the initial input plaintext as well as the output ciphertext at the end of encryption.

Two methods of hiding are used in this work, the first method is the Least Significant Bit (LSB) and the second is proposed method which is modified method used to hide bits in LSB of iterated loop in brightness, red, green and blue of hiding image. The proposed method was tested

using standard subjective measures such as Mean Square Error (MSE) and Peak Signal to Noise Ratio (PSNR). A comparison between the two methods is performed.

1. Introduction:

Digital communication has become an essential part of nowadays infrastructure, A lot of applications are Internet-based and in some cases it is desired that communication be made secret. Consequently, the security of information has become a fundamental issue, many of the techniques are available to achieve this goal some of them are the Encryption and the steganography techniques. Using cryptography, the information is transformed into some other gibberish form and then the encrypted information is transmitted. Steganography is a process that involves hiding a message in an appropriate carrier for example an image or an audio file. The carrier can then be sent to a receiver without anyone else knowing that it contains a hidden message [1].

Steganography is mostly used on computers with digital data being the carriers and networks being the high speed delivery channels. Modern steganography is generally understood to deal with electronic media rather than physical objects and texts. This makes sense for a number of reasons. First of all, because the size of the information is generally (necessarily) quite small compared to the size of the data in which it must be hidden (the cover file), electronic media are much easier to manipulate in order to hide data and extract messages. Secondly, extraction itself can be automated when the data is electronic, since computers can efficiently manipulate the data and execute

the algorithms necessary to retrieve the messages. Electronic data also often includes redundant, unnecessary, and unnoticed data spaces which can be manipulated in order to hide messages [2].

Previous attempts at achieving this goal have required the user to provide the original cover as well as the stego-object. The best areas to hide are first identified in the original cover, then these areas are mapped across to the stego-object and the hidden information is retrieved. The original cover must be provided because the information overwritten in the message hiding process may have been used to identify the best hiding areas. However, to provide the original object is not secure, because taking the differences between the two objects would be enough to suspect the existence of (and in some cases, recover) the hidden information.[3]

2. Framework of Steganography Model:

In general, the basic framework of the steganography model is illustrated in Figure (1). This model consists of two main processes, namely the Embedding process and the Extracting process. The main function of the embedding process is to hide the secret message, called Embedded message, in a given cover, called Cover-file. In hidden communication techniques, the cover-file is no more than an innocent (unrelated to the embedded message) piece of information that is used to hide the secret information. A secret key, called Stego-key is used in the embedding process such that it makes the embedded message computationally infeasible to extract without possessing this key. The output of the embedding process is called Stego-file, which is the original file holding the hidden secret message. This output becomes, at the other end, the input of the extracting process, in which the embedded message is extracted from the Stego-file to complete the hidden communication process. Since the stego-key is used in the embedding process, it needs to be used in the extracting process [4].

3. Cryptography

The process of encryption and decryption is called a ciphering as shown in figure (2). All modern algorithms use a key to control encryption and decryption; a message can be decrypted only if the key matches the encryption key.

Basically, the purpose of cryptography and steganography is to provide secret communication. Many people lump Steganography with cryptography, and while they are in many cases means to the same ends they are not the same thing.

Cryptography is the science of converting plaintext into ciphertext, which protects the contents of messages.[5], [6]

3.1-Details of RC6:

RC6 is a fully parameterized family of encryption algorithms. A version of RC6 is more accurately specified as RC6-w/r/b where the word size is w bits, encryption consists of a nonnegative number of rounds r, and b denotes the length of the encryption key in bytes. Since the AES submission is targeted at w = 32 and r = 20, we shall use RC6 as shorthand to refer to such versions.

When any other value of w or r is intended in the text, the parameter values will be specified as RC6-w/r. Of particular relevance to the AES effort will be the versions of RC6 with 16-, 24-, and 32-byte keys.

For all variants, RC6-w/r/b operates on units of four w-bit words using the following six basic operations. The base-two logarithm of w will be denoted by lgw.

a + b integer addition modulo 2w

a - b integer subtraction modulo 2w

a ⊕ b bitwise exclusive-or of w-bit words

a × b integer multiplication modulo 2w

a <<<b rotate the w-bit word a to the left by the amount given by the least significant lgw bits of b

a >>>b rotate the w-bit word a to the right by the amount given by the least significant lgw bits of b

Note that in the description of RC6 the term "round" is somewhat analogous to the usual DES-like idea of a round: half of the data is updated by the other half; and the two are then swapped.[7]

RC6 works with four 32-bit registers A;B;C;D which contain the initial input plaintext as well as the output ciphertext at the end of encryption. The first byte of plaintext or ciphertext is placed in the least-significant byte of A; the last byte of plaintext or ciphertext is placed into the most-significant byte of D. Use the (A; B; C; D) = (B; C; D;A) to mean the parallel assignment of values on the right to registers on the left, figure (3).

3.2- Key Schedule for RC6:

The user supplies a key of b bytes. Sufficient zero bytes are appended to give a Key length equal to a non-zero integral number of words; these key bytes are then loaded in little-endian fashion into an array of c w-bit words L[0],.....,L[-1].

Thus the first byte of key is stored as the low-order byte of L[0], etc., and L[c_1] is padded with high-order zero bytes if necessary. (Note that if b = 0 then c = 1 and L [0] = 0.) The number of w-bit words that will be generated for the additive round keys is 2r + 4 and these are stored in the array S [0, 2r + 3].

The constants P32 = B7E15163 and Q32 = 9E3779B9 (hexadecimal) are the same "magic constants" as used in the RC5 key schedule. The value of P₃₂ is derived from the binary expansion of e - 2, where e is the base of the natural logarithm function. The value of Q₃₂ is derived from the binary expansion of Ø-1, where Ø is the Golden Ratio. [7]

Key schedule for RC6-w/r/b

c=16, 24 or 32, w=32, r=20

Input: User-supplied b byte key preloaded into the c-word

array L[0, c - 1]

Number r of rounds

Output: w-bit round keys S [0, 2r+3]

Procedure:

S [0] = Pw // PW=0xB7E15163

```

for i = 1 to 2r + 3 do
  S[i] = S [i - 1] + Qw // QW=0x9E3779B9
  A = B = i = j = 0
for s = 1 to 132 do
  {
  A = S[i] = (S[i] + A + B) <<<3
  B = L[j] = (L[j] + A + B) <<< (A + B)
  i = (i + 1) mod (2r+4)
  j = (j + 1) mod c
  }

```

3.3- Least Significant Bit Embedding

It is one of the basic and easily implemented image steganography methods. This is done by embedding one bit from the encrypted data into one pixel of the cover; the given bit embeds in the Least Significant Bit of the blue byte of this pixel.

4-The Proposed Method

In this way the input message is divided into blocks each of which is 128 bit. The block is encrypted by using RC6 encryption algorithm. From image (cover) a 16 bit will be taken and then rearrange in to 4*4 array ,the bits of encrypted message hide in the diameter bytes of this array that is mean the encrypted bits will be hide in LSB of iterated loop in brightness, red, green and blue of hiding image. The encrypted bits will be extracted and then decrypted to check the hiding way. This modified method can be described as shown in Figure (4). The LSB method and the modified method will be used to hide the encrypted message, the comparison between the two methods are measured by using standard subjective measures such as Mean Square Error (MSE) and Peak Signal to Noise Ratio (PSNR). The results are shown in Tables (1) and (2).

5- System Evaluation Methods

Since the essential goal of steganography is the concealing of the fact that a secret message is transmitted, then it is very important to make the stego-file to be as close as to the cover-file. In fact, imperceptibility of the stego-file reflects how much it is affected due to embedding process, in other words, imperceptibility can

be decided by measuring that effect. In the proposed system, the MSE, PSNR and the Correlation Coefficient measurements are adopted.

5.1 Mean Squared Error (MSE)

The (weighted) mean squared error between the cover image and the stego-image can be used as one measures to assess the relative perceptibility of the embedded message.

$$MSE = \frac{1}{mn} \sum_{i=0}^{m-1} \sum_{j=0}^{n-1} \| C(i, j) - S(i, j) \|^2$$

Where m and n are the number of rows and number of columns respectively of the cover image, $C(i, j)$ is the pixel value from the cover image, $S(i, j)$ is the pixel value from the stego-image [7].

5.2 Peak Signal to Noise Ratio (PSNR)

The phrase **Peak Signal-to-Noise Ratio**, often abbreviated into **PSNR**, is an engineering term for the ratio between the maximum possible power of a signal and the power of corrupting noise that affects the fidelity of its representation. PSNR is most commonly used as a measure of quality of reconstruction in image compression. It is most easily defined via the **MSE** [8].

The PSNR is defined as:

$$PSNR = 10 \cdot \log_{10} \left(\frac{MAX_I^2}{MSE} \right) = 20 \cdot \log_{10} \left(\frac{MAX_I}{\sqrt{MSE}} \right)$$

Here, MAX_I is the maximum pixel value of the image. When the pixels are represented using 8 bits per sample, this is **255**. More generally, when samples are represented using linear **PCM** with B bits per sample, MAX_I is $2^B - 1$.

For color image with three RGB values per pixel, the definition of PSNR is the same except the MSE is the sum over all squared value differences divided by image size and by three. The larger PSNR dB value is the higher the image quality is (which means there is only little difference between the cover-image and the stego-image). On the contrary, a small dB value of PSNR means

the great distortion between the cover-image and the stego-image.[8]

5.3 The Correlation Coefficient Measuring Factor (The Similarity Test)

The similarity test is the correlation between the cover-image and stego-image. Correlation is one of the best known methods that evaluate the degree of closeness between two functions. This measure can be used to determine the extent to which the original image and the stego-image are close to each other, even after embedding data. When the stego-image is perceptually similar to the original cover-image; then the correlations equals one.

Pearson Correlation Coefficient (Corr) is given by; [8]

$$Corr = \frac{\sum \sum (S - \bar{S})(C - \bar{C})}{\sqrt{\sum \sum (S - \bar{S})^2 \sum \sum (C - \bar{C})^2}}$$

Where $\bar{S} = \frac{\sum \sum S}{MN}$.

S: stego-image. C: cover-image.

6. Results and Discussion

In this paper the tests are performed on text secret file using two types of hiding methods. The two hiding methods are Least Significant Bit and the modified method. In LSB hiding method is embedding in the least position, while in the modified hiding method which is hide bits in LSB of iterated loop in brightness, red, green and blue of hiding image.

Four different BMP images are used have as covers file to embed the encrypted secret message using RC6 encryption method to obtain four different stego-files. These images are Cat.bmp, Lena.bmp, Lev.bmp, and Peppers.bmp. Each of figures (5, 6, 7 and 8) shows the following:

- a- the original image,
- b- histogram for image,
- c- stego-file when LSB embedding method is used,
- d- histogram for stego-file when LSB embedding method is used,
- e- stego-file when modified method is used, and

f- histogram for stego-file when modified method is used.

As shown in histograms, cryptography techniques are used to increase the level of security and to make the system more complex to be defeated by attackers. The histograms of the four images shown, the stego-file is to be as close as to the cover-file which means that the two methods are successes to hide the message with more security.

The results of the three measuring factors for the two methods are given in Tables (1) and (2) where (MSE) indicates Mean Squared Error measure, (PSNR) indicates Peak Signal to Noise Ratio, and (Corr) indicates the Correlation Coefficient measure. The output stego-file remains of the same size as the original file. It is also rarely affected after hiding the information according to subjective measures or the objective measures (MSE and PSNR) as it appears in the results given in experimental result. These results prove that the goal of steganography is achieved where the stego-file will not look suspicious and nobody even knows that there is a hidden message.

The level of protection will be increased by using encryption algorithm. The proposed system for steganography is stronger to attack than any other existing system that does not use encryption. With measuring of the (MSE) the minimum values is the better, The larger (PSNR) dB value is the higher image quality (which means there is only little difference between the cover-image and the stego-image), and With the measuring of the Correlation Coefficient (Corr) the closer to one is the better. The results obtained from the correlation test indicate that the stego-file is similar in the two ways of hiding methods since correlation values approach to one.

From the studying of the whole system, it's clear that when the secret file size increases, MSE increases and the PSNR decrease. This result is obtained by applying different secret message sizes.

Hence a hacker must know the following in order to extract the embedded message from the stego-file:

- a. Algorithm to extract the message from the image. (stego algorithm)
- b. Encryption algorithm.
- c. Correct password for algorithm.

7- Conclusion

In this paper four different BMP images are evaluated. These images are cat.bmp (Figure 5) as an example for an image containing large areas of a single color, Lena.bmp (Figure 6) as it is the reference image used in image processing research (it does not contain many high frequency components), Lev.bmp (Figure 7) and peppers.bmp (Figure 8) as examples of images containing many high frequency components.

With The Mean Squared Error (MSR), Least Significant Bit gives MSR6.068E-2 which is the maximum value and 6.068E-2 is the minimum value for all images, the modified method gives maximum MSR 0.127, and minimum MSR 5.361E-03. The results for two ways of hiding methods are very small. With the Peak Signal to Noise Ratio (PSNR), Least Significant Bit gives maximum PSNR76.931, and minimum PSNR 60.317, and the modified method gives maximum PSNR 70.856 and minimum PSNR 57.109, in the two ways of hiding methods we obtain large values of PSNR for all images which mean there is only little difference between the cover-image and the stego-image. With the Correlation Coefficient measure (Corr) gives values approach to one which are better values, Least Significant Bit gives maximum Corr0.99999870254599, and minimum Corr0.999991403088456, the modified method gives maximum Corr0.99999479693163, and minimum Corr0.999983256264233, for all images. These results prove that the goal of steganography is achieved in the two ways of hiding methods.

References:

- [1] T. Morkel, J.H.P. Eloff and M.S. Olivier, "An Overview of Image Steganography", in Proceedings of the

- Fifth Annual Information Security South Africa Conference (ISSA2005), Sandton, South Africa, June/July 2005.
- [2] Maroney, C. Hide and Seek 5 for Windows 95, computer software and documentation, originally released in Finland and the UK, n.d. Downloadable from: <http://www.rugeley.demon.co.uk/security/hdsk50.zip>
- [3] M. Owens, “A Discussion of Covert Channels and Steganography”, as part of the Information Security Reading Room. SANS Institute 2002.
- [4] A. H. Ouda and M. R. El-Sakka, “A Step Towards Practical Steganography Systems”, Computer Science Department, University of Western Ontario, London, Ontario, Canada, ICIAR 2005, LNCS 3656, pp. 1158 – 1166, 2005.
- [5] A. Setiawan, D. Adiutama, J. Liman, A. Luther and R. Buyya, “Grid Crypt: High Performance Symmetric Key Cryptography using Enterprise Grids”, Grid Computing and Distributed Systems Laboratory, Dept. of Computer Science and Software Engineering, The University of Melbourne, Australia, 2004.
- [6] N. Sharma, J. S. Bhatia, N. Gupta, “An Encrypto-Stego Technique Based Secure Data Transmission System”, TheInfosec Writers Text Library (RSS), 2005.
- [7] Ashwaq T. Hashim "Type-3 Feistel Network of The 128-bits Block Size Improved Blowfish Cryptographic Encryption", Eng& Tech, Journal, Vol. 27, No. 2, 2009.
- [8] Venkatraman. S, A. Abraham and M. Paprzycki, “Significance of Steganography on Data Security”, Dept. of Computer Science & Engineering, University of Madras, INDIA, Dept. of Computer Science, Oklahoma State University, USA, Proceedings of the International Conference on Information Technology, 2004IEEE.

Table (1) System evaluation when using LSB embedding method

Image	MSE	PSNR	CORRELATION
Cat	9.405E-03	68.414	0.999998967271495
Lena	6.068E-2	60.317	0.999991403088456
Lev	1.323E-03	76.931	0.999999870254599
Peppers	5.298E-03	70.906	0.999999284715728

Table (2) System evaluation when using the modified method

Image	MSE	PSNR	CORRELATION
Cat	3.184E-02	63.118	0.99999654160075
Lena	0.127	57.109	0.999983256264233
Lev	5.361E-03	70.856	0.999999479693163
Peppers	2.151E-02	64.821	0.999997131589161

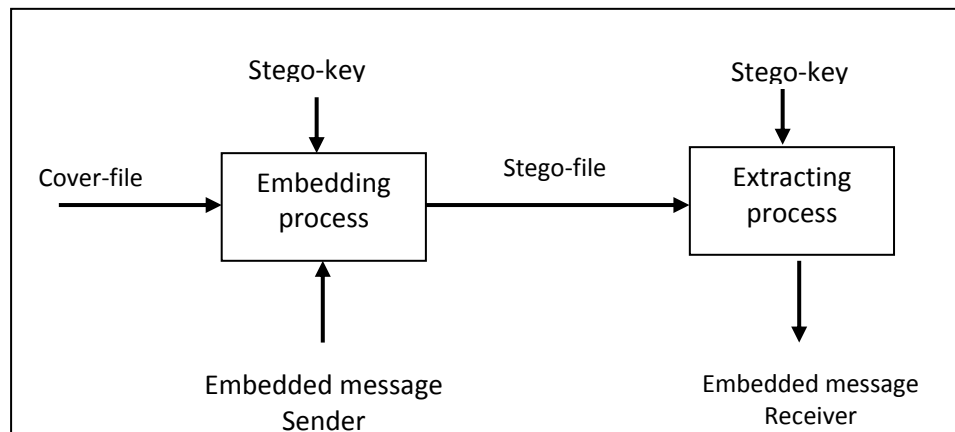


Figure (1) Framework of the embedding process

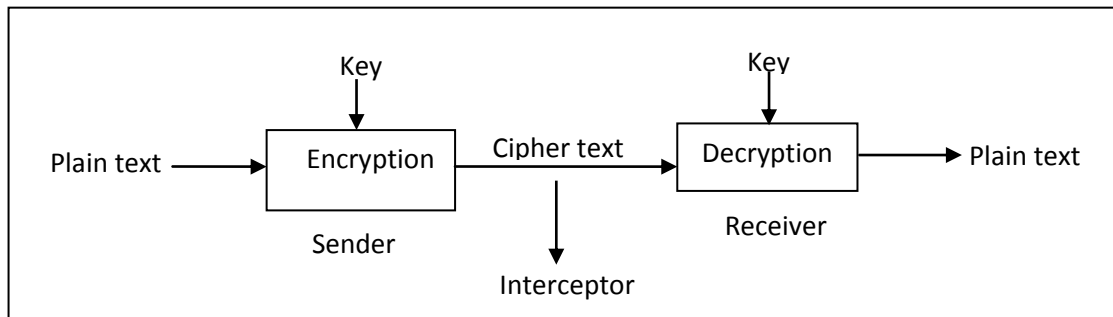


Figure (2) Block diagram of ciphering system

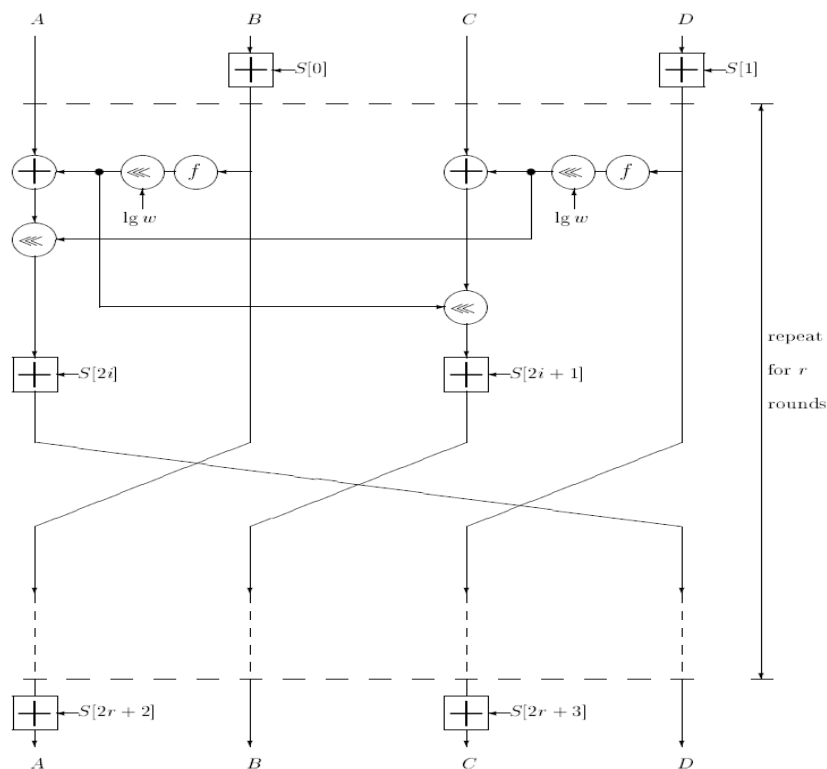


Figure (3) Encryption with RC6-w/r/b. Here $f(x) = x \ll (2x+1)$

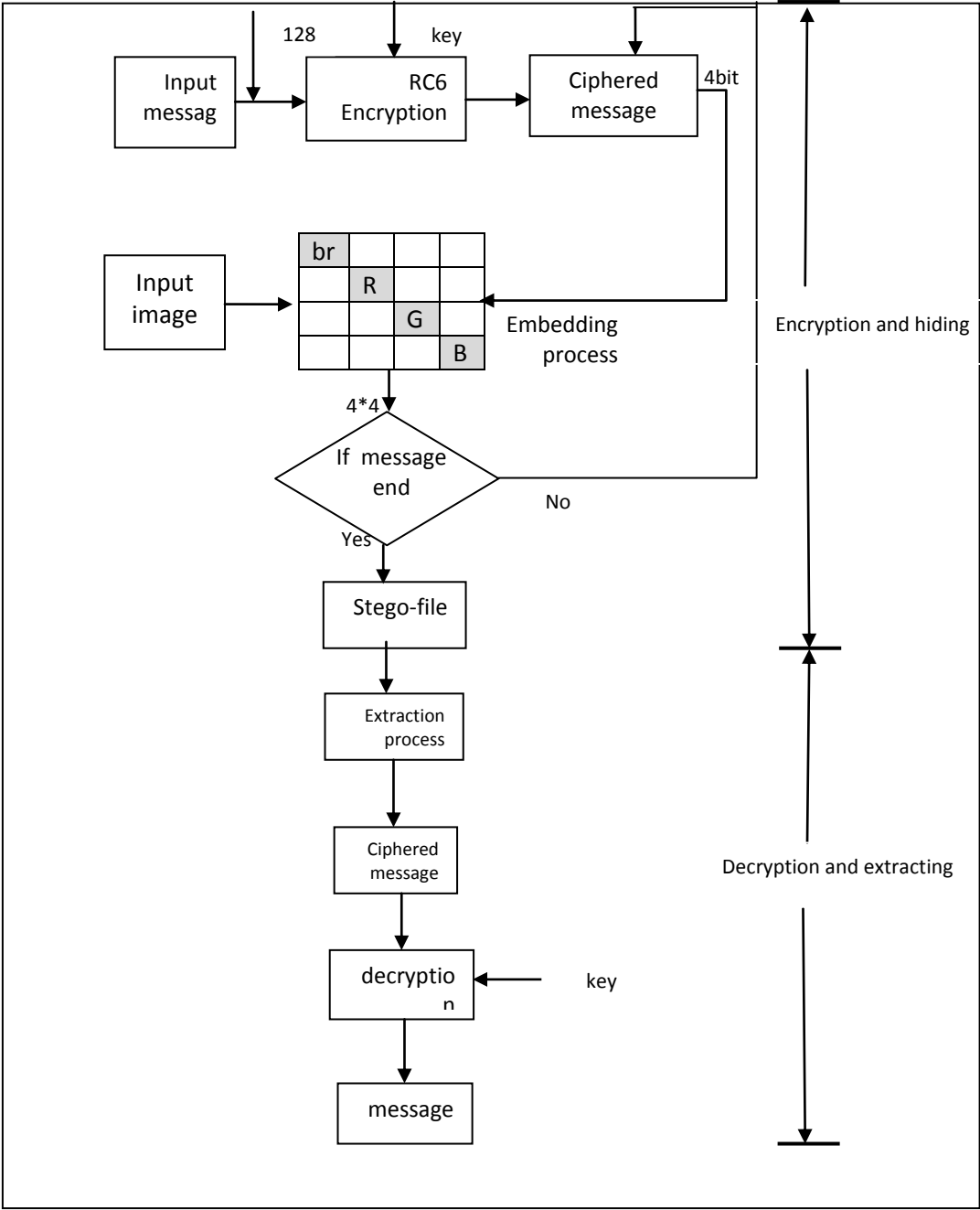


Figure (4) The flowchart of the modified method.

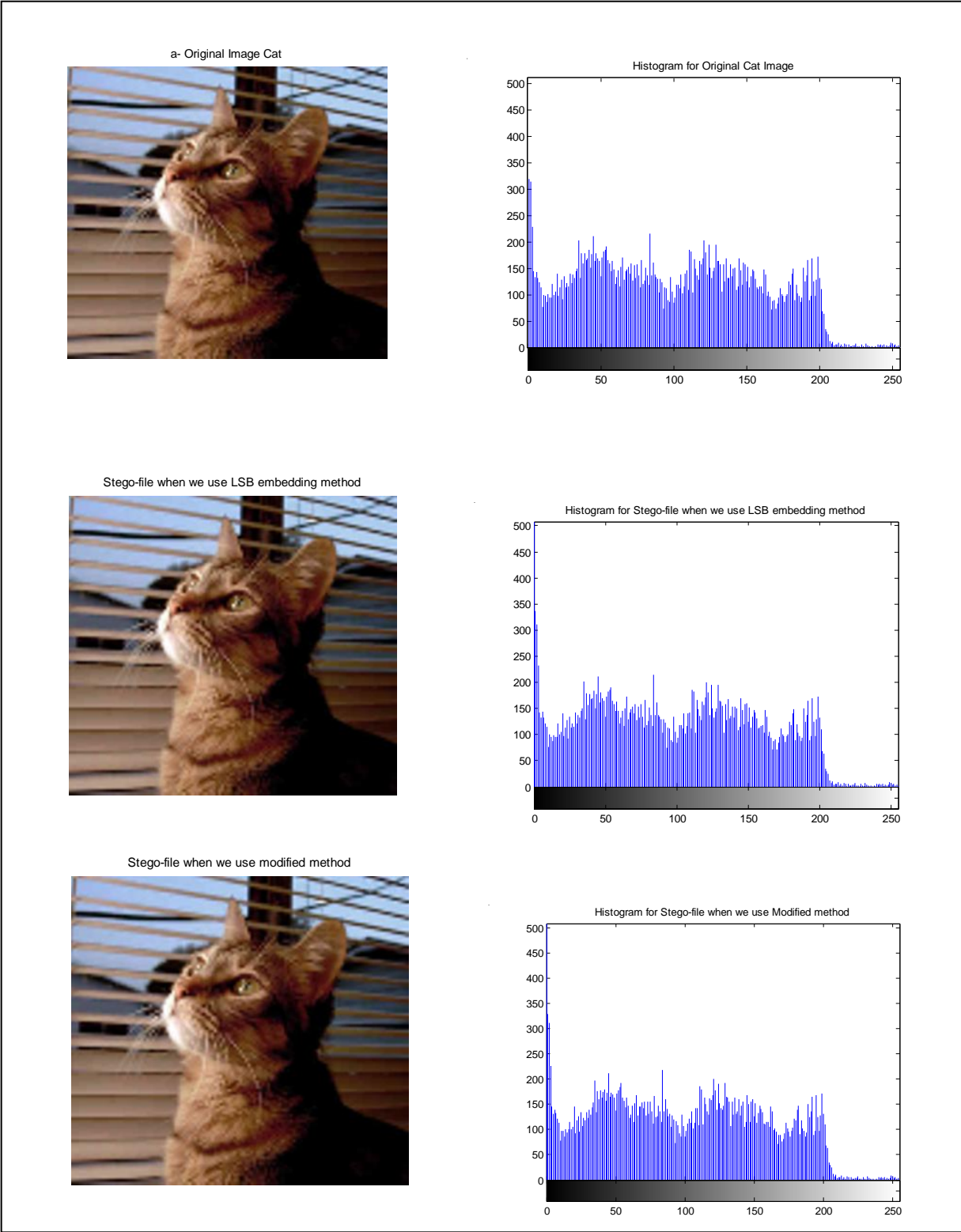
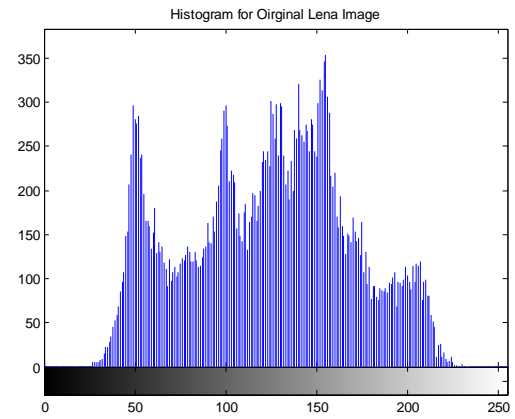
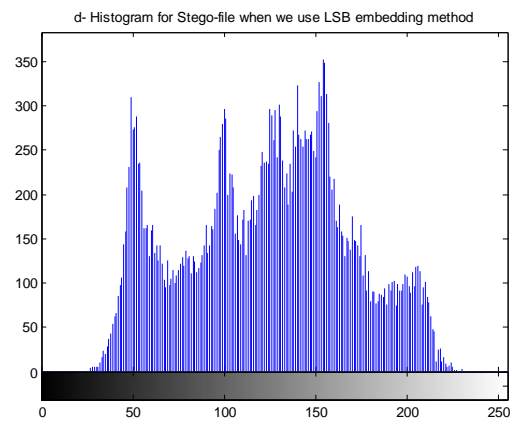


Figure (5)

a- The Original Image Lena



Stego-file when we use LSB embedding method



e- Stego-file when we use Modified method

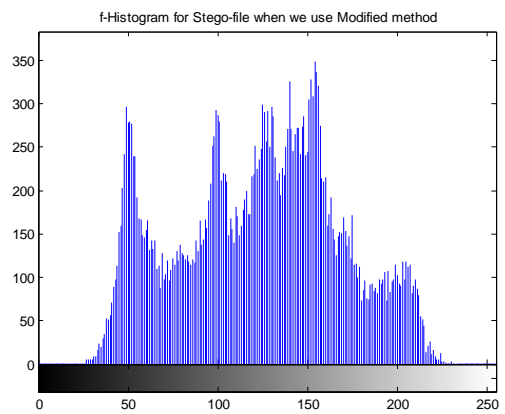


Figure (6)

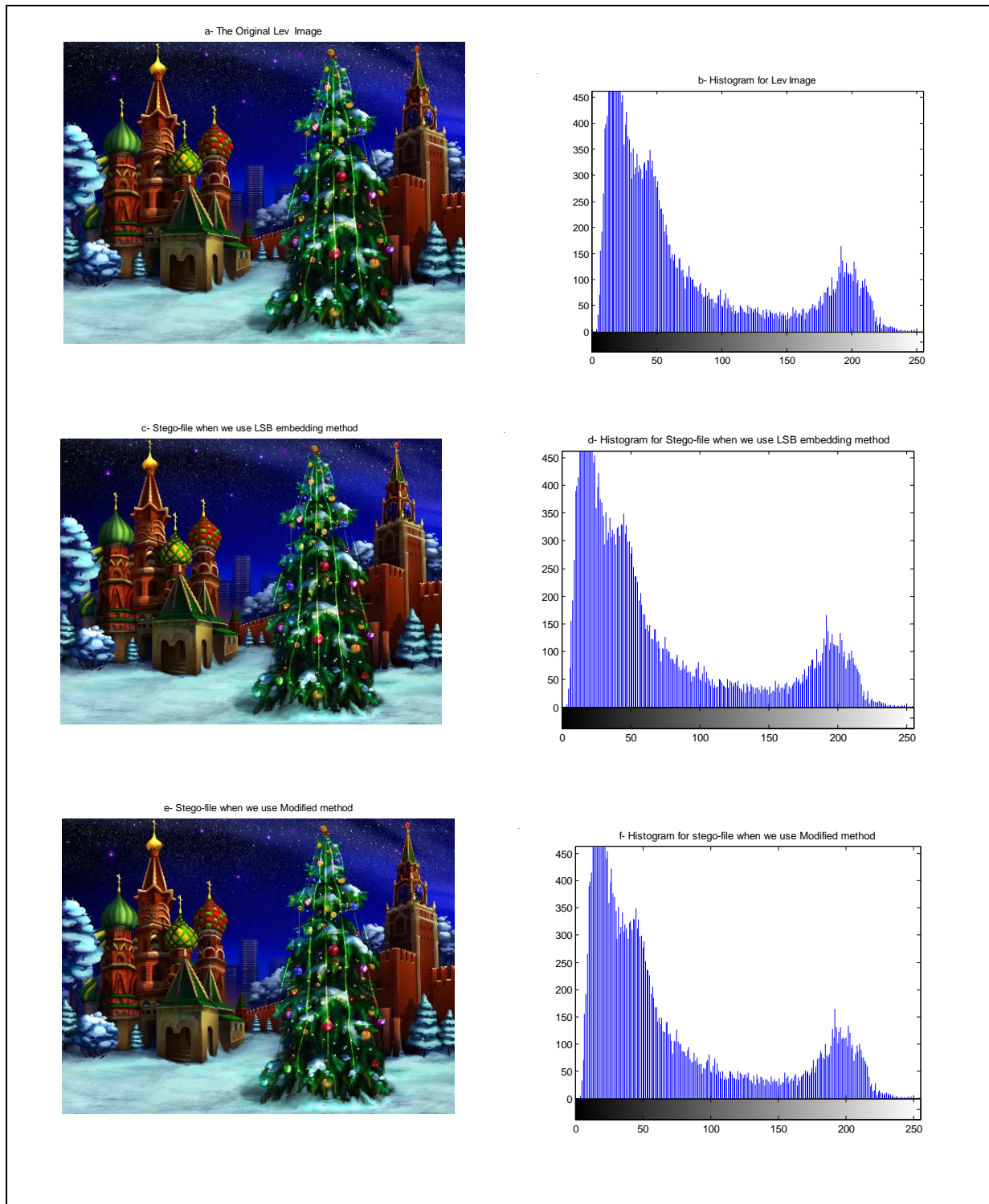


Figure (7)

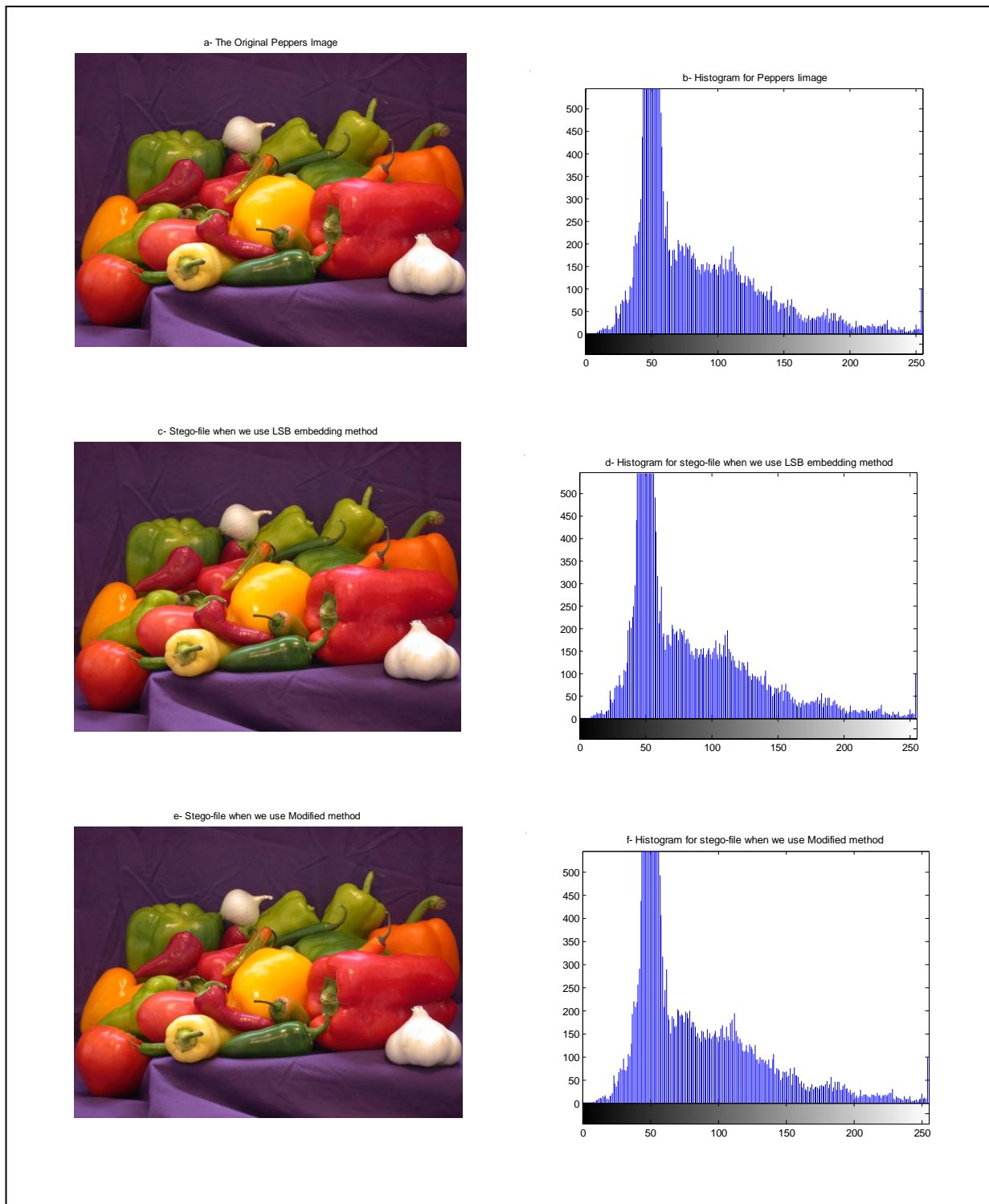


Figure (8)

KEY EXTENDED-BASE DES ALGORITHM

Dr. Mohammed Najm Abdullah Saddam Kamil Alwane Ammar Abdul-Amer Rashed
mustafamna@yahoo.com alwanesaddam@yahoo.com ammar_abed_76@yahoo.com

Computer Engineering and Information Technology Dept.
University of Technology
Baghdad-IRAQ

Abstract

Encryption is technology meant to convert plain text to encrypted text to preserve the confidentiality of this text, that the encryption algorithms based on the key used in encryption.

With the development of computing capacity, has shown its inability to DES, which showed marked weakness towards new technologies of cryptanalysis such as linear cryptanalysis, has been the target of many attacks for almost a quarter of a century, making the need for a new algorithm is stronger and more important strengthen the level of confidentiality.

In this paper, a proposal for the design and implementation of encryption technology is derived from the algorithm DES to provide more security; the proposed method depends directly on an algorithm to generate the subkey, so that order S-Box based on the subkey that has created a different way to choose S-Box in each round.

The experimental results showed that the proposed algorithm to improve security, as these results showed that the proposed method improved security by 16 times compared with the traditional method.

Keywords: *DES, Encryption algorithms, S-Box, Cryptography*

1. Introduction:

The aim of all Internet users is access to information and transfer of security, where the Internet has become an easy and enjoyable enable millions of people access to a wealth of information, in addition to communication and exchange of information

and messages among themselves. However, some factors (the open nature of this network, the absence of any party can claim that it owned and controlled, there are no laws central deterrent), helped to spread many of the crimes on the network. Such as (packet sniffing, computer hacking, hoaxes, Virus attack on the e-mail). From the foregoing, we find that Internet security is becoming important to be solving its problems, given the importance of security in the exchange of personal information and business information.

This made the encryption of information is necessary to prevent unauthorized persons from access to information or understanding [1].

The paper is organized as follows: In section 2, we summarize Cryptography, where was mention of a general overview as well as the kinds. In section 3, we discuss the original DES, where was mention of an overview of the algorithm, as well as explain the structure. In section 4, we briefly the proposed system is described, as well as compared with the original DES algorithm and in section 5, conclude the paper.

2. Cryptography

Cryptography is the science that uses mathematics to encrypt and decrypt data. You can store the encryption of sensitive information transmitted over networks or unsafe - such as the Internet - and it can not be read by anyone except the person sent to him. Because the encryption is the flag used to maintain the security and confidentiality of information, analysis and decoding (Cryptanalysis) was aware of a

breach of the break and secure communications [2].

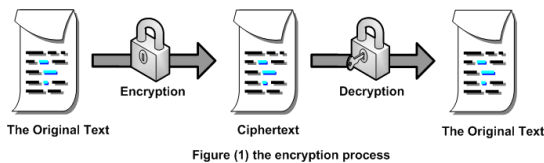
There are four main objectives behind the use of cryptography are as follows:

1. **Confidentiality:** This service is used to store content information from all persons except that told them to look at them.
2. **Integrity:** This service is used to store information of the change (delete or add or modify) by persons unauthorized to do so.
3. **Authentication:** This service is used to prove the identity of dealing with the data (authorized).
4. **Non-repudiation:** This service is used to prevent the person from doing something undeniable.

The primary goal of encryption is to provide these services to the people to be maintaining the security of their information.

Encryption algorithm is a mathematical function used in the process of encryption and decryption. It works in combination with the key or password, number or phrase, to encrypt the text read [2].

Reading the same text encrypts to different texts encrypted with different keys. And security of the encrypted data depends on two important strength encryption algorithm and secret key. As shown in the Figure (1)



2.1. Types of Cryptography:

2.1.1. Conventional Cryptography:

Also called Symmetric Cryptography. It uses one key to the process of encryption and decryption of data. This type supports of encryption on the secret key of the user. Where the person who holds the key can decode the encryption and read the content of the messages or files [2]. As shown in the Figure (2)

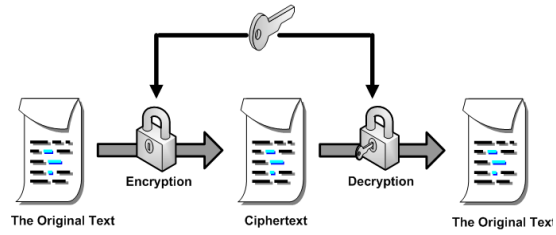


Figure (2) Symmetric Cryptography

2.1.2 Public Key Cryptography:

Public key cryptography (called Asymmetric Cryptography) are designed so that the key used encryption different from the key used for decryption. Furthermore, the decryption key can not be calculated from the encryption key. In these systems, the encryption key is often called the public key and the decryption key is often called private key [3]. The system as shown in the Figure (3)

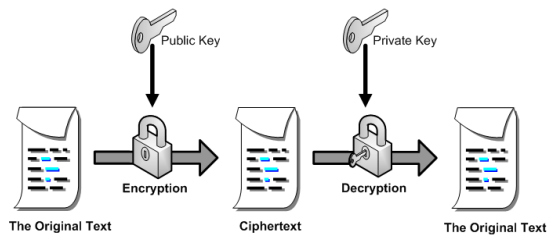


Figure (3) Asymmetric Cryptography

3. DES algorithm

DES is a complex system is not linear and is capable of operations with high speed when it is implemented components of the material allow it [4].

The DES algorithm is a substitution cipher which takes a block of 64 bits of input (plaintext) into a unique block of 64 bits of output (ciphertext), under the control of a 64-bit key. In this system, plaintext information is divided into several blocks which are then operated upon independently to generate a sequence of ciphertext blocks.

The DES encryption system is based on a system of transpositions and permutations. The permutation box or P-box is used to transpose, or map a sequence of input values to another sequence of values of the same length. Substitutions are performed by what are called S-boxes. Each combination of the S-box and P-box comprises a single weak

component of the algorithm. By including a sufficiently large number of stages in the product cipher, the output can be made to be a nonlinear function of the input.

The mapping of input to output is one-to-one and invertible, since the encrypted messages can be decrypted. The DES has three distinct components: key schedule, cipher function, and invertibility[5].

DES is characterized by the following:

1. Key used to encrypt the data to be known by authorized users in order to be able to decode the data that they receive.
2. Encryption security depends on the confidentiality that is provided for the key user in the process of encryption and decryption code.
3. DES is the first system in terms of deployment of its own algorithm, since the Analyzer code should be replaced by a large number of equations to solve nonlinear systems, the DES code.

3.1 Data structures used in the DES algorithm [6]:

1. Packet data prepared for the encryption

This data consists of 64 bits divided into the left side (32 bit) and the right side (32 bit).

2. Encryption key

Consists of 64-bit derived from 16 sub-key length of each 48-bit.

3. Initial Permutation (IP):

That the 64-bit change under the site to take action described in the Figure (4) to generate 64-bit data and then divides into the left side (32 bit) and the right side (32 bit). This table is used once for each section entered.

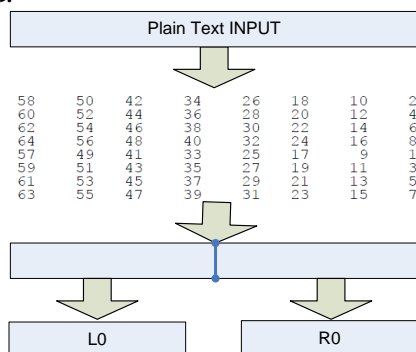


Figure (4) Initial Permutation

4. E-Bit Selection table:

This table takes the 32-bit input to give the 48-bit as output by combining bits depending on the sites indexed in a table(1) which uses 16 times (many of the locations of bits in the table repeats itself and this makes the expansion possible).

Table (1) Expansion Permutation

32	1	2	3	4	5
4	5	6	7	8	9
8	9	10	11	12	13
12	13	14	15	16	17
16	17	18	19	20	21
20	21	22	23	24	25
24	25	26	27	28	29
28	29	30	31	32	1

5. Permuted Choice -1:

This table replaces the original key, consisting of 64-bit to generate 56-bit key consists of two parts left and right of each table, including 28-bit (This table is used once for each section of the income).

Table (2) PC1 Table

Left						
57	49	41	33	25	17	9
1	58	50	42	34	26	18
10	2	59	51	43	35	27
19	11	3	60	52	44	36
Right						
63	55	47	39	31	23	15
7	62	54	46	38	30	22
14	6	61	53	45	37	29
21	13	5	28	20	12	4

6. Left Shift LS:

That each round of the 16 rounds of the algorithm uses a different key depending on the number of the session, it is Jeb, and he turned the key component of the 56-bit by one site or two to the left.

Table (3) Left Shift Table

No. round	No. of shifts to the left
1,2,9,16	1
3,4,5,6,7,8,10	2
11,12,13,14,15	3

7. Permuted Choice -2:

Is a table arrangement that turns the key, consisting of 56-bit output of the table LS to

key is composed of 48-bit which is added to 48-bit derived from (Table 4), and this table is used 16 times (once for each round).

Table (4) PC2 Table

14	17	11	24	1	5
3	28	15	6	21	10
23	19	12	4	26	8
16	7	27	20	13	2
41	52	31	37	47	55
30	40	51	45	33	48
44	49	39	56	34	53
46	42	50	36	29	32

8. Substitution Boxes S:

Is an eight tables, each table takes a 48-bit resulting from the process E+K_n 6-bit input to each box to give out 4 bits of each fund and the result is a 32-bit eight of these tables is used 16 times (once for each round). Figure (6) shows the S-Box rule while Figure (7) shows the architecture of S-Box and table (5) represents one of eight tables.

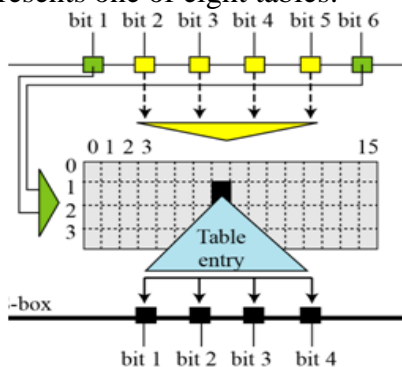


Figure (6) the S-Box rule

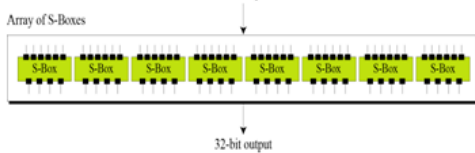


Figure (7) S-boxes

Table (5) S-Box Table

S ₁															
14	4	13	1	2	15	11	8	3	10	6	12	5	9	0	7
0	15	7	4	14	2	13	1	10	6	12	11	9	5	3	8
4	1	14	8	13	6	2	11	15	12	9	7	3	10	5	0
15	12	8	2	4	9	1	7	5	11	3	14	10	0	6	13

9. Permutation P:

The permutation function P yields a 32-bit output from a 32-bit input by permuting the bits of the input block. Such a function is defined by the following table (6).

Table (6) Permutation P

16	7	20	21
29	12	28	17
1	15	23	26
5	18	31	10
2	8	24	14
32	27	3	9
19	13	30	6
22	11	4	25

10. Inverse Initial Permutation (IP⁻¹):

That 64-bit result of 16 turns round to the locations shown in the figure (8)

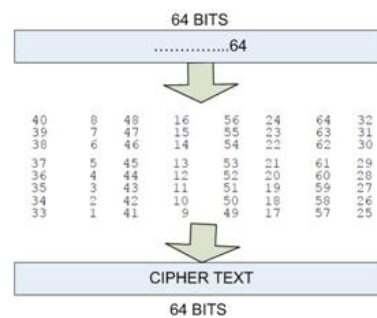


Figure (8) Inverse Initial Permutation

3.2 Key generation:

The DES uses a 64-bit key for encryption and decryption process. Initially, the original 64-bit key is reduced to 56-bit by ignoring every eighth bit. In general these bits are used as parity bits to make sure that there were no errors when entering the key or during key transmission. After the 56-bit key is extracted a different 48-bit key, referred to as subkey, is generated for each of the 16 rounds of the DES. These keys, K_i, are determined as shown in Figure (9). The 56-bit key is divided into two 28-bit halves C_i and D_i which are then shifted left by either 1 or 2 digits, depending on the round. (Table 3) shows the number of circular left shifts for C_i and D_i halves. After the shifting operation, 48 out of the 56 bits are selected. Since this operation permutes the order of the bits as well as selecting a subset of the original bits, it is called compression permutation or permuted choice. The permuted choice 1 and

permuted choice 2 matrices are shown in (Table 2) and (Table 4) respectively[7].

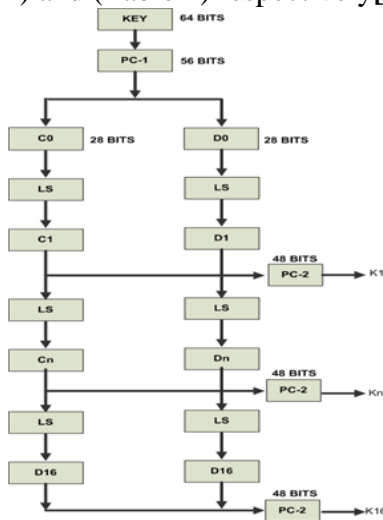


Figure (9) key generate Process

3.3 The encryption process [6]:

Figure (10) shows outline of the encryption process after a first arrangement of the constituent bits of the block to be encrypted.

With the development of computing capacity, has shown its inability to DES, which showed marked weakness towards new technologies of cryptanalysis such as linear cryptanalysis, has been the target of many attacks for almost a quarter of a century, making the need for a new algorithm is stronger and more important strengthen the level of confidentiality.

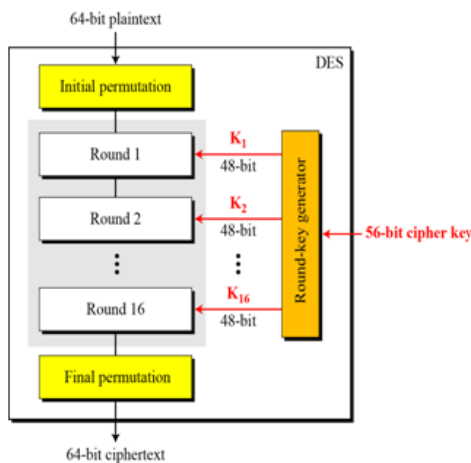


Figure (10) The encryption

4. Proposed system Description

The modification to the DES algorithm will be on the key-processing algorithm, so

that the arrangement of the S-Boxes will be dependent on the sub-keys, this will create a different way for choosing S-Boxes for each round. In the proposed systems the length of the key processing 88-bit the bits (8, 16, 24, 32, 40, 48, 56, 64, 72,80,88) are bits of error detection and after we get shot down on 84-bit being the initial permutations, as shown in table(7).

Table (7) Initial Permutation of the proposed system

57	43	47	25	62	2	61	66	45	4	83
34	70	30	77	87	5	76	20	42	55	22
75	38	81	50	52	79	23	67	51	21	74
73	19	33	17	9	44	13	82	10	27	35
29	1	31	86	14	65	33	11	28	6	18
3	58	12	78	7	37	85	15	63	26	39
54	84	71	36	59	60	68	49	69	46	41

The 77-bits result is divided into three parts. The first part consists of 48-bits will be enter S-Boxes to generate 32-bits. The second part consists of a 16-bit enters a permutation box to produce 16 bits permuted output, as shown in table (8).

Table (8) Permutation of the proposed system

12	9	10	5	1	13	16	11
14	4	6	3	8	2	7	15

The third part consists of 13-bits, where the first four bits are XORed, last four bits are XORed and (6, 7, 8, 9) bits are XORed to produce four bits. 32-bits output from the S-Boxes is divided into two parts left and right of each section is 16-bits.16-bits left are swapped with the permuted 16 bits(output from table 7) and all the output are combined to produce 48-bit block to be sent to the main algorithm as K1.

The 4 bit output from third part is used twice after adding (1) to the two least significant bits and discarding the carry, first the 4 bits are sent to the main algorithm to control the arrangement of the S-Boxes.The first bit determines whether to switch the boxes 2 and 3, The second bit determines whether to switch the boxes 1 and 7, The third bit determines whether to switch the boxes 4 and 6, The fourth bit determines whether to switch the boxes 5 and 8, Then

the four bits are recombined with the 48 bits to prepare for the next subkey of the next round.

For the next round the 52 bits are shifted 7-bits to the left, the 48 bits are sent to the main algorithm, the left four bits are processed like the 4 bit output from third part, and so on for 16 rounds. Figure (11) shows the proposed system architecture.

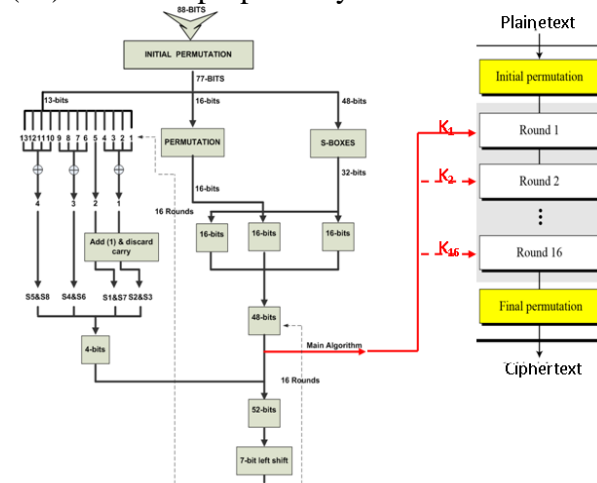


Figure (11)The Proposed system the Modified DES

The study of the characteristics of both systems (original DES and the proposed system) will give clearly which one is the strongest. One simple and clear calculation is the operation of effective-key length calculation, for the original DES: length of the key 48 bits that gives 2^{48} possible keys. And for the proposed system: 48 bits+4 bits controlling S-Boxes, that gives 2^{52} possible keys.

This shows that the proposed system is more secured than the original DES with a factor of 24. This means that if all the other features of the proposed system are put aside, it will take 16 times the time required to break the DES.

Table (9) shows the difference between the original DES algorithm and the proposed system.

Table (9) The difference between two systems

	Length of K	possible keys	Iteration	S-Boxes	Security	Permutation box
original DES	48-BITS	2^{48}	2^{16}	no	Security	no
proposed system	52-BITS	2^{52}	2^{17}	s-box	More Security	Permutation box

5. Conclusions

- ❖ The 88 bits instead of 64 bits give a more secure information and to ensure more safety from tampering by hackers and vandals and thieves, this increases the required iterations by a factor of 2^{21} , that is when using the most basic attack of trying every possible key the needed iterations will be increased from 2^{56} to 2^{77} .
- ❖ The S-Boxes inside the key generation algorithm are aimed to reduce linearity. This is to resist the linear cryptanalysis providing a non-linear operation. The non-linear operation was chosen to be the same S-Boxes of the main algorithm to reduce the needed components (in hardware) or disk space (in software), it is done only once to increase the speed of generation of sub-keys, and it is convenient for key generation.
- ❖ The permutation inside the key generation algorithm is to provide more diffusion. Diffusion dissipates the redundancy of the plaintext by spreading it out over the ciphertext. A cryptanalyst looking for those redundancies will have a longer time finding them.
- ❖ Controlling the S-Boxes of the main algorithm by the key is a very important feature that is aimed to resist differential cryptanalysis. The key dependent swapping of the S-Boxes in each iteration makes the differential cryptanalysis inconvenient to apply because it will require more time than the brute-force attack
- ❖ The addition of 1 and neglecting the carry provides two benefits; first, there will be no weak, semi-weak, or possibly-weak keys. Second, it will cancel the complement keys property
- ❖ The 7-bit shift left will provide at least, 15 different sub-keys for each key. Any number less than 7 will provide more similar sub-keys. It is clear that the number of shifts should not be a factor of 52, because it will cause alike patterns.

References:

- [1] Farmer W. M. (2003), "Overview of Cryptography" 07- Cryptography Overview. Pdf".
- [2] Wilson S (2004), "An Introduction to Cryptography". IntroToCrypto.pdf.
- [3] Schneier B. (2009), "Applied Cryptography (Protocols, Algorithm, and Source Code)", " New Yourk"
- [4] Pfleeger C.P. (2006), "Security In Computing", Prentice Hall.
- [5] Daemen J. and Rijmen V. (2008) ,"The Design of Rijndael" (AES- The Advance Encryption Standard), "Belgium".
- [6] Whiley. J. & Sons (2006), "Information: Security Principles and Practice", "New Jersy".
- [7] Stamp M, (2009) "Information Security Principles and Practice" "Canada"
- [8] Topping C., (2003). "General Cryptographic Knowledge". White Paper"general_cryptographic_knowledg e3. pdf".

RULE INDUCTION TECHNIQUE FOR FINGERPRINT IDENTIFICATION

Awad Kadhim Hammoud
awad_kh2007@yahoo.com

Hattam Nahi Muhaisen, B.Sc.
hattamal_amery@yahoo.com

Directorate of Information Technology
Ministry of Science and Technology

Abstract:

Pattern recognition problems computer based are very important and essential in our real life.

There are many approaches have been used in pattern recognition problem such as: Fourier Descriptor, Moment Invariant. But the main defect of these methods is the long time processing and large computer space. This paper, presents a new approach Artificial Intelligence, of Rule Induction technique. By this approach, the essential and specific features of object have been extracted from contour of object to be recognized. The characteristics of these features, are easy computed, and require fewer amounts of time and space, and then high speed in recognition and decision. Such features are (number of curves inside the fingerprint, number of check point for each curve). It efforts a good and accurate results. We test the performance of this system using many contours of fingerprint, and get a good and accurate results.

Keywords: *Fingerprint, pattern recognition, Image processing, Artificial Intelligence, Rule Induction, B_Spline.*

1-Introduction:

Pattern recognition techniques are the important tools used in the field of machine intelligent,[Julius T. Ton and R. C. Gonzalez, 1974].

Pattern recognition could be defined as: “the categorization of input data into identifiable classes via the extraction of significant feature of attributes of the data from background of irrelevant detail”,[Julius T. Ton & R. C. Gonzalez, 1974].

We recognize characters, pictures, music and the objects around us. This process may be referred to as sensory recognition which includes aural and visual recognition. This recognition process involves the identification and classification of spatial and temporal patterns.

There are many techniques have been largely and earliest used in pattern recognition fields, such that Fourier descriptor, [R. C. Gonzalez, 1992], and moment invariants, [W. Pratt, 1978].

The pattern recognition techniques are widely used in real life, such that, we need system for handwritten recognition. We need a system for target detection and classification. We need system for blood cell analysis and classification, etc.

In this paper, presentation of Artificial Intelligence technique of rule induction for fingerprint recognition, was employed to generate a classification rule from features extracted from examples for contour of the object of the fingerprint to be recognized. The induction technique was first developed, by Hunt at 1966, who produce the (Concept learning Algorithm) CLS, and was subsequently improved by Quinlan at 1979, by using ID3 algorithm (Iterative Dichotomies 3) ,[Anna Hart,1986],[Paul R. Cohen and Edward A. Fiegenbaum, 1982] . This approach presented in this paper adopts the features are essentially and specific of object such as (number of curves inside the fingerprint, number of check point for each curve ...). The classification of unknown objects using rule induction was computationally inexpensive compared to the conventional approaches, (Fourier Descriptor, Moments Invariants).

2- Induction Algorithm:

This algorithm is based on inductive inference which is “the process of inferring general law from particular examples, [Paul R. Cohen and Edward A. Figenbaum,1982],[4]

In order to be able to use induction, we require the following [Anna Hart,1986]:

1-Examples: The examples or training set from the basis of induction process.

2-Attributes: The examples have sets of characteristics that describe them, and enable comparisons to be made between different examples. The attributes may be:

a-Descriptive categories,(e.g.small, medium, large).

b-Real measurements, (e.g. height in meter).

c- Integer values (e.g. age in years).

d- Logical descriptive, (e.g. true, false, on top of).

3-Classes: the classes represent the decision or classification. The ID3 algorithm is the tool of the classification mechanism, which it will describe, in the following article.

Figure (1): Block diagram of FingerPrint Recognition system.

2-1 ID3 Algorithm:

The ID3 algorithm uses a training set of examples to induce IF... THEN ... rules, which is form a simple decision tree [Anna Hart, 1986]. These examples are describe the attributes and the resulting classes. The training set contains at least one type of cases, which the expert has deal with. The expert draws up a set of examples, then inductive system read and analysis, these examples, which describe the pattern involved. Induction rules can be produced for these examples.

3- The Developed System:

The structure of the object recognition system, which designed and implemented to recognize the object of fingerprint using ID3 algorithm consist from the following major part :-

1- Input Image of the fingerprint.

2- Feature extraction by using B_spline method to determine the check point for each curve of the fingerprint.

3- Object classification Using Rule Induction.

Figure (1) shows the major part of the system.

3-1 Input Image:

The input image of the fingerprint is captured by scanner, the image size is (160,160) pixel, as shown bellow in fig(2).

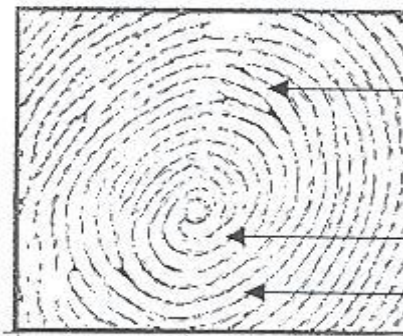


Figure (2): The input Image of fingerprint

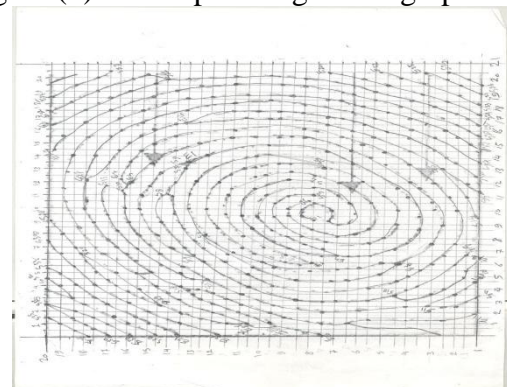


Figure (3): Processed Input FingerPrint image.

3-2 Feature Extraction:

In this step, we have to extract the features of the fingerprint by using B_spline method to determine the check point for each curve in the fingerprint image, as shown in the next paragraph.

which represent the control points of the finger were employed to generate a classification rule extracted from examples for contour of the fingerprint to be recognized.

The detailed of extracted control Points will be shown in the experimental result part, as shown in figure (4).

3-3 B_Spline Method:

From a mathematical point of view, a curve which is generated by using the vertices of a defining polygon is dependent on some interpolation or approximation scheme to establish the relationship between the curve and the polygon.

Let P(t) be the position vector along the curve, as a function of a parameter t, a curve generated by the use of the B_spline basis is given by [6]:

$$p(t) = \sum_{i=0}^n p_i N_{i,k}(t) \quad \dots\dots(1)$$

Where p_i are the n+1 defining polygon vertices.

For the ith normalized B_Spline basis curve of order k, the weighting function $N_{i,k}(t)$ are defined by the recursion formulas

$$N_{i,1}(t) = \begin{cases} 1 & \text{if } X_i \leq t < X_{i+1} \\ 0 & \text{Otherwise} \end{cases}$$

And

$$N_{i,k}(t) = \frac{(t-x_i)N_{i,k-1}(t)}{x_{i+k-1}-x_i} + \frac{(x_{i+k}-t)N_{i+1,k-1}(t)}{x_{i+k}-x_{i+1}} \quad \dots\dots(2)$$

Where the x_i are element of a knot vector which is the parameter t varies from 0 to t(max) along the curve p(t).

3-4 Fingerprint Identification Using Rule Induction:

A rule tree is automatically generated from examples by ID3 algorithm. So, we have been designed and implemented a Visual Basic program to generate and produce a decision rule tree for fingerprint identification system.

Rule induction is chosen for these approach, because it provides solution that that uses a minimum number of features (curve no., control no.), and give fast decision and accurate distinction between objects of fingerprint.

4-The System Implementation and Experimental results:

An experiment was designed to test the performance of fingerprint identification system to identify the contour of the fingerprint were selected to train the system.

After reading image of fingerprint, features of fingerprint have been measured, and then a rule tree was generated via used ID3 algorithm.

This system was implemented by written a Visual BasicVer. 6.

The following steps explain the detailed description of implementation of the designed system. This section consist of two sections:

Section one provides a full description of the developed system.

Section two deals with the experimental results obtained by the implementation of the system.

4-1 System Algorithms:

The system is built on a set of algorithms, which can be described as follows:

- 1-Input Fingerprint Image algorithm.
- 2-Feature Extraction algorithm.
- 3-ID3 Fingerprint Identification algorithm.

4-1-1 Input Fingerprint Image algorithm:

This algorithm shows how to read the image of the fingerprint , display on the screen, save in data file.

Input : Image file of finger print

Output : Data file (curve number., control number)

Step1: scan image file of fingerprint by scanner device.

Step 2: read image file.

Step 3 : save the coordinate of the fingerprint object in data file.

Step 6 : close data file.

End.

4-1-2 Feature extraction algorithm

Input : Data file1

Output : Data file2 (curve number., control number)

Step 1 : calculate number of curves for fingerprint in image file.

Step 2: calculate number of control points in each curve.

Step 3: save (Finger_no, curve_no, control_point) data file (table1).

Step 4: Call B-Spline function to draw the new image of the original fingerprint.

End.

4-1-3 ID3 Fingerprint Identification algorithm

The following decision tree is produced by Id3 algorithm to get the type of the fingerprint.

Begin

If (curve_no <= 35) then

 If (control_point[1] < 35)

 Else if If (control_point[2] < 20)

 Else If (control_point[3] < 25)

 Else If (control_point[4] < 8)

 Else If (control_point[35] < 4)

 Output :FingerTyepe= : ("Finger1")

End.

4-2: The Experimental results

4-2-1.Input Image:- The figure (2), shows the input image of fingerprint.

4-2-2- Measurement of the fingerprint Features Extraction:

In order to extract features of the object from an image, there are several significant and essential features that should be extracted from the object of the fingerprint. So, the image of the fingerprint will be breakdown into the many curves. Each curve contain many of control points, as shown in figure(3) and figure(4).

The origin fingerprint consist of 35 curves. Curve number 1 for example consist of 32 control points and Curve number 2 consist of 20 control points, and so on, into curve number 35 which contain four curves as shown bellow in the table(1):

Table (1): curves number, control points and fingerprints identification.

Control point No.	Curve No.	Fingerprint Class	No.
32	Curve no.1	Finger1	1
20	Curve no.2	Finger1	2
25	Curve no.3	Finger1	3
8	Curve no. 4	Finger1	4
30	Curve no. 5	Finger1	5
8	Curve no. 6	Finger1	6
32	Curve no. 7	Finger1	7
14	Curve no. 8	Finger1	8
7	Curve no. 9	Finger1	9
16	Curve no. 10	Finger1	10
5	Curve no. 11	Finger1	11
7	Curve no. 12	Finger1	12
9	Curve no. 13	Finger1	13
37	Curve no. 14	Finger1	14
3	Curve no.15	Finger1	15
12	Curve no 16	Finger1	16
14	Curve no. 17	Finger1	17
9	Curve no.18	Finger1	18
29	Curve no. 19	Finger1	19
19	Curve no. 20	Finger1	20
7	Curve no. 21	Finger1	21
6	Curve no. 22	Finger1	22
5	Curve no. 23	Finger1	23
6	Curve no. 24	Finger1	24
4	Curve no. 25	Finger1	25
3	Curve no. 26	Finger1	26
4	Curve no. 27	Finger1	27
12	Curve no. 28	Finger1	28
4	Curve no. 29	Finger1	29
8	Curve no. 30	Finger1	30
9	Curve no. 31	Finger1	31
7	Curve no. 32	Finger1	32
5	Curve no. 33	Finger1	33
5	Curve no. 34	Finger1	34
4	Curve no. 35	Finger1	35

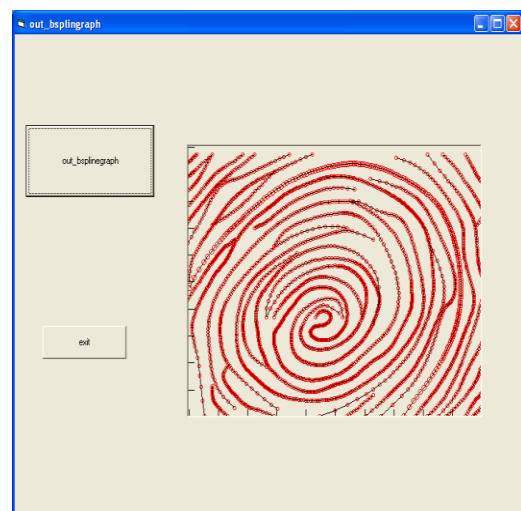


Figure (4) : The output processed curves of the origin fingerprint

4-3-3 The Decision Making and Identification Result:

The curve no. and control point that extracted from the step 2, are passed into decision tree (rule induction) to make a decision making and then get an accurate type of fingerprint identification, as shown in Figure (5).

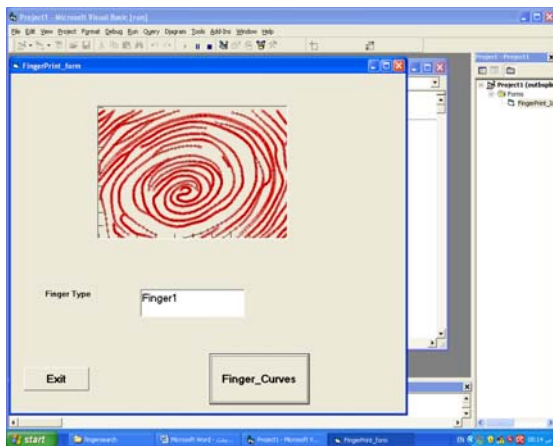


Figure (5): The output of the final fingerprint and its type.

The sub code implementation of the some function of the system will be described in appendix 1.

5- Conclusion:

Using rule induction technique to generate classification rules from examples was demonstrated, and has been successfully extended to identify the true type of fingerprint via use ID3 algorithm, viewed from 35 curves. It has been demonstrated that the rule trees provided a method of identification, such fingerprint which is both computationally efficient, and faster decision and high accurate. In current research, a new technique have been adopted to segment the image of the fingerprint into many curves by using B_Spline method to make smooth and accurate curves, which each curve contain a number of check point using later in rule induction to make decision making of fingerprint type as demonstrate in the last steps.

References:

- [1] Parsye K., M. Chignell, "Expert Systems for Experts", John_wiely,1989.
- [2] Anna Hart, "Knowledge Acquisition for Expert Systems", Kogan Page,1986.
- [3] Mowforth,P. H. and Grant E., "Rule Based Integration Of vision and taction", Tuning Institute, 1987.
- [4] (Rule Induction) some material adopted from internet notes.2011 <http://lightning.eecs.ku.edu/Rule-Induction>
- [5] R.C. Gonzaleze, "Digital Image Processing", Printice_Hall, 1992.
- [6] W. Pratt, "Digital Image Processing", A Wiley-Interscience publication, 1978.
- [7] Rogers, D. F., "Mathematical Elements for Computer Graphics", McGraw-Hill, New york, 1976.

Appendix 1

```

Private Sub outbsplinegraph_Click()
Dim xx(1000), yy(1000), zz(1000), t As Double
Dim ff(1000), vv(1000), xx1, yy1, xs, ys, gg, jj As Double
Dim curveno, controlno As Integer

yt = 10: xt = 10: aa = 8
k = 0
For i = 1 To 21
k = k + 1
xx(i) = k
yy(i) = k
Next i
minx = xx(1): miny = yy(1): maxx = xx(1):
maxy = yy(1)
For i = 1 To 20
If (xx(i) >= maxx) Then
maxx = xx(i)
End If
If (yy(i) >= maxy) Then
maxy = yy(i)
End If
If (xx(i) <= minx) Then
minx = xx(i)
End If
If (yy(i) <= miny) Then
miny = yy(i)
End If

```

```
Next i
  xx1 = maxx - minx: yy1 = maxy - miny
  X1 = minx: Y1 = miny: X2 =
  p1.ScaleWidth: Y2 = p1.ScaleHeight
  gg = (X2 - X1) / xx1: jj = (Y2 - Y1) / yy1
  Open "F:\outcurve19.txt" For Input As #1
  Input #1, m
  For i = 1 To m
  Input #1, xx(i), yy(i)
  Next i

  For z = 1 To m
  xs = X1 + (gg * (xx(z) - minx))
  ys = Y2 - (jj * (yy(z) - miny))
  ff(z) = xs: vv(z) = ys
  p1.Circle (xs, ys), 3, RGB(255, 0, 0)
  Next z
```

Topic 6

Communications, Sensors and Signal Processing in Modern Control Systems

MULTISPECTRAL FUSION FOR SYNTHETIC APERTURE RADAR (SAR) IMAGE BASED FRAMELET TRANSFORM

Mohammed Hussein Miry

Department of Electrical and Electronic Engineering, University of Technology.

mohammed_miry@yahoo.com

Abstract

The technique of fusing a panchromatic (Pan) SAR image that has a high-spatial and low-spectral resolution with multispectral (MS) SAR images that have a low-spatial and high spectral resolution is very useful in many remote sensing applications that require both high-spatial and high-spectral resolution. Recently, some studies showed that a wavelet-based image fusion method provides high quality spectral content in fused SAR images. In this paper, a new method based on a Framelet transform is introduced, which represents discrete wavelet transforms based on over sampled filter banks, that are analogous to Daubechies wavelets. The design of minimal length wavelet filters satisfy certain polynomial properties. In the proposed method, we replace max rule in high frequency with new relation depending on an input SAR image. Experimental results show that the framelet transform based SAR image fusion method provides richer information comparing with wavelet transform. Simulation experiments show that fused SAR image of proposed method is efficiently.

Keywords: *Fusion, Multispectral, Panchromatic, SAR Image, Framelet Transform*

1. Introduction

In recent years, synthetic aperture radar (SAR) image fusion technology has been widely used in various fields such as remote sensing and military applications for the

purpose of object detection, target recognition, better human perceptibility, and other computer processing tasks[1]. To date, many techniques and software tools for fusing SAR images have been developed. The well-known methods include the intensity–hue–saturation (IHS) color model, and principal component analysis (PCA), both IHS and PCA mergers are based on the same principle: to separate most of the spatial information of an MS image from its spectral information by means of linear transforms. The IHS transform separates the spatial information of the MS image as the intensity (I) component. In the same way, PCA separates the spatial information of the MS image into the first principal component. The limitation of these methods is that some distortion occurs in the spectral characteristics of the original MS images. Recently, developments in wavelet analysis have providing a potential solution to this problem by provides a high spectral quality in fused SAR images. Nune developed an approach for fusing a high-resolution Pan image with a low-resolution MS [2]. In this paper, a multispectral fusion for SAR image based on framelet transform is introduced. The results clearly demonstrate the advantages of this approach. The paper is organized as follows: Section 2, describes the theoretical basis of the framelet transform. In section 3, we will introduce and motivate the IHS color conversion. In section 4, we introduce the stages of the proposed fusion method. Experimental results of the proposed method are shown in section 5. Then, the proposed fusion is scheme is compared to the

wavelet and HIS, PCA methods. Finally, conclusions are outlined in Section 6.

2. Framelet Transform

Though standard Discrete Wavelet Transform (DWT) is a powerful tool for analysis and processing of many real world signals and images, it suffers from three major disadvantages, shift sensitivity, poor directionality, and lack of phase information. These disadvantages severely restrict its scope for certain signal and image processing applications (e.g. edge detection, image registration /segmentation, motion estimation) [3, 4, 5]. Other extensions of standard DWT such as Wavelet Packet Transform (WPT) and Stationary Wavelet Transform (SWT) reduce only the first disadvantage of shift-sensitivity but with the cost of very high redundancy and involved computation. Recent research suggests the possibility of reducing two or more of these disadvantages [3]. Introducing the Double-Density Wavelet Transform (DDWT) as the tight-frame equivalent of Daubechies orthonormal wavelet transform; the wavelet filters are of minimal length and satisfy certain important polynomial properties is an oversampled framework. Because the DDWT, at each scale, has twice as many wavelets as the DWT, it achieves lower shift sensitivity than the DWT [4].

2.1. Computation of Framelet Transform for 2-D Signal using Non- Separable method [6,7]

To compute a single level orthogonal-based discrete Framelet for 2-D signal the next steps should be followed:

- 1) Checking input dimensions: Input matrix should be of length $N*N$ where N must be even and $N \geq \text{length}$ (analysis filters).
- 2) For an $N*N$ matrix input 2-D signal X , construct a $3N/2*N$ transformation matrix, W using transformation matrices for length-7 given as equation (1)

$$W = \begin{bmatrix} h_0(0) & h_0(1) & h_0(2) & h_0(3) & h_0(4) & h_0(5) & h_0(6) & 0 & 0 & \dots & 0 & 0 \\ 0 & 0 & h_0(0) & h_0(1) & h_0(2) & h_0(3) & h_0(4) & h_0(5) & h_0(6) & \dots & 0 & 0 \\ \vdots & \vdots \\ h_0(2) & h_0(3) & h_0(4) & h_0(5) & h_0(6) & 0 & 0 & \dots & 0 & 0 & h_0(0) & h_0(1) \\ h_1(0) & h_1(1) & h_1(2) & h_1(3) & h_1(4) & h_1(5) & h_1(6) & 0 & 0 & \dots & 0 & 0 \\ 0 & 0 & h_1(0) & h_1(1) & h_1(2) & h_1(3) & h_1(4) & h_1(5) & h_1(6) & \dots & 0 & 0 \\ \vdots & \vdots \\ h_1(2) & h_1(3) & h_1(4) & h_1(5) & h_1(6) & 0 & 0 & 0 & 0 & \dots & h_1(0) & h_1(1) \\ h_2(0) & h_2(1) & h_2(2) & h_2(3) & h_2(4) & 0 & 0 & 0 & 0 & \dots & 0 & 0 \\ 0 & 0 & h_2(0) & h_2(1) & h_2(2) & h_2(3) & h_2(4) & 0 & 0 & \dots & 0 & 0 \\ \vdots & \vdots \\ h_2(2) & h_2(3) & h_2(4) & 0 & 0 & 0 & 0 & 0 & 0 & \dots & h_2(0) & h_2(1) \end{bmatrix} \quad (1)$$

- 3) Apply transformation by multiplying the transformation matrix by the input matrix by the transpose of the transformation matrix

$$Y = W \cdot X \cdot W^T \quad (2)$$

Then multiplication of the three matrices result in the final discrete framelet transformed matrix.

2.2. Computation of Inverse Framelet Transform for 2-D Signal [8]

To reconstruct the original signal from discrete Framelet transformed signal, Inverse Discrete Framelet Transformed (IDFT) should be used. The inverse transformation matrix is the transpose of the transformation matrix as the transform is orthogonal. To compute a single level 2-D inverse discrete Framelet Transform using non-separable method the next steps should be followed:

- 1) Let Y_0 be the $3N/2 \times 3N/2$ Framelet transformed matrix.
- 2) Construct $N \times 3N/2$ reconstruction matrix, $R = W^T$ using transformation matrix given in equation (1).
- 3) Reconstruction of the input matrix by multiplying the reconstruction matrix by

the input matrix by the transpose of the reconstruction matrix.

$$X=R \cdot Y_o \cdot R^T \quad (3)$$

At a given level in the iterated filter bank, this separable extension produces nine 2D subbands. These subbands are illustrated in figure (1). Since L is a low-pass filter ($h_0(n)$) while both H1 and H2 are high-pass filters ($h_1(n)$ and $h_2(n)$), the H2H2, H1H2, H2H1, H1H1 subbands each have a frequency-domain support comparable to that of the HH subband in a DWT. A similar scheme creates the H1L, H2L LH1, and LH2 subbands the same frequency-domain support as the corresponding HL (LH) subbands of the DWT, but with twice as many coefficients. Finally, note that there is only one subbands LL with the same frequency-domain as the LL subbands in a DWT.

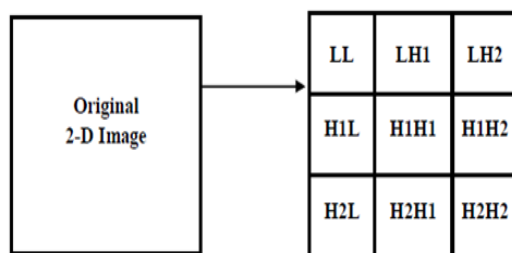


Figure (1) Image subbands after a single-level Decomposition of Framelet

3. IHS Color Conversion

The IHS conversion can effectively separate a RGB (Red, Green, Blue) color image into IHS (Intensity, Hue, and Saturation). Intensity (I) refers the total brightness that corresponds to the surface roughness, hue (H) the wavelength contribution and saturation (S) is its purity[9].The Intensity-Hue-Saturation (IHS) transformation decouples the intensity information from the color carrying information. The hue attribute describes a pure color and saturation gives the degree to which pure color is diluted by white light. This transformation permits the separation of spatial information into one single intensity band. The changes in the intensity values are not distributed evenly in all the three R, G,

and B components when the inverse transform is performed [10]. In fusion, the IHS transformation is used to convert three bands of an MS image from the RGB color space to the IHS color space. The I component is related to the spatial frequencies and is highly correlated with the PAN image. However, PAN has higher spatial frequencies than the MS images. These high frequencies represent the finer details present in the PAN image. Therefore, replacing the I component with the PAN image and transforming back to the RGB color space will introduce high frequencies from PAN into the MS image [11].

4. Proposed Model for SAR Image Fusion

The proposed system for SAR image fusion based Framlet transform is show in Figure(2). The main procedure of the system is described as follow:

Step (1): Conversion of multispectral (RGB) image to IHS space

In this step the MS image will be converted from the RGB model to the IHS model.

Step (2): Computation of two dimensions Framelet transform

In this step, the two dimensional Framelet should be applied to the pan image and I components

Step (3): Fusion rule

The most used of SAR image fusion rule using wavelet transform is maximum selection, compare the two coefficients of wavelet of the two images and select the maximum one, but this rule lead to a color distortion. All the high frequency bands (LH, HL, HH) contain transform values that fluctuate around zero. While the lowpass subband is an approximation of the input image, the three detail subbands convey information about the detail parts in horizontal, vertical and diagonal directions. Different merging procedures will be applied to approximation and detail subbands. Lowpass subband will be merged using simple averaging operations since they both

contain approximations of the source images. In this paper the selection rule (equation (4)) used for the detail subbands rule is:

$$\text{Fused image} = K * \min(\text{image1}, \text{image2}) + K1 * \max(\text{image1}, \text{image2}) \quad (4)$$

Where K vary from zero to 0.5 and K1=1-K

Step (4): Inverse fast discrete Framelet transforms

After selected the fused low frequency and high frequency bands, fused coefficient is reconstructed using the Inverse Framelet transform to get the fused image which represent the new I band .

Step (5): Inverse (IHS) to (RGB) image

The resultant image which represents the new I band will be back transformed with the original H & S bands to the RGB model. Then these three bands represent the new MS image.

5. Evaluation Criteria

Assessing image fusion performance in a real application is a complicated issue. In particular, objective quality measures of image fusion have not received much attention. Some techniques to blindly estimate image quality are proposed in our research. Such quality measures can be used to guide the fusion and improve the fusion performance.

- The Combination Entropy:

The combination entropy (C.E.) of an image is defined as equation (5):

$$C.E = -\sum_n p_n \log_2(p_n), \text{bit / pixel} \quad (5)$$

Where p is the combination probability of the image. The combination entropy represents the

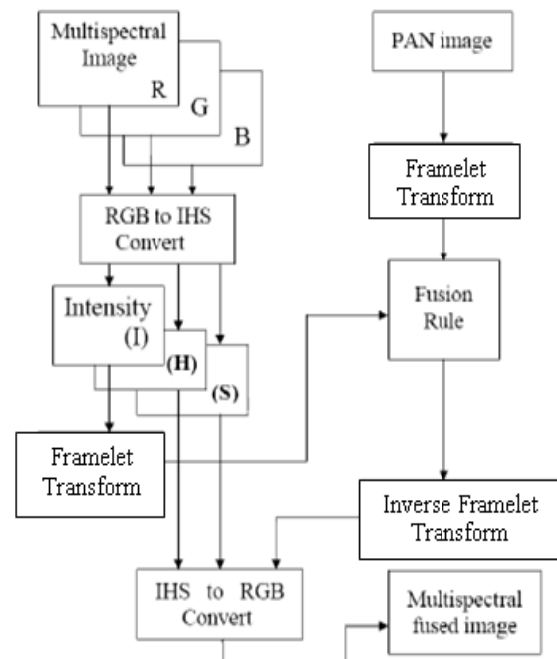


Figure 2: Block Diagram of the Proposed Model

property of combination between images. The larger the combination entropy of an image, the richer the information contained in the image.

- Correlation Coefficient:

The closeness between two images can be quantified in terms of the correlation function. The correlation coefficient ranges from -1 to $+1$. A correlation coefficient value of $+1$ indicates that the two images are highly correlated, i.e., very close to one another. A correlation coefficient of -1 indicates that the two images are exactly opposite to each other. The correlation coefficient is computed from

$$\text{Corr}(I, F) = \frac{\sum_{r=1}^N \sum_{c=1}^N (I(r,c) - \bar{I})(F(r,c) - \bar{F})}{\sqrt{\left(\sum_{r=1}^N \sum_{c=1}^N (I(r,c) - \bar{I})^2 \right) \left(\sum_{r=1}^N \sum_{c=1}^N (F(r,c) - \bar{F})^2 \right)}} \quad (6)$$

Where I is the ideal image, F is the fused image, \bar{I} and \bar{F} stand for the mean values of

the corresponding data set, and $N \times N$ is the image size. Here I and F are the two images which the correlation is computed between them. The correlation between each band of the multispectral image before and after sharpening was computed. The best spectral information is available in the multispectral image and hence the pansharpened image bands should have a correlation closer to that between the multispectral image bands. The spectral quality of the sharpened image is good if the correlation values are closer to each other. Another set of correlation coefficients was computed between each band of the multispectral image and the panchromatic image. Since the panchromatic image has better spatial information, the correlation between the sharpened image bands and the pan image is expected to increase compared to that of the original multispectral. An increase in the correlation indicates an increase in the spatial information compared to the multispectral image.

- The Peak Signal to Noise Ratio:

The Peak SNR (PSNR) is defined as equation (7):

$$SNR_{\text{PEAK}} = 10 \log \left(\frac{(255)^2}{\frac{1}{N^2} \sum_{r=1}^N \sum_{c=1}^N [I(r,c) - F(r,c)]^2} \right) \quad (7)$$

Where I is the ideal image, F is the fused image, and $N \times N$ is the image size. In this measure a larger number implies a better result.

6. Simulation and Result

The SAR Panchromatic and multispectral images are shown in figures 3(a,b), 4(a,b), 5(a,b) and 6(a,b). The proposed model is applied to these data set to produce the fused multispectral images in figures 3(c), 4(c), 5(c) and 6(c), a good fusion approach should retain the maximum

information from the original images and should not damage the internal relationship among the original bands. From the fused images, they should be noted that both the spatial and the spectral resolutions have been enhanced, in comparison to the original images. The spectral information in the original panchromatic images has been increased and the structural information in the original multispectral images has also been enriched. Hence, the fused image contains both the structural details of the higher spatial resolution panchromatic image and the rich spectral information from the multispectral images. Different fusion methods applied to this data set to produce the fused multispectral images, the combination entropy, correlation coefficient and PSNR were computed as shown in tables (1) and (2). The correlation coefficient and PSNR values are computed between the fused image bands with their corresponding MS image bands, and also computed between the fused image bands with the original panchromatic image. In tables 1 and 2, the combination entropy of the Framlet based image fusion is greater than that of other methods. The PSNR values between the fused image bands with their corresponding MS image bands (in table 1) indicate that the pixel values are less distorted in the proposed method compared to the IHS, PCA and DWT methods. The correlation coefficient values between each new image band with its original MS band (in table 1) indicate that the proposed fusion method produce the best correlation result. The PSNR values between the fused images bands with the original PAN image (in table 2) indicate that the pixel values are less distorted in the proposed method compared to HIS, PCA and DWT methods. The correlation coefficient values between each new image band with the original panchromatic image (in table 2) indicate that the proposed fused method produces the closest correlation with the panchromatic bands compared to PCA and DWT methods.

Thus, the Framlet based image fusion method is superior to the IHS, PCA and DWT methods in terms of combination entropy, PSNR and correlation coefficient and the Framlet based image fusion method is very efficient for fusing SAR images.

7. Conclusion

This paper presented a newly developed method based on the Framelet transform for fusing SAR images. The experimental study was conducted by applying the proposed method and compared with other image fusion methods, namely IHS, PCA and wavelet transform methods. Three performance measure definitions combination entropy, correlation coefficient and PSNR have been introduced. Experimental results indicate that the proposed method preserves the image contrast and obtains better region similarity than other method. The Framlet technique is found to give an output which is better and it also preserves the spectral content of data in a better fashion. This is evidenced by the highest combination entropy, correlation coefficient and PSNR for the image fused with Framlet technique. Also increasing the value of k make the fused image is produced better quality but to value (0.5).

References

- [1] Wang Q., Shen Y., May 2004, "The effects of fusion structures on image fusion performances" IMTC 04. Proc. 21st IEEE, Vol. 1, pp. 468-471.
- [2] Choi M., Kim R. Y., Nam M., and Kim H. O., April 2005, "Fusion of Multispectral and Panchromatic Satellite Images Using the Curvelet Transform", IEEE Trans. Geosciences and Remote Sensing, Vol. 2, No. 2, pp. 136-140.
- [3] Shkla P.D., October 2003, "Complex Wavelet Transform and Their Applications", Ph.D. Thesis, A Dissertation Submitted of Signal Processing Division Department of Electronic and Electrical Engineering, University of Strathclyde Scotland United Kingdom.
- [4] K.Sukumar, T.Hemalatha, K.P.Soman, 2009, "Multi Image-Watermarking scheme based on Framelet and SVD", IEEE, International Conference on Advances in Recent Technologies in Communication and Computing, pp 379-383
- [5] Abd M. K., 2009, "Electricity Load Forecasting based on Framelet Neural Network Technique", American Journal of Applied Sciences, Vol 6, Issue5, pp 970-973
- [6] Sabri A. A., Abdul_Qader T. T., 2010, "New Proposed Algorithm To Conceals Error In Wireless Image Transmission Based on Framelet Transform", Eng. and Tech. Journal, Vol.28, No.4, pp. 664-675.
- [7] Abdulmunim M. E., May 2005 "Color Image Denoising Using Discrete Multiwavelet Transform", Ph.D Thesis, University of Technology, Department of Computer Science, Baghdad.
- [8] Umbaugh S. E., 1998 "Computer Vision and Image Processing: A Practical Approach Using CVIP Tools", Prentice Hall PTR.
- [9] Zhang N., Zhong S., 2008, "Adjustable Transforms of IHS and PCA for QuickBird Panchromatic and Multispectral Images", CISP '08. Congress on Image and Signal Processing, Vol 3, pp. 471-474
- [10] Meenakshisundaram V., 2005, "Quality Assessment of Ikonos and Quickbird Fused Images for Urban Mapping" Department of Geometrics Engineering, University of Galary.
- [11] Zhenhua Li, Leung H., May 2009, "Fusion of Multispectral and Panchromatic Images Using a Restoration-Based Method" IEEE Transaction on Geoscience and Remote Sensing, Vol. 47, No 5, pp. 1482-1491.

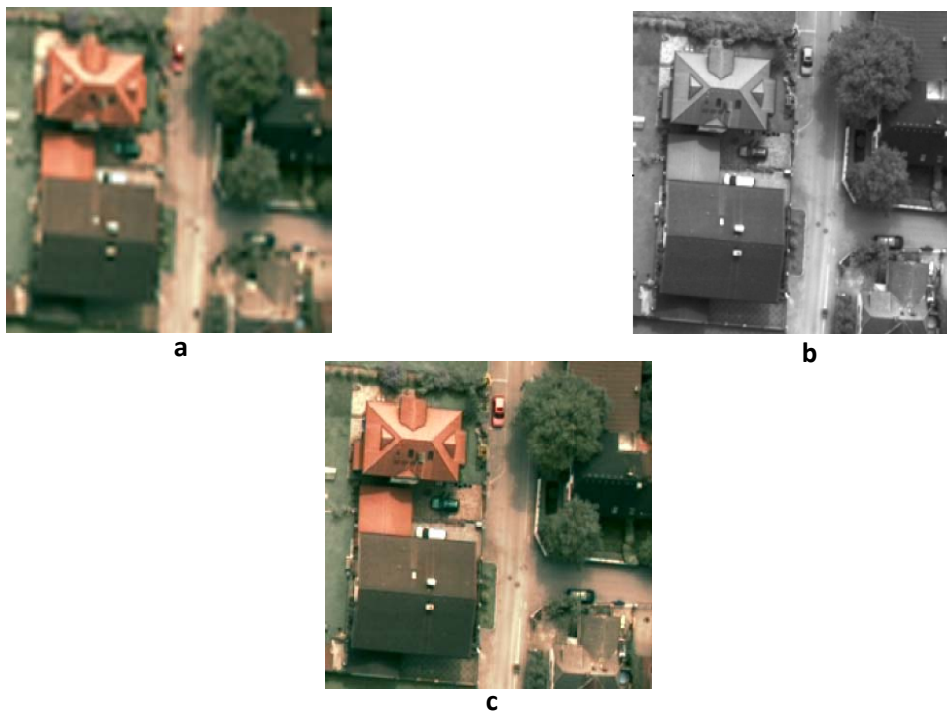


Figure 3. The original SAR images 1 and fused image: (a) the original MS image; (b) the original PAN image; (c) the fused image using our proposed new fusion method.

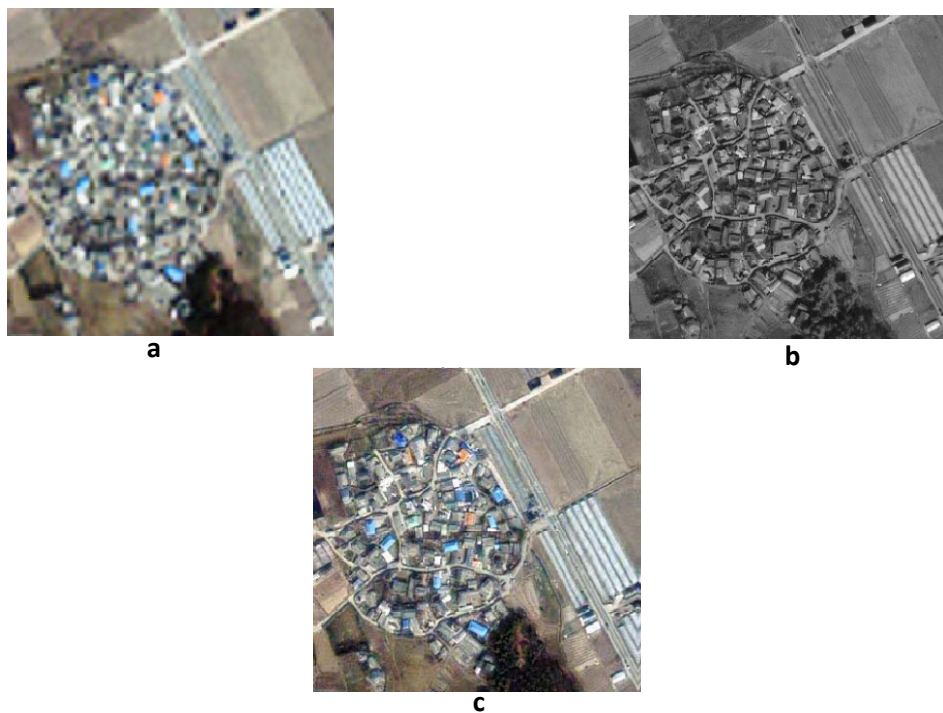


Figure 4. The original SAR images 2 and fused images: (a) the original MS image; (b) the original PAN image; (c) the fused image using our proposed new fusion method.

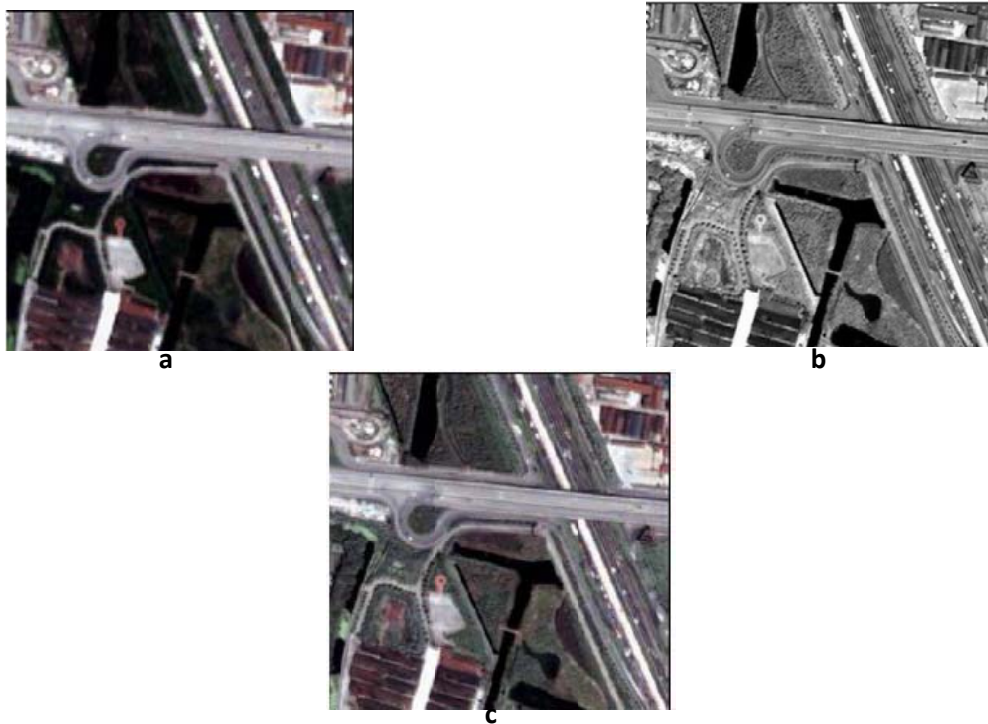


Figure 5.The original SAR images 3 and fused images: (a) the original MS image; (b) the original PAN image; (c) the fused image using our proposed new fusion method.

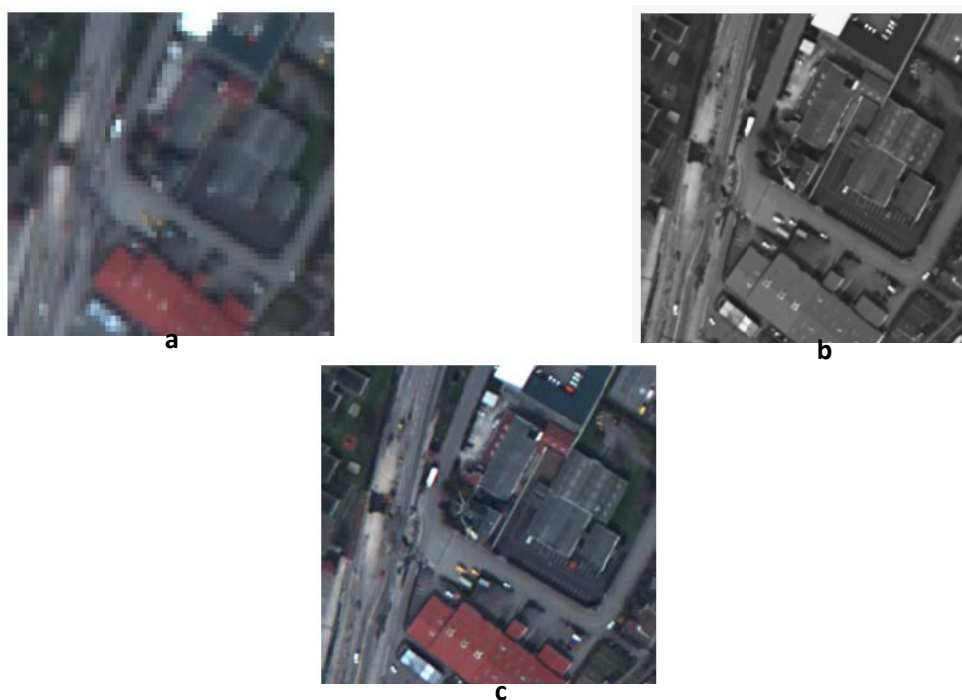


Figure 6.The original SAR images 4 and fused images: (a) the original MS image; (b) the original PAN image; (c) the fused image using our proposed new fusion method.

Table 1
 The (Combination Entropy, Correlation Coefficient, PSNR) values between the fused image bands with their corresponding MS image bands computed for the different fusion methods.

SAR Image	Method	Combination Entropy of fused image	Correlation Coefficient Between each new fused image bands with their corresponding original MS bands			PSNR values Between each new fused image bands with their corresponding original MS bands		
			R & new R	G & new G	B & new B	R & new R	G & new G	B & new B
1	IHS	4.1380	0.8539	0.8098	0.7869	65.7045	66.8819	68.1162
	PCA	5.0952	0.9682	0.9537	0.9440	71.5586	72.6991	73.9199
	Wavelet	5.3693	0.9680	0.9538	0.9446	71.5323	72.7053	73.9614
	Framelet with k= 0.1	5.4727	0.9695	0.9554	0.9460	71.6748	72.8400	74.0687
	Framelet with k= 0.3	5.6584	0.9776	0.9669	0.9596	72.8559	74.0332	75.2676
2	IHS	3.8322	0.7678	0.7593	0.7499	63.0350	62.9486	62.9509
	PCA	5.0327	0.9483	0.9466	0.9455	68.9987	68.9122	68.9151
	Wavelet	5.2241	0.9409	0.9390	0.9377	68.7866	68.7012	68.7024
	Framelet with K= 0.1	5.3487	0.9498	0.9482	0.9470	69.0445	68.9579	68.9605
	Framelet with K= 0.3	5.5741	0.9626	0.9615	0.9607	70.1757	70.0894	70.0917

Table 1 (continued)

SAR Image	Method	Combination Entropy of fused image	Correlation Coefficient Between each new fused image bands with their corresponding original MS bands			PSNR values Between each new fused image bands with their corresponding original MS bands		
			R & new R	G & new G	B & new B	R & new R	G & new G	B & new B
3	IHS	4.3220	0.7784	0.7531	0.7428	68.5982	68.3389	67.7877
	PCA	5.0988	0.9325	0.9204	0.9149	74.0433	73.7840	73.2328
	Wavelet	5.4276	0.9382	0.9270	0.9217	74.4658	74.2010	73.6438
	Framelet with K= 0.1	5.5205	0.9403	0.9294	0.9243	74.5827	74.3235	73.7700
	Framelet with K= 0.3	5.6718	0.9466	0.9368	0.9305	74.8916	74.5694	73.9063
4	IHS	4.3706	0.6552	0.6211	0.5934	61.0722	60.6863	60.3297
	PCA	5.4015	0.9272	0.9150	0.9148	66.9713	66.5970	66.2412
	Wavelet	5.4607	0.8982	0.8895	0.8861	65.9650	65.7809	65.4116
	Framelet with K= 0.1	5.5522	0.9297	0.9174	0.9175	67.0637	66.6798	66.3240
	Framelet with K= 0.3	5.6532	0.9614	0.9542	0.9551	69.2783	68.8923	68.5357

Table 2
The (Combination Entropy, Correlation Coefficient, PSNR) values between the fused image bands with the original PAN image computed for the different fusion methods.

SAR Image	Method	Combination Entropy of fused image	Correlation Coefficient Between each new fused image bands with the original PAN image			PSNR values Between each new fused image bands with the original PAN image		
			PAN & new R	PAN & new G	PAN & new B	PAN & new R	PAN & new G	PAN & new B
1	IHS	4.1380	0.9743	0.9395	0.8411	77.4286	69.9783	65.0104
	PCA	5.0952	0.9322	0.9337	0.8720	69.9618	69.9599	65.3941
	Wavelet	5.3693	0.9370	0.9323	0.8660	70.3752	69.8651	65.3112
	Framelet with K= 0.1	5.4727	0.9425	0.9387	0.8730	70.7405	70.1693	65.4070
	Framelet with K= 0.3	5.6584	0.9432	0.9401	0.8744	70.8105	70.2266	65.4199
2	IHS	3.8322	0.9790	0.9803	0.9735	77.6569	78.6696	76.0071
	PCA	5.0327	0.8918	0.8998	0.8697	68.1559	68.3407	68.2718
	Wavelet	5.2241	0.8989	0.9072	0.8787	68.8060	69.0364	68.9048
	Framelet with K= 0.1	5.3487	0.9054	0.9140	0.8853	69.0110	69.2571	69.1157
	Framelet with K= 0.3	5.5741	0.9074	0.9161	0.8874	69.0696	69.3192	69.1766

Table 2 (continued)

SAR Image	Method	Combination Entropy of fused image	Correlation Coefficient Between each new fused image bands with the original PAN image			PSNR values Between each new fused image bands with the original PAN image		
			PAN & new R	PAN & new G	PAN & new B	PAN & new R	PAN & new G	PAN & new B
3	IHS	4.3220	0.9758	0.9547	0.9640	74.1657	73.4453	76.5087
	PCA	5.0988	0.9056	0.8944	0.9108	72.4548	72.1576	72.9855
	Wavelet	5.4276	0.8654	0.8521	0.8696	71.1788	70.9232	71.4399
	Framelet with K= 0.1	5.5205	0.8936	0.8819	0.8983	72.0808	71.7902	72.4319
	Framelet with K= 0.3	5.6718	0.8957	0.8845	0.9012	72.1531	71.8718	72.5397
4	IHS	4.3706	0.9189	0.9420	0.9616	68.4169	68.8201	71.6017
	PCA	5.4015	0.7030	0.7493	0.7368	62.3167	62.5541	62.8651
	Wavelet	5.4607	0.7547	0.8015	0.7948	63.2924	63.6017	64.0866
	Framelet with K= 0.1	5.5522	0.7570	0.8038	0.7975	63.3337	63.6439	64.1391
	Framelet with K= 0.3	5.6532	0.7668	0.8119	0.8062	63.3843	63.6898	64.1980

LOW DENSITY PARITY CHECK (LDPC) CODES FOR PROPOSED SLANTLET TRANSFORM OFDM SYSTEM IN A RAYLEIGH FADING CHANNELS WITH PERFECT AND PILOT CHANNEL ESTIMATION FOR M-ARY PSK MODULATION

Ghanim Abd Al-Kareem Mugheer

Electrical Engineering Department

College of Engineering, Al-Mustansiriya University.

gha2014nim@yahoo.com

Abstract

Orthogonal Frequency Division Multiplexing (OFDM) is a very attractive technique for high bit rate data transmission in a multipath fading environment that causes intersymbol interference (ISI). In this paper, two steps is used to improve the error rate performance of OFDM system: first, we proposed the Slantlet Transform (SLT) is used instead of Fast Fourier Transform (FFT) to obtain high orthogonality properties between subcarriers and hence reduce (ISI); And second: we proposed the Low Density Parity Check (LDPC) Codes for proposed SLT-OFDM system to improve the system error rate performance and reduced energy needed to transmit data on fading channel. LDPC codes can be decoded by using a probability propagation algorithm known sum product algorithm.

In mobile communications the high bandwidth efficiency is required, and thus the multilevel modulation is preferred. In this paper, Bit Error Rate (BER) and Packet Error Rate (PER) are evaluated for the proposed LDPC-based SLT-OFDM systems with BPSK and 16PSK modulation in a two typical channels, AWGN channel and Rayleigh fading channels with a pilot-aided data compensation and perfect compensation to compensate phase error due to the fading channels with comparison the results with the traditional OFDM system which is used FFT. The goal of the proposed SLT method is to decrease the complexity of the system and

that leads to reduce the number of computations (complex addition and multiplication) and hence increase the speed of the system additional to obtain high orthogonality between subcarriers. Hence, the proposed LDPC-based SLT-OFDM system is a promising solution to high efficient data transmission over fading mobile wireless channels.

The proposed system has been tested and validated using MATLAB 7 package.

Keywords: *Low-Density Parity-Check (LDPC) Codes, Orthogonal Frequency Division Multiplexing (OFDM), Slantlet Transform (SLT), Rayleigh Fading Channels, Channel Estimation*

1-Introduction

The basic principle of OFDM is to split a high rate data stream into a number of lower rate streams that are transmitted simultaneously over a number of subcarriers. Because the lower rate parallel subcarriers increases the symbol duration so the relative amount of dispersion in time caused by multi-path delay spread is decreased. Inter symbol interference (ISI) is eliminated almost completely by introducing a guard time in every OFDM symbol. The guard time is chosen larger than the expected delay spread such that the multipath components form one symbol cannot interfere with the next symbol. However, the problem of Inter Carrier Interference ICI

would arise. ICI is a crosstalk between different sub carriers, which means that they are no longer orthogonal (orthogonality is lost).

Hence, to eliminate ICI, the OFDM symbol is cyclically extended in the guard time, which is done by taking symbol period samples from the end of OFDM symbol and appending them to the start of OFDM symbol. This ensures that the OFDM symbol always has integer number of cycles within the FFT interval, as long as the delay is smaller than the guard time. As a result, the multipath signals with delays smaller than the guard time cannot cause ICI. In this case, the total length of the symbol is^[1-5].

$$T_f = T_G + T_{FFT} \quad \dots(1)$$

Where T_f is the total length of the symbol in samples, T_G is the length of the guard period in samples, and T_{FFT} is the size of the IFFT used to generate the OFDM signal and usually T_G is smaller than $(\text{symbol time} / 4)$ ^[1-5].

2-Channel Estimation

In this paper, the method used to compensate phase error due to fading is a pilot symbol –aided OFDM modulation scheme which is the most sensible for channel estimation especially when the channel is time variant. In this method, pilot symbols are inserted at the transmitter at fixed time intervals and at the receiver, the channel characteristics are estimated by using the pilot symbol because the level of fluctuation is independent in each sub carrier channel. The pilot carried in all frequency domains can be inserted at a known time period. Then, by using the estimated channel characteristics, the transmitted data can be recovered. The pilot data are inserted only in the in phase channel. The relation between the transmitted pilot data (ice_0 , qce_0) and the received pilot data (ice_1 , qce_1) is given By^[6].

$$\begin{pmatrix} ice_1 \\ qce_1 \end{pmatrix} = A \begin{pmatrix} ice_0 \\ qce_0 \end{pmatrix} \quad \dots(2)$$

Where A is the transition matrix of the fading environment

$$A = \begin{pmatrix} iv & -qv \\ qv & iv \end{pmatrix} \quad \dots(3)$$

To compensate the phase error all the received data are multiplied by the complex conjugate of A

$$A^{-1} = \frac{1}{\sqrt{iv^2 + qv^2}} \begin{pmatrix} iv & qv \\ -qv & iv \end{pmatrix} \quad \dots(4)$$

The values of iv and qv are given by

$$iv = \frac{1}{\sqrt{ice_1 + qce_1}} (ice_0 * ice_1 + qce_0 * qce_1) \quad \dots(5)$$

$$qv = \frac{1}{\sqrt{ice_1 + qce_1}} (qce_0 * ice_1 - ice_0 * qce_1) \quad \dots(6)$$

3- Slantlet Transform (SLT)

The Slantlet Transform (SLT) is an orthogonal Discrete Wavelet Transform (DWT) with two zero moments, improved time localization, and is based on designing different filters that are not product for each scale instead of using filter bank iteration. In general, the algorithm to obtain the L-scale Slantlet filter banks is, as follows^[5,7]:

1- The L -scale Slantlet has 2L filterbanks. The first filterbank is called the low pass filter (LPF), and its transfer function is $h_L(n)$. The adjacent to the LPF filterbank has transfer function $f_L(n)$. Both $h_L(n)$ and $f_L(n)$ are to be followed by down sampling of 2L.

2- The remaining 2L -2 filterbanks, there transfer functions are $g_i(n)$ and its shifted time reverse $g_i((2i+1-1)-n)$ for $i = L - 1, L - 2, \dots, 1$. Each $g_i(n)$ and its shifted time reverse are to be followed by down sampling of $2i+1$ for each value i .

The Slantlet filter bank appears each $g_i(n)$ with its time reverse $g_i((2i+1-1)-n)$, while $h_L(n)$ does not appear with its time reverse, It always appears paired with the filter $f_L(n)$. The transfer functions $h_L(n)$, $f_L(n)$ and $g_i(n)$ for L-scale Slantlet are calculated using the following expressions^[7] and the parameters is shown in Tables (1) and (2) respectively.

$$h_i(n) = \begin{cases} b_{0,0} + b_{0,1}n & \text{for } n=0, \dots, 2^i - 1 \\ b_{1,0} + b_{1,1}(n-2^i) & \text{for } n=2^i, \dots, 2^{i+1} - 1 \end{cases} \dots(7)$$

$$f_i(n) = \begin{cases} c_{0,0} + c_{0,1}n & \text{for } n=0, \dots, 2^i - 1 \\ c_{1,0} + c_{1,1}(n-2^i) & \text{for } n=2^i, \dots, 2^{i+1} - 1 \end{cases} \dots(8)$$

$$g_i(n) = \begin{cases} a_{0,0} + a_{0,1}n & \text{for } n=0, \dots, 2^i - 1 \\ a_{1,0} + a_{1,1}(n-2^i) & \text{for } n=2^i, \dots, 2^{i+1} - 1 \end{cases} \dots(9)$$

Table 1: $h_L(n)$ and $f_L(n)$ parameters

$$\begin{aligned} m &= 2^i \\ u &= 1 / \sqrt{m} \\ v &= \sqrt{(2m^2 + 1) / 3} \\ b_{0,0} &= u(v + 1) / (2m) \\ b_{1,0} &= u - b_{0,0} \\ b_{0,1} &= u / m \\ b_{1,1} &= -b_{0,1} \\ q &= \sqrt{3} / (m(m^2 - 1)) / m \\ c_{0,1} &= q(v - m) \\ c_{1,1} &= -q(v + m) \\ c_{1,0} &= c_{1,1}(v + 1 - 2m) / 2 \\ c_{0,0} &= c_{0,1}(v + 1) / 2 \end{aligned}$$

Table 2: $g_i(n)$ parameters

$$\begin{aligned} m &= 2^i \\ s_1 &= 6\sqrt{m} / ((m^2 - 1)(4m^2 - 1)) \\ t_1 &= 2\sqrt{3} / (m(m^2 - 1)) \\ s_0 &= -s_1(m - 1) / 2 \\ t_0 &= ((m + 1)s_1 / 3 - mt_1)(m - 1) / (2m) \\ a_{0,0} &= (s_0 + t_0) / 2 \\ a_{1,0} &= (s_0 - t_0) / 2 \\ a_{0,1} &= (s_1 + t_1) / 2 \\ a_{1,1} &= (s_1 - t_1) / 2 \end{aligned}$$

4-Proposed Slantlet Transform for OFDM system

Many researchers appeared recently to improve the performance of OFDM system, the way is done by replacing the FFT transform by any other transforms such as Discrete Wavelet Transform (DWT) and Discrete Multiwavelet Transform (DMWT). In this paper, first the Slantlet Transform (SLT) is proposed to use instead of Fast Fourier Transform (FFT) in the OFDM modulator and demodulator to obtain better performance for OFDM system. The filters in the SLT depends on the wavelet function namely Daubechies basis functions where these functions are simple in design with respect to sine and cosine functions of FFT and IFFT. The SLT is better than DWT because the length of the filters will be reduced, and that leads to reduce the number of computations which lead to increase the speed of operations in the system^[7].

Figure (1) shows the block diagram of the proposed SLT-OFDM system. In the transmitter, the Inverse Slantlet Transform (ISLT) is used instead of Inverse Fast Fourier Transform (IFFT) to modulate a block of input modulated values onto a number of sub-carriers and in the receiver; the sub-carriers are modulated by a Slantlet Transform (SLT) instead of Fast Fourier Transform (FFT), which perform a reverse operation of an ISLT.

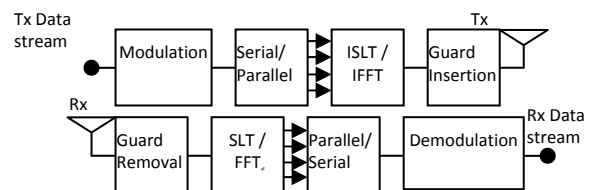


Figure (1) Proposed SLT-OFDM system (transmitter & receiver)

In the future. The high-bit rate transmission is required for high quality mobile communication systems. Orthogonal Frequency Division Multiplexing (OFDM), is a very attractive technique for the high-bit-rate data transmission in a multipath environment that causes intersymbol

interference (ISI). The ISI in OFDM can be eliminated by adding a guard interval. In a multipath environment, some subcarriers of OFDM may be completely lost because of the deep fades. Hence, even though most subcarriers may be detected without errors, the overall bit error rate (BER) will be largely dominated by a few subcarriers with small amplitudes. To avoid this domination by the weakest subcarriers, forward-error correction coding is essential. Many error correcting codes have been applied to OFDM, Convolutional codes, Reed Solomon code and Turbo code [8]. In this paper, Low Density Parity Check (LDPC) Code is proposed for the proposed SLT-OFDM system.

5-Low Density Parity Check (LDPC) Code

LDPC codes and their iterative decoding algorithm were proposed by Gallager in 1962 have been excellent properties. The, LDPC codes are now recognized as good error correcting codes achieving near Shannon limit performance [9]. The name of the LDPC codes comes from the characteristic of their parity-check matrix which contains only a few 1's in comparison to the amount of 0's [10].

LDPC codes are defined as codes use a sparse parity-check matrix with the number of 1's per column (column weight) and the number of 1's per row (row weight), both of which are very small compared to the block length. LDPC codes are classified into two groups, regular and irregular LDPC codes. Regular LDPC codes have a uniform column weight and row weight, and irregular LDPC codes have a nonuniform column weight. (N,K) LDPC code is defined by M x N parity-check matrix H, where K = N - M and the code rate is R = K/N. If the H doesn't have full rank, K > N - M the error performance of an LDPC code becomes worse. Thus, when we construct the parity-check matrix H, we will ensure that all the rows of the matrix are linearly independent [8,9,11].

LDPC codes can be represented by a Factor Graph or Tanner Graph that contains two types of nodes: the "bit nodes" and the "check nodes". Figure 2(a) shows an example of the Factor Graph. Each bit node corresponds to a column of a parity-check matrix, which also corresponds to a bit in the codeword. Each check node corresponds to a row of a parity-check matrix, which represents a parity-check equation. An edge between a bit node and a check node exists if and only if the bit participates in the parity-check equation represented by the check node [8,9,11]. LDPC codes can be decoded by using a probability propagation algorithm known as the sum product or belief propagation algorithm, which is implemented by using a Factor graph. LDPC codes have

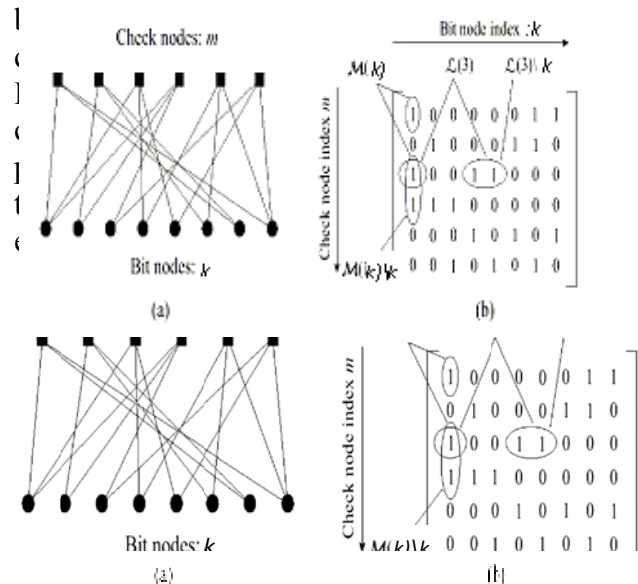


Figure 2 (a) Factor graph and (b) notation of the sum-product algorithm

5-1- Sum Product Algorithm

The notations of the sum-product algorithm are described in Figure 2 (b). M(k) denotes the set of check nodes that are connected to the bit node k, i.e., positions of "1"s in the kth column of the parity-check matrix. L(m) denotes the set of bits that participates in the mth parity-check equation, i.e., the positions of "1"s in the mth row of the parity-check matrix. $q_{k \rightarrow m}^0$ and $q_{k \rightarrow m}^1$ denote the probability information that the bit

node k sends to the check node m , indicating $P(x_k=0)$ and $P(x_k=1)$ respectively. $r_{m \rightarrow k}^0$ and $r_{m \rightarrow k}^1$ denote the probability information that the m^{th} check node gathers for the l^{th} bit being 0 and 1, respectively. The posteriori probability for a bit is calculated by gathering all the extrinsic information from the check nodes that connect to it, which can be obtained by the following iterative belief propagation procedure [11,13].

For binary codes, the sum-product algorithm can be performed more efficiently in Log domain, where the probabilities are equivalently characterized by the log-likelihood ratios (LLRs):

$$\begin{aligned} L(r_{m \rightarrow k}) &\equiv \log(r_{m \rightarrow k}^1 / r_{m \rightarrow k}^0), L(q_{m \rightarrow k}) \equiv \\ \log(q_{m \rightarrow k}^1 / q_{m \rightarrow k}^0), L(p_k) &\equiv \log(p_k^1 / p_k^0), \\ L(q_k) &\equiv \log(q_k^1 / q_k^0) \quad \dots(10) \end{aligned}$$

Initialization

Each bit node k is assigned an a priori LLR $L(p_k)$. In the case of equiprobable inputs on a memoryless AWGN channel with BPSK,

$$L(p_k) = \log \frac{P(y_k | x_k \approx +1)}{P(y_k | x_k \approx -1)} = \frac{2}{\sigma^2} y_k \quad \dots(11)$$

where x, y represent the transmitted bit and received bit, respectively, and σ^2 is the noise variance. For every position (m, k) such that $H_{mk} = 1$, where H_{mk} represents the element of the m^{th} row and the k^{th} column in the parity-check matrix H , $L(q_{k \rightarrow m})$ and $L(r_{m \rightarrow k})$ are initialized as:

$$L(q_{k \rightarrow m}) = L(p_k) \text{ and } L(r_{m \rightarrow k}) = 0 \quad \dots(12)$$

1-Checks to Bits

Each check node m gathers all the incoming information $L(q_{k \rightarrow m})$'s, and updates the belief on the bit k based on the information from all other bits connected to the check node m .

$$L(r_{m \rightarrow k}) = 2 \tanh^{-1} \left(\prod_{k' \in L(m) \setminus k} \tanh(L(q_{k' \rightarrow m}) / 2) \right) \dots(13)$$

2-Bits to Checks

Each bit node k propagates its probability to all the check nodes that connect to it.

$$L(q_{k \rightarrow m}) = L(p_k) + \sum_{m' \in M(k) \setminus m} L(r_{m' \rightarrow k}) \quad \dots(14)$$

3-Check Stop Criterion

The decoder obtains the total a posteriori probability for the bit l by summing the information from all the check nodes that connect to the bit l .

$$L(q_l) = L(p_l) + \sum_{m \in M(l)} L(r_{m \rightarrow l}) \quad \dots(15)$$

Hard decision is made on the $L(q_k)$, and the resulting decoded input \hat{x} is checked against the parity-check matrix H . If $H\hat{x} = 0$, the decoder stops and outputs \hat{x} . Otherwise, it repeats the steps (1-3). The sum-product algorithm sets the maximum number of iterations. If the number of iterations reaches the maximum, the decoder stops and outputs \hat{x} is the result of the hard decision [11,13].

6- System Description of LDPC Coded For the Proposed SLT-OFDM

Orthogonal Frequency Division Multiplexing (OFDM) is a very attractive technique to achieve the high bit rate data transmission required for the future mobile communications. A major drawback of OFDM is its high peak to average power ratio (PAPR). Many researches have been done to reduce the PAPR. In a multipath fading channel, some subcarriers of OFDM may be completely lost because of the deep fades. Hence, even though most subcarriers may be detected without errors, the overall bit error rate (BER) will be largely dominated by a few subcarriers with the smallest amplitudes [11]. To improve the error rate performance of proposed SLT-OFDM; forward error correction coding is essential. Recently, low density parity check (LDPC) codes, which can achieve the near Shannon limit performance, attracted much attention. We proposed the LDPC coded for proposed SLT-OFDM (LDPC-SLT-OFDM) systems to improve the error rate performance of

proposed SLT-OFDM system on a Rayleigh fading channel. In mobile communications the high bandwidth efficiency is required, and thus the multilevel modulation is preferred. LDPC codes have been applied to Mary PSK modulation on additive white Gaussian noise (AWGN) channel and a Rayleigh fading channels.

Figure (3) shows the modified model of the proposed LDPC-SLT-OFDM system. At the transmitter, information bits are encoded at the LDPC encoder and modulated at the Mary PSK modulator. After the serial-to-parallel conversion, the OFDM sub-channel modulation is implemented by using an inverse slantlet transform (ISLT) and assigned to some OFDM symbols for the purpose of compensating two dimensional errors in the OFDM system. On a fading channel the guard interval is inserted for the purpose of eliminating the ISI. At the receiver, the guard interval is removed on a fading channel. After the serial-to-parallel conversion, the OFDM subchannel demodulation is implemented by using a slantlet transform (SLT). The received OFDM symbols generated by the SLT are demodulated at the Mary PSK demodulator. The demodulated bits are decoded with each LDPC encoded block and data bits are restored.

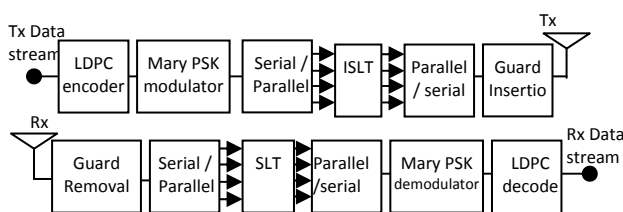


Figure (3) Proposed LDPC-SLT-OFDM system model (transmitter & receiver)

7- Performance by Computer Simulation

7-1 Performance of the Proposed SLT-OFDM System in AWGN Channel

All the implementation concepts have been verified in MATLAB Version 7 and the evaluation of the proposal SLT-OFDM system is presented and compared with traditional FFT-OFDM system with Mary

PSK modulation using the Gray mapping. The measurement for the performance is displayed as Bit Error Rate (BER) and Packet Error Rate (PER) in comparison to signal to noise ratio (SNR) of the AWGN channel or a Rayleigh fading channel. The block diagram of the computer simulation for the proposed SLT-OFDM modulator and demodulator are shown in Figure(1).

The standard parameters used in our simulations which are affecting the performance of the proposal SLT-OFDM system are shown below.

Number of parallel channel = ISLT length = IFFT length = 64

Channel Spacing = 20 MHz which is used for 64 point ISLT or for IFFT

Symbol Rate = $S_r = 312.5$ (ksymbol/sec)= Carrier Spacing (F_c) (=20 MHz/64)

Symbol time = $T_s = 1/S_r = 3.2$ μ sec

Guard time = $T_G = T_s/4 = 800$ nsec

OFDM block length = $T_f = T_G + T_s = 4$ μ sec

Rate in OFDM = $1/T_f = 250$ (ksymbol/sec)

Number of OFDM symbol for one loop = 6

Pilot Symbol = 1 for 6 symbol

Modulation Schemes BPSK and 16PSK

Figure (4) and Figure(5) illustrates the performance of the proposed SLT-based OFDM (SLT-OFDM) and the traditional FFT-based OFDM (FFT-OFDM) systems in AWGN channel compared with theoretical OFDM results for BPSK and 16PSK modulation. It is clearly shown that, the BER decreases when we increase the SNR, which is normal because the signal becomes stronger than the noise. Also we can see from these two figures that the proposed SLT-based OFDM and FFT-based OFDM has almost the same BER and PER performance and close to theory BER results for OFDM system in AWGN channel.

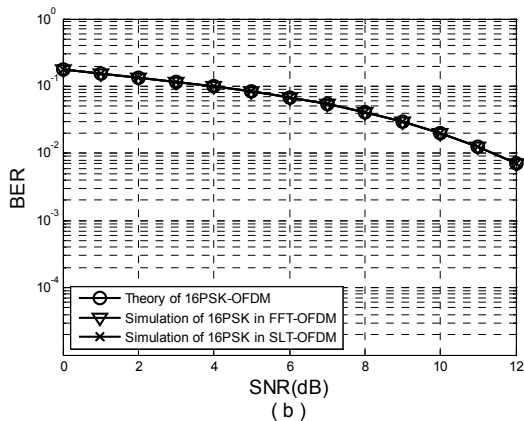
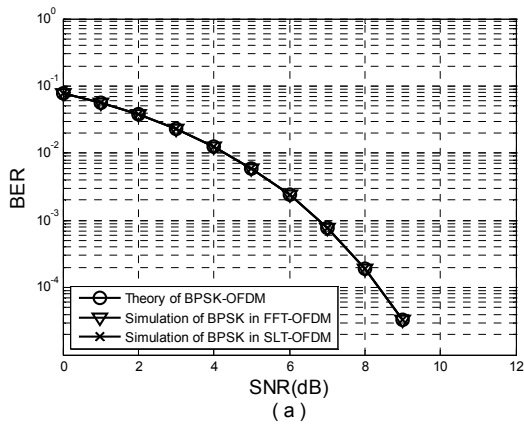


Figure (4) BER performance of the proposed SLT-based OFDM system and the traditional FFT-based OFDM system in AWGN channel compared with theoretical OFDM results for (a) BPSK modulation (b) 16PSK modulation

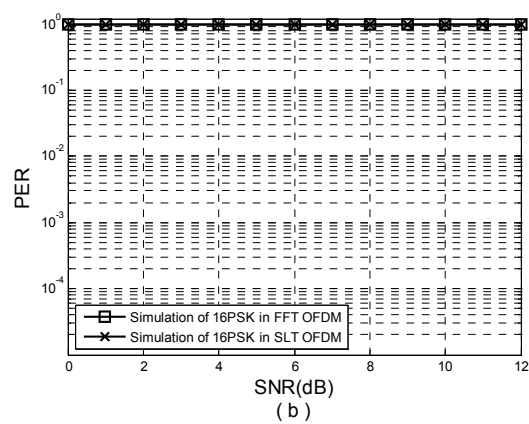
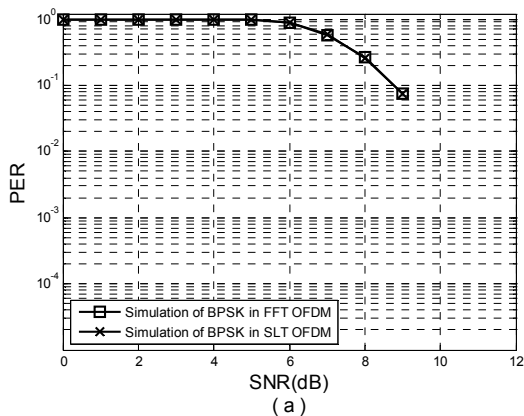


Figure (5) PER performance of the proposed SLT-based OFDM system and the traditional FFT-based OFDM system in AWGN channel for (a) BPSK modulation (b) 16PSK modulation

7-2 Performance Of The Proposed SLT-OFDM System In A Rayleigh Fading Channel With And Without Perfect Compensation

Fading is a more realistic mobile channel where multiple paths are received from the signal that is transmitted through the channel. This phenomenon introduces ISI (inter symbol interference) which is one of the major interference factors for a SLT-OFDM system that significantly degrades the system performance.

Figure (6) and Figure (7) show the BER and PER performance in a Rayleigh fading channel. The fading period is equal to 4 msec when the Doppler frequency shift equal to 250Hz (15 m/s @ 5 GHz). from simulation, if cannot compensate the amplitude and phase fluctuation caused by propagation characteristics, the data cannot be recovered, and both BER ≈ 0.5 and PER between (1 and 0.55) for all the values of SNR for two system BPSK-SLT-OFDM and BPSK-FFT-OFDM while the BER ≈ 0.5 and PER ≈ 1 for all values of SNR for two system 16PSK-SLT-OFDM and 16PSK-FFT-OFDM .

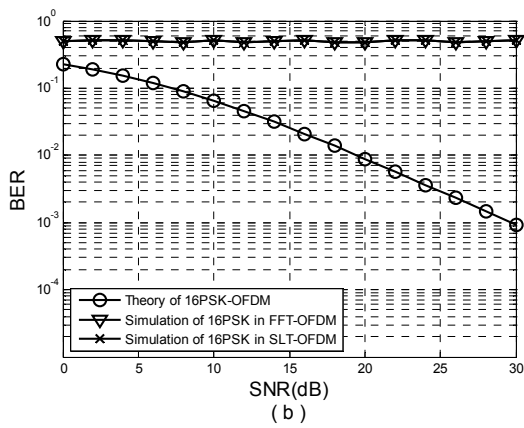
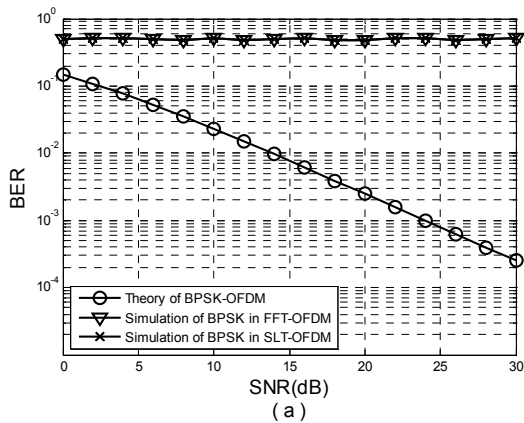


Figure (6) BER performance of the proposed SLT-based OFDM system and the traditional FFT-based OFDM system in a Rayleigh fading channel compared with theoretical OFDM results for (a) BPSK modulation (without compensation) (b) 16PSK modulation (without compensation)

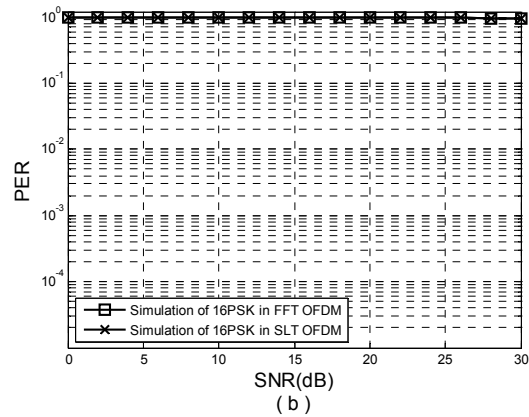
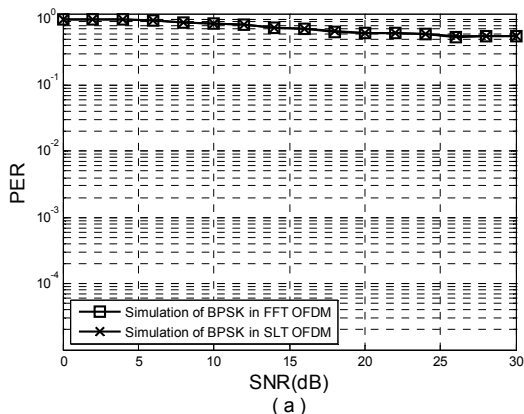


Figure (7) PER performance of the proposed SLT-based OFDM system and the traditional FFT-based OFDM system in a Rayleigh fading channel for (a) BPSK modulation (b) 16PSK modulation

Figure (8) and Figure(9) show the BER and PER performance of the proposed SLT-based OFDM (SLT-OFDM) and the traditional FFT-based OFDM (FFT-OFDM) compared with the theoretical results for the OFDM system in a Rayleigh fading channel which have a Doppler frequency shift equal to 250Hz. To obtain real OFDM simulation we add 11 zeros in the center of data & one zero at the beginning (over sampling present) before fed the modulated data into the 64-point ISLT.^[1,5]

In this simulation, we assume ideal channel estimation is achieved (perfect compensation). The proposed SLT based OFDM is much better BER performance than the FFT based -OFDM, since the filters in the SLT depend on the wavelet functions. This is a reflection of the fact that the orthogonal bases of the Slantlet are more significant than the orthogonal bases used in FFT which are capable to reduce the intersymbol interference (ISI) and intercarrier interference (ICI) which are lead to loss the orthogonality between the carriers as a result of multipath propagation over the wireless fading channels. So that, the results of the proposed SLT-OFDM system operates at its optimum BER performance with traditional FFT-OFDM system.

It is also clear that the BER of the proposed SLT-OFDM system with BPSK modulation is about 2dB better than that of the FFT-OFDM system with BPSK modulation for all values of SNR, moreover. The proposed SLT-OFDM system with 16PSK modulation is about 2.5dB over than that of the FFT-OFDM system with 16PSK modulation for all values of SNR

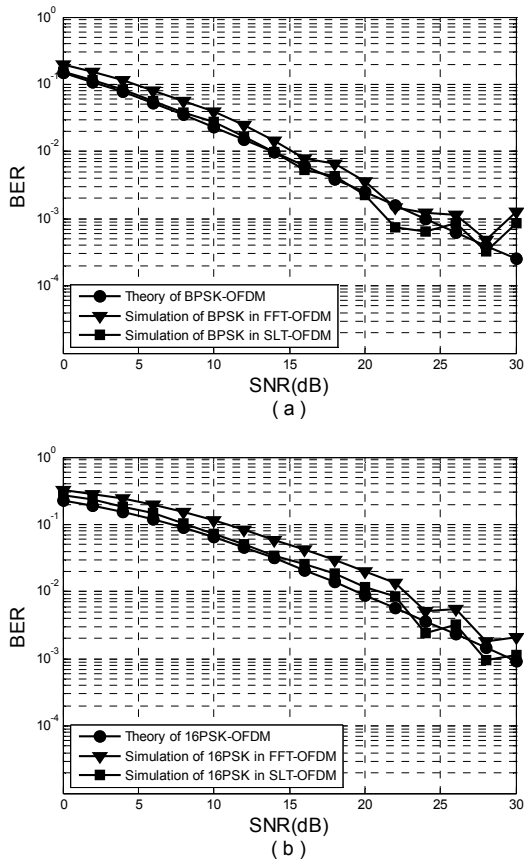


Figure (8) BER performance of the proposed SLT-based OFDM and FFT-based OFDM system in a Rayleigh fading channel with perfect compensation compared with theoretical OFDM results for (a) BPSK modulation (b) 16PSK modulation

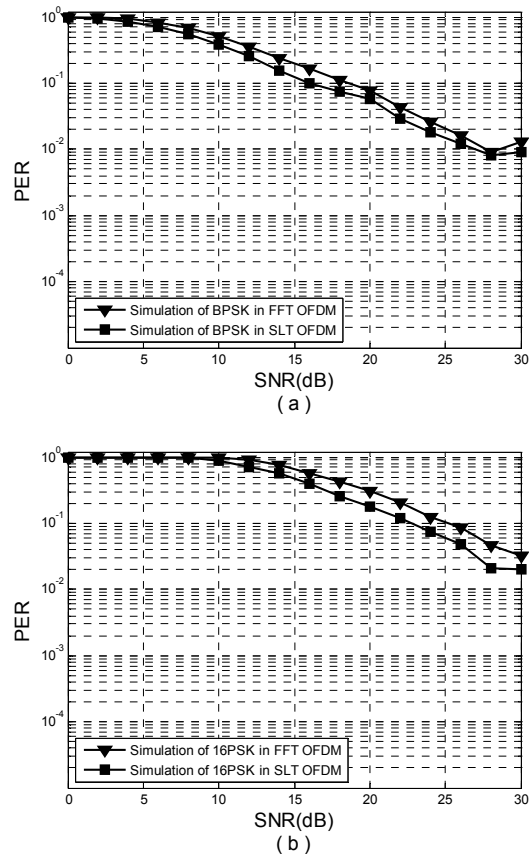


Figure (9) PER performance of the proposed SLT-based OFDM and FFT-based OFDM system in a Rayleigh fading channel with perfect compensation for (a) BPSK modulation (b) 16PSK modulation

7-3 Performance of the Proposed SLT-OFDM System in a Rayleigh Fading Channel with Pilot Symbol-Aided OFDM Modulation

In this simulation, we use one channel estimation symbol (pilot symbol) and six transmitted data symbols as one frame (packet) unit. Figure (10) and Figure (11) show the BER performance for the proposed SLT-OFDM system and traditional FFT-OFDM system compared with the theoretical results for OFDM system in a Rayleigh fading channel for channel estimation compensation. If a pilot signal for the proposed SLT-OFDM transmission system with BPSK modulation is used, approximately 3 dB shift from the theoretical result is obtained because of the pilot data of

1/7 in one frame (packet) unit & use high value of Doppler frequency shift ($f_d=250$) so the fading period is 4 ms. Also the channel estimation is not accurate enough to follow the fast fading. While, for pilot symbol FFT-OFDM transmission system with BPSK modulation approximately 5dB shift from the theoretical result is obtained. Also, can see that the proposed SLT-OFDM system with BPSK modulation is about 2dB better than that of the FFT-OFDM system for all values of SNR. Moreover, for pilot symbol SLT-OFDM transmission system with 16PSK modulation, approximately 3dB shift from the theoretical result is obtained. While for the FFT-OFDM transmission system with 16PSK modulation approximately 6dB shift from the theoretical result is obtained. It is also clear that the proposed SLT-OFDM system with 16PSK modulation is about 3dB better than that of the FFT-OFDM system for all values of SNR.

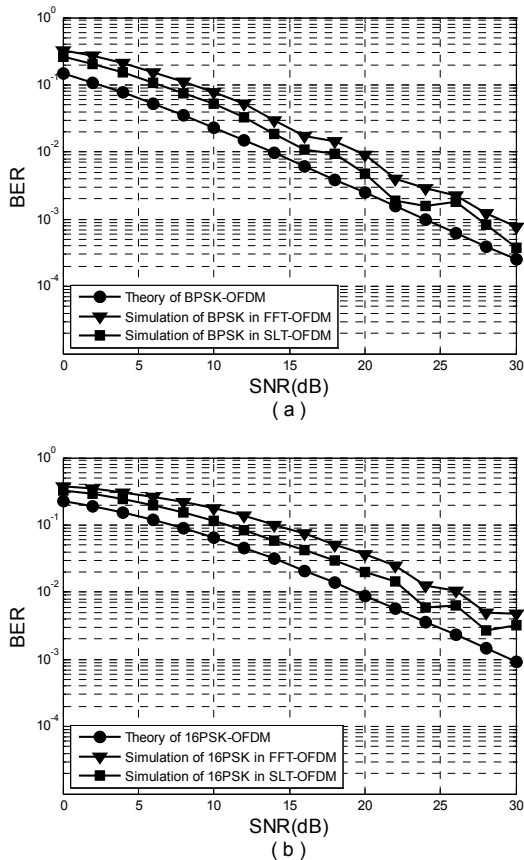


Figure (10) BER performance of the proposed SLT-based OFDM system and

FFT-based OFDM system in a Rayleigh fading channel with Pilot Symbol-Aided compared with theoretical OFDM results for (a) BPSK modulation (b) 16PSK modulation.

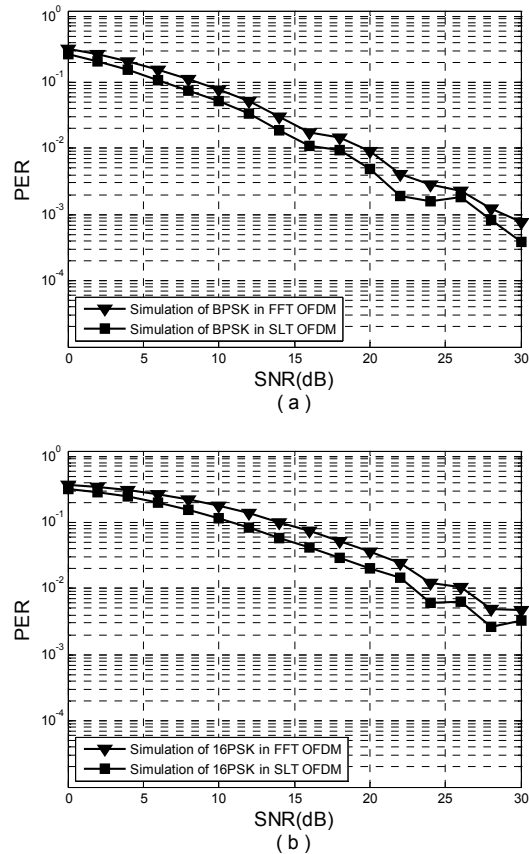


Figure (11) PER performance of the proposed SLT-based OFDM system and FFT-based OFDM system in a Rayleigh fading channel with Pilot Symbol-Aided for (a) BPSK modulation (b) 16PSK modulation

7.4 Performance of the Proposed LDPC Codes for the SLT-OFDM System with Pilot Symbol Aided OFDM Modulation

In this section, we evaluate the bit error rate (BER) of the proposed LDPC-SLT-OFDM system with BPSK and 16 PSK modulation using the Gray mapping in a Rayleigh fading channel with pilot channel estimation. We use (20,10)LDPC code Rate 1/2 with column weight of 3 and set the number of iterations in decoding to 2 and 8

and compare the results with the LDPC-FFT-OFDM system.

Figure-3 shows the block diagram of proposed LDPC-SLT-OFDM system for BPSK and 16PSK modulation over a Rayleigh fading channel with pilot symbol aided channel estimation. First, a block of k bits information data is encoded by a rate 1/2 LDPC code. The encoder output is then pass through the modulator which modulates the data using BPSK or 16PSK modulation. The modulated data is converted from serial to parallel and mapped on the subcarriers using an inverse SLT. Each OFDM block is prefixed by a cyclic copy of the last few samples in the same block. At the receiver the inverse operation is performed. After LDPC code is decoded the data bit by using sum-product algorithm and then the bit error rate (BER) is calculated.

In a multipath fading channel, some subcarriers of OFDM may be completely lost because of the deep fades. Hence, it is expected that lots of errors fix on continuous some subcarriers and the two dimensional errors in both time and frequency domains occur. So that, LDPC codes can compensate for two dimensional errors in both time and frequency domains for the OFDM system.

Figure 12, shows the BER performance of the LDPC-SLT-OFDM system and LDPC-FFT-OFDM system with BPSK and 16PSK modulation. With each iteration in the figures, the estimation of the message bits improve, and they usually converge to a correct estimate of the message. The number of corrected error increases as the number of iterations increases. However, the improvement of the estimation does not increase linearly, and so, in practice, it is enough to utilize a reasonable small number of iterations to achieve acceptable performance. Therefore, as the number of iterations for the iterative LDPC code decoding algorithm increases, the LDPC decoder performs significantly better.

From this figure, the BER performance of the LDPC-SLT-OFDM system with BPSK

modulation is about 3dB better than that of the LDPC-FFT-OFDM system after 2 and 8 iteration and for all values of SNR in a Rayleigh fading channel with pilot symbol aided channel estimation. The BER performance of the LDPC-SLT-OFDM system with 16PSK modulation is about 4dB better than that of the LDPC-FFT-OFDM system after 2 and 8 iteration and for all values of SNR in a Rayleigh fading channel with pilot symbol aided channel estimation. Therefore, the overall performance of the proposed LDPC code SLT OFDM is considered very well in operation under fading channel which is also efficient in terms of power consumption as compared to the LDPC code FFT-OFDM system.

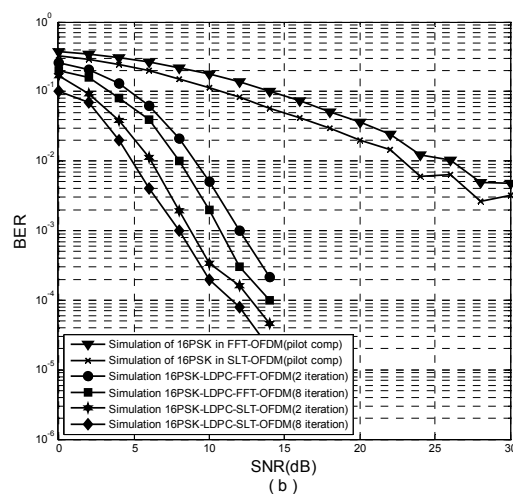
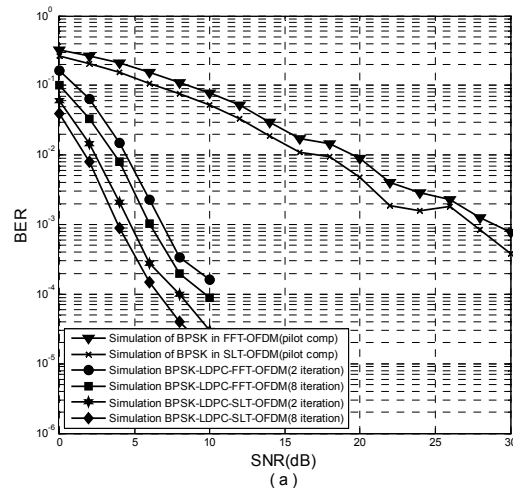


Figure (12) BER performance of the proposed LDPC codes for the proposed SLT-based OFDM system and the proposed

LDPC codes for FFT-based OFDM system in a Rayleigh fading channel with Pilot compensation with 2 and 8 iterations for (a) BPSK modulation (b) 16PSK modulation

From the figure-12(a) the coding gain at $BER = 7 \cdot 10^{-4}$ between uncoded traditional FFT-OFDM system and coded LDPC-FFT-OFDM system with BPSK modulation and with pilot compensation in a Rayleigh fading channel is about 22.5 dB for 2 iteration and about 23 dB for 8 iteration. While the coding gain at $BER = 7 \cdot 10^{-4}$ between uncoded proposed SLT-OFDM system and coded LDPC-SLT-OFDM system with BPSK modulation and with pilot compensation in a Rayleigh fading channel is about 23 dB for 2 iteration and about 24 dB for 8 iteration.

Finally, the coding gain between the proposed LDPC-SLT-OFDM and LDPC-FFT-OFDM is about 2.5dB for 2 iteration and about 3dB for 8 iteration.

While, from the figure-12(b) the coding gain at $BER = 5 \cdot 10^{-3}$ between uncoded traditional FFT-OFDM system and coded LDPC-FFT-OFDM system with 16PSK modulation and with pilot compensation in a Rayleigh fading channel is about 18 dB for 2 iteration and about 19 dB for 8 iteration. While the coding gain at $BER = 5 \cdot 10^{-3}$ between uncoded proposed SLT-OFDM system and coded LDPC-SLT-OFDM system with 16PSK modulation and with pilot compensation in a Rayleigh fading channel is about 20 dB for 2 iteration and about 21 dB for 8 iteration.

Finally, the coding gain between proposed LDPC-SLT-OFDM and LDPC-FFT-OFDM is about 3dB for 2 iteration and about 3dB for 8 iteration.

7- Conclusions

In this paper, a SLT for OFDM system is proposed to improve the BER performance on a Rayleigh fading channel. The SLT is less frequency sensitive than equivalent DWT or FFT due to the shorter length of the SLT filters. The LDPC-SLT-OFDM system with BPSK and 16PSK modulation

using gray mapping have a better error rate performance and more effective than the LDPC-FFT-OFDM system with BPSK and 16PSK modulation on a Rayleigh fading channel with pilot channel estimation in the term of iterations for the decoding algorithm. The reason for this improvement on a Rayleigh fading channel could be explained by the decoding algorithm. The proposed system employs the sum product algorithm as a decoding algorithm. The sum product algorithm exchanges likelihoods among frequency and time directions, so it can compensate for the two dimensional errors in both frequency and time domains. Thus, the LDPC codes are effective to improve the error performance of the proposed SLT-OFDM system on a Rayleigh fading channel.

References

- [1] Ahmad R. S. Bahai and Burton R. Saltzberg, 2004, "Multi-Carrier Digital Communications Theory and Applications of OFDM", Kluwer Academic Publishers, 2nd edition , 418 pages
- [2] T. Magesacher (ed.), 2010 , "OFDM for Broadband Communication.", EIT, Lund University.
- [3] Dr.S.S.RiazAhamed, 2008, "Performance Analysis Of OFDM", Journal of Theoretical and Applied Information Technology, pp 22-30, www.jatit.org
- [4] L. J. Cimini, Jr, 1985, "Analysis and simulation of a digital mobile channel using orthogonal frequency division multiplexing ", IEEE Trans .on comm., pp . 665-675
- [5] Saif Al-deenA.Mohamed, 2007 , "Space Time Block code for PCC, MC-CDMA using Slantlet Transform", Thesis submitted to college of engineering, Baghdad, Iraq
- [6] P. Hoher, S. Kaiser, and P. Robertson, 1997, "Pilot-symbol-aided channel estimation in time and frequency",

- Proc. IEEE Global Telecommun. Conf., USA, pp. 90-96
- [7] Ivan W. Selesnick, 1999, "The Slantlet Transform", IEEE Transactions On Signal Processing, VOL. 47, NO. 5
- [8] Hisashi Futaki and Tomoaki Ohtsuki, 2002, "Performance of Low-Density Parity-Check (LDPC) Coded OFDM Systems", IEEE JSAC, vol. 19, no.5, pp. 924 ~ 934
- [9] Robert G. Gallager, 1963, "Low-Density Parity-Check codes", Information Theory and Reliable Comm. vol. IT-g, pp. 143-156
- [10] Othman O. Khalifa, Sheraz Khan, Mohamad Zaid, and Muhamad Nawawi, 2008, "Performance Evaluation of Low Density Parity Check Codes", International Journal of Computer Science and Engineering
- [11] Hisashi Futaki and Tomoaki Ohtsuki, 2002, "Low Density Parity Check (LDPC) coded OFDM Systems", IEEE Trans on Information Theory, vol. 47, No. 2
- [12] Alexandre de Baynast, Ashutosh Sabharwal, Behnaam Aazhang, 2008, "LDPC Code Design for OFDM Channel: Graph Connectivity and Information Bits Positioning", Nokia Corporation, Electrical and Computer Engineering Dept, Rice University
- [13] Hisashi Futaki and Tomoaki Ohtsuki, 2001, "Low Density Parity Check (LDPC) coded OFDM Systems with M-PSK", IEEE JSAC, pp. 924 - 934

MODELING AND SIMULATION OF INTELLIGENT TRAFFIC LIGHT

Bassam H. Abed

Department of Electrical and Electronic Engineering,
University of Technology
eng.bassam77@yahoo.com

Abstract

The fixed time traffic light strategy is time and cost consumptive. Intelligent light trafficking based on car numbers is of impotence in recent studies to save time and cost. The present work focuses on modeling and calculating the time intervals needed to each side of traffic light. The calculations are based on the number of cars which is fed by sensors set up at each side. The model equations have been simulated using visual basic software. The simulation program can be divided into two parts; the first stage computes the number of cars at each side, and then gives the result to the second part which is responsible for time interval calculation. The result of second stage is fed again to first one and so on. Two case studies have been considered and the result has been compared to fixed time policy. Results based on this strategy show that the time interval and cost has been much reduced and; therefore, the suggested policy could enhance the traffic light system.

Keywords: *Intelligent Traffic light system, Intelligent Traffic mathematical model, Traffic light algorithm.*

1-Introduction

Traffic congestion is a severe problem in many modern cities around the world. Traffic congestion has been causing many critical problems and challenges in the major and most populated cities. To travel to different places within the city is becoming more difficult for the travelers in traffic. Due to these congestion problems, people lose time, miss opportunities, and get frustrated [1].

In fixed time traffic light control system, we can not get optimal solution for the traffic congestion. This leads to using other systems. One of these systems is intelligent traffic light system.

Many traffic light systems operate on a timing mechanism that changes the lights after a given interval. An intelligent traffic light system senses the presence or absence of vehicles and reacts accordingly. The idea behind intelligent traffic systems is that drivers will not spend unnecessary time waiting for the traffic lights to change. An intelligent traffic system detects traffic in many different ways [2-3].

We can see the need to intelligent system from raising the number of cars. As example in the city of Kuala Lumpur, the registration of new vehicles each year increased by about twenty per cent [4-5]. May be the intelligent system alone will not solve this problem but it still the important parts of the solution. I here suggest mathematical modal for the intelligent traffic light.

2-System Requirements

The whole system can be seen as in Fig (1-a). First part is cars counting system (can be sensors or any other instrument satisfies our requirements), in my example, I supposed sensor system Fig (1-b). First part is useful for counting cars in wait state and computing density of input cars for each side. Second part is the interface between traffic light and the computer. This part is useful for solving interfacing problems. The third part is the dedicated computer which is responsible for all computing according to

my algorithm by taking the input and calculating the time interval for each side then sending these intervals for the traffic light.

3-Mathematical Modal (Initial computation)

Firstly, we will take Fig (2) as a first case study in my research (we can record this case as a first case). As in Fig (2), we have four sides (0, 1, 2 and 3). Each side has traffic forwarding and to the left. This means if any side has the green light, the others three sides will have red light. Suppose that we have two sensors at each side, the first count input cars (Cin) and the seconds count the output cars (Cout). Then the number of cars in each side is (Cin – Cout) which for four sides are C0, C1, C2 and C3. The density of input cars can be estimated for fixed time t (constant time, which is specified previously) by:

CinD equal to number of incoming cars during the time t (Cin) dividing by this time.

$$CinD = Cin / t \quad \dots\dots\dots(1)$$

I suppose this can be gotten from the sensor system. The time for one period of the traffic light is T. the time which will be given to the sides is:

T0, T1, T2, and T3.

Before any computation, I mentioned that all computations are done in waiting state (when the yellow light effective).

The time initially can be estimated by estimating the time needed to one care (Tcar):

$$T_{car} = \frac{T}{C_0 + C_1 + C_2 + C_3} \quad \dots\dots\dots(2)$$

The time needed to side 0 is:

$$T_0 = T_{car} * C_0 \quad \dots\dots\dots(3)$$

Now we can give the side 0 time T0 but the computation not accurate because we did not take into account the expected rising cars in each side.

Firstly, we need to know the side active now. Let us take the side 3 active (have green light) and when this side gets yellow light then:

$T_{s,e}$: Time for side s which are estimated.

$$\left. \begin{aligned} T_{0,e} &= T_{car} * C_0 \\ T_{1,e} &= T_{car} * C_1 \\ T_{2,e} &= T_{car} * C_2 \\ T_{3,e} &= T_{car} * C_3 \end{aligned} \right\} \quad \dots\dots(4)$$

The expected cars rising in side 0 is equal to density of inputted cars in it multiply by the time taken by it because the side 0 is directly after side 3 and will not wait more:

$$C_{0EXP} = CinD_0 * T_{0,e} \quad \dots\dots(5)$$

The expected cars rising in any side can be estimated as:

$$\left. \begin{aligned} C_{1EXP} &= CinD_1 * (T_{0,e} + T_{1,e}) \\ C_{2EXP} &= CinD_2 * (T_{0,e} + T_{1,e} + T_{2,e}) \\ C_{3EXP} &= CinD_3 * (T_{0,e} + T_{1,e} + T_{2,e} + T_{3,e}) \end{aligned} \right\} \quad \dots\dots(6)$$

Then the total cars in each side equal to the number of cars in fixed time plus the expected rising cars:

$$\left. \begin{aligned} TotalC_0 &= C_0 + C_{0EXP} \\ TotalC_1 &= C_1 + C_{1EXP} \\ TotalC_2 &= C_2 + C_{2EXP} \\ TotalC_3 &= C_3 + C_{3EXP} \end{aligned} \right\} \quad \dots\dots(7)$$

According to the new numbers of cars, we will repeat our calculation:

$$T_{car} = \frac{T}{TotalC_0 + TotalC_1 + TotalC_2 + TotalC_3} \quad \dots\dots(8)$$

$$\left. \begin{aligned} T_0 &= T_{car} * TotalC_0 \\ T_1 &= T_{car} * TotalC_1 \\ T_2 &= T_{car} * TotalC_2 \\ T_3 &= T_{car} * TotalC_3 \end{aligned} \right\} \dots(9)$$

Summation of these times (T_0, T_1, T_2 and T_3) will be exactly T .

4-Mathematical Modal (General form):

If we have junction have n sides and the effective side is i (our computing will be after this side) then we can generalize the equation to:

$$\left. \begin{aligned} T_{car} &= \frac{T}{\sum_{j=0}^{j=n-1} C_j} \\ T_{je} &= T_{car} * C_j \text{ where } j=0, 1, 2 \dots n-1 \\ C_{EXP_j} &= CinD_j * \sum_{k=1}^{k=(j-i+n) \bmod (n+1)} T_{(i+k) \bmod n,e} \\ TotalC_j &= C_j + C_{EXP_j} \\ T_{car} &= \frac{T}{\sum_{j=0}^{j=n-1} TotalC_j} \\ T_j &= T_{car} * TotalC_j \end{aligned} \right\} \dots(10)$$

5-General Form for Other Case Study:

We can apply the above equations on the case in Fig (3). As we can see in Fig (3) there are four sides but the turn to left was not permitted, which leads to two sides have a green light in the same time. We can apply the above equations on this case by taking the apposite sides as one side (the sides which take a green light at the same time). From this, we have practically two sides only as shown in Fig (3). Now we have $n=2$ and i depends on the sides which we want to

estimate the time to them. With taking into account the number of cars C_0 is the average of the car's number of the two apposite sides. The density of input cars is the average too. We can record this case as the second case.

6-Testing the Mathematical Model

Testing of my equations are done with a simple simulator (program written by visual basic) which consists of two parts. The first part produce cars in each side and give this to the second part which calculates the time interval for the sides and sends it to the first part which in turn calculate the leaving cars and so on. Fig (4) shows the flowchart of the two parts. All the calculation of the interval is done in the last seconds of the last period (when the last side has yellow light). These tests were done on the two cases which are explained previously. The same tests are done on the same cases with fixed time interval traffic light. Fig (5) and (6) shows the relation between waiting time with respect to progress of time for first and second cases. The Y-axis represent waiting time for all cars for a specific slice of time (X-axis). Fig (7) and (8) shows the number of cars with respect to waiting time for first and second cases. Fig (5-8) drawing using Microsoft excel according to numerical data results from the mathematical model. From the test, clearly, when use the new model the average (over all time) will be reduced to 0.4 while it 0.6 when used the fixed time system. Therefore, the efficiency of the new model will be increasing approximately 33%. Then, this increasing of efficiency will tend to reduce the time loss and this loss in time mean increase in cost like time, money, emission of Co_2 . (If we suppose that the cost is unity).

7-Conclusions

As we can see the results ensure that using this mathematical modal decrease the waiting time (travel time) of each car and then decreasing the cost in fuel, which results

from waiting time. In the worst case, the fixed time system will not be best than using mathematical modal as can be seen from second case testing. The expected numbers of cars will not be same as the true cars. This will lead to small errors. The solution of it is by using smoothing factor, which depends on the difference between the true cars and the expected cars.

References

- [1] P. Krishnani, D. Sul, and C. Anyanwu, 2008, "Automatic Traffic Light Control System", Spring, ME 233 Final Project Report, CaliforniaStateUniversity, Sacramento
- [2] A. Albagul, M. Hrairi, Wahyudi, and M.F. Hidayathullah, 2006, "Design and Development of Sensor Based Traffic Light System", American Journal of Applied Sciences 3 (3): 1745-1749.
- [3] K. L. Shunmuganathan, V. Vasudevan and P. Yogesh, 2007, "Intelligent Communicating Agent and Their Performance for Multi-Agent Based Traffic Controller- A New Approach for Roads Using JADE", International Journal of Soft Computing Vol. (2), No. (1), pp. (17-20).
- [4] KokKiang Tan, 1Marzuki Khalid and RubiyahYusof, December 1996, "Intelligent Traffic Lights Control By Fuzzy Logic". Malaysian Journal of Computer Science, Vol. 9 No. 2, pp. 29-35.
- [5] A. S. Khalid, A. Y. Jaiz and F. Wajdi, , 2008, "Dynamic Traffic Light Sequence Algorithm Using RFID", Journal of Computer Science, Vol. (4), No. (7), pp. (517-524).

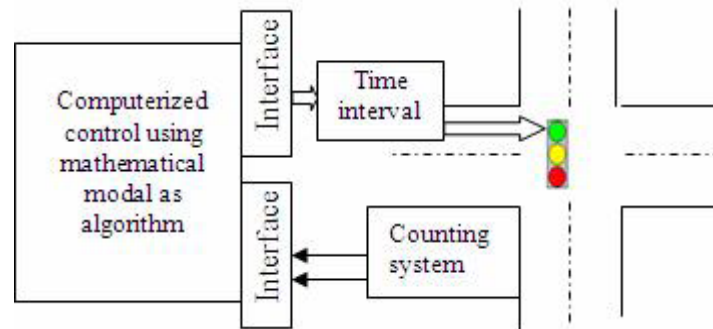


Figure (1-a) Main parts of the system

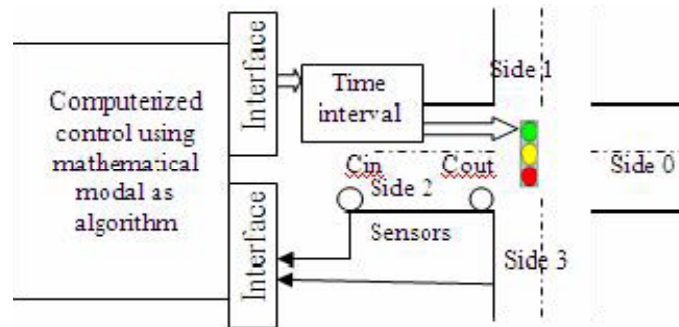


Figure (1-b) Main parts of the system with sensor as first part

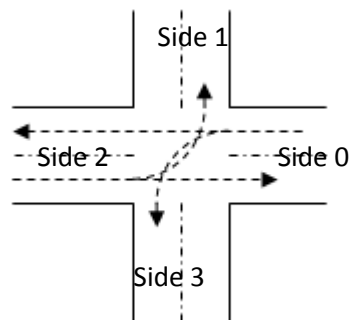


Figure (2) Four sides junction with permit to turn to left

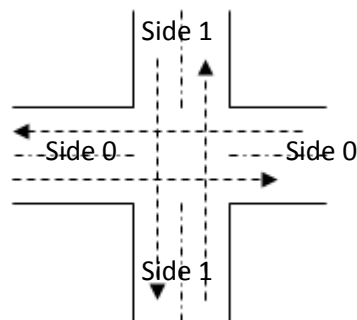


Figure (3) Four sides junction with turn to left not permitted

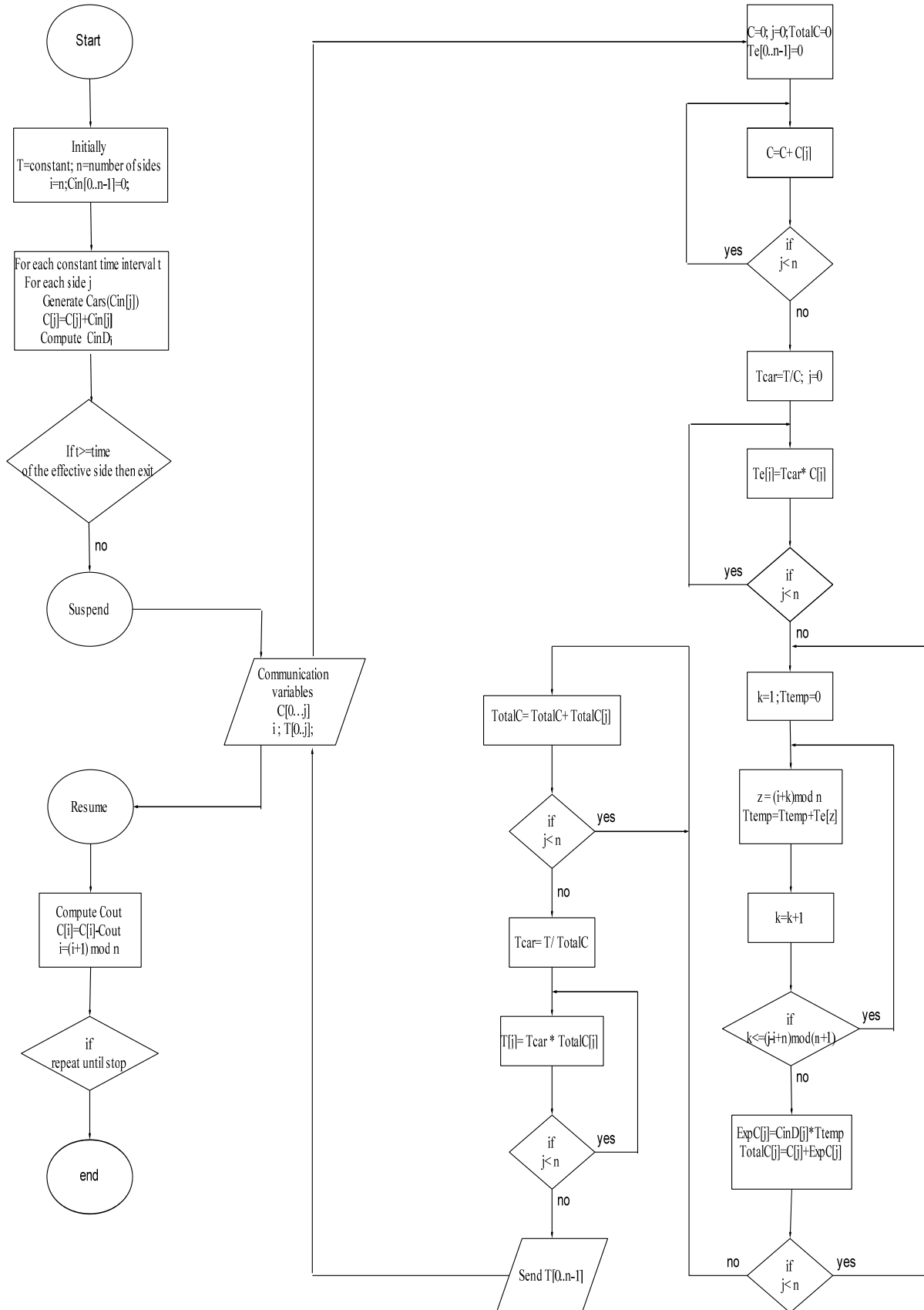


Figure (4) The Flowchart of Two Parts

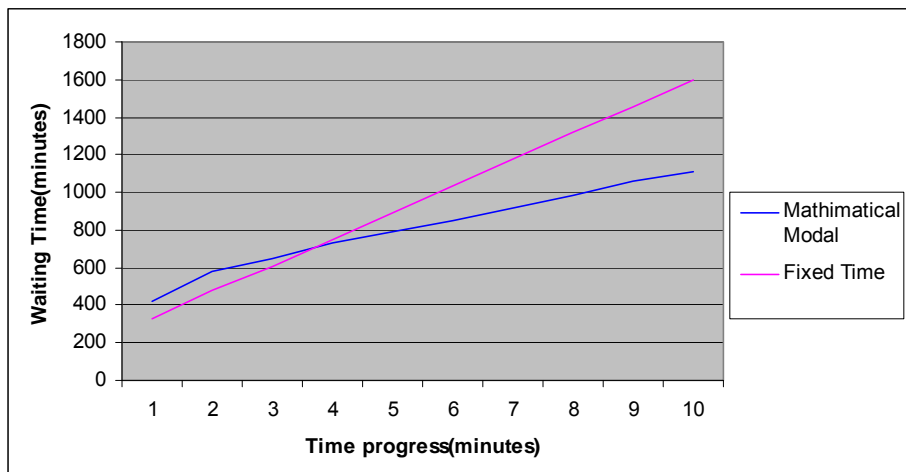


Figure (5) Waiting time of all cars per slice of Time (First Case)

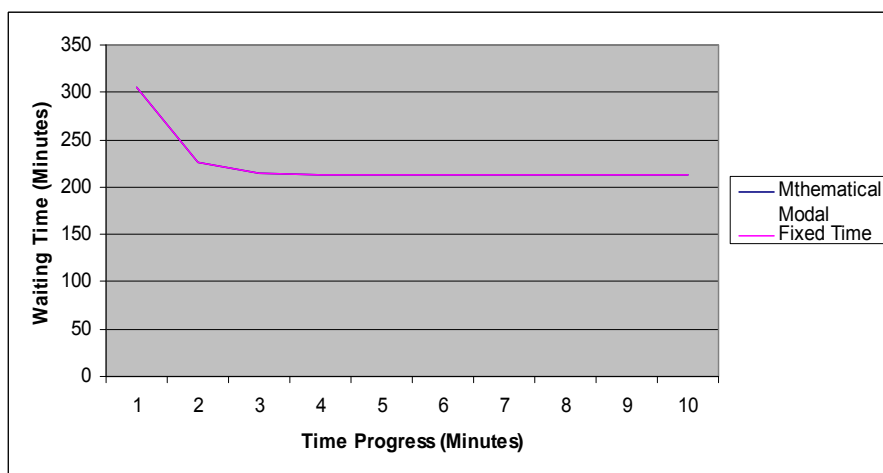


Figure (6) Waiting time of all cars per slice of Time (Second Case)

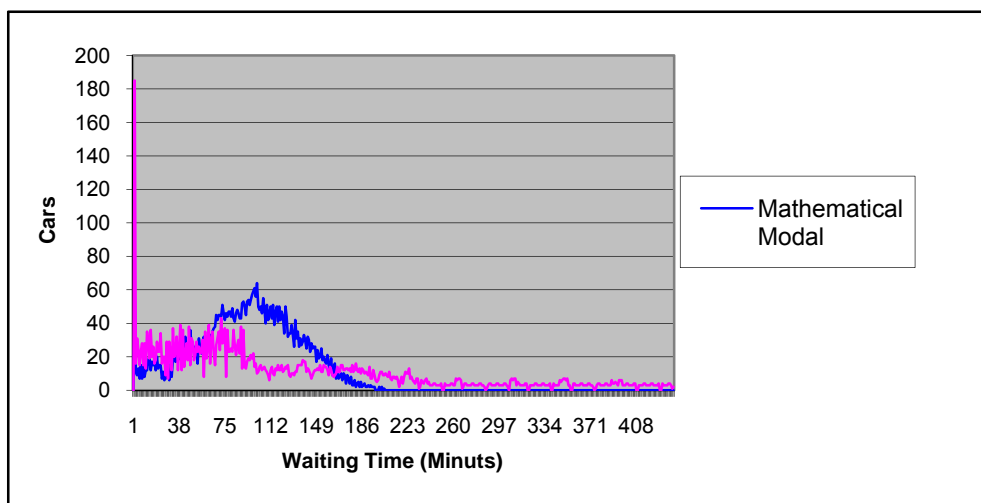


Figure (7) Relation between number of cars and Waiting time (first Case)

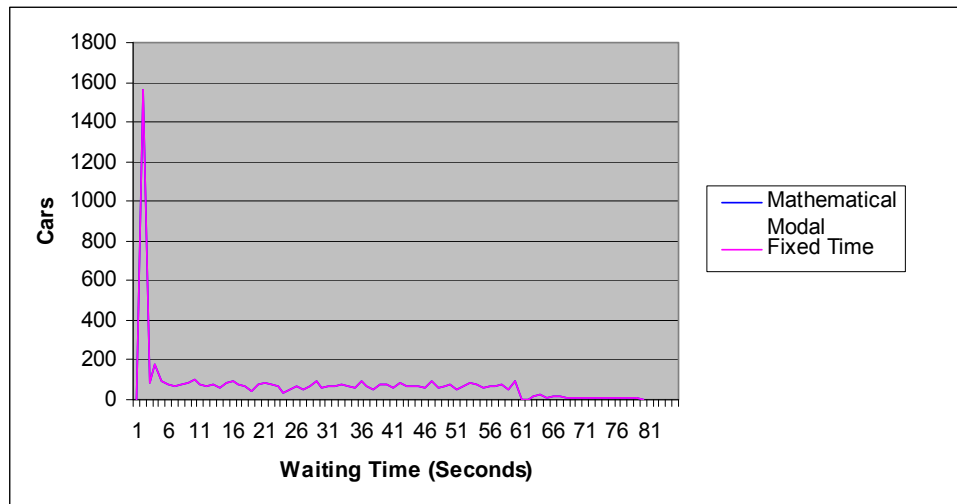


Figure (8) Relation between number of cars and Waiting time (Second Case)

SELF HEATING CALCULATION AND RESISTANCE MEASUREMENT CIRCUIT DESIGN OF MEZZO-STRUCTURE RESISTANCE TEMPERATURE DETECTOR (μ SRTD) SENSOR

Dr. Dlear Hassan Abed

Electrical Engineering Department
College of Engineering, University of Sulaimani.
dlear7419@yahoo.com

Abstract

The paper addresses: (1) Designing a new type of temperature measurement sensor named Mezzo-Structure Resistance Temperature Detector (μ SRTD). (2) Designing an accurate circuit to measure sensor resistance which is about (0.25 – 1 Ω). (3) Driving a mathematical equation to determine the self heating value in (μ SRTD) sensor.

Keywords: RTD sensor, temperature sensor, temperature measurement.

1- Introduction

Two types of temperature measurement sensors among all RTDs (Resister Temperature Detector) sensors are used. They are: Wire Wound RTD and Thin Film RTD. The basic characteristics of temperature sensors are:

1. Internal characteristics: size; vibration tolerance, mechanical and thermal shock immunity; sensitivity; operating range; stability; accuracy; ability to measure the temperature of a small and sprayed particles; sensor effect on measuring process; self heating coefficient; homogeneity; cost; interchangeability. [1]
2. External characteristics: contact or non-contact temperature measurement needs; measurement accuracy; temperature change range; maximum temperature applied; explosion conditions; additional requirements of environments. [2]

Despite of a high linearity of RTD sensor, it does not withstand high temperature and mechanical shock which is result to break the

sensor. μ SRTD sensor made by coating thin layers of metallic powders on dielectric substrates, therefore it will strong enough to withstand mechanical shocks and high temperature impulses. [3]

Applications of μ SRTD sensor are in critical and exploitation loads conditions like self propagation, high temperature synthesis (SHS) and detonation gun spray. [3]

2-Mezzo-Structure RTD Sensor Specifications [3]

1. μ SRTD sensor is able to measure effective temperature in detonation spray coating processes.
2. μ SRTD sensor built by coating thin layers of metallic powders on dielectric substrates which is withstand mechanical shocks and vibrations.
3. Physical topology model of μ SRTD sensor consists of layers in the form of mezzo-structure split-particles.
4. Electrical equivalent circuit topology model of μ SRTD sensor is in the form of a group of resistors with different values connected on series and parallel. Connection quality between split-particles borders are represented as resistor. Resistor with large value represents bad connection between split-particles and resistor with small value represents good connection between split-particles.
5. μ SRTD sensor has “hysteresis” characteristic.
6. μ SRTD sensor has “memory” characteristic which can remember maximum temperature of environment

after removing it from measurement process.

7. μ SRTD sensor can be used in computerized real time measurement systems. [4]

3- μ SRTD Sensor Design & Build Method

The method which is used to build μ SRTD sensor helps sensor to withstand vibrations and mechanical shocks. μ SRTD sensor is build in conditions similar to conditions in which it would be used in future. Detonation-gas spray and plasma spray are the most suitable technologies to build μ SRTD sensor. Thin layers of micro-diameter metallic particles are coated on the ceramic substrate by using detonation-gas gun spraying in our research. Collision speed of powders with substrate is between (0.4 - 1.5 Mach). Powder particles supply pressure (100 - 800 MegaPascal) in collision point. Pressure on substrate depends on size and weight of metallic powders. The temperature of metallic powder particles approximately is between (600 to 2300 °C). Building μ SRTD sensor under above conditions helps it to withstand working under these conditions. μ part of μ SRTD sensor name derived from “mezzos” which mean medial or intermediate. We designated an abbreviation μ SRTD (Mezzo-Structure Resistance Temperature Detector) to recognize a new sensor from others. μ SRTD sensors based on metallic powders of (Ti, Ni, Al) are shown in Fig.1. [3]

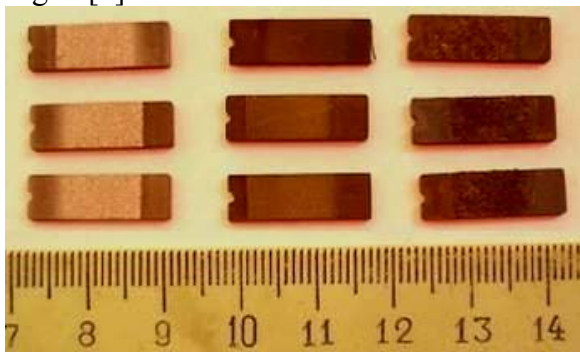


Fig. 1 - μ SRTD sensors based on metallic powders of Al, Ni, Ti respectively

Each layer of sensor formed from collision of melted metallic powders particles with insulator substrate. During interaction between melted metallic particles and solid surface of substrate a heat transfer and crystallization will happen. Fig. 2 & 3 shows mechanical formation of one particle during process of interaction between particle and substrate [6].

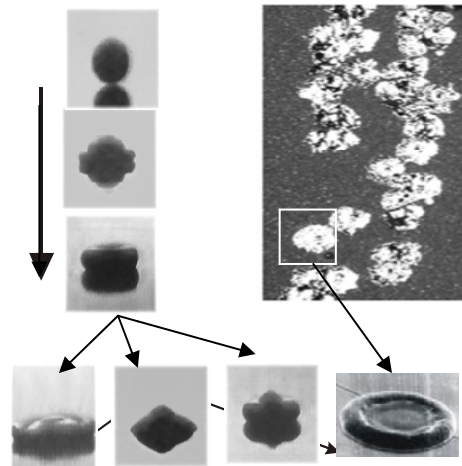


Fig. 2 - high speed video recorder shows the process of mezzo-structure layers formation.[6]

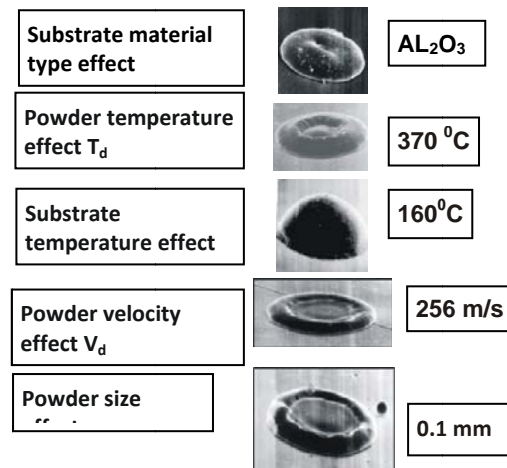


Fig. 3 - The factors which effect on metallic particles formation process during their collision with solid surface of substrate

The factors which effect on metallic particle form during their collision with solid surface of substrate are:

1. Natural interaction between particle and substrate.

2. Particles temperature (T_d) and substrate temperature effect on formation process.
3. Particles velocity (V_d).
4. Particles size.

4-Temperature Characteristic Of μ SRTD Sensor

Linear increasing of resistance with temperature of classic RTD sensor is because of thermal energy which causes the atoms of sensor to vibrate. At any instant, the atom may not be in its equilibrium position and therefore interacts with and scatters electrons. The mean free path decreases, the mobility of electrons is reduced, and the resistivity increases. This increase in sensor resistance continues until fusion temperature of metal. [6]

μ SRTD sensor shows non linear resistance versus temperature characteristic as shown in Fig.4. Non-linearity characteristic of μ SRTD sensor obviously appears at high temperatures above destruction temperature (T_{des}). T_{des} represents the temperature in which the layers of μ SRTD sensor start to destruct. At T_{des} μ SRTD sensor resistance starts to increase non-linearly and increases two or three times more than average. μ SRTD sensor resistance value after T_{des} point depends on connection quality between borders of split-particles. μ SRTD sensor resistance does not retain to its' initial value, when it cooled to room temperature (300°K). This behavior shows hysteresis characteristic of μ SRTD sensor. μ SRTD sensor destroys after a number of thermo-cycling (heating & cooling cycles). The parameters which are determining period of using of μ SRTD sensor are:

1. Number of times in which μ SRTD sensor used in thermo-cycle process.
2. Chemical properties of sensor material.
3. Thickness of sensor coat layers.

Therefore by increasing the number of sensor layers, we can increase operation period of sensor in critical and exploitation conditions.

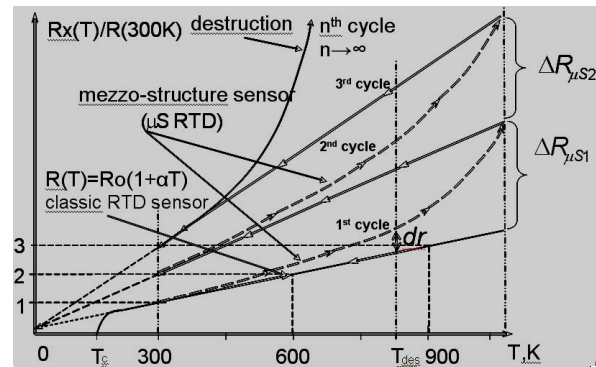


Fig. 4 - Comparison between resistance versus temperature characteristic of RTD and μ SRTD sensors

$$\Delta R_{\mu S1}(kT) = \Delta R_{\mu S2}(kT) = D * dr * e^{-E/kT}$$

μ SRTD sensor used to measure maximum temperature in any process. μ SRTD sensor resistance will be measured two times (at room temperature); first time before temperature measurement process, Second time after the measurement process. Sensor resistance value in second time will be greater than first time. The increasing in sensor resistance is proportional to maximum temperature of a process. Therefore, this fact shows “memory” characteristic of μ SRTD sensor. This explanation confirms theoretical hysteresis characteristic in Fig. 4. Because of the non-linearity of μ SRTD sensor characteristic, an accurate resistance measurement system is necessary.

5-Pinciple Work Of μ SRTD Sensor [3]

The difference between μ SRTD sensor and RTD sensor is in sensor structure. μ SRTD sensor formed from split-metallic particles layers. Resistance of μ SRTD sensor depends on two factors:

1. First factor is resistivity of metal particles used in sensor (this factor similar to classic RTD sensor).
2. Second factor is number and quality connections between particles surfaces of sensor layers.

At low temperatures less than 300 °K, linear characteristic relation between resistance and temperature determines

μ SRTD sensor output response. At higher temperatures (more than > 300 °K), contact destruction between surfaces of coat particles will determines μ SRTD sensor output response, therefore we observe at high temperatures gradual diversion in linear relation between resistance and temperature characteristic of sensor.

Sensor layers have mezzo-structure form and can be represented as resistors connected together in three-dimensional matrix form. We will consider that layers of μ SRTD sensor are flat. Electrical equivalent circuit represented as a series and parallel resistors connection Fig. 5. In general, total resistance of μ SRTD sensor is determined by number, size, contact quality between particles, topology of conductor layer (or effective layer length) and metal type.

Surface layers of μ SRTD sensor are destroyed because of high temperature effect in explosion process. As a result, number of contact between particles of mezzo-structure sensor will decrease. The decreasing in number of contact, in electrical equivalent circuit of μ SRTD sensor (Fig. 5) can be described as some of resistors will burn in circuit. This leads to suddenly change in total resistance of sensor. Number and connections type between particles of μ SRTD sensor can not predict.

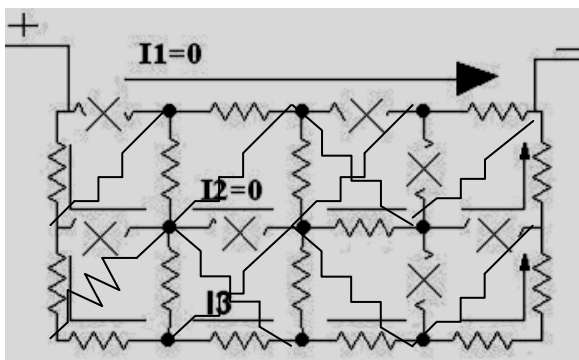


Fig. 5 - Destruction in sensor surface will change total resistance value and current flow path in it.

6- μ SRTD Sensor Characteristic According To Practical Results. [3]

Nonlinear characteristic of resistance versus temperature of μ SRTD sensor (Al type) is because of sequentially destruction of connections between particles. This nonlinear characteristic confirms theoretical principles which depended to explain the principle work of μ SRTD sensor. At 300°C a small decreasing in sensor resistance will obvious (Fig. 6). The reason is that at high temperature, thermal expansion of particles increase there sizes and increases the number of contacts between them. Increasing particles size will decrease holes volume in coat structure. Increasing the number of contacts between particles will decrease the total resistance value of μ SRTD sensor.

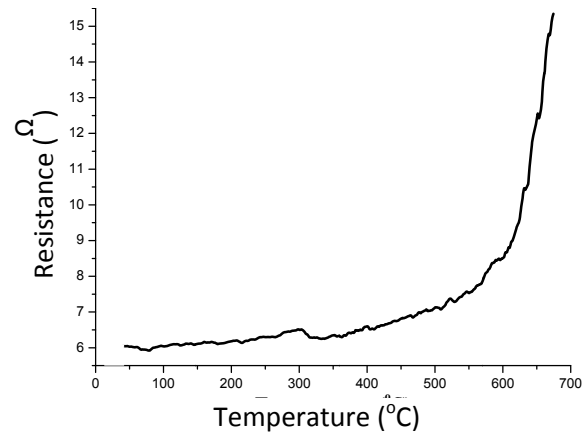


Fig. 6 - Resistance vs. temperature characteristic of μ SRTD sensor (Al type)

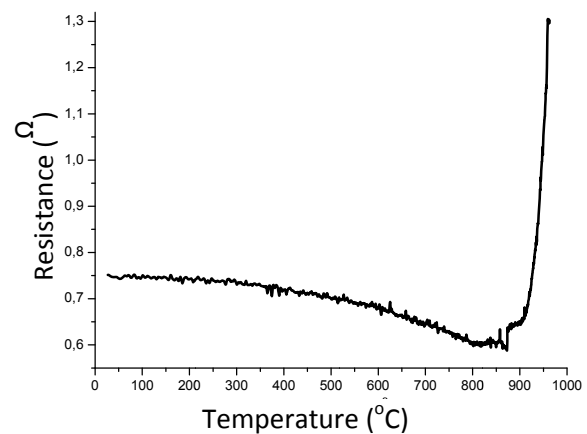


Fig. 7 - Resistance vs. temperature characteristic of μ SRTD sensor (Ni type)

Resistance versus temperature characteristic of μ SRTD sensor (Ni type) in 1st heating cycle is shown in Fig. 8. A smooth decreasing in sensor resistance value happens to 800°C. Sensor resistance degrades by 15%. The reason is that, thermal expansion of particles will increase there sizes and number of contacts. Holes volume in coat will decrease due to increasing particles size. Total resistance of μ SRTD sensor will decrease due to increase in number of contacts between particles.

In general, there are two mechanisms to explain μ SRTD sensor (Ni type) characteristic in Fig. 9. The first is “holes filling” mechanism which is happens because of size expansion “thermal expansion” of particles. The second is “destruction” mechanism which is happens because of destruction between particles contacts of mezzo-structure sensor. The “holes filling” mechanism to “destruction” mechanism in Nickel is more intensively than in Aluminum. “destruction” mechanism of μ SRTD sensor (Ni type) dominate at 800°C and higher temperatures.

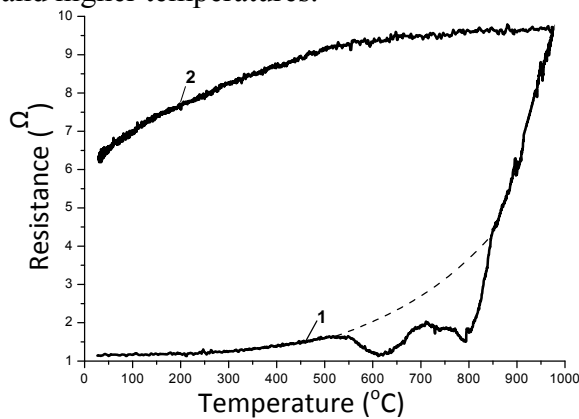


Fig. 9 - Resistance vs. temperature characteristic of μ SRTD sensor (Ni type) after 2nd heating (curve1) & cooling (curve2) cycle[3]

7-Resistance Measurement Circuit Of μ SRTD Sensor

Using Wheatstone bridge to measure resistance between $(10 - 10^{-6}) \Omega$ causes errors because of wire resistance value and contact resistance effects between wires. It is

difficult to connect copper lead wires to low resistors value without introducing contact resistances of the order of 0.0001% Ω or more. The contact resistance would amount to 0.01% for a resistance of 1 Ω and as high as 10% for a resistance of 0.001 Ω . [6] Kelvin double bridge (fig 10) is chosen to measure the resistance of μ SRTD sensor. Kelvin double bridge eliminates the lead resistance between wires connections of bridge. R_x is (μ SRTD) sensor and R_o is a standard resistor. R_x and R_o have nearly equal values. R_1, R_2, R_3 and R_4 are four known non-inductive resistors. R_x and R_o are represented as they connect to bridge by four contact resistors to increase measurement accuracy. Each resistors $c_1, c_2, c_3, c_4, p_1, p_2, p_3, p_4$ represent wire resistance and contact resistance between wires. Variable resistance is to control the current passing through sensor to make it as small as possible to decrease self heating in μ SRTD sensor.

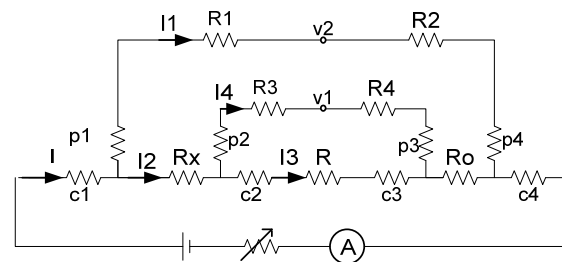


Fig. 10 - Connection diagram of the Kelvin double bridge circuit

$$I_1 (p_1 + R_1) = I_2 R_x + I_4 (p_2 + R_3)$$

$$I_1 (p_4 + R_2) = I_2 R_o + I_4 (p_3 + R_4)$$

$$I_4 (p_2 + R_3 + R_4 + p_3) = I_3 (c_2 + R + c_3)$$

$$I_2 = I_3 + I_4$$

μ SRTD sensor resistance value is determined by equation:

$$R_x = \frac{V_{R_x}}{I_{R_x}} = R_o \cdot \frac{R_1}{R_2} + \frac{R \cdot R_4}{R + R_3 + R_4} \cdot \left(\frac{R_1}{R_2} - \frac{R_3}{R_4} \right)$$

We can obtain balance condition ($v_1 = v_2$) by two methods:

1. First method by making the ratio R_1/R_2 equal to R_3/R_4 and varying R_o . This is done

by observing a null ($V_1 - V_2 = 0$) on the galvanometer, G.

2. Second method by making R_o constant and varying the ratio $R_1/R_2, R_3/R_4$.

In order to prevent any mistake effect on measurement results, R value must be very small this can be done by using a wire with a large cross section area for R .

We choose $R_1 = R_2 = R_3 = R_4 = 10 \Omega$ to cancel wire resistance and contact resistance in measurement. c_2 and c_3 do not enter bridge balance equation because they do not effect on measurement result. c_1 and c_4 enters in total current (I) calculations and they do not have effect on bridge balance condition. The effect of thermo-electric e.m.f.s may be eliminated by passing the current through R_x and R_o in a reverse direction and taking the mean of the readings.

A mathematical equation for μ SRTD sensor resistance value in case of unbalanced bridge is derived. According to Fig. 10, the equations are:

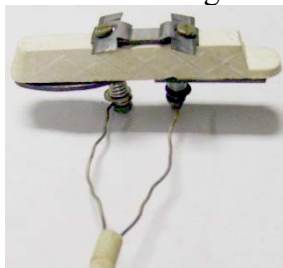
$$V_1 = \frac{V \cdot \{RR_4 + R_o \cdot (R + R_3 + R_4)\}}{R_x \cdot (R + R_3 + R_4) + R(R_3 + R_4) + R_o(R + R_3 + R_4)}$$

$$V_2 = \frac{V \cdot R_2}{R_1 + R_2}$$

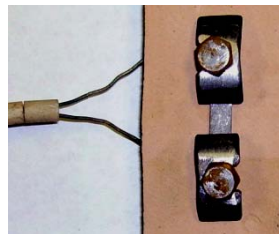
When $V_1 - V_2 \neq 0$, then

$$R_x = \frac{V \cdot [R \cdot R_4 + R_o \cdot (R + R_3 + R_4)] \cdot (R_1 + R_2)}{V \cdot R_2 - [V_1 \cdot (R_1 + R_2)] \cdot (R + R_3 + R_4)} + \frac{R_2}{R + R_3 + R_4} - (R + R_o)$$

Practical circuits of Kelvin double bridge are shown in Fig. 11.



A



b



C

D

Fig. 11 - (a,b,c) show sensor connection to lead wire; (d) shows Kelvin double bridge circuit

8-Self Heating In μ SRTD Sensor

In order to accurately measuring resistance of μ SRTD sensor, it is necessary to pass a small current through it. Small current in μ SRTD sensor will not cause self heating. In this case μ SRTD sensor resistance will change only with temperature change. Equation which calculates self heating in μ SRTD sensor is:

$$\frac{P}{A} = -kU'(0)$$

where:

P – Heating energy in μ SRTD = $V^2/R(T)$,

(W)

A – Surface area of μ SRTD, (m^2)

k - Substrate heat transfer coefficient, (m^2/c).

$$\frac{P}{A} = -\gamma \frac{(T_2 - T_1)}{l}$$

$$T_1 = \frac{lP}{\gamma A} + T_2 = \frac{lV^2}{\gamma AR(T)} + T_2, \text{ where } \gamma = k\beta$$

β - Heat transfer resist parameter of substrate, ($\beta = \text{Jule}/m^3.K$)

$$I^2 \cdot R_{layer} \cdot t_{rel} \geq C_{layer} \cdot m_{layer} \cdot \Delta T_{layer}$$

Left part is “Joule” heat energy due to current passing through μ SRTD sensor. Right part is “Joule” heat energy which causes heating of μ SRTD sensor layers.

Temperature increasing ΔT_{layer} of μ SRTD sensor layers because of self heating is:

$$\Delta T_{layer} \leq \frac{I^2 \cdot R_{layer} \cdot t_{rel}}{C_{layer} \cdot m_{layer}}$$

Where $m_{layer} = \rho \cdot V_{layer}$, $V_{layer} = a \cdot l \cdot h$; ρ is volume density of metal. For example, if μ SRTD sensor (Al type) has $\rho = 2,7 \cdot 10^3 \text{ kg/m}^3$; a is layer width ($a = 5 \cdot 10^{-3} \text{ m}$); l is layer length ($l = 10^{-2} \text{ m}$); h is layer thickness ($h = 10^{-4} \text{ m}$); C_{layer} is specific heat capacity, Aluminum has $C_{layer} \approx 0,2 \text{ joule/g}$. Layers mass is about 0.01 – 0.015 g. the layers resistance R_{layer} of different samples of μ SRTD sensor lies between a few ohms to 10-20 ohm (layers resistance of Aluminum samples may have $R_{layer} \approx 2 \text{ ohm}$ at high temperatures). Power supply voltage is between a few voltages to 12V. Therefore sensor current at these conditions is about 10 mA. Relaxation time t_{rel} for self heating of layers can not exceed several seconds. If t_{rel} is equal to 5 seconds then ΔT_{layer} will be ($\Delta T_{layer} \leq 0.5 \text{ }^\circ\text{K}$). Therefore self-heating in μ SRTD sensor because of current passing through it can be neglected.

9-Conclusion

1. Kelvin double bridge is a best circuit to measure the resistance of μ SRTD sensor with a high accuracy. The accuracy of circuit is: 0.05% for resistors (from 100 micro ohms to 1 ohm); 0.2 – 0.05% for resistors (from 100 to 1000) micro ohms; 0.2 - 0.5% for resistors (from 10 to 100 micro ohms).
2. Mathematical equation which calculates self heating in μ SRTD sensor determines exactly the factors which effect on μ SRTD sensor resistance.

References

- [1] Hashemian H.M., "Comparing RTDs and Thermocouples In Industrial Applications", Sensors magazine, February, 2003, <http://www.sensormag.com/articles/0203/temp/main.shtml>
- [2] Nelson S., Chen D., Ralph J., Herde D. E., "The Development Of a RTD Temperature Sensor For Exhaust Applications", SAE, 2004. <http://delphi.com/pdf/techpapers/2004-01-1421.pdf>
- [3] Abed D.H., Evstigneev V.V., "Mezzo-Structure Sensor For Temperature Measurement In Conditions Of Critical And Explosion Loads", Ph.D. thesis, engineering faculty, Altai state technical university, Barnaul, Russia, July 2006. 143 pages (thesis in Russian language).
- [4] Krikor K.S., Abed D.H., Abbood F.A. "A PC Based Speed Controller for PM DC Motor", II national conference on computer, communication, control and system engineering, university of Technology, Baghdad, Iraq, 23-24 Dec. 2001.
- [5] Predtechensky M.R., Varlamov Yu.D., Uliankin S.N., Cherepanov A.N., Popov V.N., "Spreading and Solidification of Liquid Metal Droplets on a Substrate: Experiment, Analytical Model and Numerical Simulation", Proceedings of 32nd International Symposium on Microelectronics, October 26-28, 1999, Chicago Hilton & Towers, Chicago, Illinois, IMAPS-International Microelectronics and Packaging Society, 1999, pp. 166-171.
- [6] Indulkar C.S., Thiruvengadam S., "An Introduction to Electrical Engineering Materials", S. Chand & Company LTD, India, 2004.

[THIS PAGE IS INTENTIONALLY LEFT BLANK]

Author Index

- Abbas, A. Y., 42
Abdullah, M. N., 291
Abdul Muhsin, H. A., 224
Abed, B. H., 330
Abed, D. H., 338
Abood, Q. K., 129, 241
Akkar, H. A. R., 270
Al-Faiz, M. Z., 90, 206
Algailany, M. Y., 110
Ali, A. A., 90
Ali, L. T. A., 82
Al-Mashhadany, Y. I., 100
Alneby, M. E., 145
Al-Qassar, A. A., 121
Alradh, J. A. A. A., 134
Al-Samarraie, S. A., 2
Al-Ubaidi, S. N., 134
Alwane, S. K., 291
Ameen, S. Y., 235
Haider, H. T., 213
Hameed, S. M., 198
Hammoud, A. K., 298
Hasan, Q. F., 60
Hasan, S. D., 270
Hassan, M. Y., 263
Hawas, M. N., 42
Helal, B. H., 279
Humaidi, A. J., 22, 134
Humod, A. T., 34
Kareem, E. S., 160
Khalil, Y. A., 247
Maher, R. A., 160
Mahmood, A. M., 65, 206
Mahmoud, W. A., 129, 145
Mary, A. H., 14
Miry A. H., 90
Miry, M. H., 305
Mohammed, A. G., 263
Mugheer, G. A., 317
Muhaisen, H. N., 298
Nafia, A. H., 75
Naji, M. A., 254
Obaid, A. K., 230
Oliewe, B. K., 171
Othman, M. A., 241
Othman, M. Z., 121
Rashed, A. A., 291
Sa'id, W. K., 110, 171
Saleh, M. H., 121
Shareif, A. Q., 75, 129
Saud, L. J., 182, 235
Thanoon, A. A., 188
Yasein, F. R., 51
Younis, M. F., 241
Zayer, W. H., 145

Looking forward to see you on the next conference
Looking forward to see you on the next conference
Thank you
Thank you

ECCCM 2011 Full Papers Conference Proceeding
Copyright © University of Technology - Control and Systems
Engineering Department, 2011